Properties of the Higgs boson in the 4 leptons final state with the ATLAS experiment at the LHC : mass, limit on the high mass contribution and on the Higgs width

Alessandro Calandri

UNIVERSITÉ PARIS SUD

Comprendre le monde, construire l'avenir®

Université Paris-Sud

École Doctorale: Particules, Noyaux et Cosmos (ED 517)
Laboratoire CEA-Saclay - IRFU-SPP

Discipline: Physique

Thèse de doctorat

Soutenue le 29/6/2015 par

Alessandro Calandri

Propriétés du Boson de Higgs se désintégrant en 4 leptons au LHC dans l'expérience ATLAS: masse, limite sur la contribution à haute masse et sur la largeur

Directeur de thèse : Bruno Mansoulié

Composition du jury :

Bruno Mansoulié	CEA-Saclay
Achille Stocchi	LAL-Orsay
Chiara Mariotti	INFN Torino
Yves Sirois	Ecole Polytechnique
Anne-Isabelle Etienvre	CEA-Saclay
Christos Anastopoulos	University of Sheffield
Frank Martin Krauss	University of Durham

Contents

Introduction

The Large Hadron Collider (LHC) and its experiments installed at the CERN laboratory in Geneva (Switzerland) were built to unravel the missing pieces associated to the comprehension of the theory of fundamental interactions.
One of the main objectives of the LHC collider is to probe the experimental consistency of the Standard Model (SM). An essential aspect is the understanding of the electroweak symmetry breaking mechanism that is exploited in the Standard Model by adding a scalar boson, whose associated particle is the Higgs field. This particle, whose mass cannot be predicted by the theory, had never been observed in past experiments until July 4th, 2012 when the ATLAS and CMS collaborations announced its discovery at around $m_H \sim 125$ GeV.
Among the Higgs decay channels, the one characterised by lepton final state (electrons and muons) is extremely relevant despite its low branching ratio, thanks to the reduced background rate and the excellent mass resolution due to a clean decay state with energetic and isolated leptons. An additional advantage is that the decay products are fully reconstructed.
The general context of this thesis is therefore the measurement of the Higgs boson properties, its mass and width as well as the contribution of this resonance in the high mass region. The analysed data was collected in proton-proton collisions at a center-of-mass energy $\sqrt{s}$=7 TeV and $\sqrt{s}$=8 TeV recorded with the ATLAS detector comprising a total integrated luminosity of approximately 4.6 fb^{-1} and 20.5 fb^{-1} respectively.

In Chapter 1, the Standard Model framework is quickly summarised, with particular focus to the $H \to ZZ \to 4$l decay channel. The signal and background features of this channel will be presented as well as the various aspects of the Monte Carlo simulations, such as the generators employed and the theoretical uncertainties affecting each specific calculation. As for Chapter 2 and Chapter 3, the main characteristics of the LHC and the ATLAS detector are presented in addition to a detailed dissertation on the reconstruction and identification of the physics objects used in the analysis, i.e. electrons, muons, jets, neutrinos.
In order to achieve a good mass measurement, an accurate calibration of the energy related to the final state particles plays a major role in the game. This task represents my technical work accomplished for the ATLAS authorship during the first year of my doctoral programme within the ATLAS EGamma Calibration Working Group. Chapter 4 will detail the implemented procedure to extract the electron calibrated energy starting from the raw cluster inputs. Especially Section 4.5 will illustrate the energy-momentum combination algorithm on electrons I studied to improve the electron energy resolution. This method has been conceived as the last step of the standard electron calibration chain; it has been exploited in the $H \to ZZ \to 4$l analysis and culminated to the documentation for the final Run 1 legacy paper.

Chapter 5 is devoted to documenting the analysis to extract the Higgs mass in the $H \to ZZ \to 4$l decay channel. The primary step is the description of the kinematic selection, the reducible, and the dominant irreducible ZZ background with particular emphasis on the beneficial effects stemming

from the new electron calibration. Conclusively, the results of the event selection in light of the expected and observed yields are scrutinised and the Higgs Boson mass is calculated.

Chapter 6 will examine the study developed in the $H \to ZZ \to$ 4l high-mass region (m_{4l} >220 GeV) to extract indirect limits on the Higgs boson width through the determination of the off-shell signal strength. This study includes the $H \to ZZ \to$ 4l, $H \to ZZ \to 2l2\nu$ and the H$\to WW \to l\nu\nu$ final states, yet the description will be limited to my personal contribution to the final picture in the $H \to ZZ \to$ 4l channel. In this regard, a brief study on prospects in the high-luminosity LHC scenario (HL-LHC) is reported in Chapter 7.

Chapter 1

The Standard Model and the Higgs Mechanism

Contents

1.1 The Standard model

The Standard Model is the gauge theory that describes the strong and electroweak interactions. Elaborated and proposed in the sixties, it has obtained various experimental confirmations and it is currently the model employed to describe the high energy physics even though it does not explain satisfactorily a certain number of cosmological aspects, mostly associated with the existence of Dark Matter and Dark Energy. The inclusion of the Higgs boson in the theoretical framework of

Family	Symbol	Name	Electric charge	Mass
1^{st}	e	electron	-e	511 keV
	ν_e	neutrino e	0	< 1.5 eV
	u	up quark	$2/3e$	2.5 MeV
	d	down quark	$-1/3e$	5 MeV
2^{nd}	μ	muon	-e	105.7 MeV
	ν_μ	neutrino μ	0	$<$1.5 eV
	c	charm quark	$2/3e$	1.3 GeV
	s	strange quark	$-1/3e$	95 MeV
3^{rd}	τ	tau lepton	-e	1.8 GeV
	ν_τ	neutrino τ	0	$<$1.5 eV
	t	top quark	$2/3e$	173 GeV
	b	bottom quark	$-1/3e$	4.1 GeV

Table 1.1: Names, symbols associated, electric charges and masses for the three families of particles of the matter fields in the Standard Model framework.

the Standard Model allows to describe the spontaneous symmetry breaking mechanism thanks to which the observed particles acquire their mass.
In this first Chapter, the main features of the theoretical apparatus will be exposed, starting from the quantum electrodynamics up to the electroweak unification all the way through the illustration of the Higgs mechanism (Sections 1.1.1 and 1.2). Secondly, Section 1.6 will give an overview of the main production and decay mechanisms of the Higgs boson at the LHC. Finally, Section 1.5 will be devoted to the analysis of the theoretical limits on the Higgs boson mass as well as the direct and indirect searches carried out at LEP, TeVatron and LHC.

1.1.1 General features of the model

The need for a theory that comprises the principles of Special Relativity and the Quantum Mechanics has led to the introduction of the so-termed quantum field theory, where the parameters of interest are fields, linear operators in the Hilbert space of the states (the scalar field, ϕ, the gauge, vectorial field, A^μ, the fermionic, Dirac field ψ and so forth) with precise transformation rules. Under certain conditions, the fields can be written as quantised plane-waves through the linear combination of creation and annihilation operators [1], [2].
The Standard Model distinguishes the fermionic fields (half-integer spin) and the bosonic (integer spin) fields, mediators of the interactions. The fields of matter are divided into two distinct families, quarks and leptons, both with spin $\frac{1}{2}$. These fields are organised in three internal generations composed by a couple of quarks and leptons whose quantum numbers are well defined. As for the matter fields, Table 1.1 illustrates the names of the particles, as well as the symbols associated to these name, the electric charge and their masses.

The quarks and leptons corresponding to the first, second and third families are coupled in a doublet of isotopic spin. As exposed in Table 1.1, the first element of the doublet has charge $\frac{Q}{e} = +\frac{2}{3}$, while the second element has charge $\frac{Q}{e} = -\frac{1}{3}$. As for the leptons, the first element of the

Interaction	**Gauge boson**
Electromagnetic	photon (γ)
Weak	W e Z bosons ($W^{\pm}$, Z)
Strong	8 gluons (g)
Gravitational	graviton (not observed)

Table 1.2: Fundamental interactions and mediators in the Standard Model framework.

doublet has 0 charge and the second one (electron, muon, τ) has $\frac{Q}{e} = -1$.
The gauge fields, on the contrary, are subdivided into four classes, corresponding to the four fundamental interactions and each field has its gauge boson, mediator of that specific interaction, strong, electromagnetic, weak and gravitational. The gravitational interaction is not included in the Standard Model but on the scales of particle physics it is completely negligible, hence it will not be taken into account in this Chapter. The fundamental interactions in the Standard Model framework as well as the mediators are detailed in Table 1.2. The complete unification of the four forces is still an open issue in the world of physics.

The dynamics of the quantised fields is described through the lagrangian density, $\mathcal{L}(q, \dot{q})$, that is a local function of the fields and their spatial and temporal derivatives. The equation of the motion can be then derived using the principle of Least Action:

$$\frac{d}{dt}\frac{\partial \mathcal{L}}{\partial \dot{q}} - \frac{\partial \mathcal{L}}{\partial q} = 0. \tag{1.1}$$

The gauge symmetry group the Standard Model lagrangian is built upon is:

$$SU(3)_C \otimes SU(2)_L \otimes U(1)_Y \tag{1.2}$$

- $SU(3)_C$ represents the non-abelian group of the strong interactions among quarks, mediated by an octet of massless particles, the gluons, that carries the charge of the interaction, the *colour* (red, green and blue). Quantum Chromodynamics (QCD) comprises the explanation of these interactions and will be illustrated in Section 1.1.3.

- $SU(2)_L \otimes U(1)_Y$ represents the minimal symmetry group for the electromagnetic and weak interactions between quarks and leptons and it is described by the unification theory of Weinberg-Salam. Three massive bosons ($W^{\pm}$ and Z) and one massless boson, the photon (γ), are the mediators of this interaction. The quantum electrodynamics will be the main topic of Section 1.1.2, whereas an overview of the electroweak unification will be given in Section 1.2.

1.1.2 Quantum Electrodynamics (QED)

The first field theory that has been developed is the Quantum Electrodynamics (QED), formulated to explain the electromagnetic interactions of sub-atomic particles. QED is an abelian gauge [3] theory that describes a fermion field Ψ and its electromagnetic field. The fermionic contribution of the QED lagrangian can be written as follows:

$$\mathcal{L} = i\bar{\Psi}\gamma_\mu \partial^\mu \Psi - m\bar{\Psi}\Psi \tag{1.3}$$

where $\bar{\Psi} = \Psi^\dagger \gamma^0$ and γ_μ are the Dirac matrices whose anticommutator is equal to $2g^{\mu\nu}$, being $g^{\mu\nu}$ the metric tensor, m is the mass of the fermionic particle and Ψ its Dirac field. The lagrangian (1.3) is required to satisfy the local gauge invariance principle, i.e. its invariance under local gauge transformations. The equation (1.3) is not locally gauge invariant; in order to restore the gauge invariance, a covariant derivative, D_μ, replacing the global partial derivative ∂_μ, needs to be introduced in the lagrangian. Its definition is the following:

$$D_\mu = \partial_\mu - ieA_\mu \tag{1.4}$$

where e is identified as the elementary charge and A_μ is a new field, the gauge field. This stems from the fact that the covariant derivative in equation (1.4) transforms under local U(1) symmetries in the following way:

$$D_\mu \Psi \rightarrow e^{i\alpha(x)} D_\mu \Psi. \tag{1.5}$$

By working out this new definition, we are able to write down the QED lagrangian in a different manner:

$$\mathcal{L}_{QED} = \left[i\bar{\Psi}\gamma_\mu \partial^\mu \Psi - m\bar{\Psi}\Psi \right] + e\bar{\Psi}\gamma_\mu A^\mu \Psi. \tag{1.6}$$

The equation (1.6) presents three terms: the first contribution is the fermionic lagrangian of the Dirac field Ψ, the second one is the mass term of the fermionic lagrangian (the constant m is multiplied to the quadratic terms in the field Ψ) and the third term, $e\bar{\Psi}\gamma_\mu A^\mu \Psi$, describes the interaction of the gauge field A^μ with the electromagnetic current J_μ. Adding up the fermionic term brought by the Dirac field Ψ in equation (1.3) and the bosonic contribution, originated by the gauge field A_μ, we reach the full expression of the QED lagrangian:

$$\mathcal{L} = -\frac{1}{4} F_{\mu\nu} F^{\mu\nu} + \bar{\Psi}(i\gamma_\mu D^\mu - m)\Psi. \tag{1.7}$$

In conclusion, a vector field A_μ has been introduced in the usual fermionic lagrangian (1.3) in order to restore the local gauge invariance under the abelian group U(1). This contribution denotes the photon field. Moreover, this field must be described by a massless particle to keep the gauge invariance of the lagrangian. Its lagrangian (Maxwell's lagrangian) is:

$$\mathcal{L}_{Maxwell} = -\frac{1}{4} F_{\mu\nu} F^{\mu\nu} + e\bar{\Psi}\gamma_\mu A^\mu \Psi. \tag{1.8}$$

One important characteristic of the QED is that the coupling constant associated to it, α_{EM}, is very small ($\alpha_{EM} \sim \frac{1}{137}$); hence, the quantum electrodynamics can be developed through perturbative calculations.

1.1.3 Quantum Chromodynamics (QCD)

Quantum chromodynamics explains how the strong interactions work through the $SU(3)_C$ group. This theory describes the interactions and the behaviour of quarks (present in three colours, blue, green and red) as well as the force carriers, namely the gluons.

Gell-Mann [4] and Zweig proposed the quark-model in 1964 as a classification scheme for hadrons that postulates the existence of three fundamental particles (the quarks u, d and s), bonded in a triplet of flavour, degenerate in mass, constituting the hadrons. According to the number of quarks and their antiparticles, antiquarks, the hadrons can be divided in two categories and their pictorial representation can be exploited in the hypercharge-isospin plane:

- the mesons are formed by a $q\bar{q}$ couple and their multiplets can be written as $3 \otimes \bar{3} = 1 \oplus 8$ (one octet, plus one singlet). They have integer spin and baryonic number $B=0$.

- the baryons are constituted by three quarks and they are organised as $3\otimes3\otimes3=1\oplus8\oplus8\oplus10$ (one decuplet, plus two representations of octets and one singlet). They have half-integer spin and baryonic number $B=+1$.

The discovery of the resonance Δ^{++}, formed by three quarks u, created a problem in the current scheme (Pauli's exclusion principle) and was the first hint of something beyond the rudimental quark model proposed by Gell-Mann. The solution proposed by Han and Nambu was the introduction of a new quantum number, colour, produced by a gauge symmetry, $SU(3)_C$.

The minimal number of colours was set to $N_c = 3$ by various experiments. One first check was shown by the calculation of the ratio $\mathcal{R}$ of the cross sections of the following processes in a e^+e^- accelerator:

- $e^+e^- \to \mu^+\mu^-$;
- $e^+e^- \to q\bar{q}$.

that exhibit a clear evidence of the presence of the colour. Another strong hypothesis of the theory is that only particles that are colour singlet can be experimentally observed.

The β function of the QCD theory, dealing with the evolution of the coupling constant α_S with the probing energy, unlike the QED case (Section 1.1.2), diminishes as the probing energy increases. An important consequence is that in the low energy range quarks are confined inside the hadron, QCD is non-perturbative and is therefore impossible to compute the internal interactions of a neutron, a proton or a pion with perturbative techniques [5].

As for the QED case (Section 1.1.2), the introduction of the quarks in the lagrangian goes in parallel with the bosons associated to the strong interactions. They are 8 massless spin 1, gauge bosons, the gluons. The direct test of the existence of gluons has been carried out at PETRA (DESY) in 1979 where events with three jets, $e^+e^- \to q\bar{q}g$, one of which comes from a gluon radiation from a quark were observed [6]; other experimental evidences followed.

In analogy with Section 1.1.2, quantum chromodynamics is extracted from local gauge invariant transformations under the quark colour field group SU(3). The free lagrangian density [5] for a fermionic field, q gets the form of:

$$\mathcal{L} = \sum_j \bar{q}_j \left(i\gamma^\mu \partial_\mu - m_j\right) q_j \tag{1.9}$$

where the sum is extended for $j = 1, ..., 6$, the colour triplet corresponding to the six quark flavours and $q_j = (q_r, q_b, q_g)_j$ is the quark triplet whose indices refer to the colour charge of the strong interactions. As for the previous Section, the lagrangian above must be invariant for SU(3) gauge transformations. The procedure explained in Section 1.1.2 holds: we need to restore SU(3) local gauge invariance and the lagrangian (1.9) does not exhibit it. Hence, eight gauge fields G^a_μ are included in the lagrangian computation transforming as:

$$G^a_\mu \to G^a_\mu - \frac{1}{g}\partial_\mu \alpha^a - f_{abc}\alpha^b G^c_\mu. \tag{1.10}$$

The resultant lagrangian is:

$$\mathcal{L} = \bar{q}\left(i\gamma_\mu \partial^\mu\right) q - g\left(\bar{q}\gamma_\mu T^a q\right) G^\mu_a. \tag{1.11}$$

The partial derivative can be replaced by the covariant derivative in such a way that the newly-produced lagrangian is now locally invariant under the gauge group SU(3). Including the kinematic terms for each G_a^μ gauge field, the final form of the gauge invariant QCD lagrangian is:

$$\mathcal{L}_{QCD} = -\frac{1}{4} G^a_{\mu\nu} G^{\mu\nu}_a + \bar{q}\,(i\gamma_\mu D^\mu - m)\,q \tag{1.12}$$

where $G_a^{\mu\nu}$ is the gluon field tensor and is defined as follows:

$$G^{\mu\nu}_a = \partial^\mu G^\nu_a - \partial^\nu G^\mu_a - g f^{abc} G^\mu_b G^\nu_c. \tag{1.13}$$

Equation (1.13) displays the non-abelian structure of the QCD in the third term where, unlike the abelian QED case, the gluon-gluon self-interaction terms ($G^\mu_b G^\nu_c$) are visible leading to vertices with three or four gluons.

In the QCD framework, perturbation theory [5] is a method to improve the accuracy of theoretical cross-section predictions. Processes can be computed at leading-order (LO) if no radiative corrections are added to the initial or final states but only the $|\mathcal{M}|^2$ matrix element computation is present. Next-to-leading-order (NLO) diagrams arise if real emissions (extra partons) or virtual corrections are included, each of them carrying a proportionality to α_S. The same applies to NNLO corrections and so forth. In the case that the perturbative series do not converge because of the presence of large logarithms coming from the phase-space integration of soft ($E_g \to 0$) and collinear ($\theta_{qg} \to 0$) gluon singularities, the so-called logarithmic resummation technique is employed. This technique involves a definition of another convergent function in which the individual terms of the original functions are rescaled and summed to the fixed order contribution to restore the convergence. The first term of the series represents the leading-log (LL) contribution, the second one the next-to-leading-log (NLL) and so on.

1.2 The electroweak interactions

The nuclear β decay is one of the many facets of weak interaction. The basic reactions involving weak interactions in nuclei may be characterised by the decay of a neutron:

$$n \to p\, e\, \bar{\nu}$$

In the forties, the studies on the β radioactivity led by Fermi [7] were the first attempt to draw a comprehensive picture of these interactions. These phenomena are described by a four-fermion coupling, whose intensity is proportional to the Fermi constant, $G_F \sim 10^{-5}$ GeV^{-2} in such a way that the lagrangian of the interaction is written:

$$\mathcal{L}_F = \frac{G_F}{\sqrt{2}} \left[\bar{p}\gamma_\mu(1+\alpha\gamma_5)n\right] \left[\bar{e}\gamma_\mu(1-\gamma_5)\nu\right] \tag{1.14}$$

where p, n, e, ν are the fermionic fields of the proton, neutron, electron and neutrino respectively. The discovery of the parity violation in the framework of the weak interactions by Wu [8] as well as the measurement of the neutrino helicity by Goldhaber, Grodzsins and Sunyar [9] improved the general knowledge of the theory.

It was later observed that under precise working hypothesis and generalisations the electromagnetic and the weak theories can be unified in a common structure (electroweak unification). The theory of the electroweak unification, postulated by Glashow, Weinberg and Salam, is based on

the concept of gauge symmetry under the local symmetry group $SU(2)_L \otimes U(1)_Y$. As illustrated in Section 1.1.1, the matter fields are identified with three chiral fermionic fields, for quarks and leptons, so that the two components of different chirality ψ_L and ψ_R of the wave function ψ, can be written as follows:

$$\psi_L = \frac{1}{2}(1 - \gamma_5)\psi; \tag{1.15}$$

$$\psi_R = \frac{1}{2}(1 + \gamma_5)\psi; \tag{1.16}$$

being γ_5 a matrix belonging to the Dirac formalism.

The left-handed (L) fermions are represented by a weak isospin doublet: $I^2{=}\frac{1}{2}$; $I_3 = \pm\frac{1}{2}$:

$$\psi_L = \begin{pmatrix} \nu_L \\ e_L \end{pmatrix} \tag{1.17}$$

while the right-handed (R) fermions are represented by a weak isospin singlet $I_3 = 0$. The right component of the fermions is not in a doublet structure:

$$\nu_R, \;\; e_R. \tag{1.18}$$

The lagrangian of the doublet (Dirac lagrangian) of the electronic doublet in terms of the right and left-handed fields is:[1]

$$\mathcal{L} = \bar{\psi}_L \imath \partial\!\!\!/ \psi_L + \bar{e}_R \imath \partial\!\!\!/ e_R + \bar{\nu}_R \imath \partial\!\!\!/ \nu_R \tag{1.19}$$

where the left-handed fields have been included in the isospin doublet ψ_L and the right-handed contributions are isospin singlets. Equation (1.19) exhibits an asymmetry in the treatment of the left and right components of the fields. The transformations below leaves the left component of the lagrangian invariant (1.19):

$$\psi_L^{'} = e^{\imath\beta\frac{\tau_i}{2}}\psi_L. \tag{1.20}$$

where the τ_i are the three Pauli matrices, generators of the SU(2) group (Section 1.1.2) and β a numerical constant. As a consequence, $\mathcal{L}$ is proved to be invariant under local $SU(2)_L$ transformation acting only on the left contribution. The application of the Noether theorem implies that the conserved currents (weak isospin currents), associated to the $SU(2)_L$ transformations of the lagrangian, should be expressed as follows:

$$\mathcal{J}_\mu = \bar{\psi}_L \gamma_\mu \frac{\tau_i}{2} \psi_L. \tag{1.21}$$

From this formulation, the weak isospin is extracted from the temporal component of the quadrivector:

$$I_3 = \int d^3x \, \mathcal{J}^0. \tag{1.22}$$

The electromagnetic current is:

$$\mathcal{J}^\mu_{\mathrm{em}} = -\mathrm{e}\bar{e}\gamma^\mu e \tag{1.23}$$

where e is the electron charge, e is the fermionic Dirac field of the electron and by explicitly expressing Q as the integral of the temporal component of the electromagnetic current, we are able to introduce a new quantity, the weak hypercharge:

$$\mathcal{Y} = 2(Q - I_3) \tag{1.24}$$

[1] $\partial\!\!\!/ = \partial_\mu \gamma^\mu$.

defined in such a way that it is related to the invariance of the lagrangian (1.19) under $U(1)_Y$ transformations, namely phase transformations. The generator of the $U(1)_Y$ group is the parameter α:

$$\psi^{'} = e^{\imath\alpha}\psi. \tag{1.25}$$

Not only is the left component of the lagrangian (1.19) invariant under this gauge transformation but also the right contribution even if it carries the singlet-based structure.
Wrapping up, the general scheme achieved is sketched out below:

- invariance of the lagrangian under $SU(2)_L$, explicitly defined by the transformations (1.20) $\Longrightarrow$Weak isospin $\mathcal{I}$ conservation;
- invariance of the lagrangian under $U(1)_Y$, whose transformations are displayed in equation (1.25) $\Longrightarrow$Weak hypercharge $\mathcal{Y}$ conservation.

In conclusion, the minimal symmetry group of the electroweak interaction is $SU(2)_L \otimes U(1)_Y$.

1.2.1 The Glashow theory

The theory proposed by Glashow [3] is the first attempt towards a unification of the electromagnetic and weak interactions. Defining the following gauge fields of the electroweak sector:

- B_μ - the gauge field that corresponds to the generator of the $U(1)_Y$ group;
- the triplet W^i_μ fields, where $i = 1, 2, 3$, associated to the three generators of the $SU(2)_L$ group.

In analogy with the formulation illustrated in Sections 1.1.2 and 1.1.3, the lagrangian of the gauge fields is:

$$\mathcal{L} = -\frac{1}{4}W^i_{\mu\nu}W^{\mu\nu\,i} - \frac{1}{4}B_{\mu\nu}B^{\mu\nu}. \tag{1.26}$$

As it is now, the theory would allow massless Goldstone-like bosons (Section 1.3.1). In order to remove them, Glashow [10] proposed to add a mass term, $\mathcal{L}_m$, to the above-defined lagrangian (1.26):

$$\mathcal{L}_m = \frac{1}{2}[M^2 W^i_{\mu\nu}W^{\mu\nu}_i + M_0^2 B_{\mu\nu}B^{\mu\nu} + 2M_{03}^2 W^3_\mu B^\mu] \tag{1.27}$$

The resultant gauge invariance of the total lagrangian ($\mathcal{L}_{tot} = \mathcal{L} + \mathcal{L}_m$) is spoilt as the mass term breaks explicitly the symmetry. Let us analyse the mass spectrum of the theory produced by the insertion of the mass term on the basis (W^3,B), that is the one of the neutral fields of the gauge boson Z and the γ.

$$\mathcal{M} = \begin{pmatrix} M^2 & M_{03}^2 \\ M_{03}^2 & M_0^2 \end{pmatrix} \tag{1.28}$$

This matrix must possess a null eigenvalue, correspondent to the photon mass and the other non-zero eigenvalue refers to the mass of the Z boson. By imposing the condition $\det(\mathcal{M}) = 0$, the following equation is obtained:

$$M_{03}^2 = M^2 M_0^2. \tag{1.29}$$

By including the physical fields A^μ (electromagnetic field) and Z^μ (Z boson field) as a linear combination of W^3 and B through a rotation, the following relations are proposed:

$$Z^\mu = \cos\theta_W W_3^\mu - \sin\theta_W B^\mu; \tag{1.30}$$

$$A^{\mu} = \sin\theta_W W_3^{\mu} + \cos\theta_W B^{\mu}; \tag{1.31}$$

where θ_W is the Weinberg angle that guarantees the mixing between the physical fields, A^{μ}, Z^{μ}, and the gauge field W_3^{μ} and B^{μ} with which we have started the calculation.

The mutual equations that govern the masses of the bosons and the coupling constants are:

$$M_W = M_Z \cos\theta_W; \tag{1.32}$$

$$\tan\theta_W = \frac{g'}{g} \tag{1.33}$$

meaning that the electromagnetic field A^{μ} couples to the electron through the electromagnetic current, with $g\sin\theta_W = g'\cos\theta_W = e$.

1.3 The Higgs Mechanism

1.3.1 The Goldstone model

The approach introduced by Glashow described in Section 1.2.1 did not satisfactorily treat the massless Goldstone bosons: his mass term added in the lagrangian (1.27) breaks explicitly the gauge symmetry. Let us now consider the lagrangian [3] of a complex scalar field, ϕ, being μ^2 the mass coefficient that multiplies the quadratic terms of the fields and a quartic self-interaction term, with a positive coefficient λ:

$$\mathcal{L} = \partial_{\mu}\phi\partial^{\mu}\phi^{\dagger} - \mu^2\phi\phi^{\dagger} - \lambda(\phi\phi^{\dagger})^2. \tag{1.34}$$

This lagrangian exhibits an invariance under global phase transformations:

$$\phi(x) \to \phi^{'}(x) = e^{\imath\alpha}\phi(x); \tag{1.35}$$

$$(\phi^{\dagger})(x) \to (\phi^{\dagger})^{'}(x) = e^{-\imath\alpha}\phi^{\dagger}(x). \tag{1.36}$$

where α is an arbitrary phase term that does not depend on the phase-space where the field is embedded. The theory can be farther developed by introducing two real scalar fields, $\phi_{1,2}$ where the following relation holds:

$$\phi^{(\dagger)} = \frac{\phi_1 \pm \imath\phi_2}{\sqrt{2}} \tag{1.37}$$

and ϕ, $\phi^{\dagger}$ are the complex scalar fields. The lagrangian (1.34) becomes:

$$\mathcal{L} = \frac{1}{2}(\partial_{\mu}\phi_1\partial^{\mu}\phi_1 + \partial_{\mu}\phi_2\partial^{\mu}\phi_2) - V \tag{1.38}$$

and the potential term is:

$$V = \frac{\mu^2}{2}(\phi_1^2 + \phi_2^2) + \frac{\lambda}{4}(\phi_1^2 + \phi_2^2)^2. \tag{1.39}$$

The functional form of the potential V depends on the mass term μ^2; two possible theories can arise depending on the sign of μ^2, being $\delta(\phi_{1,2})$ the complex plane of the scalar fields ϕ_1 and ϕ_2.

- $\mu^2 > 0$. The potential is a concave function of the fields ϕ_1 and ϕ_2, with an absolute minimum in the origin of the axis, i.e. $\phi_1 = \phi_2 = 0$. The state of minimal energy of the field is unique as well as the vacuum expectation value of the field ϕ. The symmetry is therefore exact:

$$< 0|\phi(0)|0 >= 0. \tag{1.40}$$

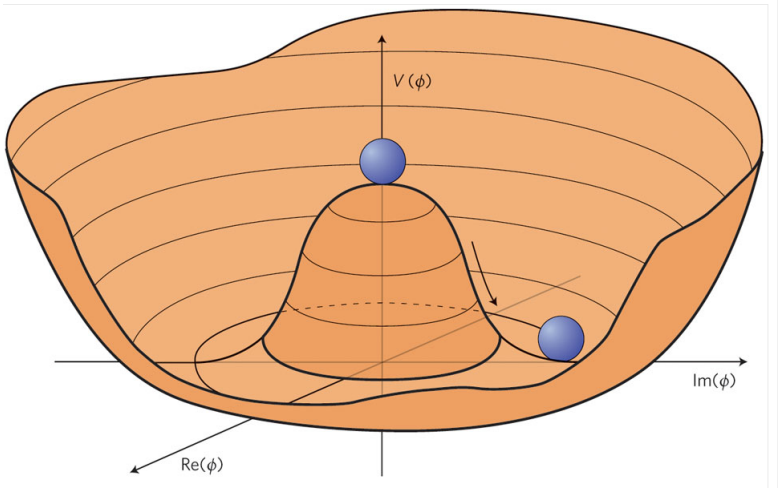

Figure 1.1: Functional form of the potential V as defined in equation (1.39) as a function of the real fields ϕ_1 e ϕ_2 when $\mu^2 < 0$.

- $\mu^2 < 0$: The functional form of the potential V is shown in Figure 1.1. It is clear that the configuration ϕ=0 is still a solution of the equation, but it is not the configuration that minimises the potential. On the contrary, ϕ=0 represents a local maximum of the potential, whereas the local minimum corresponds to the circumference centred in the origin.

In order to solve the degeneracy of the circumference of the minima and choose a unique state, a small, complex *driving* term, ϵ, can be introduced in the lagrangian:

$$\mathcal{L}^{'} = \epsilon^{*}\phi + \epsilon\phi^{\dagger} \tag{1.41}$$

The minimum of the energy is extracted by computing the first derivatives of the potential in the fields ϕ and $\phi^{\dagger}$:

$$\phi[\mu^2 + 2\lambda(\phi\phi^{\dagger})] = \epsilon. \tag{1.42}$$

The equation has two solutions: the former coincides with the origin of the axis (local maximum) and the latter is the one that cancels the term within parenthesis, corresponding to the minima of the circumference. Consequently, the above-defined driving term enables the quantum system to have one minimum only on the circumference shown in Figure 1.1. Noting η as the non-zero vacuum expectation value (VEV), the following equation:

$$< 0|\phi(0)|0 >= \eta \neq 0 \tag{1.43}$$

displays that the configuration of minimal energy is no longer symmetric and the symmetry of the system is *spontaneously* broken in the fundamental state.

The fluctuations of the minima when $\mu^2 < 0$

Let us investigate the fluctuations of the field around the fundamental state. They are described by quantum oscillations of the scalar field ϕ around its expectation value in the vacuum:

$$\phi(x) = \eta + \frac{\sigma_1(x) + \imath\sigma_2(x)}{\sqrt{2}} \tag{1.44}$$

where the second term, including a real and an imaginary part, represents the fluctuation around the VEV. Replacing (1.44) into (1.38), and developing the equation in powers of σ, we find the following identities:

$$M_{11}^2 = 4\lambda\eta^2; \tag{1.45}$$

$$M_{12}^2 = M_{21}^2 = 0; \tag{1.46}$$

$$M_{22}^2 = 0. \tag{1.47}$$

that coincide with the matrix that defines the mass spectrum of the theory. It is noticeable that the mass spectrum is equal to matrix of the curvature of the potential since it is computed with the second derivatives of the potential. The two degrees of freedom associated to the complex field ϕ are now represented by two particles whose masses are $M_{11}^2 = 4\lambda\eta^2$ and M_{22}^2=0 respectively. The massless particle that is produced by the theory is known as the Goldstone boson and it is the result of the spontaneous symmetry breaking à la Goldstone.

1.3.2 The Higgs model and its coupling to the gauge fields and to the fermions

In analogy with the procedure explained in Section 1.1.2 and 1.1.3, let us replace the global phase transformation symmetries (1.35) and (1.36) with local phase transformation functions [11] [12]. Consequently, the partial derivative gets replaced by the covariant derivative and a new gauge field, A^μ, must be added to restore the local gauge invariance. The new lagrangian is:

$$\mathcal{L} = (D_\mu\phi)^\dagger(D^\mu\phi) - V(\phi,\phi^\dagger) - \frac{1}{4}F_{\mu\nu}F^{\mu\nu} \tag{1.48}$$

where the covariant derivative, D_μ, is defined as follows:

$$D_\mu = \partial_\mu - \imath e A_\mu \tag{1.49}$$

and $F_{\mu\nu}$ is the Yang-Mills tensor in analogy with the Maxwell tensor of the electromagnetic field. If we let the gauge field A^μ coincide with the electromagnetic field, e denotes a coupling constant describing the electron charge. The lagrangian $\mathcal{L}$ in (1.48) is invariant under local gauge transformations:

$$\phi(x) \to \phi^{'}(x) = e^{\imath\alpha(x)}\phi(x); \tag{1.50}$$

$$\phi^\dagger(x) \to (\phi^\dagger)^{'}(x) = e^{-\imath\alpha(x)}\phi^\dagger(x). \tag{1.51}$$

$$A^\mu \to A^\mu + \frac{1}{e}\partial^\mu\phi(x) \tag{1.52}$$

where $\alpha(x)$ is an arbitrary local phase.
As stated in Section 1.3.1, the condition $\mu^2 < 0$ leads to the spontaneous symmetry breaking of the system. Developing the equation (1.50) in this operating scheme up to the second order, we obtain:

$$\phi(x) \to \phi(x) + \imath\alpha\phi(x). \tag{1.53}$$

Replacing (1.53) in (1.44), we verify that $\sigma_{1,2}$ transform in the following way:

$$\sigma_1(x) \to \sigma_1^{'}(x) = \sigma_1(x) \tag{1.54}$$

$$\sigma_2(x) \to \sigma_2^{'}(x) = \sigma_2(x) + \sqrt{2}\eta\alpha(x). \tag{1.55}$$

$\alpha(x)$ is the term associated to the local phase of the symmetry. A specific choice of this parameter enables us to remove the field $\sigma_2^{'}$, expression of the massless particle of the Goldstone theory (1.47). Choosing the so-termed unitary gauge,

$$\alpha = \frac{-\sigma_2(x)}{\sqrt{2}\eta} \Longrightarrow \sigma_2^{'} = 0. \tag{1.56}$$

the fields are now expressed as follows:

$$\phi = \eta + \frac{\sigma}{\sqrt{2}} = \rho(x) \text{ real.} \tag{1.57}$$

By substituting the above-extracted functional form of ϕ in the lagrangian (1.48), we obtain:

$$\mathcal{L} = \frac{1}{2}\partial_\mu\sigma\partial^\mu\sigma + e^2\rho(x)^2 A_\mu A^\mu - V(\rho) - \frac{1}{4}F_{\mu\nu}F^{\mu\nu}. \tag{1.58}$$

From this equation, the quadratic terms in the fields turn out to be (lagrangian of the Higgs field):

$$\mathcal{L} = \frac{1}{2}\partial_\mu\sigma\partial^\mu\sigma - \frac{1}{2}M_H^2\sigma^2 - \frac{1}{4}F_{\mu\nu}F^{\mu\nu} + \frac{1}{2}M_A^2 A_\mu A^\mu \tag{1.59}$$

where σ is the scalar field of the Higgs boson, $M_H = 2\lambda\eta^2 = -2\mu^2$ is the mass term of the Higgs field, $M_A = 2e^2\eta^2$ is the mass contribution of the gauge field A^μ that appears in the game because of its coupling with the Higgs field.
In presence of a local gauge symmetry, the spontaneous symmetry breaking implies that the corresponding gauge field acquires a mass through the coupling with the Higgs field. The mass spectrum changes dramatically when moving from an exact symmetry to a broken one but the total number of degrees of freedom of the theory is conserved:

- **No spontaneous symmetry breaking**: two degrees of freedom associated to the spin 0 scalar fields σ_1 and σ_2, plus two degrees of freedom produced by the massless spin 1 gauge field A^μ. In total, four degrees of freedom.
- **Spontaneous symmetry breaking**: One degree of freedom coming from the scalar field of the Higgs boson (spin 0 particle), plus three degrees of freedom of the spin 1 gauge field A^μ that has now acquired mass. The total number of degrees of freedom of the theory does not change.

As for the electromagnetic field, the gauge boson, the photon, is massless because the gauge symmetry is not spontaneously broken as illustrated in Section 1.1.2.

The masses of the fermions are generated by Yukawa couplings between the fermions themselves and the Higgs boson. These Yukawa terms appear in the lagrangian in the form:

$$\mathcal{L}_{\text{Yukawa}} = -(\frac{\sigma}{\sqrt{2}})\lambda_f \bar{f} f \tag{1.60}$$

for each fermionic field f, where λ_f represents its coupling with the Higgs field.

1.4 The Weinberg-Salam theory

The development by Weinberg [13] and Salam [14] of the Standard Model is the continuation of Glashow's theory without the usage of the mass term in the lagrangian that explicitly breaks the

gauge symmetry of the theory, and introducing spontaneous symmetry breaking. Let us promote the global transformation of the fields into local ones. This derivation proceeds in analogy with what has been already shown in Sections 1.1.2 and 1.1.3 for the QED and QCD cases. In order to keep the gauge symmetry of the lagrangian, the partial derivative needs to be replaced by the covariant derivative and the weak lagrangian becomes:

$$\mathcal{L} = \bar{\psi}_L \imath \not{D} \psi_L + \bar{e}_R \imath \not{D} e_R + \bar{\nu}_R \imath \not{D} \nu_R \tag{1.61}$$

where D is the covariant derivative that is defined in the following way:

$$D^\mu = \partial^\mu + \imath g \frac{\tau_i}{2} W^\mu + \imath \frac{g'}{2} B^\mu. \tag{1.62}$$

The lagrangian (1.61) is invariant under the set of local transformations $SU(2)_L \otimes U(1)_Y$.

Let us now make use of the Higgs mechanism to generate the masses of bosons and leptons. Firstly, a scalar doublet, the Higgs doublet Φ, is introduced in the calculation. The Higgs field needs to be a doublet in order not to spoil the gauge invariance of the lagrangian (1.61) under local transformations $SU(2)_L \otimes U(1)_Y$:

$$\begin{pmatrix} \phi_a \\ \phi_b \end{pmatrix} \tag{1.63}$$

From here, we obtain the final lagrangian:

$$\mathcal{L} = \mathcal{L}_B + \mathcal{L}_F + \mathcal{L}_H \tag{1.64}$$

where $\mathcal{L}_B$ is the gauge bosons lagrangian (1.26), $\mathcal{L}_L$ is the lagrangian of the lepton contribution (1.61) and $\mathcal{L}_H$ is the lagrangian of the Higgs doublet:

$$\mathcal{L}_H = (D^\mu \Phi)^\dagger (D_\mu \Phi) - \mu^2 \phi \phi^\dagger - \lambda (\phi \phi^\dagger)^2. \tag{1.65}$$

By recalling the gauge choice (unitary gauge), specified in equation (1.56), the doublet Φ is equivalent to:

$$\begin{pmatrix} 0 \\ \eta + \frac{\sigma(x)}{\sqrt{2}} \end{pmatrix} \tag{1.66}$$

In the Higgs doublet there is only one physical field left, σ, hence one neutral, scalar particle, the Higgs boson. By replacing this term into (1.64), we obtain the mass term of the electroweak lagrangian:

$$\mathcal{L}_{ew} = \frac{g^2 \eta^2}{4} W^i_\mu W^{\mu\, i} - \frac{g g'}{4} \eta^2 W^3_\mu B^\mu - \frac{g g'}{4} \eta^2 B_\mu W^{\mu\, 3} + \frac{g'^2}{4} \eta^2 B_\mu B^\mu. \tag{1.67}$$

that is the final outcome of the electromagnetic and weak unification. Grouping the quadratical terms multiplying the fields, we are also able to examine the mass spectrum of the theory:

$$\mathcal{M} = \begin{pmatrix} g^2 & -g g' \\ -g g' & g'^2 \end{pmatrix} \tag{1.68}$$

and Glashow's final result $\frac{g'}{g} = \tan \theta_W$, exposed in Section 1.2.1 can be derived again.

1.5 The Higgs Boson in the Standard Model

The electroweak theory has been deeply verified in the last thirty years of the 20th century, proving that the Standard Model offers a valid explanation of the nature of particle interactions. The Higgs boson has represented the only missing piece for more than a decade and has been searched by experiments at LEP, TeVatron and LHC until it was discovered by both ATLAS and CMS experiments at the LHC in 2012.

1.5.1 Theoretical limits on the Higgs boson mass

The assumptions in [15] based on the current formulation of the quantum field theory place strong theoretical constraints on the possible mass range of the Higgs boson. They are listed below and analysed in this Section.

- Unitarity;
- vacuum stability and triviality.

Unitarity

The Fermi theory does not respect the unitarity limit. Indeed, in this model the cross section of the process $\nu_\mu\, e \to \nu_e\, \mu$ is proportional to $G^{-1/2}E_{CM}^2$ in the high energy range and it is divergent in s when the available energy of the centre-of-mass increases. The constraint would have been violated for $\sqrt{s}_{cut-off} = 300$ GeV and the theory would not have been unitary.

A similar issue was found in the high energy WW scattering (vector-boson scattering):

$$W^+W^- \to W^+W^- \tag{1.69}$$

where the Higgs boson can be exchanged both in the s and t channel. An upper limit for m_H is found at $m_H \sim 870$ GeV beyond which the cross section of the WW scattering process diverges and the unitarity principle would be then violated. By including higher order calculations to the tree level, the value of the limit reaches ~ 1 TeV: other mechanisms need to be introduced to prevent the vector boson scattering amplitudes from being divergent.

Vacuum stability and triviality

The coupling constants depend on the energy scale Q^2 of the process. Be v^2 the scale of the electroweak spontaneous symmetry breaking (~ 246 GeV^2) and λ the Higgs self-interaction coupling constant. Its value is dependent (running) on the energy scale of the process, $\lambda = \lambda(Q^2)$. There are essentially two different behaviours of the Q^2-dependent coupling constant:

- $Q^2 \ll v^2$. The system cannot reach the energy needed for the symmetry breaking. As a consequence, the running coupling constant λ is very small. The quartic self-interaction term in the Higgs lagrangian (1.48) disappears and the theory is trivial.
- As the value of Q^2 of the process increases, the energy of the system approaches the scale of the electroweak symmetry breaking; the coupling constant λ gets larger and larger until it diverges (Landau pole) and the theory is no longer perturbative.

However, if we include all the virtual contributions to the constant $\lambda(Q^2)$, we obtain the following relation:

$$\lambda(Q^2) = \lambda(v^2) + \frac{1}{16}[-12\frac{m_t^4}{v^4} + ...] \log \frac{Q^2}{v^2}. \tag{1.70}$$

If the tree level term $\lambda(v^2)$ is very small, then $\lambda(Q^2) < 0$ and the vacuum state is unstable. Given the Higgs mass dependency on the vacuum expectation value v, equation (1.70) implies a lower limit on m_H, being the physical non-plausibility of the vacuum instability. The combination of the stability and triviality [15] hypotheses produces an upper and lower limit on the Higgs mass that constraint an allowed range in the Λ-m_H phase-space as illustrated in Figure 1.2. As the cut-off scale Λ increases, the limits on the allowed Higgs masses get tighter , favouring a low-mass Higgs boson scenario. The plot in Figure 1.2 illustrates that as the cut-off scale Λ increases, the limits on

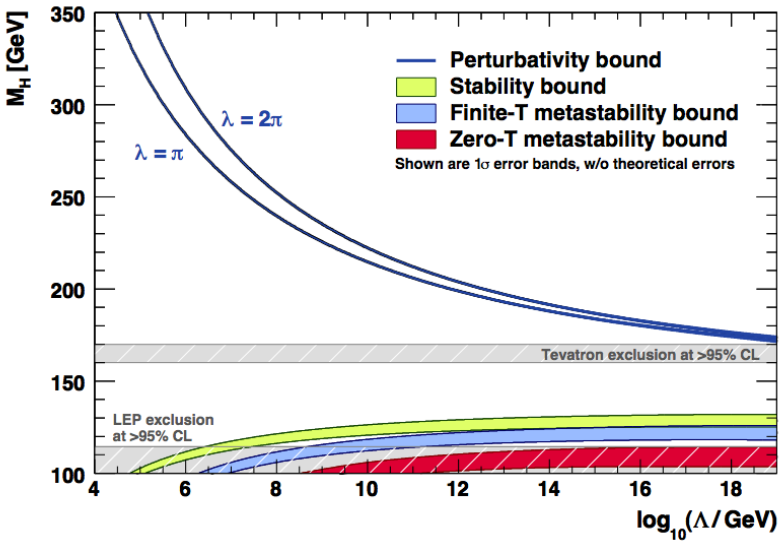

Figure 1.2: The scale Λ [16] at which the two-loop corrections to the self-coupling constant drive the quartic SM Higgs coupling to be non perturbative and the scale up to which the theory creates an instability of the electroweak vacuum (λ <0). The triviality upper bound is given for $\lambda = \pi$ (lower bold line in blue) and $\lambda = 2\pi$ (upper bound line in blue). Their difference indicates the size of the theoretical uncertainty in this bound. The absolute vacuum stability bound is displayed by the light shaded green band. The theoretical uncertainties in these bounds have been ignored in the plot. The grey hatched areas indicate the LEP and TeVatron exclusion domains.

the allowed Higgs masses get tighter, favouring a low-mass Higgs boson scenario.

1.5.2 Experimental limits on the Higgs boson mass before the discovery

Indirect searches of the Higgs boson

The Higgs boson contributes to the radiative corrections of the electroweak theory as it enters in the perturbative loops, with a correction proportional to $\ln m_H$. It is then possible to extract information on m_H from precise measurements of the other particles masses and couplings.

The precision measurements at LEP [17] and TeVatron [18] processed by LEP Electroweak Working Group with the GFitter collaboration in 2011 [19], are indicated below:

- The observables from the profile of the Z peak at LEP: the total decay width Γ_Z, the hadronic cross section at the peak, σ_{had}, the partial decay widths of the Z boson in leptons and in hadrons, the backward-forward asymmetries.
- The longitudinal polarisation asymmetries A_{LR} measured at SLC through a polarised beam.
- The W mass m_W and its total decay width Γ_W, measured at LEP and TeVatron.

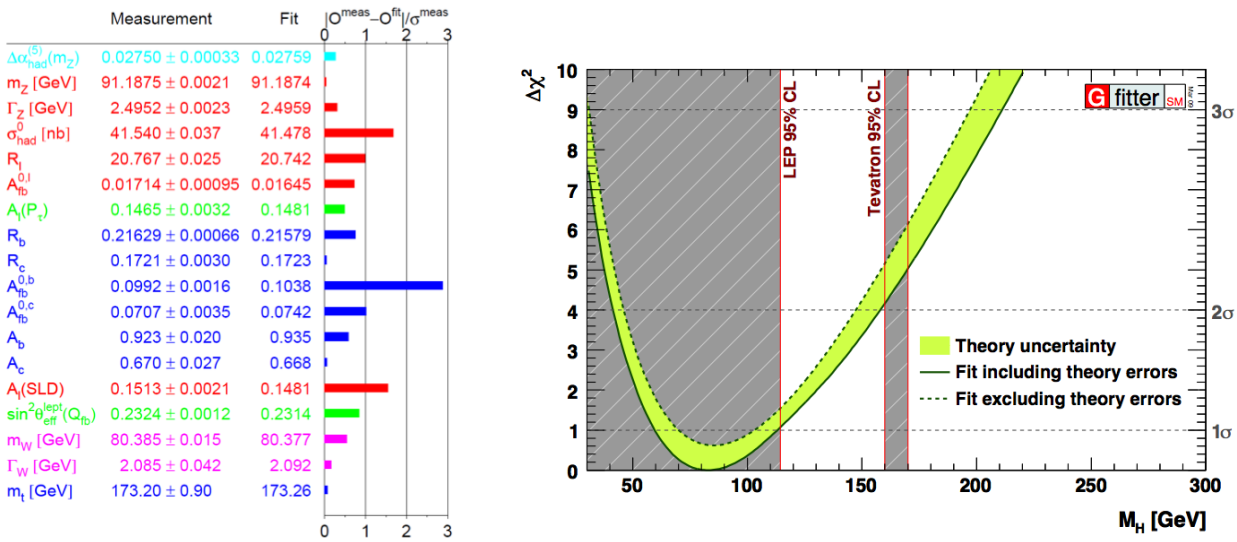

(a) **(b)**

Figure 1.3: (a) Summary of the results on the precision measurements at LEP, TeVatron and SLC. (b) $\Delta\chi^2$ fit of electroweak data as a function of m_H. The solid (dashed) line gives the results when including (ignoring) theoretical errors.

- The top quark mass measurement performed at TeVatron.
- The measurement of the strong coupling constant α_s and its running behaviour as a function of Q^2.

These measurements are summarised in Figure 1.3 (a). Figure 1.3 (b) indicates the $\Delta\chi^2$ fit for the electroweak data as a function of m_H which gives a favoured Higgs mass at $m_H = 91 \pm 30$ GeV if the results from direct searches at LEP and TeVatron are ignored.

The indirect determination mainly relies on the measurements of m_W and m_t. The Higgs mass can be therefore parametrized in the m_t, m_W phase space: Figure 1.4 shows in the m_T-m_W plane the trajectories corresponding to various Higgs masses from 114 GeV to 1000 GeV.

Direct searches of the Higgs boson

The Higgs boson has been seeked at LEP and at TeVatron as well as the LHC until its discovery by ATLAS and CMS announced in a seminar at CERN on July, 4^{th} 2012.
In 1989 the Large Electron Positron (LEP) collider became operational at CERN and the four experiments (ALEPH, L3, DELPHI and OPAL) started to collect data at $\sqrt{s}$=89-93 GeV in the first phase (LEP1) and $\sqrt{s}$=161-209 GeV in the second phase (LEP II). At LEP, the Higgs boson was expected to be produced mainly in the association with a W or Z boson.
The final state topologies the searches were concentrated on were:

- four jet final state $H \to bb$ and $Z \to q\bar{q}$;
- tau lepton production $H \to \tau\tau$ and $Z \to q\bar{q}$ or $H \to bb$ and $Z \to \tau\tau$;
- missing energy final states $H \to bb$ and $Z \to \nu\bar{\nu}$
- leptonic final states $H \to bb$ and $Z \to e^+e^-$ or $Z \to \mu^+\mu^-$.

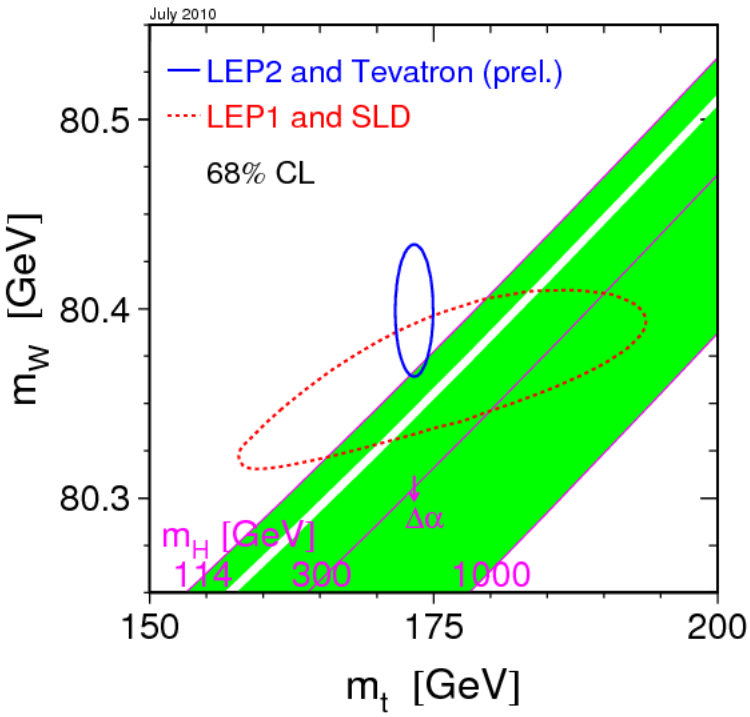

Figure 1.4: Compatibility among the W and the top mass measurements with the possible mass of the Higgs boson. The W and t masses extracted at LEP2 and TeVatron are comprised into a 68% confidence level contour.

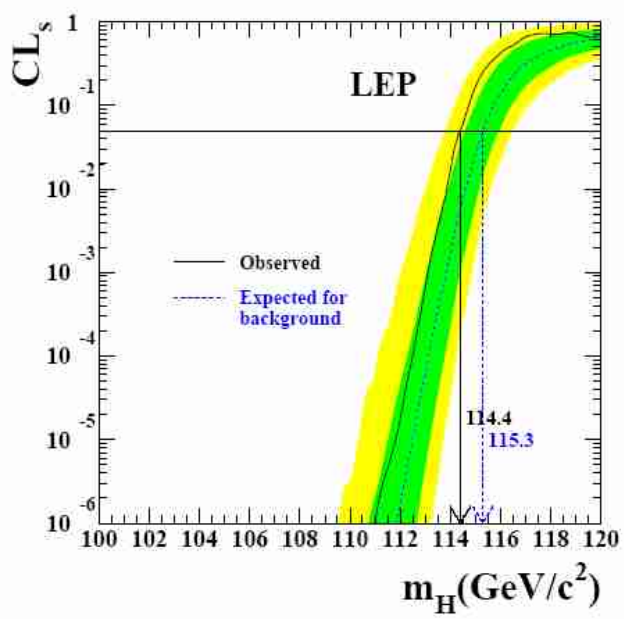

Figure 1.5: Exclusion limits produced by the combination of the results from the four experiments (ALEPH, OPAL, L3 and DELPHI) at the LEP. The dashed line indicates the median background expectation whilst the solid line represents the observation on data and the coloured bands correspond to the 68% (1 standard deviation) and 95% (2 standard deviations) probability contours.

The combination of the various searches performed at LEP are shown in Figure 1.5 where a 95 % Confidence Level lower limit at 114.4 GeV is extracted. In the exclusion plot, the dashed line indicates the median background expectation whilst the solid line represents the observation on data and the coloured bands correspond to the 68% (1 standard deviation) and 95% (2 standard deviations) probability contours.

The TeVatron experiments at Fermilab, CDF and D0, started the data taking in 1985 until 2011. The TeVatron was a $p\bar{p}$ collider operating at $\sqrt{s}$=1.96 TeV. The Higgs searches were conducted in the following decay channels:

- jet-related final states $H \to b\bar{b}$;
- bosonic final states, $H \to WW \to l\nu l\nu$ or $H \to ZZ \to$4l.

As for LHC, the discovery of a new resonance compatible with the long-sought Higgs boson of the Standard Model at $m_H \sim$125 GeV by both ATLAS and CMS was finally accomplished in July 2012. Further detailed studies on this particle and its kinematic properties were carried out all through 2012, 2013 and 2014. The final results for what concerns the ATLAS experiment in the so-called Run 1 period ($\sqrt{s}$=7 TeV and $\sqrt{s}$=8 TeV) are now published.

The measurement of the Higgs boson mass comprises the $H \to ZZ \to$ 4l and $H \to \gamma\gamma$ channels with the available integrated luminosity of $\sim$ 25fb^{-1} recorded in 2010, 2011 and 2012. The measured value of the mass is m_H=125.36 $\pm$ 0.37 (stat) $\pm$ 0.18 (syst) GeV [20]. Chapter 5 will illustrate the analyses that have been employed to derive the Higgs mass in the H→ZZ→4l channel and Chapter 6 will present the measurement of the same channel for an off-shell Higgs which can be used to constrain the width under some hypotheses.

1.6 The Higgs boson phenomenology at the LHC

1.6.1 Parton density functions at the LHC

A proton is not an elementary particle but it consists of three valence quarks (two up-quarks and one down-quark), sea quarks and gluons. The pp collisions can be therefore described by the mutual interactions between valence, sea quarks and gluons. Depending on the factorisation scale, μ_F, of the process, that corresponds to the resolution with which the hadron is being probed, the scattering between hadrons is written as the sum of hard processes, with high momentum transfer Q^2, computed in perturbative QCD, and soft interactions, domain of the non-perturbative QCD, characterised by low Q^2.

Let p be the modulus of the momentum of each proton, each constituent carries a fraction x of the momentum of its parent proton. Given two colliding partons, a and b, in two protons, the total cross section of the hard scattering depends on the cross section of the two partons, a and b ($\sigma_{a+b\to c}$ where c is the final state of the process) and their parton density functions (PDFs) $f_a(x_a, \mu^2)$ and $f_b(x_b, \mu^2)$ corresponding to the probability density function of finding a parton of a fraction x of the momentum of the proton:

$$\sigma_{pp\to c} = \sum_{a,b} \int dx_a dx_b f_a(x_a, \mu^2) f_b(x_b, \mu^2) \cdot \sigma_{a+b\to c} \tag{1.71}$$

where the sum above is overal all partonic processes. This model also implies that the transverse momenta of the partons into the nucleons are negligible. In a hard scattering process, initial and final state quarks and gluons can radiate gluons which further radiate or create new quark anti-quark pairs, developing a *parton shower* modelled by splitting functions [21] and Sudakov form factors [22]. As coloured hadrons cannot exist freely for the theory of the confinement (Section 1.1.3), the resulting partons form colourless hadrons (hadronisation). When a bunch of hadrons are produced in a narrow cone, they are experimentally reconstructed as jets.

The PDFs determination relies on phenomenological analysis based on data collected mostly from deep-inelastic scattering experiments and precision measurements exploited in hadron colliders. Their evolution as a function of the energy scale Q^2 of the process can be calculated by the DGLAP equations [23] [24] [25] (Dokshitzer-Gribov-Lipatov-Altarelli-Parisi). Various PDF sets are available: their main difference is the number of parameters of the model and the series of data used to fit the processes. The most common ones are CTEQ [26], MSTW [27] or NNPD [28].

1.6.2 Higgs boson production

From the electroweak lagrangian (1.67), the following coupling constants of the Higgs boson to bosons and fermions are extracted:

$$g_{Hff} = \imath \frac{m_f}{\eta}; \tag{1.72}$$

$$g_{HVV} = -2\imath \frac{M_V^2}{\eta}; \tag{1.73}$$

$$g_{HHVV} = -2\imath \frac{M_V^2}{\eta^2}. \tag{1.74}$$

The Standard Model predicts everything except the Higgs boson mass, therefore, by assuming a mass, production rates and branching ratios can be univocally calculated.
In the Standard Model, the Higgs coupling is preferential to the heaviest particles, namely the

massive bosons W and Z and to the quark top through virtual loops. The main production mechanisms at the LHC [29] [30] will be illustrated in this Section and the relative Feynman diagrams are displayed in Figure 1.6. The cross sections for the same processes are shown in Figure 1.7 for $\sqrt{s}$=7 TeV, $\sqrt{s}$=8 TeV and the total cross section of the process pp→H+X at $\sqrt{s}$=7 TeV, $\sqrt{s}$=8 TeV and $\sqrt{s}$=14 TeV. The coloured bands around the curves represent the theoretical uncertainties on each production mechanism.

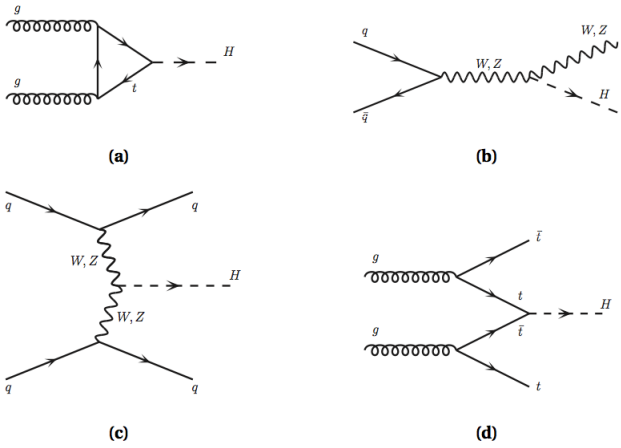

Figure 1.6: Feynman diagrams for the main production mechanisms of the Higgs boson at the LHC: (a) gluon-gluon fusion, (b) associated production with a $W^{\pm}$ or Z bosons, (c) vector boson fusion and (d) $t\bar{t}$ associated production.

Gluon gluon fusion

The gluon gluon fusion (ggF) mechanism:

$$pp \rightarrow gg \rightarrow H \tag{1.75}$$

is dominant at the LHC in the whole Higgs mass range. The coupling of the gluons to the Higgs boson is mediated through a triangular loop of virtual quarks where the t contribution plays the dominant role because of the large top mass. The theoretical cross section has been computed including the QCD corrections up to next-to-next-to-leading-order (NNLO) and next-to-next-leading-log (NNLL), whereas the electroweak corrections are known to next-to-leading order (NLO).

Vector boson fusion

The vector boson fusion mechanism (VBF):

$$pp \rightarrow qq \rightarrow V^*V^* \rightarrow qqH \tag{1.76}$$

is the second-most important mechanism at the LHC. For example, for a Higgs boson of m_H=125 GeV, its contribution to the total cross section is of the order of 8% and its value gets comparable to ggF for Higgs masses $\sim$ 1 TeV. The VBF production mode has a distinctive kinematics: two energetic jets ($p_T^{jets} > 20$ GeV) in the forward and backward regions of the detector with a large rapidity gap between them. The Higgs production is therefore lying inside this gap and the analyses may take advantage of it for identification and reconstruction of VBF-like events. The VBF cross section has been calculated up to NNLO.

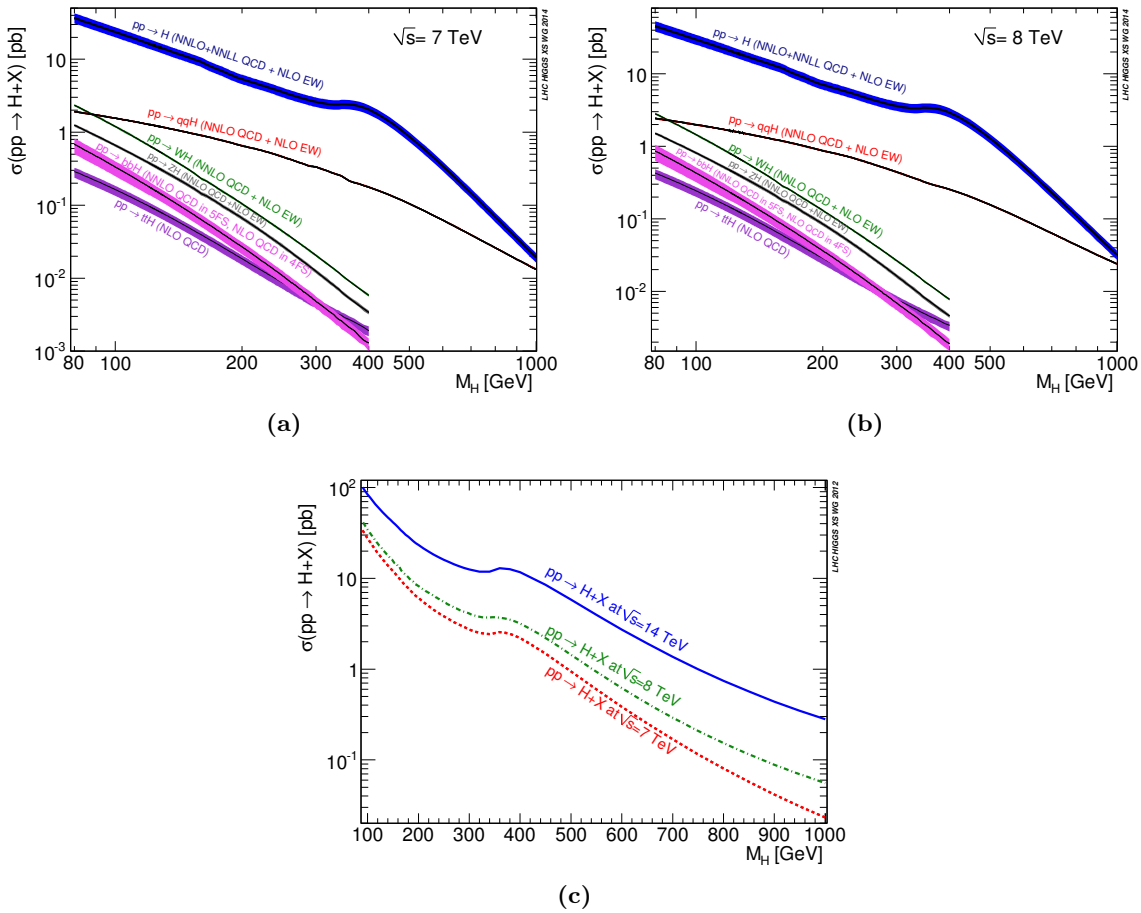

Figure 1.7: Higgs boson production cross section for pp collision at $\sqrt{s}$= 7 TeV (a), and $\sqrt{s}$= 8 TeV (b) as a function of the Higgs mass m_H. Total cross section for pp→ H+X for $\sqrt{s}$= 7 TeV, $\sqrt{s}$= 8 TeV and $\sqrt{s}$= 14 TeV [29].

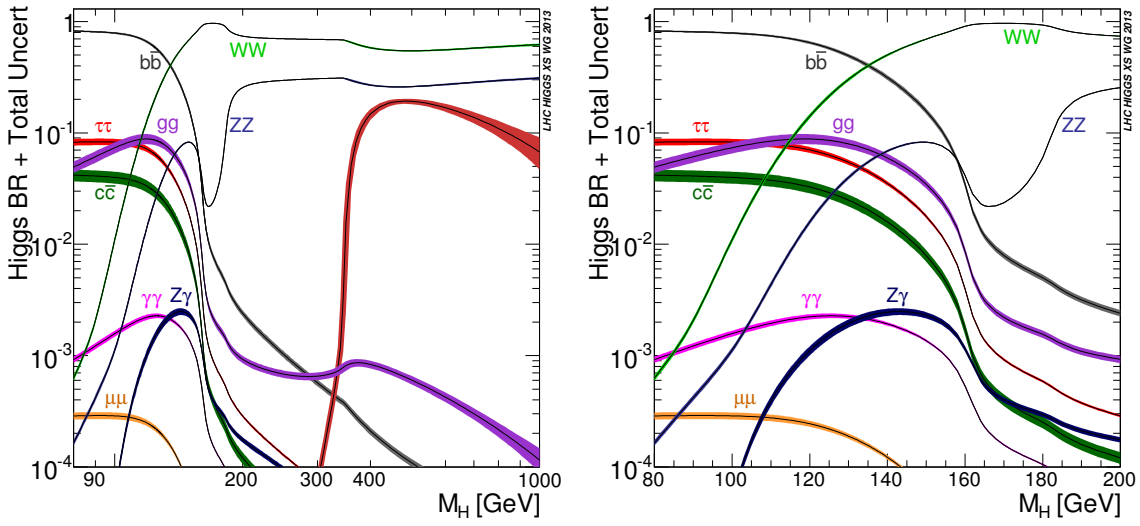

(a) **(b)**

Figure 1.8: Standard Model Higgs decay branching ratios at $\sqrt{s} = 8$ TeV in the whole mass range up to 1 TeV (a) and in the low mass region, 80< m_H <200 GeV (b) [30].

Associated production

The associated production mechanism, described by the process:

$$pp \to q\bar{q} \to VH \tag{1.77}$$

is penalised by the necessity of the presence of an antiquark that, in a pp machine, does not come from the valence but from the sea. In this case, the selection of an event can be performed by reconstructing the original boson that radiated the Higgs. This production cross section has been calculated up to the QCD correction at NNLO and electroweak corrections at NLO.

Associated production to a $t\bar{t}$ pair

The production mechanism of the Higgs boson associated with a $t\bar{t}$ couple is the production mechanism with the smallest yields:

$$pp \to q\bar{q} \to t\bar{t}H \tag{1.78}$$

This process has been computed with a precision NLO.

1.6.3 Higgs boson decay

As previously stated (Section 1.3), the Higgs decay is correlated to the value of its mass and the final state particles due to the dependency of the coupling constants on the mass of the particles the Higgs couples to and the available phase-space. The branching ratios are known at NNLO, including both QCD and electroweak corrections and they are presented in Figure 1.8 as a function of the Higgs mass. Figure 1.9 displays the product of the production cross section σ and the branching ratio for the various final states.

We may subdivide the channels according to the Higgs mass:

- **High mass Higgs** (180 GeV $< m_H <$ 1 TeV). This range is characterised by the fact that $m_H > 2M_Z$, $2M_W$. The Higgs boson decays into two massive bosons, W^+, W^- or ZZ pairs,

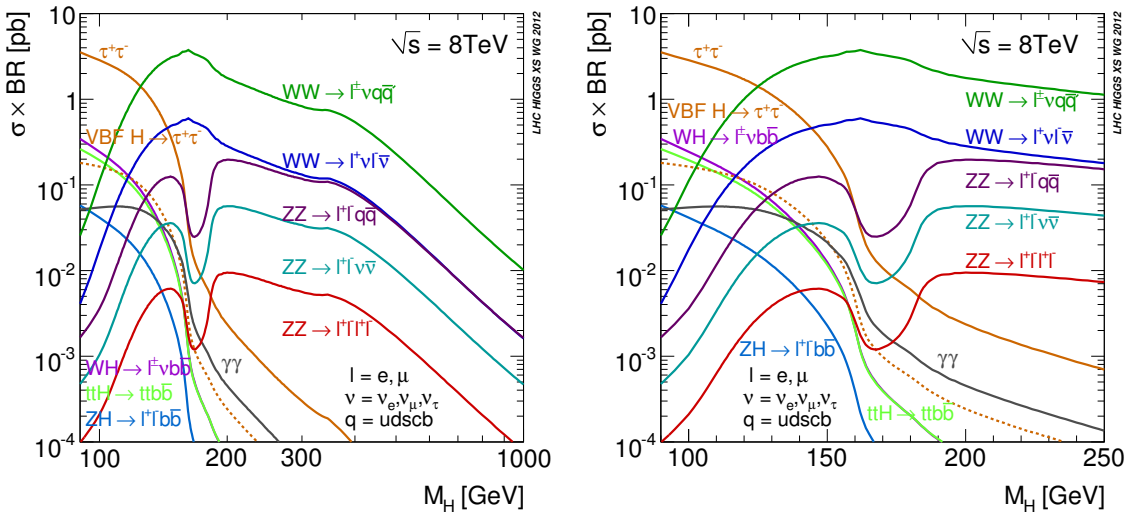

Figure 1.9: Standard Model Higgs boson production cross section times branching ratio at $\sqrt{s}$= 8 TeV in the whole mass range up to 1 TeV (a) and in the low mass region, 80< m_H <250 GeV (b) [30].

with a branching ratio of $\sim$ 70 % in the WW and $\sim$ 30 % in the ZZ final state. In the WW case ($l\nu l\nu$ or $l\nu q\bar{q}$ are the final states that are included in the analysis), its $\sigma\times$BR is high; however, the presence of neutrinos does not allow reconstruction of the final state: the measurement of the rate is important but difficult since several backgrounds can mimic the signals. On the other hand, the ZZ decay channel into 4 leptons, electrons or muons (H $\rightarrow$ ZZ $\rightarrow$ 4l) possesses an excellent resolution for what regards the Higgs mass as well as a negligible background rate. Chapter 5 will develop the main characteristics of this analysis as well as the various steps that led to the mass extraction in that channel.
For $m_H > 200$ GeV, the decay channels $H \rightarrow$ ZZ $\rightarrow$ llqq and $H \rightarrow$ ZZ $\rightarrow$ ll$\nu\nu$ are also included in the ZZ analysis because of their good sensitivity in the high mass region.

- **Intermediate Higgs** (130 GeV $< m_H <$ 180 GeV). The Higgs boson still decays into 4 fermions, through a pair of massive gauge bosons, being one of them virtual. As m_H approaches 130 GeV, the decay channel into $b\bar{b}$ pairs is present as well, with a branching ratio $\sim$ 50 %. When the WW threshold ($m_H \sim 2M_W$) is reached, the $b\bar{b}$ decay channel contribution gets less important. Until the production threshold of two real Z bosons ($m_H \sim 2M_Z$), the WW decay completely dominates the branching ratio.

- **Low mass Higgs** (110 GeV $< m_H <$ 130 GeV). In the low mass range, the main decay channel is $b\bar{b}$, then $\tau^+\tau^-$ and $c\bar{c}$. In spite of its high value of $\sigma\times$BR, the $b\bar{b}$ mode is not easily accessible because of the overwhelming QCD background. The decay channels that are characterised by a virtual top or bottom loop, namely $H \rightarrow \gamma\gamma$ and $H \rightarrow Z\gamma$, are much rarer than $b\bar{b}$ or $\tau^+\tau^-$ although they are experimentally precious because of their very distinctive signature due to two high energetic photons forming a narrow invariant mass peak over a falling background.

1.6.4 Higgs boson total width

The functional form (Figure 1.10) of the the total width above the ZZ production threshold as a function of m_H is illustrated in the equation below:

$$\Gamma_H \propto m_H^3. \tag{1.79}$$

The detector resolution dominates over the Higgs width contribution below the WW threshold

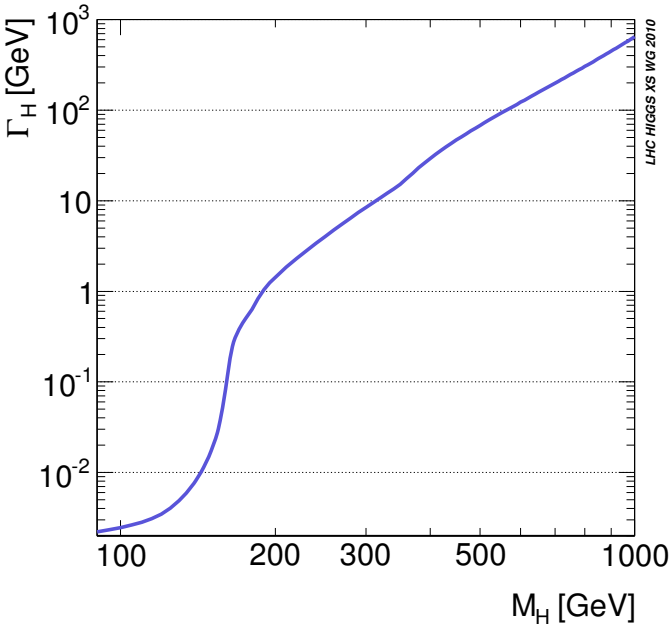

Figure 1.10: Total decay width of the Higgs boson as a function of its mass, m_H [29].

where the Higgs width is of the order of few MeV and the detector term $\sim$ 1 GeV. Above this value, the intrinsic width of the resonance takes over and it reaches $\sim$ 500 GeV for m_H=1 TeV.

1.7 The H $\rightarrow ZZ^* \rightarrow$ 4l channel - Signal and Background simulations

The ZZ decay mode of the Standard Model Higgs boson has a low branching fraction over the range of the Higgs mass hypotheses inspected; nevertheless the final state with four leptons (electrons and muons) from the ZZ decay is very clean and almost background-free so it is one of the main discovery channel at the LHC.
The four leptons are associated in two pairs: when the Higgs mass is below $2m_Z \sim$ 180 GeV, one of the two Z bosons is on-shell and the other one is off-shell.
Other final states with two leptons and two jets (H $\rightarrow ZZ^* \rightarrow$ llqq) or two neutrinos (H $\rightarrow ZZ^* \rightarrow$ ll$\nu\nu$) have been also investigated but will not be comprised in this dissertation. They are particularly relevant for a Higgs-boson mass above the ZZ threshold ($m_{4l} > 2m_Z \sim$ 180 GeV) where the contributions coming from the background processes can be significantly reduced.

1.7.1 The H $\rightarrow ZZ^*$ signal process

The simulation of the production and the decay of the Higgs boson in the ZZ final state has been performed by using several Monte Carlo generator programs. The multi-purpose generator program PYTHIA version 6 [31] [32] and the generator program POWHEG BOX [33] have been used for the current Higgs simulation covering all the various production mechanisms. PYTHIA is a leading-order (LO) generator while POWHEG BOX implements calculations at the next-to-leading order (NLO). PYTHIA is interfaced to PHOTOS [34] for QED radiative corrections in the final state. PYTHIA is also employed for the production of a Higgs boson in association with a W or a Z boson (VH) and with a $t\bar{t}$ pair. As for the last production mechanism, the production of a Higgs boson in association with a $b\bar{b}$ pair is included in the signal yield assuming the same m_H dependence for the two processes.

- The cross sections for the gluon-gluon fusion process have been calculated to NLO, and NNLO in QCD [30]. In addition, QCD soft-gluon resummations calculated in the NNLL approximation are applied for the ggF process as explained later in this Section. NLO electroweak (EW) radiative corrections are also computed.

- For the VBF process, full QCD and EW corrections up to NLO [35] and approximate NNLO QCD [36] corrections are used to calculate the cross section.

- The cross sections for the associated WH/ZH production processes are calculated at NLO [37] and at NNLO in QCD [38], and NLO EW radiative corrections are applied [39].

- The cross sections for associated Higgs boson production with a $t\bar{t}H$ pair are calculated at NLO in QCD [40] [41] [42] [43].

- The cross section for the $b\bar{b}H$ process is calculated at NLO [44] [45] and NNLO in QCD [46].

The Higgs boson decay branching ratios [47] to the different four lepton final states are provided by Prophecy4f [48], which includes the complete NLO QCD+EW corrections and interference effects between identical final-state fermions.

Theoretical uncertainties

The two main sources of uncertainties affecting the cross section are discussed below.

- QCD radiation corrections. The usual method (used for ggF and VBF Higgs productions) applied to generate these uncertainties is varying the renormalisation and factorisation scales around a central value chosen to be the hard scale of the process. These scales are changed by a factor two up and down from their nominal value. The choice of this nominal parameter is $\mu_0 = m_H$ or $\mu_0 = \frac{m_H}{2}$ according to two different calculations [49] [50] leading to very similar results.

- PDF choice + α_S. The MSTW2008 PDF set [27] provides 40 different grids that allow the evaluation of the experimental uncertainties. These grid variations are then compared to other PDF set variations, namely NNPDF [28] and CTEQ [26]. Another related source of theoretical uncertainties comes from the value of the QCD coupling constant α_S. This value is known up to the order of 3-4% in the Higgs mass range m_H=100-300 GeV and its uncertainty is usually incorporated into the PDF-related systematics.

The use of the large m_t approximation induces another source of uncertainty, nonetheless the two calculations [49] and [50] both include the exact NLO corrections with dependence on the masses

of the top and bottom quarks, thence this uncertainty is not taken into account.
The QCD scale uncertainties for a Higgs boson of m_H=125 GeV amount to approximately +7% and -8% for the gluon fusion process, $\sim \pm 1\%$ for the VBF and associated WH production processes and +4% and -9% for the $t\bar{t}$ production process. The uncertainty on the production cross section due to uncertainties on the parton distribution functions and the strong coupling constant α_S is of the order of ±8% for gluon-initiated processes and ±3% for quark-initiated processes.

Wrapping up, for a Higgs boson of m_H=125 GeV, the cross section values as well as the uncertainties on the QCD and PDF scales calculated for $\sqrt{s}$=8 TeV in the complex pole scheme (CPS) [51] computed at NNLO QCD + NLO EW are charted in Table 1.3.

$\sigma_{\text{production}}$ [pb]	QCD up/down scales	PDF +α_S up/down scales
$\sigma(gg \to H)$=19.27	+7.2%, -7.8%	+7.5%, -6.9%
$\sigma(qq' \to Hqq')$=1.578	+0.2%, -0.2%	+2.6%, -2.8%
$\sigma(q\bar{q} \to WH)$=0.7046	+1.0%, -1.0%	+2.3%, -2.3%
$\sigma(q\bar{q} \to ZH)$=0.4153	+3.1%, -3.1%	+2.5%, -2.5%
$\sigma(q\bar{q} \to t\bar{t}H)$=0.1293	+3.8%, -9.3%	+8.1%, -8.1%

Table 1.3: Cross section of the Higgs production mechanisms and uncertainties on the QCD and PDF scales calculated for $\sqrt{s}$=8 TeV in the complex pole scheme (CPS) computed at NNLO QCD + NLO EW.

Higher-order corrections to the Higgs boson transverse momentum spectrum

The total inclusive cross sections for the Higgs-boson production have been computed at NNLO+NNLL [29] [52] [53] [50]. In this Section we focus on the analysis of the transverse-momentum (p_T) spectrum of the Higgs boson. When studying the Higgs p_T distribution, it is convenient to distinguish two regions of transverse momenta.

- In the large p_T region, $p_T > m_H$, perturbative QCD calculations are available and theoretically justified. In this region, the spectrum is known up to LO with the correct dependence of the masses of the top and bottom quarks and up to NLO in the large m_T-limit.
- In the low p_T region ($p_T < m_H$), the bulk of events produced with fixed-order in α_S expansion needs to be parametrized with the presence of large logarithmic terms due to soft gluon radiations. These terms need to be resummed (soft resummation) to the fixed order calculations up to a given scale (resummation scale, μ_R).

These two regimes are implemented in the HqT program [175]; the differential distributions with NNLL accuracy are then compared with those from the NLO generator program POWHEG BOX. The transverse-momentum distribution of the Higgs boson produced via gluon fusion is illustrated in Figure 1.11 (a) as obtained by using the POWHEG generator and the HqT tool; the two distributions are normalised to the gluon-fusion cross section. The p_T is significantly affected over the full range and for low Higgs-boson masses ($m_H < 150$ GeV); HqT gives a larger differential cross section at low p_T with respect to POWHEG, while at large p_T the opposite behaviour is observed. The ratio between the p_T distributions for each p_T bin can be used as a weight for the POWHEG spectrum that has been used for the current ZZ analysis (Figure 1.11 (b)).
This difference in the Higgs boson transverse momentum spectrum affects other variables that are correlated with the p_T, hence the number of accepted events passing the kinematic selection after the cutflow. The impact of the reweighting of POWHEG events on the acceptance of the four

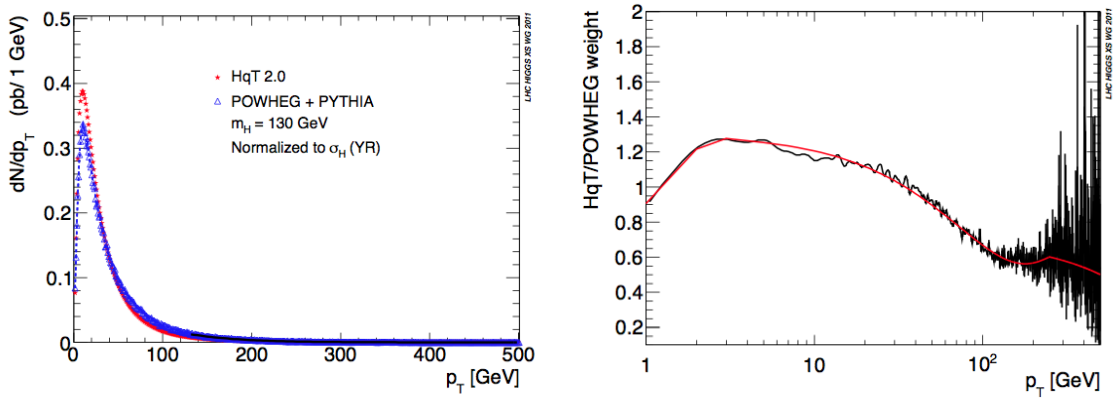

(a) **(b)**

Figure 1.11: (a) p_T spectrum of the Higgs boson of mass m_H=130 GeV produced via gluon-gluon fusion as obtained by using the POWHEG generator (and PYTHIA for parton shower, hadronisation and underlying event) and the HqT tool. (b) The ratio HqT *vs* POWHEG as a function of the Higgs-boson p_T generates the weights that are applied as a function of m_H to the POWHEG-based Higgs p_T distribution [30].

lepton kinematics has been therefore addressed and displayed in Figure 1.12 when the reweighting is turned on or off. The ratio between the acceptance values in the four electron, four muons and mixed channel can be monitored as a function of m_H. The impact of such a procedure on the final acceptance is mass-dependent, it amounts to 1−2% at low Higgs boson mass and it reduces significantly as the Higgs mass grows.

In 2012, a new Monte Carlo generator was later introduced and finally used for the Run 1 publications: HRES [54] implementing the Higgs boson production by gluon-gluon fusion channel (at the NNLO+NNLL accuracy). It was meant to replace HqT; in this regard, the HRES spectrum was cross-checked against that of HqT and found to be identical. The Higgs boson transverse momentum spectrum in the gluon gluon fusion process is therefore reweighted to HRES to match the NNLO+NNLL accuracy.

1.7.2 The background processes

ZZ^* continuum irreducible background

The main background to the Higgs decay in 4 leptons is the Standard Model di-boson non resonant production. It is mostly an irreducible background because its final state is similar to the one of the Higgs, with two pair of isolated leptons. Note that the quantum interference between the Z/γ final state needs to be properly taken into account as well. If the ZZ continuum production is LO, it is characterised by the diagram $q\bar{q} \rightarrow$ ZZ in a t-channel as illustrated in Figure 1.13 (a). The NLO contribution is generated by a s-channel diagram as shown in Figure 1.13 (b) and 1.14. As displayed in Figure 1.13 (c), the gg→ ZZ production is LO and it involves diagrams with quark loops at LO. Such a contribution is negligible in the low m_{ZZ} mass region (below the ZZ threshold at 180 GeV) and it accounts for approximately 8% of the total ZZ→ 4l cross section in the high mass m_{ZZ} region (above the ZZ threshold). The cross section of the non-resonant $ZZ \rightarrow$ 4l is of the order of 5.3 fb.
The continuum background is parametrized using POWHEG [55] for $q\bar{q}$ annihilation (NLO calculation) and gg2ZZ [56] (LO) for gluon fusion with the CT10 and CT10NNLO for $q\bar{q}$ and gg-initiated background respectively. The parton shower is performed through the usage of PYTHIA 8.

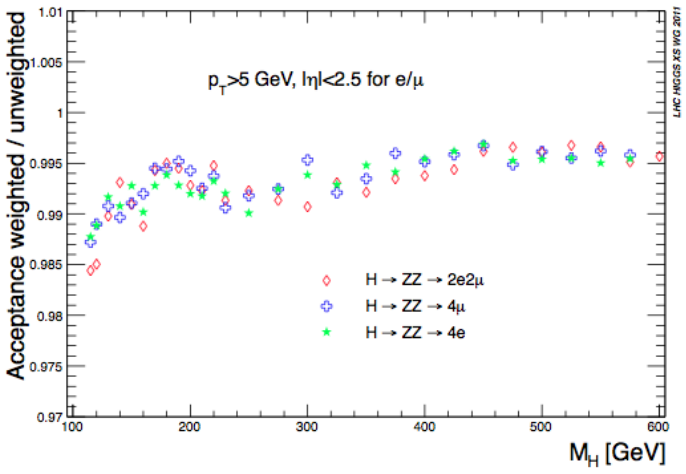

Figure 1.12: Ratio between the acceptance values for POWHEG events with four electrons, four muons, and two electrons and two muons final state from $H \to ZZ$ decay, when turning on-off the reweighting with HqT [30].

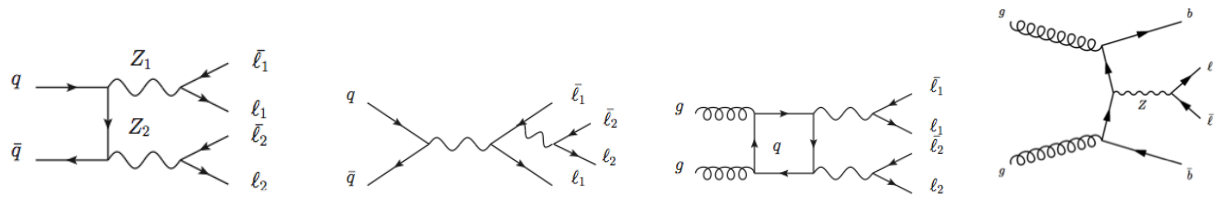

Figure 1.13: Feynman diagram of the non-resonant ZZ production in the t channel (a), in the s channel (b) and through the gluon fusion (c). The t channel is a LO process, whereas the s channel is NLO. Feynman diagram of the Z$b\bar{b}$ irreducible background production (d).

Another important difference between the Higgs signal and the ZZ irreducible background stems from the fact that the Higgs is a scalar particle (spin=0), hence the angular distributions of the ZZ decay (mostly produced by $q\bar{q} \to ZZ$ in the t channel) are different with to respect to those of the signal. The analysis of the angular distributions in the 4 lepton final state can therefore improve the ZZ background rejection and notably enrich the signal region through the employment of multivariate techniques (Chapter 5).

Theoretical uncertainties

The two main sources of theoretical systematic uncertainties for the ZZ^* non-resonant background, QCD and PDF + α_S scale uncertainties, as well as the different treatments to compute them, are listed below. Note that this study refers to a centre-of-mass-energy of 7 TeV, even though the results still hold in the configuration at 8 TeV. QCD scale uncertainties do not strongly depend on centre-of-mass energy as they account for the estimation of unknown higher-order corrections. Likewise,

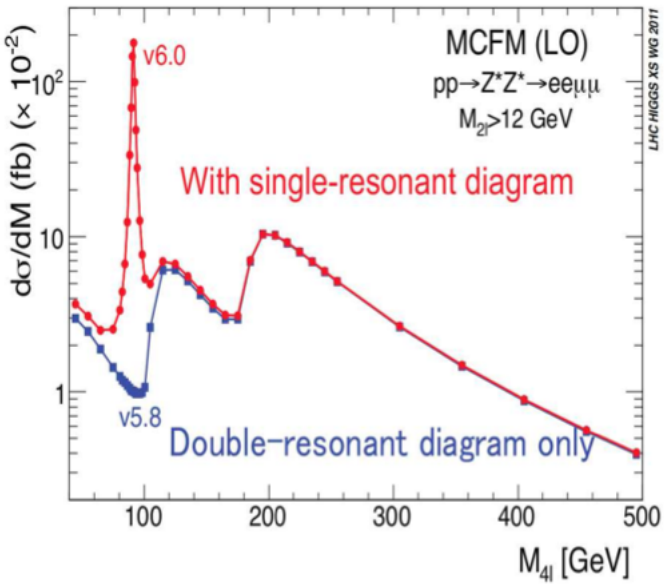

Figure 1.14: Invariant mass of the 4 leptons final state (ZZ^*) with the LO Monte Carlo MCFM if there is only the leading-order contribution (blue curve) or if the NLO diagram is added (red curve). The effect of the NLO is the opening of the single Z production illustrated by the peak at ∼ 91 GeV [30].

PDF + α_S uncertainties do not change between $\sqrt{s}$=7 TeV and $\sqrt{s}$=8 TeV because processes at these two energies hit quasi-equivalent Bjorken regimes.

- PDF-related systematic uncertainties. The prescriptions reported in [57] are applied: the up and down variations taken as the envelope of the distributions are computed with three PDF sets: CT10 [58], MSTW2008 [27] and NNPDF [28]. These variations can be parametrized as follows:

$$\mathcal{K}(m_{4l}) = 1 + 0.0035\sqrt{m_{4l} - 30}\ \ (q\bar{q}) \tag{1.80}$$

and

$$\mathcal{K}(m_{4l}) = 1 + 0.0066\sqrt{m_{4l} - 10}\ \ (gg). \tag{1.81}$$

Figure 1.15 (a) and (b) show the difference between the central value of the cross section and the cross section computed with plus and minus 1σ of the total PDF variations. The red line is the parametrisation of the equations (1.80) and (1.81).

- QCD scale systematics. In order to compute the QCD scale theoretical uncertainties, the differential cross section $\frac{d\sigma}{dm_{4l}}$ is computed when the renormalisation and factorisation scales are changed by a factor two up and down from their nominal value, namely μ_R=μ_F=m_Z. As for the PDF-related systematics, the dependence on the mass of the QCD systematics can be extracted as follows:

$$\mathcal{K}(m_{4l}) = 1.00 + 0.01\sqrt{(m_{4l} - 20)/13}\ \ (q\bar{q}) \tag{1.82}$$

and

$$\mathcal{K}(m_{4l}) = 1.04 + 0.10\sqrt{(m_{4l} + 10)/40}\ \ (gg). \tag{1.83}$$

Figure 1.15 (c) and (d) illustrate the cross section for $q\bar{q} \to ZZ^*$ and gg→ ZZ^* as a function of m_{4l} at 7 TeV computed with CT10 PDF and varying the QCD scale up and down by a

factor two. Figure 1.15 (e) and (f) report the ratio of the cross section as a function of the 4 lepton final state. The red line is the parametrisation defined in (1.82) and (1.83).

Conclusively, the quark-initiated (gluon-initiated) process have a PDF and a QCD scale uncertainty of approximately ±4% (±8%) and ±5% (±25%).

Z+jets (Z+light jets and $Zb\bar{b}$) and $t\bar{t}$ reducible backgrounds

This background generates a final state with 4 leptons, two of them are high-momentum isolated leptons and the other two are produced by the semileptonic decay of heavy quarks (mostly b quarks) as illustrated in Figure 1.13 (d) or fake-leptons. The $t\bar{t}$ background comes from the decay of the W in leptons. This background is estimated by data-driven methods (Chapter 5). There are two main experimental quantities that can be measured to reduce the contribution of these background processes:

- **Impact parameter**: as the leptons are produced by the decay process of hadrons have a long lifetime (mostly b-related hadrons), they acquire an impact parameter that can be measured with respect to the primary vertex. Hence, provided that the resolution on the trajectory of the leptons is accurate enough, a simple cut on the impact parameter can remove a large percentage of this background.

- **Isolation**: A semileptonic decay of a hadron produces leptons, neutrinos and hadrons in the final state. Hence, there is activity around the leptons and a cut on the transverse activity in a cone of radius ΔR around the leptons:

$$\Delta R = \sqrt{(\Delta\eta)^2 + (\Delta\phi)^2} \tag{1.84}$$

  can remove several background events. The isolation cut can be performed both at the inner detector (track isolation) and the calorimeter level (calorimetric isolation).

The $t\bar{t}$ background does not have a resonance at the Z peak for the two isolated leptons - the invariant mass distribution of this contribution is therefore relatively flat.
Another background for the Higgs decay channel in 4 leptons final state is the Z+ (light) jets background, where jets are reconstructed as fake-leptons. As for the $Zb\bar{b}$ and $t\bar{t}$, this background plays a role only in the low mass region, below the ZZ threshold (m_{ZZ} <180 GeV). In any event, the treatment of this background proceeds in parallel with the one relative to the $Zb\bar{b}$ and $t\bar{t}$: isolation and impact parameter cuts are applied both at the inner detector and the calorimeter level.

The Z+jets production is modelled using Alpgen [59] and is divided into two sources: Z+light jets which includes $Zc\bar{c}$ in the massless c-quark approximation and with $Zb\bar{b}$ from parton showers, and $Zb\bar{b}$ using matrix element calculations that take into account the b-quark mass. The set of PDFs used for Alpgen is CT10.

The MLM [60] matching scheme is exploited to remove any double counting due to identical jets produced via the matrix element calculation and the parton shower: this scheme is applied to gluons and light quarks but it is not implemented for b-jets. First, a sorting algorithm is based on a cut on a cone around the lepton ΔR_{min} and a minimal energy E_{min}. Then a matching is performed between the partons coming from the matrix element and the reconstructed jet. In order not to include any double counting in the procedure, an event is kept if and only if each parton of the matrix element is matched to a jet and vice-versa.

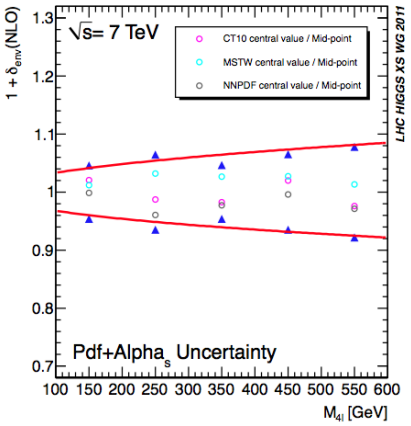

(a) PDF scale for $q\bar{q} \to ZZ^*$

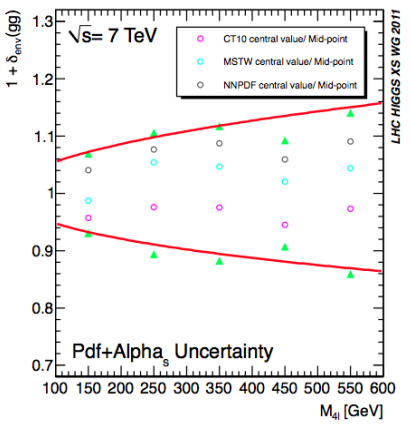

(b) PDF scale for $gg \to ZZ^*$

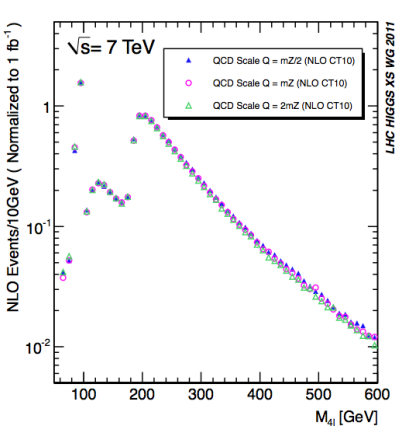

(c) QCD scale for $q\bar{q} \to ZZ^*$

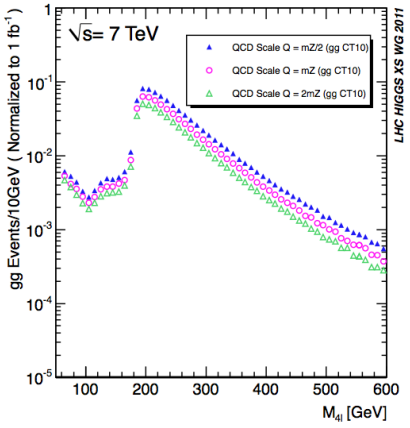

(d) QCD scale for $gg \to ZZ^*$

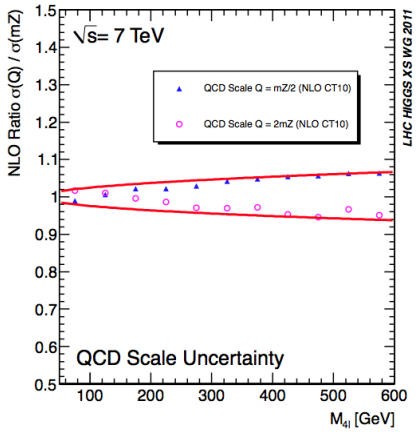

(e) Ratio of the QCD scales for $q\bar{q} \to ZZ^*$

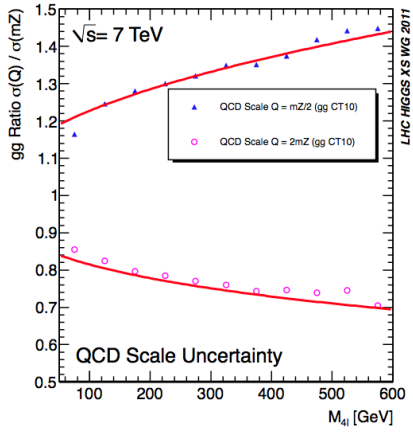

(f) Ratio of the QCD scales for $gg \to ZZ^*$

Figure 1.15: (a) and (b) - Difference between the central value of the ZZ cross section and the ZZ cross section computed with 3 different sets of PDF varying them by plus and minus 1σ for $q\bar{q} \to$ ZZ and gg$\to$ ZZ processes as a function of the 4 lepton final state mass. The red line is the parametrisation of the variation reported in equations (1.80) and (1.81). Cross section for $q\bar{q} \to ZZ^*$ (c) and gg$\to ZZ^*$ (d) as a function of m_{4l} computed with CT10 PDF and varying the QCD scale up and down by a factor two. Ratio of the cross section, (e) and (f), as a function of the 4 lepton final state. The red line is the parametrisation defined in (1.82) and (1.83) [30].

The $t\bar{t}$ background is modelled using POWHEG interfaced to Pythia 8.1 for parton shower and hadronisation; with PHOTOS used for quantum electrodynamics (QED) radiative corrections and TAUOLA for the simulation of the τ lepton decays [61].

Chapter 2

The ATLAS detector and the LHC

Contents

2.1 The Large Hadron Collider

The Large Hadron Collider (LHC) [62] is a hadron collider installed at CERN (Geneva) along the border between France and Switzerland in the existing 26.7 km tunnel that was previously constructed between 1984 and 1989 for the LEP (Large Electron Positron collider) machine. The tunnel has eight straight sections and eight arcs and lies between 45 m and 170 m below the surface on a plane inclined at 1.4% towards the Leman lake. The construction started right after the end of LEP-era, early in 2000. The centre-of-mass energy, $\sqrt{s}$, of the accelerator was set to 7 TeV for the 2010 and 2011 data-taking and subsequently increased to 8 TeV for 2012. By February 2013, the accelerator ceased to be operative for about two years (Run 1 shut-down) and it will resume between April (first beam injected in the accelerator) and June 2015 (expected first collisions for

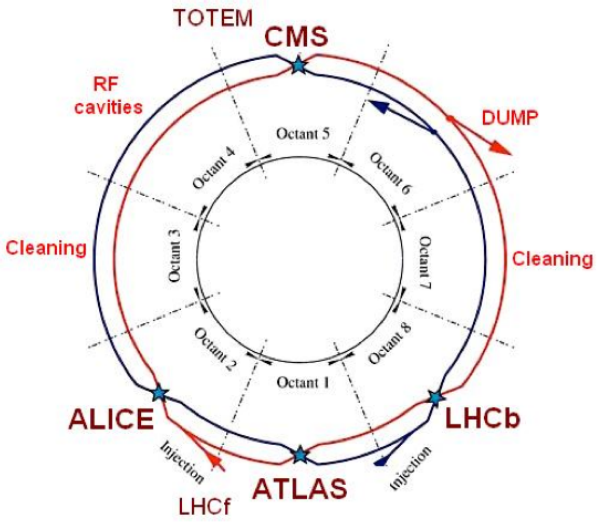

Figure 2.1: Schematic overview of the structure of the LHC. The various interaction points as well as the position of the experiments are shown.

physics) with an increased $\sqrt{s}$= 13-14 TeV (Run 2). The broad physics programme expressed by the LHC has been previously exploited by the proton-anti proton collider at $\sqrt{s}$=1.96 TeV located at TeVatron (Fermilab) [18] before it shut down on September 29th 2011.
The exploration project of the LHC, as well as for the TeVatron in the past decades, is vast: the main goal of the analyses is to unravel the still-unknown features of the Standard Model (Chapter 1), especially in line of the Higgs boson quest.

The LHC is constituted by two rings (Figure 2.1) instrumented with superconductive magnets. The tunnel is sectioned in eight octants and linear sections 528 meters each. The two maximal-luminosity zones, where the ATLAS (A Toroidal LHC ApparatuS) [63] and CMS (Compact Muon Solenoid) [64] experiments reside, span along two rectilinear sections, addressed as Point 1 and Point 5. The other two main experiments at the LHC, ALICE (A Large Ion Collider Experiment) [65] dedicated to heavy ions physics and LHCb (LHC beauty experiment) [66] studying flavour physics, are hosted respectively at Point 2 and Point 8. In the other four rectilinear sections there are no further intersections between beams. The injection zones are in the octant 2 and 8 for the clockwise and anticlockwise bunch filling. In the octants 3 and 7 the apparati for the *cleaning* and *collimation* of the beams are lodged whereas sector 4 has two independent radiofrequency cavities enabling proton acceleration. The area of Point 6 contains the equipment to extract the dumped beam from the tunnel. Most notably, two other detectors are installed: they are mostly devoted to diffraction and forward physics, TOTEM (Total cross-Section, Elastic Scattering and Diffraction Dissociation at the LHC) [67] and LHCf (LHC forward experiment) [68] housed in the very forward regions of CMS and ATLAS respectively.

2.1.1 The acceleration chain

The acceleration process [69] of the two proton beams is performed in different phases and LHC is just the last part of this chain bringing protons to their final center-of-mass energy of 7-8 TeV. The injection chain is composed of the following systems:

- Linac,

- Proton Synchrotron Booster (PSB),
- Proton Synchrotron (PS),
- Super Proton Synchrotron (SPS),
- Large Hadron Collider (LHC).

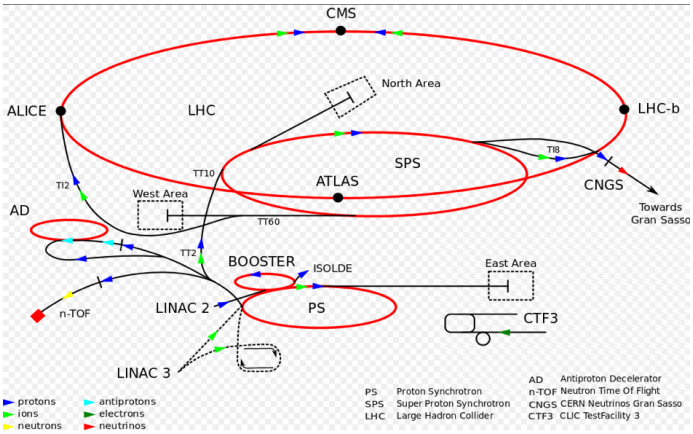

Figure 2.2: Schematic view of the accelerators operated at CERN. The path of protons and ions towards their injection inside the LHC is marked in blue and green respectively.

Protons are brought to a beam current of approximately 300 mA. At this stage, the protons are injected in the LINAC that accelerates them up to 50 MeV. The particles are now ready to enter the PSB that increases their energy to 1.4 GeV before being transferred to the PS that goes up to 25 GeV and creates the typical structure of bunches. Finally, the SPS accelerates the protons to 450 GeV, the bunches are finally injected to the LHC using two different tunnels. Then, when all bunches are inside the ring, the LHC raises its energy to $\sqrt{s}$=7 TeV (in 2010 and 2011) or $\sqrt{s}$=8 TeV (in 2012).
In the LHC, the two beams circulate in two vacuum chambers whose horizontal distance is 194 mm. Time-wise, it takes 4 minutes to fill each LHC ring, and 20 minutes for the protons to reach their maximum beam energy of 4 TeV. Lastly, beams circulate for many hours inside the LHC beam pipes under normal (stable beam) operating conditions. Additional details on the acceleration chain are presented in Figure 2.2.

The LHC is also used for research programmes with heavy-ions exploiting lead-lead collisions at a center-of-mass energy significantly lower than the proton case, namely 2.76 TeV. In 2012, special LHC runs were performed using proton-lead collisions at $\sqrt{s}$=5.02 TeV.
The acceleration inside the tunnel is provided by eight radiofrequency cavities and the proton trajectory is controlled by 9593 magnets, mostly superconductive. The proton beams are kept on a given circular trajectory using $\sim$ 1232 superconductive magnetic dipoles producing a magnetic field of 8.33 Tesla (for 7 TeV beams). Such an intense field can curve the proton trajectory by $\sim$ 0.6 mm for each meter. These dipoles are embedded in superfluid liquid helium at 1.9 K and 0.13 MPa. The quadrupoles ($\sim$ 390) shape the beam width by modifying its optics [70].
The particle beam is divided into discrete packets called *bunches*. The instantaneous luminosity of the run depends on the number of protons in each bunch: for instance, a bunch in a high-luminosity run contains $\sim 10^{11}$ protons with a design timing separation between successive bunches of 25 ns (50 ns during the Run 1 data-taking period). Each of them is 7.55 cm long and 16.7 μm wide at the

Parameter	2010-2011	2012
$\sqrt{s}$ (TeV)	7	8
$\mathcal{L}$ (10^{33}cm^{-2}s^{-1})	3.7	7.7
Δt (ns) between collisions	50	50
Particles per bunch (10^{10})	15	15
Full crossing angle (μrad)	240	$\sim$300
Beam radius (10^{-6}m)	26	20
Transverse emittance ($10^{-9}\pi$·rad·m)	0.7	0.6
β^* at the IP (m)	1	0.6

Table 2.1: Parameters of the LHC collider [71] referring to the the data-taking period 2010-2012.

interaction point. Each proton beam at full intensity consists of $\sim$ 2800 bunches per beam at 25 ns. The superconductive radiofrequency cavities on the LHC are housed in four cryomodules (two per beam).
Important parameters [71] of the LHC colliders referring to the data taking periods 2010-2011 and 2012 are reported in Table 2.1. The transverse *emittance* describes the typical beam width while β^* is the value of the *betatron* function calculated at the impact parameter. This observable represents the level of expected focalisation of the colliding beams.

2.1.2 The calculation of the instantaneous luminosity

The number of events of a given process described by a cross section σ and characterised by an efficiency $\mathcal{E}$ (trigger, reconstruction and identification), generated at the LHC per second can be parametrised as follows:

$$N = \mathcal{L}\sigma\mathcal{E} \tag{2.1}$$

where $\mathcal{L}$ is the instantaneous luminosity of the system, and $L = \int \mathcal{L}\, dt$ is the integrated luminosity of the run. The luminosity is a function of the beam parameters; under the hypothesis of gaussian distributions of protons in the beam, the luminosity factor is modelled as:

$$\mathcal{L} = \frac{N_b^2 n_b f_{rev} \gamma_r}{4\pi\epsilon_n\beta} F. \tag{2.2}$$

N_b is the number of particle for each bunch, n_b is the number of bunches per beam, f_{rev} is the rotation frequency, γ_r the relativistic factor, ϵ_n the normalised transverse emittance[1] and β^*, the betratron function, is extracted at the interaction point. F is a luminosity reduction factor introduced to parametrise the non-zero crossing angle θ_c between the two colliding beams (non head-on collisions) with respect to the orthogonal axis of the bunches (at the LHC, θ_c=0.85 μrad). The luminosity exponentially decreases during a run because of the degradation of intensity and emittance of the circulating beams. Other effects can play a marginal role in the process of luminosity degradation, namely the beam interaction with the gas left inside the beam pipe and the local scattering inside the beams. Figure 2.3 shows the ATLAS instantaneous luminosity profile as measured online for a representative LHC fill with $\sqrt{s}$=8 TeV center-of-mass energy in 2012. The green curve shows the delivered luminosity during stable beam conditions and the yellow distribution gives the ATLAS recorded luminosity with the entire detector available. The exponential decrease of the

[1]The emittance, already mentioned in the previous paragraph, is defined as the product of the width in position, σ, and angle, σ', of the distributions of the particles in the bunch under the assumption that the distribution of the particles is gaussian.

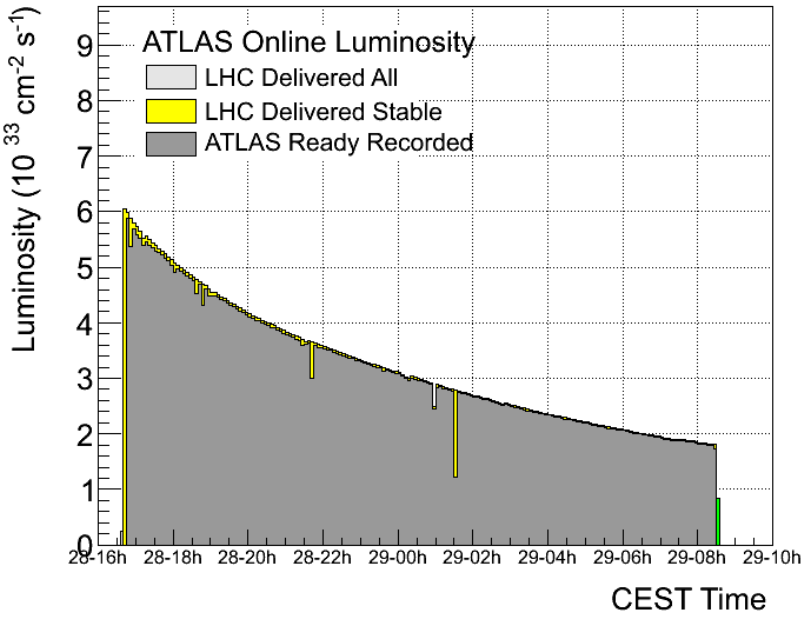

Figure 2.3: Exponential decrease of the instantaneous luminosity during a run characterised by stable beam at $\sqrt{s}$=8 TeV recorded in 2012. The grey area illustrates the delivered luminosity by the LHC whilst the yellow distribution specifies the LHC luminosity produced in stable beam conditions and the dark grey area the recorded luminosity by ATLAS in this run.

instantaneous luminosity is therefore visible in the plot.
The luminosity is measured without the knowledge of the cross section by the Van der Meer scan [72]. This scan determines the transverse profiles of the beams: this method requires the knowledge of the beam currents in order to deduce the absolute luminosity and is employed by LUCID (Section 2.7). Then, these detectors are used during normal fills to extract the luminosity by comparing it to their measurement during the dedicated Van der Meer scans.

Given the high total inelastic, σ_{pp} cross section at the LHC ($\sim$ 70 mb), several proton-proton interactions take place during the same bunch-crossing. Thence, at the nominal instantaneous luminosity of $10^{34}\text{cm}^{-2}\text{s}^{-1}$, for each interesting hard-scattering event, there are approximately 25 additional inelastic interactions that can perturbate the measurement. This phenomenon is the pile-up: the *in-time* pile-up is originated by particles emerging from vertices within the same bunch crossing; the *out-of-time* pile-up is due to the superimposition of signals in the detector that come from different bunch crossings. The number of proton-proton interactions in a bunch crossing at the LHC resulting in vertices varies according to Poisson statistics with a mean value $< N >$ given by:

$$< N >= \sigma_{pp} \cdot \mathcal{L}_b, \tag{2.3}$$

where σ_{pp} is the total inelastic cross section and $\mathcal{L}_b$ is the instantaneous luminosity per bunch crossing. Section 3.7 gives a complete overview of the pile-up scheme in 2011 and 2012 data as well as its treatment in the Monte Carlo simulation.

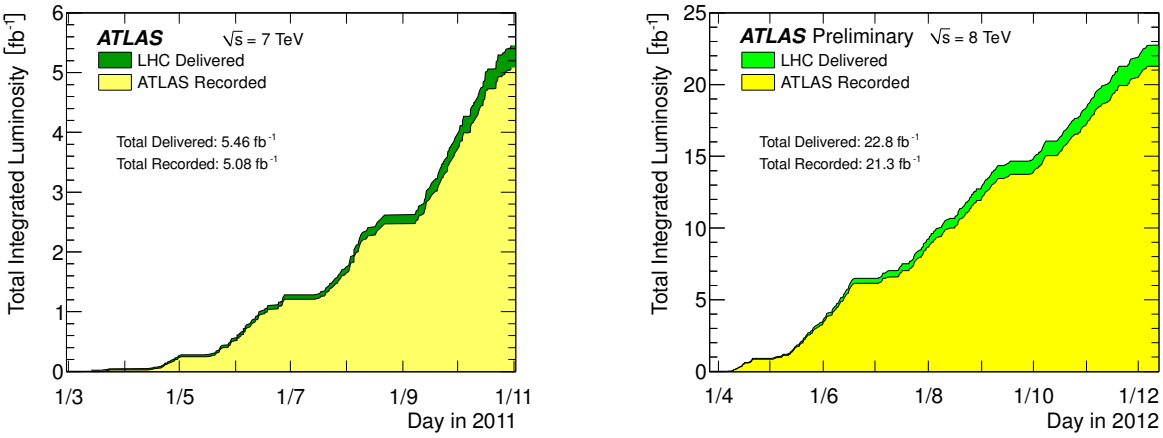

(a) **(b)**

Figure 2.4: Cumulative luminosity versus time delivered to (green), and recorded by ATLAS (yellow) during stable beams and for proton-proton collisions at 7 TeV centre-of-mass energy in 2011 (a) and 8 TeV centre-of-mass energy in 2012 (b). The delivered luminosity accounts for the luminosity produced from the start of stable beams until the LHC requests ATLAS to put the detector in a safe standby mode to allow a beam dump or beam studies.

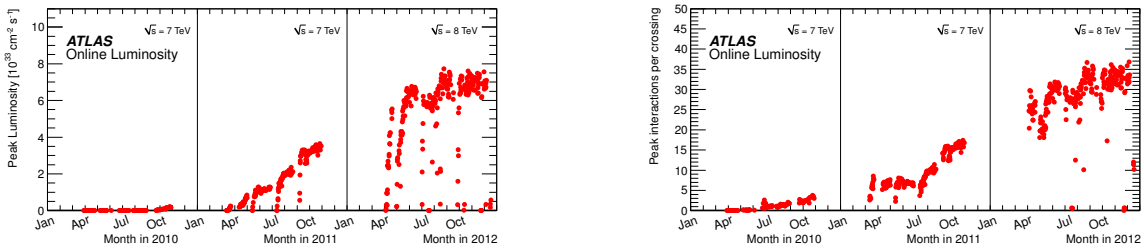

(a) **(b)**

Figure 2.5: (a) The peak instantaneous luminosity delivered to ATLAS per day versus time during the proton-proton runs of 2010, 2011 and 2012. (b) The maximum mean number of events per beam crossing (pile-up) versus day during the proton-proton runs of 2010, 2011 and 2012. This version shows the average value for all bunch crossings in a given lumiblock interval.

2.1.3 Data taking conditions in 2011 and 2012 (proton-proton runs)

During 2010 and 2011 [73], the LHC has collided proton beams at $\sqrt{s}$=7 TeV reaching a peak instantaneous luminosity of 3.65 10^{33}cm^{-2}s^{-1} and delivering an integrated luminosity of 5.6 fb^{-1}. In 2012, the LHC has increased its center-of-mass-energy from 7 to 8 TeV and the peak luminosity grew to 7.73 10^{33}cm^{-2}s^{-1}, the total integrated luminosity is 22.8 fb^{-1}. Figure 2.4 illustrates the behaviour of the integrated luminosity delivered by the LHC and recorded by the ATLAS experiment as a function of time in 2011 and 2012.

The recorded luminosity reflects the data quality inefficiencies as well as the inefficiencies of the *warm-start*: as soon as the stable beam flag is raised, the tracking detectors (Section 2.4) undergo a ramp of the high-voltage that may provoke a tiny timing-latency resulting in unavailability of data recording. The number of pile-up is directly proportional to the instantaneous luminosity and inversely proportional to f_{rev} as in (2.2). Figure 2.5 reports the distribution of the peak luminosity as a function of the data taking time, both at 7 and 8 TeV and the peak pile-up versus time during the proton-proton runs in 2010, 2011 and 2012. This distribution shows the average value for all

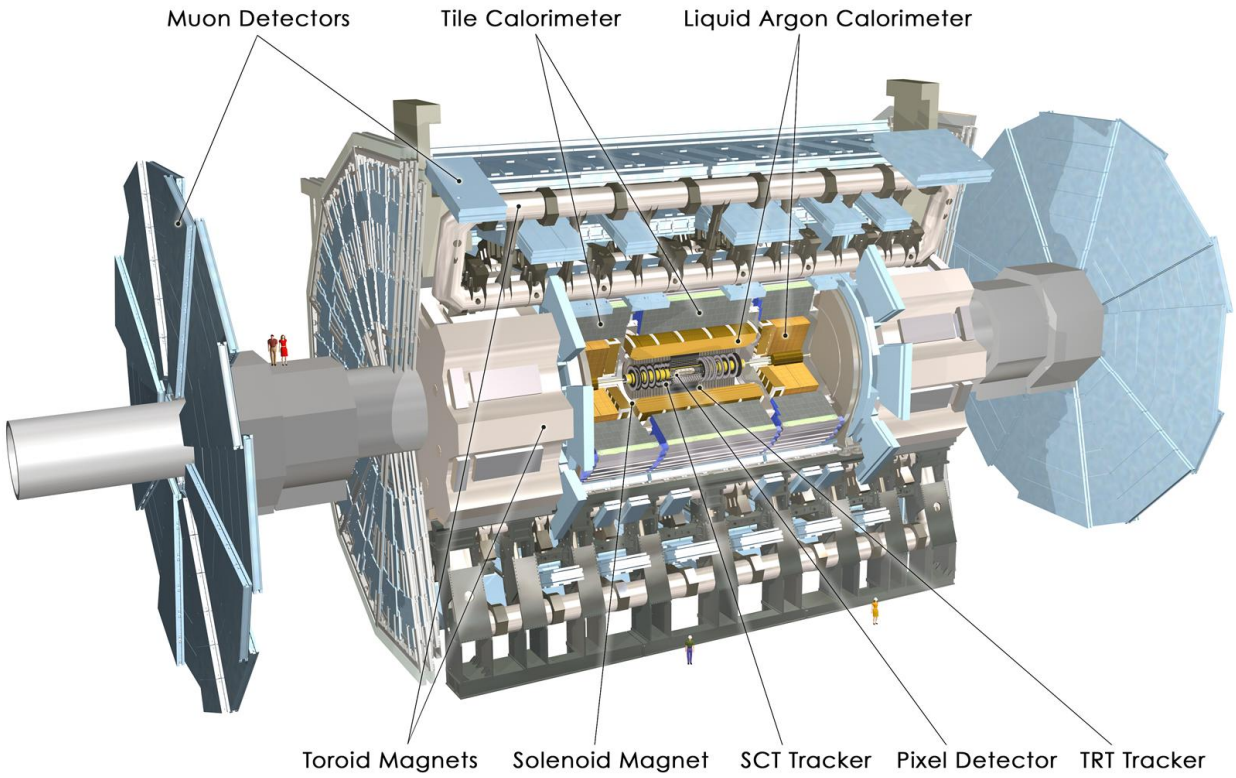

Figure 2.6: Schematic layout of the ATLAS experiment.

bunch crossings in a fixed integrated luminosity period (*lumiblock* interval). The collision data delivered in 2010, 2011 and 2012 with $\sqrt{s} = 7$ and $\sqrt{s} = 8$ TeV is referred to Run 1.

2.2 The ATLAS detector: general features and its coordinate system

The structure of the ATLAS detector [63] (Figure 2.6) is typical of a multi-purpose experiment situated at a collider. It is composed of the *barrel*, a cylindrical section around the beam axis whose length is 21 m and radius $\sim$ 11 m and two *end-caps* housed in the detector extremity.
The ATLAS subdetectors are listed below. They will be detailed later in this Chapter.

- an Inner Detector (*tracker*) which measures the trajectory of a charged particle under the presence of the magnetic field, as well as the primary and secondary interaction vertices, close to the interaction point (Section 2.4);
- an Electromagnetic Calorimeter for the detection of electromagnetic showers induced by electrons and photons (Section 2.5.1);
- a Hadronic Calorimeter for the study of hadronic showers and jet kinematical structures (Section 2.5.2);
- a Muon Spectrometer that provides the tracking of muons (Section 2.6);

Component	Radius [m]	Length [m]	η-coverage
barrel muon spectrometer	11	26	$\|\eta\|$ <1.4
end-cap muon spectrometer	11	2.8	1.1< $\|\eta\|$ <2.8
barrel hadronic calorimeter	4.25	12.2	$\|\eta\|$ <1.0
end-cap hadronic calorimeter	2.25	2.25	1.5< $\|\eta\|$ <3.2
barrel electromagnetic calorimeter	2.25	6.42	$\|\eta\|$ <1.4
end-cap electromagnetic calorimeter	2.25	0.63	1.4< $\|\eta\|$ <3.2
barrel + end-cap inner detector	1.15	6.8	1.4< $\|\eta\|$ <2.4

Table 2.2: Dimensions of the ATLAS sub-detectors and η-coverage.

- a system of *solenoid* and *toroidal* magnets (Section 2.3) generating strong magnetic field allowing charged particles in the ID and muon trajectories in the spectrometer to bend.

The reference frame defines a right-handed coordinate system with the x-axis pointing towards the centre of the LHC ring, the z-axis along the beam line and the y-axis on the vertical direction. Cylindrical coordinates are also employed: ϕ is the azimuthal angle and θ is the polar angle measured with respect to the positive z axis. Be a particle of energy E and momentum $\vec{p}$. By defining $\vec{p_L}$ as the longitudinal component of the momentum $\vec{p}$, the quantity *rapidity* is: $y \doteq \frac{1}{2}\log\frac{E+p_L}{E-p_L}$. In the ultra-relativistic limit (E$\gg$m) the expression above is approximated by another quantity, the *pseudorapidity*, η:

$$\eta = -\log(\tan(\frac{\theta}{2})). \tag{2.4}$$

Another useful variable of ATLAS analyses is the angular separation of tracks in the η-ϕ plane:

$$\Delta R = \sqrt{\Delta\eta^2 + \Delta\phi^2}. \tag{2.5}$$

ΔR is relativistically invariant under boost transformations along the z axis.
The dimensions (radius and length) of the various ATLAS sub-detectors (both for barrel and end-cap) and their coverage in pseudorapidity are summarised in Table 2.2.

2.3 The Magnetic field

In order to measure the momenta and the charges of the particles, the magnetic field permeates the volume of the inner detector and the muon spectrometer. Figure 2.7 (a) displays the magnetic system and its spatial geometry [74]: it is constituted of a central superconductive solenoid [75] for the inner detector and three superconductive air-core toroids [76] [77].

- **Central Solenoid**. It consists of one coil with 1173 turns fully surrounding the Inner Detector. The central solenoid is designed to provide for the Inner Detector an axial magnetic field of 2 T. Its axis coincides with the beam axis. The axial length of the solenoid is 5.3 m and the circulating current is 7.73 kA. It has been conceived to minimise the presence of dead material in front of the calorimeter, therefore its total thickness accounts for ~ 0.66 X_0.

- **Toroid magnets**. The barrel toroid consists of eight superconductive coils of 35.3 m length and 5.4 m width, each with 120 (barrel) and 116 (end-cap) turns inside an individual cryostat, located around the calorimeter. The toroid magnets generate a toroidal magnetic field configuration for the Muon Spectrometer. The advantage of a toroidal magnetic field is that its direction is almost perpendicular to the direction of flight of the particles and the particle

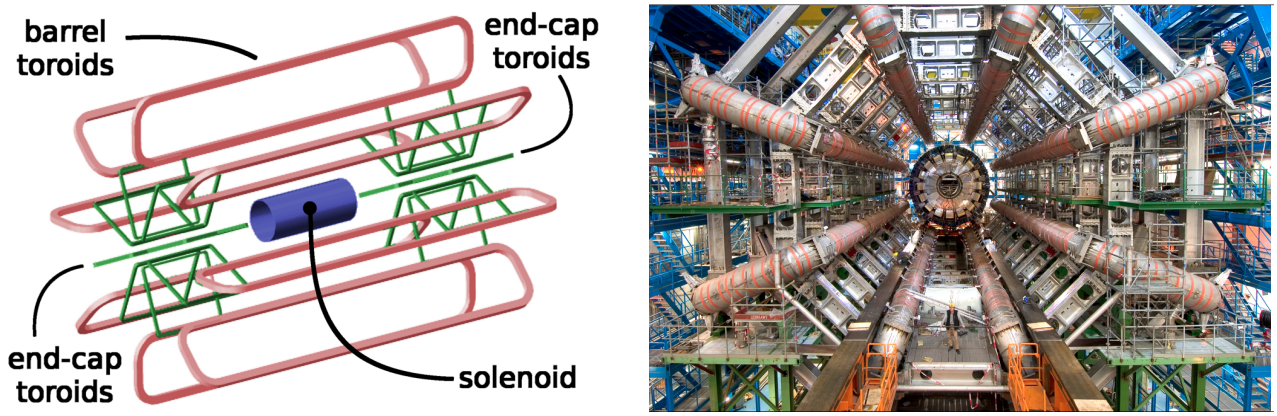

(a) (b)

Figure 2.7: (a) Geometry of the coils comprising the solenoid, the barrel and end-caps toroids. (b) Frontal view of the barrel toroid operating inside the muon system.

trajectory under the presence of the field is deviated in η. Its magnetic field is generated by a current $\sim$ 22.3 kA, the peak field is of the order of 3.9 T in the barrel (η <1.4) and 4.1 T in the end-caps (1.6< η <2.7) where the two toroids are positioned beyond the forward hadronic calorimeter. In the transition region between barrel and end-caps, the contribution of the magnetic field is characterised by a complex structure and its magnitude is weaker than the one in the barrel or in the end-caps. Figure 2.7 (b) shows a frontal view of the barrel toroid operating inside the muon system.

The field integral over the track length within the tracking volume, I, represents a measurement of the bending power of the field; its typical value for the toroidal magnets is $\sim$ 3 T·m in the barrel and 6 T·m in the end-caps regions, while the solenoidal fields provides a bending power of the order 2.1 T·m.

2.4 The Inner Detector

The ATLAS Inner Detector (ID) covers the region $|\eta|$ <2.5, being 6.2 m long with a total radius of 2.1 m. Its main objectives are given below:

- precise measurement of the transverse momentum charge and impact parameter of the charged particle traversing it;
- reconstruction of the primary and secondary vertices;
- discrimination between electrons and photons;
- tagging of the b-jets and the τ leptons.

The design ID momentum resolution is:

$$\frac{\sigma(p_T)}{p_T} = 0.05\% \cdot p_T \oplus 1\% \tag{2.6}$$

for tracks with $p_T > 500$ MeV and $|\eta|$ <2.5. The first term denotes the intrinsic resolution, dominant in the high p_T regime, while the second term comes from multiple scattering and contributes mostly at low p_T .

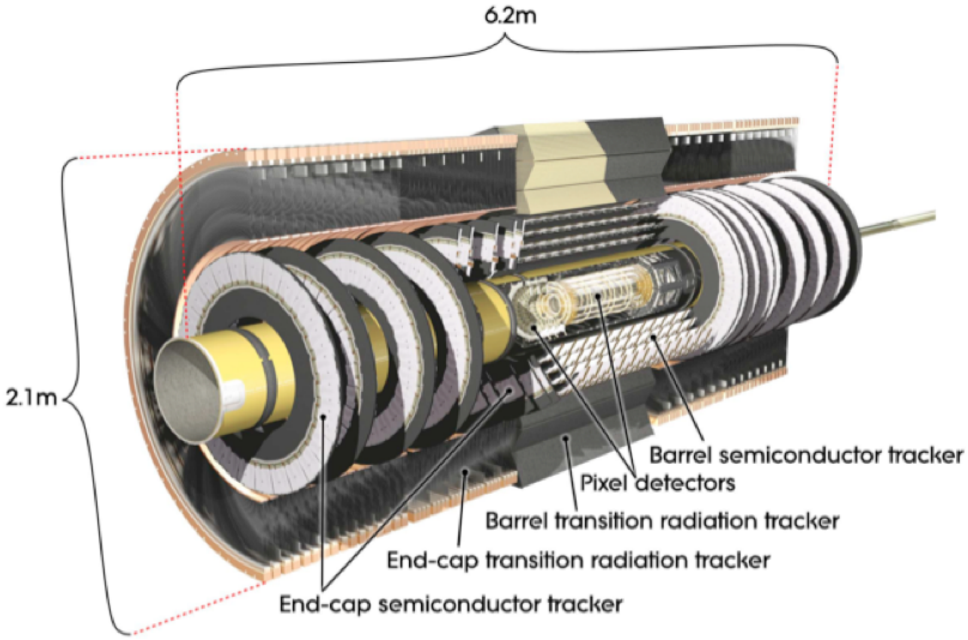

Figure 2.8: Graphic representation of the ATLAS ID and sub-detectors.

The graphic representation of the Inner Detector (ID) [78] is shown in Figure 2.8. Figure 2.9 reports a detailed view of the modules housed in the barrel (a) and in the end-caps (b) when traversed by a 10 GeV particles at η=0.3, 1.4 and 2.2. The barrel region of the sub-detector layers is shaped in cylinders around the beam axis, whereas the end-cap region houses concentric disks parallel to the transverse plane so that the $|\eta|$ coverage is maximised while minimising the detector volume.

The Inner Detector combines high-resolution detectors in its internal region with other tracking systems in its outermost layers. The structure is fully encompassed inside the internal solenoid (Section 2.3), providing a nominal magnetic field of about 2 Tesla along the beam axis, z. Given the solenoidal magnetic field, the measurement is performed on the R-ϕ plane: each track traverses three pixel layers and four semiconductor tracker layers providing few but high-precision hits and it crosses a transition radiation tracker (TRT) in the external region of the detector where it produces a very significant number of hits ($\sim$ 36) with a slightly worse precision.

The close localisation of the Inner Detector with respect to the interaction point also implies that this sub-detector receives a significant amount of radiation during data-taking. Although this issue has been fully addressed by providing a cooling system of the pixel and micro-strips at about -7 C to alleviate the radiation effects on the electronics, its intrinsic performance degrades with time and luminosity. For this reason, a new internal layer is inserted in view of the Run 2 data-taking (*Insertable B-Layer*, IBL [79]) aiming at improving *b-tagging* efficiency and the identification of the primary and secondary vertices. The specific aspects of the sub-detectors will be illustrated in the following paragraphs.

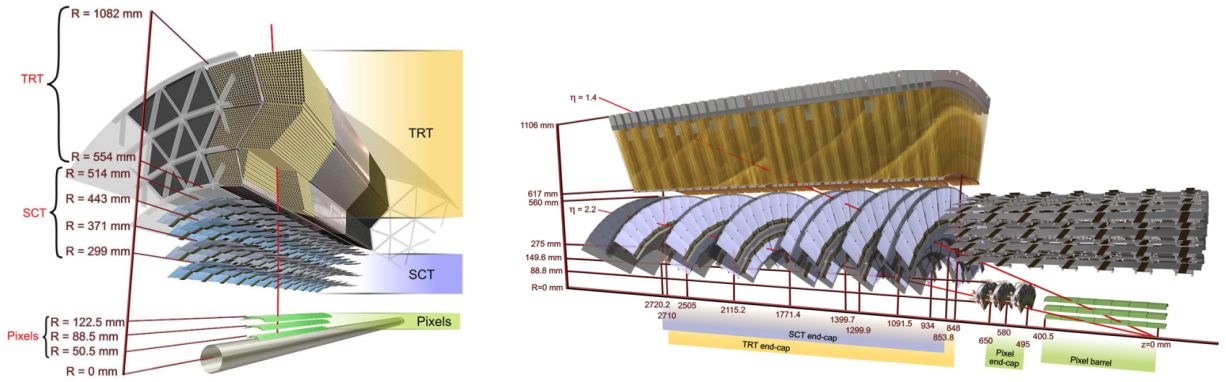

(a) **(b)**

Figure 2.9: Pictorial sketch and localisation of the different modules comprised in the Inner Detector in the barrel (a) and in the end-caps (b) when traversed by a 10 GeV charged particles (red lines) for different pseudorapidity values ($|\eta|$=0.3, 1.4, 2.2).

2.4.1 Silicon Pixel Detector

The *Silicon Pixel* detector [80] is designed to perform very high precision measurements close to the interaction point. This system contributes to the vertex and the impact parameter determination and is therefore employed for the search of displaced vertices involving long lived particles such as B-hadrons. The pixel detector system consists of 80 million sensors placed at a mutual distance of 50 μm in the R-ϕ plane and 300 μm in z. They are located in three cylindrical structures whose radius is respectively 4 cm, 11 cm and 14 cm in addition to five disks (radius between 9 and 15 cm) for each side covering the acceptance in the two end-caps. The innermost layer is called *b-layer*: its distance to the beam pipe is $\sim$ 5 cm and it plays an essential role in the reconstruction of secondary vertices and in the jet *b-tagging*.

This detector is made of approximately 1500 distinct modules in the cylinders and 700 modules in the disks. The typical spatial resolution in the R-ϕ plane is $\sigma(R-\phi) \sim 12$ μm and along the z axis, $\sigma(z) \sim 66$ μm for the barrel and $\sigma(z) \sim 77$ μm for the external disks (end-cap regions). The thickness of each layer is expected to be about 2.5% of a radiation length at normal incidence. Typically three pixel layers are crossed by each track.

In order to guarantee good performance of the pixel system against the radiation damage provoked by the beam collisions, the whole sub-detector is cooled down to approximately -10 C.

2.4.2 Semi Conductor Tracker

fibres The SCT (Semi Conductor Tracker) [81] system is designed to provide eight precision measurements for each track in the intermediate zone (299 mm $< r <$ 514 mm) contributing to the calculation of transverse momenta, vertices as well as trajectory recognition of charged particles in the region $|\eta|$ <2.5. The technology employed for the SCT sub-detector is quite similar to the one of the pixels (Section 2.4.1) but the surface is segmented in stripes rather than pixels in order to reduce the global number of readout channels. As already mentioned, in the cylindrical area, eight layers of silicium *micro-strips* are accommodated in the R-ϕ plane. There are 768 stripes with mutual distance of 80 μm. Each SCT module is composed of two grouped wafers pairs placed back-to-back, put together with an opening angle of $\pm$ 20 mrad with respect to their geometric centre. Each detection plane is segmented in 770 strips, 12 cm long and 80 μm large. The spatial resolutions in

the R-ϕ plane is $\sim$ 16 μm and on the z axis $\sim$ 580 μm and approximately 8 hits are collected in the SCT modules. The cylindrical modules in the barrel are mounted on four cylinders made of carbon fibres whilst the modules in the end-caps are assembled on nine external disks. The electronic signals are amplified and treated with discriminating filters; the ones above a certain threshold are recorded in a transient buffer. The SCT system contains an overall number of approximately 6.2 million readout channels for a total surface of about 63 m^2.

2.4.3 Transition Radiation Tracker

The Transition Radiation Tracker (TRT) [82] is based on cylindrical gas detectors. The main scope of this sub-detector is to add to the tracking information provided by the innermost silicon detectors (pixels and SCT) a large number of hits that are inputs to the pattern recognition procedure (Section 3.1). Furthermore, the TRT plays a role in the electron identification and the discrimination between electrons and light hadrons such as pions and kaons. This sub-detector is based on the

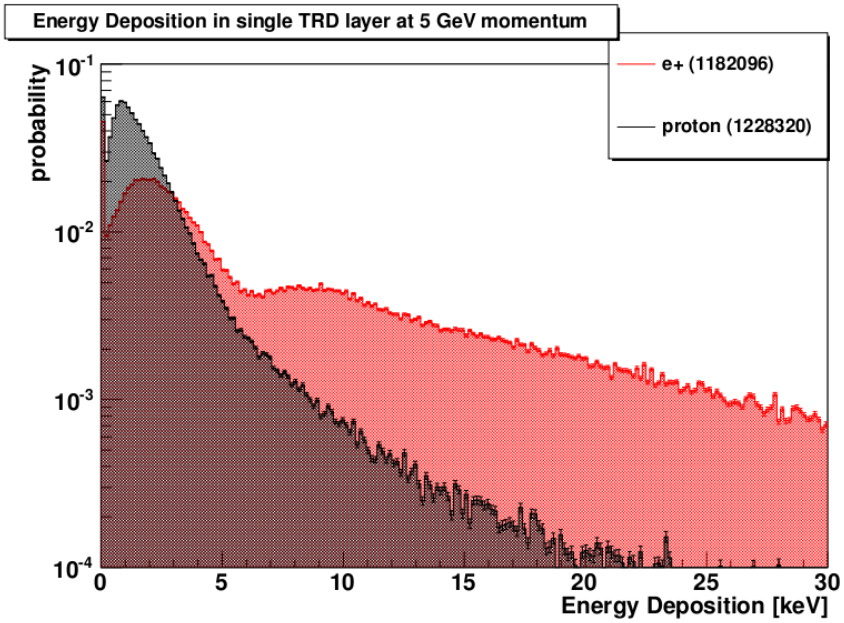

Figure 2.10: Histogram of energy entries in a layer of the TRT for 5 GeV particles. The proton spectrum is shown in black and the positron spectrum in red.

use of straw detectors. Each straw is 4 mm in diameter and equipped with a 30 μm diameter gold-plated wire. The maximum straw length is 144 cm in the barrel containing approximately 50000 straws located along the z axis. The end-caps contain 320000 radial straws measuring 37 cm with the readout at the outer radius. The straw tubes are filled with gas alternated with polypropylene fibres and foils. In the internal surface of the straws, aluminium acts as the cathode and the central gold-plated tungsten wire of 30 μm diameter is the anode. The gas admixture filling the straw is 70% Xe, 27% CO_2 and 3% O_2 in a volume of about 3 m^2. Charged particles typically cross 35 to 40 straws leaving hits with a resolution of $\sim$ 130 μm in the R$-\phi$ plane, less accurate than the one of pixel and SCT detailed in Sections 2.4.1 and 2.4.2.

When a relativistic particle traverses the TRT, it emits radiation (*transition* radiation) when crossing the interface surface between media with different dielectric constants, namely air and polypropylene. Provided that the transition radiation energy emitted by a particle is proportional to its

Lorentz factor, γ, the TRT is able to operate with two thresholds that are visible in Figure 2.10: the low threshold (energy below 0.5 keV) signals the passage of a generic charged particle in the detector, while the high threshold (above 6 keV) indicates the presence of a particle with a very large Lorentz factor. Accordingly, the TRT can discriminate between electrons and hadrons: since the Lorentz factor γ for an electron is 270 larger than the one of a pion for a fixed momentum, the high threshold regime is more likely to be triggered by electrons.

The choice of Xenon in the admixture filling the straws stems from the fact that radiated photons are absorbed by the gas (photoelectric effect) proportionally to Z^5 where Z is the atomic number of the admixture. Thus, the Xenon, characterised by a very large atomic number (Z=54) is adopted to increase the absorption of TR photons.

As reported in Figure 3.2 for the electromagnetic, and analogously for the hadronic interactions in Figure 2.11, the incoming particles cross several radiation lengths before the Calorimeter. The distribution of the material is plotted in unity of radiation X_0, Figure 3.3, and interaction lengths λ, Figure 2.11, and is strongly dependent on the $|\eta|$ of the probing particle. In the central region, the TRT volume represents the major contribution to the total material as well as the services referring to the external structures installed inside the tracker volume such as cables and cooling systems.

The main consequences of the particle interaction with matter in front of the calorimeter are the presence of photon conversions in electron pairs originated inside the inner detector volume and electron energy loss due to bremsstrahlung instances or multiple scattering.

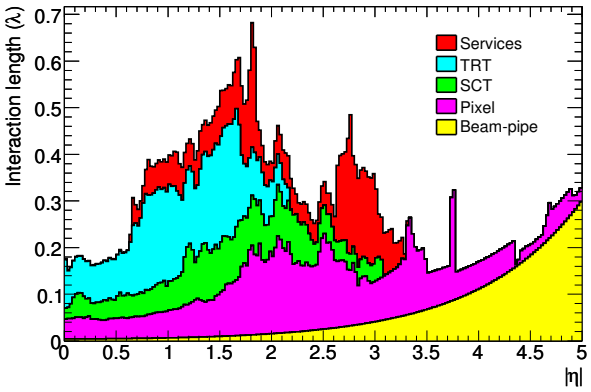

Figure 2.11: Material distribution described by the interaction length λ for hadronic interactions at the exit of the ID envelope including the services. The distribution is shown as a function of η and averaged over ϕ. The breakdown indicates the contributions of external services and individual sub-detectors.

2.5 The calorimeters

The ATLAS calorimeters are placed between the Inner Detector and the Muon Spectrometer covering the pseudorapidity range $|\eta| < 4.9$. The main purpose of calorimetry in experiments at hadron colliders is the accurate measurement of the energy of charged and neutral particles, namely electrons and photons in the electromagnetic calorimeter and hadronic jets in the hadronic calorimeter as well as the transverse missing energy, E_T. More information on the reconstruction and identification of these particles will be given in Chapter 3.

Over the region matched to the Inner Detector, the fine granularity of the electromagnetic calorimeter is ideal for precision measurements and pattern recognition whereas the coarser granularity of the hadronic calorimeter is useful to match identification and reconstruction requirements for jets.

The ATLAS calorimeter is composed of the following parts as shown in Figure 2.12:

- an electromagnetic liquid-argon calorimeter covering the pseudorapidity region $|\eta|$ <1.475 for the barrel (EMB) and 1.375< $|\eta|$ <3.2 for the two end-caps (EMEC);
- an hadronic calorimeter composed of a barrel in the acceptance $|\eta|$ <1.7 (TILE) and two end-caps in 1.5< $|\eta|$ <3.2 (HEC).
- a forward calorimeter - 3.2< $|\eta|$ <4.9 (FCAL).

The ATLAS electromagnetic and hadronic calorimeters are *sampling* calorimeters; the total thickness of the electromagnetic and hadronic calorimeter is approximately 24 X_0 in the barrel and 26 X_0 in the end-caps to achieve a sufficient containment of electromagnetic and hadronic showers and consequently limit the shower leakage inside the Muon Spectrometer (*punch-through*). Another feature of the ATLAS calorimeter is the *non-compensating* behaviour: the energy response to electromagnetic particles differs from hadronic inputs. Lastly, the calorimeters play an important role

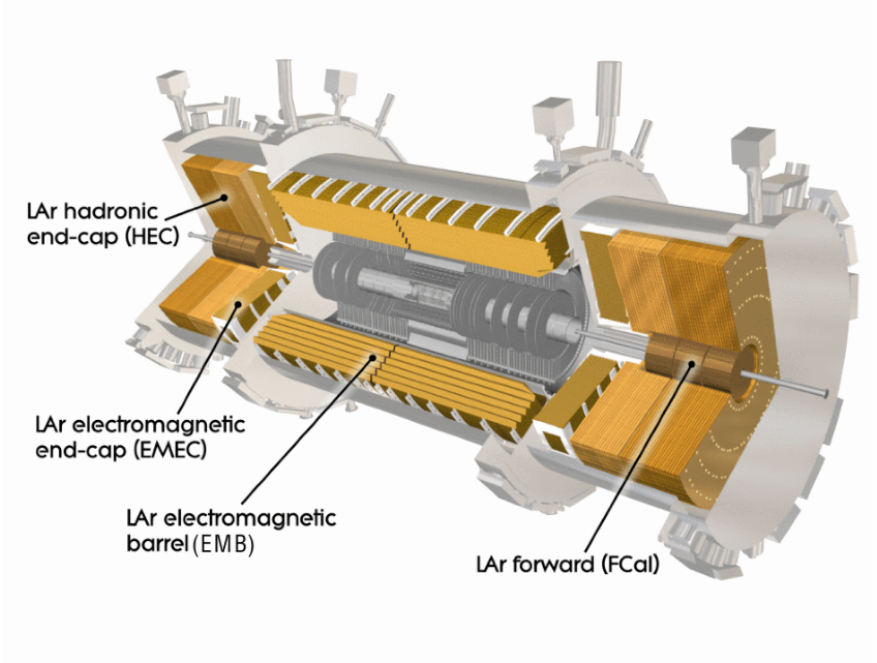

Figure 2.12: Pictorial representation of the ATLAS electromagnetic and hadronic calorimeters.

in the trigger system as explained in the Sections 2.8 and 3.3.1.

The electromagnetic calorimetry is based on Liquid Argon technology, while hadronic calorimetry uses scintillating tiles technology and its main aspects will be expanded in Sections 2.5.1 and 2.5.2.

2.5.1 Electromagnetic calorimeter

Liquid Argon calorimeter

The electromagnetic calorimeter [83] is constituted of lead absorbers, whose high density helps to develop compact electromagnetic showers inside the calorimeter volume, and Liquid Argon (LAr) with *accordion* geometry placed inside a cylindric cryostat surrounding the cavity where the detector is housed.

As shown in Figure 2.13, there are three longitudinal samplings for $|\eta|$ <2.5 and two for 2.5< $|\eta|$ <3.2. The logic of this particular geometry is that it allows rejection of π_0 and jet background

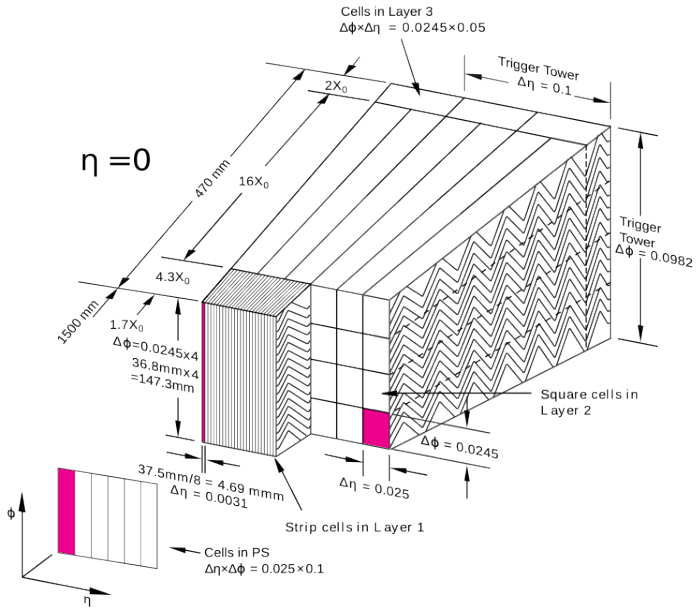

Figure 2.13: Graphic representation of the electromagnetic calorimeter and its modularity.

for physics involving individual photons and measurement of the electromagnetic shower direction (in combination with the second sampling). This geometry also ensures a complete ϕ symmetry. The active depth of the three samplings are about 6 X_0, 16 X_0 and 3 X_0 respectively at η=0. The modules are equipped with a very high granularity in the $\Delta\eta$-$\Delta\phi$ phase-space: 0.03×0.1 in the first sampling, 0.025×0.025 in the second sampling and 0.05×0.025 in the third sampling. In the range $|\eta|$ <1.8, the calorimeter is preceded by a *presampler* employed to recover the energy lost in the upstream materials (Inner Detector, superconductive coils, cryostat). Its granularity in $\Delta\eta$-$\Delta\phi$ is 0.025×0.1. The depth of the presampler is 11 mm of Liquid Argon in the barrel and 4 mm in the end-caps, contributing to 0.08 X_0 and 0.03 X_0 respectively. The calorimeter barrel is formed by two ϕ-segmented cylinders whose length is $\sim$ 3.2 m, internal radius $\sim$ 1.4 m and external radius $\sim$ 2 m. Each end-cap is divided into two coaxial wheels: an outer wheel and an inner wheel - the internal radius of the inner wheel is $\sim$ 33 cm and the external radius of the outer wheel measures $\sim$ 210 cm.

The active medium is Liquid Argon and the current is measured by the electron drift between anode and cathode. The structure of the detector is displayed in Figure 2.14. Each layer in lead is 1.53 mm thick in the barrel region $|\eta|$ <0.8 and 1.1 mm for $|\eta|$ >0.8. In the end-cap, its thickness reaches 1.7 mm ($|\eta|$ <2.5) and 2.2 mm ($|\eta|$ >2.5). The Liquid Argon gap is 2.1 mm thick in the

barrel and from 0.9 to 3.8 mm in the end-caps. The electrodes are mutually separated by insulating kapton foils and organised with a honeycomb structure. The distinct accordion geometry of the LAr calorimeter guarantees a full azimuthal coverage and a fine segmentation in η.

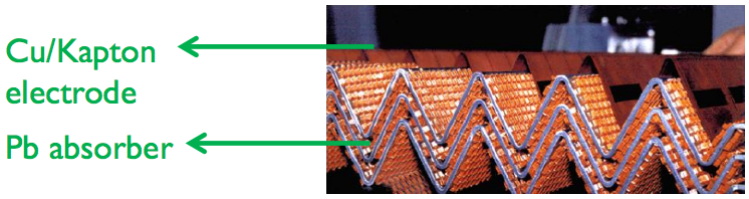

Figure 2.14: Accordion geometry of the electromagnetic calorimeter. Zoom on the internal structure: lead absorbers and LAr gaps representing the active medium are separated by insulating kapton foils.

The energy resolution of the electromagnetic calorimeter is given by the sum in quadrature of three independent terms:

$$\frac{\sigma(E)}{E} = \frac{a}{\sqrt{E}} \oplus \frac{b}{E} \oplus c. \tag{2.7}$$

a is the stochastic term that describes the statistical fluctuations of the fraction of the shower energy deposited in the sampling medium (Liquid Argon) and the fraction deposited in the absorber (lead). The value for this contribution at η=0 is $\frac{10\%}{\sqrt{E}}$. b is the noise term that is related to the electronic noise and the out-of-time pile-up. This term is significantly contributing to equation (2.7) only in the low energy spectrum. c is the constant term accounting for calibration-related effects, mechanical and electrical inhomogeneities, energy loss due to non-instrumented regions. The goal is to obtain a factor $c \sim 0.7\%$. Figure 2.15 shows the distribution of the energy resolution (2.7) and its dependence on the pseudorapidity region. Additionally, thanks to its longitudinal segmentation, the angular resolution of the electromagnetic calorimeter is $\sim$ 40 mrad, good to perform discrimination on the electromagnetic shower trajectory.

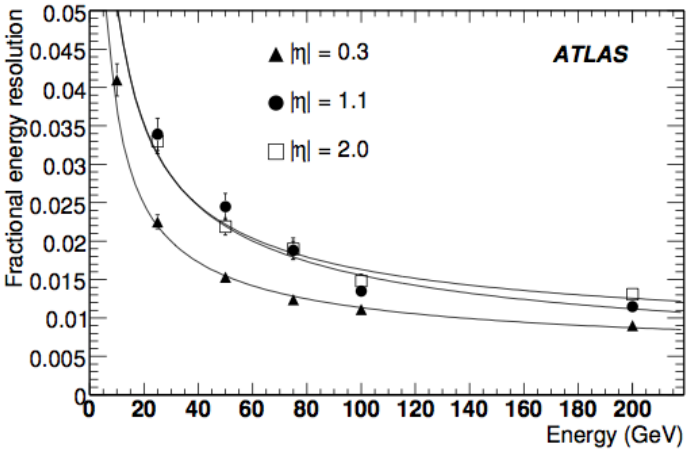

Figure 2.15: Energy resolution (2.7) as a function of the energy E of the incoming particle for different η regions.

Electromagnetic Forward calorimeter

In the forward region (3.1< $|\eta|$ <4.9), the electromagnetic calorimeter is constructed using another type of LAr calorimeter. The forward calorimeter consists of copper rods parallel to the beam axis inside an outer tube with 250 mm Liquid Argon gap in between. The matrix in which both the rods and the tubes are inserted is made of copper too. As for the Forward Hadronic Calorimeter detailed in Section 2.5.2, this sub-detector has to cope with high radiation levels. The thickness of the Forward Calorimeter is approximately 28 X_0 at η=0. The $\Delta\eta$-$\Delta\phi$ granularity is 0.1×0.1 for 1024 readout channels per end-cap.

2.5.2 Hadronic calorimeter

The objective of the hadronic calorimeter is the measurement of jet energy and the determination of transverse missing momentum. A good measurement of jet energy and its properties is achieved with a lateral segmentation; furthermore the calorimeter must be hermetic, i.e. have as complete coverage as possible to detect all energy emitted from the interaction point, thereby correctly infer missing transverse energy deposited by neutrinos (Section 3.6). The hadronic calorimeters covers the region $|\eta|$<3.2 with different techniques according to the operating region. In order to ensure the containment of the hadronic showers and to reduce the punch-through instances inside the Muon Spectrometer, the thickness of the system is about 8 λ_0. It is composed of four parts:

- a central barrel made of scintillating Tiles in the region $|\eta|$ <1;
- two scintillating Tile end-caps covering the pseudorapidity region 0.8< $|\eta|$ <1.7;
- two end-caps with Liquid Argon (1.5< $|\eta|$ <3.2);
- a forward calorimeter operating in the region 3.1< $|\eta|$ <4.9.

The overall energy resolution of the barrel/end-cap system for jets is:

$$\frac{\sigma(E)}{E} = \frac{50\%}{\sqrt{E}} \oplus 3\% \tag{2.8}$$

while for the forward detector:

$$\frac{\sigma(E)}{E} = \frac{100\%}{\sqrt{E}} \oplus 10\%. \tag{2.9}$$

Hadronic Tile calorimeter

The Hadronic Tile calorimeter [84] is situated behind the electromagnetic calorimeter. It is a sampling calorimeter using steel as absorber material and *scintillating* tiles as active material. Both sides of the tiles are analysed by shifting fibres into two separate photomultipliers. The calorimeter is split in a Barrel ($|\eta|$ <1.0) with 3 sub-samplings featured by 0.1×0.1 granularity in $\Delta\eta \times \Delta\phi$ for the first and second sampling and 0.2×0.1 for the third sampling and 5760 readout channels and an Extended Barrel (0.8< $|\eta|$ <1.7) with the same number of samplings and granularity scheme of the Barrel and 1792 electronics channel. The three longitudinal layers are approximately 1.4, 4.0 and 1.8 interaction lengths at η=0. The internal and external radii are 2.28 m and 4.25 m respectively.

A graphic representation of the hadronic Tile calorimeter and a zoom of a single module are reported in Figure 2.16. The scintillating tiles are placed in planes orthogonal to the beam axis and staggered in depth simplifying the mechanical construction and the fibre routing. As soon as ionising particles traverse the detector, the tiles emit scintillation light that is collected by the wavelength-shifting

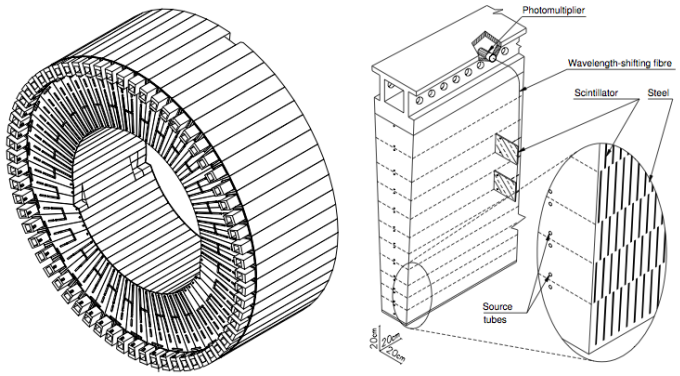

Figure 2.16: Graphic representation of the hadronic Tile calorimeter. The full sketch is shown on the left and the architecture of a single module is on the right.

fibre located on the sides of the modules. It then reaches the photomultipliers where it is amplified and sent to the readout electronics. Fibres are grouped together in calorimeter cells and analysed by the same photomultiplier. Light is collected on each side of each tile, hence a calorimeter cell is read by two different photomultipliers.

End-cap Hadronic calorimeter

In the end-cap region, the calorimeter uses Liquid Argon as active material and cooper plates as absorber. The geometry is composed by parallel planes, orthogonal to the beam axis. The external radius is 2.03 m. Both the hadronic end-cap and the forward calorimeters are integrated in the same cryostat housing also the electromagnetic end-caps. Each hadronic end-cap calorimeter consists of two independent wheels of equal diameter. The first wheel is built out of 25 mm copper plates, while the second one uses 50 mm plates; in both wheels the gap between consecutive copper plates is 8.5 mm, and is equipped with 3 electrodes that split it in 4 drift spaces of $\sim$ 1.8 mm each. The thickness of the active part of the end-cap calorimeter is $\sim$ 12 λ. The typical granularity in $\Delta\eta$-$\Delta\phi$ is 0.1$\times$0.1 for 1.5$<|\eta|<$2.5 and 0.2$\times$0.2 for 2.5$<|\eta|<$3.2 employing 3072 readout channels.

Forward Hadronic calorimeter

The forward calorimeter [85] (3.1$<|\eta|<$4.9) is a particularly challenging detector due to the high level flux of particles resulting in substantial radiation doses to which it is exposed. Its purpose is to cover the very forward region of the detector by ensuring a better hermeticity of the detector with clear advantages on the forward jet tagging and the determination of the missing transverse energy of the event. This detector is very dense since it accommodates 9 λ of material in a rather short longitudinal space. It incorporates three longitudinal sectors made of copper and tungsten. The active medium is Liquid Argon. The granularity of the Forward Calorimeter in $\Delta\eta$-$\Delta\phi$ is 0.2$\times$0.2 with 768 readout channels.

2.6 The Muon Spectrometer

Figure 2.17 shows the general layout with barrel chambers ($|\eta|<$1) arranged in three cylindrical layers and end-cap chambers (extending to $|\eta|$=2.7) mounted on wheels that are orthogonal to the

detector axis. The detector size is about 22 m in diameter and 44 m in length. The Muon Spectrometer is also equipped with an independent trigger system as studied in Section 3.4.1. Figure 2.18 reports a schematic view of the Muon Spectrometer in the $x-y$ (a) and $z-y$ (b) projections. As the magnetic field is toroidal, unlike the Inner Tracker where the precision coordinate was ϕ because of the solenoidal development of the field, here, the most accurate measurement is deployed along η. Tracks are deflected in the $R-z$ plane: four detection chambers are adopted for different goals, precision measurements (Section 2.6.1) and trigger (Section 2.6.2). The Muon Spectrometer sub-detectors are composed by precision and trigger chambers. The precision chambers are organised in three stations (Figure 2.18 (a)) whose radius is 5, 7.5 and 10 m respectively for the internal (*Inner*), median (*Middle*) and external station (*Outer*). The end-cap chambers cover the region $1< |\eta| <2.7$ and are organised in concentric disks with respect to the beam axis whose distance to the interaction point is 7.4, 10.8 and 21.5 m. The *Monitored Drift Tubes* (MDT) covers the large majority of the η range. In the forward region and close to the interaction point in the Inner station, the *Cathode Strip Chambers* (CSC) guarantee a fine granularity.

The trigger system (Section 3.4.1) sketched in Figure 3.8 selects muons in a large momentum range and is based on the search of coincident hits in the $\eta-\phi$ plane. In the barrel, *Resistive Plate Chambers* (RPC) are employed, while *Thin Gap Chambers* (TGC) are used in the end-caps. Moreover, having to identify the reference bunch-crossing, the trigger chambers carry an excellent timing resolution. The parametrisation of muon momentum resolution will be addressed in Section 3.4.3.

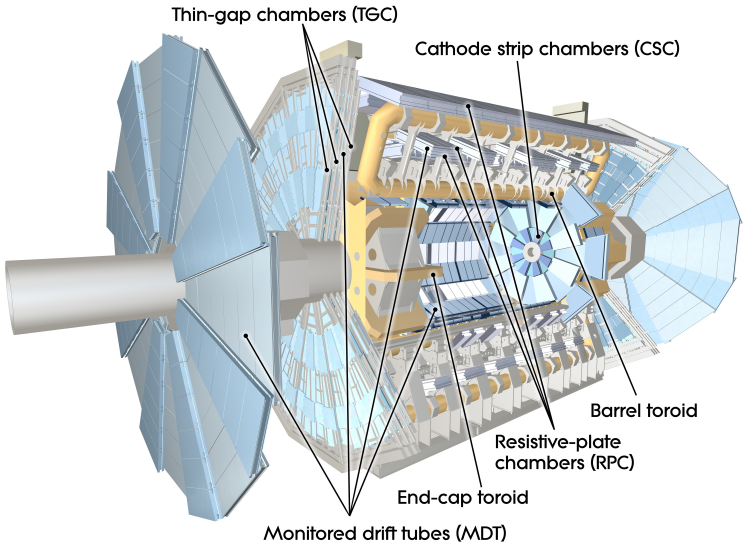

Figure 2.17: Computed-generated image of the ATLAS Muon Spectrometer and its sub-detectors.

2.6.1 The Precision chambers

MDT

The MDT sub-detectors are employed to reconstruct muon tracks. Each module has 3 layers of aluminium drift tubes on both sides for a total of 400000 tubes of 30 mm diameter each. Tubes are filled with an admixture of 93% Ar and 7% CO_2 gas with a pressure of 3 Bar. The tube acts as a cathode (Figure 2.19) and a gold-plated tungsten-rhenium wire, operating in a potential of 3080

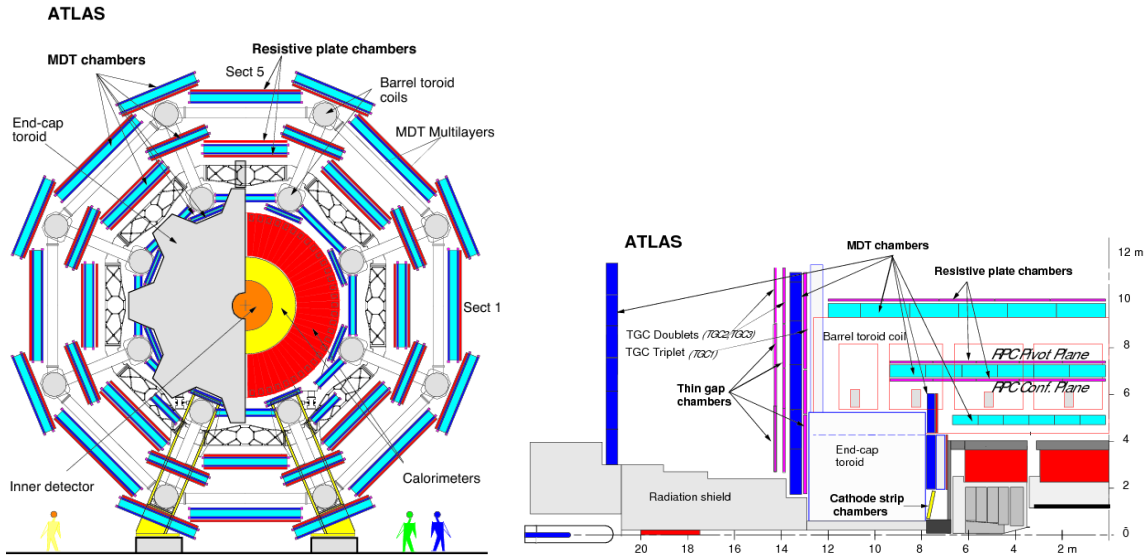

(a) **(b)**

Figure 2.18: Schematic view of the muon spectrometer in the $x-y$ (a) and $z-y$ (b) projections.

V, characterised by a diameter of 50 μm lying in the centre of the tube, works as the anode. The measurement of the time drift estimates the value of the drift path of the particle. Tubes function in proportional regime and the typical drift time is $\sim$ 700 ns. Tubes are also grouped in chambers that are superimposed one on top of each others: 1194 chambers are lodged in 5500 m^2 exploiting $3.7 \cdot 10^5$ readout channels. The track position in each chamber is calculated with a maximum resolution of 80 μm per tube and 30 μm per chamber.

CSC

The CSC are multiwire proportional chambers instrumented with a symmetric cell in the pseudo-rapidity range $2< |\eta| <2.7$ where the expected interaction rate is higher than 1150 Hz/cm^2. The selected gas admixture chosen for the chambers is 80% Ar, 20% CO_2. In each module (Figure 2.20), the anodes are rhenium-tungsten wires of 30 μm diameter operating at 1900 V and set parallel to each other. The cathode planes are segmented into strips. The typical drift time is approximately 30 ns, well within the timing of bunch-crossing occurrences at the LHC, while the spatial resolution is 60 μm.

2.6.2 The trigger chambers

RPC

The technology employed for the barrel is based on Resistive Plate Chambers (RPC) illustrated in Figure 2.21 (a). These are gas detectors composed by a pair of parallel layers made of bakelite whose typical resistivity is ρ_B=2×10^{10} Ω·cm, separated by a gap of 2 mm with insulating polycarbonate foils. The volume between the two layers is filled with a gas admixture of 94.7% tetrafluorethane, 5% isobutane and 0.3% sulfur hexafluorure. The external surfaces of the bakelite layers are covered by a thin foil of graphite dressed with an insulating film of 200 μm polyethylene (PET) . Both layers are connected to tension providing an electric field of $\sim$ 4.9 kV/mm.

The avalanche is generated by the primary ionisation created by the particle acceleration traversing

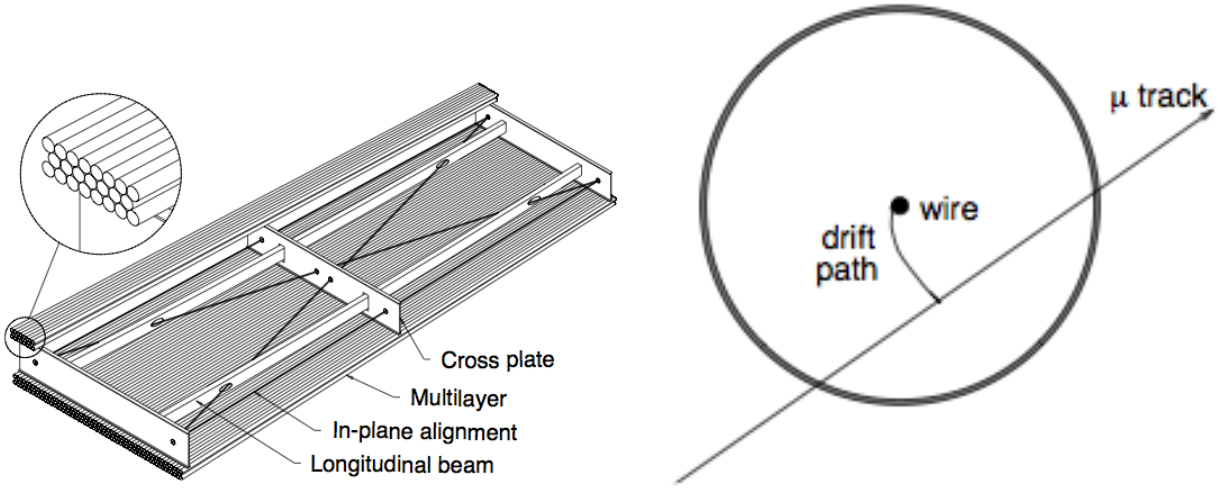

(a) (b)

Figure 2.19: (a) Schematic drawing of an MDT chamber where structural components are indicated. (b) Drift tube operation in a magnetic field with curved drift path.

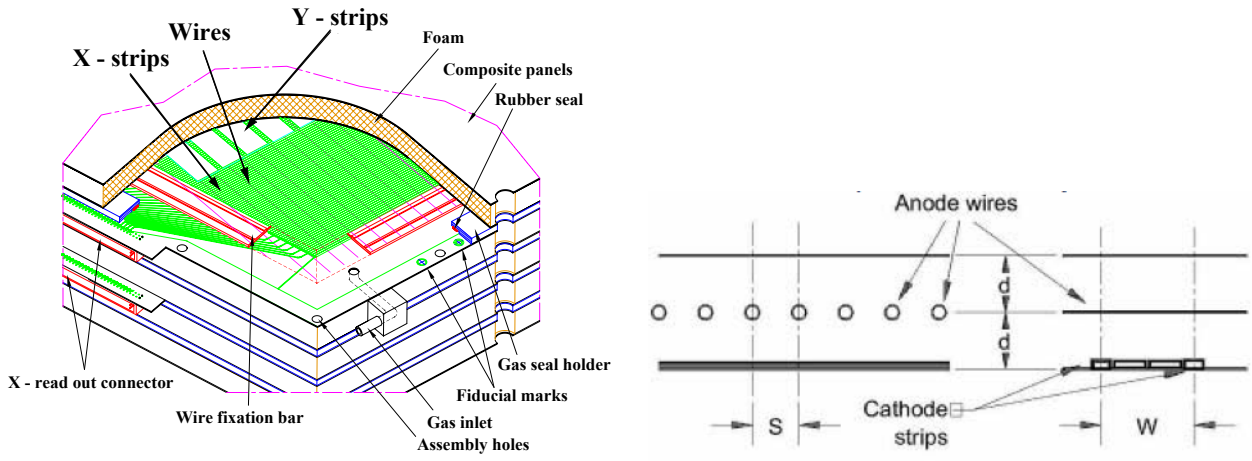

(a) (b)

Figure 2.20: (a) Schematic drawing of a CSC chamber where structural components are indicated. (b) Sketch of a CSC chamber.

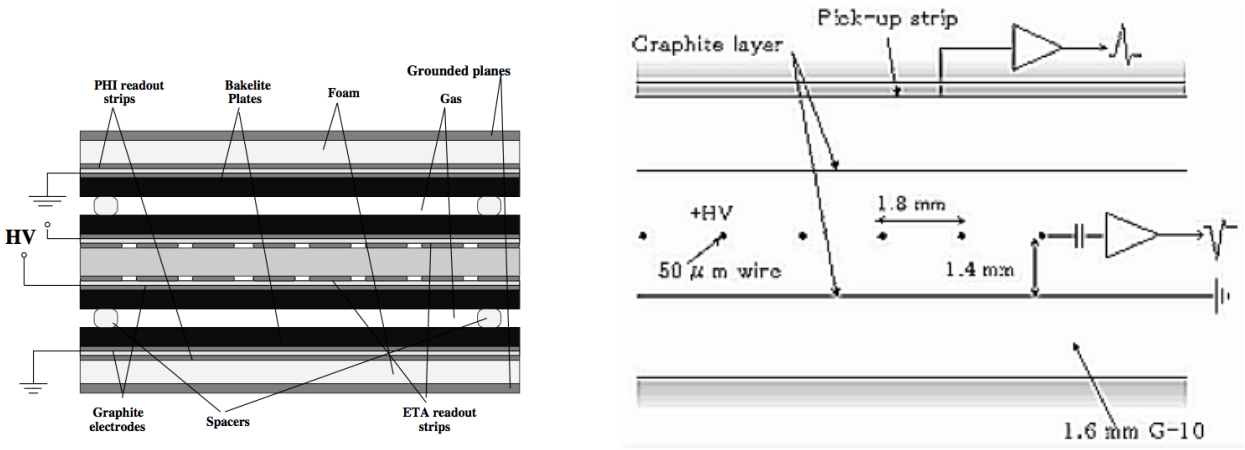

(a) **(b)**

Figure 2.21: Sketch of a RPC (a) and a TGC (b) chambers.

the gas under the external electric field. Each strip works as a transmission line allowing the signal to propagate in two opposite directions with respect to the detection points. The strips segmentation guarantees an approximate spatial resolution of 10 mm on each coordinate per chamber. The total number of RPC sub-detector is 1116 for a total surface of about 4000 m^2.

TGC

The Muon Spectrometer end-cap is instrumented with Thin Gap Chambers (TGC). These are multiwire proportional chambers, Figure 2.21 (b), whose structure is similar to the CSC. The main difference is that the anode-anode distance (2.8 mm) is greater than the cathode-anode one (1.4 mm). The anodes are oriented to measure η: they are 50 μm diameter wires encompassed by two graphite cathodes placed 1.4 mm far from the anodic plane. The detection volume is filled with a combination of 55% CO_2 and 45% n-pentane. Cathode planes are also divided into strips.
A mandatory requirement of a trigger chamber is an adequate temporal resolution for the identification of the bunch-crossing: the small gap between anode and cathode (1.4 mm) associated to a tension of 2900 V results in a quick drift time for particle traversing the TGCs leading to a good timing resolution of $\sim$ 4 ns.

2.7 Forward detectors

In addition to the main ATLAS detector, three instruments are located along the beam line at a very high distance from the interaction regions:

- LUCID (LUminosity measurement using Cherenkov Detector) [86] is composed of two modules around the beam pipe at $\sim$ 17 m far from the interaction point on both forward extremities of ATLAS. In each module, 16 photomultipliers are housed. The charged particles traversing the detector produce Cherenkov light detected by the photomultipliers.

- The detector ZDC (Zero Degree Calorimeter) [87] is located 140 m far from the interaction point, exactly on the proton beam axis and covers the region $|\eta|$ >8.3. It is composed of 2 quartz-tungsten samplings.

- ALFA (Absolute Luminosity For ATLAS) [88] is an ultra-small-angle detectors located at 240 m on both sides of ATLAS. It is built to calculate the amplitude of the elastic diffraction at small angle. It consists of so-called Roman Pots inserted above and below the beam axis, equipped with scintillating fibre detectors.

2.8 Trigger and Data Acquisition

The trigger system in ATLAS is articulated into the following three levels:

- first level trigger (L1);
- second level trigger (L2);
- event filter (EF).

The first level trigger is entirely based on hardware and electronics and is usually executed in the online mode while the second level trigger and the event filter step are mainly software-based.

The first level operates very basic cuts and produces an output rate of approximately 75 kHz, while the second level trigger further reduces the rate to $\sim$ 1 kHz. The L2 trigger processes events by focusing on the regions individuated at L1. The selection on each physical object is tightened by stringent cuts and the use of calculated physical quantities (isolation, impact parameter,...). The last step of the chain, the *event-filter*, is tuned for an approximate output rate of 300 Hz. The main features of the L1, L2 and EF triggers regarding electrons and muons will be presented in Sections 3.3.1 and 3.4.1.
The online L1 and L2 trigger time latencies are $\sim$ 2.1 μs and 40 ms respectively, the computing time for the trigger algorithms at the EF level is $\mathcal{O}(s)$, on average 4 s.

Depending on the trigger chains the particles are associated to, the events are added to different *streams*: the *EGamma* stream, involving electron and photon-like objects that fulfilled the specific trigger requirements on electrons and photons, the *Muons* and *JetTauEtMiss* streams. Other channels are employed to generate offline checks on data quality and consistency. A *debugging* stream is reserved for events that could not be evaluated in the time allotted to a trigger. Furthermore, streams called *express stream* and *calibration stream* contain an assortment of events which are deemed interesting or useful for calibration of the sub-detectors. Certain trigger items are also prescaled, meaning that only a given fraction of occurrences fulfilling the trigger criteria are recorded, to limit the bandwidth. Figure 2.22 sketches a view of the trigger and DAQ system in ATLAS.

2.9 Computing: the ATLAS Software and the Grid Infrastructure

A single data taking run in stable beam condition can last for hours. These runs are divided into luminosity blocks that are a few minutes long each. Luminosity blocks are the smallest units of data for an analysis in ATLAS; each block can be included or excluded in the final analysis using requirements on data-quality and integrity.

Data are primarily processed at CERN with the *Tier0* computing facilities before being distributed. CERN is responsible for the safe keeping of the raw data (millions of digital readings from across the detectors), and performs the first step at reconstructing the raw data into meaningful information. Tier 0 distributes (Large Computing Grid, LCG [89]) the raw data and the reconstructed output to

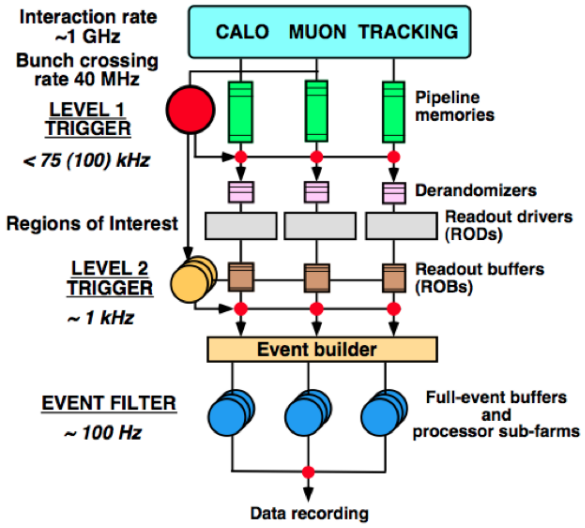

Figure 2.22: Trigger and DAQ systems developed in ATLAS

*Tier 1*s, and reprocesses data when the LHC is not running. Tier 1 consists of 13 computer centres large enough to store LHC data. They provide support for the Grid, and are responsible for storing a proportional share of raw and reconstructed data, as well as performing large-scale reprocessing and storing the corresponding output as well as distributing data to *Tier 2*s. The main role of this local computing system is to provide computing power and manage to data storage for the analysers.

ATLAS has developed different data treatments [89] to store information collected by the various sub-detectors to be re-extracted for the various physics analyses. As mentioned in Section 2.8, events passing the EF are addressed as raw-data. These data packets can reach a size of 1.6 Mb and are written in binary. *Event Summary Data* (ESD) store raw-data in a user-readable framework, ROOT. The typical size of these events is reduced to 500 kilobytes. From ESD, the data format is modified to the *Analysis Object Data* (AOD), directly derived from ESD with all the features of a C++-like object-oriented representation. The main scope of the ESD - AOD conversion is to limit the file size ($\sim$ 100 kilobytes). AOD are converted in *Derived Physics Data* (DPD). This data format is particularly suitable for final analyses because it can be easily accessed by standard tools (ROOT).

The main goal of the ATLAS offline software is to process data fulfilling trigger requirements, create simulation events for a given physics process, and produce objects that can be easily accessed by the analysers. In order to accomplish this, the ATHENA framework [90] was developed. The paradigm that lies beneath the concept of this framework is the creation of an object-oriented architecture where C++ is the implemented language for the software and PYTHON for the configuration files (*JobOptions*).

Chapter 3

Reconstruction and identification of the physics objects

Contents

Electrons and muons are employed to reconstruct the Higgs decay final state in the H→ ZZ→ 4l channel. Good identification and reconstruction performance is crucial for this search and it is achieved using the various features of the ATLAS detector systems. In this Chapter, the key points of the definition, reconstruction and identification of the physics objects used in the electron calibration procedure as well as in the Higgs mass and width analyses for the H →ZZ→4l channel developed in Chapters 4, 5, 6 and 7 (electrons, muon, jets and neutrinos) are reviewed.

3.1 Track reconstruction

A particle's trajectory inside a magnetic field can be defined by 5 parameters that exploit the full kinematic of the system and are calculated in the ATLAS coordinate system (Chapter 2):

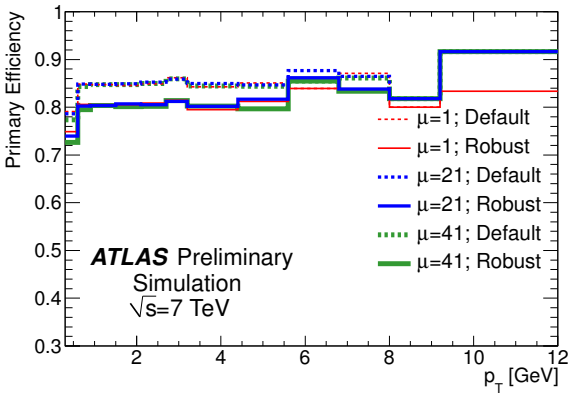

(a) Primary particles - p_T

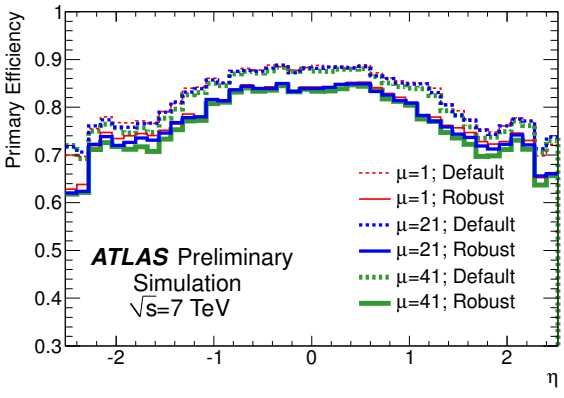

(b) Primary particles - η

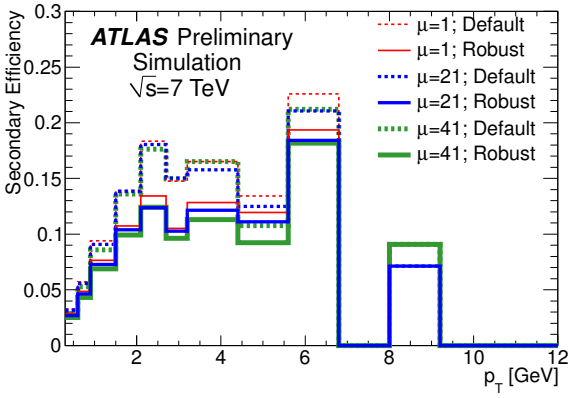

(c) Secondary particles - p_T

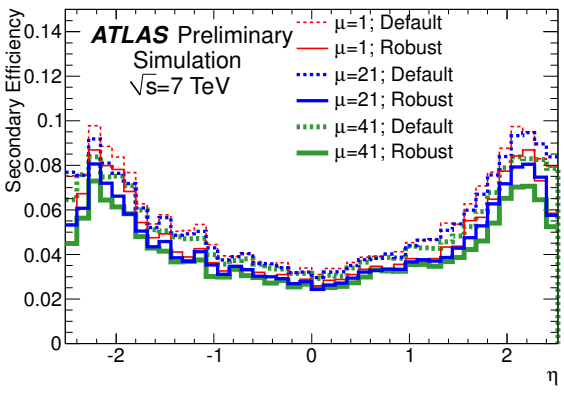

(d) Secondary particles - η

Figure 3.1: The primary and secondary track reconstruction efficiency as a function of the transverse momentum of the tracks (a) and (c) and their pseudorapidity (b) and (d) in minimum bias Monte Carlo samples when testing the inside-out algorithm for primary and secondary particles with three pile-up schemes, μ=1, 21 or 41. The histograms are provided for tracks surviving the *loose-primary* menu (default quality cuts requirements) and the *tight-primary* configuration (robust track requirements).

- $\frac{q}{p}$ is the charge over momentum magnitude. It accounts for the track curvature of the particle inside the magnetic field,
- d_0, the transverse impact parameter, is the distance in the transverse plane xy of the closest approach (perigee) of the helix produced by the particle to the z-axis;
- z_0, the longitudinal impact parameter, is the z coordinate situated at the perigee.
- ϕ_0 is the azimuth angle of the momentum at the perigee, measured in the range $[-\pi, \pi]$;
- θ is the polar angle of the perigee, measured in the range $[0, \pi]$,

By travelling under the presence of the magnetic field, charged particles traversing the ID leave hits that enable to reconstruct their trajectory. In addition, particles will also interact with the dead material in the detector and this will lead to a deviation from their original trajectory due to multiple scattering; they can also loose energy via ionisation and bremsstrahlung. The tracking reconstruction algorithms extracts the trajectory and the kinematic of the charged particles by looking at the series of hits that are being produced and such algorithms need to be robust against the presence of multiple interactions in the same bunch-crossing (pile-up).

The track reconstruction strategy in the ID is different for primary and secondary particles [91] [92]. Primary particles are directly produced in a pp interaction or with the decay of another particle whose lifetime τ is smaller than τ_{primary}. For these objects, an inside-out algorithm is employed. On the contrary, a secondary particle is reconstructed through the usage of the outside-in algorithm.

3.1.1 Inside-out algorithm

For primary particles, the *inside-out* algorithm [93] starts from a seed of 3 hits in the innermost part of the silicon detectors. Once the seed is defined, a combinatorial Kalman filter is deployed and successive hits are added while moving away from the interaction point. This filter accounts for the various interactions of the particles with the detector materials causing energy loss and multiple scattering so that the position of each track is predicted until the external layers of the ID is reached. The trajectory is then recursively refitted by minimising a χ^2 function that describes the distance of each hit with respect to the most probable inferred trajectory.

As a large number of tracks in the tracking detectors are fakes, ambiguities in the track candidates found in the silicon detectors need to be resolved in order to complete the procedure and extend the trajectories to the external layer of the ID, represented by the TRT. The tracks are therefore ranked using a reward/penalty system based on quality criteria such as cuts on the number of hits and the goodness of the refitted χ^2 with respect to the most probable direction. If missing hits (holes) are present in the trajectory of a given track, a penalty is assigned and the candidate is likely not to be chosen. Tracks with a score below a certain threshold are discarded so that each ambiguity is resolved by choosing the track that obtained the highest score.

In the present analysis, quality criteria on tracks rely on a sufficient (9) number of successive hits in the silicon detectors (pixel and SCT) and no holes in the b-layer. Once the algorithm has extracted the best candidates in the internal layer of the ID, the tracks are extended to the TRT.

First, a longer track is computed by adding hits compatible with the extension of the silicon information to the TRT. Tracks that do not fulfil the basic quality requirements are deemed as outliers and are discarded from the fit.

The inside-out algorithm covers tracks whose transverse momentum p_T is greater than 400 MeV. Figure 3.1 displays the track reconstruction efficiency as a function of p_T and η. This parameter is computed as the fraction of primary particles matched to a well reconstructed track. High pile-up scenarios may induce a large increase in occupancy leading to nearby hits from other particles that spoil the pattern recognition algorithm. Nevertheless, as illustrated in Figure 3.1, the efficiency of the inside-out algorithm in the default configuration (the loose-primary menu) is nearly independent on pile-up up to a level of approximately 5%. The robust requirements (tight-primary) however decrease the efficiency by a factor 5% approximately for all pile-up schemes.

3.1.2 Outside-in algorithm

The inside-out algorithm [93] is effective when the number of hits in the silicon layers is sufficient to trigger and complete the pattern recognition procedure. Nonetheless, secondary particles coming from decay vertices which are displaced along the z axis with respect to the interaction point or tracks produced by photon conversions cannot be properly selected and reconstructed with the inside-out method. Moreover, the inside-out approach is not efficient for electrons with high energy loss as well.

A second recognition procedure is therefore performed after the reconstruction of the primary vertex (*outside-in* algorithm). The track candidate is built through the exploitation of a back-tracking pattern recognition starting from the TRT-based information back to the innermost layers silicon hits. Note that track segments in the TRT that are backported to the internal layers are not already associated to an extension of a silicon track in order to avoid double-counting and interferences with the previous procedure (inside-out).

The distributions of the efficiency of the secondary track reconstruction in minimum bias Monte Carlo samples for different pile-up schemes and quality cuts requirements are displayed in Figure 3.1.

3.2 Vertex reconstruction

A key ingredient of analyses is the correct determination of the primary vertex of the pp interaction as well as the secondary vertices. Primary vertices are reconstructed employing an iterative vertex finding algorithm where vertex seeds are calculated from the z position at the beam line of the various reconstructed tracks. In order to remove fake instances, each track carries a weight measuring its compatibility with the fitted vertex based on a χ^2 fit. When a track is displaced more than 7σ from its vertex, it is assigned to another vertex and the algorithm continues.

The typical resolution on the vertex position is of about 30 μm in the xy plane and 50 μm in the z direction.

3.3 Electrons

Electrons are charged particles that experience a bending in the ID due to the presence of its solenoidal magnetic field, deposit energy in the EM (cluster) and radiate a significant amount of photons through bremsstrahlung in the material of the Inner Detector. The main point in the reconstruction and identification of these objects is to locate energy deposits in the EM calorimeter that are compatible with electrons and match such clusters with a charged particle in the ID

(reconstruction) accounting for possible changes in direction and kinks caused by bremsstrahlung events. In order to achieve a good discrimination against background (mostly light hadrons or photon conversions) faking genuine electrons, various identification schemes are deployed in the analysis. Sections 3.3.1, 3.3.2 and 3.3.3 detail the various successive procedures, namely trigger, reconstruction and identification, adopted to define the particle *electron* in ATLAS.

3.3.1 Electron trigger

The ATLAS trigger detailed in Section 2.8 is employed to select interesting events containing electrons in the final state [94].

- At the L1 trigger level, the identification of the positions of the Regions of Interest (RoIs) exploits the usage of trigger towers covering a portion of the phase-space $\Delta\eta \times \Delta\phi \sim 0.1 \times 0.1$ lying in the calorimeter surface. The transverse energy of the electromagnetic cluster is therefore computed inside these RoIs with an accuracy of approximately 1 GeV. The outputs of neighbouring trigger towers are summed and EM-clusters are built by choosing local E_T maxima inside a sliding window of 4×4 group of trigger towers. The central core of this agglomerate, located within the region of 2×2 trigger towers, is checked and if it contains a sufficient amount of energy that passes an E_T threshold, the L1 trigger is satisfied and L2 trigger requirements are applied.

- At the L2, the trigger algorithm creates cell clusters in the domain $\Delta\eta \times \Delta\phi$=0.4×0.4 within the RoIs that have already been identified in the previous trigger step. The L2 analysis is performed both at the calorimeter and the ID level.

  As for the calorimeter clustering, the final position of the RoI, is obtained by calculating the energy weighted-average cell position on a 3×7 grid inside the already-built cell cluster. According to its position, two different sizes are deployed: 3×7 ($\Delta\eta \times \Delta\phi$=0.075×0.175) when the cluster lies in the barrel ($|\eta|$ <1.4) and 5×5 ($\Delta\eta \times \Delta\phi$=0.125×0.125) if the cluster is in the end-cap (1.4< $|\eta|$ <2.7).

  On the tracking side, specialised fast algorithms process signals from the innermost layers of the ID (pixel and SCT) and extrapolate them onwards into the outer layer of the TRT volume. A fast pattern recognition algorithm is also employed comprising a determination of the z position of the primary vertex along the beam axis and a subsequent combinatorial analysis to locate the correct tracks associated to that vertex.

- The EF, mostly operating in offline mode, fulfils the same reconstruction and identification criteria used in the offline selection of electron candidates (Sections 3.3.2 and 3.3.3) although characterised by looser cuts. These cuts are based on the kinematic features of hadron and electron-induced showers.

The E_T trigger threshold at the EF level for the single electron trigger was initially set to 20 GeV and was raised to 24 GeV close to the end of Run 1 to cope with the high values of the instantaneous luminosity delivered by the LHC and to maintain sustainable trigger rates. Similarly, the threshold was raised to 16 GeV from 14 GeV at the L1 trigger.

3.3.2 Electron reconstruction

Electron reconstruction algorithms in the ATLAS detector [95] start from energy deposits in the EM calorimeter (cluster energies) that are matched to reconstructed tracks of charged particles in the inner detector. The reconstruction is achieved along the following three points:

- electron seed-cluster reconstruction and cluster building;
- electron track-candidate reconstruction and the GSF refitting;
- electron candidate reconstruction.

Within the acceptance of the internal detector ($|\eta|$ <2.5), the $\eta-\phi$ phase-space of the EM calorimeter system is divided into a grid of $N_\eta \times N_\phi$=200×256 towers whose size is 0.025 ×0.025. In order to compute the tower energy, the energy of the cells in all longitudinal layers is summed. The reconstruction of the clustering at the calorimeter level is exploited with sliding-window algorithm: clusters of longitudinal towers with total energy above 2.5 GeV are searched and then the window size in 3×5 towers of η-ϕ is formed - a pre-cluster is therefore defined (*cluster-seeding* procedure). As soon as close-by seed clusters are found, duplicate removal algorithms are applied to avoid energy double-counting.

The final Section of the algorithm (cluster building) assigns to the cluster all cells that are within a specific window in η and ϕ around the position of the cluster. The cluster size is $N_\eta \times N_\phi$=3×7 in the barrel and $N_\eta \times N_\phi$=5×5 in the end-cap. The values of the sliding windows in η and ϕ is more pronounced in the barrel because of the structure of the magnetic field.
The efficiency in Monte Carlo simulations is of the order of 95% for electrons of E_T below 7 GeV and it reaches 99.9% for electron with $E_T \sim 45$ GeV.

The second part of the reconstruction chain is done with the electron-track candidate reconstruction via the GSF refitting [96]. This part of the reconstruction algorithm proceeds in two sub-steps:

i pattern recognition;

ii track fit.

The standard pattern recognition [97] starts from the pion hypothesis: if a track seed is not successfully extended to a full track of at least seven hits, then the electron hypothesis is employed and energy loss is allowed. This procedure is carried out with a global χ^2 fit [98]: if a track candidate is characterised by a very large value of the χ^2 estimator due to non negligible energy losses throughout its trajectory, the pion hypothesis is rejected and the track is refitted with the electron hypothesis.

Moreover, as observed in Figure 3.2, the distribution of the amount of material traversed by an electron before reaching the calorimeter is not uniform, leading to a different impact of bremsstrahlung energy loss in different detector regions. In order to improve the resolution of the tracking of the electron candidates, all but TRT-only tracks are re-fitted using an optimised electron track fitter, namely *Gaussian Sum Filter* (GSF) [99]. This algorithms accounts for energy loss by bremsstrahlung in the silicon detectors through the refitting of the ID tracks that have failed the pion hypothesis.

The electron energy loss caused by bremsstrahlung is parametrised by the Bethe-Heitler distribution, $f(z)$, expressing the probability of an electron to retain a fraction z of its initial energy when traversing a material being t its thickness and X_0 its radiation length:

$$f(z) = \frac{(-\log(z))^{a-1}}{\Gamma(a)} \tag{3.1}$$

where $a = t\log(2)$ and Γ is the Euler function. In fact, for electrons above the GeV, additional effects must be taken into account, namely the corrections due to interference effects to the scattering processes for ultra-relativistic electrons (Landau-Pomeranchuk-Migdal effect). As a result, the

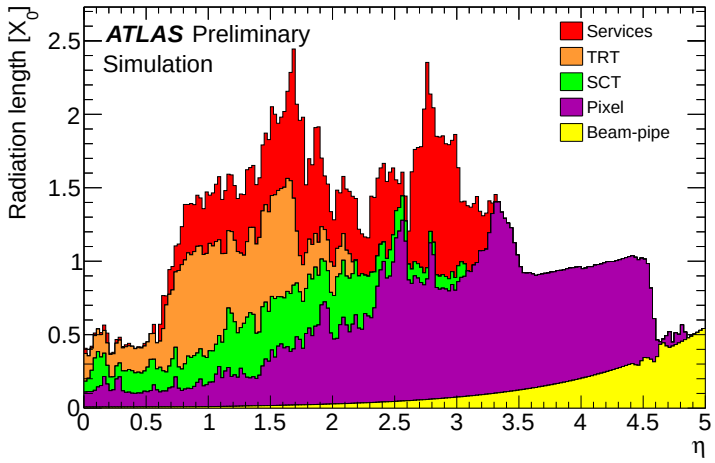

Figure 3.2: Distribution of the material in units of radiation lengths X_0 traversed by electrons before reaching the calorimeter. The filled colour areas matches with contributions of different detector elements.

equation (3.1) that generates the probability density function of the process cannot be computed analytically but numerically and does not exhibit a gaussian behaviour. Consequently, the Kalman filter [99], a regressive least square estimator employed in the pattern recognition of particles and based on the gaussian hypothesis for all measurement uncertainties, is no longer valid. The GSF is a generalisation of the Kalman filter where the PDF uncertainties are approximated as a sum of gaussian components treated by local Kalman filters.

In the 2011 electron reconstruction chain, the GSF algorithm was not used for technical reasons; only at a later stage of the data taking period, electron tracks started to exploit the beneficial features of the GSF fitting. On the contrary, during the 2012 data taking, the GSF was included from the very beginning leading to an increase in reconstruction efficiency of 2% in the barrel and 5% in the end-cap. As illustrated in Figure 3.3 (a) and (b), this procedure reduces the dependence of the momentum measurement on the amount of materials in a given pseudorapidity range. It is to be noted that the GSF is not a real reconstruction algorithm, but rather a track refitter.

The validation on Monte Carlo simulations has been carried out [96] employing an estimator given by the ratio of $\frac{q}{p}$ reconstructed over truth variable for electrons between 7 and 80 GeV in p_T. Be f_{Brem} a parameter that represents the amount of bremsstrahlung experienced by an electron with a given p measured in the ID:

$$f_{\text{Brem}} = \frac{(q/p)^{\text{reco}} - (q/p)^{\text{truth}}}{(q/p)^{\text{truth}}}. \tag{3.2}$$

Although the GSF-based algorithm brings an overall improvement in resolution of the f_{Brem} variable as noted in Figure 3.3 (c), its full distribution is not gaussian because in some cases the fitting procedure fails and the algorithm is unable to distinguish tracks generated by electrons in the ID.

The improvement of the GSF refitting algorithm is expected to be for low p_T electrons that are likely to be affected by energy losses due to bremsstrahlung. For this purpose, a full check of the procedure was accomplished on the $J/\Psi \rightarrow$ ee resonance characterised by low transverse momenta

electrons in the final state (Figure 3.4). The brem-related tails on the left for standard electrons representing the incorrect treatment of these energy losses is reduced in the case of GSF. These tails are still present because of the cases where the algorithm is unable to correctly refit the track when electrons radiate a large amount of energy in the first layers of the Pixel detector. However, the improvement of the resolution in the peak is manifest when the electrons are treated with the GSF-based algorithm. In addition, the GSF successfully stabilises the position of the peak, i.e. by shifting it towards its true value.

The pull distribution, $\mathcal{P}_{GSF}^{J/\Psi}$, defined as:

$$\mathcal{P}_{GSF}^{J/\Psi} = \frac{m_{\text{reco}} - m_{\text{truth}}}{\delta m_{\text{reco}}} \tag{3.3}$$

is expected to be a Gaussian distribution peaked at 0 with σ=1 for an ideal fitter (Figures 3.4 (c) and (d)). As already stated, the residual non gaussianity of the left tails is traced back to the treatment of the cases where the GSF fit is not applicable. Even so, the gaussian core is left intact and its mean value is peaked at 0. Conclusively, the non-gaussian behaviour of Figure 3.4 (c) is largely recovered by the presence of the GSF fitter.

The usage of the GSF fitting algorithm for electrons also paves the way for an improvement of the electron reconstruction efficiency with respect to the standard approach. Figure 3.5 illustrates the distribution of the electron reconstruction efficiency as a function of η with a given electron identification menu (*tight++*), detailed in Section 3.3.3. Electrons refitted with the GSF show a non negligible improvement in the efficiency ($\sim$ 5 %) when particles fall in the forward region of the detectors.

Finally, calorimeter clusters matched to tracks in the electron fitting hypothesis and refitted with the GSF algorithm build the electron candidate. The final electron four-momentum is extracted using the inner detector information for the charge determination and the measurement of d_0, z_0, η and ϕ, while the cluster output is adopted to compute the transverse energy E_T of the electron.

3.3.3 Electron identification

The goal of the electron identification is to provide robust set of selection requirements to allow discrimination power between true electrons (isolated electrons or non-isolated electrons produced in jets due to the semileptonic decay of heavy flavour quarks), hadronic jets faking electrons or photon conversions. The electron identification [95] strategy used in this analysis is specific to each of the two different data samples available and it is optimised in the selection efficiency *vs* the rejection against fake electrons phase-space. For the 2011 data sample, a cut-based identification analysis has been deployed [96], whereas for the 2012 dataset, a dedicated multivariate likelihood discriminant is used.

Cut-based identification

The cut-based electron identification is optimised to provide good separation between signal and background. The available menus are tight++, *medium++* and *loose++* accessing different working points and cuts on the variables of interest. In the early 2012, the performance of the various menus was improved by loosening cuts and introducing additional information and variables that carry extra discriminant power between signal and background. The $H \rightarrow$ZZ$\rightarrow$ 4l analysis uses the loose++ identification criteria for what concerns the 2011 data at $\sqrt{s}$=7 TeV and the cut-based menu for the first part of 2012 dataset at $\sqrt{s}$=8 TeV.
The cut-based electron identification is based on:

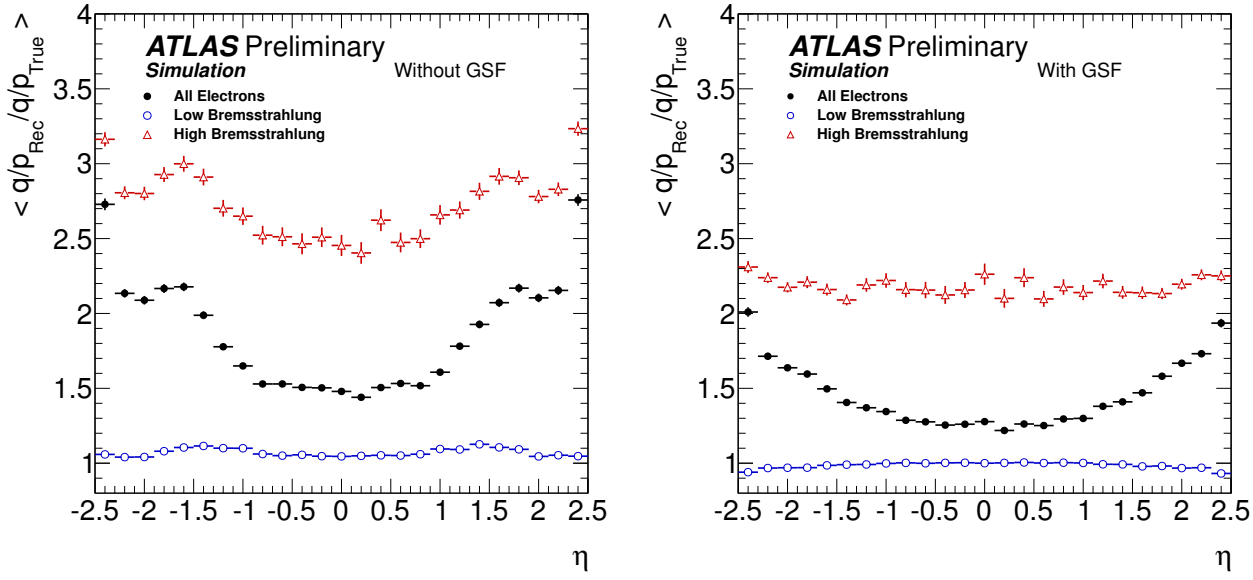

(a) (b)

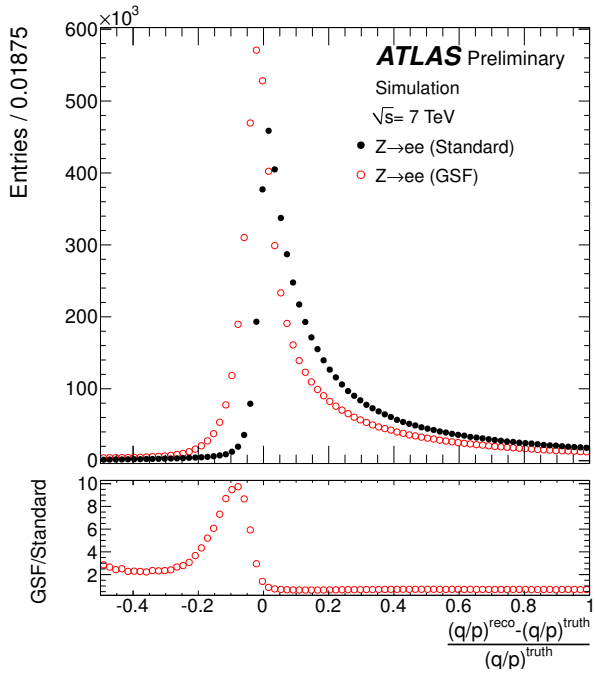

(c)

Figure 3.3: Mean value of the ratio of the reconstructed over the true electron inverse momentum times charge as a function of pseudorapidity for single electrons with transverse momentum between 7 and 80 GeV that lose less than (open points) and greater than (open triangles) 20% of their energy due to bremsstrahlung in the silicon detector and surrounding infrastructure without (a) and with (b) GSF refitting applied. Distribution of the f_{Brem} variable (c) defined in the text for both GSF (open red) and standard (solid black) Monte Carlo from $Z \rightarrow$ ee decays. The bottom plot shows the ratio of the entries of the GSF and the standard electron for each bin.

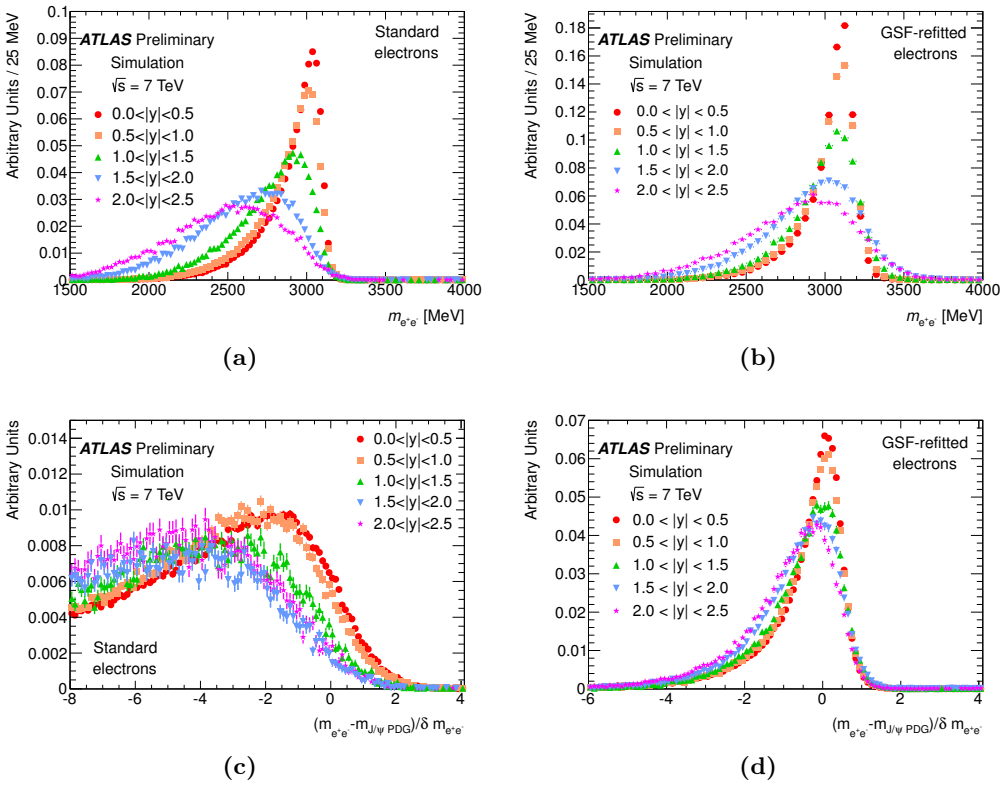

Figure 3.4: Invariant mass distributions of simulated $J/\Psi \rightarrow ee$ decays in various pseudorapidity ranges for the standard (a) and GSF reconstruction (b). Pull distributions (3.3) of standard (c) and GSF-treated (d) electrons from simulated $J/\Psi \rightarrow ee$ decays in various pseudorapidity regions.

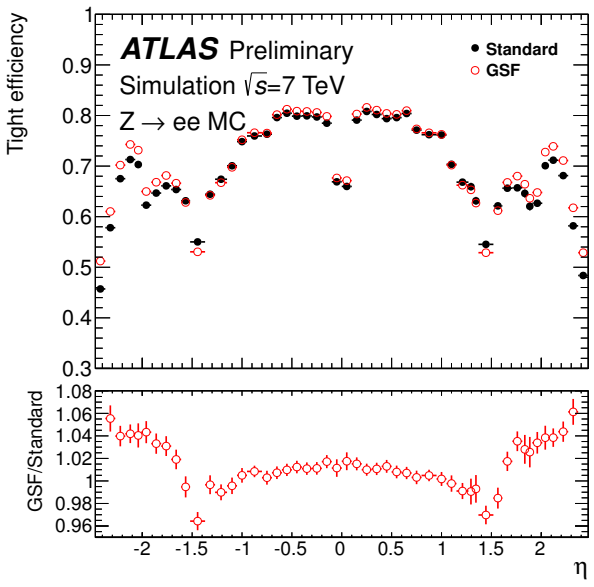

Figure 3.5: Electron reconstruction efficiency for a specific identification menu as a function of the pseudorapidity range for GSF (open red) and standard (solid black) electrons. The ratio of the GSF to the standard distribution is also provided in the bottom part of the plot.

- requirements on the track quality, i.e. the number of hits in the B-layer to discriminate against photon conversions, the total number of hits in the pixel, in the SCT and the TRT, the transverse impact parameters d_0 and its significance defined as the ratio of d_0 and its uncertainty;
- track-cluster matching, namely the η, ϕ matching between cluster and ID tracks as well as the ratio of the cluster energy and the track momentum, $\frac{E}{p}$;
- the hadronic leakage defined as the ratio of E_T in the first layer of the hadronic calorimeter to E_T of the EM cluster (true electron candidates are expected to release energy mostly in the electromagnetic calorimeter);
- the ratio of the energy in the third layer of the calorimeter and the total energy of the object inside the calorimeter;
- requirements on the geometrical structure of the lateral shower shape created by the electron: isolated electrons are featured by a narrower cluster than all other components, in particular hadrons;
- the ratio of the energy in 3×7 cells over the energy in 7×7 cells centred at the electron cluster position;
- ratio of the energy in the strip layer to the total layer;
- ratio of the energy between the largest and the second largest energy deposit in the cluster over the total energy of the cluster.
  This criterion, explicitly addressed as E_{ratio}, is employed to distinguish jets with one or more neutral particle (π_0) which create significant electromagnetic showers inducing a non-negligible contribution to the electron background. Rejection is therefore accomplished by using the first calorimeter layer and its fine granularity: true electrons leave an energy deposit with a single maximum E_1 whilst these jets can produce an adjacent second maximum E_2.

Likelihood-based identification

An improved identification scheme aiming at replacing the cut-based approach detailed in Section 3.3.3 for 2012 is also developed. Out of the possible multivariate techniques, the maximum likelihood procedure is chosen for electron identification. As a starting point, the probability density functions (PDFs) of signal and background are built. An overall probability is consequently calculated for each electron to look more signal or background-like based on the structure of those PDFs. Be $\mathcal{P}_{s,i}(x_i)$ the signal PDF for the i^{th} variable evaluated at x_i and $\mathcal{P}_{b,i}(x_i)$ its correspondent background PDF, the likelihood discriminant can be parametrised as follows:

$$d_{\mathcal{L}} = \frac{L_S}{L_S + L_B} \tag{3.4}$$

where:

$$\mathcal{L}_S(\mathbf{x}) = \prod_{i=1}^{n} \mathcal{P}_{s,i}(x_i) \tag{3.5}$$

for the signal and analogously for the background:

$$\mathcal{L}_B(\mathbf{x}) = \prod_{i=1}^{n} \mathcal{P}_{b,i}(x_i). \tag{3.6}$$

In equations (3.5) and (3.6), $\mathbf{x}$ is the vector of variable values. Signal and background PDFs used for the likelihood identification menu are derived from data and consist of a set of 9×6 PDFs (9 bins in η and 6 bins in E_T). Each cut on the likelihood discriminant is made with a different set of variables entering into the parametrisation of the signal and background PDFs depending on the type of likelihood menu. For instance, the loose likelihood selection is characterised by a set of variables that is essentially in common with the cut-based menu (Section 3.3.3).

The loose likelihood identification menu is used in the $H \rightarrow$ZZ$\rightarrow$ 4l (Chapter 5) analysis and it is tuned in such a way that it carries the same identification efficiency as the loose++ ID menu but better background rejection by improving the light flavour jet exclusion. The identification efficiency as a function of E_T and η is shown in Figure 3.6 both for the cut-based scenario, (a) and (b), and for the likelihood approach (c) and (d). The plots marked with (e) and (f) illustrate the ratio of the background efficiency for electrons of $Z \rightarrow$ ee events treated with the likelihood and its relative cut-based menu. It can be noticed (Figure 3.6) that the likelihood menus let through only about 40-60% of the background compared to the cut-based menus, while keeping essentially the same signal efficiency. The efficiency is measured with the *tag-and-probe* method from $Z \rightarrow$ ee events from data.

3.4 Muons

Muons are charged particles that cross the whole detector: they leave minimum amount of energy in the electromagnetic and hadronic calorimeter as well as a series of hits in the ID and in the MS that can be exploited to measure their trajectories and reconstruct their kinematic properties. Events with muons in the final state involve several physics processes, like $H \rightarrow$ZZ$\rightarrow 4\mu$, and they guarantee a very clean signature. As for the previous Section, Section 3.3, the following paragraphs will cover the main aspects of the muon trigger, reconstruction and identification [100] [101] as well as a digression on the determination of muon momentum scale and resolution.

3.4.1 Muon triggers

The ATLAS muon trigger system [102], [103] has been designed to select muons in a wide momentum range with high efficiency. The muon trigger consists of three steps and the the trigger logic is based on the search of coincident hits in the η-ϕ plane. The geometrical coverage of the trigger system is about 99% in the end-cap and 80% in the barrel because of the presence of the crack around η=0. Figure 3.7 shows the structure of the muon system as well as the location of the main trigger detectors.

- At L1, the RPCs in the barrel and the TGC in the end-cap are used. In the barrel, the low p_T triggers require a coincidence of three out of four layers of the two RPC planes while the high-p_T triggers start from the output of the low p_T trigger and look for hits in the RPC layers of the third plane. The same trigger match is employed for the TGC in the end-cap.

- At L2, each muon candidate is required to have additional precise hits in the MDTs and CSCs chambers in a spacial region around the muon candidate. At this stage, muon spectrometer tracks are combined and matched with ID tracks in a narrow cone so to select precisely the region where the interesting candidates reside. The first estimation of the transverse momentum of the particle is computed using the position and the direction of the hits. The amount of data is partially reduced to 3-7% of the total volume.

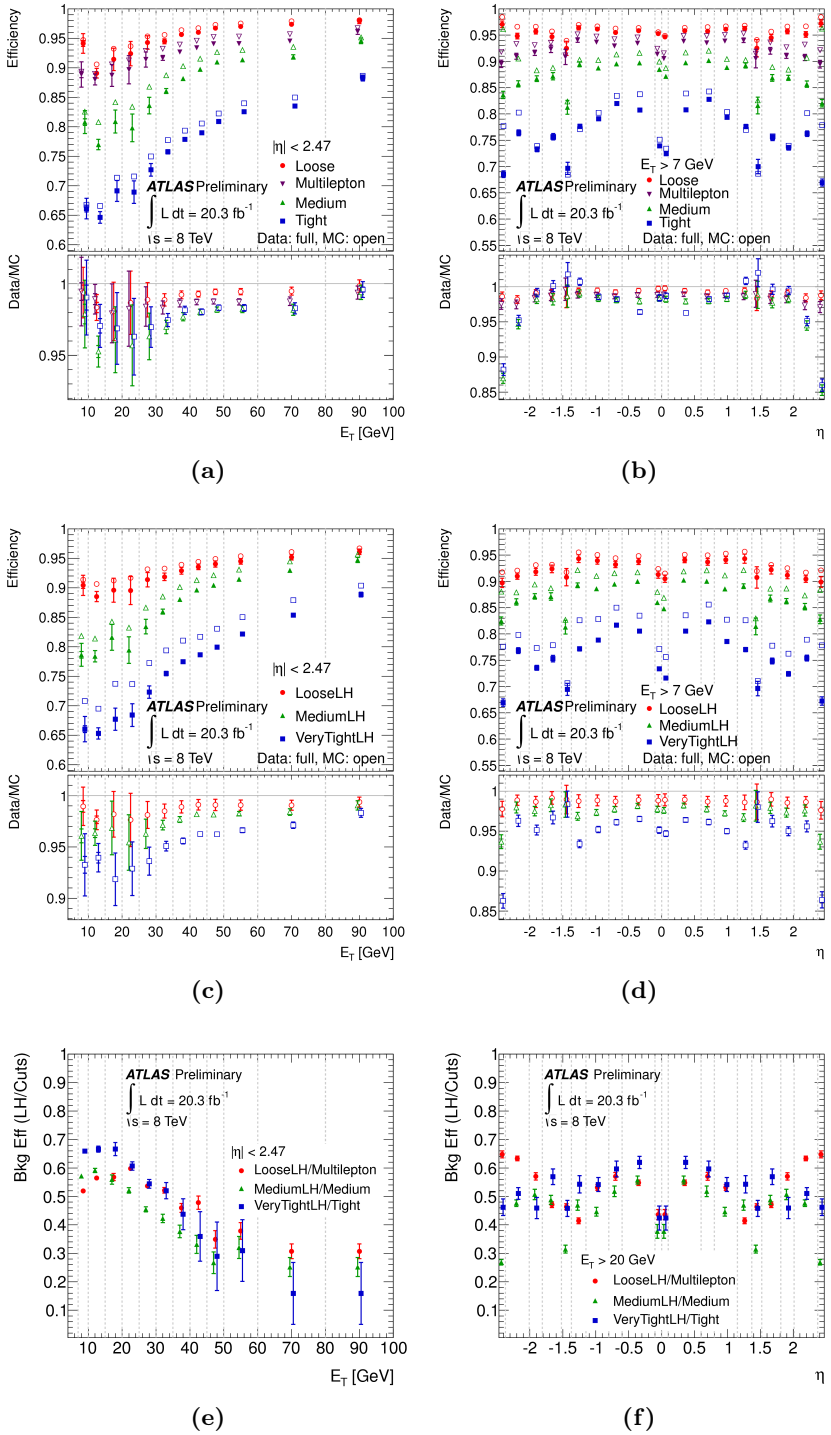

Figure 3.6: Measured identification efficiency as a function of E_T(a), (c) and η (b), (d) for the cut-based loose, medium and tight menus as well as for the closest-efficiency likelihood-based ones, compared to MC expectation for electrons from $Z \rightarrow$ ee decay. Ratio of background efficiencies for the likelihoods and the closest-efficiency cut-based menu as a function of η (e) and η (f). The uncertainties are statistical only. The lower panel shows the data-to-Monte Carlo efficiency ratios.

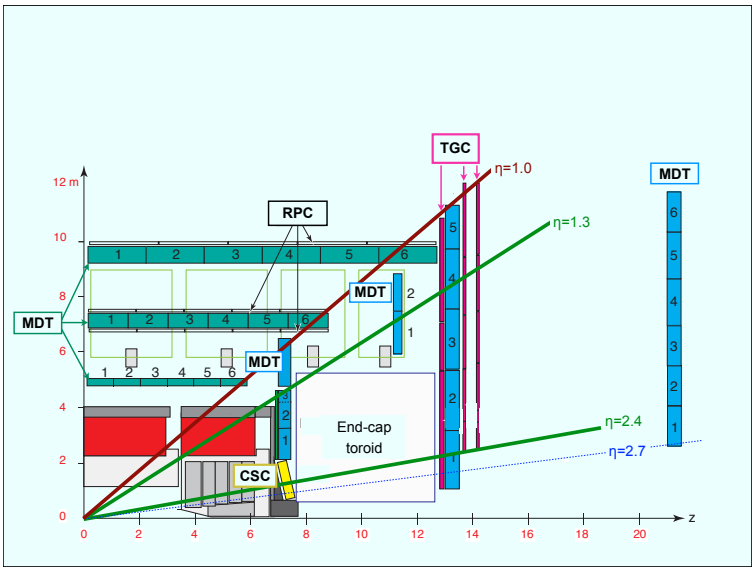

Figure 3.7: Schematic picture showing a quarter-section of the muon system in a plane containing the beam axis. The position of MDTs, RPCs, TGCs and CSCs is indicated in figure.

- At the EF, the full offline reconstruction on muon candidates is applied when the region of interest has already been determined by the first two trigger steps. The track is then extrapolated back to the beam line to locate the track parameter in the ID (inside-out strategy). Subsequently, as a complementary approach, the reconstruction starts from an ID track and tries to extrapolate upwards in the MS (outside-in). The momentum and the track parameters are finally re-fitted and improved so that a p_T measurement is assigned to the muon candidate. The p_T threshold used for the single muon trigger is 18 GeV for 2011 data and 24 GeV for 2012 data.

3.4.2 Muon reconstruction and identification

Mainly two sub-detectors, the MS and the ID, are involved in muon reconstruction and identification. As they provide an independent measurement of the transverse momentum of the particle as well as its trajectory in the magnetic field, they can be simultaneously used. In some cases, the energy deposit compatible with the muon hypothesis can be also detected in the EM calorimeter and therefore combined to the ID tracks.

ATLAS employs various definitions of muons resulting in different kinematic features of the objects.

i Standalone muons: particles are reconstructed only in the MS without any track left in the ID. Standalone track reconstruction in MS starts with a search for patterns among hits throughout the whole detector outside the ID geometrical coverage ($|\eta|$ >2.5) extending to $|\eta|$=2.7, the limit of the acceptance of the MS. In the selected areas, close hits in the same chambers are fitted along a line to produce segments. Segments from the three chamber stations are then used to perform a fit of the tracks whose trajectory is extrapolated back to the interaction point, through the calorimeters including effects caused by energy loss and multiple scattering.

ii Combined muons: standalone muon tracks extrapolated back to the vertex are matched to ID tracks, inside its coverage ($|\eta|$ <2.5), and combined into a single track, in order to benefit from

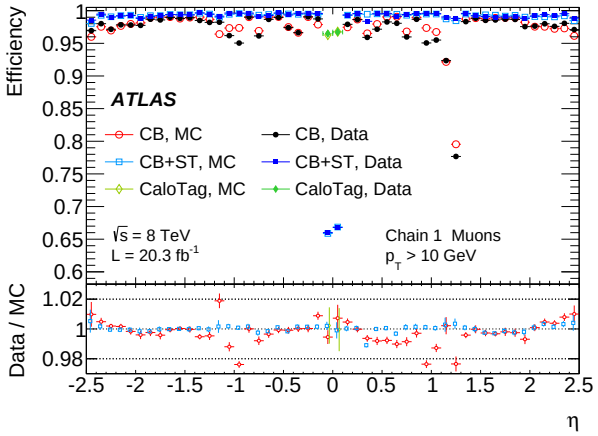

Figure 3.8: Muon reconstruction efficiency as a function of η measured in $Z \to \mu\mu$ events for muons with p_T >10 GeV and different muon reconstruction types. The error bars on the efficiencies indicate the statistical uncertainty. The panel at the bottom shows the ratio between the measured and predicted efficiencies with statistical only uncertainties.

the complementary momentum sensitivities of MS and ID over the whole p_T range. The statistical treatment of the combination uses the covariance matrices of the two tracks representing the uncertainty on the measurements of the parameters. Two different algorithms are available in ATLAS: STACO [104] performing a statistical combination of track parameters of the MS and ID using the covariance matrices of both parameters (default) and MUID [105] based on a global refit of the muon track with hits selected in the ID and the MS.

iii Segment-tagged muons: additional muon candidates are obtained by tagging incomplete ID track with the MS. This strategy is less sensitive to Coulomb scattering and energy loss; to maximise the accuracy of this measurement, segment-tagged muons utilise the measured parameters coming from the associated track in the ID.

iv Calorimeter-tagged muons: since the region of $|\eta|$ <0.05 is not instrumented with muon chambers, in order to measure very central muons, the trajectory in the ID is identified as a muon if there is a connected calorimetric deposit compatible with the hypothesis of a minimum ionising particle.

In order to reject muon background (mostly represented by pions and kaons decays in flight generating genuine muons or punch-through showers, i.e. showers not fully contained in the calorimeter leaking outside and developing tracks in the MS) a set of cuts based on ID hit requirements is carried out. Another possible source of background is associated to muon tracks from cosmic rays and beam backgrounds. These items show different timing characteristics with respect to muons produced in pp collision and fail the trigger requirements detailed in Section 3.4.1. After applying these cuts, the fraction of muon background was found to be negligible, well below the percent level. A tag-and-probe technique, already detailed in Section 3.3.3, on $Z \to \mu\mu$ candidates is employed to calculate the reconstructed efficiency. As presented in Figure 3.8, the efficiency is practically uniform within the pseudorapidity range. The main drop in efficiency is located at η=0, the crack-region for the muon chambers. In the very forward region of the detector (2.5< $|\eta|$ <2.7) there is no ID coverage and the reconstructed efficiency may suffer from severe degradation.

3.4.3 Muon momentum resolution

The physics model of the muon interaction is described by Monte Carlo simulations. However, detector conditions during data taking and possible misalignment between ID and MS can create local differences in data distributions reflecting in imperfect accuracy of data-Monte Carlo comparison. Therefore, a set of corrections is applied to Monte Carlo-generated events to match data expectations.
The muon momentum resolution can be parametrised as follows:

$$\frac{\sigma(p_T)}{p_T} = \frac{a}{p_T} \oplus b \oplus c \cdot p_T, \tag{3.7}$$

where a refers to the fluctuations of the muon energy loss when the particle is traversing the material, b describes the multiple scattering effect and c accounts for the intrinsic resolution of the muon chambers, depending for instance on the spatial positions of the hits, and residual misalignment effects between ID and MS. Two corrections are applied to Monte Carlo events to restore data-simulation agreement. A set of smearing parameters directly acting on the resolution model of the distribution are derived in 36 η-ϕ regions by fitting the Z$\rightarrow$ $\mu\mu$ data mass spectrum with Monte Carlo templates. The fitting procedure [106] selects the best value of these parameters in specific regions of the phase space. Correction factors are derived separately in the transverse momentum measurement in the ID and in the MS and are consequently combined employing a weighted sum of their relative contributions. These momentum smearings correct the Monte Carlo spectrum with a multiplicative gaussian contribution with mean 0 and variance 1 in front of each parameter reported in equation (3.7).

The dimuon invariant mass resolution, $\sigma(m_{\mu\mu})$ which results from the momentum resolution effect of each single muon is shown in Figure 3.9 separately for ID and MS and the combined contribution (Z, J/Ψ and $\Upsilon \rightarrow \mu\mu$). The importance of the simultaneous usage of the ID and MS measurements for the extraction of the combined p_T is testified by the improvement in resolution of the CB mass throughout the whole η range with respect to the ID and MS outputs. A second correction that is applied to Monte Carlo templates is the so-termed scale correction. It is a multiplicative correction modifying the typical muon momentum scale with the factor Δs_1 as well as the offset Δs_0 modelling data Monte Carlo differences due to the energy loss:

$$p_T^{\mathrm{MC,corrected}} = \Delta s_0 + \Delta s_1 \cdot p_T^{\mathrm{MC}}. \tag{3.8}$$

Figure 3.10 (a) reports the $Z \rightarrow \mu\mu$ mass distribution in data and Monte Carlo before and after applying the smearing and scale correction factors on the Monte Carlo sample. Better agreement is obtained as shown in Figure 3.10 (b) where the dimuon invariant mass resolution in data is compared with Monte Carlo simulation before (the width of the uncorrected Monte Carlo is 5-10% smaller than that of the data) and after smearing corrections. Figure 3.10 (c) shows the data/Monte Carlo ratio of the mean mass $< m_{\mu\mu} >$ obtained from the fits to the Z, J/Ψ and Υ samples, as a function of the pseudorapidity of the highest-p_T muon for a pair of combined muons. For the uncorrected Monte Carlo, the ratio deviates from unity in the large η region of the J/Ψ and Υ cases by up to 5%. This is mainly due to imperfections in the simulation of the muon energy loss that have a larger effect at low p_T and in the forward η region where the MS measurement has a larger weight in the MS-ID combination. The corrected Monte Carlo is in very good agreement with the data, well within the scale systematics that are $\sim 0.035\%$ in the barrel region and increase with η to reach $\sim 0.2\%$ in the region $|\eta| > 2$ for the $Z \rightarrow \mu\mu$ case.

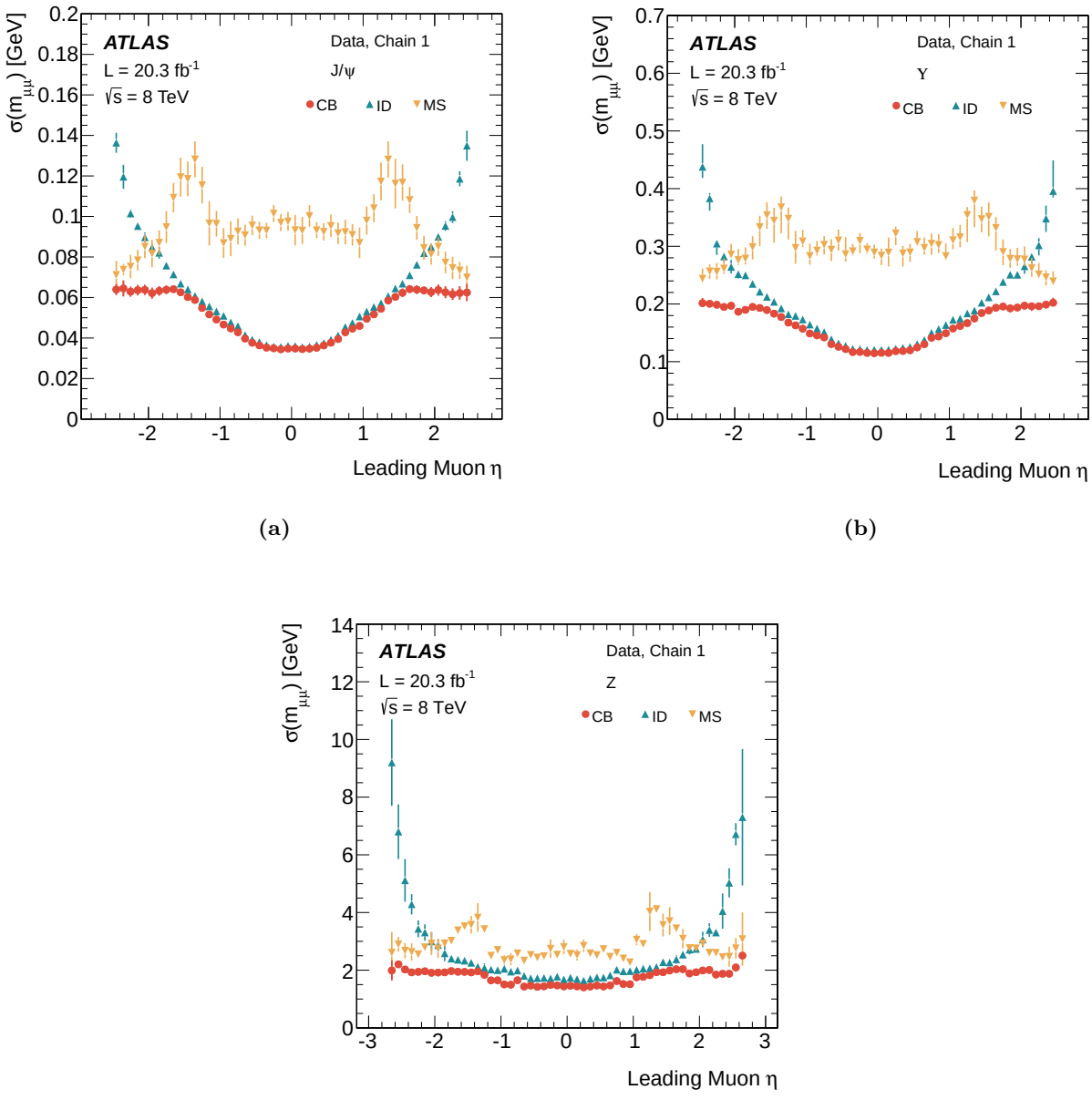

Figure 3.9: Invariant mass resolution $\sigma(m_{\mu\mu})$ for ID, MS and combined measurements observed in data at $\sqrt{s}$= 8 TeV for J/$\psi \to \mu\mu$ (a), $\Upsilon \to \mu\mu$ (b) and Z$\to \mu\mu$ (c) as a function of η of the highest p_T muon of the pair.

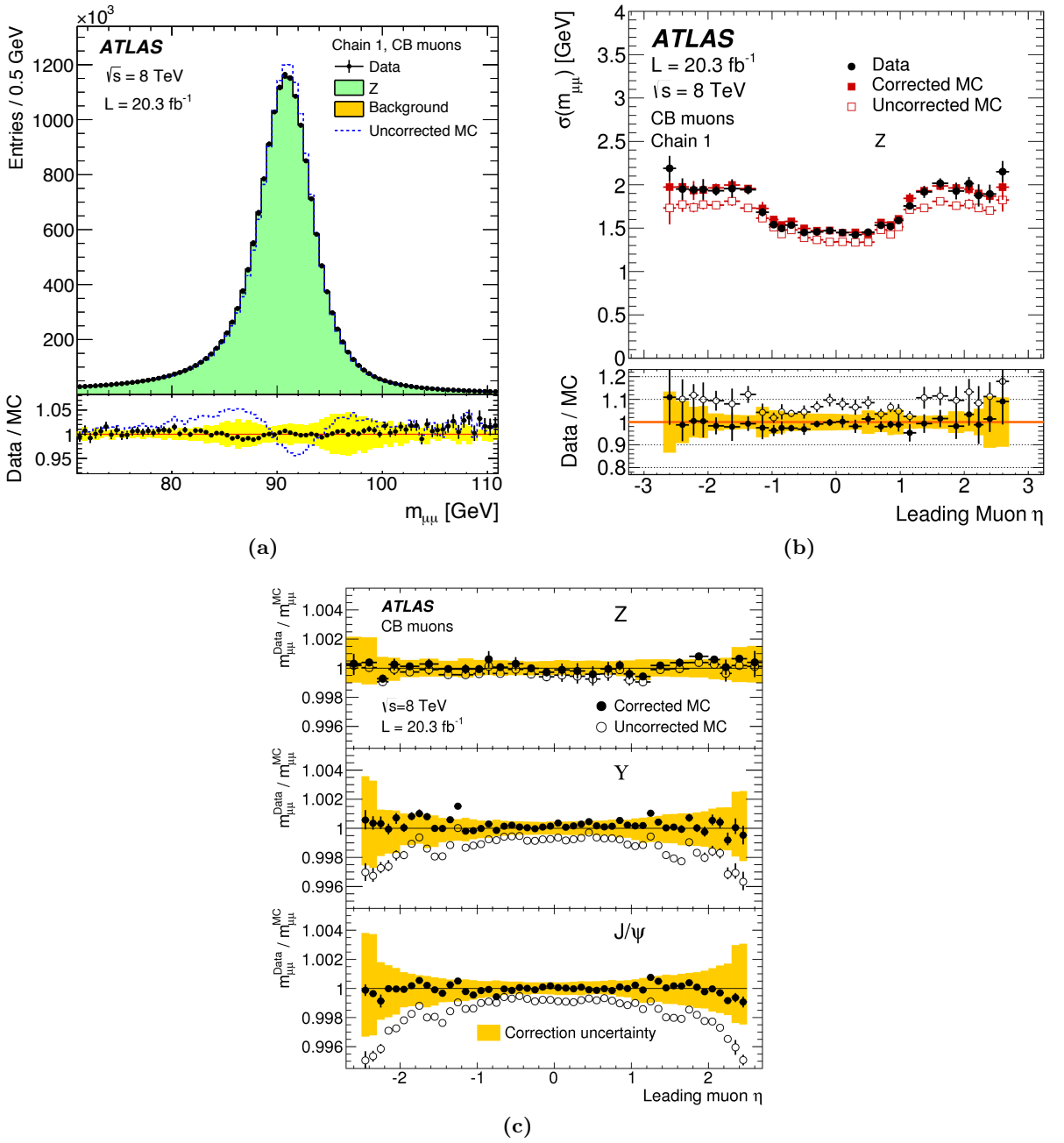

Figure 3.10: Dimuon invariant mass for combined muons reconstructed with STACO algorithm with p_T>25 GeV as obtained from data at $\sqrt{s}$=8 TeV. Data are compared to Monte Carlo simulation for $Z \to \mu\mu$ events before and after (a) applying smearing and scale corrections on Monte Carlo. Background estimates are added to the signal simulation. The lower panels show the Data/MC ratios. The band represents the effect of the systematic uncertainties on the MC momentum corrections. (b) Dimuon invariant mass resolution for combined muons of $Z \to \mu\mu$ events for data and for uncorrected and corrected Monte Carlo as a function of the pseudorapidity of the highest-p_T muon. The upper plots show the fitted resolution parameter for data, uncorrected Monte Carlo and corrected Monte Carlo. The lower panels illustrates the data-to-Monte Carlo ratio, using uncorrected and corrected Monte Carlo. The error bars represent the statistical uncertainty and the systematic uncertainty on the fit added in quadrature. The bands in the lower panels represent the systematic uncertainty on the correction. (c) Ratio of the fitted mean mass in data and in simulations for the dimuon final state produced by Z, J/Ψ and ϒ decays as a function of η of the leading muon. The ratio is shown for corrected Monte Carlo (filled symbols) and uncorrected Monte Carlo (empty symbols). The yellow band defines the systematic correction uncertainty.

3.5 Jets

Jets appear [5] in the detector as collimated bunches of hadrons originated from gluons and quarks after fragmentation and hadronisation.

3.5.1 Jets reconstruction and identification

Topological clusters [107] [108], *topoclusters*, formed by jet deposits, are extracted in the hadronic calorimeter using neighbouring cells with significant energy deposit over the noise. The contribution of noise is measured in each calorimetric cell and is computed as the expected RMS of the electronic noise for the current gain and conditions in addition to the contribution from pile-up. Topoclusters formation relies on seed cells where the signal to noise ratio, labelled as S/N, is above a certain threshold. As a second step, adjacent cells to the seeded ones are added to the topocluster regardless of their S/N ratio. The energy of the topocluster is therefore the sum of energies of the various cells belonging to that topocluster.

In order to select the object jet, ATLAS employs an *anti-kt* algorithm [109]. For the jet constituents, the algorithm computes the following quantity:

$$d_{i,j} = \min(\frac{1}{k_{ti}} \cdot \frac{1}{k_{tj}}) \frac{\Delta R_{ij}^2}{R^2}. \tag{3.9}$$

k_{ti} is the transverse momentum of the i^{th} constituent, $R_{ij} = \sqrt{\Delta\eta^2 + \Delta\phi^2}$ between the two constituents i and j, and R is a parameter of the algorithm that models the size of the jet. Typical values for R are $R = 0.4$ or 0.6. Intuitively, the algorithm tends to define high energy clusters and to further combine the other lower energy clusters lying close to the first aggregation. Once the procedure is completed, the jet four-momenta are computed by the vectorial sum of all the four-momenta of the topocluster. The anti-kt algorithm has been used in every jet-related physics analysis in ATLAS. A key advantage is that it is infrared safe, that is to say not affected by soft QCD radiation emission that can lead to divergences, and collinear safe, i.e. robust against parton splitting into two collinear partons because soft radiations and splitted partons are clustered into more energetic objects. Furthermore, the anti-kt algorithm was also tested to be robust against pile-up.

Pile-up-motivated corrections are then applied to the jet energy: they subtract the contribution produced by multiple interactions from the same (in-time pile-up) or previous (out-of-time pile-up) bunch crossing. These corrections depend on the jet pseudorapidity are calculated as a function of the number of reconstructed vertices in the event and on the average number of interactions per bunch crossing, μ in data.
Another variable that is employed to gauge the jet performance is the jet vertex fraction (JVF), namely the fraction of tracks that are associated to the jet which are consistent with being originated from the primary vertex: the higher the JVF, the more probable the jet-to-vertex match assignment was correctly accomplished.

3.5.2 Jet energy scale calibration

The raw jet energy resulting from cluster deposits needs to be properly calibrated to account for the following effects:

- calorimeter non-compensation: the energy response to hadron is lower than that to electrons of the same energy;

- dead materials, inactive regions of the detectors where the energy deposit is not properly recorded;
- electromagnetic leakage due to the punch-through showers developing electromagnetic deposits leaking inside the hadronic calorimeter.

For the 2011 and 2012 analyses, a simple and robust approach, named jet energy scale (JES), has been carried out and applied to the simulation. These calibration factors are derived from Monte Carlo samples and correct the jet direction through a match in a ΔR cone of calorimetric jets with Monte Carlo true jets. The correction factors, $\mathcal{R}_{\text{jet}}$, are extrapolated from the ratio of energies of the reconstructed and true jets, $\mathcal{R}_{\text{jet}} = \frac{E_{\text{reco}}}{E_{\text{truth}}}$ inside the geometrical acceptance of the ΔR cone. These constant factors are parametrised both in the transverse momentum and the pseudorapidity regions of the jets. For the 2012 analysis, a more sophisticated calibration procedure, the local calibration weighting (LCW), is employed on top of the JES calibration. Its main purpose is the classification of the formed topological cluster as either electromagnetic or hadronic. Based on this difference, preliminary energy corrections are derived before starting the JES procedure. A final calibration is applied after the LCW+JES procedure and it corrects Monte Carlo-based results using data.

The jet energy scale uncertainties come from the experimental uncertainty on the detector knowledge, mostly due to the imperfect parametrisation of the dead materials, the effects of pile-up and its treatment for close-by jets. The theoretical physics models and parameters underneath the concept of QCD jet (treatment of the fragmentation and underlying events) in the Monte Carlo event generators used to derive the JES corrections are also an important source of uncertainty on the jet scale corrections. For the 8 TeV analyses, the total JES uncertainty in absence of pile-up varies between 2.5% for central high-p_T jets ($0< |\eta| <0.8$ and $60< p_T <800$ GeV) up to $\sim 14\%$ for forward low p_T jets ($3.2< |\eta| <4.5$ and $20< p_T <30$ GeV). Furthermore, the dependancy of the scale on multiple interactions in the same bunch crossing introduces an additional systematic uncertainty that accounts for approximately 0.5% for jets with $p_T \sim 50$ GeV. Figure 3.11 shows the the relative systematic uncertainty for inclusive jets as a function of the transverse momentum of the jet. The various sources comprised in the total uncertainty, explicitly the generation and tuning of the Monte Carlo, the material description, the jet resolution and the tracking in the jet core, are also reported in the same p_T^{jet} range.

3.6 Missing energy

The missing transverse momentum (MET) [110], generated by the presence of particles escaping the detector, like neutrinos, is defined as the momentum imbalance in the xy plane, transverse to the beam axis z. Given the parton model employed to describe the proton interactions, the sum of the longitudinal momenta is unknown. However, the sum of the transverse momenta of all particles in the final state must be zero. The momentum conservation should therefore hold in the transverse plane of the event, the missing transverse energy is defined as:

$$E_T^{\text{miss}} = -|\sum_i \vec{p_{T}}_i|. \tag{3.10}$$

The computation of the transverse energy for a given event comprises all the collection of particles that are present in the final state, hence sources of electronic noises, unknown dead regions, cosmic rays and beam-halo muons crossing the detector can be a source of fake missing E_T - the maximisation of the detector coverage and the reduction of the effects due to finite effect resolution are key ingredients to reach a good E_T^{miss} performance.

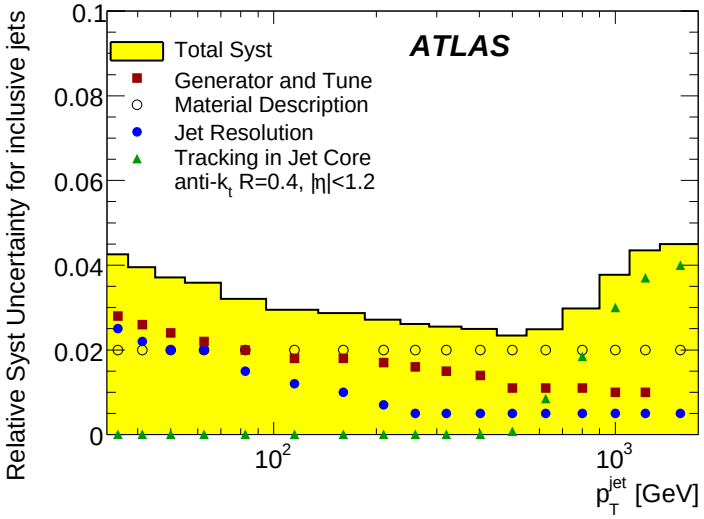

Figure 3.11: Relative systematic uncertainty on the jet energy scale for inclusive jets treated with the anti-kt algorithm (R=0.4) and $|\eta|$ <1.2. The various contributions to the total uncertainty are reported as a function of p_T^{jet}.

The reconstruction uses energy deposits in the EM and hadronic calorimeters as well as muons reconstructed in the MS. The contribution of tracks is added to recover the low p_T particles that are bended in the magnetic field and miss the calorimeter. The calculation of the subterms contributing to the definition of the MET is a comprehensive equation as follows:

$$E_{(x,y)}^{\text{miss}} = E_{(x,y)}^{\text{miss,e}} + E_{(x,y)}^{miss,\gamma} + E_{(x,y)}^{miss,\tau} + E_{(x,y)}^{\text{miss,jets}} + E_{(x,y)}^{\text{miss,SoftTerm}} + E_{(x,y)}^{miss,\mu} \tag{3.11}$$

where each term is extracted in the xy plane projecting the components of the transverse momentum onto the x and y axis and is extracted as the negative sum of the calibrated values for the relevant objects. Precisely, electrons (as detailed in Chapter 4) and photons are calibrated according to [111], τ-jets are calibrated with the local cluster weighting algorithm and the τ energy scale correction is also applied [112]. Jets [113] are reconstructed using the k_T algorithm [109] with R=0.4 when $p_T^{\text{jet}} > 20$ GeV. Each jet is then corrected for the pile-up contribution as detailed in Section 3.5.1. In order to suppress the noise contribution at the calorimeter cells level as much as possible, only the calorimeter energy deposits up to a certain threshold should be included into the computation. For this reason, the $E_{xy}^{\text{miss, SoftTerm}}$ is added and it accounts for the small energy deposits that are not associated to any high p_T object. In the formula (3.11) there is also a muonic term, $E_{(x,y)}^{miss,\mu}$ calculated by taking into account muons that are reconstructed in the MS and matched to tracks in the ID (combined muons). In the very forward region of the detector (2.5< $|\eta|$ <2.7) the measurement is entirely extracted by the MS (standalone muons). In the transition region (1.0< $|\eta|$ <1.3) tagged muons are considered as well.

Figure 3.12 (a) shows the excellent data - Monte Carlo (minimum bias) agreement of the parametrisation of the E_T^{miss}. As for Figure 3.12 (b) $Z \to \mu\mu$ events are well-suited to the study of the missing energy performance because of its very clean signature. Each contribution is weighted with its relevant cross section and the integral of the distribution is normalised to the corresponding luminosity in data. No genuine E_T^{miss} is expected from these events, thus the MET reconstructed in these events directly comes from imperfections in the reconstruction process of the energy response.

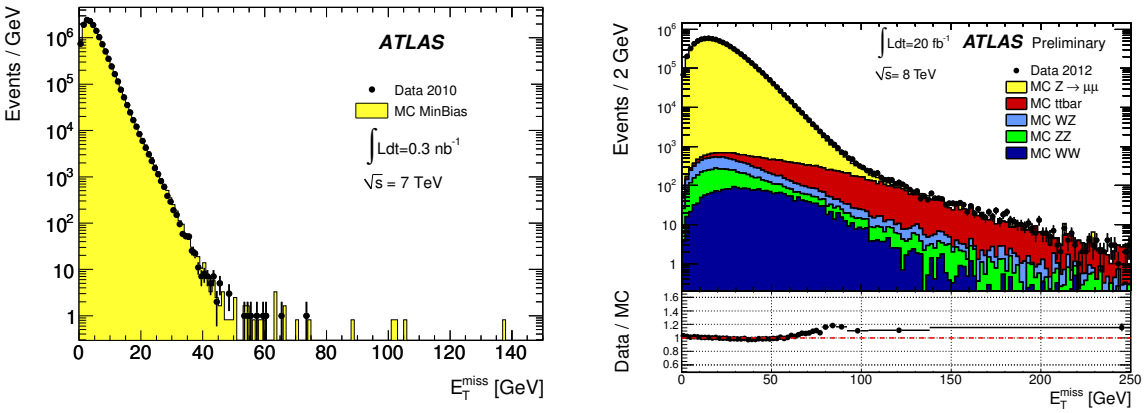

(a) **(b)**

Figure 3.12: (a) Data and minimum bias Monte Carlo comparison of E_T^{miss} using 0.3 nb^{-1} at $\sqrt{s}$=7 TeV. The Monte Carlo distribution is normalised to the luminosity in data. (b) Distribution of E_T^{miss} in $Z \to \mu\mu$ events in data using an integrated luminosity of 20 fb^{-1} at $\sqrt{s}$=8 TeV. The Monte Carlo expectations of the signal ($Z \to \mu\mu$) and the various background contributions are superimposed, stacked one on top to the others and normalised to data. The lower section of the plot shows the data to Monte Carlo ratio.

This fair agreement proves that the instrumental effects are accounted for by the simulation and the parametrisation of the E_T^{miss} term is correctly added. The dominant backgrounds of this analysis are also superimposed in this plot ($t\bar{t}$, WZ, ZZ, WW).

3.7 Pile-up conditions in the simulation

The various pile-up conditions [114] need to be thoroughly comprised in the simulation samples in order to have a realistic picture of physics conditions and to match them with data inputs. The total inelastic cross section is σ_{in}= (57.2 ± 6.3) mb [115] at $\sqrt{s}$= 7 TeV.
From the performance point of view, the main effects of the presence of pile-up are listed below:

- potential inefficiency in track reconstruction and identification due to very busy environment (occupancy) that affects the typical event processing time of the local recognition algorithm;
- degradation of the isolation requirements at the ID and calorimeter levels;
- distortion or mis-measurement of energy in calorimeters, mostly resulting in inefficiencies of the electromagnetic (electrons and photons) objects or increasing noise terms on the treatment of the jet energy resolution;
- degradation of the resolution of the missing energy.

It is therefore important that identification and reconstruction performance of the algorithms should guarantee robustness against the presence of pile-up. Figure 3.13 illustrates the plot of the luminosity-weighted distribution of the mean number of the interaction per bunch crossing for 2011 and 2012 with a timing bunch crossing difference of 50 ns. The modelling of the effects of pile-up events inside bunch crossings, both in-time and out-of-time contributions, is included in a separate process of the reconstruction chain that is applied to the Monte Carlo simulation, namely the digitalisation. The treatment of this procedure works as follows:

i Monte Carlo samples are simulated with a fixed distribution of additional minimum-bias interactions.

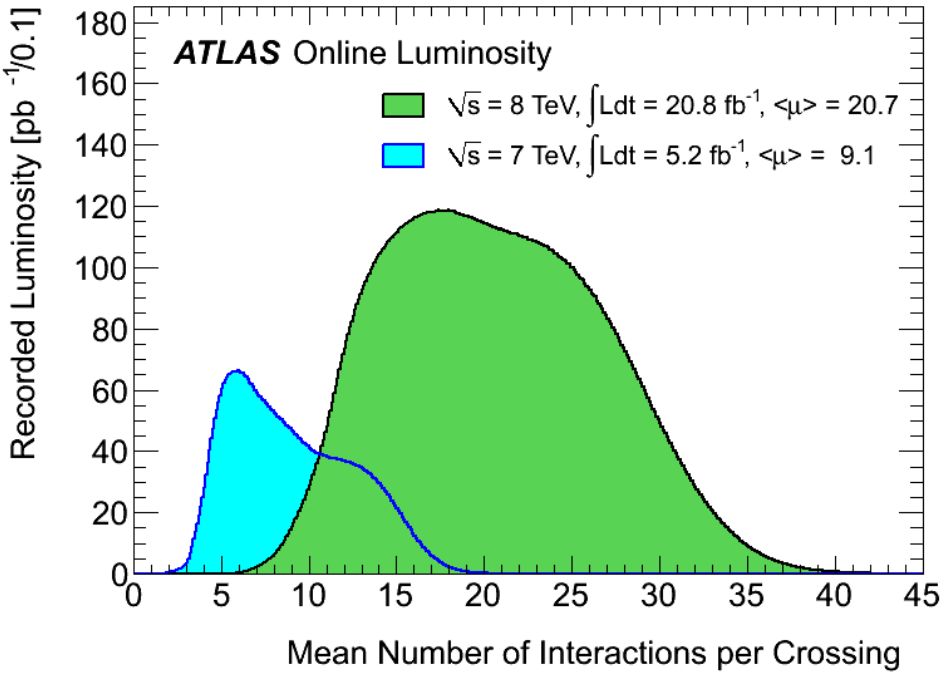

Figure 3.13: Luminosity-weighted distribution of the mean number of the interaction per crossing in data for 2012 at $\sqrt{s}$=8 TeV using an integrated luminosity of 20.8 fb^{-1} and 2011 at $\sqrt{s}$=7 TeV for 5.2 fb^{-1}.

ii This distribution is then reweighted to the one observed in data measured in LUCID and ALFA (Chapter 2) as a function of the lumiblock representing the data-taking periods.

iii This reweighting gives a scaling factor that is applied to the Monte Carlo events to correctly reproduce the distributions of pile-up measured in data. Hence, these weights vary in each event according to the actual number of interactions and to the pile-up conditions characterising a precise run and its instantaneous luminosity (number of bunches and ΔT between bunches) ensuring full compatibility of simulations with data.

Chapter 4

Energy calibration of the electrons and $E - p$ combination

Contents

A precise calibration of the energy measurement of electrons is a fundamental need of many physics measurements in ATLAS particularly after the discovery of the Higgs boson by the ATLAS and CMS experiments [20], for the measurement of the Higgs boson mass.

This Chapter explains the present scheme that derives the calibrated energy of the electrons starting from the energy deposits in the electromagnetic calorimeter as the electron reconstruction and identification have already been analysed in the previous Chapter.
Finally, a method that combines the calorimeter energy measurement with the momentum measured in the tracking detectors will be presented. This method has been exploited [20] in the extraction of the Higgs boson mass in the $H \to ZZ \to 4l$ channel as illustrated in Chapter 5.

4.1 General overview of the calibration procedure

The different steps in the procedure to calibrate the energy response of electrons are summarised below, with the items referring to the calibration chains sketched in Figure 4.1. The results presented in this Chapter are based on 20.3 fb^{-1} of pp collision data at $\sqrt{s} = 8$ TeV, collected in 2012.
The energy of an electron candidate is built from the cell responses in the electromagnetic calorimeter as explained in Chapter 3. The calibration then proceeds as follows:

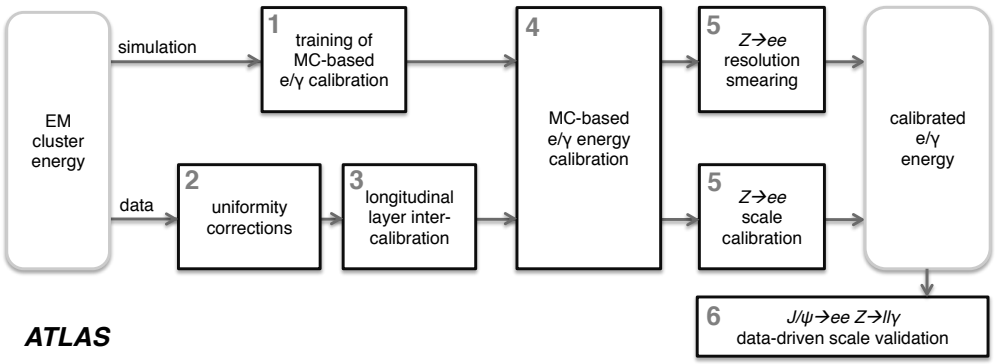

Figure 4.1: Schematic overview of the procedure used to calibrate the energy response of electron in ATLAS.

- The energy extracted from the deposits in the calorimeter cells is calibrated to the real energy of the electron. The procedure is illustrated in Section 4.2.
- A set of corrections is applied to the cluster energy that is reconstructed in data in order to account for effects that are not present in the simulation, namely non-optimal high voltage regions and geometrical effects that are associated with the calibration of the LAr calorimeter. Furthermore, in order to achieve a consistent measurement in data, the uniformity of the calorimeter energy response as a function of ϕ and η and its stability as a function of time t and different pile-up μ conditions (collectively contributing to the η-ϕ-t-μ *linearity* of the energy response) need to be checked to derive correction factors restoring the linearity of the measurement.

  The sources of non-uniformities of the energy responses that are investigated in the current round of the analysis and reported in the calibration paper [111] are listed below.

  – High-voltage inhomogeneties. In few sectors of the accordion electromagnetic calorimeter, the high voltage is set to a non-nominal value due to the presence of short circuits in the LAr gaps.
  – Time dependance of the pre-sampler response. The high voltage in the barrel pre-sampler is set to 2000 V but it was sometimes limited to lower values because of the occurrences of electronic noises.
  – Energy response in High-Medium gain. To accommodate the wide range of expected energies in the calorimeter cells and their amplifications, the electronic signals are treated with different linear gains [116]. Some processes, like Z→ee are recorded by cells in the high gain, whereas this is not the case for H→ $\gamma\gamma$ as the events have a photon with at least one cell in the medium gain.

  Figures 4.2 and 4.3 present the residual non uniformity after applying the above-discussed corrections as well as the residual instabilities of the measurement as a function of time and pile-up conditions.
- The non-linearities (Figures 4.2 and 4.3) in data can produce responses that do not match Monte Carlo expectations. Thence, correction scales are extracted from $Z \to ee$ events in data. The Monte Carlo response is also modified to account for the slight difference in resolution between data and simulation. The calibrated energy and the values of the extracted scale factors are additionally validated from J/Ψ →ee events so to ensure data - Monte Carlo

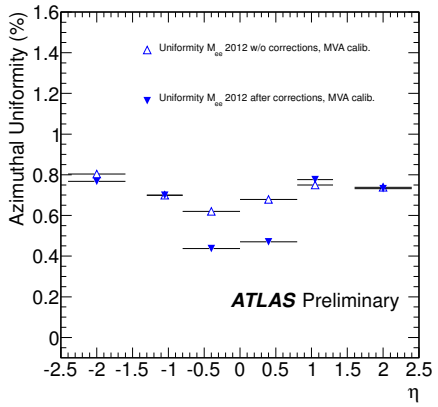

Figure 4.2: Non uniformity of the energy response of an electron candidate as a function of η with and without corrections.

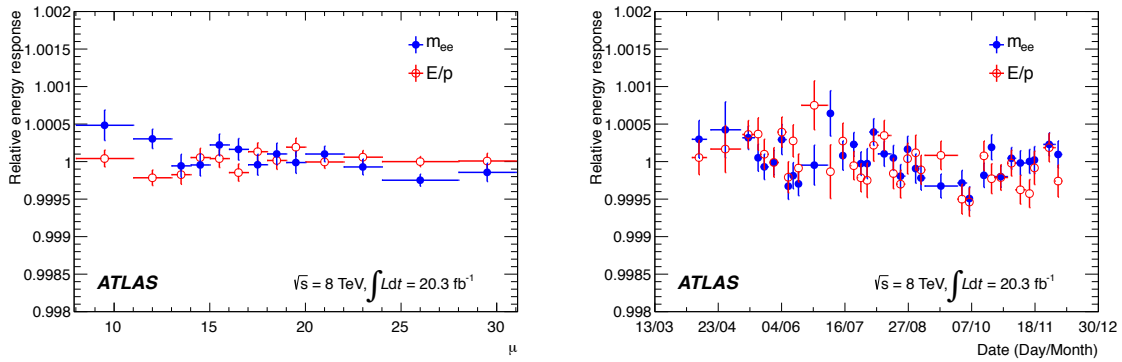

(a) **(b)**

Figure 4.3: (a) - Energy response as a function of μ normalised to its average quantity. (b) - Energy response as a function of time, normalised to its average quantity.

consistency. The procedure of the extraction of the correction factors on $Z \to ee$ will be the main theme of Section 4.3.

As the corrected energy of the electron candidate is returned by the calibration chain, the $E-p$ combination algorithm is deployed and the cluster-based electron energy is combined with the track momentum. This method will be detailed in Section 4.5.

4.2 Energy calibration of electrons

The goal of the calibration is to estimate the true energy of the particle from the quantities measured by the calorimeter. An electron (or a photon) deposits energy in several cells of the calorimeter due to electromagnetic showers created by the interaction with matter. A cluster of cells is then defined such that it contains most of the energy deposits, hence, the electron (photon) energy can be computed.

The calibration chain progresses as follows. The LAr calorimeter calibration converts the electronic signal readout into an energy inside one cell in the calorimeter [116]. However, several effects distort this calculation at the cell-level (energy lost by the candidate electron or photon in the

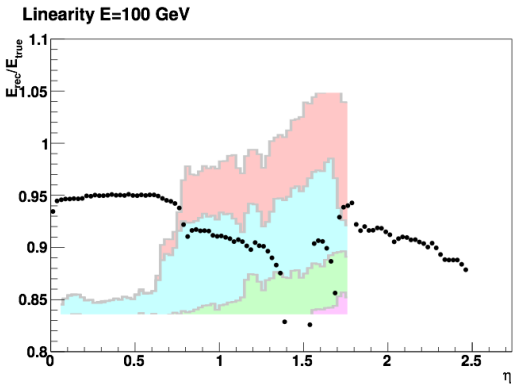

Figure 4.4: Linearity of the raw energy *vs* η for 100 GeV electron candidates. The distribution of the material in front of the calorimeter is shown in the background [117].

matter in front of the calorimeter energy leakage behind the calorimeter and the energy outside the defined cluster of the calorimeter cells), therefore, the calibration is applied to produce corrections to the cell-based energy.
Wrapping up, the calibration uses the energy of the cells (the *raw*-energy) and returns the energy of the cluster. Figure 4.4 illustrates the linearity of the response of the uncalibrated (raw) energy, defined as the ratio of the sum of the energies in the four layers to the true energy of the electron, as a function of the pseudorapidity η for 100 GeV electrons. The distribution of the material in front of the calorimeter is shown in the background [117]. The returned corrections of the energy calibration are parametrised as a function of measurable quantities and are obtained from Monte Carlo simulations.

The present calibration method [111], based on a multivariate approach [118], replaced the previous one (the calibration hit method) detailed in [119]. The constants determined by the method are applied separately for electrons, converted and unconverted photons in η and p_T regions. For this study, a sample of single electrons is employed, its E_T distribution covering the energy range from 1 GeV to 3 TeV, maximising the statistics between 7 and 100 GeV.

The new calibration scheme [111] is implemented using the Toolkit for Multivariate Analysis (TMVA) framework [118]. The framework provides a machine learning environment for the processing and parallel evaluation of multivariate classification and regression techniques. Several distributions of input variables extracted from the training sample are included in the machine learning algorithm and one output is produced as a result. The quantities used as input variables for the training of the multivariate approach are tabled below.

- **Total energy in the accordion**: E_{acc}, defined as the sum of the uncalibrated energies of the accordion layers (strips, middle and back).
- **Ratio of the energy in the presampler to the energy in the accordion**: E_0/E_{acc}, used only for clusters within $|\eta| < 1.8$.
- **Shower depth**: $X = \sum X_i E_i / \sum E_i$, where X_i is the amount of material (in X_0) in each layer i or in front of the presampler.
- **Pseudorapidity in the ATLAS frame**: η_{cluster}.
- **Cell index**: an integer number between 0 an 99 defined as the integer part of the division

$\eta_{\text{calo}}/\Delta\eta$ where η_{calo} is the pseudorapidity of the cluster in the calorimeter frame and $\Delta\eta = 0.025$ is the size of one cell in the middle layer.

- η **with respect to the cell edge**: defined as the pseudorapidity (in the calorimeter frame) modulus the width of one cell of the middle layer ($\Delta\eta = 0.025$).
- ϕ **with respect to the lead absorbers**.

In order to help optimising the energy response in different regions of the phase space, the sample is divided into bins of $|\eta_{\text{cluster}}|$, E_T, and according to the particle type (electron, unconverted photon or converted photon). The binning is chosen to match known detector geometry variations and significant changes in the energy response:

- $|\eta_{\text{cluster}}|$: 0 - 0.05 - 0.65 - 0.8 - 1.0 - 1.2 - 1.37 ; 1.52 - 1.55 - 1.74 - 1.82 - 2.0 - 2.2 - 2.47;
- E_T: 0 - 10 - 20 - 40 - 60 - 80 - 120 - 500 - 1000 and 5000 GeV.

An independent optimisation, through a different training procedure of the input variables of the algorithm, is performed for each bin of $|\eta_{\text{cluster}}|$, E_T and particle type. Among the various options the TMVA package offers (likelihood, neural networks,...), the *gradient boosted decision tree* is the algorithm with which the analysis is performed [120].

In order to assess the quality and the performance of the algorithm, the linearity and the resolutions of the distributions $\frac{E}{E_{\text{truth}}}$, where E is the electron energy reconstructed after the calibration, are tested. The mean and the standard deviation cannot be adopted as estimators since the energy response is usually non-gaussian and those estimators would not correctly account for the presence of tails in the distributions of $\frac{E}{E_{\text{truth}}}$. The linearity is therefore extracted as the peak position of $\frac{E}{E_{\text{truth}}}$ in bins of E_{truth} when fitting a gaussian core to the distribution in the region [-1,2] standard deviations around the mean value. The resolution is defined as the interquartile range $\frac{E}{E_{\text{truth}}}$, namely the distance between the first and the last quartile in each bin.

The linearity and the resolution of the MVA calibration are illustrated in Figure 4.5. The resulting non-linearity is below 0.3% in the barrel for E_{truth} above 10 GeV and it reaches ~ 0.8 % in the end-cap. The performance of the multivariate calibration and its improvement compared to the previous calibration scheme [116] has been verified on physical processes involving electrons in the final state. Figure 4.6 displays the invariant mass of the electron final states on the $J/\Psi \rightarrow ee$, $Z \rightarrow ee$ and $H \rightarrow ZZ^* \rightarrow 4e$ decay channels with and without the MVA calibration in action. These distributions clearly reflect the expected improvement in the linearity of the calibrated response by exhibiting a shift of the mean value of the distributions, displaced towards the PDG-mass of the resonance.

A second longitudinal layer intercalibration [111] of the first and second layer, containing most of the energy deposited by the electrons, is also performed because an accurate estimate of this intercalibration is critical to achieve good linearity in the energy response. Such intercalibration uses muons as probes. These results are verified by a study of the electron energy response as a function of the shower depth [111] and extra corrections, around 2% on average, are derived.

The relative calibration of the presampler layer (shown in Figure 4.7) is extracted from electrons, produced in W and Z decays, by comparing the presampler energy in data and in Monte Carlo simulations as a function of the longitudinal shower development measured in the calorimeter. The accuracy of this calibration is at the level of 5%. The measured presampler energy scale defines a correction factor that is applied to data.

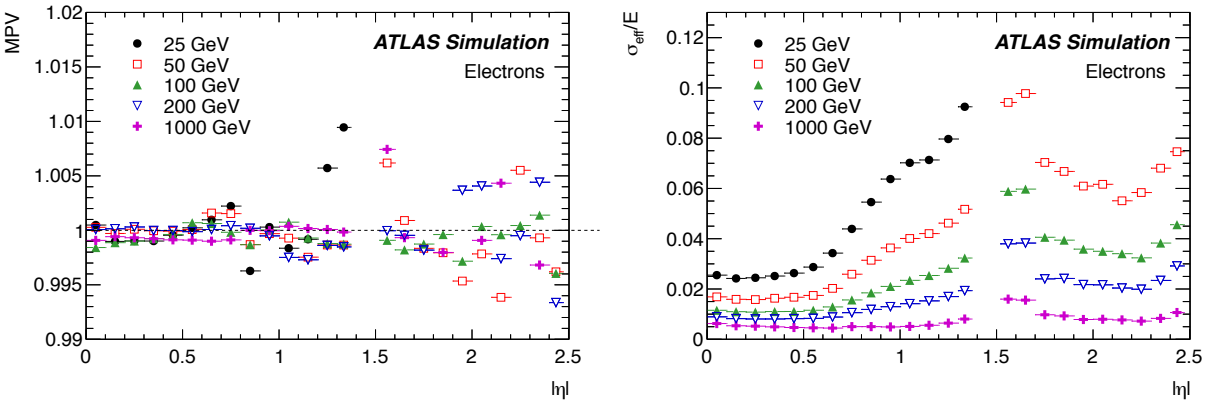

Figure 4.5: Most probable value (MPV) of $\frac{E}{E_{\text{truth}}}$ and relative effective resolution σ_{eff}/E as a function of $|\eta|$ for different energies.

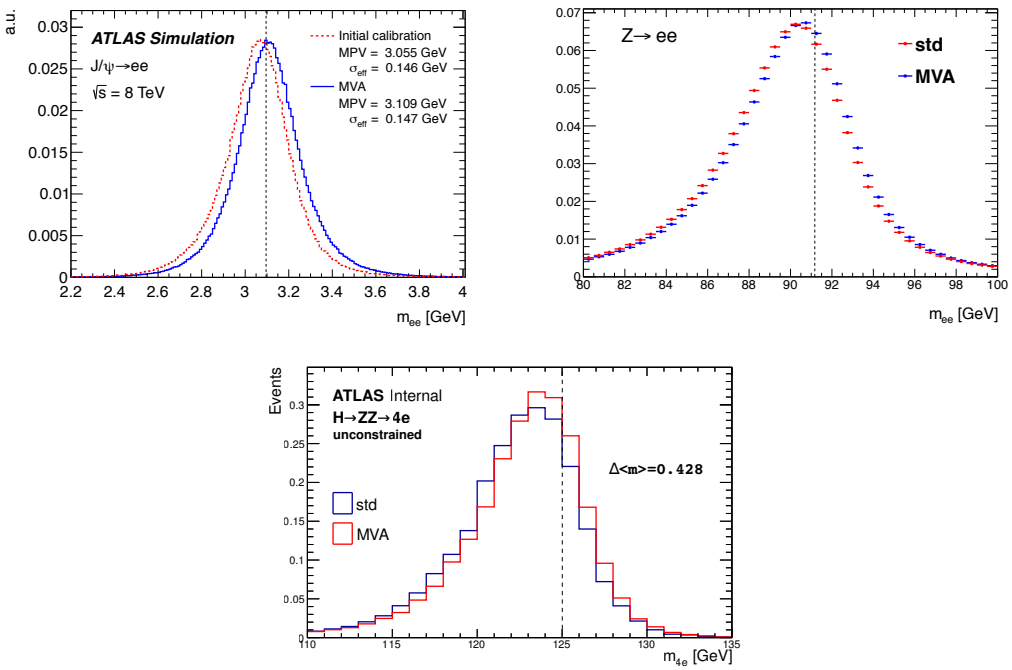

Figure 4.6: Di-electron invariant mass distributions for simulated J/Ψ $\rightarrow$ee, Z $\rightarrow$ee and H$\rightarrow$ ZZ^* $\rightarrow$4e decays comparing the standard and the MVA calibration responses. The dashed line indicate the PDG-mass [71] of the resonances.

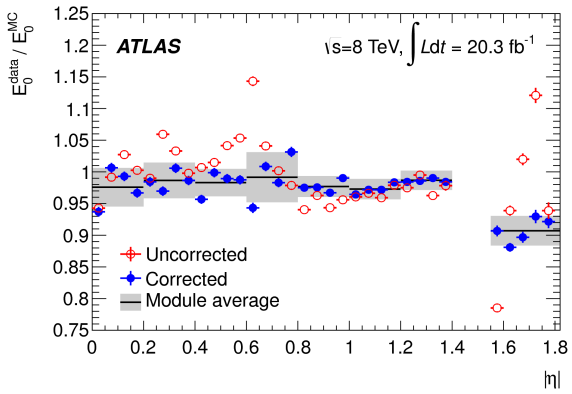

Figure 4.7: Ratio of average presampler energies for electrons in data and simulation as a function of pseudorapidity, before and after corrections to the first and second layer intercalibrations as well as the calibration of the presampler layer. The full lines with shaded bands represent the energy scale and its uncertainty

4.3 Energy scale and resolution determination from Z→ee events

As shown in Section 4.1, after the various corrections applied to data, the residual non-uniformity is at the level of approximately 0.8% (Figure 4.2). Moreover, the energy response is stable as a function of time and pile-up (Figure 4.3) up to 0.05%. The last step of the calibration process [111] comprises the corrections of the remaining differences between data and simulation (the *in-situ* calibration).

As for data, the energy scale correction α_i of the already-calibrated energy in a specific pseudorapidity bin i is defined as follows:

$$E^{data} = E^{MC}(1 + \alpha_i) \tag{4.1}$$

where E^{data} and E^{MC} are the electron energy in data and simulation respectively, α_i represents the departure from the optimal calibration of data. For Z→ee events, the effect of electron miscalibration in data on the electron pair invariant mass can be written as follows:

$$\begin{aligned} m_{ij}^{\text{data}} &= m_{ij}^{\text{MC}}(1 + \alpha_{ij}), \\ \alpha_{ij} &\sim \frac{(\alpha_i + \alpha_j)}{2}, \end{aligned} \tag{4.2}$$

m_{ij}^{data} and m_{ij}^{MC} are the invariant mass in data and simulation for an electron pair reconstructed in pseudorapidity bins i and j, herein α_{ij} is the shift on the mass peak. This derivation works under the hypothesis that the second order term of the expansion (4.2) is neglected and the angle between the two electrons is perfectly known.

Secondly, the Monte Carlo simulation is corrected to match the distribution seen in data by applying electron resolution correction (*smearing*) factors to the lineshape of the histograms. These smearing factors are derived under the assumption that the resolution curve is correctly modelled up to a Gaussian contribution that produces a constant term:

$$\left(\frac{\sigma_E}{E}\right)^{\text{data}} = \left(\frac{\sigma_E}{E}\right)^{\text{MC}} \oplus c. \tag{4.3}$$

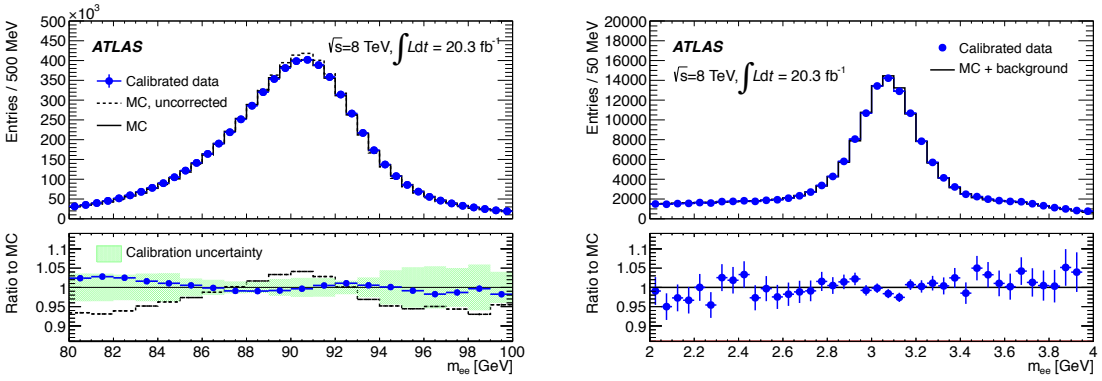

(a) **(b)**

Figure 4.8: (a) - Electron pair invariant mass distribution for Z resonance in data and Monte Carlo, Energy scale corrections are applied to data. The Monte Carlo contribution is shown before and after energy resolution corrections and is normalised to the number of events in data. Bottom: ratio of the data and uncorrected Monte Carlo distributions to the corrected Monte Carlo distributions with the calibration uncertainty bands. (b) - J/Ψ resonance in data and Monte Carlo after energy corrections on data and resolution smearing on Monte Carlo. The background is determined from the data and added to the simulated J/Ψ resonance.

For each η (i, j) category, equation (4.3) gives:

$$\begin{aligned}
\left(\frac{\sigma_m}{m}\right)_{ij}^{\text{data}} &= \left(\frac{\sigma_m}{m}\right)_{ij}^{\text{MC}} \oplus c_{ij} \\
&= \frac{1}{2}\left[\left(\frac{\sigma_E}{E}\right)_i^{\text{MC}} \oplus c_i \oplus \left(\frac{\sigma_E}{E}\right)_j^{\text{MC}} \oplus c_j\right], \\
c_{ij} &= \frac{(c_i \oplus c_j)}{2},
\end{aligned} \tag{4.4}$$

where c_{ij} is the invariant mass resolution correction for (η_i, η_j). To determine the energy scale corrections to data (α) and the smearing corrections (gaussian term c) to Monte Carlo, template histograms of the invariant mass of the dielectron final state in the $Z \rightarrow$ee channel are created from the simulation and built separately for the electron configurations in bins of η. They form a two-dimensional grid along α_{ij} and c_{ij}. The optimal value of the two parameters are obtained by a χ^2 minimisation [111].

After all corrections, the final state invariant mass distribution agrees in data and Monte Carlo to a level of 1%. Figure 4.8 (a) presents the dielectron invariant mass distribution of the data corrected with the energy scale factors α and of the Monte Carlo simulation with and without the resolution corrections in actions. The small excess located in the low mass region is explained by the presence of tails in data that are not properly modelled in the simulation. An orthogonal cross-check on the procedure of the extraction of the scales has been performed on a J/Ψ $\rightarrow$ee sample. Figure 4.8 (b) shows the electron pair invariant mass distribution in data and Monte Carlo; the corrected data and the simulation agree within statistical uncertainties throughout the whole mass range.

4.4 Analysis of the systematic uncertainties

4.4.1 Systematic uncertainties on the energy scale

The scale for electrons with transverse energy E_T close the to that of $Z \rightarrow$ee events ($E_T \sim 40$ GeV) is determined by the calorimeter energy scale adjustments illustrated in Section 4.3. The main sources of systematic uncertainties [111] that are accounted for in the analysis are listed below.

- Uncertainty on the $Z \rightarrow$ ee electron calibration.
- Uncertainty on the non-linearity of the energy measurement at the cell level: it is mostly produced by the relative calibration of the different gains used in the calorimeter readout (Section 4.1). The measurement is performed on data by comparing the Z peak position for electron clusters whose cells are recorded in High Gain to electron with at least one cell recorded in the Medium Gain. The full size of the effect is taken as a systematic uncertainty. Another verified effect was the impact of the energy pedestal of electrons comparing pile-up only events in data and Monte Carlo. The induced energy non-linearity is negligible at high energies.
- Uncertainty on the relative calibration of the different calorimeter layers.
- Uncertainty on the amount of material in front of the calorimeter (Chapter 2).
- Uncertainty on the reconstruction of photon conversion: converted and unconverted photons are calibrated in a different way [111] [121] to account for different energy losses before the calorimeter, hence the misidentification of the particles can lead to an energy shift of approximately 2%.
- Uncertainty on the modelling of the lateral shower shape: differences between data and simulation for the lateral development of the electromagnetic showers can contribute to the uncertainty on the energy scale of the particle.

Other sources of systematics are sub-leading and are therefore not explicitly included. All the above-defined sources are treated as independent and their quadratic sum defines the total uncertainty at a given E_T and η. Table 4.1 shows the summary of the energy scale systematic uncertainties estimated from electrons with E_T=11 GeV and E_T=40 GeV. The last two items on the list above are labelled as *other sources*.

The total uncertainty on the electron energy scale is strongly η-dependent: at E_T of 40 GeV (electrons from the Z decays) it is on average 0.03% for $|\eta| <1.37$, 0.2% for $1.37< |\eta| <1.82$ and 0.05% for $|\eta| >1.82$. At a transverse energy of approximately 10 GeV, the electron energy scale uncertainty spans form 0.4% to 1% for $|\eta| <1.37$; it is about 2% for $1.37< |\eta| <1.82$ and 0.4% for $|\eta| >1.82$.

To fully validate the procedure of the energy scale extraction, an independent check is performed using sample of $J/\Psi \rightarrow$ee decays. The results are in very good agreement with the values determined from the $Z \rightarrow$ee sample. Figure 4.9 summarises the verification of the electron energy scale from $Z \rightarrow$ee and $J/\Psi \rightarrow$ee samples in bins of pseudorapidity. To check the non-linearity in the electron energy scale, namely the shift with respect to 0 of the relative scale difference between the measured electron energy and the nominal energy scale, the plots are also shown in bins of electron E_T. The same analysis has been performed on the 7 TeV dataset and results are found to be fully consistent.

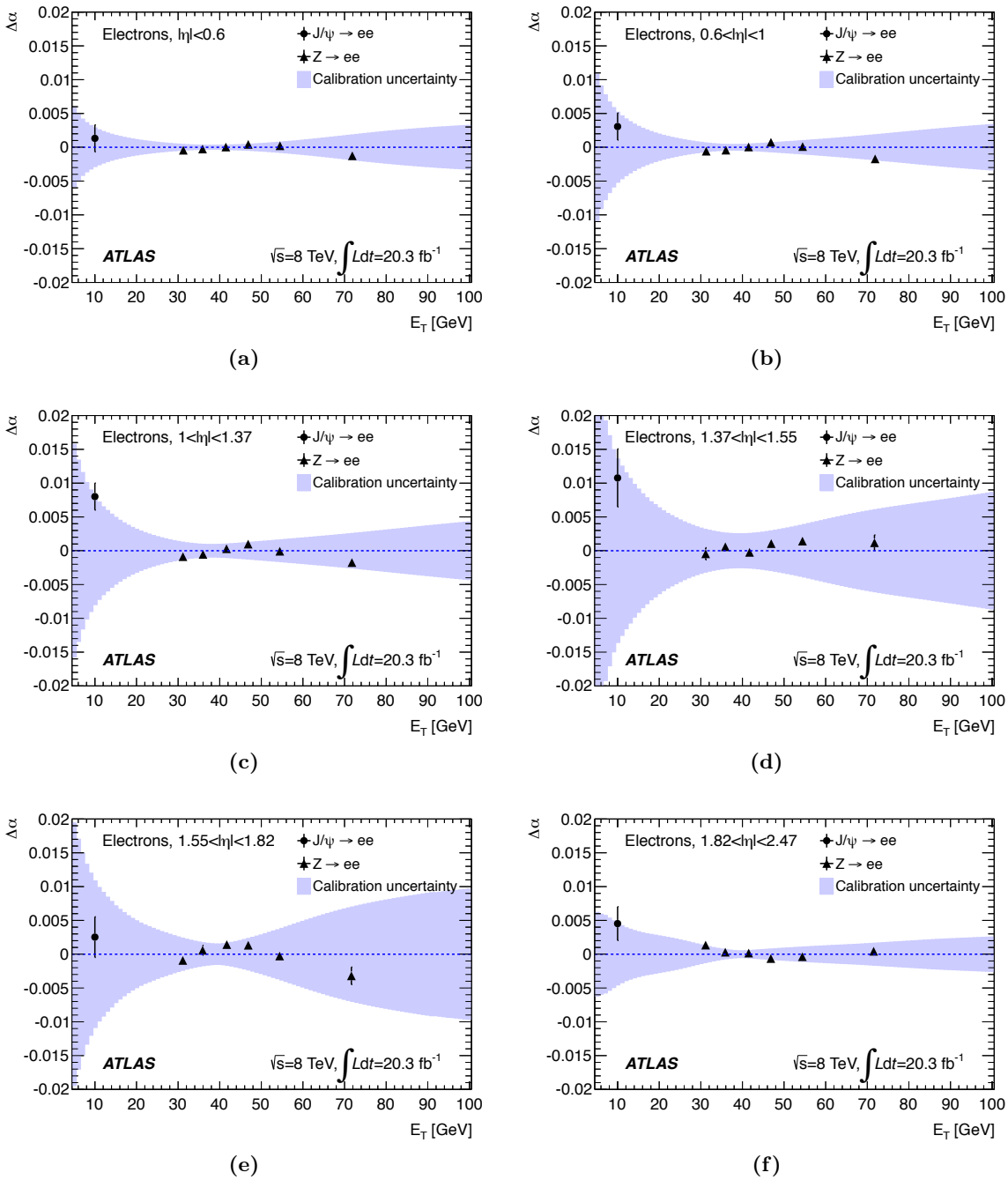

Figure 4.9: Energy scale factors $\Delta\alpha$ obtained after Z-based calibration from the J/Ψ →ee and Z →ee analyses, as function of E_T and in different pseudorapidity bins (a) to (f). The band represents the calibration systematic uncertainty. The error bars on data points represent the total statistical uncertainty.

$\|\eta\|$ range - E_T=11 GeV	0-0.6	0.6-1	1-1.37	1.37-1.55	1.55-1.82	1.82-2.47
$Z \rightarrow$ee calibration	0.03	0.04	0.08	0.22	0.22	0.05
Energy non linearities	0.09	0.09	0.07	0.00	0.09	0.24
Layer calibration	0.15	0.19	0.14	0.16	0.13	0.19
ID Material	0.03	0.03	0.31	0.88	0.33	0.10
Other sources	0.12	0.38	0.58	0.20	1.00	0.15
Total	0.22	0.44	0.69	0.94	1.09	0.36
$\|\eta\|$ range - E_T=40 GeV	0-0.6	0.6-1	1-1.37	1.37-1.55	1.55-1.82	1.82-2.47
$Z \rightarrow$ee calibration	0.03	0.04	0.08	0.22	0.22	0.05
Energy non linearities	0.00	0.00	0.00	0.00	0.02	0.01
Layer calibration	0.01	0.01	0.01	0.00	0.00	0.01
ID Material	0.00	0.00	0.01	0.00	0.00	0.00
Other sources	0.00	0.01	0.02	0.00	0.02	0.00
Total	0.03	0.04	0.08	0.22	0.22	0.05

Table 4.1: Summary of energy scale systematic uncertainties contributions (in %) estimated for electrons with E_T=11 GeV and E_T=40 GeV.

4.4.2 Systematic uncertainties on the calorimeter energy resolution

The main sources on the systematic uncertainties of the calorimeter energy resolution are related to the modelling of the sampling term and to the measurement of the constant term c in Z boson decays and from the uncertainty in the modelling of the small contribution to the resolution from fluctuations in the pile-up regime, from other proton-proton interactions in the same or neighbouring bunch crossing. The value of the uncertainty on the calorimeter energy resolution is typically 5% to 10% for electrons in the E_T range from 10 to 45 GeV. The resolution curve is shown for electrons in Figure 4.10 (a), as a function of energy for $|\eta| = 0.2$. The different contributions to the resolution uncertainty are shown in 4.10 (b) . The relative uncertainty is minimal for electrons at 40 GeV, where the measurement of the constant term of the electron resolution translates into an uncertainty of the order of 5%. At higher transverse energy, the sampling term and detector material contributions are significant; at low energy, the pile-up contribution dominates.

4.5 Improving the energy resolution using the E-p combination

4.5.1 Motivation of the E-p combination

The motivation for performing a combination of the track momentum and cluster energy ($E - p$ *combination*) is to improve electron energy resolution, particularly for particles with low transverse momentum (p_{T}). This motivation stems from the fact that momentum resolution provides the best energy estimate for low p_T particles, whereas the calorimeter energy measurement is superior for high p_T particles, as illustrated in Figure 4.11. The main physics channel that profits from the track momentum and cluster energy combination is the $H \rightarrow ZZ \rightarrow 4\mathrm{l}$ (detailed in Chapter 5) decay mode with electrons in the final state.

Before the inclusion of the $E - p$ combination algorithm [122] in the treatment of the electrons in the final state [20], the electron four-momentum used to be derived from the calorimeter-based cluster energy, the track position and direction. However, since the lowest electron transverse momentum cut of the Higgs candidate quadruplet lies at 7 GeV, the room for energy resolution

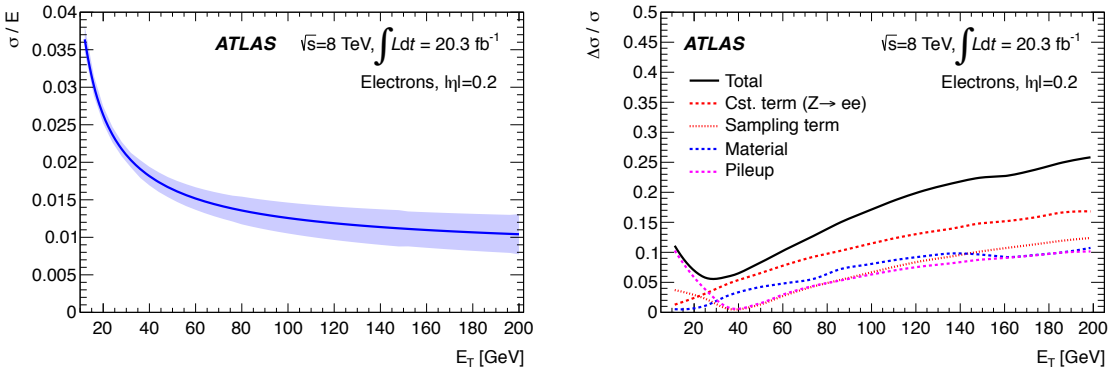

(a) **(b)**

Figure 4.10: (a) - Resolution curve and its uncertainty as a function of E_T for electrons with $|\eta|$ <0.2. (b) -Contributions of the different uncertainties to the relative resolution uncertainty as a function of E_T for electrons with $|\eta|$ <0.2.

improvements in the low p_T range can be exploited by performing the track-cluster combination. The combination also stands to benefit energy resolution in problematic parts of the electromagnetic calorimeter, such as the crack region in $1.37 < |\eta| < 1.52$, where the response tends to be poorer for electrons. Another beneficial point is that the systematic uncertainties on the overall electron energy scale are reduced due to the excellent energy scale of the track.

The *likelihood* method uses Monte Carlo modelling to generate profiles of track and cluster p_{T} relative to truth information, and forms a combined measurement based on the maximisation of a likelihood function derived from these profiles. The performance of the method is evaluated and compared using data and Monte Carlo samples of J/Ψ and Z dielectron resonances, as well as Monte Carlo samples of gluon fusion-mediated $H \to ZZ \to 4l$ decays. A brief description of the software developed for the ATLAS reconstruction chain comprising the $E-p$ combination algorithm is included in Appendix A.

4.5.2 The likelihood combination algorithm

In order to use the $E-p$ combination in an optimal manner, it is necessary to derive criteria that demarcate a phase space in which the track momentum measurement can potentially improve the resolution of the cluster energy. In this analysis, these criteria took the form of rectangular cuts on quantities related to the quality of the track measurement at reconstruction-level, and also relate to the truth-level behaviour of the electron.
Three quantities are used to define criteria for each of the methods presented here. The first quantity is the absolute value of the difference in track and cluster measurements, relative to the track momentum,

$$\mathrm{diff} = \frac{|E_{\mathrm{Clus}} - P_{\mathrm{Track}}|}{P_{\mathrm{Track}}}. \tag{4.5}$$

The difference in track momentum between the reconstructed perigee, and the last space-point before entering the ECAL, is defined as f_{Brem}. This quantity is given by,

$$f_{\mathrm{Brem}} = \frac{|p_{\mathrm{LM}} - p_{\mathrm{Perigee}}|}{p_{\mathrm{Perigee}}} \tag{4.6}$$

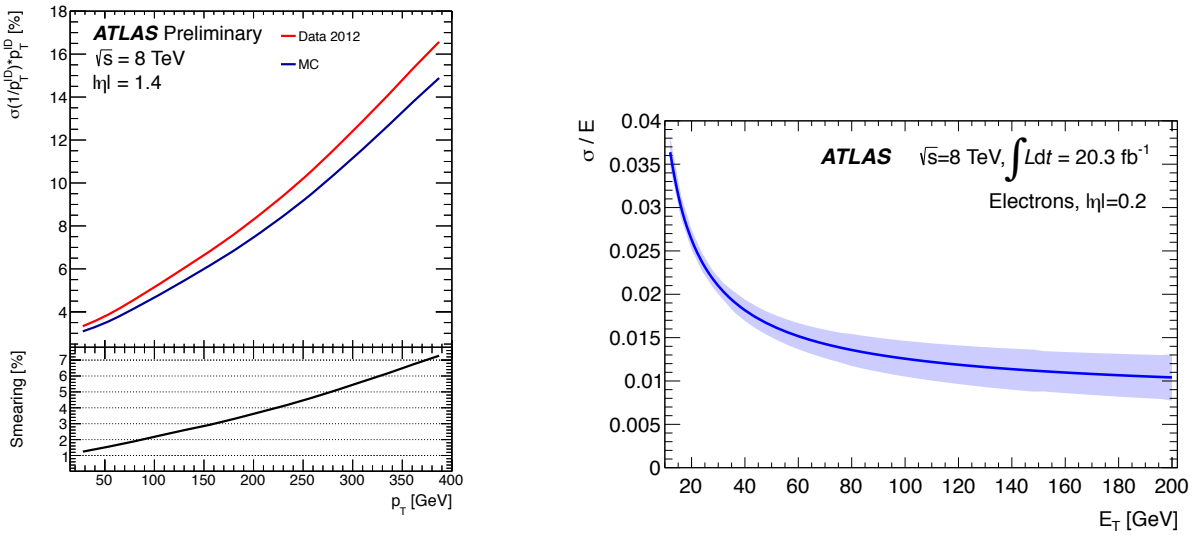

(a) **(b)**

Figure 4.11: Inner detector (a) and calorimeter resolution (b) for electrons as a function of p_T and E_T in various pseudorapidity regions.

where p_{Perigee} is the momentum measurement at the closest approach to the beam axis, and p_{LM} is the momentum measurement at the last measurement (LM) point in the tracker. The agreement between the track momentum and cluster energy measurements, relative to their respective measurement uncertainties, is also calculated as,

$$\sigma(E-p) = \frac{|E-p|}{\sqrt{\sigma_E^2 + \sigma_p^2}}. \tag{4.7}$$

Description of the method

To begin the likelihood combination approach, single electron transverse momenta (p_{T}), as measured in the Inner Detector, and cluster energies are both compared with their values using a Monte Carlo control sample. Electrons are placed in 12 categories according to their transverse momentum and pseudorapidity (η), as given in Table 4.2.

p_{T} Region	Definition
Low	$7 < p_{\text{T}} < 15\,\text{GeV}$
Medium	$15 < p_{\text{T}} < 30\,\text{GeV}$
High	$p_{\text{T}} > 30\,\text{GeV}$

$\lvert\eta\rvert$ Region	Definition
Central	$\lvert\eta\rvert < 0.8$
Medium	$0.8 < \lvert\eta\rvert < 1.37$
Crack	$1.37 < \lvert\eta\rvert < 1.52$
Forward	$1.52 < \lvert\eta\rvert < 2.5$

Table 4.2: Definitions of the p_{T} and $|\eta|$ regions used in this analysis.

Another categorisation is performed through the usage of the variable f_{Brem}, as defined in Section 4.5.2 shown in Figure 4.12. This criterion is implemented to isolate electrons which have lost relatively little energy due to bremsstrahlung in the Inner Detector (i.e. $f_{\text{Brem}} \sim 0$), with respect to those with higher brem losses ($f_{\text{Brem}} \to 1$). Based on f_{Brem} distributions in η and p_{T} categories, additional cuts are employed to select two different low and high bremsstrahlung kinematic regions.

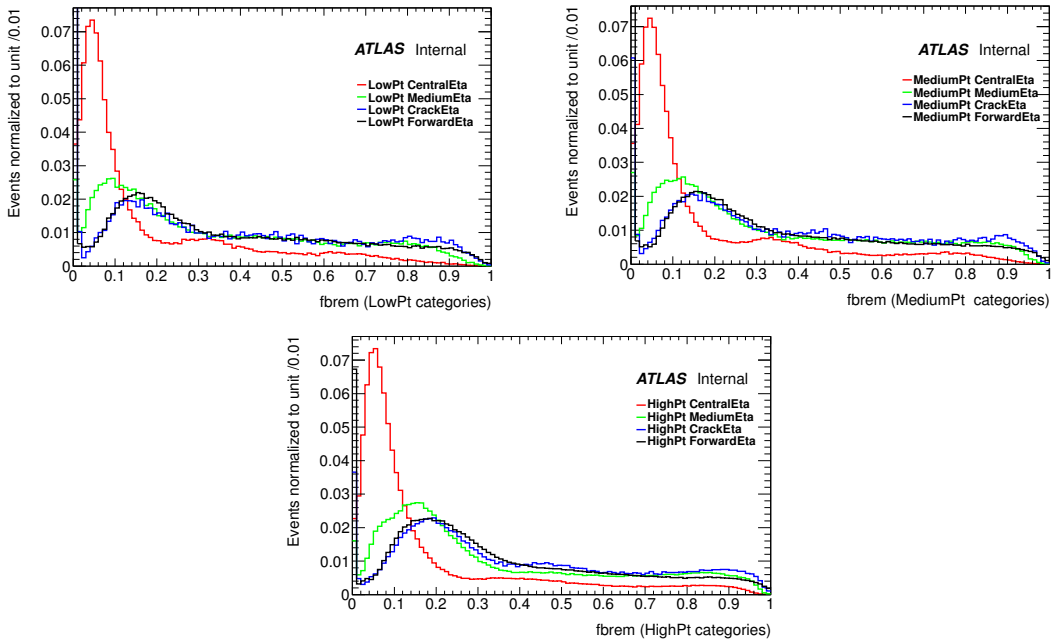

Figure 4.12: Distribution of f_{Brem}in the low, medium and high p_{T} regions as a function of the pseudorapidity of the electrons.

For each category in η, p_{T} and f_{Brem}, the ratios $p_{\text{T}}^{\text{Cluster}}/p_{\text{T}}^{\text{Truth}}$ and $p_{\text{T}}^{\text{Track}}/p_{\text{T}}^{\text{Truth}}$ are calculated.

In specific zones - mostly the one with low p_{T} electrons, in the central pseudorapidity region - the track-based p_{T} produces a better resolution than that which is calculated through the cluster-based method. A Crystal Ball fit [123] is then applied for both $p_{\text{T}}^{\text{Cluster}}/p_{\text{T}}^{\text{Truth}}$ and $p_{\text{T}}^{\text{Track}}/p_{\text{T}}^{\text{Truth}}$, with the parameters extracted from the fit, and used in the algorithm. This parametrisation is chosen because this functional form takes into account the Gaussian core resolution and the radiative tail. The parameters extracted by the fit are then used as input variables in the combination algorithm. Figures 4.13 and 4.14 show some examples of Crystal Ball fits for cluster and track in the central, medium, and high transverse momentum regions for electrons in the central and medium $|\eta|$ regions, respectively. These probability density functions (PDFs) are computed for each η, p_{T}, and f_{Brem} categories, and only when electrons pass the $\sigma(E-p)$ cut (see 4.5.2). In other words, these functions are computed exclusively for electrons whose energy and momentum will be combined by the algorithm.

A maximum-likelihood fit of $p_{\text{T}}^{\text{Track}}$ and $p_{\text{T}}^{\text{Cluster}}$ is implemented based on these ratios, with two functions defined,

$$\mathcal{F}_1\left(\frac{p_{\text{T}}^{\text{Track}}}{x}\right) \quad \text{and} \quad \mathcal{F}_2\left(\frac{p_{\text{T}}^{\text{Cluster}}}{x}\right), \tag{4.8}$$

where $\mathcal{F}_{1,2}$ are respectively track and cluster ratio Crystal Ball PDFs. For each electron, characterised by $p_{\text{T}}^{\text{Track}}$ and $p_{\text{T}}^{\text{Cluster}}$, a product is computed,

$$-\log\left[\mathcal{F}_1\left(\frac{p_{\text{T}}^{\text{Track}}}{x}\right)\cdot\mathcal{F}_2\left(\frac{p_{\text{T}}^{\text{Cluster}}}{x}\right)\right]. \tag{4.9}$$

The combined transverse momentum ($p_{\text{T}}^{\text{Comb}}$) for a given electron, as well as its error, are extracted through the minimisation of this product with respect to the independent variable x.

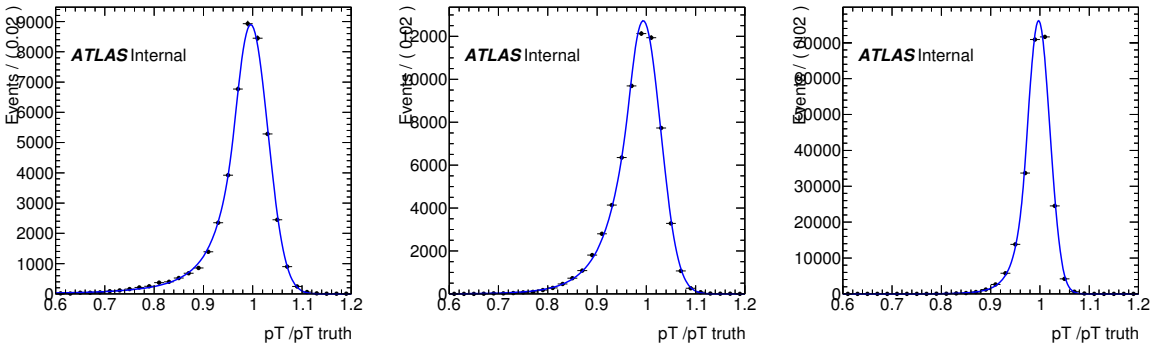

(a) Low p_{T}, central $|\eta|$ **(b)** Medium p_{T}, medium $|\eta|$ **(c)** High p_{T}, medium $|\eta|$

Figure 4.13: Crystal Ball fits to $p_{\mathrm{T}}^{\mathrm{Cluster}}/p_{\mathrm{T}}^{\mathrm{Truth}}$ distributions in various transverse momentum and pseudorapidity regions.

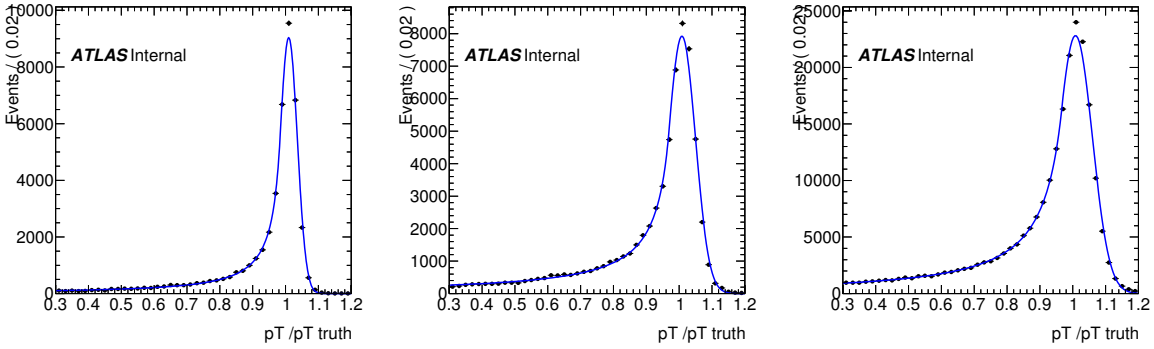

(a) Low p_{T}, central $|\eta|$ **(b)** Medium p_{T}, medium $|\eta|$ **(c)** High p_{T}, medium $|\eta|$

Figure 4.14: Crystal Ball fits to $p_{\mathrm{T}}^{\mathrm{Track}}/p_{\mathrm{T}}^{\mathrm{Truth}}$ distributions in various transverse momentum and pseudorapidity regions.

The track-cluster parametrisation through PDFs is exploited in fixed bins of p_T, η and f_{Brem} categories hence it is prone to boundary effects for electrons lying in regions that are close to the border between one category and another. The performance of the algorithm was therefore cross-checked by exploiting more bins in p_T and η. As a preliminary closure test and validation of the method, the parameters defining the Crystal Ball PDFs have been analysed and they smoothly evolve from one region to another as expected. For instance, Figure 4.15 illustrates that the standard deviations of the Crystal Ball distributions regularly decrease proportionally to $\frac{1}{\sqrt{p_T}}$. A continuous parametrisation of the probability density functions was also worked out so that for each electron, relevant values of the Crystal Ball parameters (mean value of the distribution, its standard deviation, ...) are used instead of the binned values. This approach has not yielded significantly better results than the present procedure (fixed parametrisation of the PDFs in bins of transverse momentum, pseudorapidity and f_{Brem}) thence the fixed PDF parametrisation has been adopted.

The combination

The first step of the likelihood-based procedure is to decide whether the combination is to be applied or not for a given electron, based on a rectangular cut on $\sigma(E-p)$. If $\sigma(E-p)$ is lower than a certain threshold, the cluster and track measurements are deemed consistent, and the combination algorithm

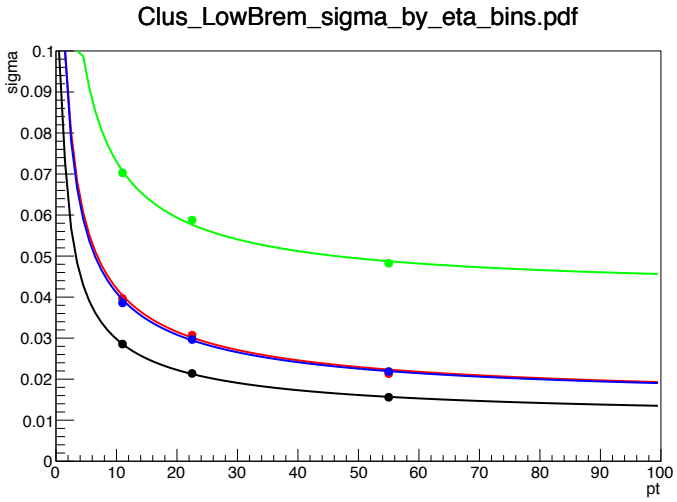

Figure 4.15: Functional form of the σ parameter of the Crystal Ball with which the distributions of $p_T^{\text{track}}/\ p_T^{\text{truth}}$ and $p_T^{\text{cluster}}/\ p_T^{\text{truth}}$ are fitted. The different colours stands for different η regions of the electron candidates: central η (black), medium η (red), crack η (green) and forward η (blue).

can be applied. On the other hand, if $\sigma(E-p)$ is larger than the threshold, the two measurements are deemed incompatible, and the cluster energy is returned. This procedure is explained in the two-dimensional distribution of $p_{\text{T}}^{\text{Cluster}}/p_{\text{T}}^{\text{Truth}}$ and $p_{\text{T}}^{\text{Track}}/p_{\text{T}}^{\text{Truth}}$ (see Figure 4.16): electrons with small $\sigma(E-p)$ populate the bulk of the distribution, while the other, external regions demonstrate a larger difference in the cluster and track measurements. The threshold value for $\sigma(E-p)$ has been optimised with the best cut found to be $\sigma(E-p) < 4$. Note the small clustered population along the equation $p_{\text{T}}^{\text{Track}}/p_{\text{T}}^{\text{Truth}} + p_{\text{T}}^{\text{Cluster}}/p_{\text{T}}^{\text{Truth}} = 1$, due to electrons where the track misses completely its relative cluster. This population is isolated in the track-cluster phase space and for these electrons the combined p_{T} is taken as the sum of cluster and track measurements. To conclude, the algorithm can be summarised as follows:

- If $\sigma(E-p) < 4$, then the $E-p$ combination is applied (else the cluster is returned);
- If $p_{\text{T}}^{\text{Cluster}}/p_{\text{T}}^{\text{Truth}} < 0.4$ for the central p_{T} region (0.16 for the medium p_{T} region): $p_{\text{T}}^{\text{Comb}} = p_{\text{T}}^{\text{Cluster}} + p_{\text{T}}^{\text{Track}}$.

4.5.3 Results - Validation of the algorithm on Monte Carlo and data samples

Samples and event selection

The validation of the combination method was performed using both Monte Carlo and data samples. Parton-level interactions in the Monte Carlo events were produced using the POWHEG [124] [125] generator, with pp collisions simulated at $\sqrt{s} = 8\,\text{TeV}$. Parton showering is handled by interfacing the initial hard scattering interactions with the PYTHIA [126] showering Monte Carlo package, with the truth-level information run through a full detector simulation in GEANT4 [127] [128]. The detector-level information is then reconstructed using the ATLAS offline reconstruction software. All data samples used in this analysis were obtained using the full 2012 ATLAS dataset, corresponding to $20.7 \pm 0.7\,\text{fb}^{-1}$ of $\sqrt{s} = 8\,\text{TeV}$ proton-proton collisions, with a total data taking efficiency of 93%.

In order to be considered for inclusion in the combination analysis, all electrons were required

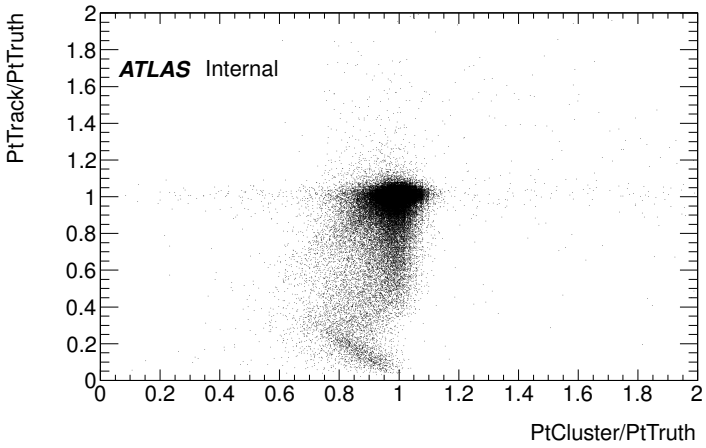

Figure 4.16: Two-dimensional phase space of $p_{\mathrm{T}}^{\mathrm{Track}}/p_{\mathrm{T}}^{\mathrm{Truth}}$ as a function of $p_{\mathrm{T}}^{\mathrm{Cluster}}/p_{\mathrm{T}}^{\mathrm{Truth}}$.

to pass loose electron ID requirements and have an uncombined $p_{\mathrm{T}} > 7\,\mathrm{GeV}$[1]. For dielectron resonances (i.e. $J/\psi \to ee$ and $Z \to ee$), the constituent electron pairs were required to have opposite charge, and for events with more than one candidate pair, the highest p_{T} pair is chosen. All electrons are subjected to energy corrections in data, while an energy smearing factor is applied to electrons in Monte Carlo to match the resolution in data [111].

Single electron Monte Carlo

To perform an initial examination of the performance of the combination algorithm, single electron Monte Carlo samples were produced with nominal detector geometry. Single electrons are generated with flat E_T in the range $[7-80]$ GeV, and passed through the ATLAS offline reconstruction software. In terms of selection, electrons are required only to have loose ID, and uncombined $p_{\mathrm{T}} > 7\,\mathrm{GeV}$. Shown in Figure 4.17 are distributions of $p_{\mathrm{T}}/p_{\mathrm{T}}^{\mathrm{Truth}}$ for electrons before and after the likelihood $E-p$ combinations are applied, respectively. Table 4.3 reports the change in mean of each distribution, along with the fraction of tails, as quantified by a Gaussian fit to each distribution between $[0.9, 1.2]$.

For single electrons, the likelihood combination method shows the best potential for improvement in cases of low p_{T} electrons, and electrons in the central region of the detector. Electrons in the forward region, or those with high p_{T}, do not benefit in a significant way from the combination. The reason is that the presence of a greater amount of material outside of the medium $|\eta|$ region leads to a significant degradation in the track momentum resolution, and the combination is therefore entirely driven by the cluster energy. As for the p_T dependence in the high transverse momentum category, the cluster resolution is better than the one of the track.

Since there is no benefit in using this procedure for forward electrons and in the high transverse momentum region, in proceeding studies ($\mathrm{J}/\Psi \to ee$, $Z \to ee$ and $H \to ZZ \to 4l$) , the final state invariant mass is computed using this algorithm only for electrons lying in the central, medium, and crack $|\eta|$ regions, for low and medium p_{T}, where the resolution is significantly improved by the track-cluster combination. For the forward η, and the high p_{T} categories, the cluster-based transverse momentum is kept.

[1]The combination threshold on p_T has been defined in such a way to be the same to the one used in the $H \to ZZ \to$ 4l analysis for electrons.

Low p_{T}				
$\lvert\eta\rvert$ region	σ_{Clus}	% tails (cluster)	σ_{Comb}	% tails (combined)
Central	4.4	9.7	2.5	9.8
Medium	6.5	11.5	3.7	11.4
Crack	13.0	9.1	7.0	9.4
Forward	5.6	14.1	5.6	15.0
Medium p_{T}				
Central	3.0	6.4	2.4	6.2
Medium	4.6	6.6	4.1	6.7
Crack	8.9	8.7	8.1	9.7
Forward	4.0	9.0	4.0	10.1
High p_{T}				
Central	2.0	1.5	2.0	2.0
Medium	2.8	3.0	2.9	3.5
Crack	6.0	6.5	5.7	6.4
Forward	2.7	5.2	2.7	5.3

Table 4.3: Energy resolution width and tails for Monte Carlo single electron events before and after the combination.

In addition, distributions of pulls for cluster and combined energies were computed:

$$\mathcal{P}(p_{\mathrm{T}}^{\mathrm{Reco}}) = \frac{p_{\mathrm{T}}^{\mathrm{Reco}} - p_{\mathrm{T}}^{\mathrm{Truth}}}{\sigma(p_{\mathrm{T}}^{\mathrm{Reco}})}. \tag{4.10}$$

The pulls are calculated in the categories where the combination is applied (low and medium p_{T}, in the central, medium, and crack $|\eta|$ regions). The results are displayed in Figure 4.18. The widths of the combined energy pulls are almost always smaller or equal to those of the uncombined energy pulls. The explanation for this behaviour is that the cluster energy error relies on a purely Gaussian approximation, which does not account for the non-Gaussian tail from cases where $E_{\mathrm{Reco}} < E_{\mathrm{Truth}}$. Consequently, the cluster energy uncertainty is frequently underestimated, whereas the combined error returned by the combination is given by the uncertainty on the likelihood functional form, thus it takes into account the real PDF lineshape.

J/Ψ $\rightarrow$ee Monte Carlo and data

A generation of J/Ψ Monte Carlo samples is used in this analysis and is composed of prompt (direct production) and non-prompt ($b \rightarrow J/\Psi$ decays) productions, with nominal ATLAS detector geometry [111]. All J/$\Psi \rightarrow ee$ candidates are required to pass initial selection criteria on object quality, electron ID, and transverse momentum prior to combination [111]. Beyond the cuts on electron p_{T} and quality, it is required that each selected dielectron pair has $1 < m_{ee} < 5\,\mathrm{GeV}$. Moreover, if more than one J/Ψ candidates is found, the highest oppositely-charged p_{T} pair is chosen. Figure 4.19 shows the excellent data - Monte Carlo agreement of the samples.

The prompt and non-prompt J/Ψ Monte Carlo samples used in this study are reweighted to their expected proportions in data, with different triggers applied, based on the following sample filters:

- **e3e3:** Leading $p_{\mathrm{T}} \in [4, 9]$ GeV $\rightarrow$ `EF_e5_tight1_e4_etcut_Jpsi`
- **e3e8:** Leading $p_{\mathrm{T}} \in [9, 14]$ GeV $\rightarrow$ `EF_e5_tight1_e9_etcut_Jpsi`

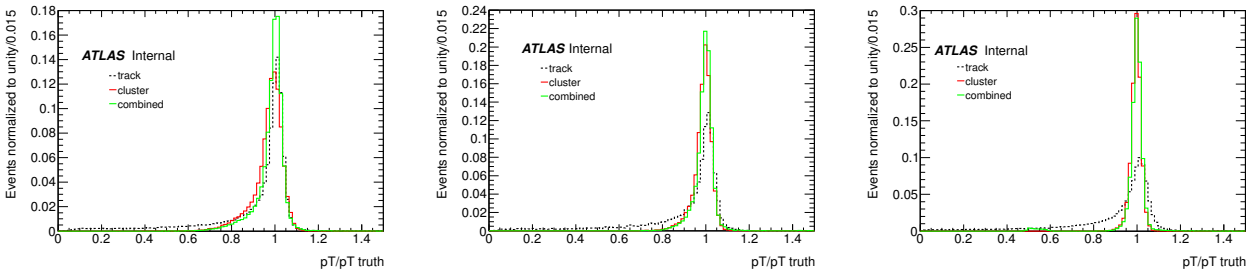

(a) Central, low p_{T} **(b)** Central, medium p_{T} **(c)** Central, high p_{T}

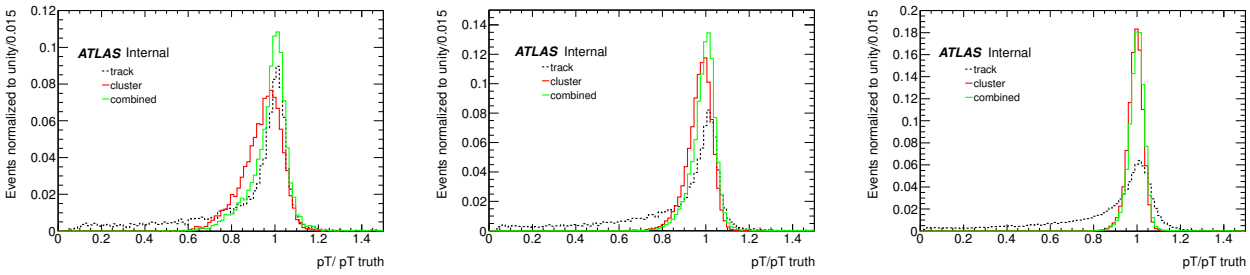

(d) Medium, low p_{T} **(e)** Medium, medium p_{T} **(f)** Medium, high p_{T}

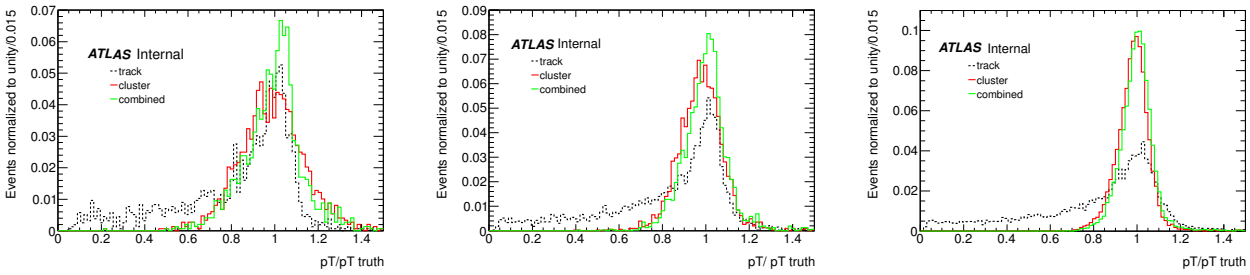

(g) Crack, low p_{T} **(h)** Crack, medium p_{T} **(i)** Crack, high p_{T}

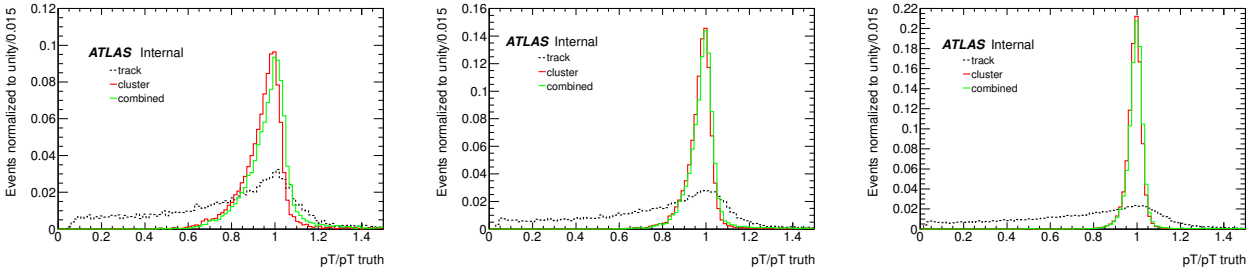

(j) Forward, low p_{T} **(k)** Forward, medium p_{T} **(l)** Forward, high p_{T}

Figure 4.17: Improvement in $p_{\mathrm{T}}/p_{\mathrm{T}}^{\mathrm{Truth}}$ for Monte Carlo single electrons after the $E-p$ combination, as compared to the standard approach (E_{Clus} only) and the track distribution as well.

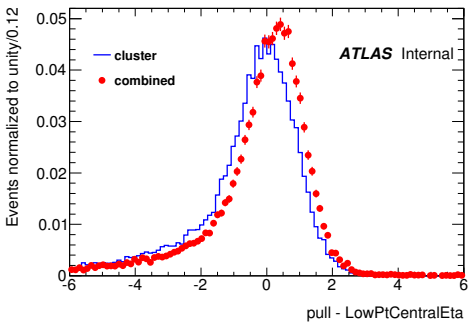

(a) Pull: central $|\eta|$, low p_{T}

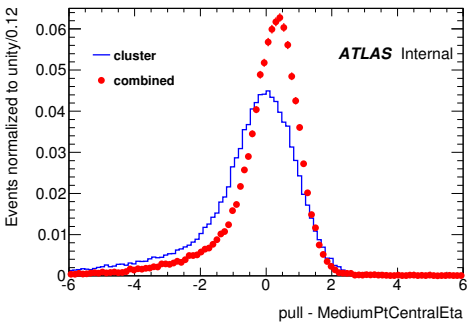

(b) Pull: central $|\eta|$, medium p_{T}

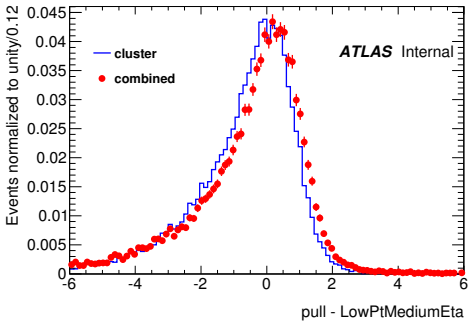

(c) Pull: medium $|\eta|$, low p_{T}

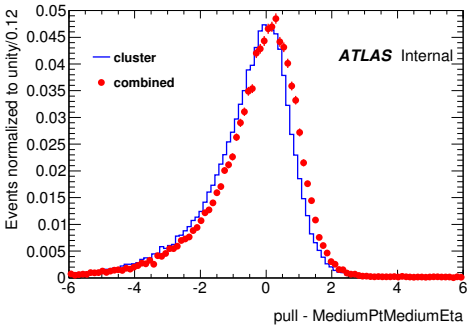

(d) Pull: medium $|\eta|$, medium p_{T}

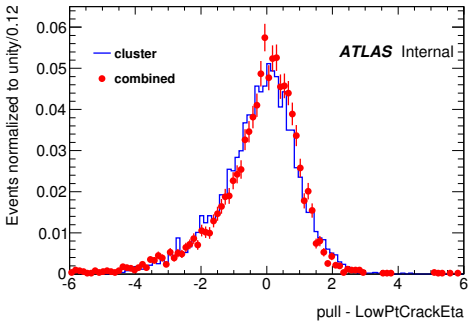

(e) Pull: crack $|\eta|$, low p_{T}

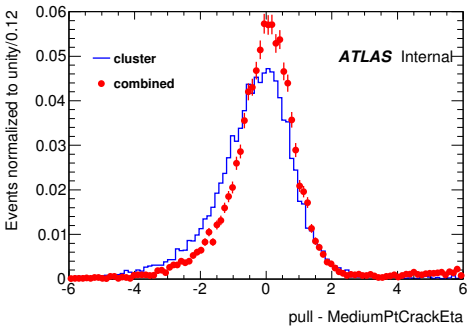

(f) Pull: crack $|\eta|$, medium p_{T}

Figure 4.18: Pull distributions of the cluster and combined transverse momentum.

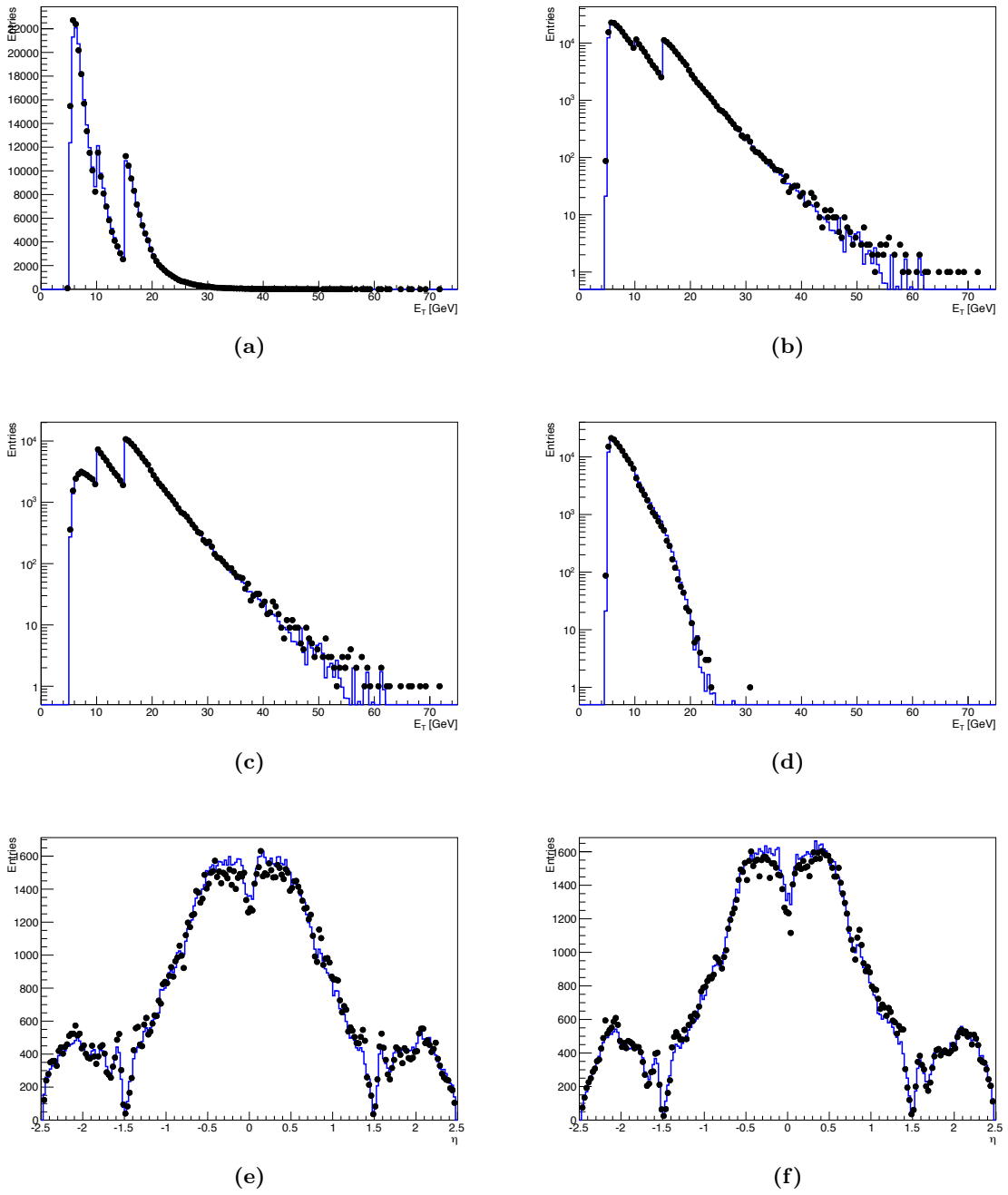

Figure 4.19: Data distributions (in black) compared with the corresponding ones from combined (prompt and non-prompt samples) Monte Carlo prediction (in blue) for $J/\Psi \rightarrow$ee decays. (a) and (b) - both electrons E_T in linear and logarithmic scale. (c) and (d) - E_T for leading and sub-leading electron. (e) and (f) - η for leading and sub-leading electron.

- **e3e13:** Leading $p_{\mathrm{T}} \in [14, \infty)$ GeV $\rightarrow$ `EF_e5_tight1_e14_etcut_Jpsi`

These triggers are at the Event Filter level and require leading and sub-leading p_T electrons of 5, 4, 9 and 14 GeV respectively. The identification criteria for these electron is *tight* (Chapter 3).

The invariant mass distributions for Monte Carlo $\mathrm{J}/\Psi \rightarrow ee$ events, with and without the combination in effect, are presented in Figure 4.20. The distributions are shown in pseudorapidity regions, with the requirement that both electrons fall in the designated pseudorapidity bin, e.g. for a central J/Ψ candidate, both electrons must have $|\eta| < 0.7$. The most noticeable improvement in the invariant mass resolution appears in the central regions; the peak is sharper for the combined distribution, and the tails of the distribution have narrowed with respect to those of the cluster-based distribution. Reasonable improvement is also observed in the medium and crack regions. However, for the forward region, little to no improvement is observed in performing the combination.

The invariant mass distributions for data $\mathrm{J}/\Psi \rightarrow ee$ candidates are shown in Figure 4.21 for the same $|\eta|$ regions noted above. The trends in resolution improvement observed in the Monte Carlo events hold true of data, as well. The most significant improvement is observed for J/Ψ candidates with both electrons in the central region ($|\eta| < 0.7$), with J/Ψ candidates in the medium $|\eta|$ region showing mild improvement, the forward region displaying no improvement due to the combination.

Another way to quantify the improvement in energy resolution is to look at the change in the tails of the electron energy resolution, considered in this analysis to be the region outside of $\pm 1\sigma$ about the peak of the function $p_{\mathrm{T}}/p_{\mathrm{T}}^{\mathrm{Truth}}$. The width ($\sigma$) is taken from a Gaussian fit to the distribution of $p_{\mathrm{T}}/p_{\mathrm{T}}^{\mathrm{Truth}}$ on $[0.9, 1.2]$. In performing the $E-p$ combination, one would ideally expect both a narrower width of the resolution function, and a decrease in the size of the response tails. The electron energy response, in particular, has a non-Gaussian tail that is primarily the result of bremsstrahlung in the Inner Detector, as shown in Figure 4.22. Thereby, the $E-p$ combination would ideally also mitigate cases where the cluster energy is combined with a track measurement that is affected severely by bremsstrahlung.

To obtain a robust parametrisation of the J/Ψ invariant mass distribution, a detailed study on this spectrum in data is pursued. The flat, non-resonant, combinatory background is fitted with a 3^{rd} order polynomial and the J/Ψ decay signal with a Crystal Ball function, mean and resolution values scale as 3.7/3.1 and as $\sqrt{3.7/3.1}$, respectively. This scaling is set in this way to incorporate the J/Ψ_{2S} resonance, at $m_{2S} \sim 3.7$ GeV. Likewise, the other Crystal Ball parameters, namely α and n, are floating in the fit procedure. An example of the fit is illustrated in Figure 4.23.

Table 4.4 shows the improvement in the tails of $p_{\mathrm{T}}/p_{\mathrm{T}}^{\mathrm{Truth}}$ for Monte Carlo $J/\Psi \rightarrow ee$ events using the combination whilst Table 4.5 displays the mean and width for both Monte Carlo and data events. In both Monte Carlo and data samples, the mean of the invariant mass distribution shifts closer to $m_{J/\Psi}$ when the $E-p$ combination is applied.

Since the constituent functions are built with respect to $p_{\mathrm{T}}/p_{\mathrm{T}}^{\mathrm{Truth}}$, the combination method shifts the electron p_{T} to its assumed truth value.
The width of the invariant mass distribution also narrows after performing the combination, indicating a more precise reconstruction of the dielectron system. For instance, the width of the resolution improves by $25\% - 27\%$ in the central and medium regions, both for data and Monte Carlo. Furthermore, the values of μ and σ for each $|\eta|$ region for both data and Monte Carlo are in good agreement, indicating that the decision-making criteria used (i.e. $|E-p|/p$ and f_{Brem}) are valid for both simulated and experimental J/Ψ candidate events.

Z→ee Monte Carlo and data

This analysis employs $Z \rightarrow ee$ Monte Carlo samples with nominal geometry. Along with the nominal selection outlined in Section 4.5.3, each electron in the Z candidate is required to have $p_{\mathrm{T}} > 20\,\mathrm{GeV}$.

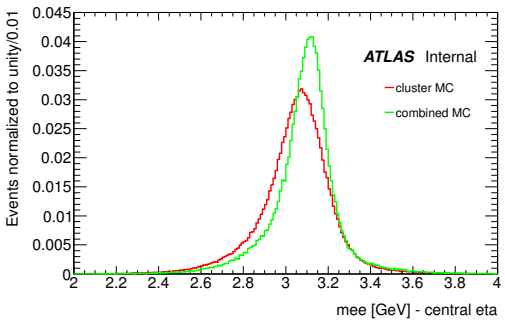

(a) Central $|\eta|$

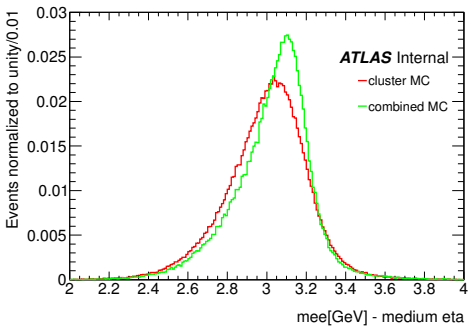

(b) Medium $|\eta|$

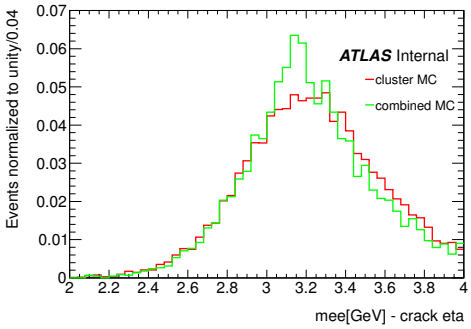

(c) Crack $|\eta|$

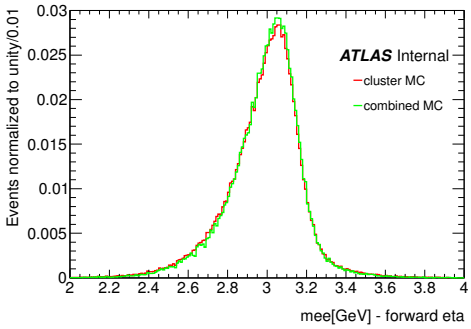

(d) Forward $|\eta|$

Figure 4.20: Monte Carlo $J/\Psi \to ee$ mass distributions with and without the combination in effect, for the likelihood method.

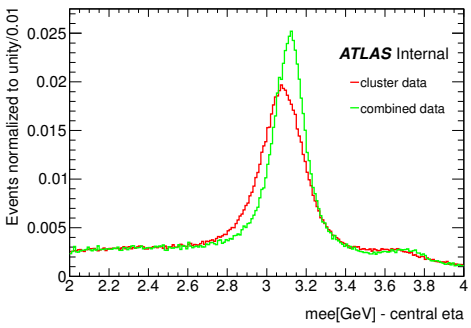

(a) Central $|\eta|$

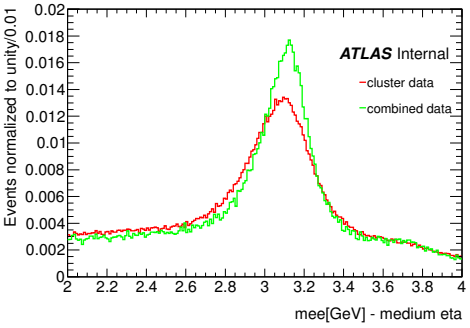

(b) Medium $|\eta|$

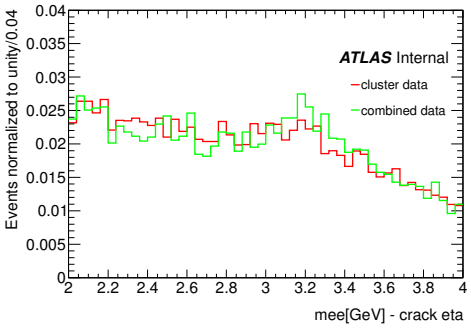

(c) Crack $|\eta|$

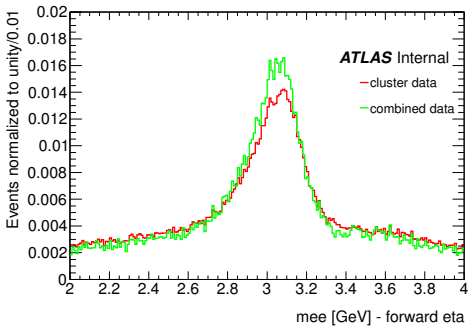

(d) Forward $|\eta|$

Figure 4.21: Invariant mass distributions of $J/\Psi \to ee$ data events, with and without the combination in effect. The data used corresponds to 21 fb^{-1} of pp collisions at $\sqrt{s} = 8$ TeV, recorded during 2012.

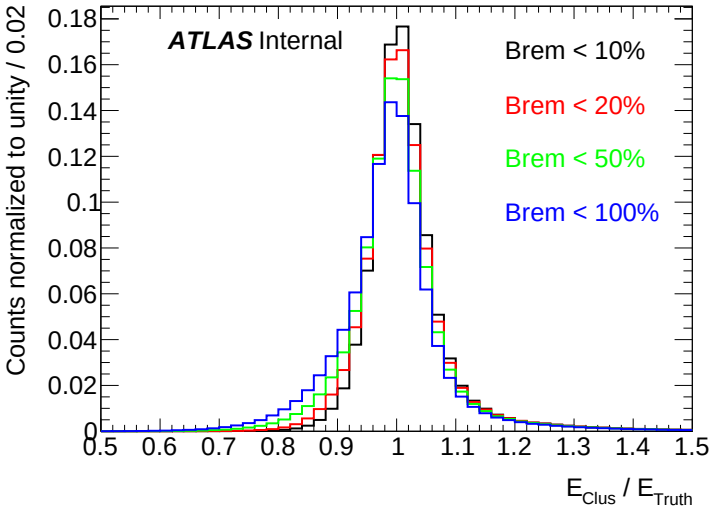

Figure 4.22: Evolution of the left tail of the energy response distribution for leading electrons in Monte Carlo $J/\Psi \rightarrow ee$ decays.

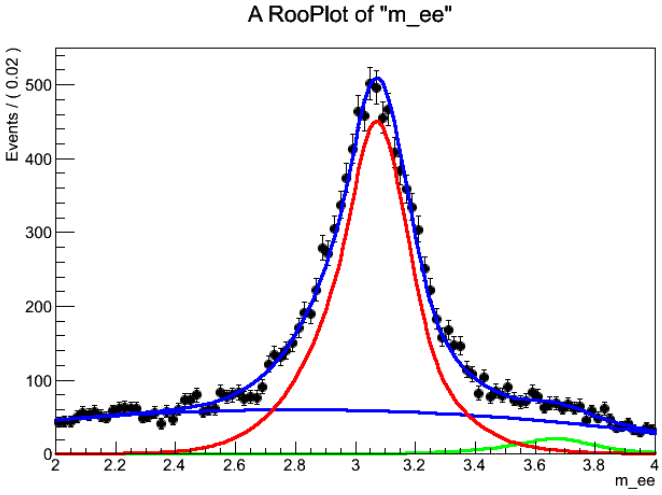

Figure 4.23: Invariant mass distribution of $J/\Psi \rightarrow$ ee resonance, for electrons lying in the central η region, namely $0 < \eta < 0.6$. The final state histograms for J/Ψ events from data (black points) is compared with the sum of the signal (red line) and the J/Ψ_{2S} (green line) component (each parametrised with the sum two Crystal Ball functions), and the combinatorial background (blue line parametrised with a third order degree polynomial function).

Low p_T				
$\|\eta\|$ region	σ_{Clus}	% tails (cluster)	σ_{Comb}	% tails (combined)
Central	5.7	10.1	3.2	8.8
Medium	7.5	9.7	5.3	9.7
Crack	11.9	9.5	7.4	15.0
Forward	6.1	11.0	6.0	10.8
Medium p_T				
Central	3.9	5.9	3.4	6.1
Medium	5.2	6.3	4.5	5.4
Crack	8.0	9.3	7.0	10.2
Forward	4.3	6.4	4.3	6.1
High p_T				
Central	2.9	9.3	2.8	8.4
Medium	3.6	7.7	3.6	7.0
Crack	7.5	12.7	7.2	11.7
Forward	3.1	13.0	3.1	13.0

Table 4.4: Energy resolution width and tails for Monte Carlo $J/\Psi \rightarrow ee$ events before and after the combination.

Monte Carlo $J/\Psi \rightarrow ee$				
$\|\eta\|$ region	μ_{Clus} [GeV]	σ_{Clus} [GeV]	μ_{Comb} [GeV]	σ_{Comb} [GeV]
Central	3.087	0.114	3.124	0.093
Medium	3.072	0.141	3.129	0.110
Crack	3.363	0.450	3.221	0.261
Forward	3.062	0.120	3.060	0.114
Data $J/\Psi \rightarrow ee$				
Central	3.071	0.127	3.112	0.091
Medium	3.079	0.140	3.115	0.101
Crack	3.435	0.684	3.245	0,454
Forward	3.041	0.113	3.0551	0.101

Table 4.5: Improvement in the mean and width of the invariant mass distribution for $J/\Psi \rightarrow ee$ Monte Carlo and data events before and after the combination.

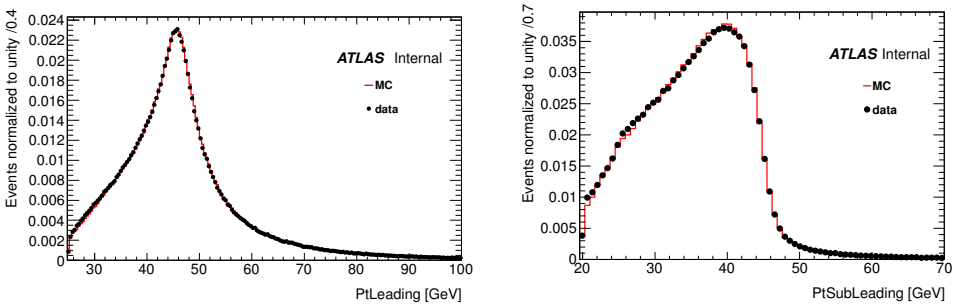

(a) Leading p_{T} **(b)** Sub-leading p_{T}

Figure 4.24: Transverse momentum distributions of the leading and sub-leading p_{T} electron pairs of the Z boson, as shown for data and Monte Carlo events.

It is further asked that the dielectron pair has an invariant mass $m_{ee} > 50\,\mathrm{GeV}$. Energy scale corrections are applied on data sample as well as smearing correction on Monte Carlo as explained in Section 4.

Overall, excellent agreement between data and Monte Carlo is found in the leading and sub-leading electron p_T distributions for simulation and data respectively as noted in Figure 4.24.

The final combined and uncombined $Z \to ee$ invariant mass distributions for Monte Carlo and data, respectively, are shown in Figures 4.25 and 4.26. Table 4.6 displays the mean and the σ of the combined and uncombined $Z \to ee$ invariant mass distributions for the combination algorithm.

In these distributions, there is little benefit to performing the $E - p$ combination on high p_{T} electrons of the Z resonance. One notable exception to this behaviour is the m_{ee} distribution of the crack region where the combination produces a shift in the peak of the combined distribution towards the true Z mass (taken to be $m_Z = 91.188\,\mathrm{GeV}$). This result is a consequence of the comparatively poorer energy resolution of the ECAL in the crack region (relative to the momentum resolution of the Inner Detector), which leads to a greater importance of track measurements in the combined distribution. The invariant mass distributions from the 2012 data agree with the results of the Monte Carlo study, with a noticeable improvement in resolution only observed in the crack region. Overall, these plots demonstrate that the $E - p$ combination for high p_{T} electrons is only effective in the crack region.

H→ZZ → 4l Monte Carlo

The effect of the $E - p$ combination method was also studied using Monte Carlo samples of gluon fusion-mediated $H \to ZZ \to 4l$ with pp collisions simulated at $\sqrt{s} = 8\,\mathrm{TeV}$. The sample was generated using nominal ATLAS geometry. The standard $4l$ selection cuts [20] were applied, as detailed in Chapter 5. Furthermore, all necessary event weights were in place, including pile-up reweighting, z-vertex smearing, gluon fusion and ZZ overlap reweighting as well as muon, electron trigger and efficiency scale factors. In addition, energy resolution smearing factors are applied to electron cluster energy. In these samples, the $E - p$ combination is applied exclusively for electrons after the standard selection (detailed in Chapter 5), with muons reconstructed in the same manner as the standard $4l$ analysis. To ensure the consistency of the combination approach, the performance of the algorithm has also been examined when using the combination before the standard cut-based selection and the results were found to be similar to the previous case. In any event, by keeping the

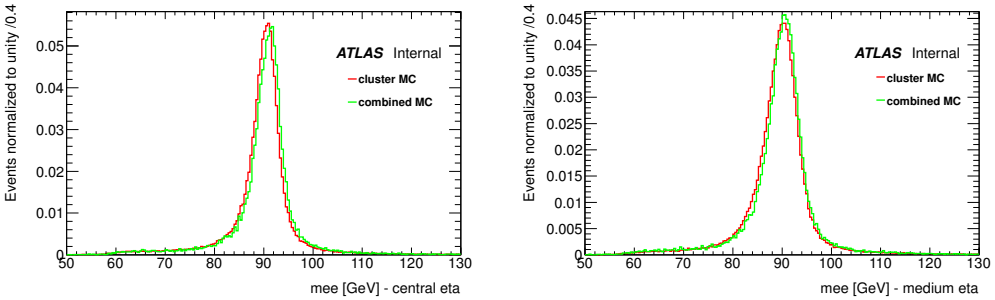

(a) Central $|\eta|$ **(b)** Medium $|\eta|$

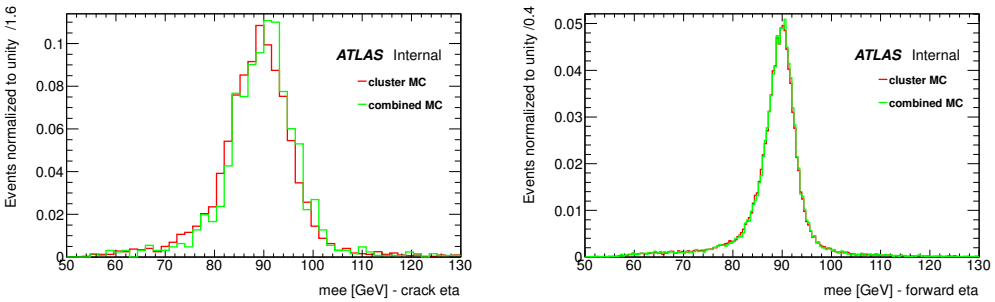

(c) Crack $|\eta|$ **(d)** Forward $|\eta|$

Figure 4.25: Monte Carlo $Z \to ee$ mass distributions with and without the combination in effect.

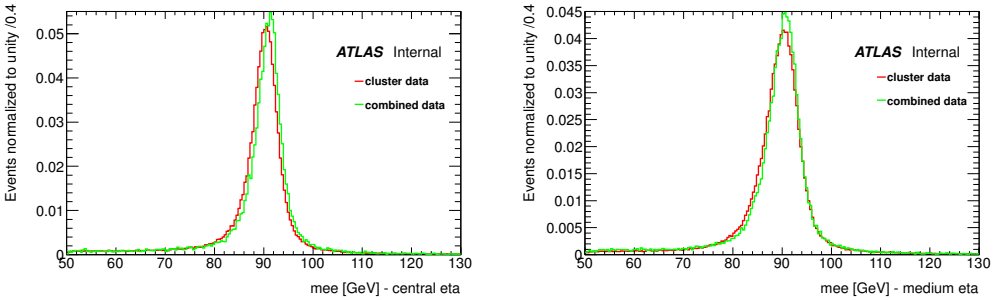

(a) Central $|\eta|$ **(b)** Medium $|\eta|$

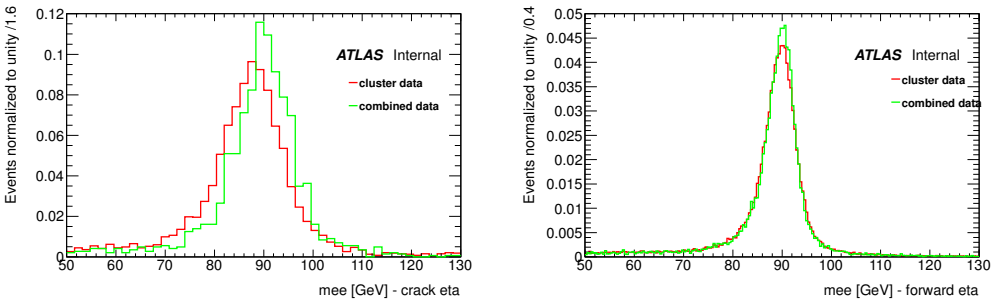

(c) Crack $|\eta|$ **(d)** Forward $|\eta|$

Figure 4.26: Invariant mass distributions of $Z \to ee$ data events, with and without the combination in effect. The data used corresponds to 21 fb^{-1} of pp collisions at $\sqrt{s} = 8$ TeV, recorded during 2012.

Monte Carlo $Z \to ee$				
$\|\eta\|$ region	μ_{Clus} [GeV]	σ_{Clus} [GeV]	μ_{Comb} [GeV]	σ_{Comb} [GeV]
Central	90.403	2.839	90.641	2.778
Medium	89.694	3.530	90.811	3.440
Crack	88.845	5.295	89.920	5.105
Forward	89.201	3.305	89.340	3.298
Data $Z \to ee$				
Central	90.339	2.820	90.821	2.689
Medium	90.046	3.320	90.501	3.197
Crack	87.852	6.053	91.202	6.011
Forward	89.752	3.501	89.799	3.404

Table 4.6: Improvement in the mean and width of the invariant mass distribution for $Z \to ee$ Monte Carlo and data events.

combination after the standard selection, the re-calculation of efficiencies and acceptances can be avoided. The percentage of electrons undergoing combination is 42% in the $4e$ channel, and 63% in the $2\mu 2e$ channel. With regard to the $2e2\mu$ channel, given that the p_{T} spectrum of the on-shell Z is sensibly harder, and the combination threshold is placed at 30 GeV, the combination is practically never applied.

Four lepton invariant mass distributions before and after the $E-p$ combination, with the Z mass constraint applied, are displayed in Figure 4.28. Candidate events are separated out into $4e$, $2e2\mu$, and $2\mu 2e$ categories, with the on-shell pair (i.e. the pair with the mass closest to the PDG-given Z boson mass) listed first. The set of values that are used to gauge the improvement of the combination algorithm was calculated by applying a Gaussian fit using iterative fit on $[-1\sigma, 2\sigma]$ around the mean of the distributions. Tables of the resolution, and relative size of the tails, with and without applying the $E-p$ combination, are shown in Table 4.7. The largest improvement is seen in the $H \to 4e$ and $H \to 2\mu 2e$ channels, showing an approximate reduction of 5% and 4%, respectively, in the width of the m_{4l} distribution. In addition, the combination produces a reduction of the tails of the m_{4l} distribution, mostly in the $4e$ channel.

Before applying the $E-p$ combination on events from data, its outcome is first scrutinised in the sideband regions, i.e. the signal-free region in data. Figure 4.27 (a) displays a 2D map of $|m_{4l}^{\text{Comb}} - m_{4l}^{\text{Clus}}|$ as a function of m_{4l}^{Clus} in the 4e decay channel for what concerns the two sideband regions (50< m_{4l} <100) GeV and (140< m_{4l} <450) GeV. The σ of the difference $|m_{4l}^{\text{Comb}} - m_{4l}^{\text{Clus}}|$ is about 1 GeV, but at an average mass of approximately 200 GeV, 0.5% in relative difference. Figure 4.27 (b) exhibits the same 2D distribution $|m_{4l}^{\text{Comb}} - m_{4l}^{\text{Clus}}|$ *vs* m_{4l}^{Clus} for the signal Monte Carlo. In this specific case, the standard deviation of the difference between the cluster and combined-based measurements is 0.5 GeV, fully consistent with the typical behaviour shown in the sideband.

Validation of the $E-p$ combination on the 2011 simulation

A validation of the track-cluster combination algorithm has been performed at single electron level for Monte Carlo samples with $\sqrt{s}$=7 TeV (mc11 in what follows).
In particular, single electrons are produced with the same flat E_T range of [7-80] GeV used in the 8 TeV analysis and passed through the ATLAS offline reconstruction software. Additionally, the p_T cut is kept at 7 GeV. As a second step of the analysis, the PDFs for mc11 are computed from

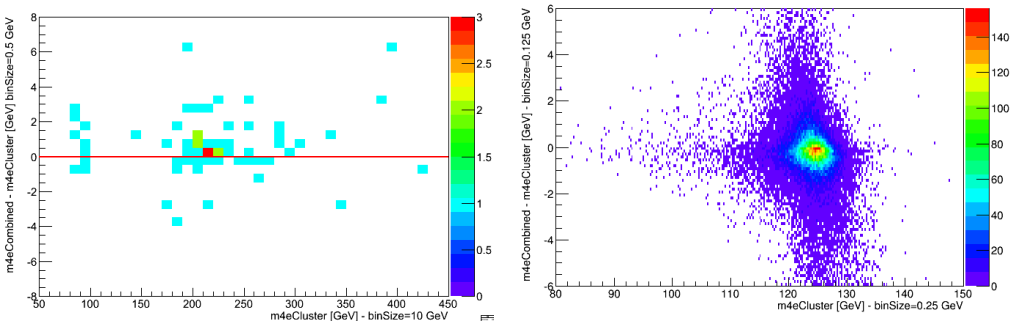

(a) **(b)**

Figure 4.27: 2D map of $|m_{4l}^{\text{Comb}} - m_{4l}^{\text{Clus}}|$ *vs* m_{4l}^{Clus} for electron candidates in the sidebands (a) and in the Higgs signal Monte Carlo (b). The standard deviation of the difference cluster-combined is fully compatible between the two plots.

Channel	μ_{Clus}	σ_{Clus}	μ_{Comb}	σ_{Comb}	% tails (Cluster)	% tails (Combined)
$4e$	123.67	2.248	123.98	2.132	16.9%	15.8%
$2e2\mu$	124.20	1.655	124.54	1.609	14.5%	14.4%
$2\mu2e$	123.91	2.223	124.25	2.170	13.5%	13.6%

Table 4.7: Energy resolution and size of tails for Monte Carlo $H \to ZZ \to 4l$ events before and after the track-cluster combination.

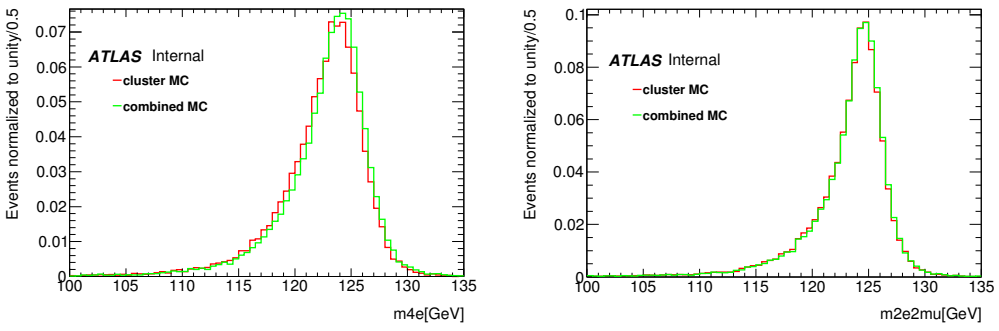

(a) $4e$ **(b)** $2e2\mu$

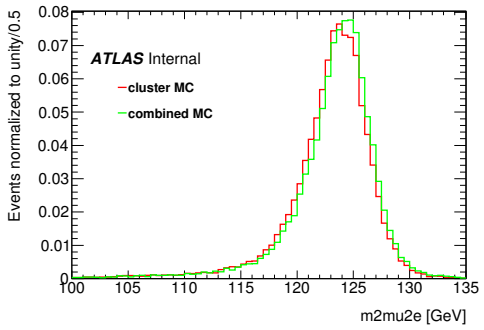

(c) $2\mu2e$

Figure 4.28: Monte Carlo $H \to ZZ \to 4l$ mass distributions with and without the combination in effect.

$\|\eta\|$ Region	Definition
Central	$\|\eta\| < 0.6$
Semi-central	$0.6 < \|\eta\| < 1$
Medium	$1 < \|\eta\| < 1.37$
Crack	$1.37 < \|\eta\| < 1.52$
Semi-forward	$1.52 < \|\eta\| < 1.82$
Forward	$1.82 < \|\eta\| < 2.47$

Table 4.8: Definitions of the $|\eta|$ regions used in the computation of material systematic uncertainties.

mc11-based Monte Carlo single electron samples in the usual bins of p_T, η and f_{Brem} as illustrated earlier on in the text. The σ cut, σ(E-p), is re-computed in this new configuration and it is found to be 3 unlike the previous case, σ (E-p)=4 for mc12. The improvement of the p_T/p_T^{truth} distributions in width and amount of tails found at single electron level for mc11 is found to be compatible with the one described above for mc12.

4.5.4 Systematic uncertainties associated to detector geometry and material

The track-cluster combination method depends to varying degrees on the energy calibration of the electrons studied, as well as the accuracy of the simulated ATLAS geometry used to reconstruct the Monte Carlo events. A difference between the simulated detector and the real detector (mostly due to the amount of material) would induce a shift in the reconstructed energy. Hence, the uncertainty on the knowledge of the real detector is the source of a systematics. Such a systematics is applicable to the cluster-based energy and to the combined one - in what follows the procedure to extract it will be detailed for the two measurements. Accordingly, the effect of the different simulation, calibration, and geometry-based systematic uncertainties must be evaluated. The systematic uncertainties in these Sections, unless otherwise specified, are computed using single electron Monte Carlo samples described in Section 4.5.3 and the energy is extracted after the MVA-based calibration.

In order to assess the systematic uncertainties due to differences in simulated detector geometry, various Monte Carlo samples with distorted geometries are used:

- A: ID material scaling by 5%;
- $C^{'}$+$D^{'}$: SCT and Pixel services scaled by 10%;
- $E^{'}$+$L^{'}$: + 7.5 X_0 at SCT/TRT end-cap, + 5 X_0 between ID and PS;
- $F^{'}$+$M^{''}$+$X^{''}$: + 7.5 X_0 at ID endplate, + 5.0 X_0 between PS and strips, LAr material increase in transition region.
- $G^{'}$: All above variations applied together.

Linearity

Electrons were placed in six $|\eta|$-based categories, as listed in Table 4.8, and nine $p_{\mathrm{T}}^{\mathrm{Truth}}$ categories (with bin edges defined by [6, 10, 15, 20, 25, 30, 40, 50, 65, 80] GeV).
As a preliminary step, a detailed study was pursued on the ideal estimator to be employed in evaluating the material uncertainties. The estimators that were considered are the average values of the

distributions of $p_{\mathrm{T}}/p_{\mathrm{T}}^{\mathrm{Truth}}$ in bins of $|\eta|$ and $p_{\mathrm{T}}^{\mathrm{Truth}}$, or the mean of the Gaussian core of the same ratio. The main drawback of the first approach is that the computation of the calibration is extremely dependent on the configuration in $|\eta|$ and p_{T} of the electrons. Some particular zones in the $|\eta|$-p_{T} phase-space, in particular, demonstrate non-negligible tails that may skew the average value of the distribution far below the peak of the Gaussian core. This problem is not encountered when using the mean of the Gaussian core as estimator, since the fit is performed in an interval that ignores the non-Gaussian tail. For the study of non-linearity and its dependence on material distribution, the material systematic uncertainties are therefore evaluated by fitting a Gaussian function in the region $[-1\sigma,\ 2.5\sigma]$ of the mean of each $p_{\mathrm{T}}/p_{\mathrm{T}}^{\mathrm{Truth}}$ distribution (both for cluster and combined), and evaluating the uncertainty in terms of the difference in the means of the nominal and distorted cases.

The material-related uncertainty is defined as the difference in bins of $p_{\mathrm{T}}^{\mathrm{Truth}}$ between the nominal geometry and the various distorted schemes. This difference is computed for uncombined (cluster energy-based) and combined p_{T}. The overall shift between the calibration of the nominal sample with respect to the distorted samples is absorbed in the re-calibration of the peak. Thus, the constant difference between the distributions of $p_{\mathrm{T}}^{\mathrm{Clus}}/p_{\mathrm{T}}^{\mathrm{Truth}}$ (and $p_{\mathrm{T}}^{\mathrm{Comb}}/p_{\mathrm{T}}^{\mathrm{Truth}}$, as well) is trivial, and is removed by shifting the Monte Carlo-derived peak position. On the contrary, it is important to assess correctly the non-linear behaviour for the distorted profiles, as compared to the nominal profiles. This non-linearity is driven by the non-constant shape of the difference and it is quoted as a systematic uncertainty due to material distortions. Figure 4.29 shows the impact of the various distortions in the uncombined p_{T} distributions, and Figure 4.30 presents the differences in the combined version. The offset for the functional form, which produces the constant term in the difference, is defined as the value of the difference for electrons whose $p_{\mathrm{T}}^{\mathrm{Truth}} = 40\,\mathrm{GeV}$, and it is subtracted to remove the calibration-driven linear shift, shown in Figures 4.31 and 4.32. The relative change in linearity for the uncombined and combined p_{T}, in terms of the G' distorted geometry, is shown in Figure 4.33. Note that the combination algorithm improves the non-linearity of the response under each material distortion, evidenced by the reduction in magnitude of $\Delta\mu(p_{\mathrm{T}}/p_{\mathrm{T}}^{\mathrm{Truth}})$ for electrons with the combined p_{T}.

Uniformity

While the electron energy response can be examined as a function of $p_{\mathrm{T}}^{\mathrm{Truth}}$ to gauge the linearity, the response can also be studied relative to η^{Truth}, denoted the energy *uniformity*. Electrons are placed in six $|\eta|$-based categories, as listed in Table 4.8 and three $p_{\mathrm{T}}^{\mathrm{Truth}}$ categories (low, medium and high p_{T}, with bin edges defined by [6, 15, 30, 80] GeV). The uniformity of the distribution of $p_{\mathrm{T}}/p_{\mathrm{T}}^{\mathrm{Truth}}$ as a function of $|\eta|$ is estimated as the difference in bins of η between the nominal geometry and the various distorted schemes. As in the previous Section, the estimator for the distribution of (Distorted − Nominal) is the mean of a Gaussian fit to the distribution of $p_{\mathrm{T}}/p_{\mathrm{T}}^{\mathrm{Truth}}$ (both for combined and uncombined energies) on the interval $[-1\sigma,\ 2.5\sigma]$.

The distributions of $\Delta\mu(p_{\mathrm{T}}/p_{\mathrm{T}}^{\mathrm{Truth}})$ for the various distortions (in terms of the combined and uncombined p_{T}), as well as a direct comparison of the uncombined and combined approaches using the $G^{'}$ distorted geometry, are shown in Figures 4.34 and 4.36. The $E-p$ combination leads to an overall improvement in the uniformity of $p_{\mathrm{T}}/p_{\mathrm{T}}^{\mathrm{Truth}}$ for low and medium p_{T} electrons in the distorted geometries. As expected, electrons in the crack region show the largest deviation in uniformity, although as displayed in Figures 4.35, the usage of the $E-p$ combination improves the non-uniformity by more than $\sim 30\%$.
Hence, in terms of both electron p_{T} linearity and uniformity, the usage of the algorithm leads to a reduction in the overall systematic uncertainties associated with material distortions in the ATLAS detector.

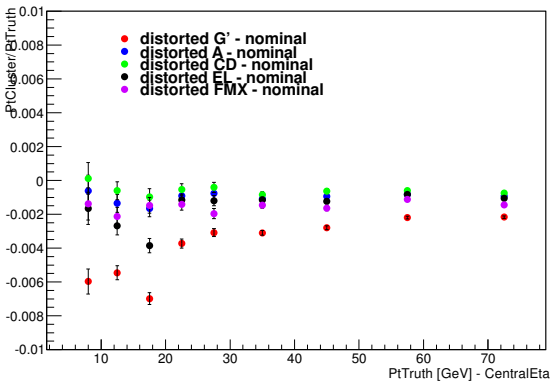

(a) Central $|\eta|$

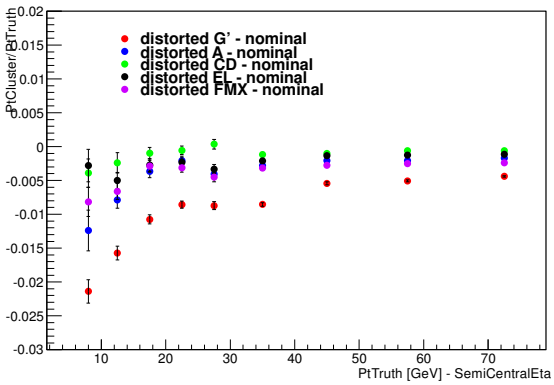

(b) Semi-central $|\eta|$

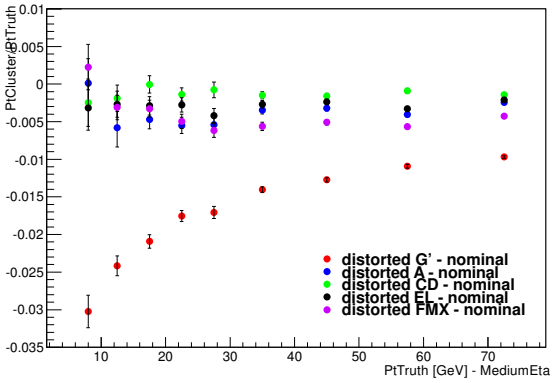

(c) Medium $|\eta|$

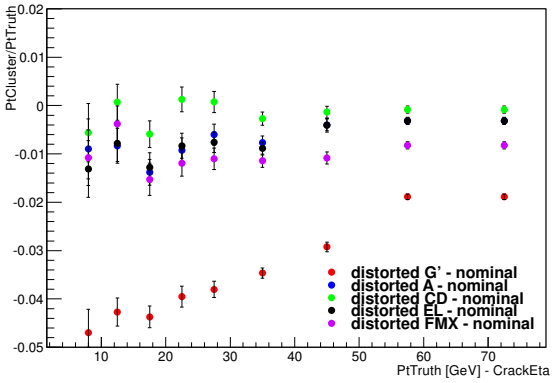

(d) Crack $|\eta|$

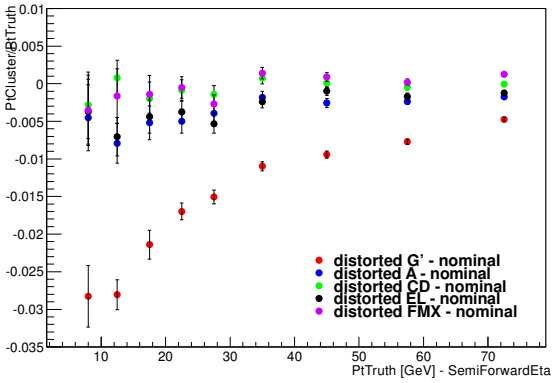

(e) Semiforward $|\eta|$

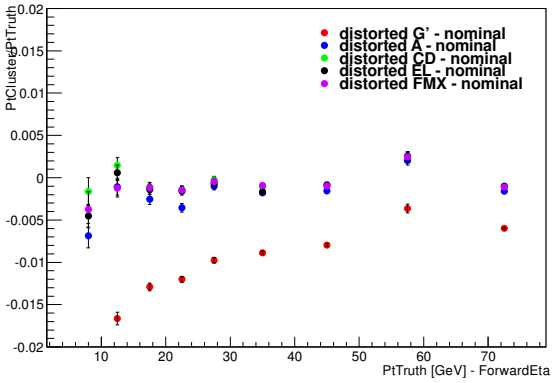

(f) Forward $|\eta|$

Figure 4.29: Distributions of $(p_{\mathrm{T}}^{\mathrm{Cluster}}/p_{\mathrm{T}}^{\mathrm{Truth}})_{\mathrm{Distorted}} - (p_{\mathrm{T}}^{\mathrm{Cluster}}/p_{\mathrm{T}}^{\mathrm{Truth}})_{\mathrm{Nominal}}$ as a function of $p_{\mathrm{T}}^{\mathrm{Truth}}$ in the various $|\eta|$ regions. The nominal geometry response is compared with the other distorted samples.

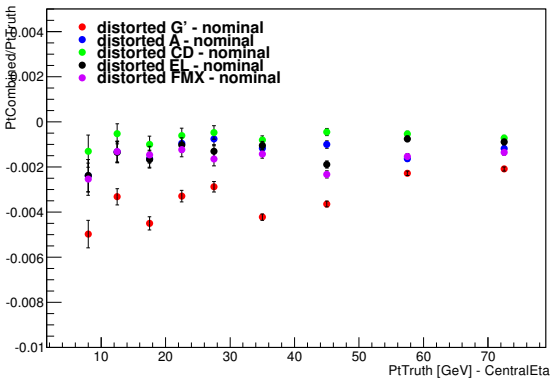

(a) Central $|\eta|$

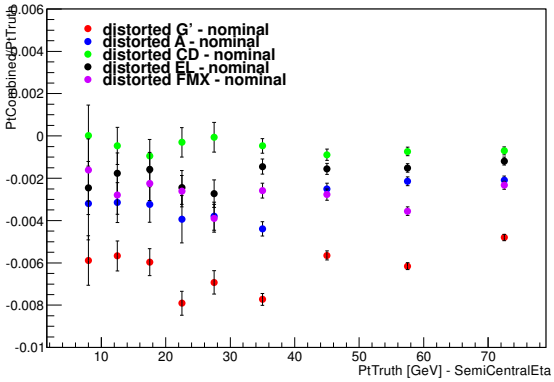

(b) Semi-central $|\eta|$

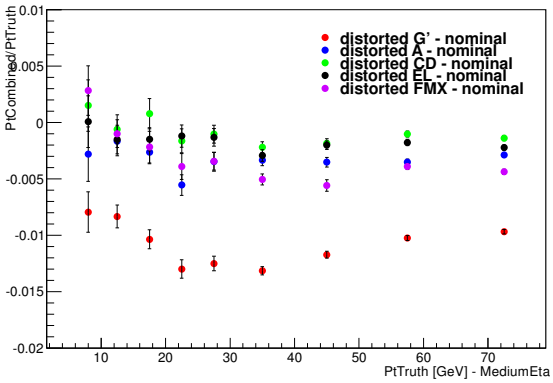

(c) Medium $|\eta|$

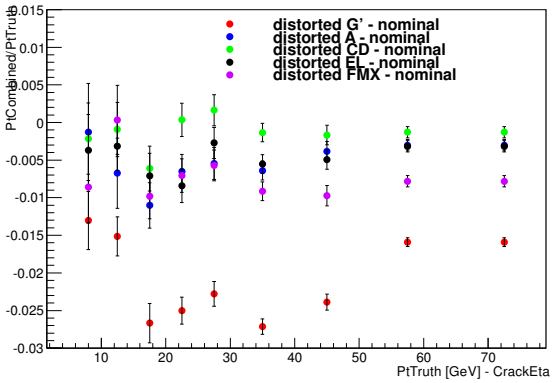

(d) Crack $|\eta|$

Figure 4.30: Distributions of $(p_{\mathrm{T}}^{\mathrm{Comb}}/p_{\mathrm{T}}^{\mathrm{Truth}})_{\mathrm{Distorted}} - (p_{\mathrm{T}}^{\mathrm{Comb}}/p_{\mathrm{T}}^{\mathrm{Truth}})_{\mathrm{Nominal}}$ as a function of $p_{\mathrm{T}}^{\mathrm{Truth}}$ in the various η regions. The nominal geometry response is compared with the other distorted samples.

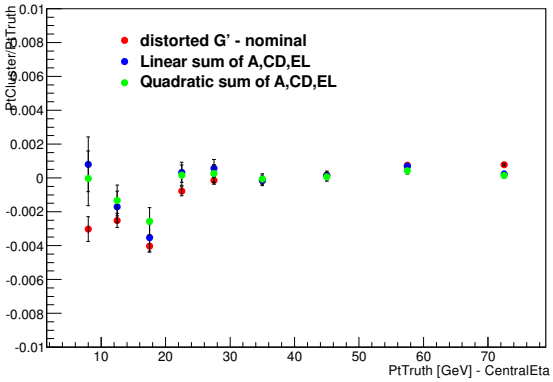

(a) Central $|\eta|$

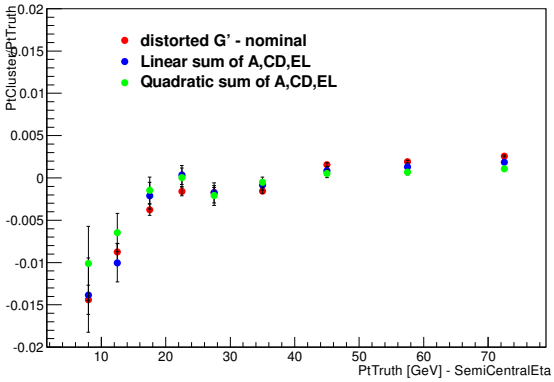

(b) Semi-central $|\eta|$

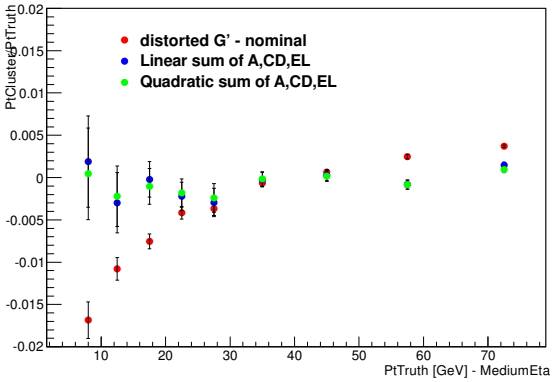

(c) Medium $|\eta|$

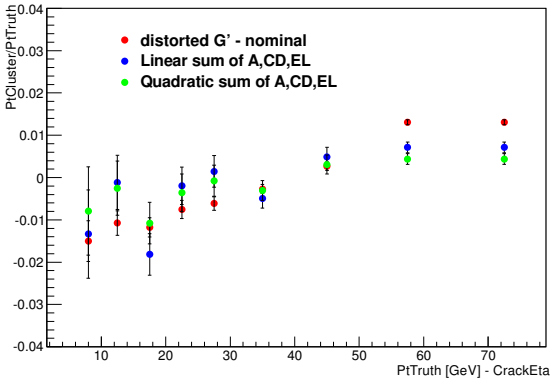

(d) Crack $|\eta|$

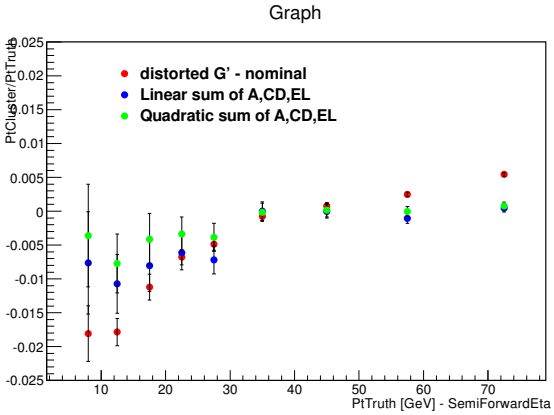

(e) Semiforward $|\eta|$

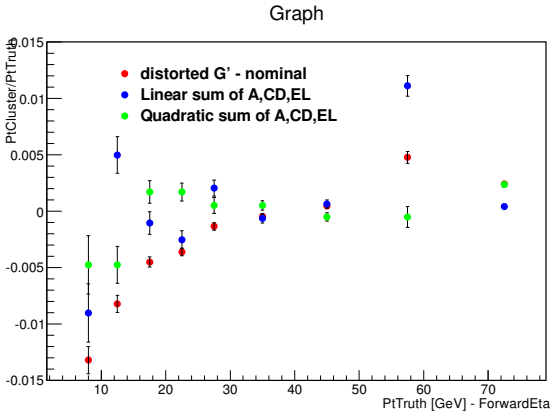

(f) Forward $|\eta|$

Figure 4.31: Distributions of $(p_{\mathrm{T}}^{\mathrm{Cluster}}/p_{\mathrm{T}}^{\mathrm{Truth}})_{\mathrm{Distorted}} - (p_{\mathrm{T}}^{\mathrm{Cluster}}/p_{\mathrm{T}}^{\mathrm{Truth}})_{\mathrm{Nominal}}$ as a function of $p_{\mathrm{T}}^{\mathrm{Truth}}$ in the various η regions. The nominal geometry response is compared with $G^{'}$ distorted sample and with the linear and quadratic sum of the various other distortions. The value of each offset is defined relative to the offset at $p_{\mathrm{T}}^{\mathrm{Truth}} = 40$ GeV.

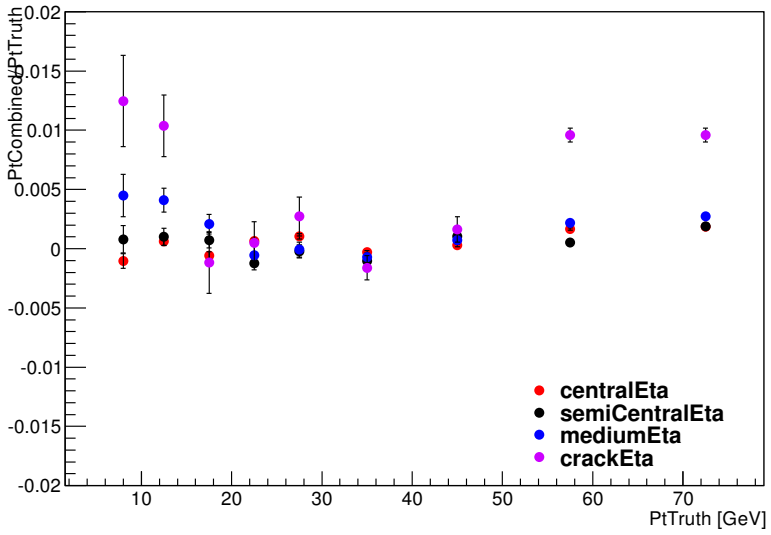

(a) Combined momentum

Figure 4.32: Distributions of the mean of $(p_{\mathrm{T}}^{\mathrm{Comb}}/p_{\mathrm{T}}^{\mathrm{Truth}})_{\mathrm{Distorted}} - (p_{\mathrm{T}}^{\mathrm{Comb}}/p_{\mathrm{T}}^{\mathrm{Truth}})_{\mathrm{Nominal}}$. The nominal geometry response is compared with the $G^{'}$ distorted sample (that encompasses the various other distortions) and the various differences are displayed as a function of the region in η where the combination is applied.

Momentum scale uncertainties from $E - p$ combination

As illustrated in Section 4.3, the invariant mass distributions of $J/\psi \rightarrow ee$ events are parameterised and used to derive in situ energy scale factors and provide a cross-check for the baseline extraction in the Z→ee channel. These energy scale factors, α, are defined, similarly to equation (4.1), in the following way:

$$E^{\mathrm{meas}} = E^{\mathrm{truth}}(1 + \alpha_i) \tag{4.11}$$

where E^{meas} is the measured electron energy, E^{truth} is the true energy and α_i represents the departure from a perfect calibration in a range of pseudorapidity, labelled as i. To evaluate the effect of introducing track momentum information into the cluster energy measurement, the same parametrisation process is employed, with the exception that J/ψ candidate invariant masses are built exclusively using track information. It is found that the resultant J/ψ momentum scale factors are very small when using the the track-based information (typically $< 1\%$ as in Figure 4.37), implying that the uncertainty on the prompt fraction of the signal sample due to the $E - p$ combination is expected to be negligible.

4.6 Conclusions

The electron energy calibration exploited in ATLAS has been illustrated in this Chapter using LHC Run 1 proton-proton collisions data corresponding to a total integrated luminosity of approximately 25 fb^{-1} at the centre of mass energy of 8 TeV. The calorimeter energy measurement is first optimised using a multivariate-based technique. The calorimeter energy response in data is stable at the level of 0.05 % as a function of time and pile-up. The local non-uniformities are at the level of 0.5% in the barrel and 0.75% in the end-cap. The residual miscalibration on data and Monte Carlo is then corrected using Z→ee samples and the data-simulation accuracy improves up to the level

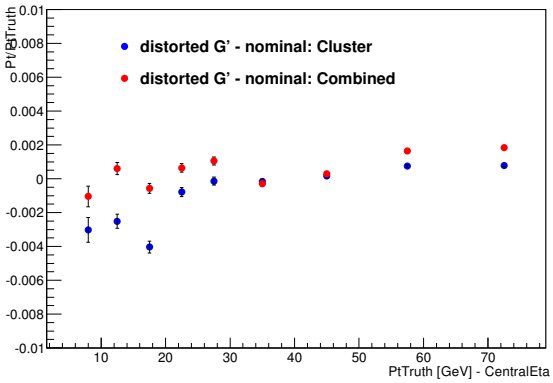

(a) Central $|\eta|$

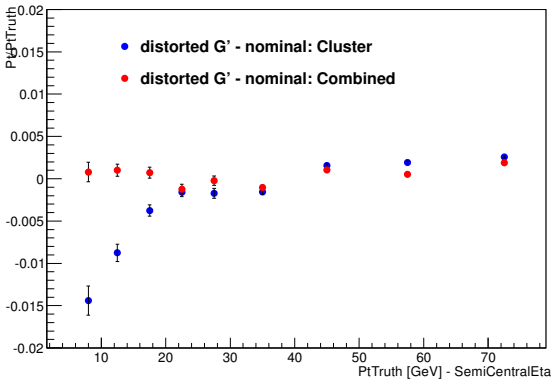

(b) Semi-central $|\eta|$

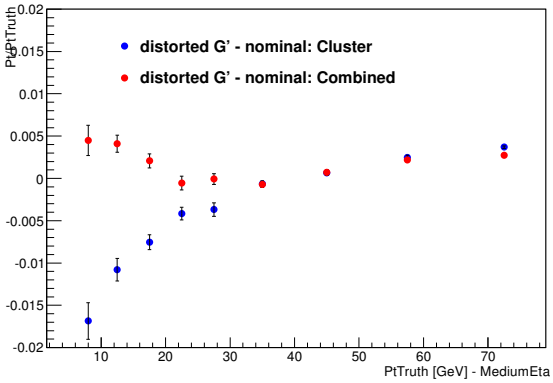

(c) Medium $|\eta|$

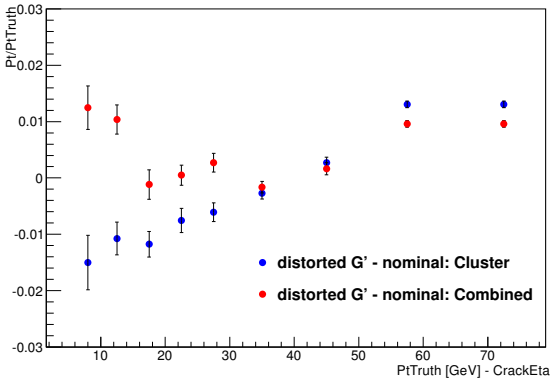

(d) Crack $|\eta|$

Figure 4.33: Distributions of $(p_{\mathrm{T}}^{\mathrm{Cluster}}/p_{\mathrm{T}}^{\mathrm{Truth}})_{\mathrm{Distorted}} - (p_{\mathrm{T}}^{\mathrm{Cluster}}/p_{\mathrm{T}}^{\mathrm{Truth}})_{\mathrm{Nominal}}$ and $(p_{\mathrm{T}}^{\mathrm{Comb}}/p_{\mathrm{T}}^{\mathrm{Truth}})_{\mathrm{Distorted}} - (p_{\mathrm{T}}^{\mathrm{Comb}}/p_{\mathrm{T}}^{\mathrm{Truth}})_{\mathrm{Nominal}}$ as a function of $p_{\mathrm{T}}^{\mathrm{Truth}}$ in the various η regions. The nominal geometry response is compared with G' distorted sample. The value of the offset (relative to the one where $p_{\mathrm{T}}^{\mathrm{Truth}} = 40$ GeV) is subtracted for each bin.

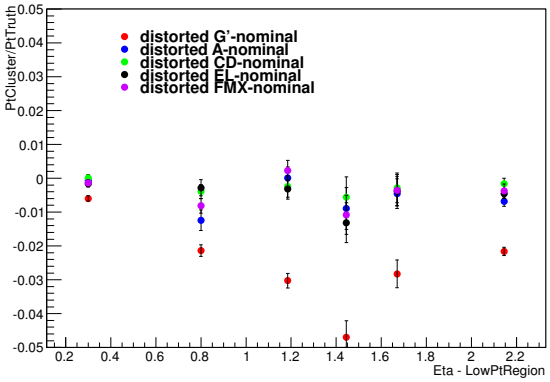

(a) Low p_{T}

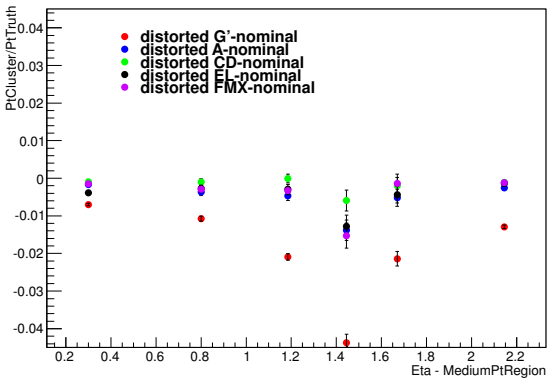

(b) Medium p_{T}

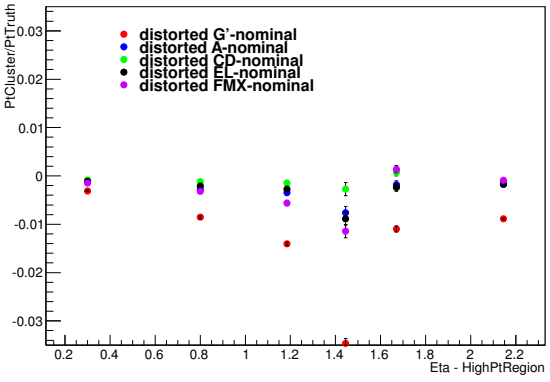

(c) High p_{T}

Figure 4.34: Distributions of $(p_{\mathrm{T}}^{\mathrm{Cluster}}/p_{\mathrm{T}}^{\mathrm{Truth}})_{\mathrm{Distorted}} - (p_{\mathrm{T}}^{\mathrm{Cluster}}/p_{\mathrm{T}}^{\mathrm{Truth}})_{\mathrm{Nominal}}$ as a function of $|\eta|$ in the low and medium p_{T} regions. The nominal geometry response is compared with the other distorted samples.

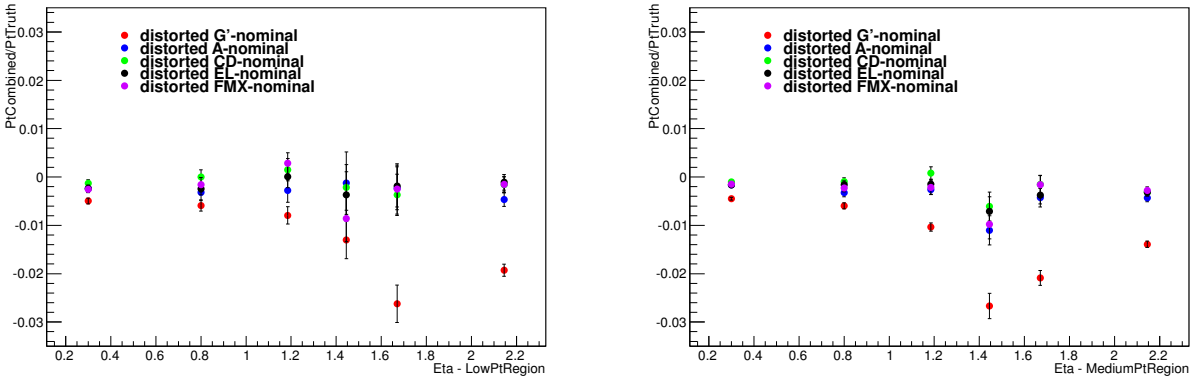

(a) Low p_{T} **(b)** Medium p_{T}

Figure 4.35: Distributions of $(p_{\mathrm{T}}^{\mathrm{Comb}}/p_{\mathrm{T}}^{\mathrm{Truth}})_{\mathrm{Distorted}} - (p_{\mathrm{T}}^{\mathrm{Comb}}/p_{\mathrm{T}}^{\mathrm{Truth}})_{\mathrm{Nominal}}$ as a function of $|\eta|$ in the low and medium p_{T} regions. The nominal geometry response is compared with the other distorted samples.

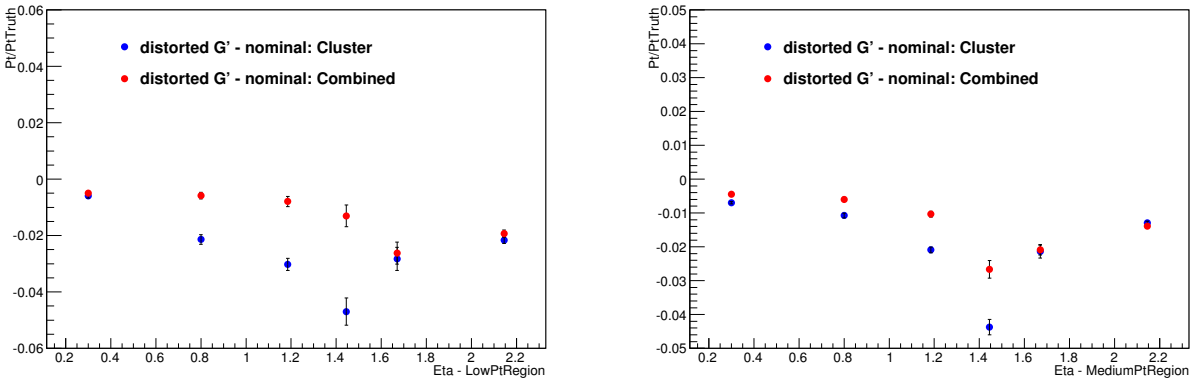

(a) Low p_{T} **(b)** Medium p_{T}

Figure 4.36: Distributions of $(p_{\mathrm{T}}^{\mathrm{Cluster}}/p_{\mathrm{T}}^{\mathrm{Truth}})_{\mathrm{Distorted}} - (p_{\mathrm{T}}^{\mathrm{Cluster}}/p_{\mathrm{T}}^{\mathrm{Truth}})_{\mathrm{Nominal}}$ and $(p_{\mathrm{T}}^{\mathrm{Comb}}/p_{\mathrm{T}}^{\mathrm{Truth}})_{\mathrm{Distorted}} - (p_{\mathrm{T}}^{\mathrm{Comb}}/p_{\mathrm{T}}^{\mathrm{Truth}})_{\mathrm{Nominal}}$ as a function of $|\eta|$ in the various p_{T} regions when applying the $G^{'}$ geometry distortion.

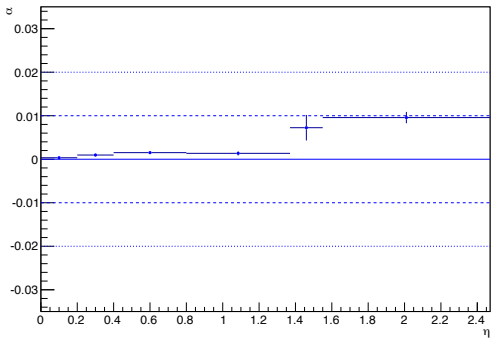

Figure 4.37: Electron momentum scale factors as defined in (4.11) in different pseudorapidity regions.

of 1%. An orthogonal cross-check on the current calibration has been carried out using J/Ψ →ee resonances leading to consistent results for what concerns the energy scales and the data - Monte Carlo agreement.

As the final step of the energy calibration procedure, a likelihood-based electron track and cluster combination has been derived and validated using the improvement in the invariant mass distributions of J/ψ, $Z \rightarrow ee$, and $H \rightarrow ZZ \rightarrow 4l$ decays. This method shows significant improvement in the width while also decreasing the bremsstrahlung-related tails of each distribution.

Studies of the efficacy of this algorithm were performed on electrons from $J/\psi \rightarrow ee$ and $Z \rightarrow ee$ decays, using both data and Monte Carlo samples. For $J/\psi \rightarrow ee$ decays, the improvement in the resolution of the dielectron invariant mass spectrum is approximately $18 - 20\%$. The order of improvement in resolution is smaller (2-3%) for $Z \rightarrow ee$ decays, as the $E - p$ combination is generally less effective for high p_{T} electrons, such as those emerging from Z boson decays. In the $H \rightarrow ZZ \rightarrow 4l$ channel, the largest gains in resolution are found in the $4e$ channel, with an improvement in resolution of approximately 5%. After having checked the geometry-related systematic uncertainties, both for the cluster-based energy and the combined momentum, it is observed that the combined momentum is less prone to material uncertainties in te whole η range, as displayed in the comparison of cluster-combined responses to geometry distortions.

Chapter 5

Measurement of the Higgs mass in the $H \to ZZ \to 4l$ channel

Contents

The final Run1 measurement of the Higgs boson mass in the decay channel $H \to ZZ \to l^+l^-l'^+l'^-$ where $l, l' = e, \mu$ will be presented in this Chapter. The main features of this channel are detailed in Section 1.6.

Section 5.1 will introduce the data and the Monte Carlo simulations relative to the Higgs signal and to the various background components. The event selection, starting from the definition of the physics objects and the trigger requirements up to the kinematic selection applied on the lepton candidates will be covered in Sections 5.2.1 and 5.2.2.
In order to enhance the sensitivity of the signal against the dominant $q\bar{q} \to$ZZ background, a BDT-based kinematic discriminant (Appendix B) has been deployed: Section 5.3 will be devoted to the

description of this method while the treatment of the reducible background of the analysis, i.e. Z+jets is detailed in Section 5.4.
Conclusively, Section 5.6 will give an overview on the main results achieved on the Higgs mass and signal strength in the four lepton decay channel as well as a digression on the beneficial effects of the improved electron calibration (Chapter 4) on the mass resolution.

5.1 Data and Monte Carlo samples

Data are collected in 2011 and 2012 from proton-proton collisions with center-of-mass energies of $\sqrt{s}$=7 TeV and $\sqrt{s}$=8 TeV respectively. In order to check data integrity, the events are subjected to quality requirements defining the so-termed Good Run List (GRL). Events collected in runs where detectors are not fully operative are discarded. As already described in Section 2.1.3, the resulting integrated luminosity comprising the 2011 and 2012 runs is approximately 4.5 fb^{-1} at $\sqrt{s}$=7 TeV and 20.3 fb^{-1} at $\sqrt{s}$=8 TeV. The $H \to$ 4l analysis applies the usual GRL delivered by ATLAS at the end of each data-taking period.
The signal with the various production mechanisms, the dominant $q\bar{q}$ →ZZ background and the reducible components Z+jets and $t\bar{t}$ Monte Carlo simulations as well as a detailed study on the theoretical uncertainties affecting each sample have been examined in Sections 1.6.1 and 1.6.2.

5.2 Event selection and analysis

5.2.1 Object definition and triggers *menus*

The electron and muon candidates fulfil the prescriptions detailed in Section 3.3 and 3.4 for the identification and the reconstruction. The cut-based identification menu is applied on the 2011 dataset while the likelihood algorithm is used on 2012 candidates. The *loose* likelihood menu has been chosen to define the electron identification and replaced the cut-based selection used in previous publications. The electrons are calibrated according to the procedure explained in Chapter 4 and the track-cluster $E - p$ combination is applied to electron candidates passing the standard cut-based selection.
Jets are used in the classification of events into VBF-like, VH-like and ggF-like categories. Reconstruction and identification prescriptions of these objects as well as dedicated correction methods to calibrate their energy are addressed in Section 3.5.

The triggers for the online selection of four leptons are based on single and dilepton menus. Due to the increased instantaneous luminosity in 2012, the typical trigger thresholds have been raised. Besides, specific isolation cuts on the leptons are implemented only for single lepton triggers. This isolation criterion is applied at the Event Filter level and requires the sum of the p_T of the tracks associated to a lepton (p_T >1 GeV) in a cone of size ΔR=0.2 around the track to be less than a certain percentage ($\sim$ 10-15%) of the lepton p_T in order to remove lepton candidates surrounded by hadronic activity. The trigger efficiency calculated for Monte Carlo simulations generated at $\sqrt{s}$= 8 TeV for a Higgs boson of m_H=125 GeV is 98% for the 4μ and the mixed channel while it goes up to $\sim$ 100% for the 4e channel. The trigger requirements of the analysis, although their impact on the efficiency of the event selection is found to be marginal, are executed as the logic OR of the following conditions:

- one of the leptons matches the single lepton trigger;
- two leptons match the dilepton trigger.

Table 5.1 shows the trigger menus, both single and dilepton triggers, used for the $H \to ZZ \to 4l$ decay channel. The efficiency of a given trigger class is measured using a *tag-and-probe* technique illustrated in Section 3.3.3 on Z→ee and Z→ $\mu\mu$ Monte Carlo events. Residual differences between trigger efficiencies determined in data and Monte Carlo are extrapolated in the p_T-η phase space and used to reweight the typical efficiency exhibited in Monte Carlo in order to match it with data. The trigger-related systematic uncertainties will be explained in Section 5.5.

Trigger type	$\sqrt{s}$=7 TeV	$\sqrt{s}$=8 TeV
Single muon	$p_T > 18$ GeV	$p_T > 24$ GeV
Single electron	$E_T > 22$ GeV	$E_T > 24$ GeV
Dimuon (symmetric)	$p_T^{(1,2)}$ >10 GeV	$p_T^{(1,2)}$ >13 GeV
Dimuon (asymmetric)	added for 2012 data-taking	$p_T^{(1)}$ >18 GeV, $p_T^{(2)}$ >8 GeV
Dielectron	$E_T^{(1,2)}$ >12 GeV	$E_T^{(1,2)}$ >12 GeV
Electron - Muon	E_T >10 GeV, $p_T > 6$ GeV	E_T >12 or 24, p_T >8 GeV

Table 5.1: Trigger menus used for the $H \to ZZ \to 4l$ decay channel. 1 and 2 label the first and the second lepton in the dilepton pair.

5.2.2 Kinematic selection

In order to define the candidate lepton quadruplet for each event, a set of sequential cuts on kinematic variables are defined. The *cutflow* is designed to be constituted by two main sub-steps, explicitly the event preselection and the event selection. The first item deals with requirements on the object quality; its main aspects are summarised below:

1. Electrons.
   - Smearing and calibration are applied to all electrons.
   - E_T >7 GeV and $|\eta|$ <2.47 (loose likelihood identification menu applied).
2. Muons.
   - Smearing functions are applied to all muons.
   - *combined* or *segment-tagged* muons with p_T >6 GeV and $|\eta|$ <2.7;
   - Maximum one *calorimeter-tagged* (p_T >15 GeV and $|\eta|$ <0.1) or *standalone muon* (p_T >6 GeV, 2.5< $|\eta|$ <2.7 and ΔR >0.2 from the closest *segment-tagged* muon).

The event selection is composed of three sub-levels, kinematic selection, isolation and impact parameter significance requirements.

1. Kinematic selection.
   - Two pairs of same flavour opposite charge leptons (SFOS); the analysis is split in four final states: 4e, 4μ, 2e2μ and 2μ2e.
   - p_T threshold for the three leading leptons in the quadruplet set at 20, 15, 10 GeV. The fourth lepton must fulfil the requirements on the transverse momentum or transverse energy ($p_T > 7$ GeV for muons and E_T >6 GeV for electrons) listed in the previous block.

- The leading dilepton pair is defined as the one closer to the PDG Z mass; its invariant mass is labelled m_{12} or alternatively m_{Z1};
- the other pair is the subleading dilepton pair, its mass is addressed as m_{34} or m_{Z2}.
- Leading dilepton mass requirement: (50< m_{12} <106) GeV.
- Subleading dilepton mass requirement: $m_{34} > m_{\text{threshold}}$, where $m_{\text{threshold}}$ varies as a function of the total four-lepton invariant mass, m_{4l}. Its value is 12 GeV for $m4l$ <140 GeV and rises linearly to 50 GeV as a function of m_{4l} in the interval 140-190 GeV. Beyond 190 GeV, the cut is kept constant at 50 GeV. In case more than one quadruplet survive the kinematic selection, the one with m_{12} closest to the Z mass is kept; additionally, if multiple quadruplets have the same m_{12}, the one with the highest m_{34} is selected.
- The standard selection of the primary vertex is also employed in the analysis: since the four leptons are originated from the primary vertex of the interaction, the lepton tracks are required to have a distance $|\Delta z_0|$ <10 mm from the primary vertex of the event along the proton beam axis.
- In order to reduce the muon cosmic background, an additional cut on the transverse impact parameter is introduced, $|\Delta d_0|$ <1 mm.
- Overlap removal on e-e: when two electrons share the same ID tracks or are too close to each other in the $\eta - \phi$ phase-space (ΔR <0.10 for the same flavour leptons and ΔR <0.20 for different flavour leptons in the final state), the highest E_T candidate is kept.
- Overlap removal on e-μ: electron and muon candidates (combined or standalone) sharing the same track are removed. Calorimeter-tagged muons sharing the same track with electrons are removed.
- Overlap removal on e-jets: jets overlapping with electrons in a ΔR=0.2 cone are discarded.
- Quadruplets whose alternative same-flavour opposite charge dilepton invariant mass is below 5 GeV are removed to eliminate the $J/\Psi \to l^+l^-$ contribution (J/Ψ veto).

2. Isolation requirements:

   - Lepton track isolation (ΔR=0.20): $\frac{\sum_i p_{T,i}}{p_T}$ <0.15;
   - Electron calorimeter isolation (ΔR=0.20): $\frac{\sum_i E_{T,i}}{E_T}$ <0.20;
   - Muon calorimeter isolation (ΔR=0.20): $\frac{\sum_i E_{T,i}}{E_T}$ <0.30;
   - Electron calorimeter isolation for standalone muons (ΔR=0.20): $\frac{\sum_i E_{T,i}}{E_T}$ <0.15.

   The normalised track isolation is defined as the sum of the transverse momenta of tracks in a cone excluding the lepton track itself. Furthermore, the tracks considered in the sum are of good quality, i.e. they have at least four hits in the pixel detector and silicon strips, in addition to $p_T > 1$ GeV for muons and at least nine silicon hits, one of them in the b-layer and p_T >0.4 GeV for electrons. Secondly, for both the track and the calorimeter-based isolation, spurious contributions from other leptons of the same quadruplet are subtracted from the final sum.

3. Impact parameter significance:

   - $\frac{d_0}{\sigma d_0}$ <6.5 for electrons;

- $\frac{d_0}{\sigma d_0}$ <3.5 for muons.

  The reason of this asymmetric behaviour between the electrons and muons regarding the impact parameter cut is related to the fact that electrons are affected by bremsstrahlung more than muons and their impact parameter is therefore larger.

The analysis is also sensitive to Higgs production enriched categories (ggF, VBF, VH hadronic and VH leptonic) characterised by specific cuts on the jet multiplicity of the event and on the kinematic features of the final state jets. The events are treated with different algorithms according to the categories they belong to, thence no candidates are discarded by the selection.

The final phase of the event selection is represented by the FSR recovery applied to all lepton candidates and the usage of the Z-mass constraint. These aspects will be investigated in the following Sections 5.2.3 and 5.2.4.

5.2.3 FSR recovery

$H \to ZZ \to 4$l decays include instances of low E_T photons radiated in the final state (*Final State Radiation*, FSR). The Monte Carlo tool modelling this QED radiative process in the Z decay is PHOTOS; some of the FSR photons can be identified in the detector and incorporated back into the final state measurement. This procedure enables to recover events having their reconstructed mass away from the signal region because of the energy depletion produced by the FSR photon. Two different conditions may arise in the FSR photon reconstruction:

- Collinear FSR [129]: the photons are emitted in a narrow cone around the final state muons or electrons in the Z decay.
- Non-collinear FSR, *far FSR*: photons are emitted in a wider area around the final states particles the photons radiated from.

Collinear FSR recovery is accomplished for muon candidates. The γ search starts from 3×5 cluster seeds in the Electromagnetic Calorimeter; if more than one possible cluster is found, the cluster with the highest E_T is selected to remove the intrinsic ambiguities associated to the correct matching of the photon candidates.

Non-collinear FSR recovery is applied for both electrons and muons. Photon candidates are supposed to pass tight requirements on the object quality. Collinear photon instances associated to the decay of the leading Z boson, both in the electron and muon channels, are searched first. The FSR correction is applied if (66< $m_{\mu\mu}$ <89) GeV and the $\mu\mu\gamma$ total mass, $m_{\mu\mu\gamma}$, is below 100 GeV. If no collinear FSR photons are found, the algorithm on the non-collinear FSR is invoked provided that the following requirements are satisfied:

- m_{ll} <81 GeV and $m_{ll\gamma}$ <100 GeV.

FSR recovery: validation on $Z \to \mu\mu$ events

The effect of adding a collinear or a non-collinear FSR photon to the Z invariant mass in the $\mu\mu$ channel is studied in order to gauge the improvement and validate the method.

A specific selection for this particular case is designed: two opposite-sign combined muons whose $p_T > 20$ GeV without overlap in a cone of ΔR=0.1 are selected. As stated before, events in the mass range 66-89 GeV such that the overall invariant mass $m_{\mu\mu\gamma}$ is below 100 GeV are evaluated. Figure

5.1 (a) illustrates the invariant mass distributions of the Z events before and after the inclusion of both collinear and non-collinear FSR photons in data and Monte Carlo for all Z events. Data to Monte Carlo agreement is found on the invariant mass of the $\mu\mu(\gamma)$ final state. On the contrary, Figure 5.1 (b) and (c) show the same distributions, with an identified FSR photon for events. The collinear FSR succeeds in recovering 70% of the FSR photons within the fiducial phase-space. Approximately 85% of the corrected events are characterised by genuine photons in the final state and the remaining 15% misidentified photons are produced by pile-up instances and muon energy losses. The total fraction of corrected events associated to collinear FSR photons in the $H \to$ 4l analysis is $\sim$ 4%; as for the signal-region (110< m_{4l} <140) GeV, 1 event goes through the FSR correction procedure.

The non-collinear FSR selection works on $\sim$ 1% of the total H$\to$ 4l events; in the above-defined signal-region, 2 events are corrected by the non-collinear FSR algorithm. This search has an efficiency of approximately 60% and a purity of 95%.

In order to gauge the improvement of the FSR method on the Z$\to \mu\mu$ invariant mass resolution, the parameter:

$$\frac{m_Z^{\text{reco}} - m_Z^{\text{true}}}{m_Z^{\text{reco}}} = \frac{m_Z^{\text{reco}}}{m_Z^{\text{true}}} - 1 \tag{5.1}$$

is plotted before and after the addition of the collinear and the non-collinear FSR photon in the Monte Carlo simulation. This approach significantly improves the bulk of the mass resolution as well as reducing the tails of the uncorrected distributions (Figure 5.2).

FSR recovery: validation on $Z \to$ ee events

A dedicated selection is applied to dielectron final states as well: two opposite sign electrons with E_T >10 GeV and $|\eta|$ <2.47 that are not overlapping in a cone ΔR=0.1 are selected. Moreover, isolation and impact parameter criteria are applied to electron candidates.

Figure 5.3 (a) indicates the invariant mass distributions with and without the non-collinear FSR corrections in place for events characterised by a radiated photon in the final state; full consistency between data and the Monte Carlo response of this parametrisation is observed. The figure of merit $\frac{m_Z^{\text{reco}}}{m_Z^{\text{true}}} - 1$ introduced for the previous Section is also drawn here for the electron final state: the usage of the non-collinear FSR correction improves the dielectron mass resolution as well as the amount of tails (Figure 5.3 (b)).

5.2.4 Z mass constraint

Given the requirements in Section 5.2.2 concerning the Z boson matching, the first lepton pair, Z_1 is predominantly associated with the decay of an on-shell Z boson, hence the Z lineshape properties and the knowledge of the lepton momenta uncertainties can be exploited to improve the Z_1 mass resolution. The ingredients of this parametrisation are listed below.

i A Z boson with a true mass μ_{12} given its reconstructed mass m_{12}.

ii Two final state leptons whose true momenta and the reconstructed ones are respectively $\mathbf{p}_{1,2}^{\text{true}}$ and $\mathbf{p}_{1,2}^{\text{reco}}$.

The following likelihood function $\mathcal{L}$ can be used to model this problem:

$$\mathcal{L}(\mathbf{p}_1^{\text{true}}, \mathbf{p}_2^{\text{true}}, \mathbf{p}_1^{\text{reco}}, \mathbf{p}_2^{\text{reco}}) = \mathcal{B}(\mathbf{p}_1^{\text{true}}, \mathbf{p}_2^{\text{true}}) \cdot \mathcal{R}_1(\mathbf{p}_1^{\text{true}}, \mathbf{p}_1^{\text{reco}}) \cdot \mathcal{R}_2(\mathbf{p}_2^{\text{true}}, \mathbf{p}_2^{\text{reco}}). \tag{5.2}$$

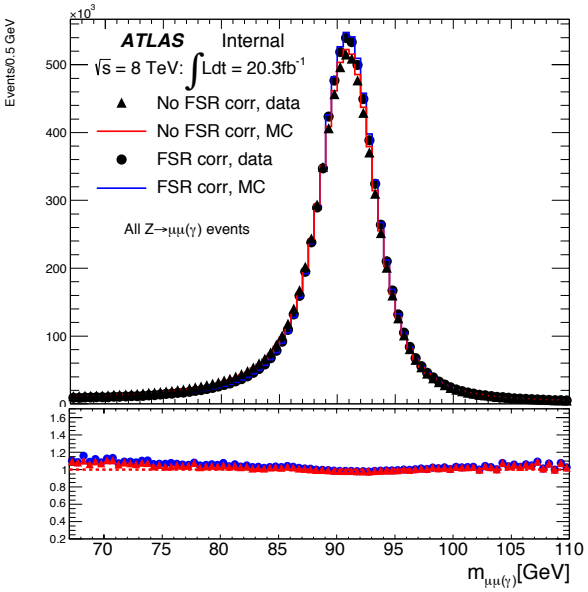

(a)

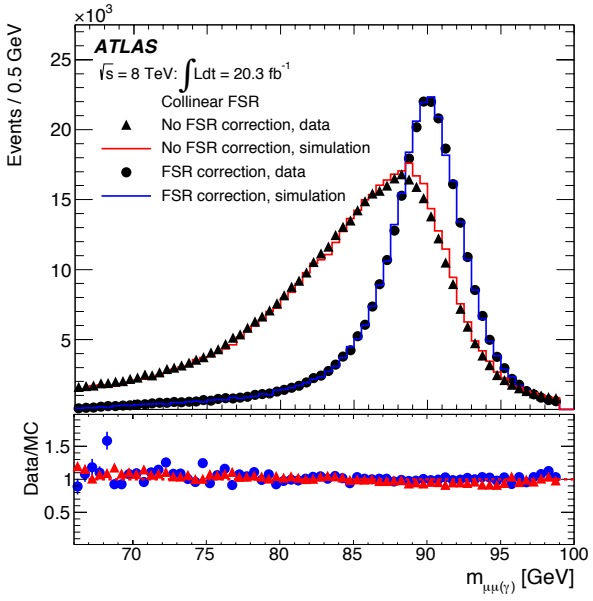

(b)

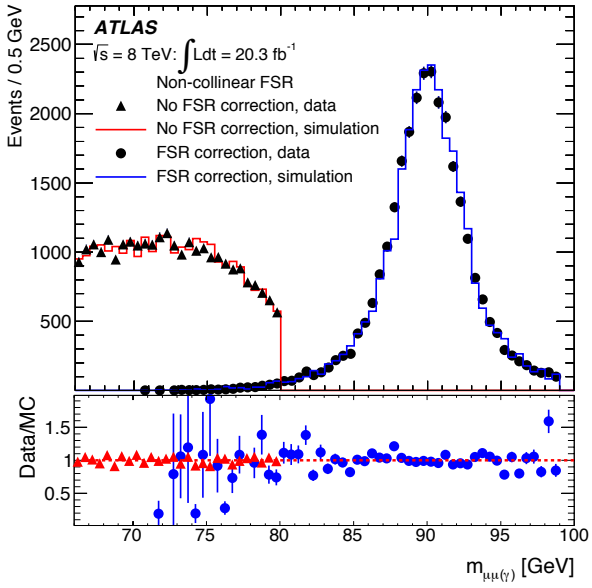

(c)

Figure 5.1: (a) Invariant mass distribution of Z→ $\mu\mu$ events in data and Monte Carlo before FSR correction (filled triangles) and after FSR correction (filled circles). The Monte Carlo predictions are illustrated before and after corrections as well. Both collinear and non-collinear corrections are herein included. The bottom plot describes the data-to-Monte Carlo ratio for the two configurations. Invariant mass distribution of Z→ $\mu\mu$ events in data and Monte Carlo before and after collinear (b) and non-collinear (c) FSR correction for events with a collinear or non-collinear FSR photon identified. The bottom plots delineate the data-to-Monte Carlo ratio for these two configurations.

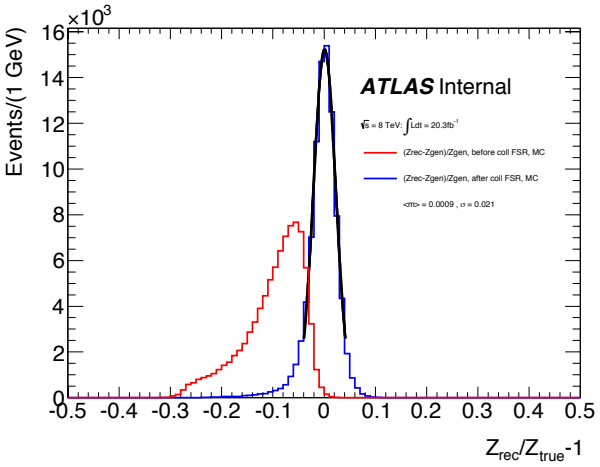

(a)

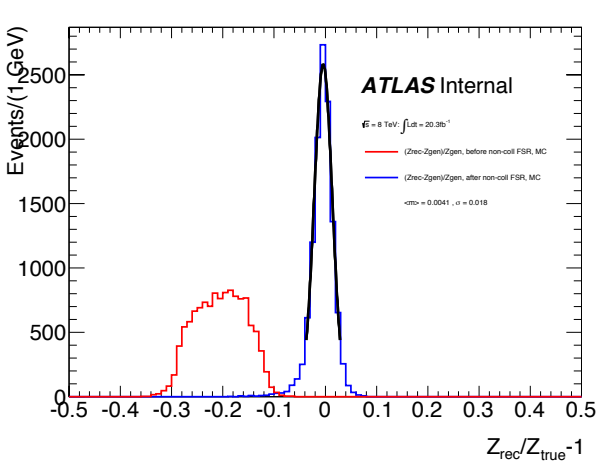

(b)

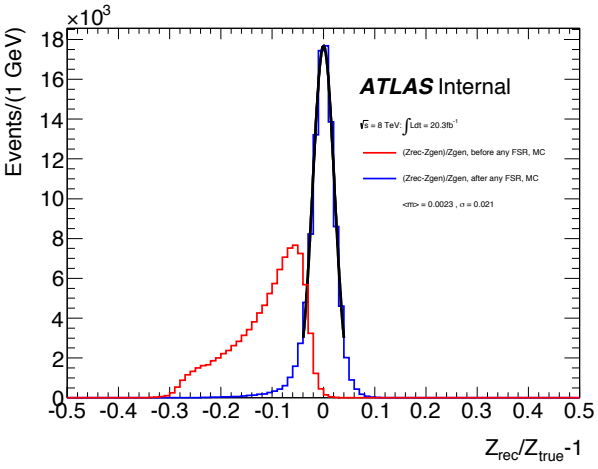

(c)

Figure 5.2: Distributions of the $\frac{m_Z^{\rm reco}}{m_Z^{\rm true}} - 1$ variable for simulated Z$\to \mu\mu$ events before and after collinear (b), non collinear (b) or both (c) FSR correction in each event where there is an FSR photon instance. The mean value $< m >$ and the σ of the various distributions are produced with a Gaussian core fit around the peak.

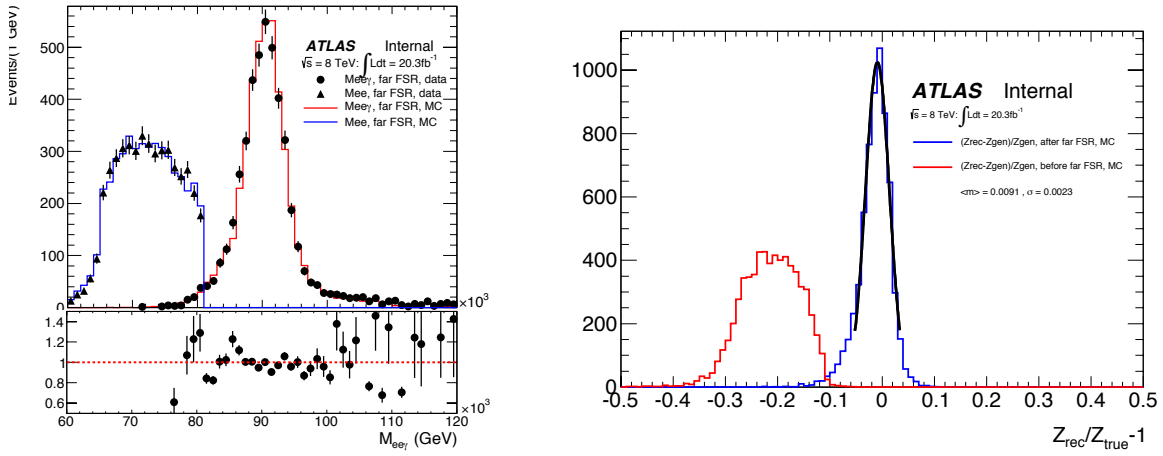

(a) **(b)**

Figure 5.3: (a) Invariant mass distribution of Z→ee events in data and Monte Carlo before FSR correction (filled triangles) and after FSR correction (filled circles). The Monte Carlo predictions are reported before and after corrections as well. (b) Distributions of the $\frac{m_Z^{\rm reco}}{m_Z^{\rm true}} - 1$ variable for simulated Z→ee events before and after non-collinear FSR correction. The mean value $< m >$ and the σ of the various distributions are computed with a Gaussian core fit around the peak

$\mathcal{B}$ is the probability density function (PDF) of the Z true lineshape at the generator level, $\mathcal{R}_{1,2}$ are the PDFs of the energy/momentum response functions for the two leading leptons. The likelihood $\mathcal{L}$ in the formula (5.2) is maximised for a given event characterised by a reconstructed and true lepton momenta so that the maximisation procedure will return the most likely reconstructed four-momenta (Z mass constraint) given the true Z lineshape. Referring to equation (5.2),

- $\mathcal{B}$ is modelled with a relativistic Breit-Wigner function, $\mathcal{B} = \mathcal{B}_{BW}(\mu_{1,2}|m_Z, \Gamma)$ with mean and width set to the Z boson mass m_Z and on the natural Z width, Γ_Z.

- $\mathcal{R}_{1,2}$, the lepton energy/momentum response functions, are approximated by a Gaussian distribution, $\mathcal{R}_{1,2} = \mathcal{R}_{\rm Gauss}(\mu_{1,2}|E_{1,2}, \sigma_{1,2})$ with mean set to the measured lepton energies, $E_{1,2}$, and variance σ^2 set to the squared lepton momentum resolution obtained from Monte Carlo studies which yields to an uncertainty on the reconstructed m_{12}. However, the lepton energy response distributions are not exactly gaussian because of the enhanced tails due to photon radiations mostly affecting electrons. For this reason, a modified parametrisation of the lepton response distributions written as a sum of three Gaussian component is also introduced in the analysis. Regarding the Z lineshape contribution in equation (5.2), the true lineshape is not exactly described by a Breit-Wigner. In order to account for this feature of the Z lineshape observed in Figure 5.4, the true distribution is smoothed and then the functional form is worked out and used as PDF in the $\mathcal{B}$ component of the likelihood fit.

Figure 5.5 illustrate the distribution of the mass response in the 4e channel for the dielectron pair and for the m_{4e} invariant mass generated for m_H =125 GeV. The response for the unconstrained mass, the default Z mass constraint and the two configurations described above are highlighted; the improvement is gauged by the usage of the variable $\frac{m_{\rm reco} - m_{\rm true}}{m_{\rm true}}$.
The Z mass constraint application highlights a clear improvement; since the gain brought by the two modified PDF parametrisations is negligible compared to the one characterising the default algorithm, it is decided to apply the Z mass constraint in its initial formulation, e.g. a Breit-Wigner PDF for the $\mathcal{B}$ term and a Gaussian response function for the $\mathcal{R}_{1,2}$ components in equation (5.2).

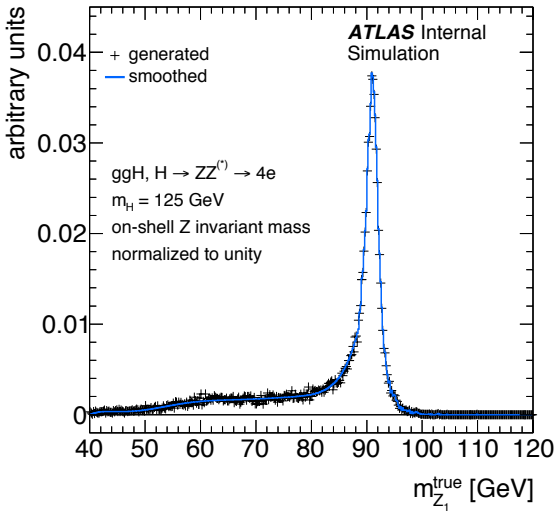

Figure 5.4: Distribution of the true leading Z boson mass, $\mu_{1,2}$, in inclusive $H \to ZZ \to$ 4e events generated at m_H= 125 GeV illustrated at generator level and smoothed.

The m_{Z1} cut is performed before the Z mass constraint as the Z mass constraint does not select and it is done on the unconstrained m_{Z1}. The Z mass constraint is modeled in such a way that it does not over-correct towards the true m_Z events that are very far from this true value if their typical momentum resolution is very bad.

Table 5.2 charts the results of the resolution studies on m_{4l} with and without the Z mass constraint in place, employing a gaussian core fit around the mean of the distributions. The improvement on the four-lepton invariant mass resolution is of the order of $\sim$ 15%.

Channel	m_{4l}^{no} [GeV]	m_{4l}^{yes} [GeV]	σ_{4l}^{no} [GeV]	σ_{4l}^{yes} [GeV]	Outside $\pm$ 2σ no Z	Outside $\pm$ 2σ yes Z
4e	123.75	124.53	2.54	2.30	17%	16%
4μ	124.52	124.89	1.98	1.64	17%	17%
2e2μ	124.18	124.86	2.08	1.76	20%	19%
2μ2e	124.30	124.67	2.30	2.08	16%	16%

Table 5.2: Four lepton invariant mass resolutions estimated from a signal Monte Carlo generated at m_H=125 GeV with and without the Z mass constraint in place. The values refer to a gaussian core fit around the mean of the distributions.

5.3 Treatment of the ZZ background - BDT kinematic discriminant

The Higgs signal $H \to ZZ \to$ 4l and the dominant ZZ background of the analysis are characterised by the same final state produced by a pair of Z boson decaying into leptons. A Boosted Decision Tree (BDT) multivariate approach is therefore developed to discriminate between the Higgs H$\to ZZ \to$ 4l signal and the irreducible $q\bar{q} \to$ ZZ background. The training of this multivariate discriminant is based on 500 decision trees on the events surviving the kinematic selection detailed in Section 5.2.2 in the mass window (115$< m_{4l} <$130) GeV. This procedure is limited to the dominant signal

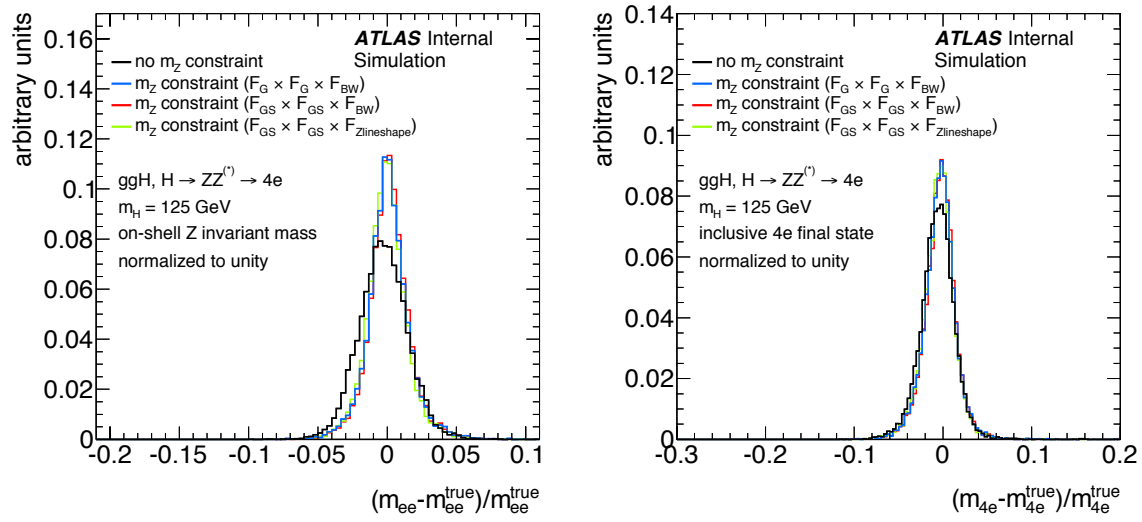

(a) **(b)**

Figure 5.5: Distributions of the mass response, $\frac{m_{\text{reco}}-m_{\text{true}}}{m_{\text{true}}}$ of the leading dielectron pair (a) and the 4-lepton pair (b) in inclusive $H \to ZZ \to 4e$ events generated at a Higgs mass M_H =125 GeV, The mass response is illustrated without Z mass constraint, with the standard Z mass constraint using a Gaussian approximation of the electron energy response, with a Z mass constraint using Gaussian sums for the response function, finally with a Z mass constraint using the Gaussian-sum response functions and the real generator m_{Z1} distributions.

production contribution, the gluon-gluon fusion, and to the ZZ background.
The input variables of the analysis are the transverse momentum and pseudorapidity of the ZZ system, p_T^{ZZ} and η^{ZZ}, and a Matrix Element (ME)-based discriminant, named KD with MADGRAPH [130]:

$$KD = \frac{\log ME^2_{\text{sig}}}{\log ME^2_{\text{ZZ}}}. \tag{5.3}$$

The equation above comprises the kinematical information of the signal and the ZZ background where the required input variables are the angular distributions of the leptons as well as the masses of the two reconstructed Z bosons, m_{Z1} and m_{Z2}. The distributions of these variables for the Higgs signal and the ZZ background in the training mass window of the BDT (115< m_{4l} <130) GeV are reported in Figure 5.6 (a) whilst Figure 5.7 testifies that no over-training is found when comparing the training and test distributions of the output BDT.

The improvement brought by the usage of p_T and η in the ZZ mass frame is visible in the ROC curve of the background rejection *vs* the signal efficiency in Figure 5.8 (a). The background separation achieved by the BDT configuration for a given signal efficiency is larger by an approximate factor 10-15% than the one of the KD-only approach.

The BDT output is used in the analysis as input to a 2-dimensional fit with the four-lepton mass, m_{4l} (Section 5.7.4). However, a set of cut-based studies on the BDT variables are done as a cross-check of the baseline shape approach illustrated in Section 5.6. For each BDT cut, the number of expected events for signal (S) and background (B) is provided and the asymptotic significance is worked out as a function of the BDT cut applied to the samples. The employed asymptotic formula,

$f(S,B)$ is:

$$f(S,B) = \sqrt{2 \cdot \left[(S+B) \cdot \left(1 + \frac{S}{B} \right) - S \right]} \tag{5.4}$$

and is plotted in Figure 5.8 (b) as a function of the BDT cut for events in the interval ($119.5 < m_{4l} < 129.5$) GeV. The proof of this formula [131] is sketched in Appendix D. The cut on the BDT discriminant that maximises the significance of the gluon-initiated Higgs signal generated at m_H=124.5 GeV over the $q\bar{q} \to$ ZZ background in the SM hypothesis (μ=1) is found to be at BDT>0 corresponding to an expected significance of $\sim 4.2\sigma$.

5.4 Treatment of the reducible background

The reducible backgrounds [132] of the analysis are represented by the Z+jets and the $t\bar{t}$-related final states. The treatment of these backgrounds is based on the definition of kinematic regions where the signal contribution is suppressed (control regions, CR) created by relaxing or inverting some analysis requirements, such as the impact parameter significance or the lepton identification and reconstruction criteria. From these regions, the expected background in the signal regions (SR) is calculated by applying *transfer factors* that are specifically associated to each control region. These transfer factors are determined on the efficiency of the relaxed or inverted selection criteria for a certain control region or by the ratio of the expected yields between control and signal regions.

Two broad categories have been introduced in the analysis: $Z + \mu\mu$ (Z boson candidates and low p_T leptons coming from heavy flavours) and $Z + ee$ (Z bosons accompanied by jets misidentified as electrons).

5.4.1 $Z + \mu\mu$ category

The three main sub-components of the $Z + \mu\mu$ category are:

- $Zb\bar{b}$: a Z boson is reconstructed in association with soft p_T leptons coming from heavy quark (heavy flavour) semileptonic decays.
- Z+light jets: a Z boson is reconstructed with π and K in-flight decays within light flavour jets.
- $t\bar{t}$: present whenever the final state leptons of the semileptonic decay produce fake Z bosons.

Different control regions are exploited in order to deal with these different background components. Each of them is designed to enrich a specific background component by minimising the spurious leakage of the signal contribution. The standard selection is always applied on the leading lepton pair.

i Same Sign CR. The standard four-lepton analysis selection is applied on the first lepton pair while the subleading lepton pair does not have impact parameter and isolation selections applied. Moreover, the leptons are required to have the same charge. This control region is not dominated by any specific background among the ones mentioned above.

ii $e\mu + \mu\mu$ CR. In this control region, mostly dominated by the $t\bar{t}$ term, the standard selection is applied on the leading pair with an additional requirement on the first lepton pair to be of different flavour. As for the subleading pair, neither the impact parameter nor the isolation requirements are present and both same and opposite charged leptons are kept in the parametrisation.

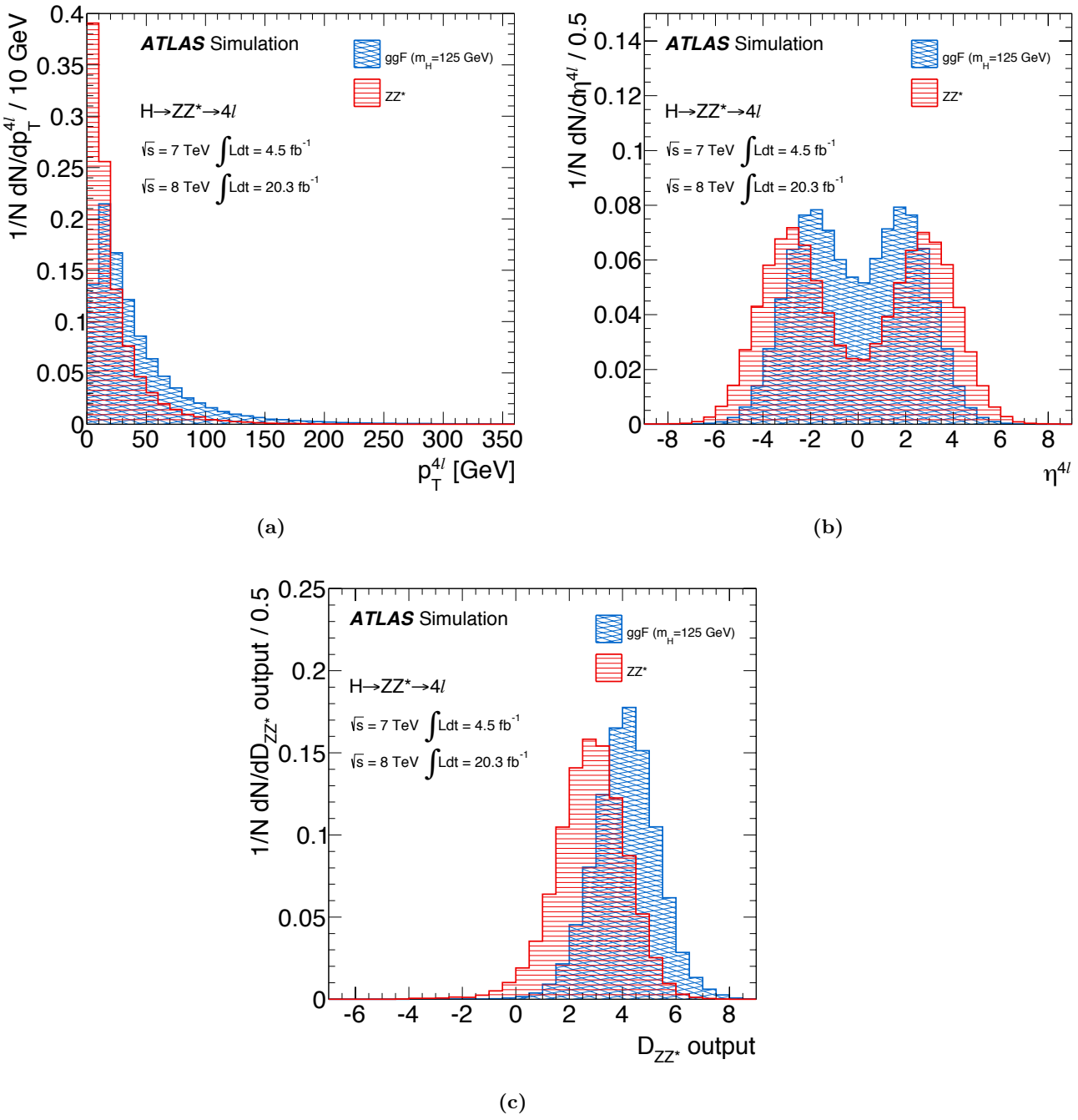

(a) **(b)**

(c)

Figure 5.6: Input variables, η^{ZZ}, p_T^{ZZ} and the KD distributions for the Higgs signal and the dominant $q\bar{q} \to$ ZZ samples after the standard cutflow in the mass range (115< m_{4l} <130) GeV used for the training of the BDT discriminant.

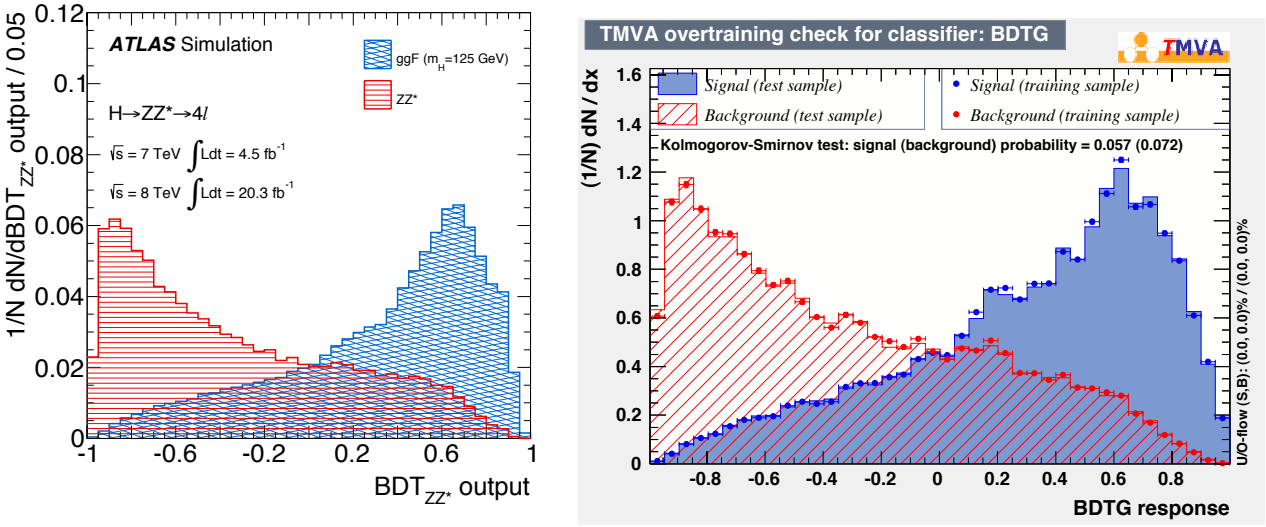

(a) (b)

Figure 5.7: Distribution of the BDT response (a) for the signal and the ZZ background normalised to the same area for shape comparison in the inclusive sample of 4e, 4μ, 2e2μ, 2μ2e final states. Signal and background distributions of the BDT response as TMVA output (b) for training and test samples.

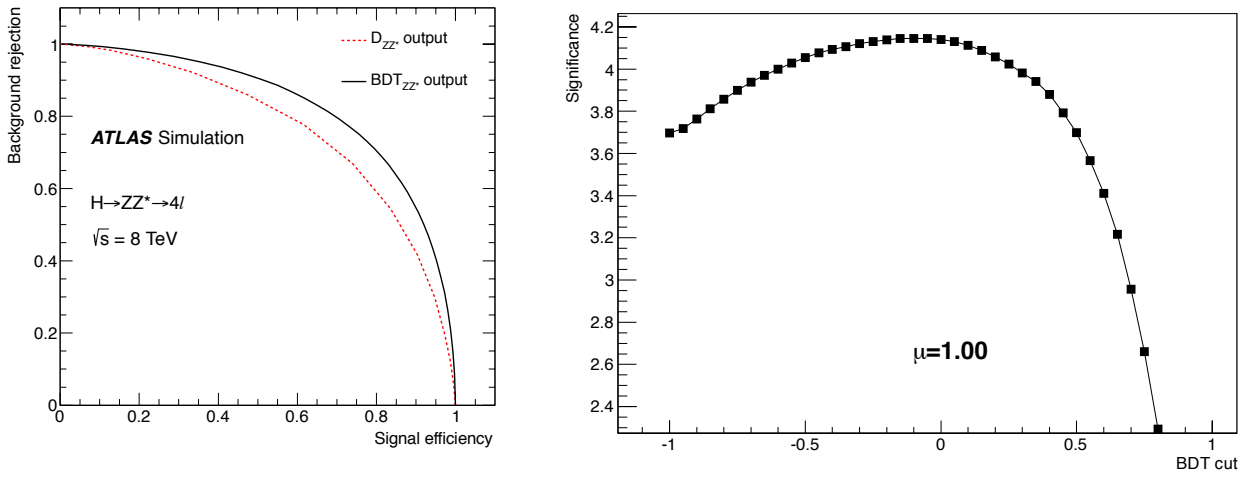

(a) (b)

Figure 5.8: (a) Background rejection versus signal efficiency curves (ROC) using KD discriminant and the BDT-based approach. (b) Figure of merit determined to estimate the significance for different BDT cuts for the SM hypothesis, μ=1. The best BDT cut that maximises the figure of merit is found at 0.

iii Inverted d_0 CR. This control region is enriched in heavy flavour from $Zb\bar{b}$ and $t\bar{t}$ decays. Indeed, leptons from b-quarks are produced in a displaced vertex, hence the impact parameter d_0 is a good variable to discriminate them. Therefore, the subleading lepton pair is submitted to the inverted d_0 requirement; in addition isolation criteria are not applied.

iv Inverted isolation CR. This control region, designed to be enriched in Z+light jets components (π and K in-flight decays) over the general $Zb\bar{b}$ component is exploited by inverting the isolation requirements for at least one lepton in the subleading pair while the first pair keeps the standard selection.

Various methods have been tried out to extract the final yields in the signal regions starting from the above CRs. In the baseline method, the four CRs are simultaneously fit to minimise statistical uncertainties. The other methods are used as internal consistency checks and developed in parallel with the simultaneous fit.

In the CRs, the observable is the mass of the leading dilepton, m_{12}, peaking at the Z mass for the resonant components of the reducible backgrounds ($Zb\bar{b}$ and $t\bar{t}$) and with a broad distribution for the non- resonant $t\bar{t}$ component.

First, the data-to-Monte Carlo agreement is tested and is found to be fairly good as reported in Figure 5.9 for two example control regions, i.e. inverted d_0 significance CR, and same-sign CR. Second, a global unbinned maximum likelihood fit is performed on m_{12} for the four control regions at the same time: the $t\bar{t}$-based m_{12} shape, provided from the $t\bar{t}$-enriched CR, is modelled by a 2^{nd} order Chebychev polynomial, whereas the $Zb\bar{b}$ and Z+light jets mass distributions are fitted with a convolution of a Crystal Ball and a Breit-Wigner that accounts for the Z lineshape component. The shape parameters of the fitting functions are determined from the Monte Carlo simulation.
The estimated yields derived in the fit for each CR are extrapolated to the signal region by calculating the selection efficiency $\epsilon = \frac{\mathcal{N}_{\text{all}}}{\mathcal{N}_{\text{relaxed}}}$ where $\mathcal{N}_{\text{all}}$ is the number of muons passing all the analysis criteria in a control region and $\mathcal{N}_{\text{relaxed}}$ is the number of muons surviving the relaxed selection specific of that given CR. This term is calculated for each muon, however the total transfer factor is assessed on a per-event basis by combining the different efficiency terms for the muons in the subleading pair. This factor is then multiplied by the yields in the CR to estimate the number of events in the signal region. In this way, the expected $Z + \mu\mu$ background yields are evaluated in the signal region.

The systematic uncertainties mostly stemming form the statistical size of the simulated samples are 6% in the $Zb\bar{b}$ component, 60% for the Z+light jets, and 16% for the $t\bar{t}$. The results of the fit are checked with data in the control regions and the good agreement of the parametrisation is found in Figure 5.10 where all the four control region components are superimposed in plot.

5.4.2 $Z + ee$ category

For the $Z + ee$ final state, the dominant reducible background comes from Z+light jets events. The electrons in the final state can be originated by jets faking electrons or photons produced by π_0 decays. The control regions of this analysis are built by relaxing or inverting the quality parameters on the electrons, X:

i CR 3l + X. The identification criteria are relaxed only for the low p_T electron in the subleading pair.

ii CR Z+ XX. The identification requirements are relaxed for both electrons composing the subleading Z pair.

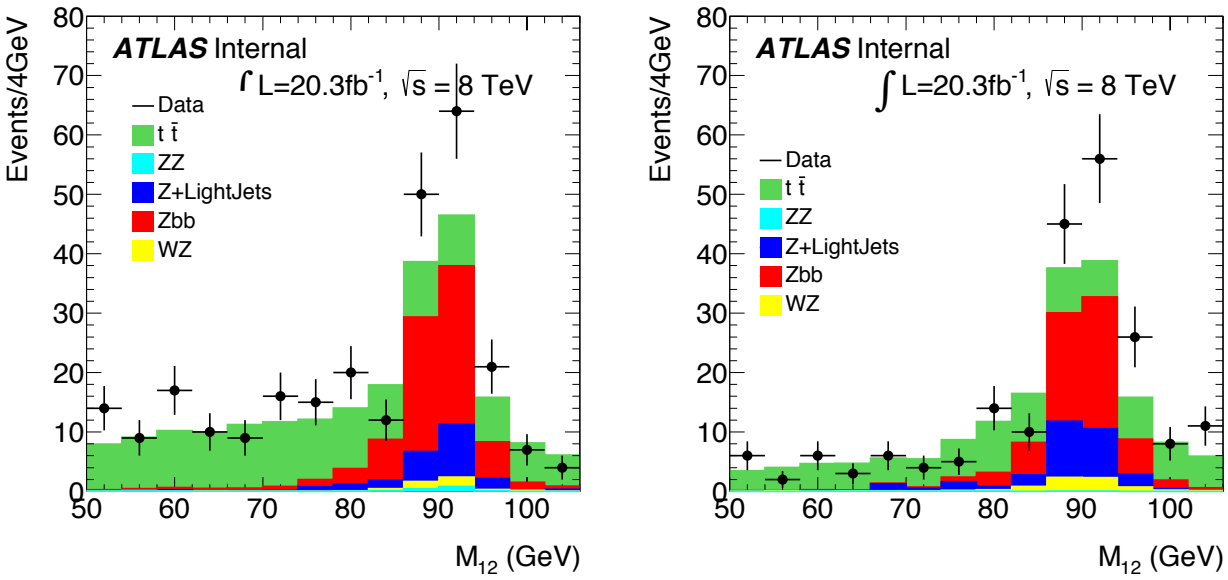

Figure 5.9: m_{12} distributions from Monte Carlo simulation normalised to the theoretical cross section for the inverted d_0 CR (a) and the same-sign CR (b). The various background contributions are superimposed in the plot..

The $3l + X$ method is the baseline approach for the $Z + ee$ background estimation. It uses data control regions with one relaxed low p_T electron in the subleading pair. Loose requirements on the probed electron of the subleading pair are used, e.g. the electron identification and isolation cuts as well as the impact parameter significance requirements are not applied.

The background components in this control region are evaluated using reconstruction-based electron categories according to which electron candidates are deemed as real electrons or fake. This approach is associated to the usage of several variables that define the object *electron* (Chapter 3) employed to reduce fake contamination. For instance, it is requested that tracks fulfil the b-layer requirement to reduce the amount of photon conversions. Another requirement is the number of high-threshold hits in the TRT to suppress hadron fakes. Candidates which do not pass the electron reconstruction are deemed as fakes.

Templates are created from the distributions of the B layer hits and the number of high-threshold hits in the TRT (Figure 5.11) and the yields of each component, light flavour jets (f), photon conversions (γ) and heavy flavour semileptonic decay (q) are extracted from the fit on data in the control region. Subsequently, in analogy with the muon case, the efficiency factors are calculated for each electron and the transverse factors are employed to extrapolate the yields of this reducible background in the signal region. The systematic uncertainty on the model is dominated by this efficiency method and it corresponds to 30%, 20% and 25% for the f, γ, q cases respectively.
The contribution of remaining contaminations derived from WZ and ZZ are estimated from Monte Carlo and found to be negligible.

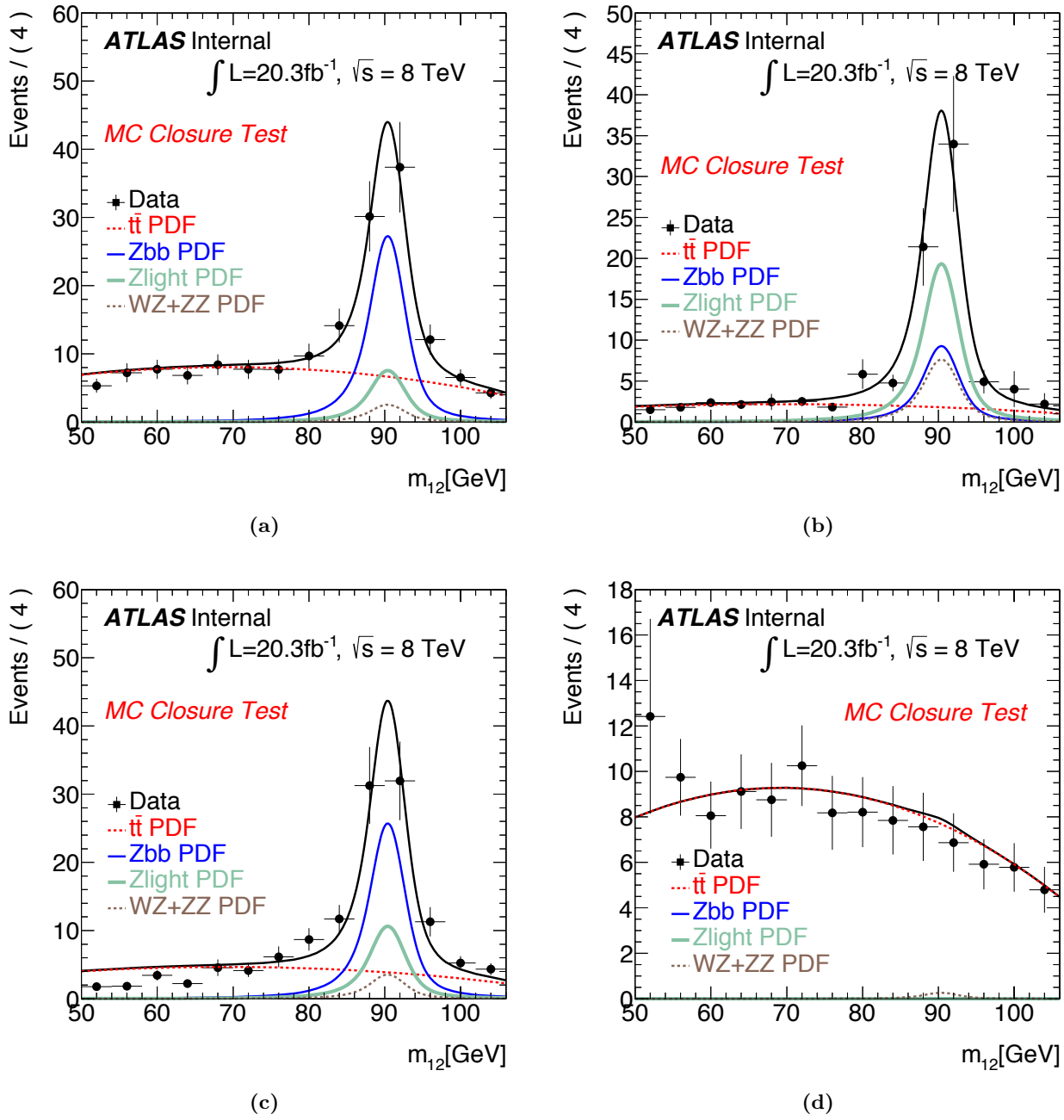

Figure 5.10: Simultaneous fit to data at $\sqrt{s}$=8 TeV using the m_{12} variable in the various control regions of the $Z+\mu\mu$ analysis, namely inverted d_0 significance (a), inverted isolation (b), same-sign (c) and $e\mu+\mu\mu$ CR (d) .

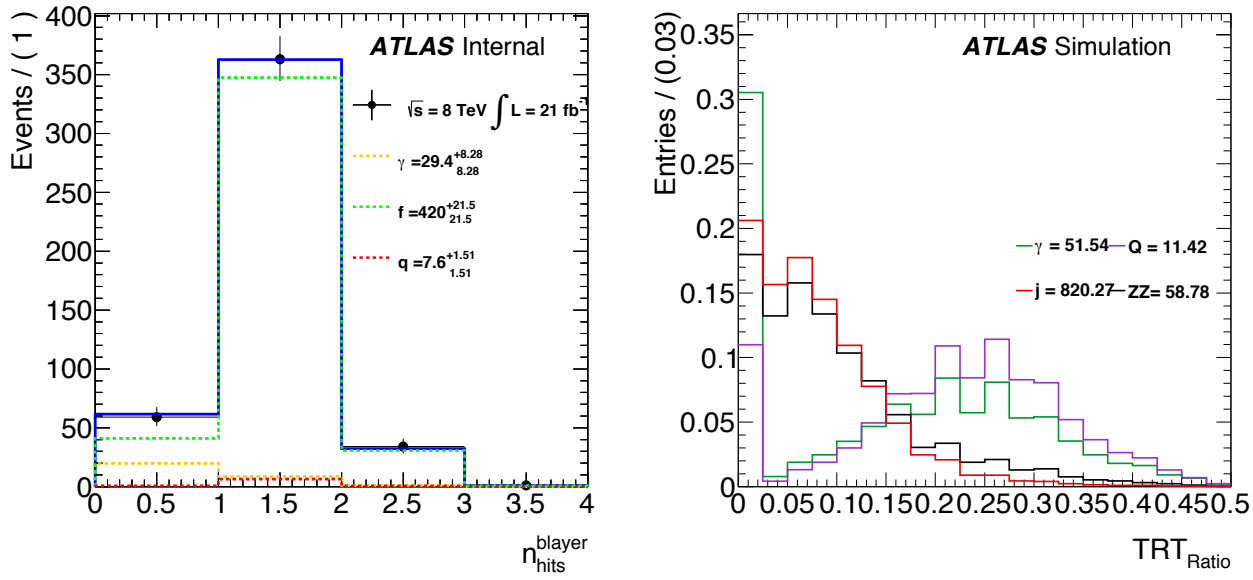

(a) **(b)**

Figure 5.11: Fit to the number of b-layer hits and the TRT ratio of the number of high threshold to low threshold TRT hits for the background components in the 3l+X control region. The source of background electrons are denoted as: light flavour jets faking an electron (f), photon conversion (γ) and electrons from heavy flavour quark semileptonic decays (q).

5.5 Systematic uncertainties

The systematic uncertainties are determined by comparing the nominal event yield with the one obtained after having modified relevant quantities by applying weights on Monte Carlo. The systematic uncertainty on the energy for electrons or momentum for muons (scale or resolution) is calculating by shifting the energy or momentum by a scale factor prior to selecting data events and by observing the impact of this shift in the number of events after the selection. The shifting procedure is effective for a nominal scale value, labelled α, and scaling values far from the nominal value of a factor 1σ, explicitly α+1σ and α-1σ. The same procedure applies to the resolution (*smearing*). Systematics are implemented in the fit as nuisance parameters: most of them carry a negligible effect on the final results and are therefore removed (*pruned*) from the fit.

The tested systematics comprised in the model are reported below.

- Electron reconstruction and identification. These systematics uncertainties on the signal Monte Carlo generated at m_H=125 GeV modify the m_{4l} yields by factors 4.36% in the 4e channel, 1.67% in the 2e2μ channel and 3.29% in the 2μ2e final state.

- Muon reconstruction and identification. There is a single nuisance parameter for the uncertainty on the muon reconstruction and identification. The yield-related uncertainties for the Higgs mass at 125 GeV are 1.86%, 0.77%, 1.09% in the 4μ, 2μ2e, 2e2μ final states.

- Trigger efficiency. As already mentioned in Section 5.2.1, the trigger efficiency of this final state due to the presence of high p_T leptons is very high. The systematic uncertainty on this trigger efficiency is given by the number of events that pass all the selection criteria with and without trigger requirements. This value is less than 0.7% on the final m_{4l} yields both for the electron and the muon triggers.

- Lepton energy scale and resolutions. The m_{4l} mass is extracted with the nominal energy scale and resolution of the physics objects, electron and muons, in the final state. In order to compute the energy scale and the resolution systematic uncertainties, the four lepton invariant mass is produced with the modified energy scale and resolution by $+1\sigma$ (up) or -1σ (down). Hence, two other mass templates are created, m_{4l}^{up} and , m_{4l}^{down}. The difference of the mean between the up/down variations and the nominal sample is extracted to compute the energy scale and resolution systematic uncertainties. The procedure is carried out for electrons and muons separately. Furthermore, since the analysis make use of collinear or non-collinear photons in the FSR recovery (Section 5.2.3) specific nuisance parameters associated to photons are also introduced.
  Total systematic uncertainties induced by electron energy scale and resolution for a Monte Carlo signal sample at m_H=125 GeV account for 0.06% in the 4e channel and 0.03%, 0.04% in the 2e2μ and 2μ2e final states respectively. As for muons, the impact of the energy scale and resolution systematics on the difference between the nominal and the modified means of the distributions is of the order of 0.02%.

- Luminosity. The normalisation uncertainty on the luminosity determination is 1.8% and 2.8% for data collected at $\sqrt{s}$=7 TeV and $\sqrt{s}$=8 TeV.

- Theory uncertainties on the signal model. The theoretical uncertainties related to the signal parametrisation are addressed in Section 1.6.1: the QCD scale uncertainties at m_H=125 GeV account for $\sim$ 7% for the ggF process, 1% for the VBF and VH productions and +4%, -9% for the $t\bar{t}$ production mechanism. The uncertainty on the parton density functions and the strong coupling constant are of the order of 8% for the gluon-initiated and 3% for the quark-based processes.

- Theory uncertainties on the background model. Theoretical uncertainties on the $q\bar{q}$ and gg-related ZZ background model are found in Section 1.6.2. The quark (gluon)-initiated processes have a PDF and a QCD scale uncertainty of approximately 4% (8%) and 5% (25%).

- p_T and η-related systematics. These two variables are used as input observables in the BDT training, hence it is essential to assess the theoretical uncertainties affecting them in order to estimate their impact on the BDT shape.

  The Higgs transverse momentum is sensitive to QCD scale uncertainties (factorisation, resummation and renormalisation scales) while the Higgs pseudorapidity depends on the PDF uncertainties. The scales μ_R, μ_F and μ_Q are varied around their central value set at μ_F=μ_R=m_H and μ_Q=$\frac{m_H}{2}$. This study has been performed using the HRES generator for a Higgs boson generated with gluon-gluon fusion at m_H=125 GeV. The largest up/down deviation to the scale is reached for μ_F=$2 \cdot m_H$ and $\mu_R = 2 \cdot m_H$ and μ_F=$0.5 \cdot m_H$ and $\mu_R = 0.5 \cdot m_H$.

  The scale variations are computed by normalising to unity the up (or down) variations with respect to the nominal case, so to account for shape-related systematic uncertainties as in Figure 5.12 (a). The systematic uncertainties on η [58] are extracted by fixing the PDF set of the analysis to CT10 and by varying its eigenvector error set. The up and down contributions are illustrated in Figure 5.13 (a).

  The impact of the p_T on the BDT shape is reported in Figure 5.12 (b); while the shape variations due to the presence of the PDF uncertainties affecting the Higgs pseudorapidity lead to negligible shape variations in the BDT, Figure 5.13 (b). In order to gauge the impact of the BDT up/down variations provoked by the p_T-related systematics, the nominal 2D

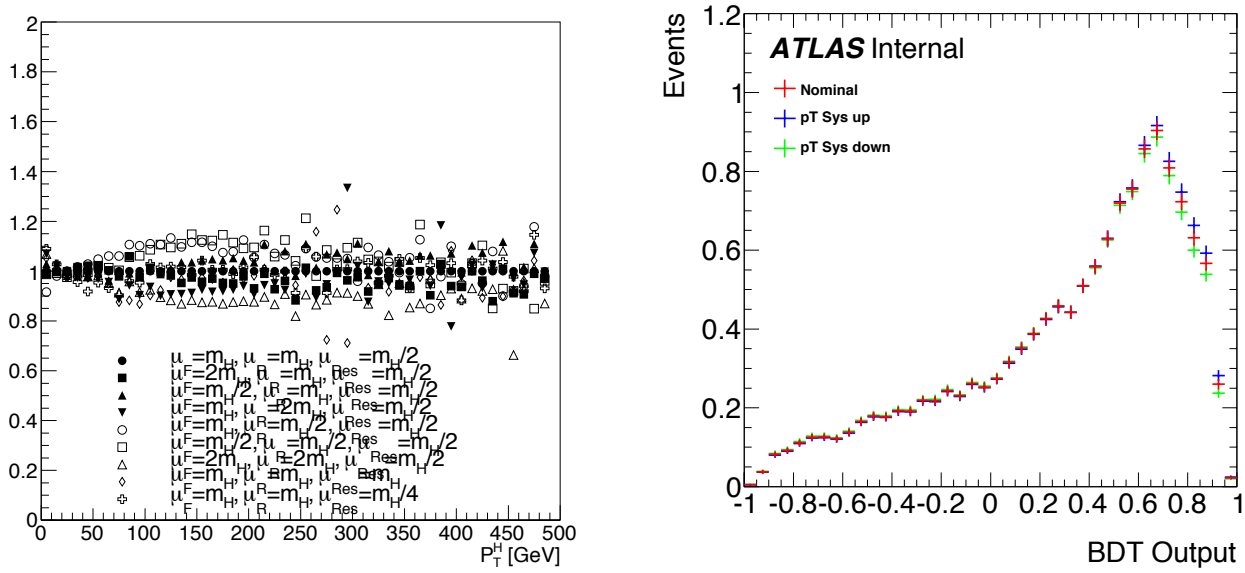

(a) (b)

Figure 5.12: Ratio of the normalised p_T distributions with the various up/down variations with respect to the central value of the relevant scales using HRES at m_H=125 GeV. (c) Variation of the signal BDT shape for $\pm$ 1σ associated to the p_T-related systematic uncertainties.

fit and the 1-dimensional approach are repeated for three configurations, e.g. BDT nominal, BDT up and BDT down. The measured effect on the best m_H fit for Asimov data at m_H=125 GeV is less than 0.01% while the impact on the measured μ fitted on the same dataset is approximately 0.1%. Due to the small impact of these systematics in the model, it was decided not to include them in the final nuisance parameter list.

5.6 Results in the $H \to ZZ \to$ 4l channel

5.6.1 Expected and observed yields in 2011+2012 analyses and control plots

This Section will take into account the data-Monte Carlo comparison of the main variables of the analysis in the 2011 and 2012 data-taking period. The kinematic selection (Section 5.2.2) is applied on 4.5 fb^{-1} events at $\sqrt{s}$=7 TeV and 20.3 fb^{-1} events at $\sqrt{s}$=8 TeV. The signal region of the analysis is defined in the interval (110< m_{4l} <140) GeV, whereas the sidebands are associated to events such that m_{4l} <110 GeV or m_{4l} >140 GeV. The low mass is referred to m_{4l} <160 GeV and m_{4l} >160 GeV defines the high mass region.

Tables 5.3 and 5.4 chart the observed number of events and the final estimate for the expected background in the low and high mass regions for the $\sqrt{s}$=7 TeV and $\sqrt{s}$=8 TeV analyses. The expected signal events are also extracted for various Higgs mass hypotheses as well as the corresponding total systematic uncertainties (Section 5.5) for signal and background. Tables 5.5 and 5.6 chart the number of expected signal Higgs with a generated mass of m_H=125 GeV and background events together with the number of events observed in data in the full 2011+2012 statistics when considering the signal region (110< m_{4l} <140) GeV and a tighter sector around the Higgs peak, i.e. (120< m_{4l} <130) GeV respectively.

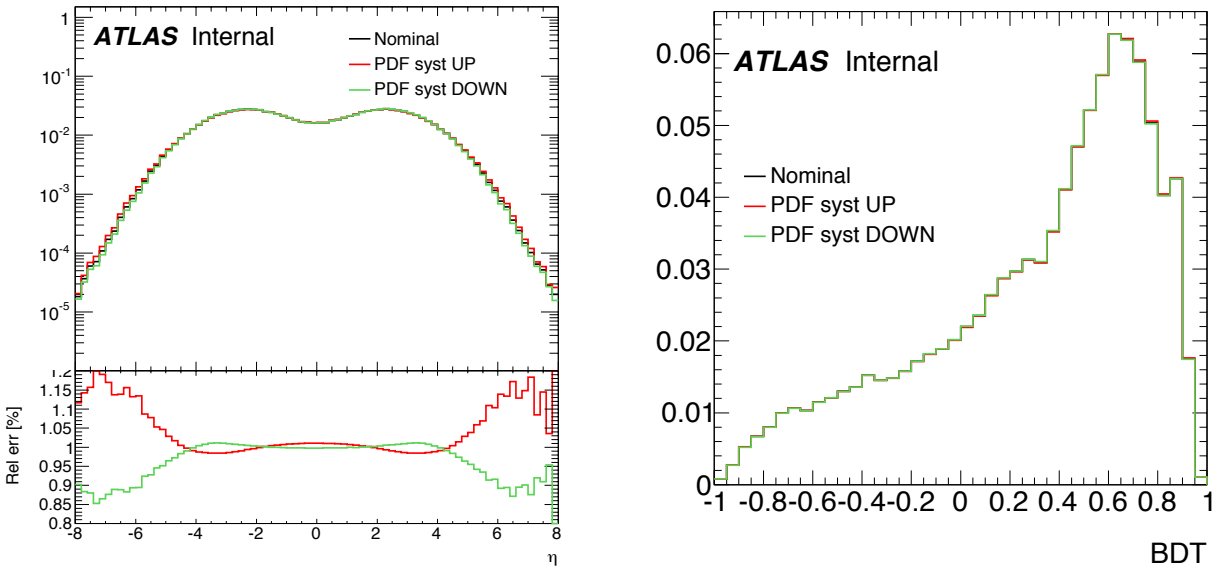

(a) **(b)**

Figure 5.13: Normalised Higgs η distribution with up and down variations due to PDF uncertainties. (b) Variation of the signal BDT shape when including $\pm$ 1σ up/down variations on the η-related systematic uncertainties.

As already mentioned in Section 4.5.3, a detailed study on the impact of the E-p combination algorithm on data candidates was pursued in the signal region as well as in the upper and lower sidebands. The previous data distribution this investigation is comparing to is detailed in [122] (Moriond 2013 analysis) where the E-p combination algorithm for electrons was not yet in place. In the signal region, thanks to the usage of the track-cluster combination that modifies the electron momenta, one candidate does not pass the selection any longer and four new Higgs-like events are now accepted. For what regards the investigation on the sidebands, the good behaviour of the algorithm is testified by the plot reported in Figure 4.27.

The remaining part of this Section will be devoted to providing the distributions of the variables of interest in the analysis. Figures 5.14 reports the invariant mass of the inclusive four-lepton final state for the full statistics generated at $\sqrt{s}$=7 TeV and $\sqrt{s}$=8 TeV in the mass region between 80 GeV and 160 GeV and in the full range up to m_{4l}=600 GeV. The background expectation is compared to the signal at m_H=125 GeV with the measured on-shell signal strength (Section 5.7.4), μ=1.51, and to the reducible background. The systematic uncertainties described in Section 5.5 on the irreducible ZZ background are drawn as hatched grey lines. The corresponding plots for the various decay channels can be found in Appendix E.
A clear peak corresponding to the Higgs signal on the continuum background is seen around m_H=125 GeV; the observed significance of this excess is $\sim 8.2\sigma$ as demonstrated by the local p_0-value [133] in Figure 5.15 representing the excess relative to the background-only hypothesis (Appendix C.2). This statistical evaluation has been obtained under the asymptotic assumption (Appendix C.3) and the p_0 value is scanned as a function of the Higgs mass, m_H.

Another observable of the analysis is the BDT output whose distribution is illustrated in Figure 5.16 in the m_{4l} region 110-140 GeV and 120-130 GeV. The m_{12} and m_{34} responses in the signal

region 110-140 GeV as well as the Higgs transverse momentum and its pseudorapidity in the same mass window can be found in Figures E.3 and E.4 respectively.

Conclusively, two-dimensional maps of m_{4l} *vs* m_{12} and BDT *vs* m_{4l} before the application of the Z mass constraint kinematic fit are shown in Figure 5.17 for the full 2011+2012 data sample. The expected Higgs distribution produced for m_H=125 GeV and the total ZZ background are also superimposed in the plots. Figure 5.17 (a) displays the m_{12} *vs* m_{4l} 2-dimensional map. The signal Monte Carlo in Figure 5.17 (b) clusters in the region where the BDT score is very high by construction of the algorithm. Besides, an excess of events in data with high BDT output is noted for values of the four-lepton invariant mass close to 125 GeV, consistent with the signal hypothesis at that mass.

	4μ		ee$\mu\mu$		4e	
	Low mass	High mass	Low mass	High mass	Low mass	High mass
ZZ	5.27±0.26	16.98±1.26	4.39±0.24	25.71±1.91	2.02±0.13	9.85±0.77
Z, $Zb\bar{b}$, and $t\bar{t}$	0.43±0.19	0.17±0.07	2.32±0.57	1.16±0.28	2.16±0.45	1.13±0.24
Total Background	5.70±0.32	17.15±1.26	6.71±0.64	26.87±1.94	4.18±0.47	10.98±0.81
Data	11.00	23.00	7.00	24.00	4.00	14.00
$m_H = 125$ GeV	1.00±0.10		1.16±0.11		0.46±0.05	
$m_H = 130$ GeV	1.55±0.14		1.89±0.18		0.72±0.07	
$m_H = 123$ GeV	0.80±0.08		0.93±0.09		0.35±0.04	

Table 5.3: Observed number of events and estimate for the expected background, separated into low mass (m_{4l} <160 GeV) and high mass (m_{4l} >160 GeV) regions presented for the $\sqrt{s}$=7 TeV analysis. The expected signal events are determined for various Higgs boson mass hypotheses. For signal and background estimates, the corresponding total systematic uncertainty is specified as well.

	4μ		ee$\mu\mu$		4e	
	Low mass	High mass	Low mass	High mass	Low mass	High mass
ZZ	27.58±1.37	95.00±7.06	23.43±1.28	145.25±10.85	11.20±0.74	56.42±4.44
Z, $Zb\bar{b}$, and $t\bar{t}$	2.90±0.53	1.14±0.21	4.44±0.87	1.98±0.40	1.89±0.40	0.99±0.21
Total Background	30.49±1.47	96.13±7.07	27.86±1.55	147.23±10.85	13.10±0.84	57.41±4.44
Data	42.00	95.00	38.00	174.00	23.00	56.00
$m_H = 125$ GeV	5.80±0.57		6.99±0.70		2.79±0.29	
$m_H = 130$ GeV	8.85±0.85		11.31±1.10		4.43±0.45	
$m_H = 123$ GeV	4.61±0.46		5.52±0.55		2.24±0.23	

Table 5.4: Observed number of events and estimate of the expected background, separated into low mass (m_{4l} <160 GeV) and high mass (m_{4l} >160 GeV) regions presented for the $\sqrt{s}$=8 TeV analysis. The expected signal events are also shown for various Higgs boson mass hypotheses. For signal and background estimates, the corresponding total systematic uncertainty is provided as well.

5.6.2 Effects of the improved electron calibration

In order to extract the impact of the new electron energy calibration detailed in Chapter 4, the Higgs boson lineshape has been compared with the results using the Moriond 2013 analysis [122]. The benefits on the muon momentum scales are much smaller than the ones introduced by the new electron calibration and are not herein discussed.
The three main aspects regarding the electron calibration that have been revisited are:

	signal	ZZ	Z+jets, $t\bar{t}$	Expected	Observed
4μ	6.65±0.66	7.75±0.38	2.04±0.34	16.45±0.84	22
$2\mu 2e$	3.48±0.35	3.78±0.23	2.03±0.33	9.28±0.54	11
$2e2\mu$	4.48±0.44	5.37±0.26	1.79±0.27	11.64±0.58	15
$4e$	3.17±0.33	3.40±0.22	2.14±0.32	8.71±0.51	12
all	17.78±1.78	20.29±1.10	8.00±0.89	46.07±2.27	60

Table 5.5: Numbers of expected signal (Higgs boson generated at m_H=125 GeV) and background events, together with the numbers of observed events in the data lying in the interval (110< m_{4l} <140) GeV, for the $\sqrt{s} = 8$ TeV and $\sqrt{s} = 7$ TeV samples.

	signal	ZZ	Z+jets, $t\bar{t}$	Expected	Observed
4μ	6.20±0.61	2.82±0.14	0.79±0.13	9.81±0.64	14
$2\mu 2e$	3.15±0.32	1.38±0.08	0.72±0.12	5.24±0.35	6
$2e2\mu$	4.04±0.40	1.99±0.10	0.69±0.11	6.72±0.42	9
$4e$	2.77±0.29	1.22±0.08	0.76±0.11	4.75±0.32	8
all	16.15±1.62	7.41±0.40	2.95±0.33	26.51±1.70	37

Table 5.6: Numbers of expected signal (m_H=125 GeV) and background events, together with the numbers of observed events in the data in a window of size (120< m_{4l} <130) GeV around the generated mass at m_H=125GeV for the combined $\sqrt{s} = 7$ TeV and $\sqrt{s} = 8$ TeV data.

1. a new MVA calibration for electrons (Section 4.2);
2. a better understanding of the passive material in front of the calorimeter leading to a generation of Monte Carlo samples characterised by a more appropriate simulation of the detector response for electrons;
3. a new combined measurement of the cluster energy with the track momentum (E-p combination) for electron in the barrel below 30 GeV in E_T (Section 4.5).

Tables 5.7 and 5.8 summarise the comparison of the mean value, the resolution and the amount of events outside the gaussian kernel of the mass distributions in the four lepton channels when applying a gaussian core fit to the mass histograms produced by the Moriond 2013 analysis (labelled as 2 in the Tables) against the current one (referred as 1), without and with the Z mass constraint in place. As already indicated in Section 4.5, the E-p combination tool is alternatively applied either

Channel	$m_2 - m_1$ [GeV]	σ_2/σ_1	events outside ± $2\sigma_{1,2}$
4μ	0.01±0.02	0.99±0.01	-2%
2μ2e	0.35±0.05	0.95±0.02	0
2e2μ	0.25±0.04	0.99±0.01	+5%
4e	0.58±0.06	0.93±0.02	+2%

Table 5.7: Comparison between the Moriond 2013 (labelled as 2) and the current analyses (1) for the four lepton invariant mass mean value, resolution and percentage of events outside the gaussian kernel of the distributions estimated from a Monte Carlo sample produced at m_H=125 GeV. The Z mass constraint is not applied on the leading Z boson.

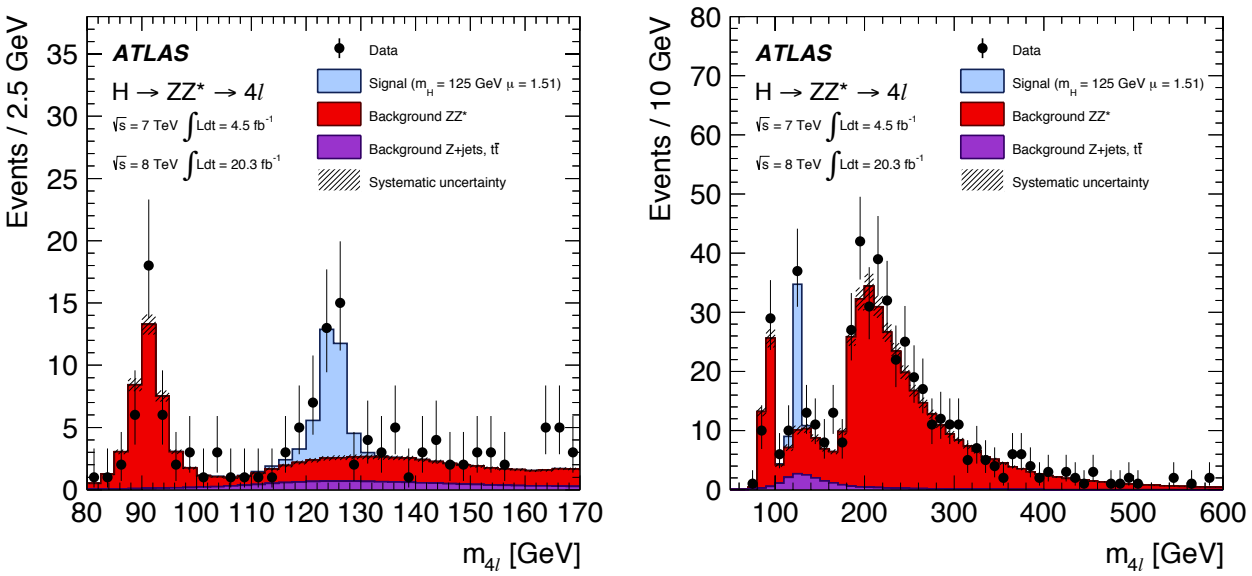

(a) **(b)**

Figure 5.14: m_{4l} distribution of the selected candidates for $\sqrt{s}$= 7 TeV and $\sqrt{s}$= 8 TeV, compared to the background expectation in the low mass region, (80< m_{4l} <170) GeV (a) and in the whole mass spectrum (b) of the analysis. The contribution of the reducible background is also separately drawn as well as the systematic uncertainties drawn as a hatched grey area.

Channel	$m_2 - m_1$ [GeV]	σ_2/σ_1	events outside $\pm$ $2\sigma_{1,2}$
4μ	0.01±0.02	1.01±0.01	-1%
2μ2e	0.41±0.04	0.95±0.02	0
2e2μ	0.36±0.03	1.04±0.02	+3%
4e	0.82±0.04	0.96±0.02	+1%

Table 5.8: Comparison between the Moriond 2013 (labelled as 2) and the current analysis (1) for the four lepton invariant mass mean value, resolution and percentage of events outside the gaussian kernel of the distributions estimated from a Monte Carlo sample produced at m_H=125 GeV. The Z mass constraint is applied on the leading Z boson.

before or after the kinematic selection; observed results on the gain with respect to the cluster-only measurement are insensitive to the position of the algorithm in the analysis workflow.

In the new analysis configuration, the m_{4l} mass is shifted towards the generated Higgs mass at m_H= 125 GeV. This aspect is more pronounced for the channels with electrons in the subleading pair because the E-p combination has a larger effect on low E_T electrons. The MVA calibration does play a role in this shift as well: out of the $\sim$ 580 MeV shift of the 4e channel, $\sim$ 100 MeV is due to the E-p combination while the remaining contribution comes from the MVA calibration. When the Z mass constraint is switched on, the shift of the m_{4l} peak is larger. This is due to the presence of a broader resolution model utilised to parametrise the $\mathcal{B}$ term in equation (5.2) which pulls the mean of the Z distribution to higher values. The same trend is found in the 2μ2e channel: the E-p-related mass shift is around 100 MeV and the remaining term ($\sim$ 250 MeV) is produced by the MVA calibration. In any event, these shifts are well accounted for by the Monte Carlo, hence they do not affect the Higgs mass determination.

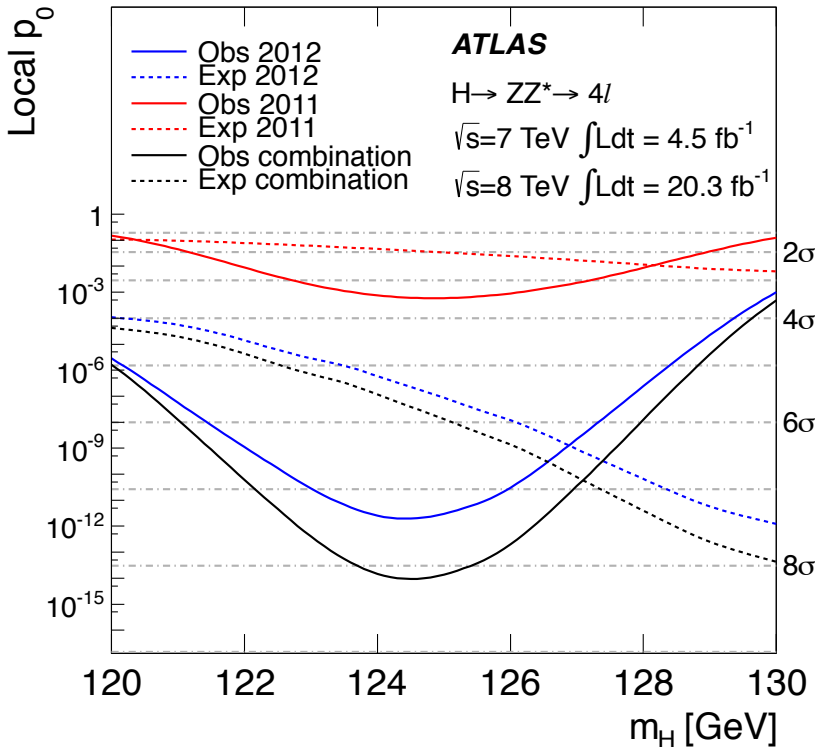

Figure 5.15: Observed and expected local p_0-value for the combination of the 2011 and 2012 datasets. The results in data at $\sqrt{s}$=7 TeV and $\sqrt{s}$=8 TeV are displayed in red and blue solid lines. The dashed curves are associated to the expected median local p-value for the signal hypothesis calculated with signal strength μ=1. The horizontal dashed lines indicate the p-values corresponding to a local significance of approximately 8σ for a measured Higgs mass of m_H=124.51 GeV

.

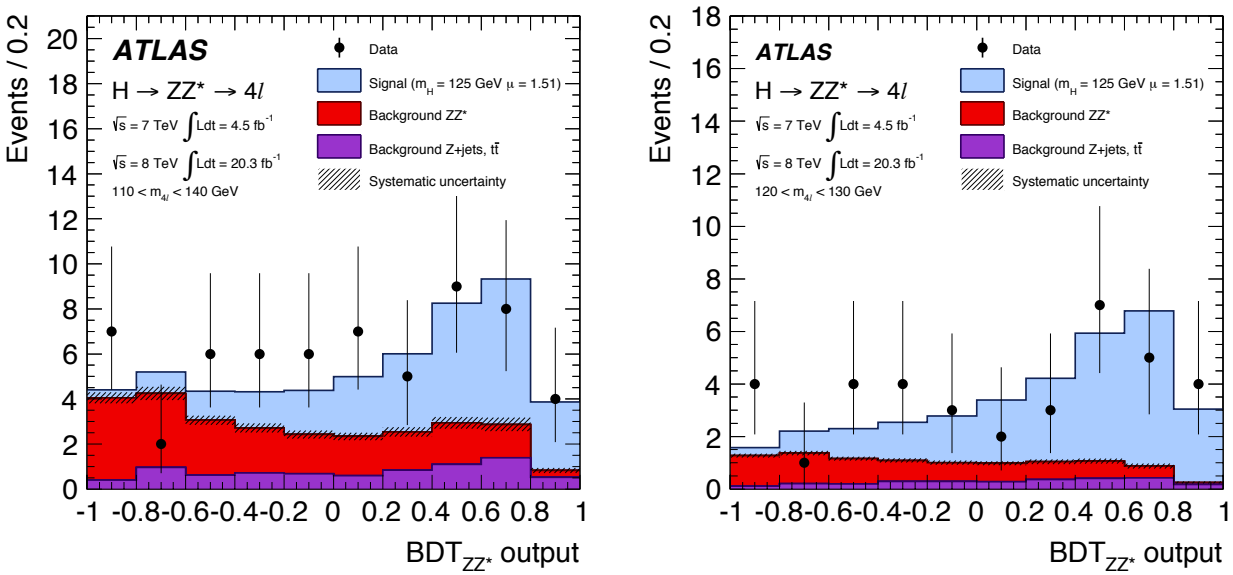

(a) **(b)**

Figure 5.16: BDT distribution of the selected candidates for $\sqrt{s}$= 7 TeV and $\sqrt{s}$= 8 TeV compared to the background expectations in the m_{4l} region (110-140) GeV (a) and (120-130) GeV (b). The contribution of the reducible background is also separately displayed as well as the systematic uncertainties drawn as a hatched grey area.

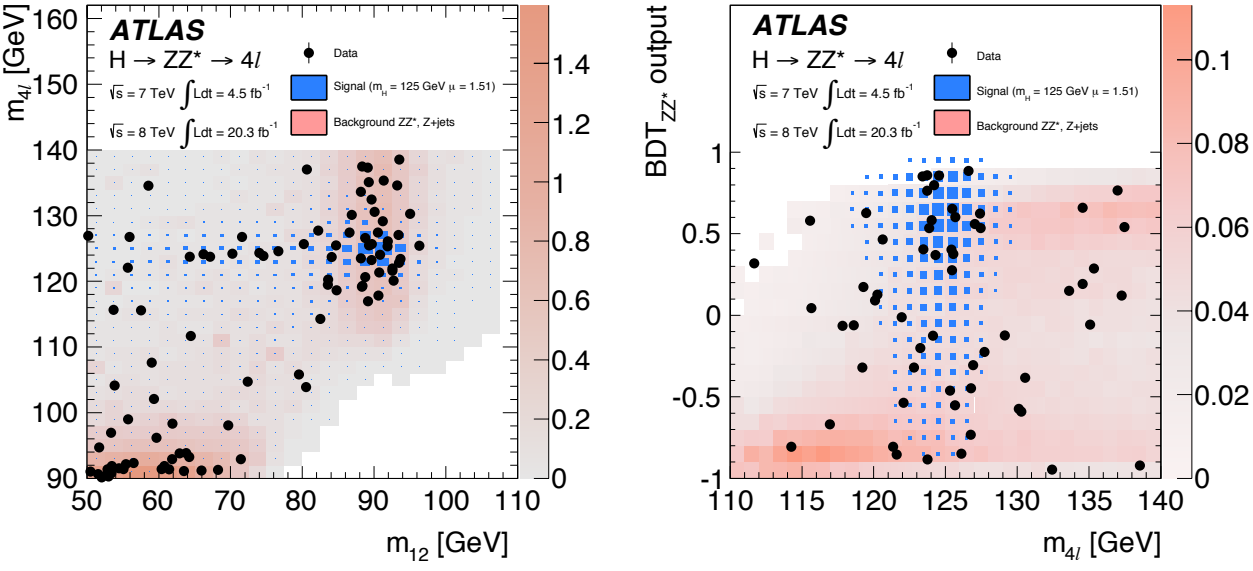

(a) **(b)**

Figure 5.17: Distribution of the m_{4l} *vs* the m_{12} invariant mass, before the application of the Z mass constraint, for the selected candidates in the m_{4l} range 80â160 GeV. (b) Distribution of the BDT discriminant against m_{4l} for the selected candidates in the m_{4l} range 110â140 GeV. Both distributions are extracted for $\sqrt{s}$ = 7 TeV and $\sqrt{s}$= 8 TeV . The expected distributions for a SM Higgs with m_H = 125 GeV (the sizes of the boxes indicate the relative density) and for the total background (the intensity of the shading indicates the density) are also presented in the plot.

Likewise, the resolution improvement is significant in the channel characterised by low E_T electrons where the E-p combination algorithm is more powerful and its impact is similar with and without the presence of the Z mass constraint, within uncertainties. Similarly to the previous point, the gain brought by the track-cluster combination compared to the cluster-only approach is partially diluted when the MVA calibration is applied on top of the E-p combination. The new Monte Carlo simulation also helps in the reduction of the mass resolution.

5.7 Mass and signal strength extraction

The following three methods are exploited to measure the Higgs boson mass and its signal strength in the four lepton channel.

- A template fit from Monte Carlo distributions of m_{4l}. This approach has been published in the previous analysis [122] and since the fit is based on one parameter of interest, this method will be addressed as one-dimensional fit.
- The second approach is characterised by a two dimensional fit m_{4l} *vs* BDT that enhances the signal discrimination against the main ZZ background (two-dimensional fit). This is the baseline method with which the Higgs invariant mass is obtained, whereas the one-dimensional parametrisation is developed as an internal cross-check.
- The last procedure is described by a fit that takes advantage of the event-by-event knowledge of the detector resolution (*per event* error fit). This fit method is the default algorithm for the direct width measurement published in [132] and it will not be covered in this text.

Signal, irreducible and reducible backgrounds are represented by probability density functions used in the fit; their modelling will be analysed in the following Sections 5.7.1 and 5.7.2. The invariant mass interval used in the fit is (110< m_{4l} <140) GeV.

5.7.1 Higgs signal modelling

For the 1D fit, the input PDFs coincide with m_{4l} generated from Monte Carlo events, while for the 2D approach PDFs, both from m_{4l} and BDT values are employed. Figure 5.18 illustrates the signal shape of the 1D PDF for the Higgs boson signal in the ggF production mode at m_H=125 GeV. The PDFs entering the fit are derived from histograms normalised to unity to predict the shape of the signal. These PDFs are represented by smoothed templates [134] to reduce the dependence of the likelihood on statistical fluctuations in the unsmoothed distributions. The amount of smoothing has been tuned to remove statistical fluctuations of the templates without biasing the distributions. Another advantage of this approach compared to the direct Monte Carlo histograms is that the PDF shape can be shifted continuously in m_{4l} - Figure 5.18 exhibits a +2 GeV shift for illustration. This feature enables to provide a continuous parametrisation as a function of m_H and interpolate the signal shape for each Higgs boson mass as in Figure 5.19 (a) (4μ channel) making use of the *B-spline* method [135].

For the ggF and VBF production mechanisms, 11 Monte Carlo samples are available in 1 GeV steps from m_H= 120 to m_H=130 GeV. It is also important to test the correct parametrisation modelled by the interpolation on the signal shape at m_H=125 GeV: an interpolated template is produced making use of all Monte Carlo samples except the one generated at m_H=125 GeV. Figure 5.19 (b) indicates (4μ channel) the normalised distribution of the Monte Carlo samples produced at m_H=125 GeV and the interpolated shapes. The plots demonstrate a perfect overlay with the

inferred shape for 125 GeV and the smoothed Monte Carlo sample generated at m_H=125 GeV. This check has been worked out also for the other channels of the analysis.

5.7.2 Background modelling

The 1D ZZ background template shapes used for the one-dimensional fit are not treated with smoothing; thus, histograms are used directly in the fit. For the m_{4l} *vs* BDT 2D fit, due to small statistics in some bins, it was decided to apply a smoothing to the m_{4l} and the BDT contributions. One dimensional projection plots for m_{4l} and BDT where the smoothed PDFs are compared to the input Monte Carlo histograms are found in Figure 5.20.

The reducible background shapes are obtained from the Z+jets and $t\bar{t}$ Monte Carlo in the ll+$\mu\mu$ and the ll+ee control regions. As for the previous ZZ component, distributions are smoothed and included in the fit. Internal closure tests determine the good agreement between the smoothed PDFs and the histogram templates (Figure 5.21).

5.7.3 One dimensional fit using m_{4l}

The first approach used in the analysis is the m_{4l}-based 1D fit that is kept as a sanity check for the 2D parametrisation that will be explained later in the text (Section 5.7.4).

The signal and background models are described with 1D templates detailed in Sections 5.7.1 and 5.7.2. The fit is performed over the four final state categories, 4e, 4μ, 2e2μ and 2μ2e. The full PDF of the model, constituted by the signal and the background (irreducible and reducible components) templates is then fitted to pseudo-data (Asimov datasets) generated for a Higgs boson at m_H=125 GeV plus background, as presented in Figure 5.22 (a) and 5.22 (b) for the 4μ and 4e cases.

A closure test on the procedure is the calculation of a likelihood fit employing the signal+background model described above on Asimov pseudo-data generated for a SM (μ=1) Higgs signal at m_H=125 GeV including the background. This validation on m_{4l} and μ, shown in Figure 5.22 (c) and 5.22 (d), confirms that there is no bias as the returned minimum of the likelihood coincides with the injected value of the mass and signal strength in the Asimov dataset. It is also verified that no bias is produced when injecting different Higgs masses in the Asimov data. The likelihood curves evaluated at the 2σ level determine the expected uncertainty on the parameter of interest.

5.7.4 Two dimensional fit

A 2-dimensional fit m_{4l} *vs* BDT is exploited as the baseline method of the analysis. The implementation of the second dimension in the fit is achieved by parametrising the signal with a conditional PDF:

$$\mathcal{P}(m_{4l}, BDT) = \mathcal{P}(m_{4l}|BDT) \cdot \mathcal{P}(BDT) \tag{5.5}$$

where $\mathcal{P}(m_{4l}|BDT)$ is the conditional 1D PDF and is modelled by splitting the signal template into four BDT bins (-1-0.5, -0.5-0, 0-0.5, 1) characterised by a different mass shape in each region. A step function is then added to retrieve the correct m_{4l} shape and combine them into a single variable. Equation (5.5) is therefore equivalent to:

$$\mathcal{P}(m_{4l}, BDT) = \mathcal{P}(m_{4l}|BDT) \cdot \mathcal{P}(BDT) = \left(\sum_{i=1}^{4} \mathcal{P}_n(m_{4l}) \theta_n(BDT) \right) \cdot \mathcal{P}(BDT) \tag{5.6}$$

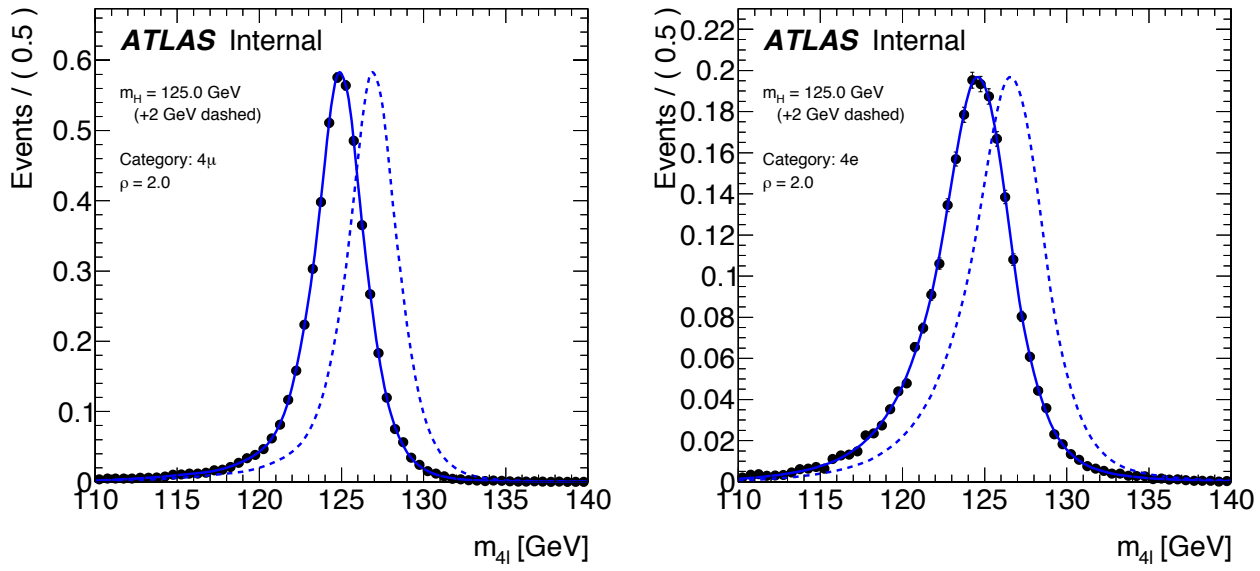

(a) 4μ

(b) 4e

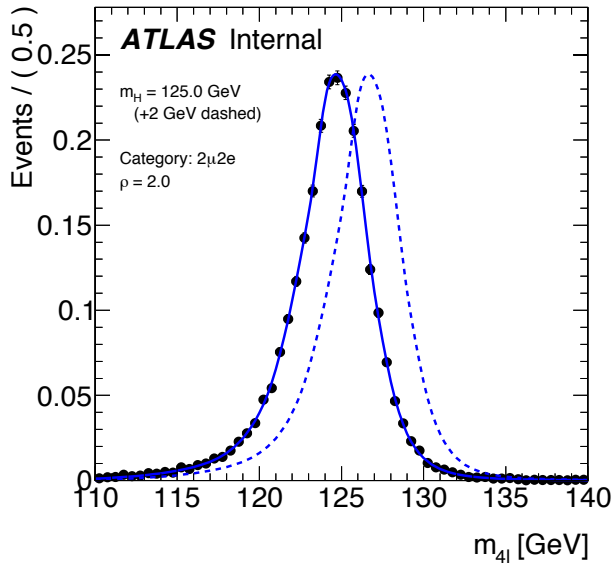

(c) 2μ2e

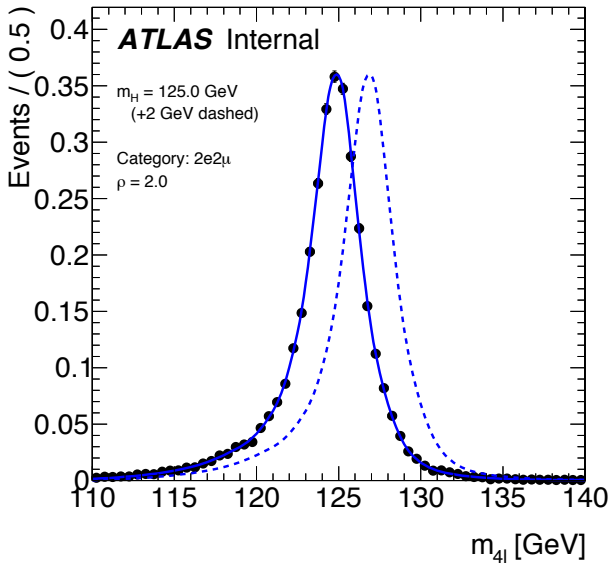

(d) 2e2μ

Figure 5.18: Invariant mass distribution of the Higgs signal Monte Carlo simulation generated at m_H=125 GeV in the gluon-gluon fusion production mode. The histogram response is represented by the black dots whereas the (smoothed) PDFs are the solid lines. A +2 GeV shift (dotted blue line) is executed on the smoothed lineshape for illustration.

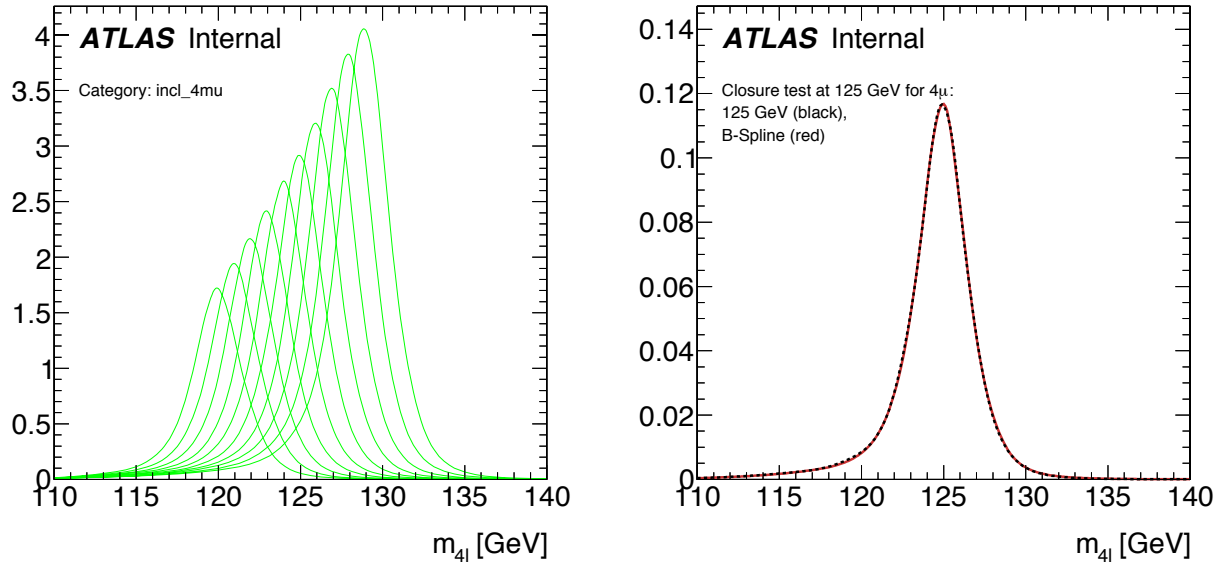

(a) 4μ **(b)** 4μ

Figure 5.19: Example of the signal shapes (continuous parametrisation in m_H) in the 4μ channel for 8 TeV Monte Carlo samples produced in 1 GeV steps between 120 and 130 GeV. The functional integral comes from Monte Carlo generations for 10 Higgs mass points between 120 and 130 GeV. (b) Distribution of the signal shapes from a signal Monte Carlo sample (4μ channel) generated at m_H=125 GeV and the interpolated shapes created by the B-spline approach using all available Higgs mass points except the tested one at m_H=125 GeV.

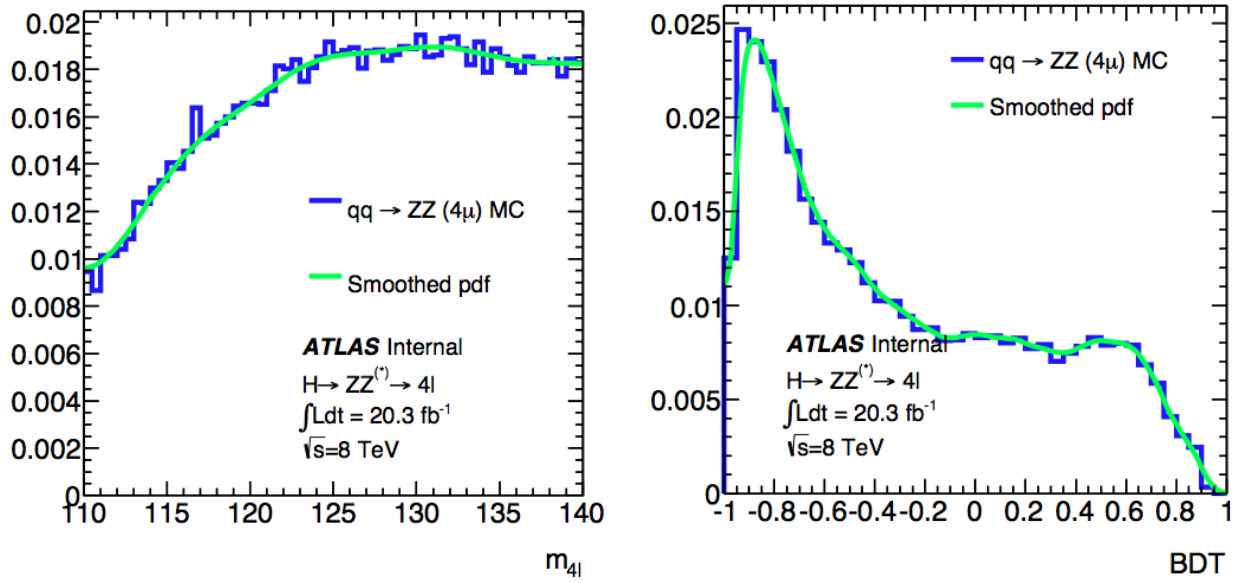

(a) **(b)**

Figure 5.20: 1-dimensional projection of the ZZ background where m_{4l} (a) and the BDT (b) distributions are determined as histogram templates or with smoothed PDF for the 4μ channel.

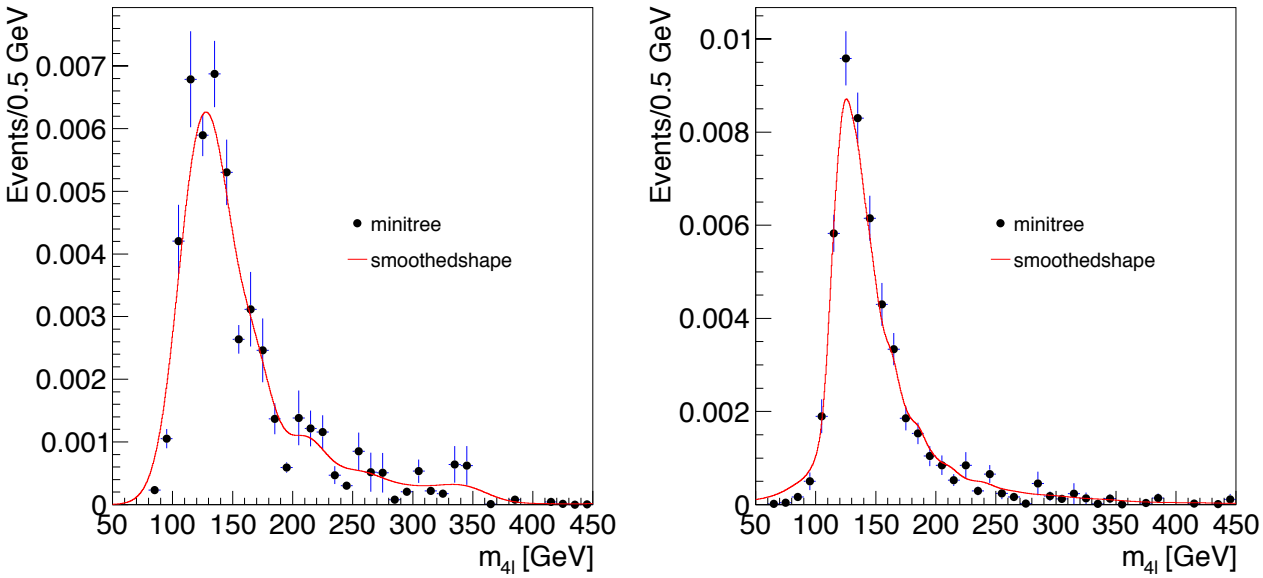

(a) ll+$\mu\mu$ **(b)** ll+ee

Figure 5.21: Reducible background distributions in the ll+$\mu\mu$ (a) and ll+ee (b) control regions for the smoothed PDF templates (black dots) and the input histograms.

where $\theta_n(BDT)$ is the step function for a given region of the BDT that selects the appropriate mass shape for a certain BDT score. In this way, the mass template in parenthesis is written as a sum of 4 different one-dimensional PDFs defined in BDT bins. As for the background, both dominant irreducible ZZ and reducible, a full 2-dimensional parametrisation is used as already mentioned in Section 5.7.2.
Figures 5.23 (a) to 5.23 (c) exhibit the distribution of the BDT shapes in the signal region for the Higgs signal, the reducible and irreducible ZZ backgrounds whilst Figures 5.23 (d) displays the mass shape for a Higgs signal Monte Carlo in BDT bins.

In analogy with the previous scenario in Section 5.7.3, basic checks are done in order to avert the presence of possible internal bias in the fit. Results do not demonstrate any bias in the procedure.

The usage of the BDT in the fit brings a 7-8% reduction in mass and signal strength error with respect to the 1-dimensional approach as observed in Figure 5.24. Likewise, the expected significance improves by an approximate factor 24% when adding the BDT output in the fit. As for the contribution of the new electron calibration and the E-p combination, the mass error is decreased by a factor 8%.

A series of other cross-checks are done on this procedure before unblinding. A selection of them is listed below.

- This approach assumes minimal variation of the m_{4l} mass shape inside the same BDT bin. It was therefore checked that this assumption is valid by comparing the mass distributions for lower and upper halves of each BDT bin. No shape deviation is observed.

- To investigate the choice of binning used in the method, instead of 4 BDT bins per channel, the binning scheme on the BDT was modified to 3 (-1-0, 0-0.5, 0.5-1): 0.5% increase is seen on the expected uncertainty on μ and 1% on the expected uncertainty on m_H.

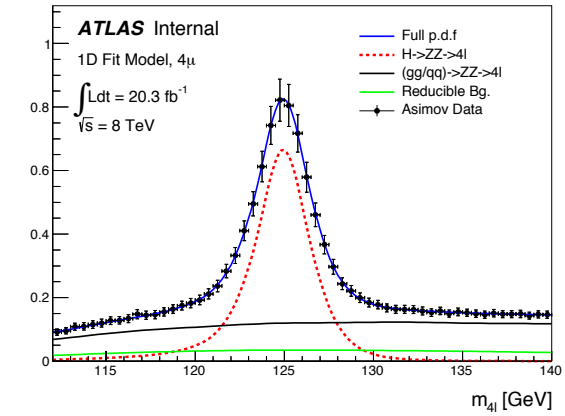

(a) 4μ

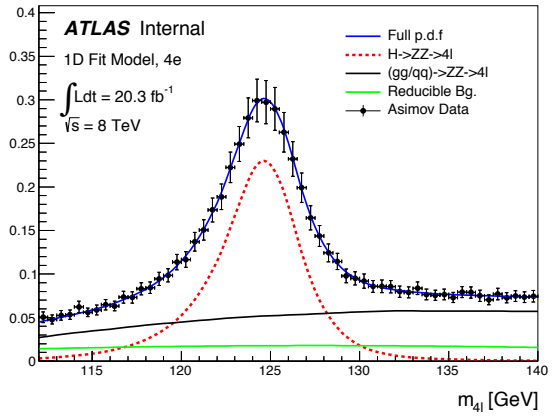

(b) 4e

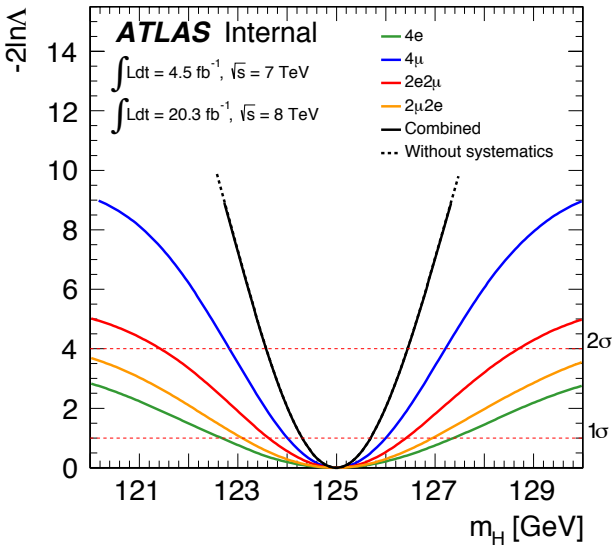

(c)

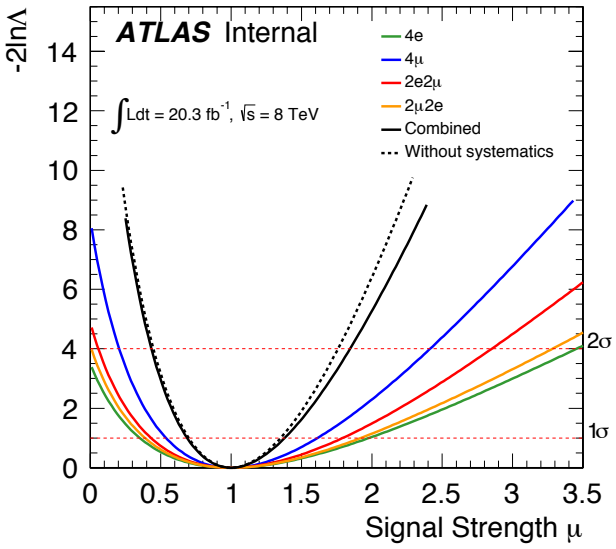

(d)

Figure 5.22: 1D fitting of signal + background model to the Asimov dataset generated for a Higgs boson at m_H=125 GeV + background in the 4μ (a) and 4e (b) categories. Likelihood scan of m_H (c) and μ (d) for 1D fit of Asimov dataset generated at m_H=125 GeV + background ($\sqrt{s}$=7 TeV and $\sqrt{s}$=8 TeV).

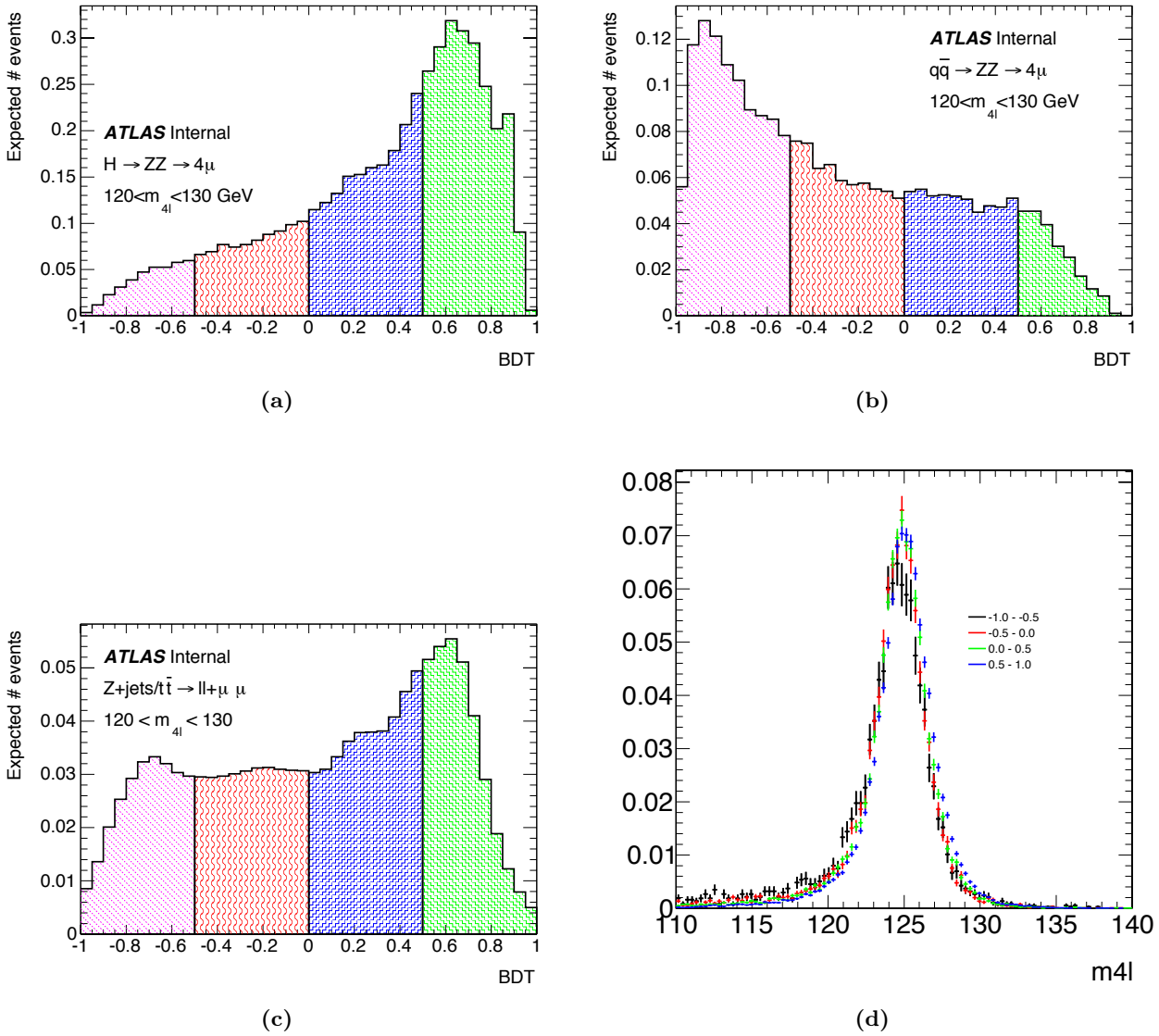

Figure 5.23: Distributions of the BDT shapes in the signal region (120< m_{4l} <130) GeV for the Higgs signal generated at m_H=125 GeV at $\sqrt{s}$=8 TeV Monte Carlo (a) for the ZZ irreducible (b) and reducible (c) backgrounds. The 4 different bins of the analysis are presented in different colours. (d) Mass shape for a Higgs signal as a function of the BDT score.

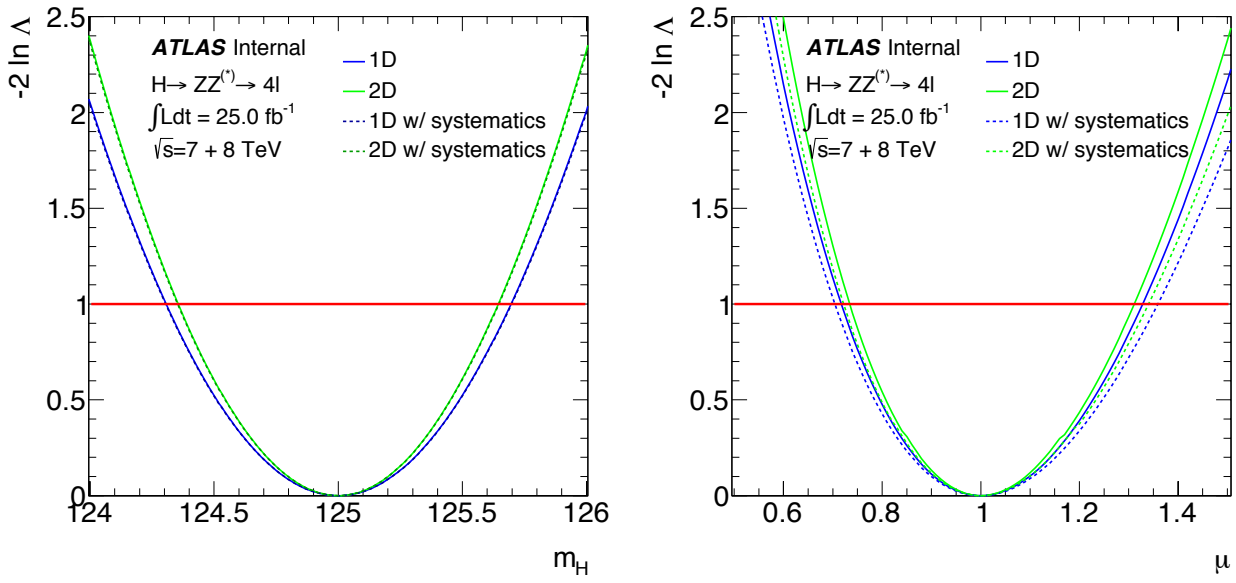

(a) **(b)**

Figure 5.24: Likelihood scan of m_H (a) and μ (b) for 1D and conditional 2D fits for the combination of 7 and 8 TeV analyses using Asimov datasets generated at a Higgs mass at m_H=125 GeV and μ=1 plus the background contribution.

- Other mass inputs are introduced in the fit and the minimum returned by the likelihood curve is always compatible with the injected mass value.

After performing all the consistency checks explained above, the 1D and 2D methods are both used to extract the Higgs mass, m_H, and the signal strength μ in data at $\sqrt{s}$=7 TeV and $\sqrt{s}$=8 TeV. The full set of results in the various decay channel as well as for the combined fit are available in Table 5.9 for the Higgs boson mass measurement and in Table 5.10 for the on-shell signal strength determination. The final Higgs mass in the four lepton channel and the on-shell signal strength μ are:

$$m_H = 124.51 \pm 0.52\,(\text{stat}) \pm 0.06\,(\text{sys}); \tag{5.7}$$

$$\mu_H = 1.66 \pm 0.41\,(\text{stat}) \pm 0.18\,(\text{sys}). \tag{5.8}$$

Figure 5.25 reports the likelihood fit on data to extract the Higgs mass m_H (a) and the signal strength μ (b) in the $H \to ZZ \to 4l$ channel with and without systematic uncertainties whilst Figure 5.25 (c) represents the contour plot corresponding to the 68% and 95% uncertainties on m_H *vs* μ as well as the best fit values.

5.8 Conclusions

This Chapter documents the final Run 1 measurement of the Higgs boson mass and signal strength in the $H \to ZZ \to 4l$ decay channel using proton-proton collisions data with an integrated luminosity of 4.5 fb^{-1} ($\sqrt{s}$=7 TeV) and 20.3 fb^{-1} ($\sqrt{s}$=8 TeV). The analysis is performed by using a kinematic selection on the events. Additionally, both the far and the collinear FSR photons produced by the final state are recovered and added to the mass measurement. Lastly, a constraint on the on-shell Z mass enables to achieve a better mass resolution and a BDT-based multivariate discriminant has been designed to cope with the irreducible ZZ background.

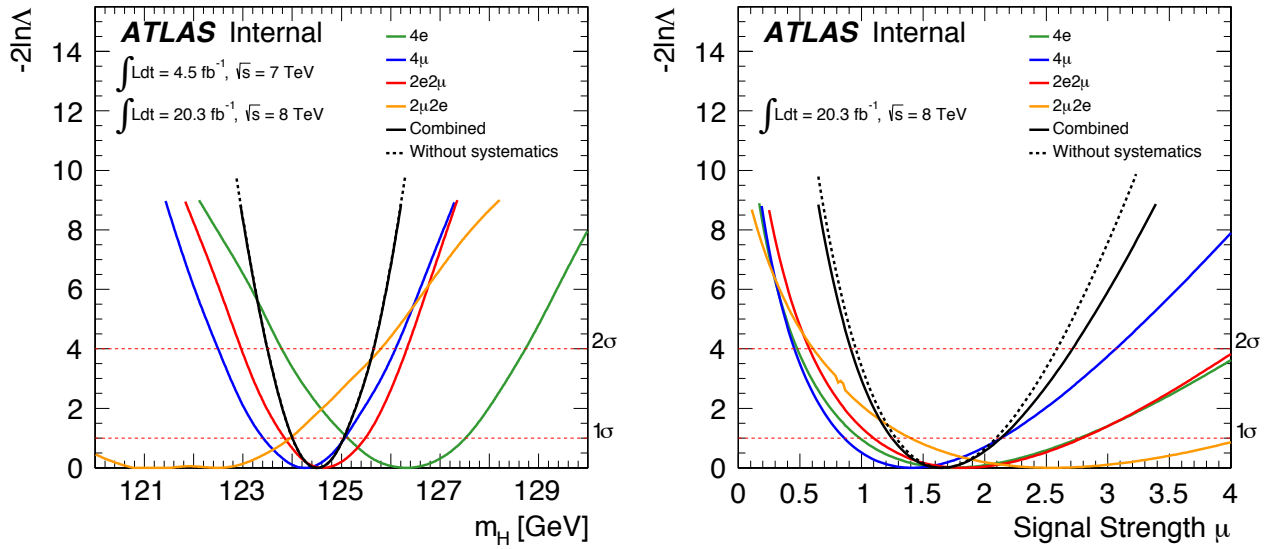

(a) (b)

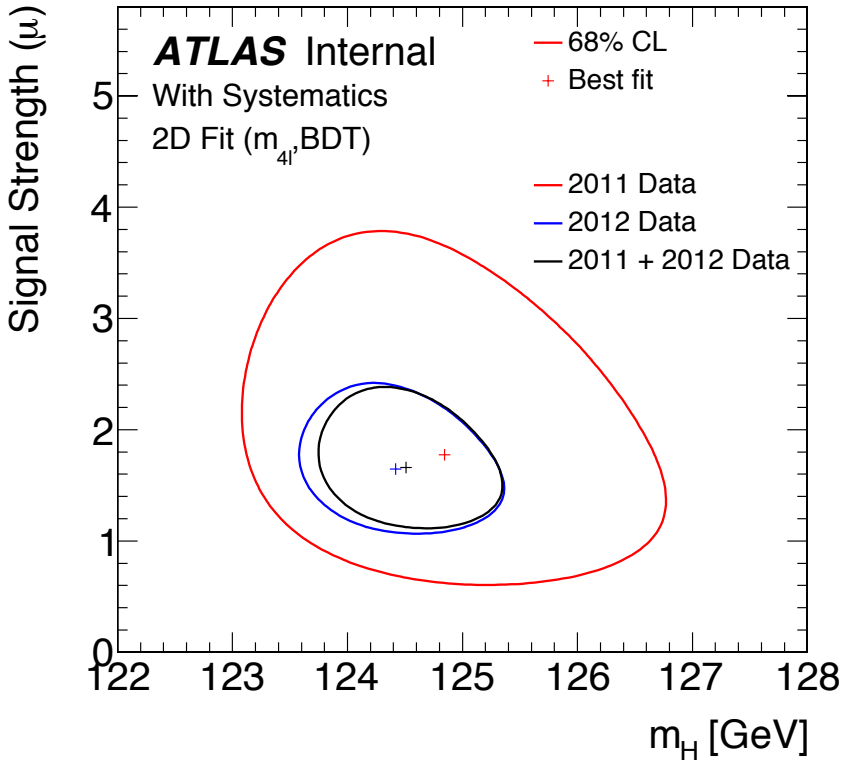

(c)

Figure 5.25: Likelihood scan of m_H (a) and μ (b) for the 2D baseline fit on data produced at $\sqrt{s}$= 7 TeV (4.5 fb^{-1}) and $\sqrt{s}$=8 TeV (20.3 fb^{-1}) where all the various channel contributions are separately displayed. (c) Contour plot representing the 68% and 95% uncertainties on m_H *vs* μ as well as the best fit from the parameter of interest m_H and μ generated for data recorded with $\sqrt{s}$= 7 TeV (4.5 fb^{-1}), $\sqrt{s}$=8 TeV (20.3 fb^{-1}) and for the combination 2011+2012.

2011+2012 data	1D No Syst.	2D No Syst.	1D with Syst.	2D with Syst.
4μ	$123.94^{+0.79}_{-0.79}$	$124.25^{+0.81}_{-0.84}$	$123.94^{+0.79}_{-0.79}$	$124.25^{+0.81}_{-0.84}$
$2e2\mu$	$124.72^{+0.83}_{-0.85}$	$124.62^{+0.86}_{-0.77}$	$124.72^{+0.83}_{-0.85}$	$124.62^{+0.86}_{-0.77}$
$2\mu 2e$	$123.73^{+1.71}_{-2.40}$	$122.49^{+1.47}_{-1.89}$	$123.74^{+1.71}_{-2.39}$	$122.50^{+1.46}_{-1.91}$
$4e$	$126.64^{+1.03}_{-1.14}$	$126.31^{+1.20}_{-1.18}$	$126.65^{+1.03}_{-1.15}$	$126.32^{+1.20}_{-1.19}$
Combined	$124.63^{+0.56}_{-0.51}$	$124.51^{+0.53}_{-0.51}$	$124.63^{+0.56}_{-0.52}$	$124.51^{+0.54}_{-0.51}$

Table 5.9: Measured Higgs boson masses in the different final states of the $H \to ZZ \to$ 4l channel with the two different methods detailed in Sections 5.7.3 and 5.7.4.

2011+2012 data	1D No Syst.	2D No Syst.	1D with Syst.	2D with Syst.
4μ	$1.80^{+0.71}_{-0.58}$	$1.47^{+0.66}_{-0.52}$	$1.79^{+0.76}_{-0.60}$	$1.47^{+0.69}_{-0.53}$
$2e2\mu$	$1.73^{+0.84}_{-0.67}$	$1.82^{+0.84}_{-0.66}$	$1.73^{+0.88}_{-0.68}$	$1.83^{+0.88}_{-0.67}$
$2\mu 2e$	$1.88^{+1.17}_{-0.87}$	$2.00^{+1.63}_{-0.91}$	$1.88^{+1.22}_{-0.88}$	$1.99^{+1.67}_{-0.92}$
$4e$	$1.80^{+0.94}_{-0.71}$	$1.72^{+0.95}_{-0.72}$	$1.80^{+0.98}_{-0.72}$	$1.72^{+0.99}_{-0.73}$
Combined	$1.76^{+0.41}_{-0.36}$	$1.67^{+0.40}_{-0.35}$	$1.76^{+0.47}_{-0.40}$	$1.66^{+0.45}_{-0.38}$

Table 5.10: Measured signal strengths μ on the different final states of the $H \to ZZ \to$ 4l channel with two different methods described in Sections 5.7.3 and 5.7.4 and using the 7+8 TeV dataset.

In the mass range (120< m_{4l} <130) GeV, 37 events have been observed in data (26.5±1.7 expected). This observation corresponds to a local significance of 8.2σ at the combined [20] ATLAS measurement Higgs mass m_H=125.36±0.41 GeV.

The Higgs mass in the four lepton final state is measured with a 2-dimensional conditional fit BDT *vs* m_{4l}. The final Run 1 value of the Higgs boson mass in the $H \to ZZ \to$ 4l decay channel is m_H =124.51±0.52 GeV and the on-shell signal strength at the best-fitted value is μ=1.66±0.42.

Chapter 6

Off-shell Higgs couplings and width measurements using diboson events

Contents

Unlike Chapter 5 where the Higgs is measured as a new *on-shell* particle showing up as a peak on the 4 leptons final state invariant mass, it was recently noted [136] [137] [138] [139] that the high mass regions of the diboson final states, H→ ZZ and H→ WW, have sensitivity to *off-shell* Higgs boson production where this particle acts as a virtual propagator. Its properties, namely the off-shell signal strength and the associated off-shell Higgs boson couplings, can be therefore determined.

This Chapter presents the analysis [140] and [141]: Section 6.1 will give a theoretical overview of the physics scenario as well as Section 6.8 while Sections 6.2, 6.3 and 6.4 will cover the Monte Carlo simulations and the various features regarding the higher order corrections applied to the generated processes. Section 6.5 will be devoted to the explanation of the analysis strategy in the 4l channel. Sections 6.6 and 6.7 will describe the two multivariate approaches employed in the analysis, namely the matrix element and the BDT. Section 6.9 will report the systematic uncertainties, both theoretical and experimental, that are included in the extraction of the off-shell measurement. Section 6.10 will address the procedure to work out the expected off-shell signal strength using a cut-based approach as well as a ME or a BDT-based configuration. Lastly, Sections 6.11 and 6.13 will show the observed results in data as well as a combination among the 4l, 2l2ν and the WW channels.
Results are elaborated for the 4 lepton channel only except that in Section 6.12 where the main ingredients on the analysis in the 2l2ν and WW channels are briefly presented.

6.1 Theory overview

In the *0-width approximation* [136] (on-peak-only contribution) the gluon-initiated Higgs signal integrated cross section is proportional to the Higgs couplings for production (κ^2_{prod}) and decay (κ^2_{decay}) divided by the Higgs width, Γ_H:

$$\sigma^{gg\to H\to VV}_{\text{on-shell}} = \frac{\kappa^2_{\text{prod,on-shell}} \cdot \kappa^2_{\text{decay,on-shell}}}{\Gamma_H}; \tag{6.1}$$

On the contrary, the cross section in the off-shell region, where the Higgs boson acts as a propagator, is independent on the total Higgs width:

$$\sigma^{gg\to H^*\to VV}_{\text{off-shell}} = \kappa^2_{\text{prod,off-shell}}\kappa^2_{\text{decay, off-shell}}. \tag{6.2}$$

This proportionality can be expressed as:

$$\mu_{\text{off-shell}} = \frac{\sigma^{gg\to H^*\to VV}_{\text{off-shell}}}{\sigma^{gg\to H^*\to VV}_{\text{off-shell, SM}}} = \kappa^2_{\text{prod,off-shell}} \cdot \kappa^2_{\text{decay,off-shell}} \tag{6.3}$$

where $\mu_{\text{off-shell}}$ is the off-shell *signal strength*:

$$\mu_{\text{off-shell}} = \frac{\sigma_{\text{off-shell}}}{\sigma^{\text{SM}}_{\text{off-shell}}} \tag{6.4}$$

and the off-shell couplings

$$\kappa^2_{\text{prod,off-shell}},\ \kappa^2_{\text{decay,off-shell}} \tag{6.5}$$

are associated to $gg \to H^*$ production ($\kappa^2_{\text{prod,off-shell}} = \kappa^2_{\text{g,off-shell}}$) and $H^* \to$VV decay ($\kappa^2_{\text{decay,off-shell}} = \kappa^2_{\text{V,off-shell}}$). Due to the statistically limited sensitivity of the current analysis, the off-shell signal strength and coupling scale factors are assumed in the following to be independent of $\hat{s}$ in the high-mass region selected by the analysis.
In contrast, the signal strength for the on-shell process $gg \to H \to$VV can be expressed as:

$$\mu_{on-shell} = \frac{\sigma^{gg\to H\to VV}_{\text{on-shell}}}{\sigma^{gg\to H\to VV}_{\text{on-shell, SM}}} = \frac{\kappa^2_{\text{g, on-shell}} \cdot \kappa^2_{\text{V, on-shell}}}{\Gamma_H/\Gamma_H^{\text{SM}}}, \tag{6.6}$$

where the explicit dependence on the total Higgs width, Γ_H, appears in the denominator.
The off-shell Higgs boson signal cannot be treated independently from the $gg \to$ VV background, as sizeable same initial-state negative interference effects appear [136]. The interference term is proportional to $\sqrt{\mu_{\text{off-shell}}} = \kappa_{g,\text{off-shell}} \cdot \kappa_{V,\text{off-shell}}$.
The dominant gg-initiated processes used in the analysis are listed below:

1. $gg \to H \to$ ZZ, the signal (S) comprising both the on-shell peak at m_H =125.5 GeV and the off-shell region where the Higgs boson is a propagator;

2. $gg \to$ ZZ, the continuum background (B);

3. $gg \to (H^*) \to$ ZZ, the signal, continuum background and interference contribution, often labelled as SBI in what follows.

The electroweak production modes are also included in the analysis bearing in mind that $pp \to VV + 2j$ configurations include both VBF-like and VH-like events. The processes are found below:

1. off-shell VBF $pp \to H^* \to VV + 2j \to$ 4l +2j signal contribution that is independent on the Higgs width, Γ_H but scales with κ^4_V;

2. VBF-like $pp \to VV + 2j \to$ 4l +2j background production in a t-channel. As for the first case, this configuration is independent on the Higgs width, Γ_H but scales with κ^4_V;

3. $pp \to (H^*) \to VV + 2j \to$ 4l +2j signal + background + interference (SBI), where the interference is caused by the same $q\bar{q}$ initial state of the off-shell VBF signal sample, $pp \to H^* \to VV + 2j$, and the continuum $pp \to$ ZZ +2j diagram.

4. on-shell VH events where the vector boson V decays into two leptons and the Higgs decays in two leptons and two jets.

The main background of this analysis is represented by the $q\bar{q} \to$ VV contribution (Section 1.6.2). Figure 6.1 shows the Feynman diagrams relative to the $gg \to H^{(*)} \to$ VV signal (a), the continuum background $gg \to$ VV (b) and the dominant $q\bar{q}$ background. The Monte Carlo simulations of the three main samples (VV final states via gluons or in the electroweak production modes as well as the $q\bar{q}$ contributions) are analysed in Sections 6.2, 6.3 and 6.4.

The workflow of the analysis is articulated along the following steps:

- an upper limit on the off-shell coupling ($\mu_{\text{off-shell}}$) will be derived in the high mass region;

- this upper limit will be interpreted as a constraint on the Higgs boson width (the predicted SM Higgs width at m_H =125.5 GeV is 4.2 MeV) when combining the off-shell results with the on-shell measurement. This *indirect* measurement is very accurate if compared to the *direct* width measurement ($\Gamma_H^{\text{dir}} <$ few GeV) performed on the Higgs boson lineshape.

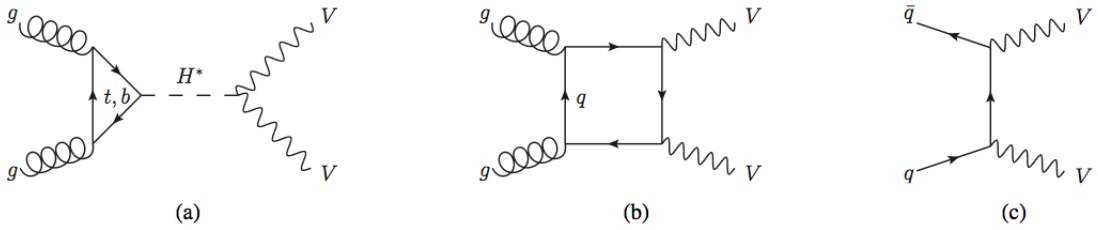

Figure 6.1: The leading-order Feynman diagrams for $gg \to H^{(*)} \to$ VV signal (a), the continuum $gg \to$ VV background (b), the $q\bar{q} \to$ VV background (c).

The analysis core assumptions

The calculation of the off-shell signal strength relies on the assumption that there is no new physics modifying the off-shell couplings [142] without varying the SM background expectations. Further, neither are there sizeable kinematic modifications to the off-shell signal nor new, sizeable signals in the search region of this analysis unrelated to an enhanced off-shell signal strength [143]. In conclusion, assuming identical on-shell and off-shell Higgs couplings ($\kappa_{\text{on-shell}} = \kappa_{\text{off-shell}}$), the ratio of $\mu_{\text{off-shell}}$ to $\mu_{\text{on-shell}}$ provides a measurement of the total width of the Higgs boson. This assumption is relevant to the running of the effective couplings $\kappa_g(\hat{s})$ for the loop-induced $gg \to$ process as it is sensitive to new physics that enters at higher mass scales and could be detected in the high mass m_{VV} signal region of the analysis.
Wrapping up, the scope of this analysis is to provide a limit on the off-shell signal strength; results will be given both employing a profile likelihood ratio scan on the parameter of interest $\mu_{\text{off-shell}}$ and with a CL_s-based approach (Appendix C) as a function of the background-to-signal gg-related k-factor ratio, $R^B_{H*} = \frac{KH^*_{gg}(m_{ZZ})}{KH^*(m_{ZZ})}$ as explained in Section 6.2.1. With the current sensitivity of the analysis, only an upper limit on the total width can be determined.

6.2 Monte Carlo simulation of the gg-initiated processes

The first step of the analysis is the generation of the Monte Carlo samples [144] [145] for the various processes involving gluons in the initial state reported in the previous Section. Only LO calculations are available, hence two LO generators are used, gg2VV [146] and MCFM [147] with PYTHIA 8 [31] showering.
The Monte Carlo production is based on two independent and consecutive processes, the *grid* integration and the *event generation*.

- The Monte Carlo grid production is a technique exploited by the VEGAS algorithm [148] for a numerical integration using random numbers: the program chooses points at which the integral of the function defining the phase-space is evaluated. The typical timescale of the VEGAS grid generation for the gg2VV process is $\sim$ 1 week, while for MCFM the integration is completed in approximately one day. We also checked the integrity and consistency of the grid production: control plots on the variables of interests of the kinematic phase space (m_{4l}, m_{Z1}, m_{Z2}, leptons transverse momenta and pseudorapidity,...) are produced and inspected.

- As a second step of the algorithm, the event-generation procedure receives in input the VEGAS grid. The format of the event generation output is a text file (*Les Houches Event* file, LHE [149]) that comprises the four-momenta of the generated particles. The LHE files

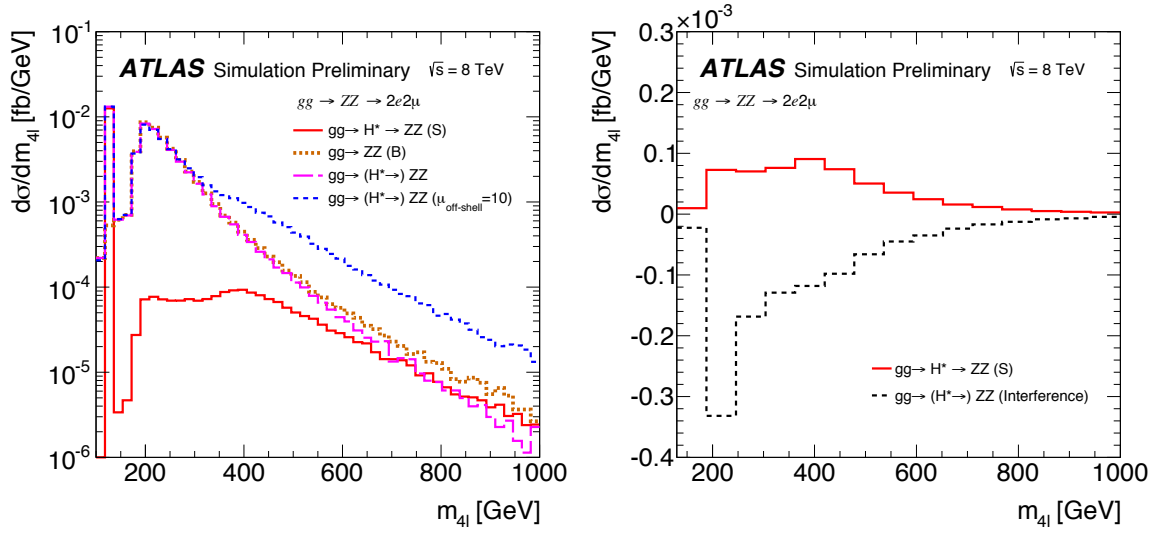

(a) **(b)**

Figure 6.2: (a) Differential cross sections generated with MCFM for the *gg*-initiated processes in the 2e2μ channel at the matrix element level. (b) Comparison of the Higgs signal with the interference contribution.

are consequently treated with *parton shower* using PYTHIA and output files are created for preliminary checks. Once the validation is accomplished and the simulation is deemed as appropriate, the LHEs are sent to the central ATLAS production that implements the GEANT4-based full simulation [127] reconstruction.

The Higgs mass is chosen to be at m_H=125.5 GeV and the QCD renormalisation and factorisation scales (dynamic scale) are set at $\frac{m_{ZZ}}{2}$. The parton density functions exploited in the matrix element calculations are CT10nnlo [150] - appropriate for this LO $gg \rightarrow$VV process being part of the NNLO calculation for pp$\rightarrow$VV. The following generation cuts are applied at the grid level both for gg2VV and MCFM:

- m_{4l} >100 GeV;
- p_T^{lep} >3 GeV;
- $|\eta^{lep}|$ <2.8;
- $m_{Z1,Z2}$ > 4 GeV.

Figure 6.2 illustrates the m_{4l} distribution for the various *gg*-related processes in the 2e2μ channel and the contribution of the signal-background interference. However, final state interference effects from same lepton flavours are negligible in the high mass region.
Figure 6.3 highlights the comparison between the two independent Monte Carlo productions with gg2VV and MCFM for the key processes entering the analysis at the matrix element level. These distributions testify full consistency in shape and cross sections between the two generators.

6.2.1 Higher order QCD corrections to the ZZ mass spectrum

The main issue characterising the *gg*-related processes is that the available Monte Carlo simulations employed in the analysis, gg2VV and MCFM, currently match LO calculations. For this reason, mass-dependent k-factors to higher order accuracy are needed to fulfil a better precision.

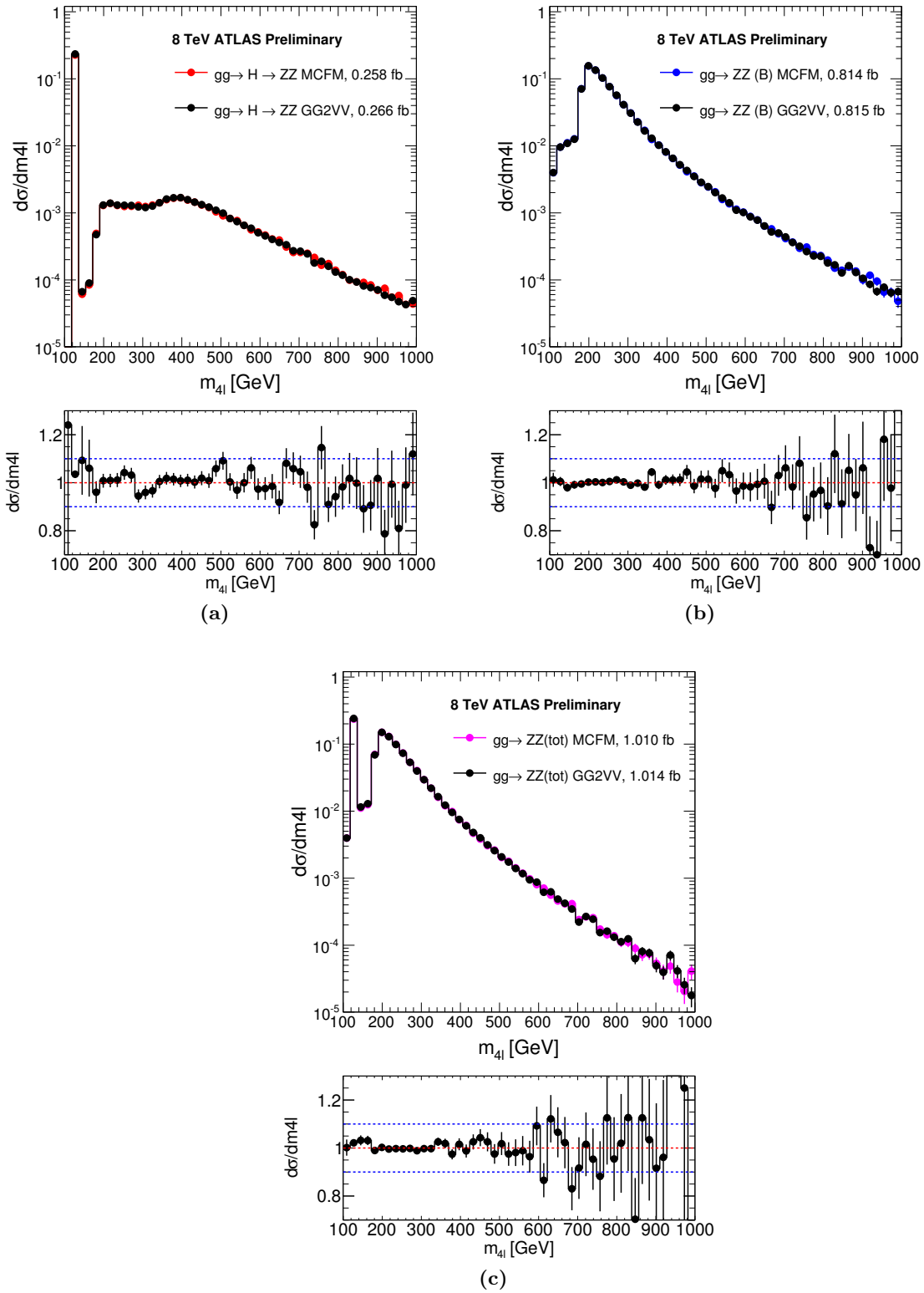

Figure 6.3: Comparison of the m_{4l} distributions between gg2VV and MCFM for the signal process (a), the background (b) and SBI (c) at the matrix element level.

i For the signal process, namely $gg \to H^* \to$ ZZ, higher order QCD corrections are computed in [151]: NNLO to LO k-factors are calculated as a function of the diboson invariant mass m_{ZZ}. Figure 6.4 (a) describes the structure of this k-factor as a function of the mass: $K(m_{ZZ})$ is the full k-factor for $gg \to H^* \to$VV which includes at NLO qg initial states and at NNLO qq initial states. $K_{gg}(m_{ZZ})$ represents the k-factor for the gg-induced only initial states, at NLO and NNLO. The reason of these two distinctive k-factors is that the LO interference calculation can only be related with the interference on gg initial states. Note that the uncertainty on $K_{gg}(m_{ZZ})$ is larger than the one on $K(m_{ZZ})$ because this k-factor comprises the full NNLO calculation, whereas $K_{gg}(m_{ZZ})$ is a truncated result, hence its uncertainty is *NLO-like*. In [151], the MSTW PDF set is used for the matrix element calculation; however in the Monte Carlo simulation of the gg-related signal process, another set of PDFs, CT10nnlo, is employed to ensure consistency with the $q\bar{q} \to$ ZZ generation. Thence, a PDF reweighting is implemented to modify the k-factors and account for this residual difference.

ii For the background process, $gg \to$ ZZ, the full k-factor from LO to NNLO accuracy is not available. Nevertheless, the effect of NLO and NNLO corrections are addressed in [152] in the *soft-collinear approximation* that is suitable for the Higgs production at high mass. According to the predictions extrapolated in this paper for the WW final state (the same conclusions hold true in the ZZ final state as well), the QCD radiative corrections are similar for $gg \to$ WW to those for the signal process in addition to a 30% uncertainty when the interference plays a role in the computation. Herewith, the gluon induced part of the Higgs signal k-factor, $K_{gg}(m_{ZZ})$, is also applicable on the gg background and the interference.

iii The uncertainty on the background k-factor is larger than the one on the signal component because of missing NNLO diagrams in the background computation. The following correlation scheme of uncertainty is therefore applied:

- the uncertainty on the signal k-factor is treated as correlated to the background k-factor;
- the quadratic difference between the uncertainties on the background and signal k-factors is also added as uncorrelated only to the background k-factor.

In order to account for the unknown background k-factor, results will be given as a function of the k-factor ratio between background and signal:

$$R^B_{H*} = \frac{KH^*_{gg}(m_{ZZ})}{KH^*(m_{ZZ})}. \tag{6.7}$$

In the analysis, results will be provided under the assumption R^B_{H*}=1 (soft collinear approximation) and by varying this ratio between 0.5 and 2. Furthermore, this ratio is assumed to be m_{ZZ} independent because the signal k-factor is almost constant as a function of m_{ZZ}. As this inference leads to large cancellations between the interference and the background, a conservative 30% uncertainty on the interference term is applied.

6.2.2 Impact of QCD variables in the analysis

Although the events are selected without any specific cut or requirement on the jet multiplicity in the 4 lepton channel, the kinematic observables used for the selection are correlated with the boost of the ZZ system. Furthermore, as the $gg \to$ ZZ Monte Carlo is a leading-order generator, the simulation of the kinematics of the ZZ system entirely relies on the PYTHIA 8 parton shower.

The impact of the selection on ZZ-related observables is examined by checking the distribution

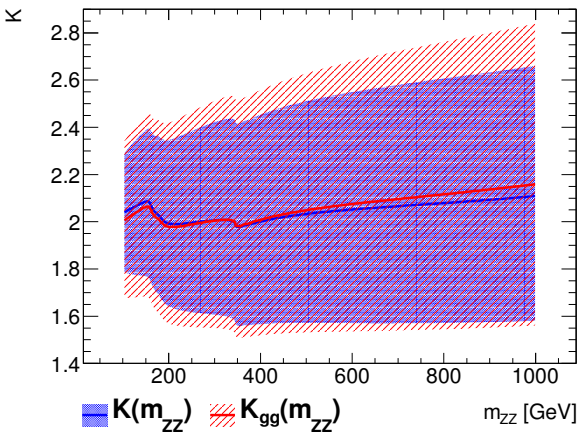

Figure 6.4: Distribution on the m_{ZZ} mass spectrum of the full *k-factors* for signal, $KH^{*}(m_{ZZ})$, and the k-factor involving the gluon-induced part of the signal, $KH^{*}_{gg}(m_{ZZ})$, and their systematic uncertainties drawn as a coloured band. The plots refer to [151].

of p_T^{ZZ} and jet multiplicity (Figure 6.5 (a) and 6.5 (b)) for the gg continuum background before and after the standard analysis cuts, in a window in m_{ZZ} equal to (600< m_{ZZ} <650) GeV. A fixed window created to remove the mass dependency is used.

Another point to be investigated is the dependence of the matrix-element based discriminant on the ZZ-frame kinematics, i.e. the transverse momentum and the jet multiplicity gauged in the same mass window. In Figure 6.5 (c) and 6.5 (d), these distributions are displayed before and after a cut on the ME discriminant at -1.5 that approximately coincides with the signal-like region of the analysis. As no change is visible in the shape comparison in Figure 6.5, the ZZ→ 4l analysis is regarded as inclusive in QCD observables. For what concerns the 2l2ν decay channel, Figure 6.6 shows the p_T(ZZ) and jet multiplicity in the same m_{ZZ} window, i.e. (600< m_{ZZ} <650) GeV before and after applying the full kinematic selection. A sizeable modification of the p_T(ZZ) and the jet multiplicity spectra is observed: the ZZ→ 2l2ν analysis is not inclusive in QCD observables and acceptance systematic uncertainties need to be applied.

Section 6.2.3 will be devoted to the explanation of the acceptance systematics extraction in the 2l2ν channel. This method refers to the first release of the analysis [140]. It relies on the comparison of different parton showers and hadronisation options using the gg2VV-based LO matrix. This treatment is replaced [141] by the procedure documented in Section 6.2.4 where the QCD-related acceptance systematics are computed from LO processes.

6.2.3 Parton shower validation

Given that no higher order matrix element calculations are available for the gg-initiated processes, the only way to simulate QCD radiation is through the parton shower [153]. However, as the generation is done at LO in QCD, there is no clear prescription to evaluate the uncertainty systematics on the QCD scale. According to the maximum jet p_T scale emission characterising the parton showers, two different configurations are exploited, the *power shower* and the *wimpy shower*. PYTHIA 8 is tuned as default with the power shower option. The comparison is carried out involving the following parton shower schemes:

- PYTHIA8 power shower including a matrix element correction on the first jet emission;

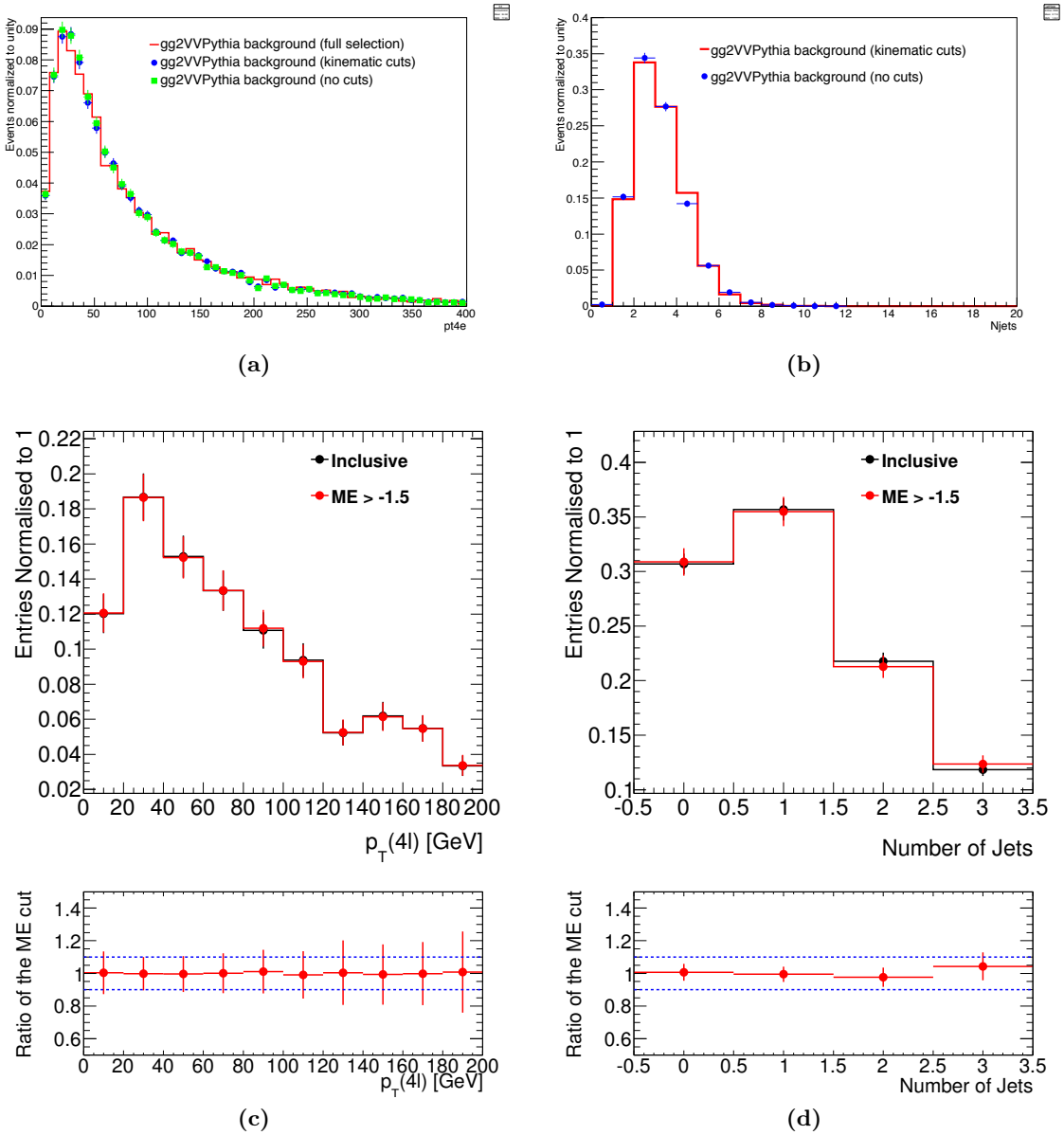

Figure 6.5: Distributions of p_T^{ZZ} (a) and the jet multiplicity (b) for the gg continuum background process before and after the basic lepton selection cuts in the 4l channel. Distributions of p_T^{ZZ} (b) and the jet multiplicity (c) for the signal process before and after the ME cut at -1.5. The plots are extracted in the same ZZ mass range, (600< m_{ZZ} <650) GeV.

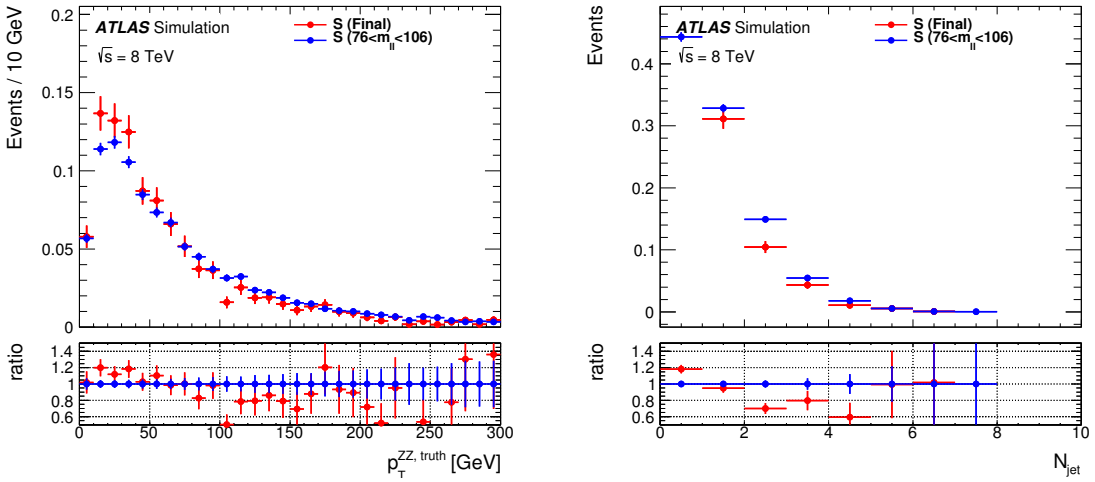

(a) **(b)**

Figure 6.6: Distributions of p_T^{ZZ} (a) and the jet multiplicity (b) for the gg continuum background process before and after the basic lepton selection cuts in the 2l2ν channel.

- PYTHIA8 power shower without a matrix element correction;
- PYTHIA8 wimpy shower without a matrix element correction;
- Herwig [154] in combination with Jimmy [155].

The items above are finally compared to high-mass POWHEG NLO $gg \to H \to$ ZZ event sample with a Higgs boson mass generated at m_H=380 GeV and a SHERPA+OpenLoops $gg \to$ ZZ background sample using merged 0-jet and 1-jet matrix element calculation.
A second validation concerns the explicit presence of the Higgs as intermediate particle in the gg2VV event record stored in the LHE file input to PYTHIA 8. This occurrence triggers a special treatment by the PYTHIA parton shower for leading jet emission based on a $gg \to H + j$ matrix element calculation (first point on the list above) in order to ensure a better NLO-like behaviour. However, this is not the case for MCFM. To check the impact of this treatment, the parton shower is repeated after removing the Higgs record from the LHE. Figures 6.7 (a) and 6.7 (b) exhibit the presence of the matrix element correction on the first jet emission. A significant effect on the Higgs p_T spectrum results in a softer NLO-like distribution in the low p_T range and a $\sim$ 30% change at high p_T(ZZ). On the contrary, no visible effect is seen on the diboson mass. As this difference could affect the extraction of the probability density function for the interference term, the gg2VV samples used in the analysis have the Higgs record removed from the LHE file.
The normalised p_T(ZZ) distributions, detailed in Figure 6.7 (c) for the sample above in the text are plotted in the same high ZZ mass range (345< m_{4l} <415) GeV in order to ensure a compatible mass of the hard interaction system. The fair agreement between the gg2VV PYTHIA distribution (regardless of the power or wimpy shower configurations) and the one of the pure NLO POWHEG indicates that PYTHIA showering achieves a good result in the simulation of the real emission component of the higher order QCD. However, the closest attempt to reproduce a pure NLO generator corresponds to Herwig+Jimmy and SHERPA where 0 and 1 jet corrections are included to the LO matrix element computation.

To conclude, the treatment of the QCD-related acceptance systematics on the gg processes are determined as follows.

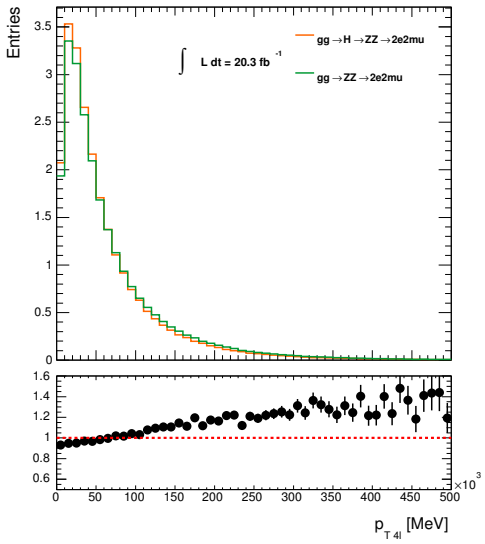

(a)

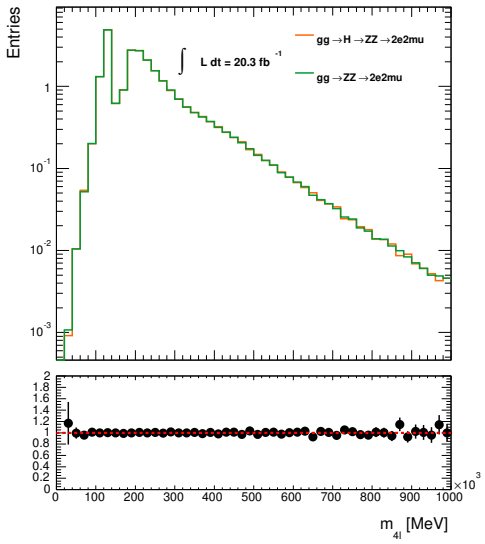

(b)

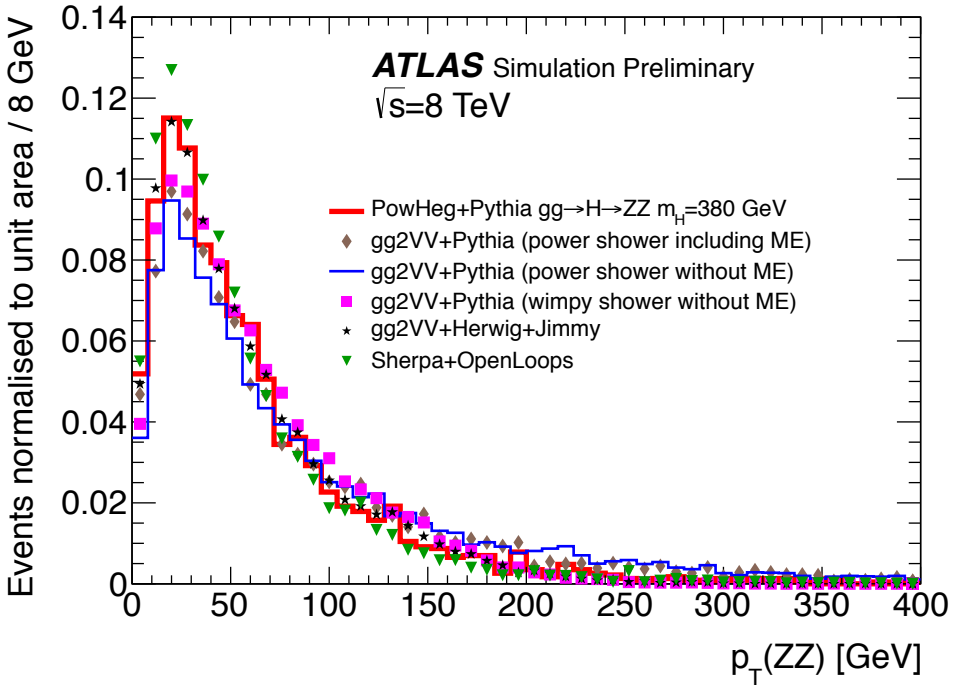

(c)

Figure 6.7: Distribution of $p_T(ZZ)$ (a) and m_{4l} (b) for the signal process with Higgs mass generated at m_H=125.5 GeV and continuum background. The signal sample has the Higgs record stored in the LHE and is therefore treated with a matrix element correction on the first jet emission. (c) Distribution of p_T(ZZ) comparing the NLO generator Powheg showered with PYTHIA8, the LO generator gg2VV + PYTHIA8 (power or wimpy shower), the LO generator gg2VV showered with Jimmy+Herwig and a SHERPA sample with a matched 0j+1j matrix element. All samples are restricted to the range (345< m_{4l} <415) GeV.

i As detailed in Section 6.2.2, the 4l analysis is inclusive in QCD observables, hence no acceptance systematic uncertainties are applied.

ii A non-negligible uncertainty is expected for the 2l2ν channel as explained in Section 6.2.2 and in Figure 6.6.

iii As the NLO Higgs signal and the matched SHERPA 0 and 1-jet matrix element samples are similar and can be considered as best estimates for the assessment of the uncertainties on the QCD effects, the following procedure is applied:

- The gg2VV-based central value of the p_T (ZZ) distribution in the 2l2ν channel is re-weighted to the POWHEG sample.
- Referring to Figure 6.7 (c), the difference between the LO gg2VV sample with PYTHIA8 parton shower in the power shower configuration (analysis default) and the full NLO POWHEG sample is regarded as the acceptance systematics on the POWHEG-reweighted p_T(ZZ) central value. This is the largest difference, accounting for $\sim 5\%$, and brackets all the other tests.

6.2.4 Higher order QCD corrections to the p_T and y of the ZZ system

This Section documents the treatment employed in the final version of the paper [141] with regard to the QCD-related corrections. This procedure superseded the method presented in Section 6.2.3.

Higher order QCD corrections for the $gg \to$ ZZ background process are studied using the SHERPA generator that includes NLO corrections at the matrix element level for the first jet emission in QCD. For the $gg \to H^* \to$ ZZ signal contribution, the POWHEG generator reweighted to HRES prediction at NNLL is also used.
Figure 6.8 includes validation plots of various comparison of the variables of interest, p_T(ZZ) and y(ZZ), in both on-shell and off-shell mass regions using POWHEG, SHERPA and gg2VV generators at truth level with no kinematic selection applied on the samples.

- Figures 6.8 (a), (b): comparison among the $gg \to H^* \to$ ZZ signal processes generated at m_H=125.5 GeV in the mass range [124,126] GeV for POWHEG, SHERPA and gg2VV;
- Figures 6.8 (c), (d): comparison between the $gg \to H^* \to$ ZZ signal off-shell processes generated at m_H=125.5 GeV produced by gg2VV and SHERPA and $gg \to H^* \to$ ZZ signal process (m_H=380 GeV) with gg2VV (on-shell) in the region [345,415] GeV;
- Figures 6.8 (e), (f): comparison between the $gg \to H^* \to$ ZZ signal off-shell processes generated at m_H=125.5 GeV produced by gg2VV and SHERPA and $gg \to H^* \to$ ZZ signal process (m_H=380 GeV) with POWHEG (on-shell) in the region [345,415] GeV;
- Figures 6.8 (g), (h): comparison among the $gg \to H^* \to$ ZZ at m_H=125.5 GeV, the $gg \to$ ZZ background and the total SBI generated with SHERPA in the mass range [345,415] GeV;
- Figures 6.8 (i), (l): comparison of the three gg2VV contributions (signal, background and SBI) in the mass region [345,415] GeV.

The errors lines in Figure 6.8 are statistical only. The systematic uncertainties, when applicable, are drawn as shaded band, extracted from scale variations on SHERPA and HRES as described in Section 6.9.2. The systematic uncertainties from the HRES are directly applicable here as the POWHEG generator (Section 1.6.1) is directly reweighted to the HRES prediction to reach

NNLO+NNLL accuracy.

As highlighted in Figures 6.8 (a) and (b) for what concerns the on-shell and Figures 6.8 (c) and (d) for the off-shell, the lack of higher QCD determination in gg2VV results in different p_T and y spectra compared to the higher order POWHEG and SHERPA Monte Carlo.
In the high mass region, the off-shell (generated at m_H=125.5 GeV) and on-shell (produced at m_H=380 GeV) Higgs productions with gg2VV match fairly well. Figure 6.8 (e) shows that the differences in p_T between SHERPA and gg2VV in the off-shell high mass region are not covered by the uncertainties assigned to SHERPA. Therefore, as the SHERPA generator has a better treatment of the first hard jet emission, gg2VV is reweighted to the SHERPA prediction in order to recover NLO-like accuracy on its central value. As for the rapidity distribution reported in Figure 6.8 (f), no significant difference between gg2VV and SHERPA is present in the high mass region; thence, the reweighting procedure on y is not necessary.
Figure 6.8 (g) stresses the fact that the ZZ-transverse momentum of the signal process $gg \to H^* \to$ ZZ differs from the $gg \to$ ZZ background process and the SBI unlike the gg2VV generator as noted in Figure 6.8 (i). This is caused by the presence of the additional matrix element correction to the first jet emission included in SHERPA that generates a different treatment of signal and background components, as explained in [156]. This statement has been explicitly validated by removing the 1-jet matrix element computation in SHERPA; as predicted, Figure 6.9 demonstrates full compatibility between signal and background.

SHERPA p_T reweigthing of gg2VV

Given the intrinsic difference between SHERPA signal and background due to the treatment of the correction on the first jet emission, Figures 6.8 (g) and Figure 6.9, the reweighting functions are separately derived for the three different processes, e.g. signal, background and interference. The main ingredient is the calculation of the ratio SHERPA *vs* gg2VV in bins of p_T for signal, background and SBI as in Figure 6.10. Likewise, the scaling of the interference term under the reweighting has also been checked.

The reweighting is derived at truth level using stable leptons after radiations. To check for a residual p_T mass dependency, three m_{4l} regions are designed for the procedure: m_{4l} >220 GeV, (220-400) GeV and (400-1000) GeV.

The most visible impact of the SHERPA p_T reweighting on the analysis resides in a small change in acceptance of the selection cuts. The assessment of this systematic effect is achieved by comparing the main kinematic distributions, namely p_T, m_{4l} and m_Z for signal, background and the total contribution including the interference before and after the SHERPA-based reweighting. Figure 6.11 (a) provides a closure test on the method: the gg2VV reweighted distribution is in agreement with the SHERPA prediction. As for m_{4l} (Figure 6.11 (b)) and m_Z (Figure 6.11 (c)), the level of agreement is approximately 4-5% and below 2% in the highly-populated bins respectively. The post-reweighting validation is also carried out at the final analysis level on the ME-based kinematic discriminant in Figure 6.11 (d). Given that the transverse momentum information on the ZZ system is not exploited in the ME-based method, the output distributions are essentially unaffected and no significant distortions are produced.

Wrapping up, the following scheme is adopted for the evaluation of the QCD corrections in the analysis.

i The ME-based discriminant is practically insensitive to the SHERPA-reweghting and the m_{4l} distribution is already scaled to higher orders in QCD with the usage of the k-factors (Section 6.2.1), hence the reweighting is not necessary for the central shape of the 4l channel.

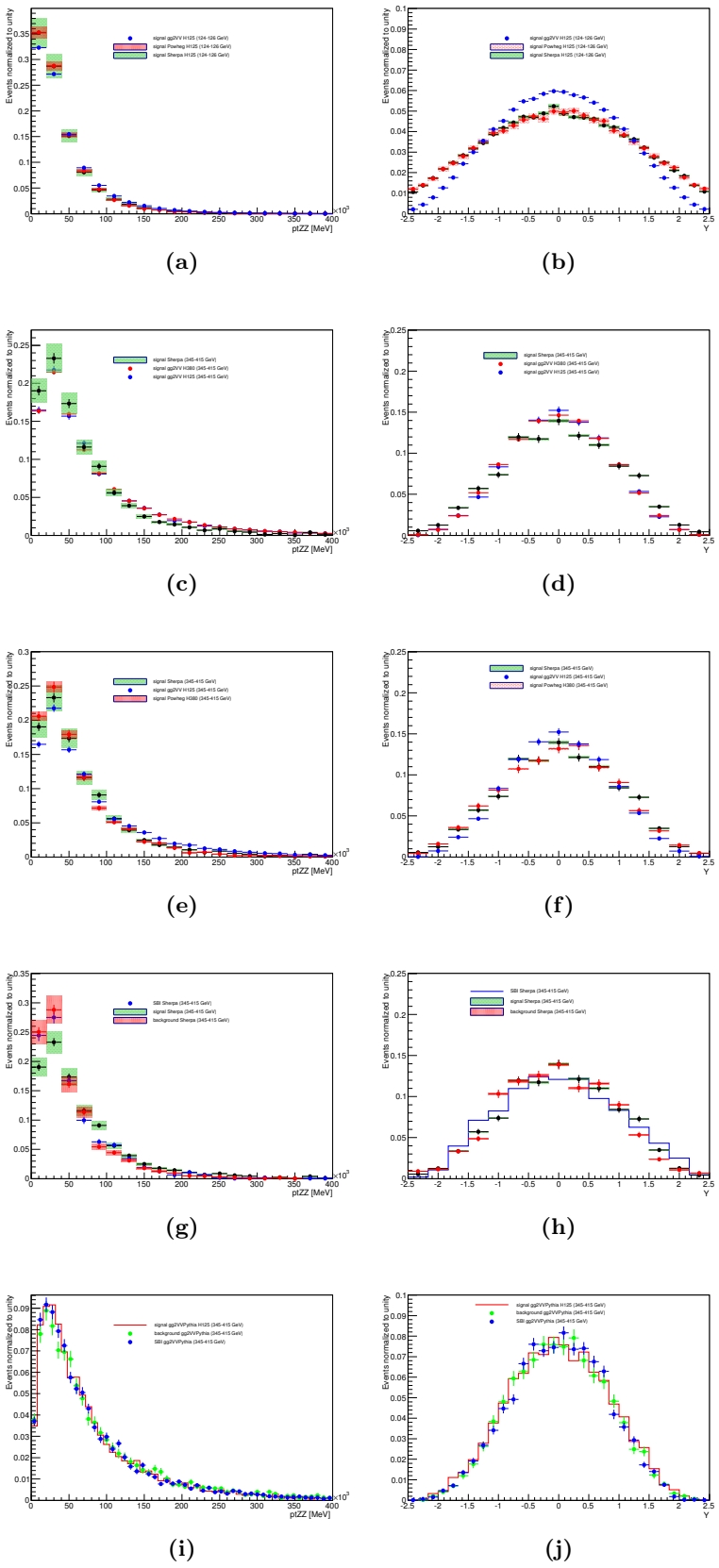

(a) **(b)**

(c) **(d)**

(e) **(f)**

(g) **(h)**

(i) **(j)**

Figure 6.8: Distributions of p_T and y exploiting the configurations specified in Section 6.2.4.

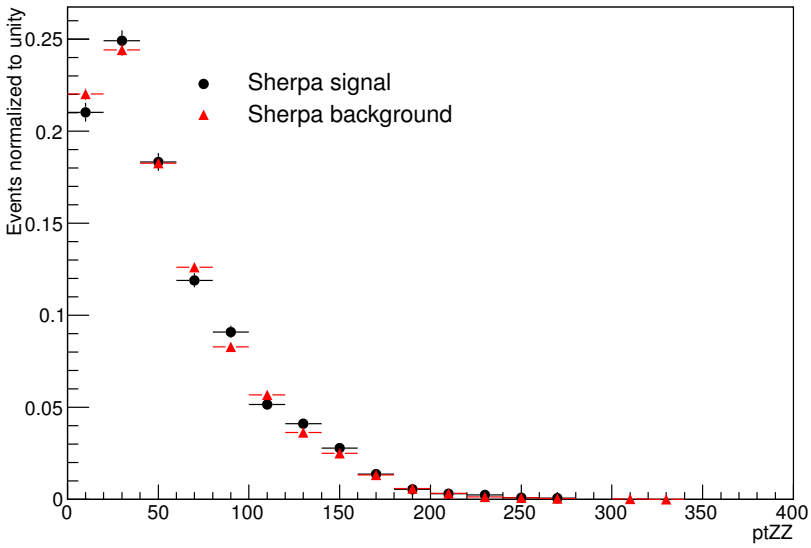

Figure 6.9: p_T(ZZ) distributions of signal generated at m_H=125.5 GeV and background in the mass window [345,415] GeV when generating events with SHERPA and disabling the 1-jet production.

ii As for the 2l2ν final state, m_T holds a dependency on p_T, thus its shape is reweighted to SHERPA.

iii The impact of the reweighting on the acceptance is well below 1% for the signal, $\sim$ 4% for the background in the 4l final state and around 6% in the 2l2ν decay mode.

iv The acceptance systematic uncertainties associated to the SHERPA-based reweighting are assessed by varying the renormalisation, factorisation and resummation scales in SHERPA (Section 6.9.2). The largest value between the QCD scale variations in SHERPA and 50% of the difference between SHERPA and gg2VV is assigned as the systematic uncertainty on the method.

6.3 Monte Carlo simulation of the $pp \to VV + 2j$ processes

The following simulations for VV final states in electroweak production modes reported in Section 6.1 are performed. MadGraph5-MCatNLO [130] showered with PYTHIA6 is used as a baseline sample with PHANTOM [157] for validation. The scales in the two generators are set to m_W following the prescriptions of the LHC Higgs Cross Section Working Group [29] and CTEQ [26] PDF set is used. These generation cuts are applied at the grid stage both for MadGraph5-MCatNLO and PHANTOM:

- p_T^{lep} >3 GeV;
- p_T^{jet} >20 GeV;
- $|\eta^{lep}|$ <2.8;
- $|\eta^{jet}|$ <6.5;
- m_{jj} >10 GeV;

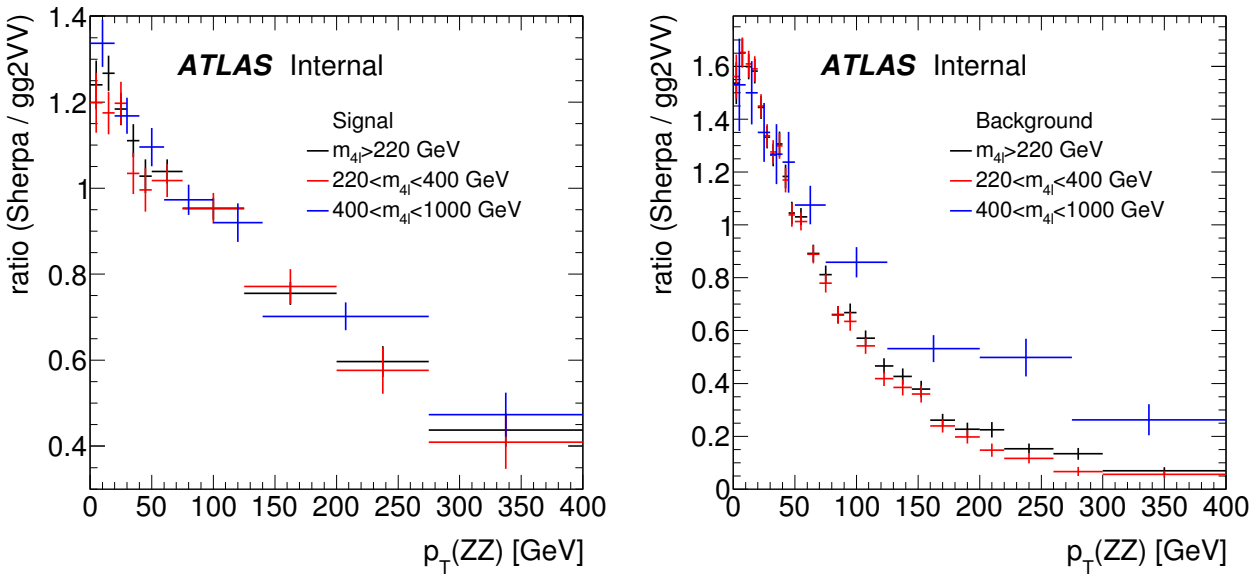

(a)

(b)

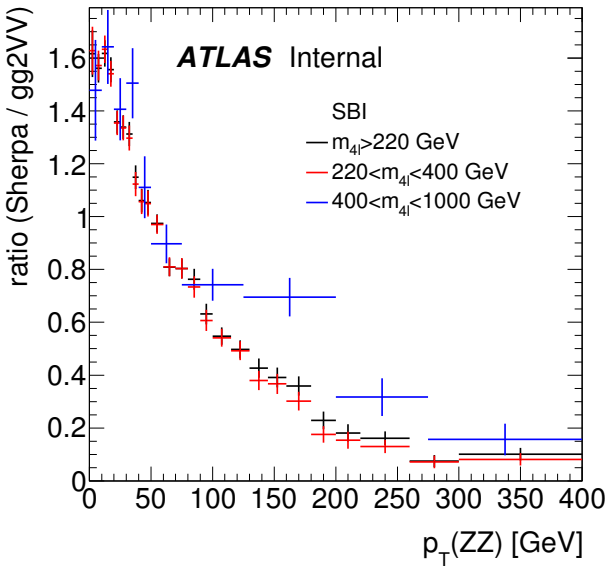

(c)

Figure 6.10: Ratio p_T^{SHERPA}/p_T^{gg2VV} for signal (a), background (b) and SBI (c) in three mass windows, m_{4l} >220 GeV, (220<m_{4l} <400) GeV and (400<m_{4l} <1000) GeV.

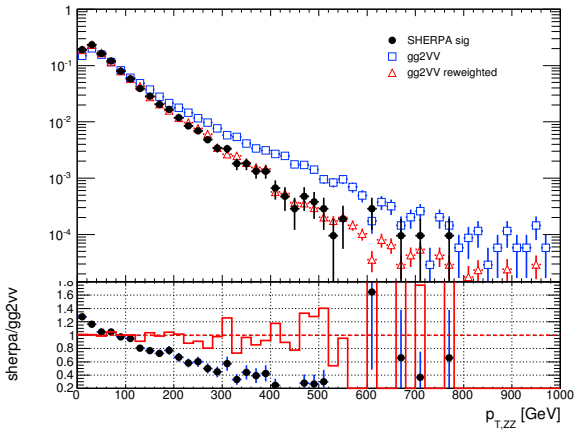

(a)

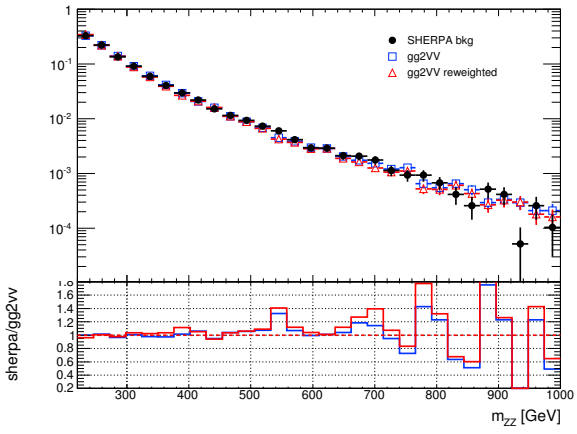

(b)

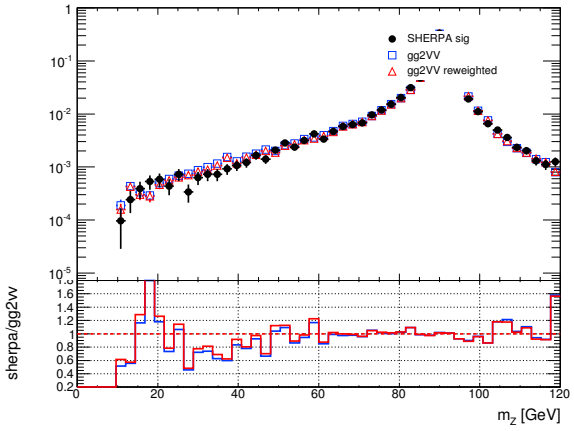

(c)

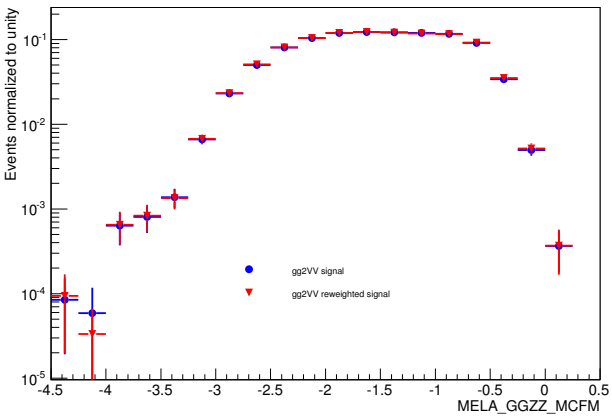

(d)

Figure 6.11: p_T(ZZ) (a), m_{4l} (b), m_Z (c) and ME (d) distribution before and after the SHERPA-based reweighting for the signal. The ratio plots with respect to gg2VV are also indicated.

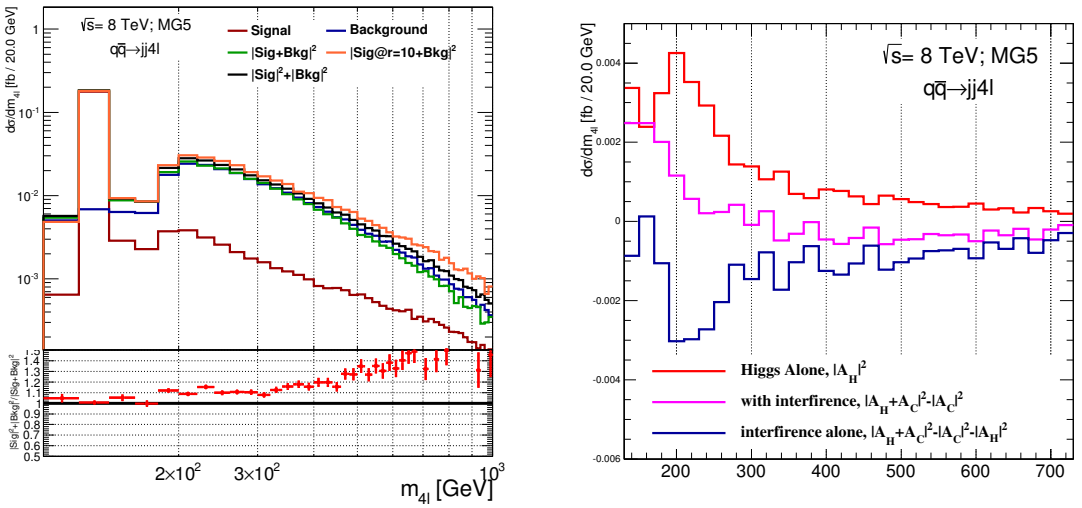

(a) **(b)**

Figure 6.12: (a) Differential cross sections for the VBF channel $q\bar{q} \to$ ZZ +2j at the matrix element level produced with MadGraph5-MCatNLO. (b) Comparison of the $q\bar{q} \to Hqq \to$ ZZ +2j signal process and its interference with the continuum $q\bar{q} \to$ ZZ +2j diagram.

- m_{ll} >20 GeV.

Figure 6.12 reports the m_{4l} distributions for the various $q\bar{q} \to$ ZZ+ 2j processes and the interference between signal and background. Figure 6.13 reproduces for validation purposes the m_{4l} spectrum comparison in shape and cross section between the two independent Monte Carlo samples MadGraph5-MCatNLO and PHANTOM for both the continuum and the total samples including Higgs and interference.

6.4 Monte Carlo simulation of the $q\bar{q} \to$ ZZ process

The $q\bar{q} \to$ ZZ background is simulated with POWHEG. Several details on the specific features used in the simulation can be found in Section 1.6.2. The theoretical uncertainties related to this process are summarised below:

- QCD scale systematic uncertainties;
- PDF scale uncertainties;
- electroweak NLO uncertainties.

The first two sources of systematic uncertainties have already been described in Section 1.6.2. A differential k-factor as a function of m_{ZZ} is computed [158] which can be directly applied to POWHEG NLO $q\bar{q} \to$ ZZ to match NNLO accuracy. This k-factor relies on the calculation of the NNLO $q\bar{q} \to$ ZZ process leading to a 6-8% increase in the $q\bar{q} \to$ ZZ cross section in the high mass region. The k-factor is produced for discrete m_{ZZ} mass points: the fitting function (Figure 6.14) for the m_{ZZ}-dependent k-factor is parametrised as follows:

$$K(m_{ZZ}) = 1.0113 + 0.000310203 \cdot m_{ZZ} - 9.2014 \cdot 10^{-8}(m_{ZZ}/GeV)^2. \quad (6.8)$$

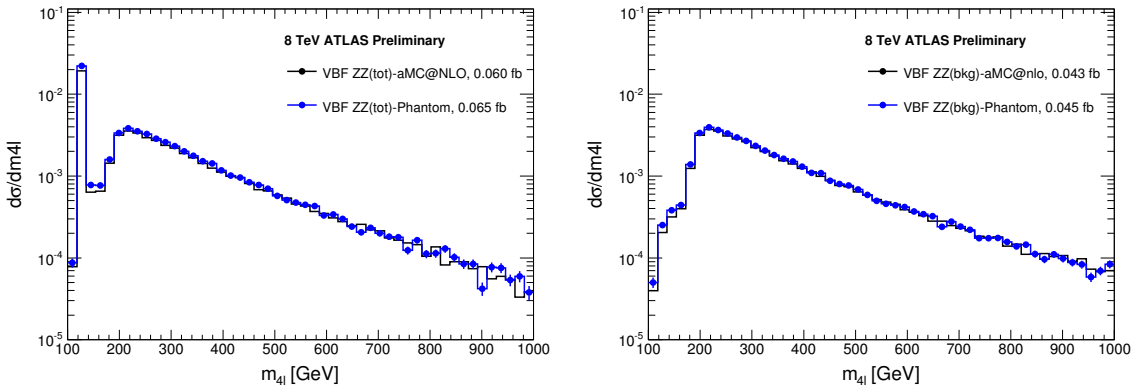

(a) **(b)**

Figure 6.13: Comparison of the m_{4l} distributions between MadGraph5-MCatNLO and PHANTOM for the SBI (a) and the continuum background (b) processes at the matrix element level.

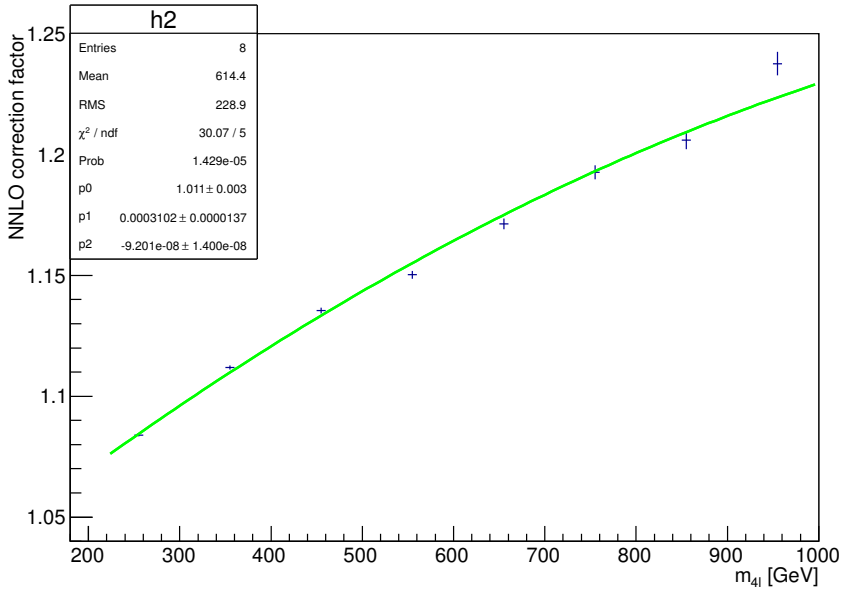

Figure 6.14: NNLO/NLO k-factor $K(m_{ZZ})$ for the $q\bar{q} \rightarrow$ ZZ process.

6.4.1 Electroweak NLO corrections

Higher order NLO electroweak corrections are not taken into account by POWHEG but are calculated in [159] [160] and found to be sizeable in the high VV mass region. The partonic production $q\bar{q} \to ZZ$ is at lowest order $\mathcal{O}(\alpha^2)$. To allow for consistent predictions with full $\mathcal{O}(\alpha^3)$ accuracy, virtual electroweak corrections as well as real corrections due to photon radiation have to be considered (Figure 6.15). On the other hand, the complete evaluation of the combined QCD and electroweak corrections, $\alpha\alpha_s$, is presently unavailable, hence this Section will be devoted to the computation of the EW term only. Worth remarking is that these contributions are not fully NNLO electroweak because they only account for *virtual* corrections. These corrections are added in the analysis by

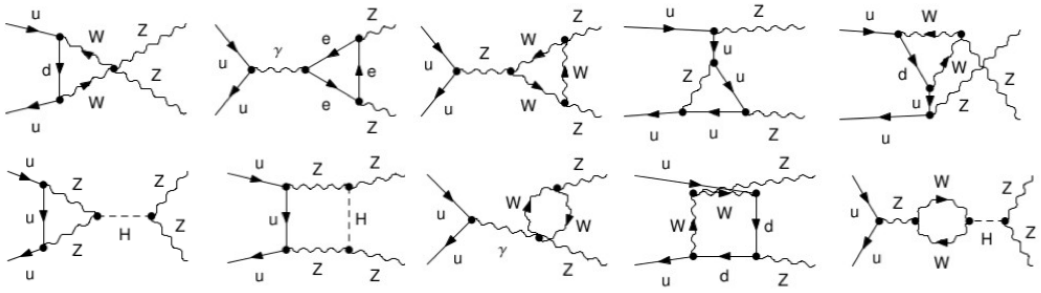

Figure 6.15: Examples of Feynman diagram for electroweak processes.

reweighting events generated with the POWHEG sample based on the particular kinematic of the diboson system. The corrections are only applicable above the diboson production threshold with both the vector bosons being on-shell. Since the analysis does not require a rigorous cut defining the diboson on-shell allowed kinematic region, corrections are applied to events with their first Z pair satisfying $|m_{ll} - m_Z^{PDG}|$ <25 GeV. Anyhow, the events with off-shell bosons amount to $\sim 0.02\%$ of the total.
A complication in the domain of the EW corrections applicability is the large theoretical uncertainty in the calculation in presence of high-QCD activity. In this topology, an additional systematic uncertainty is considered as the (NLO QCD) $\times$ (NLO EW) corrections are still unknown [159]. As for events with low QCD activity, the weights are applied without the additional uncertainty. In order to select the two QCD regions, the variable [161] ρ is defined as:

$$\rho = \frac{\left(|\sum_i \vec{l}_{i,T} + \vec{p}_T^{miss}|\right)}{\left(\sum_i |\vec{l}_{i,T}| + |\vec{p}_T^{miss}|\right)} \tag{6.9}$$

The definition (6.9) is adopted in order to make sure that the gauge-boson pairs or their decay products, the four leptons in the final state, are not produced with too much transverse momentum originated from the recoil against a system of strongly interacting particles. The index i in the sum runs to 2, 3 and 4. An additional assumption is made on the missing transverse momentum of the event: it solely stems from neutrinos originated from W decays. The numerator of (6.9) is small whenever the system has a small transverse momentum provided that the leptons recoil against each other in the transverse plane, thence, no extra QCD activity is detected. The term in the denominator works as a normalisation factor. A cut on ρ at 0.3 selects the portion of events characterised by low QCD activity where the corrections can be applied without any farther systematics. This fraction is approximately 100% in the 0-jet final state, 70% in the 1-jet final state and 42% in the 2-jet final state. Figure 6.16 illustrates the distributions of the key variables of

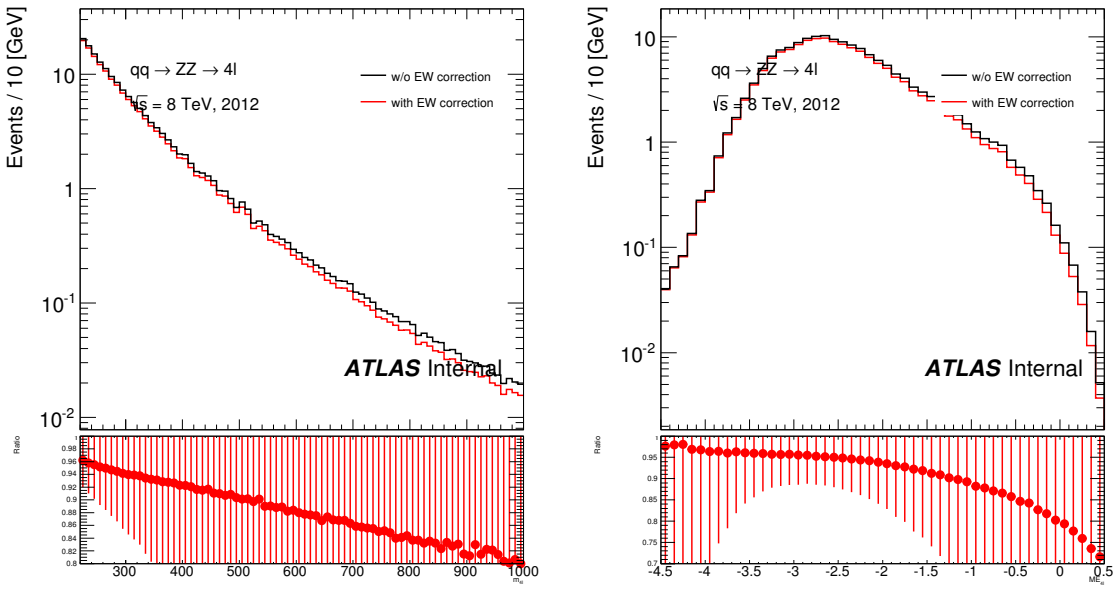

(a) **(b)**

Figure 6.16: Comparison of the m_{4l} (a) and ME (b) distributions with and without the EW corrections in place. The ratio of the distributions reweighted to account for EW corrections with respect to the configuration without EW corrections is also displayed.

the analysis, m_{4l} and the ME-based discriminant, for the background process $q\bar{q} \rightarrow$ ZZ with and without EW corrections in place. The correction increases with the mass, at m_{4l}=350 GeV, its weight is $\sim$ 10%, at m_{4l}=400 GeV, 20%; however if integrated over the full m_{4l} mass spectrum, its impact accounts for approximately 6%.

6.5 Analysis strategy in the ZZ→ 4l final state

The analysis in the ZZ→ 4l final state is identical to the one for the Higgs mass extraction detailed in Chapter 5. The event selection is identical but it is applied in the off-peak region, (220< m_{4l} <1000) GeV. As there are no explicit kinematic requirements or cuts on the number of jets, the analysis is inclusive in the jet multiplicity. In this regard, Section 6.2.2, specifically Figure 6.5 for the 4l channel and Figure 6.6 for the 2l2ν decay mode, have presented an overview on the extended checks performed on the residual QCD impact on the analysis. The study is split into 4 lepton final states (4e, 4μ, 2e2μ and 2μ2e) as in Chapter 5.
The final limit on the off-shell coupling, $\mu_{\text{off-shell}}$ is extracted with a shape-based approach based on a matrix element kinematic discriminant (Section 6.6) that enhances the sensitivity of the measurement. A BDT discriminant that exploits the full kinematic information in the ZZ decay system through the usage of p_T^{ZZ} and η^{ZZ}, is also developed in Section 6.7.
As a cross-check of the main analysis, a *cut-and-count* procedure is executed; details will be discussed in Section 6.10.1. Table 6.1 charts the expected number of events for signal, background and SBI corresponding to the distributions in Figure 6.17. The dominant background in the off-peak region is the *irreducible* $q\bar{q} \rightarrow$ ZZ, whereas the contribution of the *reducible* background, like Z+jets, top and the double parton interaction (DPI), is negligible and will not be included in the analysis.

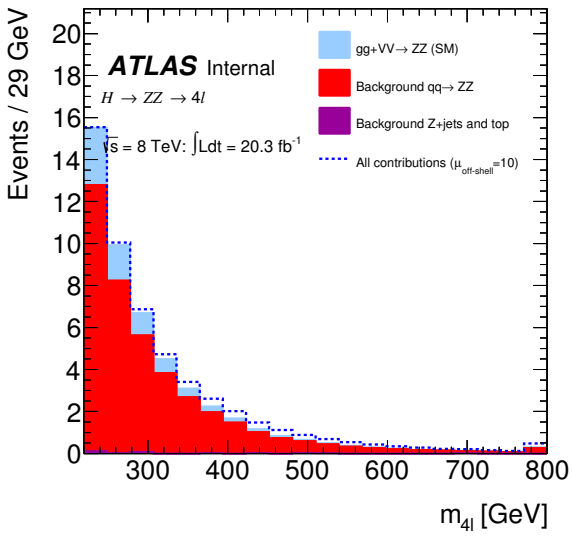

(a) 2e2μ

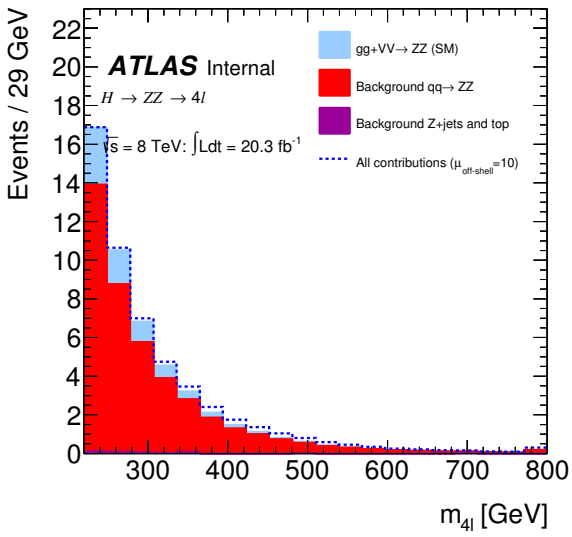

(b) 2μ 2e

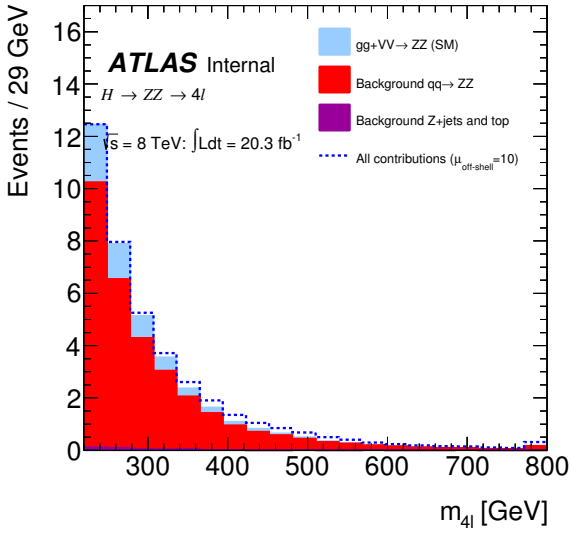

(c) 4e

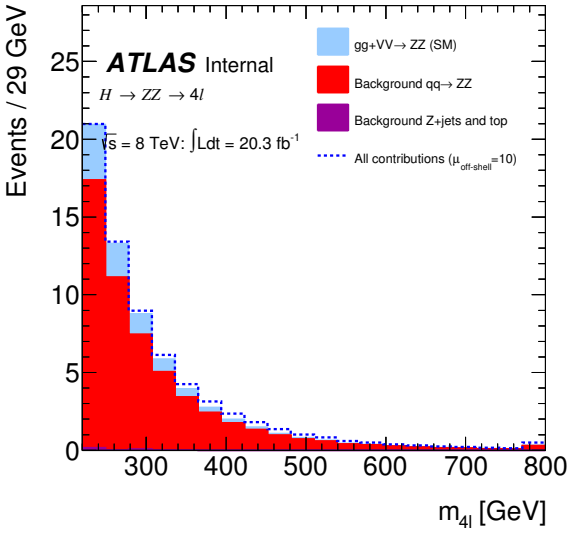

(d) 4μ

Figure 6.17: Distributions of the m_{4l} for the four different lepton final states after the baseline off-peak selections, for all signal and background processes. The last bin comprises the overflow.

	$2\mu2e$	$2e2\mu$	4μ	4e	Total
$gg \to H^* \to ZZ$ (S)	0.48 ± 0.11	0.60 ± 0.14	0.62 ± 0.14	0.45 ± 0.10	2.2 ± 0.5
$gg \to ZZ$ (B)	7.64 ± 1.74	7.57 ± 1.73	9.50 ± 2.17	5.94 ± 1.36	30.7 ± 7.0
$gg \to (H^*) \to ZZ$	7.32 ± 1.67	7.17 ± 1.64	9.05 ± 2.07	5.69 ± 1.30	29.2 ± 6.7
$gg \to (H^*) \to ZZ$ ($\mu_{\text{off-shell}} = 10$)	9.73 ± 2.22	10.3 ± 2.4	12.2 ± 2.8	7.95 ± 1.81	40.2 ± 9.2
VBF $H^* \to ZZ$ (S)	0.04 ± 0.00	0.05 ± 0.01	0.06 ± 0.01	0.05 ± 0.00	0.2 ± 0.0
VBF ZZ (B)	0.51 ± 0.03	0.56 ± 0.03	0.66 ± 0.03	0.44 ± 0.02	2.2 ± 0.1
VBF ZZ (S+B+I)	0.48 ± 0.03	0.53 ± 0.03	0.60 ± 0.03	0.40 ± 0.02	2.0 ± 0.1
VBF ZZ (S+B+I, $\mu_{\text{off-shell}} = 10$)	0.69 ± 0.04	0.79 ± 0.04	0.91 ± 0.05	0.61 ± 0.03	3.0 ± 0.2
$q\bar{q} \to ZZ$	42.0 ± 3.3	40.7 ± 3.2	53.8 ± 4.2	31.3 ± 2.5	167.9 ± 13.1
Reducible backgrounds	0.38 ± 0.06	0.30 ± 0.06	0.32 ± 0.06	0.38 ± 0.06	1.4 ± 0.1
Total Expected (SM)	50.1 ± 3.7	48.7 ± 3.6	63.8 ± 4.7	37.8 ± 2.8	200.5 ± 14.7

Table 6.1: Expected number of events for the ZZ→ 4l channel for all processes. The $gg \to ZZ$ (S+B+I) process with $\mu_{\text{off-shell}} = 10$ is created for illustration. Both statistical and systematic uncertainties are included.

6.6 Matrix element-based kinematic discriminant

It is important to extend the analysis for the off-shell coupling measurement beyond the simple cut-and-count approach. In order to enhance the sensitivity of the $gg \to$ H $\to$ ZZ production in the

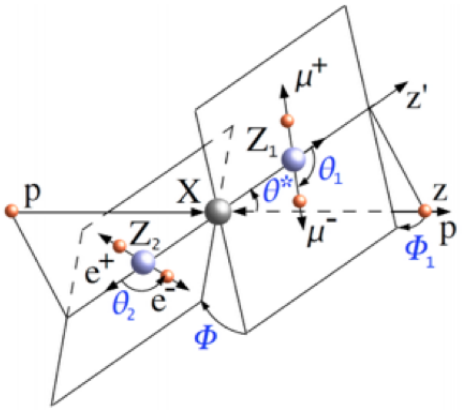

Figure 6.18: Definition of the angles used as input variables of the ME-based discriminant.

off-shell region, a matrix element-based discriminant is exploited [138] by assigning to each event a probabilistic weight associated with a given hypothesis.
This discriminant accesses the event kinematics at the centre-of-mass reference frame of the ZZ system and it is constructed on eight observables whose distributions, produced in the SM hypothesis ($\mu_{\text{off-shell}} = 1$) and generated at $\mu_{\text{off-shell}}$=10, are reported in Figure 6.19:

- m_{4l} is the invariant mass of the 4 lepton system;
- m_{Z1}, m_{Z2} represent the invariant mass of the first and second Z pairs respectively. The lepton association to the first and second Z boson is detailed in Chapter 5.
- $\cos\theta_1$, $\cos\theta_2$, the angles between the negative leptons and the direction of flight of their respective Z bosons in the Z rest frame, $\cos\theta^*$, the production angle of the Z boson in the

4l rest frame and ϕ_1, the angle between the decay plane of the first lepton pair and a plane defined by the vector of the Z_1 in the 4l rest frame with respect to the positive direction of the collision axis, are sketched in Figure 6.18.

The matrix element discriminant is therefore calculated from the above variables and is determined by the MCFM program [138]. For each event, the following matrix elements are computed:

i $P_{q\bar{q}}$: matrix element for the dominant $q\bar{q} \to \text{ZZ} \to 4\text{l}$ process;

ii P_{gg}: matrix element for the $gg \to \text{ZZ}$ and $gg \to \text{H} \to 4\text{l}$ processes including both the continuum background, the signal at m_H=125.5 GeV with SM couplings as well as the signal-background interference;

iii P_H: matrix-element for the gluon gluon fusion-mediated Higgs production process, i.e. $gg \to H^* \to 4\text{l}$ where m_H=125.5 GeV.

The following formula is calculated for each event:

$$ME = \log_{10} \frac{P_H}{P_{gg} + c \cdot P_{q\bar{q}}} \tag{6.10}$$

where c is a numerical global constant that approximately balances the overall cross sections of the $q\bar{q}$ and gg-related processes. Its nominal value is 0.1 and it is found that the sensitivity of the measurement is independent (less than 1%) on the value of c spanning in the interval 0.05-1. Figure 6.20 displays the ME distributions in the various channels for the off-shell region (220< m_{4l} <1000) GeV. The ME is limited to the interval [-4.5,0.5] for fitting reasons and the contribution of discarded events is less than $\sim$ 1%. Figure 6.21 illustrates the two-dimensional distribution of the ME discriminant compared to m_{4l}, the most discriminating variable among the ones comprising the ME definition (6.10), for signal and $q\bar{q}$-produced background. This 2D map indicates a strong correlation between the two variables. Section 6.10.3 will cover the analysis results when exploiting the matrix element-based discriminant.

6.7 BDT-based kinematic discriminant

In addition to the matrix element approach detailed in Section 6.6, a *boosted-decision-tree* (BDT) - based MVA method [118] is also exploited to improve the separation between the signal $gg \to H^* \to$ ZZ and the dominant $q\bar{q} \to$ ZZ background. This algorithm is based on the matrix element discriminant (Section 6.6), together with the ZZ system p_T(ZZ), η(ZZ) that depend on the production modes.

Figure 6.22 illustrates the shape comparison of the ZZ system p_T and η for the various contributions to the analysis, namely signal, qq-background, signal background and interference, $gg \to (H^*) \to$ ZZ, computed in the SM scenario ($\mu_{\text{off-shell}}$=1) and for a modified off-shell value ($\mu_{\text{off-shell}}$=10).

The signal sample used in the BDT training is the $gg \to H^* \to$ ZZ (m_H=125.5) process and the background sample is the dominant $q\bar{q} \to$ ZZ contribution. The training of the method is performed with a cut at m_{4l} >220 GeV and different trainings are computed for the various decay channels.
Additionally, a closure test is carried out on the BDT response when including the matrix-element input variable only: the signal *vs* background separation sensitivity coincides with the matrix-element-only case.

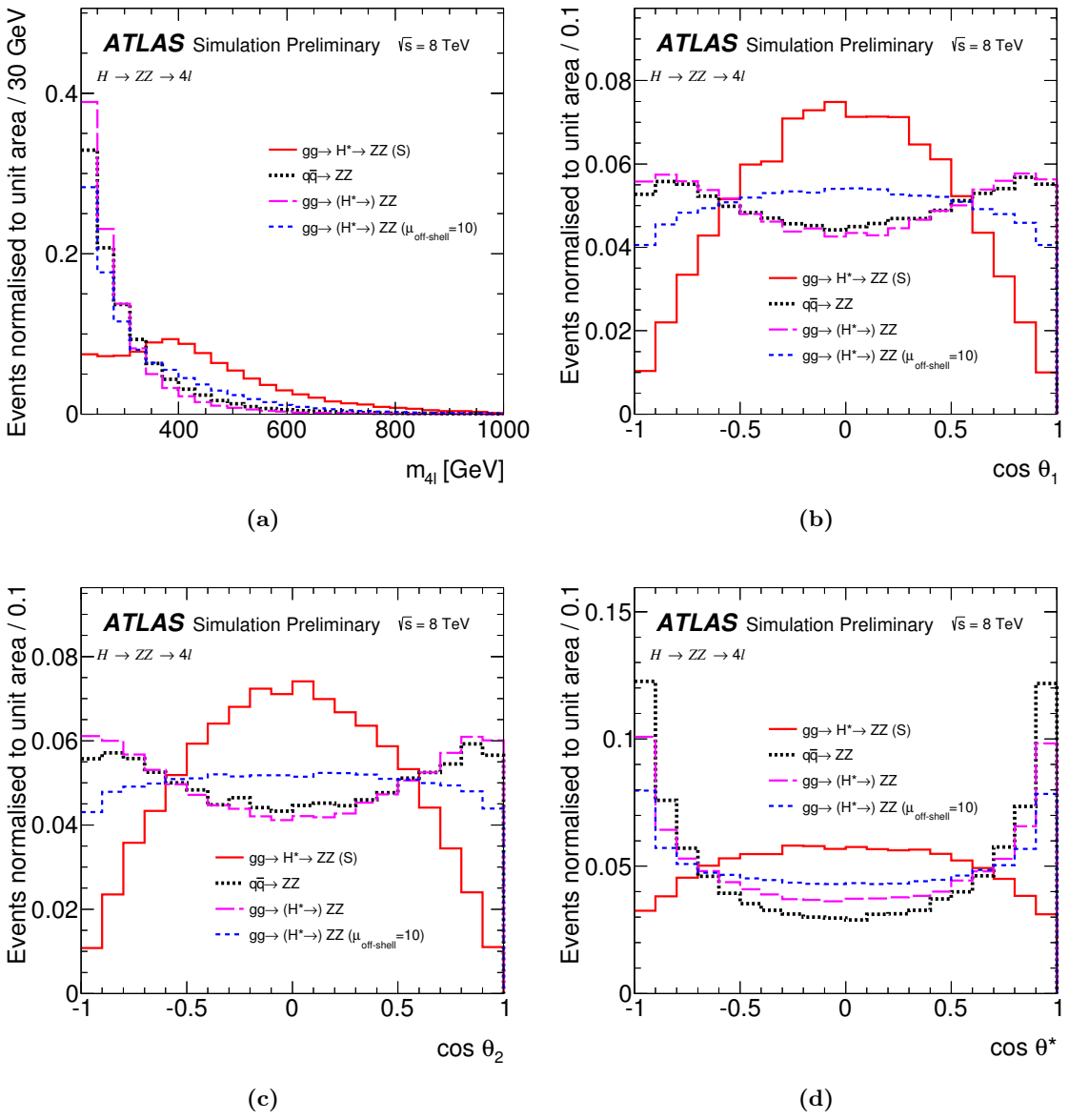

Figure 6.19: Histograms of the key input variables, m_{4l} (a), $\cos\theta_1$ (b), $\cos\theta_2$ (c) and $\cos\theta^*$ (d) to the ME-based discriminant for the $H \to$ ZZ $\to$ 4l where all the leptons in the final state are combined. The histograms are normalised to unit area for the off-shell region, i.e. (220$< m_{4l} <$1000) GeV. The red solid line coincides with the $gg \to H^* \to$ 4l signal with SM couplings, the magenta dashed line the $gg \to (H^*) \to$ 4l contribution (signal + background + interference) generated with SM $\mu_{\text{off-shell}}$, the blue dashed line is $gg \to (H^*) \to$ 4l with $\mu_{\text{off-shell}}$=10 and the black dotted line represents the $q\bar{q} \to$ ZZ background.

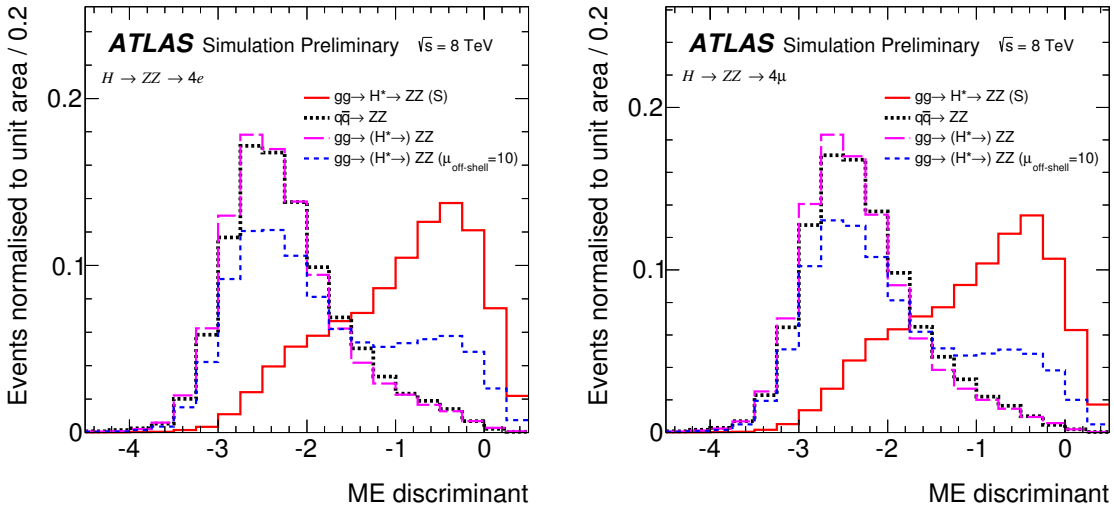

(a) ME 4e channel

(b) ME 4μ channel

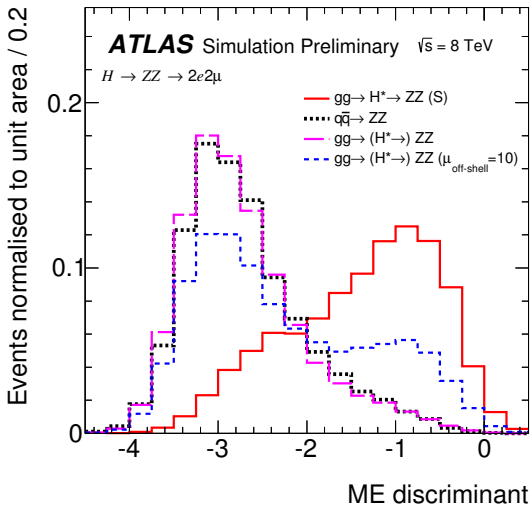

(c) ME 2e2μ channel

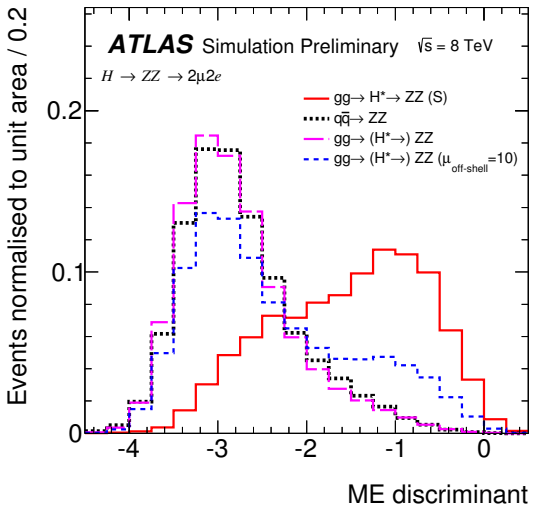

(d) ME 2μ2e channel

Figure 6.20: Distributions of the ME-based kinematic discriminant in the four lepton final states (4e, 4μ, 2e2μ and 2μ2e) normalised to unit area for shape comparison in the off-peak region ($220 < m_{4l} < 1000$) GeV. The red solid line coincides with the $gg \to H^* \to 4l$ signal with SM couplings, the magenta dashed line the $gg \to (H^*) \to 4l$ contribution (signal + background + interference) generated with SM $\mu_{\text{off-shell}}$, the blue dashed line is $gg \to (H^*) \to 4l$ with $\mu_{\text{off-shell}}=10$ and the black dotted line reproduces the $q\bar{q} \to ZZ$ background.

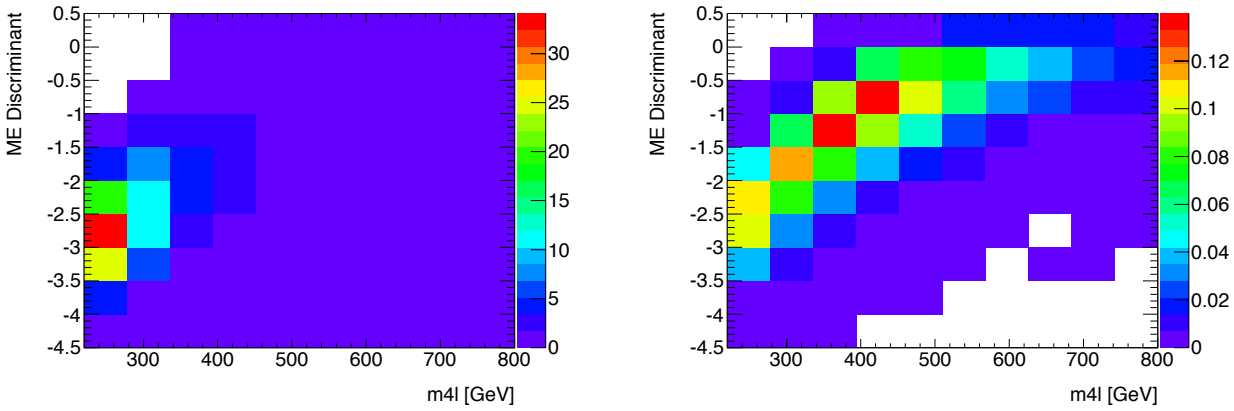

(a) **(b)**

Figure 6.21: Two-dimensional map of the ME discriminant *vs* m_{4l} in the off-peak region (220< m_{4l} <1000) GeV for the $gg \to H^* \to 4\text{l}$ (a) signal and the $q\bar{q}$ background (b).

Figure 6.23 (a) displays the response of the BDT-based MVA approach for signal and background and the signal efficiency *vs* the background rejection of the method (b). The sample is randomly divided into two halves: one of each is the training sample, the other represents the test sample and the MVA procedure is applied on both. The number of trees in the training is tuned to 1000 to avoid over-training, hence, the distributions of training and test samples in Figure 6.23, are compatible. This is also testified by the Kolmogorov-Smirnov test [162] performed on the training and test distributions. Figure 6.24 provides the shape comparison of the BDT-based discriminant for the key processes in the four final states whilst Figure 6.25 reports the strong correlation between the matrix element discriminant and the BDT output.
As for Section 6.10.3 for the ME case, Section 6.10.4 will be devoted to the description of the analysis results when employing the BDT-based discriminant.

6.8 Scaling of the signal strength in the model

A sample $\text{MC}_{gg\to(H^*)\to ZZ}$ for the $gg \to (H^*) \to \text{ZZ}$ process with an arbitrary value of the off-shell Higgs signal strength $\mu_{\text{off-shell}}$ can be constructed from:

i a pure SM Higgs $gg \to H^* \to ZZ$ signal Monte Carlo sample ($\text{MC}^{\text{SM}}_{gg\to H^*\to ZZ}$);

ii a pure $gg \to ZZ$ continuum background Monte Carlo sample ($\text{MC}^{\text{cont}}_{gg\to ZZ}$);

iii a full SM Higgs signal plus background plus interference (SBI) $gg \to (H^*) \to ZZ$ Monte Carlo sample ($\text{MC}^{\text{SM}}_{gg\to(H^*)\to ZZ}$);

by applying the following parametrisation:

$$\begin{aligned} \text{MC}_{gg\to(H^*)\to ZZ}(\mu_{\text{off-shell}}) &= K^{H*}(m_{ZZ}) \cdot \mu_{\text{off-shell}} \cdot \text{MC}^{\text{SM}}_{gg\to H^*\to ZZ} \\ &+ K^{H^*}(m_{ZZ}) \cdot \sqrt{R^B_{H^*} \cdot \mu_{\text{off-shell}}} \cdot \text{MC}^{\text{Interference}}_{gg\to ZZ} \\ &+ K^{H^*}(m_{ZZ}) \cdot R^B_{H^*} \cdot \text{MC}^{\text{cont}}_{gg\to ZZ} \end{aligned} \tag{6.11}$$

$$\text{MC}^{\text{Interference}}_{gg\to ZZ} = \text{MC}^{\text{SM}}_{gg\to(H^*)\to ZZ} - \text{MC}^{\text{SM}}_{gg\to H^*\to ZZ} - \text{MC}^{\text{cont}}_{gg\to ZZ}, \tag{6.12}$$

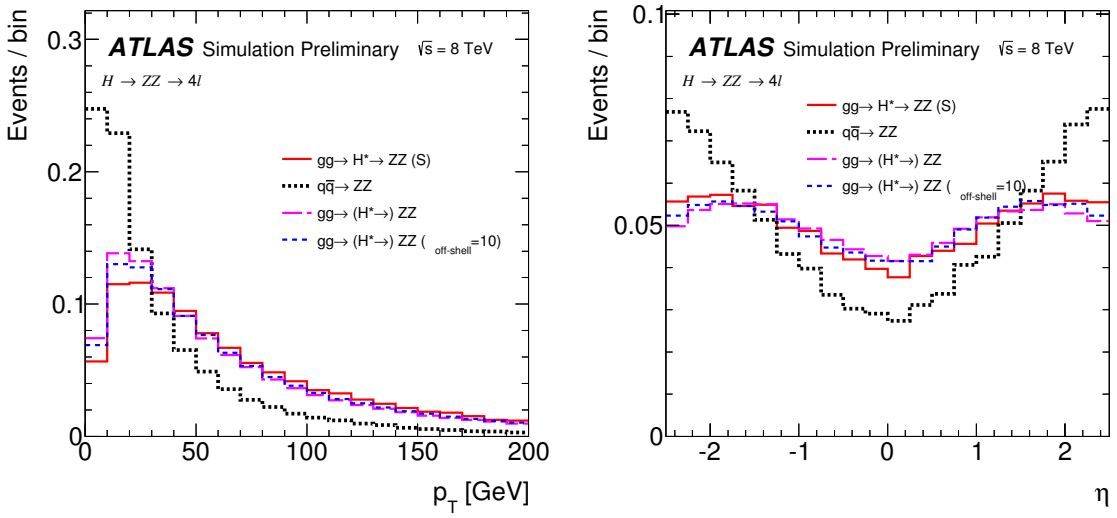

(a) **(b)**

Figure 6.22: Distributions of the ZZ→ 4l system p_T and η, for all lepton final states combined, normalised to unit area for shape comparisons, for the full off-peak region, (220< m_{4l} <1000) GeV. The thick black dotted line represents the $q\bar{q} \to$ ZZ background, the red solid line the $gg \to H^* \to$ 4l signal with SM couplings, the magenta long-dashed line the $gg \to (H^*) \to$ ZZ (signal, background and interference) with SM $\mu_{\text{off-shell}}$, and the blue dashed line is for the same contribution but with $\mu_{\text{off-shell}}$=10.

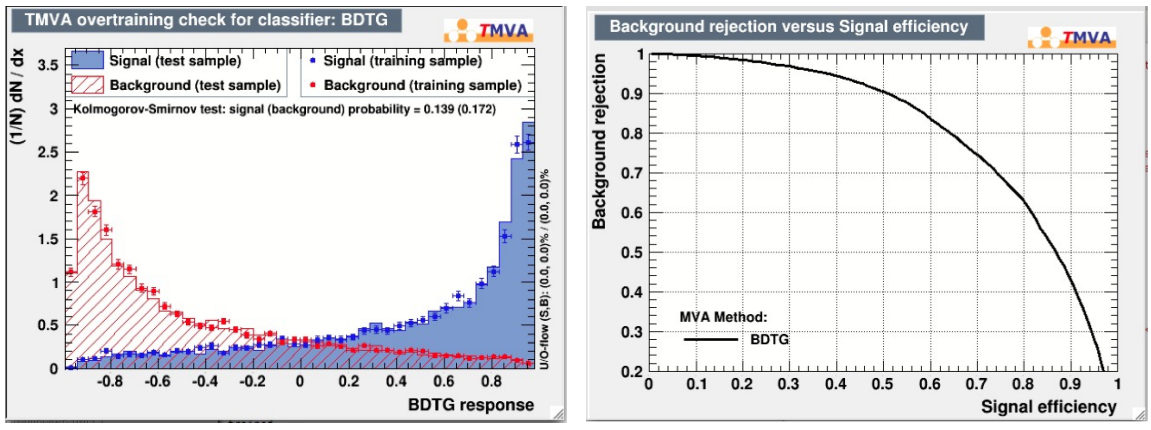

(a) **(b)**

Figure 6.23: Distribution of the BDT output for signal ($gg \to H^* \to$ ZZ) and background ($q\bar{q} \to$ ZZ) for training and test samples (a). Signal efficiency *vs* background rejection of the BDT method (b).

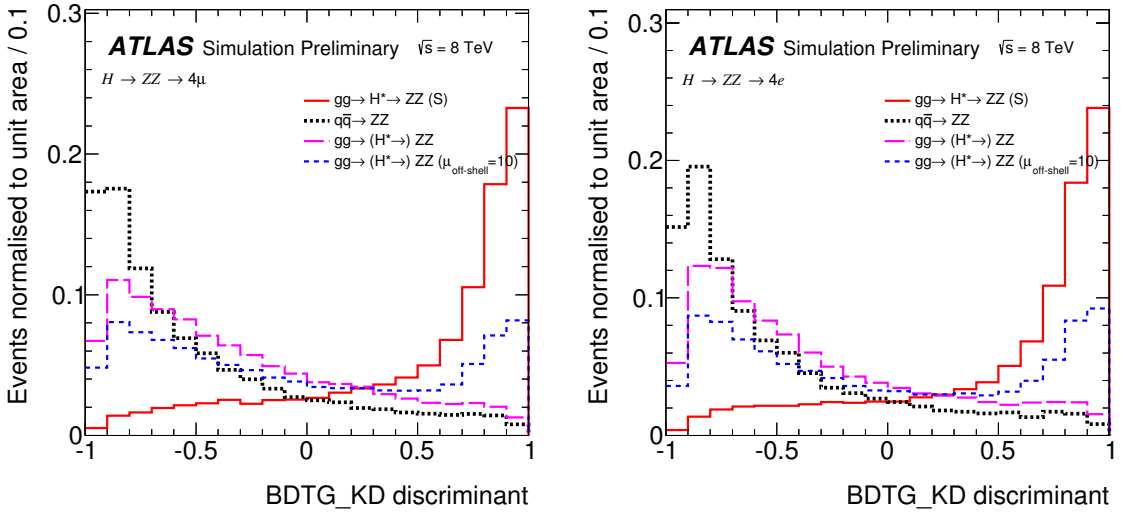

(a) 4μ

(b) 4e

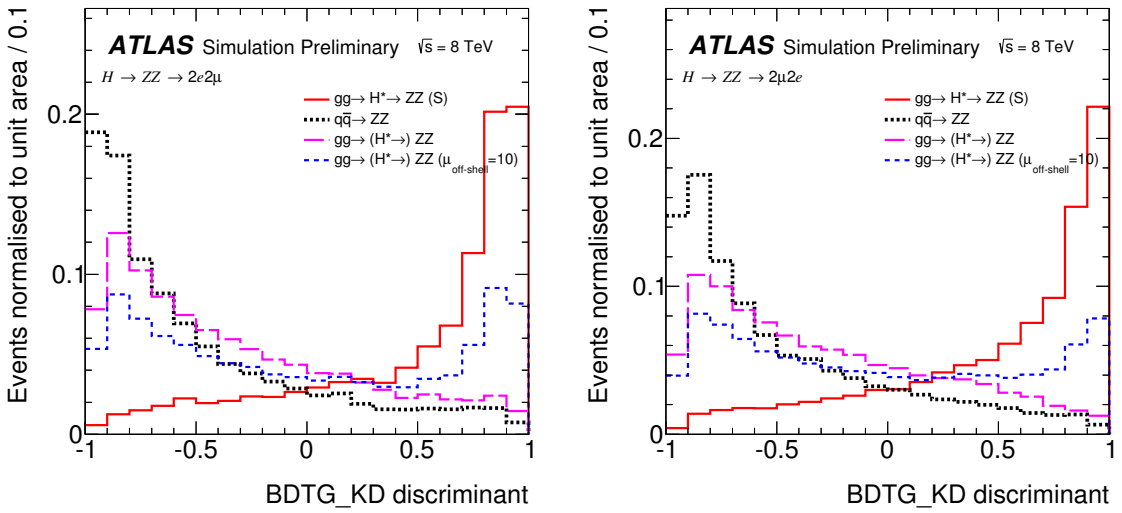

(c) $2e2\mu$

(d) 2μ2e

Figure 6.24: Distributions of the BDT-based discriminant in the four lepton final states normalised to unit area to show the shape comparisons, for the full off-peak region, (220< m_{4l} <1000) GeV. The thick black dotted line reproduces the $q\bar{q} \to$ ZZ background, the red solid line the $gg \to H^* \to$ 4l signal with SM couplings, the magenta long-dashed line the $gg \to (H^*) \to$ ZZ (signal, background and interference) with SM $\mu_{\text{off-shell}}$, and the blue dashed line is for the same contribution but with $\mu_{\text{off-shell}}$=10.

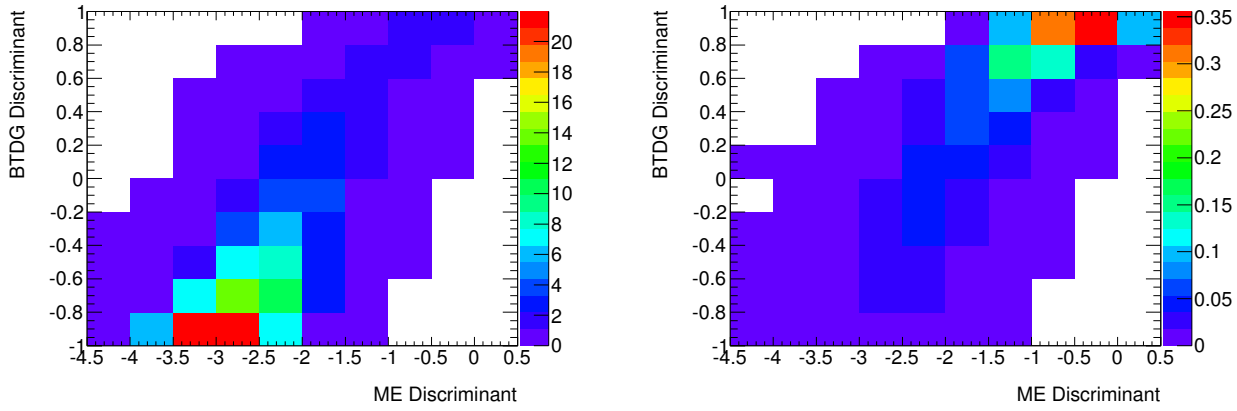

(a) **(b)**

Figure 6.25: Distributions of the BDT discriminant against the matrix element-based response for $gg \to H \to \mathrm{ZZ}$ (a) and $q\bar{q} \to \mathrm{ZZ}$ (b).

where $\mathrm{MC}^{\mathrm{Interference}}_{gg\to ZZ}$ represents a Monte Carlo sample for the interference term between signal and background; $K^{H^*}(m_{ZZ})$ and $R^B_{H^*}$ coincide respectively with the signal and the background-to-signal ratio k-factors introduced in Sections 6.1 and 6.2.1. Since a direct simulation of an interference Monte Carlo sample is not possible, (6.12) is replaced into the previous equation to obtain a parametrisation that is not directly dependent on the interference contribution:

$$\begin{aligned}\mathrm{MC}_{gg\to(H^*)\to ZZ}(\mu_{\text{off-shell}}) &= \left(K^{H^*}(m_{ZZ})\cdot\mu_{\text{off-shell}} - K^{H^*}_{gg}(m_{ZZ})\cdot\sqrt{R^B_{H^*}\cdot\mu_{\text{off-shell}}}\right)\cdot\mathrm{MC}^{\mathrm{SM}}_{gg\to H^*\to ZZ} \\ &+ K^{H^*}_{gg}(m_{ZZ})\cdot\sqrt{R^B_{H^*}\cdot\mu_{\text{off-shell}}}\cdot\mathrm{MC}^{\mathrm{SM}}_{gg\to(H^*)\to ZZ} \\ &+ K^{H^*}_{gg}(m_{ZZ})\cdot\left(R^B_{H^*} - \sqrt{R^B_{H^*}\cdot\mu_{\text{off-shell}}}\right)\cdot\mathrm{MC}^{\mathrm{cont}}_{gg\to ZZ}.\end{aligned} \tag{6.13}$$

A Monte Carlo event sample for the $pp \to \mathrm{ZZ} + 2\mathrm{j}$ process with an arbitrary value of the off-shell Higgs signal strength $\mu_{\text{off-shell}}$ can be extracted from:

i $pp \to \mathrm{ZZ} + 2\mathrm{j}$ continuum background Monte Carlo, $\mathrm{MC}^{\mathrm{cont}}_{pp\to ZZ+2j}$;

ii a full SM Higgs signal plus background $pp \to \mathrm{ZZ} + 2\mathrm{j}$ Monte Carlo, $\mathrm{MC}^{\mathrm{SM}}_{pp\to(H^*+2j)\to ZZ+2j}$;

iii a Higgs signal plus background $pp \to \mathrm{ZZ} + 2\mathrm{j}$ Monte Carlo sample with Higgs couplings and total width set to $\mu_{\text{off-shell}} = \kappa_V^4 = \frac{\Gamma_H}{\Gamma_{SM}}$=10, $\mathrm{MC}^{\kappa_V^4=10}_{pp\to(H^*+2j)\to ZZ+2j}$.

The following function is employed to produce Monte Carlo samples $pp \to ZZ + 2j$ for any given $\mu_{\text{off-shell}}$:

$$\begin{aligned}\mathrm{MC}_{pp\to(H^*+2j)\to ZZ+2j}(\mu_{\text{off-shell}}) &= \frac{\mu_{\text{off-shell}} - \sqrt{\mu_{\text{off-shell}}}}{10-\sqrt{10}}\mathrm{MC}^{\kappa_V^4=10}_{pp\to(H^*+2j)\to ZZ+2j} \\ &+ \frac{10\sqrt{\mu_{\text{off-shell}}} - \sqrt{10}\mu_{\text{off-shell}}}{10-\sqrt{10}}\mathrm{MC}^{\mathrm{SM}}_{pp\to(H^*+2j)\to ZZ+2j} \\ &+ \frac{(\sqrt{\mu_{\text{off-shell}}}-1)\cdot(\sqrt{\mu_{\text{off-shell}}}-\sqrt{10})}{\sqrt{10}}\mathrm{MC}^{\mathrm{cont}}_{pp\to ZZ+2j}.\end{aligned} \tag{6.14}$$

6.9 Systematic uncertainties

6.9.1 Inclusive theoretical uncertainty

The dominant theoretical uncertainties in the 4 lepton analysis are expressed below:

- EW correction uncertainty on $q\bar{q} \rightarrow$ ZZ;
- QCD and PDF scale uncertainties on $q\bar{q} \rightarrow$ ZZ, gg-initiated signal, continuum background and SBI.

A discussion on the source of these uncertainties is reported in Sections 6.2 and 6.4.

Figures 6.26 and 6.27 shows the up and down variations of the ME outputs in the 4e channel for the $gg \rightarrow H^* \rightarrow$ ZZ and $q\bar{q} \rightarrow$ ZZ processes using the systematic uncertainties above.
The gg-initiated contributions (signal, continuum background and SBI) are dominated by the higher order QCD systematics (Figure 6.26 (a)) concurring to an approximate difference between the central shape and the variations of 23%. In addition, a shape dependency is present. Likewise, Figure 6.26 (b) indicates the impact of the PDF systematic uncertainties on the gg initial states, accounting for a $\sim$ 13% difference in normalisation and with a mild shape dependency as well. These two uncertainties are applied both as shape and normalisation systematics to the SBI, signal and continuum samples in full correlation.

The systematic uncertainties on the $q\bar{q} \rightarrow$ ZZ background focused in Section 1.6.2 are dominated by the PDF systematics displayed in Figure 6.26 (c) and the higher order QCD corrections in Figure 6.26 (d). Finally, Figure 6.27 indicates the systematic uncertainties due to the higher order EW corrections (Section 6.4) on $q\bar{q} \rightarrow$ ZZ characterised by a shape dependency in the ME spectrum and a small normalisation contribution ($\sim$ 1.3%).

6.9.2 Additional theory systematics for the BDT

In order to adopt the BDT-based discriminant detailed in Section 6.7, additional systematic uncertainties have to be included. As the ZZ system-related variables p_T and η are used as inputs to the BDT algorithm, extra uncertainties on the treatment of higher-order QCD effects are included in the modelling. The uncertainties on the normalisation of the templates for the fit are already added in Section 6.9.1, hence in this Section only shape-related systematics are studied.
In order to evaluate the systematic effects on the uncertainties on p_T and η in the ZZ frame, the procedure reported in [29] is applied by varying the renormalisation scale (μ_R), the factorisation scale (μ_F), the resummation scale (μ_Q) and the resummation scale related to the bottom quark mass (μ_B) [163].

The impact of the PDF uncertainties is also indicated in Figure 6.28. The nominal PDF set, CT10 [150], applied on the POWHEG signal sample at m_H=125.5 GeV are compared with MSTW2008 [27] and with NNPDF2.3 [28] in bins of ZZ-transverse momentum and rapidity. As emphasised by the ratio plot in Figure 6.28, the impact of this uncertainty is found to be negligible and is consequently not included in the final list of the systematic effects affecting the BDT discriminant.

The points of the procedure are summarised below

- Beyond NLO effects are evaluated with HRES [54] (NNLO+NNLL generator) for the signal process $gg \rightarrow H \rightarrow$ ZZ generated at m_H=380 GeV;

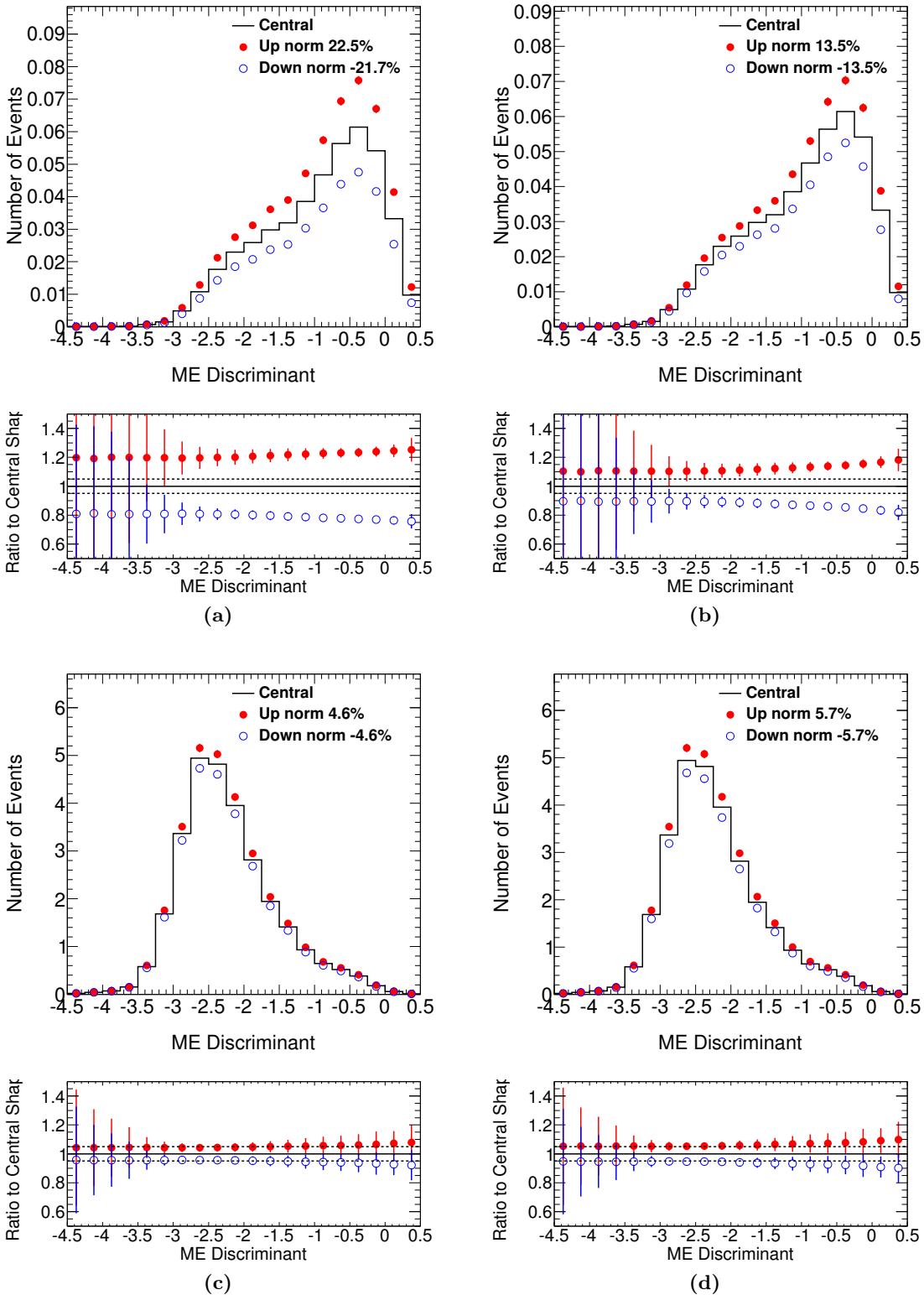

Figure 6.26: QCD scale systematic uncertainties on $gg \to H^* \to ZZ$ (a) and on $q\bar{q} \to ZZ$ (c) processes. PDF systematic uncertainties on $gg \to H^* \to ZZ$ (b) and $q\bar{q} \to ZZ$ (d) states. These systematics are evaluated on the ME discriminant shape. The ratio plots of the scale variations to the central shape are also plotted.

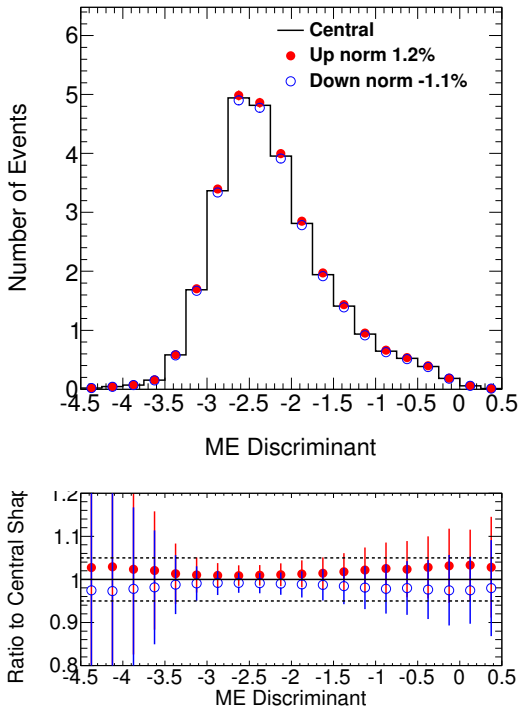

Figure 6.27: EW correction systematic uncertainties on the $q\bar{q} \rightarrow$ ZZ process evaluated on the ME discriminant shape. The ratio plot of the scale variations to the central shape is placed underneath the figure.

- NLO effects are addressed with SHERPA [164] (LO + 0 and 1 jet merged generator) for the signal process $gg \rightarrow H \rightarrow$ ZZ generated at m_H=380 GeV and the continuum background $gg \rightarrow$ ZZ;
- NLO effects for the $q\bar{q} \rightarrow$ ZZ dominant background are examined using POWHEG (NLO generator).

It is also assumed that the uncertainty of the gg$\rightarrow$ ZZ background is the same as the one of the interference between signal and gg-initiated background.

The Monte Carlo simulations employed for these studies are summarised below and the full scheme of scale variations applied to these samples are listed in Table 6.2. Assuming that the resummation scales (μ_Q and μ_B) variations are independent of the normalisation and factorisation scales (μ_R and μ_F), we fix the vector pair (μ_R, μ_F) while varying μ_Q or μ_B. Similarly we fix the resummation scales, μ_Q and μ_B, while varying μ_R and μ_F. Following the usual prescriptions [29], the nominal scale of the process is set to $\frac{m_{ZZ}}{2}$ aside from the nominal value for the resummation scale related to the bottom mass that is set to m_b and the POWHEG nominal values for renormalisation and factorisation scales that are calculated at m_{ZZ}.

Figure 6.29 shows the shape-only variations on p_T(ZZ) and Y(ZZ) for a high mass m_H=380 GeV $gg \rightarrow H \rightarrow$ ZZ signal process produced by QCD scale variations evaluated with the HRES Monte Carlo generator. The scale variations on the rapidity in Figure 6.29 (b) are neglected since they are much smaller than the one of the transverse momentum, Figure 6.29 (a). Figure 6.30 shows the variation of the signal process (a) and the background processes on p_T (ZZ) created with the SHERPA Monte Carlo sample. The envelope of these independent variations on p_T(ZZ), calculated as the maximal up and down contribution for each p_T bin is illustrated in Figure 6.31 for the HRES

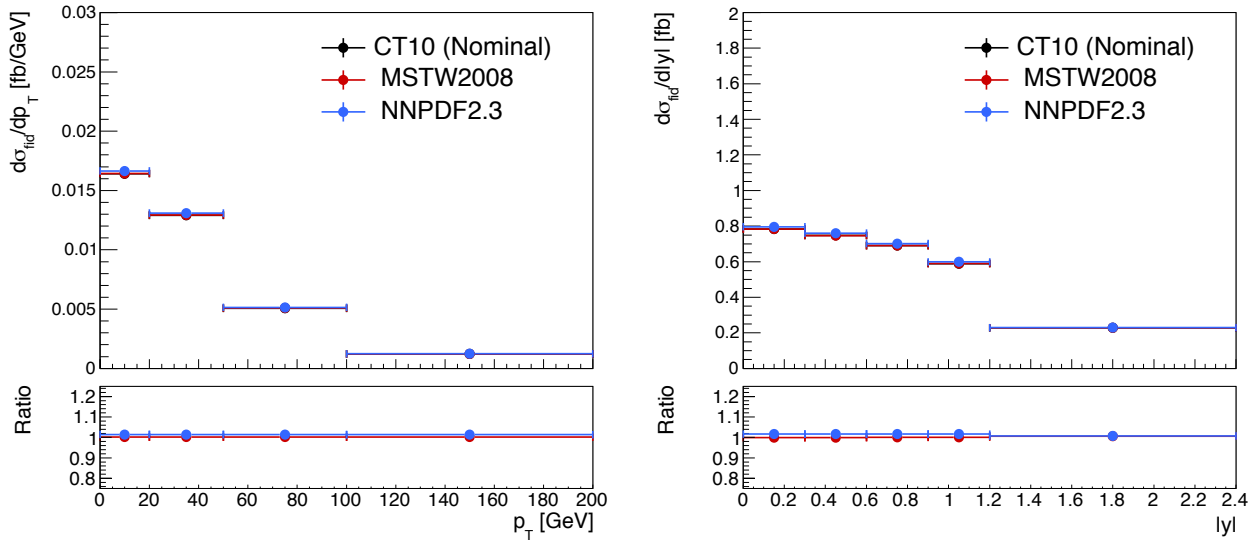

(a) (b)

Figure 6.28: Comparisons of the nominal POWHEG generated sample (CT10), the MSTW2008 and the NNPD 2.1 PDF variations, for a generated Higgs mass, m_H=125.5 GeV. The ratio plots are computed with respect to the nominal scheme (CT10).

Process	MC	Nominal Scales	Scale variations	# Variations
$gg \to H \to ZZ$	HRES	$\mu_R = \mu_F = \frac{m_{ZZ}}{2}$	$(\frac{1}{2}\mu_{R/F}, 2\mu_{R/F})$, $\frac{1}{2} \leq \mu_F/\mu_R \geq 2$	6
		$\mu_Q = m_{ZZ}/2$, $\mu_B = m_b$	$(\frac{1}{2}\mu_Q, 2\mu_Q)$, $(\frac{1}{4}\mu_B, 4\mu_B)$	8
$gg \to H \to ZZ$	SHERPA	$\mu_R = \mu_F = \frac{m_{ZZ}}{2}$	$(\frac{1}{2}\mu_{R/F}, 2\mu_{R/F})$, $\frac{1}{2} \leq \mu_F/\mu_R \geq 2$	6
		$\mu_Q = m_{ZZ}/2$, $\mu_B = m_b$	$(\frac{1}{\sqrt{2}}\mu_Q, \sqrt{2}\mu_Q)$	2
$q\bar{q} \to ZZ$	Powheg	$\mu_R = \mu_F = m_{ZZ}$	$(\frac{1}{2}\mu_{R/F}, 2\mu_{R/F})$	6

Table 6.2: Scale variations considered in the evaluation of the theoretical uncertainties related to the $p_T(ZZ)$ and Y(ZZ) for the $gg \to H \to ZZ$ and $q\bar{q} \to ZZ$ processes. The scale variations on SHERPA signal detailed in the second row are also applied on the SHERPA $gg \to$ ZZ continuum background as stated in the text.

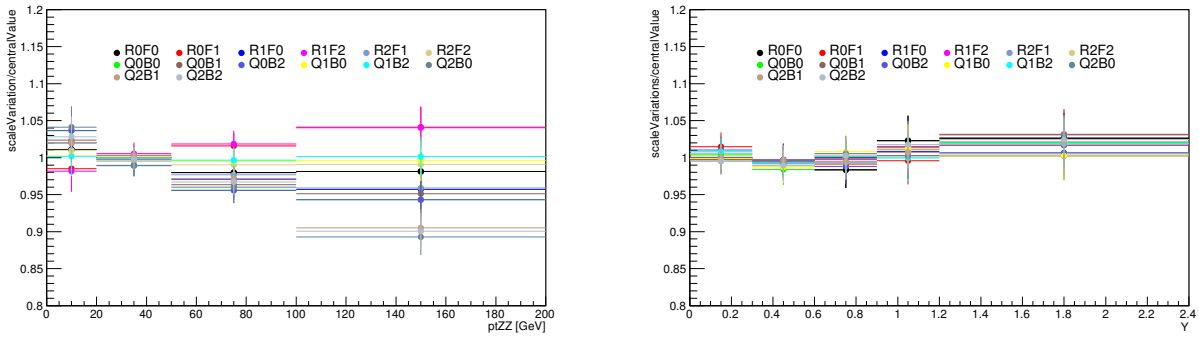

(a) **(b)**

Figure 6.29: Relative change of the p_T and y spectra due to the QCD scale variations produced with HRES signal generated at m_H=380 GeV: ratio of the up or down variations p_T or rapidity with respect to the nominal distribution. Q labels the resummation scale, B the resummation scale related to the bottom quark mass, R the renormalisation scale, F the factorisation scale. The numbers coupled with each variation characterise the nominal value (1), the down variation (0) and the up variation (2).

case (a), for SHERPA signal (b) and for SHERPA background (c). Since the contribution of the resummation scale is dominant, it was decided to compute a first envelope encompassing renormalisation and factorisation scales and sum it in quadrature with the envelope extracted from the resummation scale.
Worth noting is that the SHERPA variations enclose the variations of HRES as in Figure 6.31 (d) because SHERPA does not contain the full NLO calculations and its variations are thence larger than the typical scales of HRES. For this reason, we adopt the variations from SHERPA as systematic uncertainties, treated as correlated for all the gg-initiated processes.

The QCD scale uncertainties on p_T(ZZ) for the $q\bar{q} \rightarrow$ ZZ dominant background process are also extracted by varying the relevant scales, specifically the factorisation μ_F and the renormalisation μ_R scales. Figure 6.32 exhibits the p_T (ZZ) distribution when applying an additional cut at m_{4l} >180 GeV for all the possible independent variations. The differences are at the level of $\sim$ 5% in the high mass region, smaller than the dominant contribution carried by QCD and PDF uncertainties on POWHEG (Section 1.6.2). The scale variations on Y (ZZ) are not generated because their source is related to the treatment of the PDF model and PDF systematic errors are deemed as negligible.

6.9.3 Experimental systematics

Various sources of experimental systematic uncertainties related to the electron and muon final states are tested:

- electron reconstruction, identification and identification efficiencies;
- muon reconstruction and identification efficiencies;
- electron and photon energy-momentum scales and resolutions;
- muon momentum scale and resolution.

The implemented uncertainties having a sizeable effect on the expected sensitivity are:

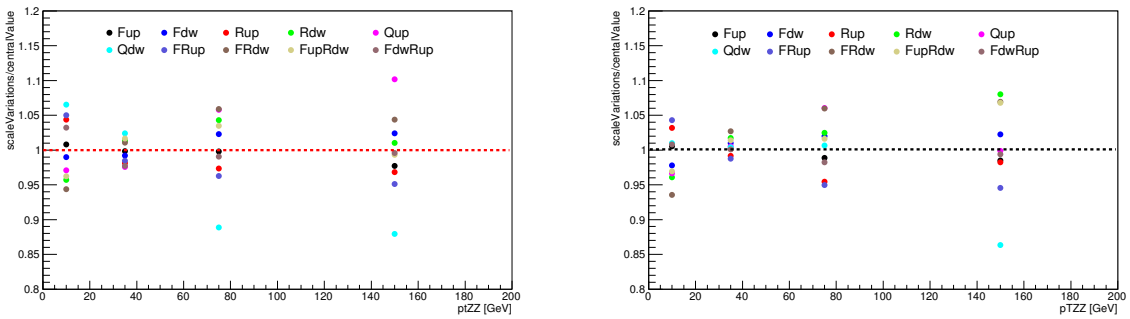

(a) **(b)**

Figure 6.30: Relative uncertainties on the p_T spectrum for the SHERPA signal (a) and background (b) samples induced by the QCD scale variations: ratio of the up or down variations with respect to the nominal distribution. Q labels the resummation scale, R the renormalisation scale, F the factorisation scale.

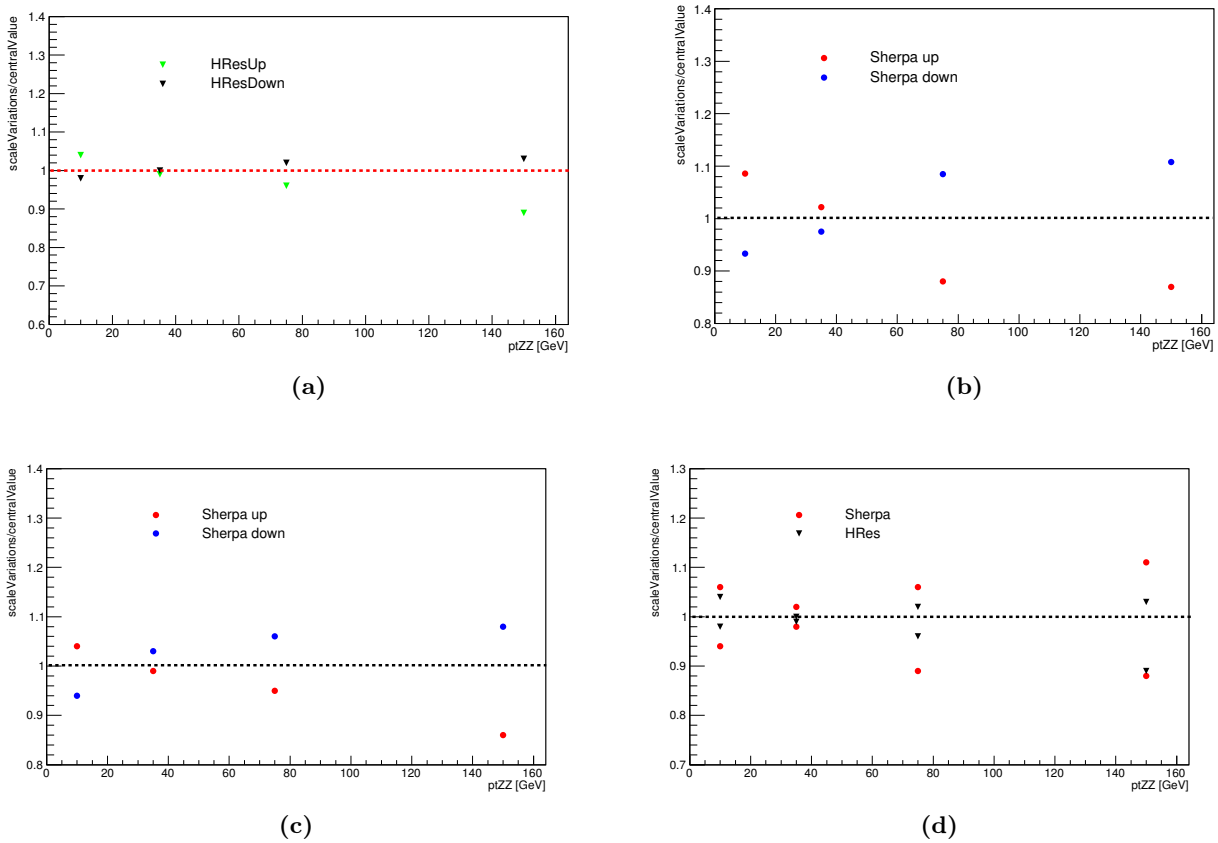

(a) **(b)**

(c) **(d)**

Figure 6.31: Envelopes of the various scale variations: HRES (a), SHERPA signal (b), SHERPA background (c) and the two contributions, SHERPA and HRES, superimposed on the same plot (d).

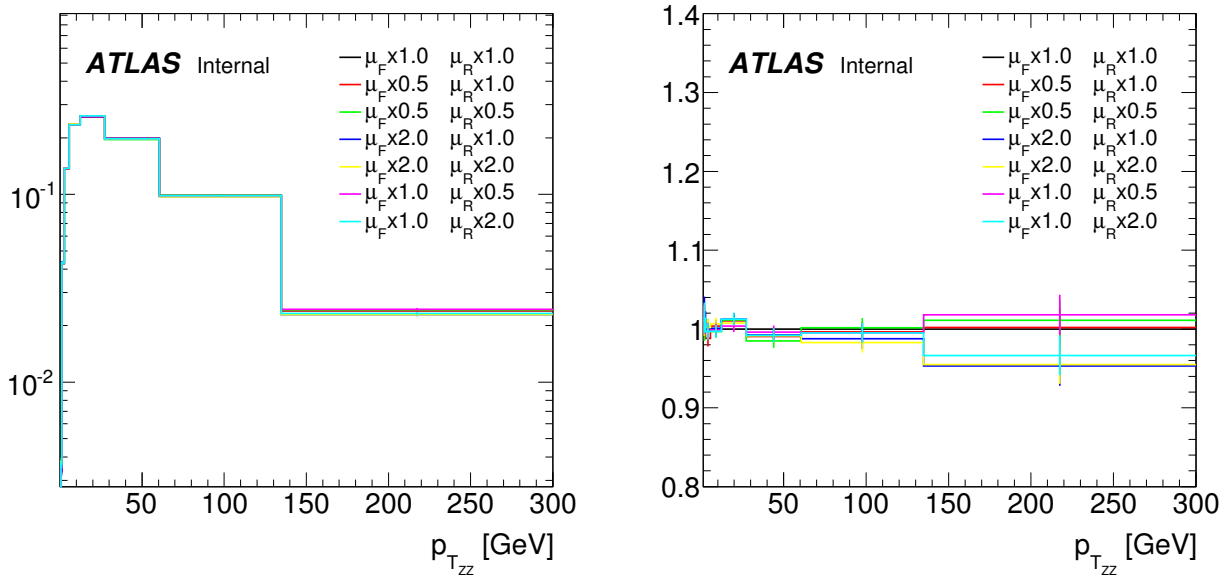

(a) **(b)**

Figure 6.32: (a) Normalised p_T distribution of the ZZ system for different variations of QCD scales. R stands for renormalisation scale, F factorisation scale. (b) Ratio to the central shape.

1. electron reconstruction efficiency for high p_T (> 20 GeV) electrons $\Rightarrow \sim 3\%$ in the 4e channel;

2. muon reconstruction efficiency $\Rightarrow \sim 2\%$ in the 4μ channel.

Figure 6.33 describes the effect of these two dominant systematic uncertainties on the m_{4l} shape for the $gg \to H^* \to ZZ$ signal process. The final impact of the experimental uncertainty on the off-shell signal strength measurement is very small, of the order of 0.3% for the electron-related components and less than 0.1% for the muons.

6.10 Extraction of the off-shell couplings and total width

6.10.1 Cut-based analysis

In parallel with the shape-based analysis on the ME and the BDT detailed in Sections 6.10.3 and 6.10.4, a cut-based feasibility study on m_{4l} and the BDT output is executed. To assess the sensitivity of the measurement, the following figure of merit is defined:

$$\mathcal{S} = \frac{N_{SBI}(r) - N_{SBI}(r=1)}{\Delta N_{SBI}(r)}. \tag{6.15}$$

where $r = \mu_{\text{off-shell}}$ and $\Delta N_{SBI}(r)$ comprises both the statistical and systematic errors on the $q\bar{q}$ (N_{qq}) and gg (N_{gg}) yields. In this study, a 10% systematic uncertainty on the main background $q\bar{q} \to ZZ$ is used to account for the dominant theoretical uncertainty on the QCD and PDF scale variations. Yields for gg and $q\bar{q}$-initiated processes are produced when scanning r according to the formula in Section 6.8. The 2-sided 95 % C.L. upper limit on r is roughly estimated as the value of r that corresponds to $\mathcal{S}$=3.84 in the formula (6.15).
The optimisation is designed in two successive steps:

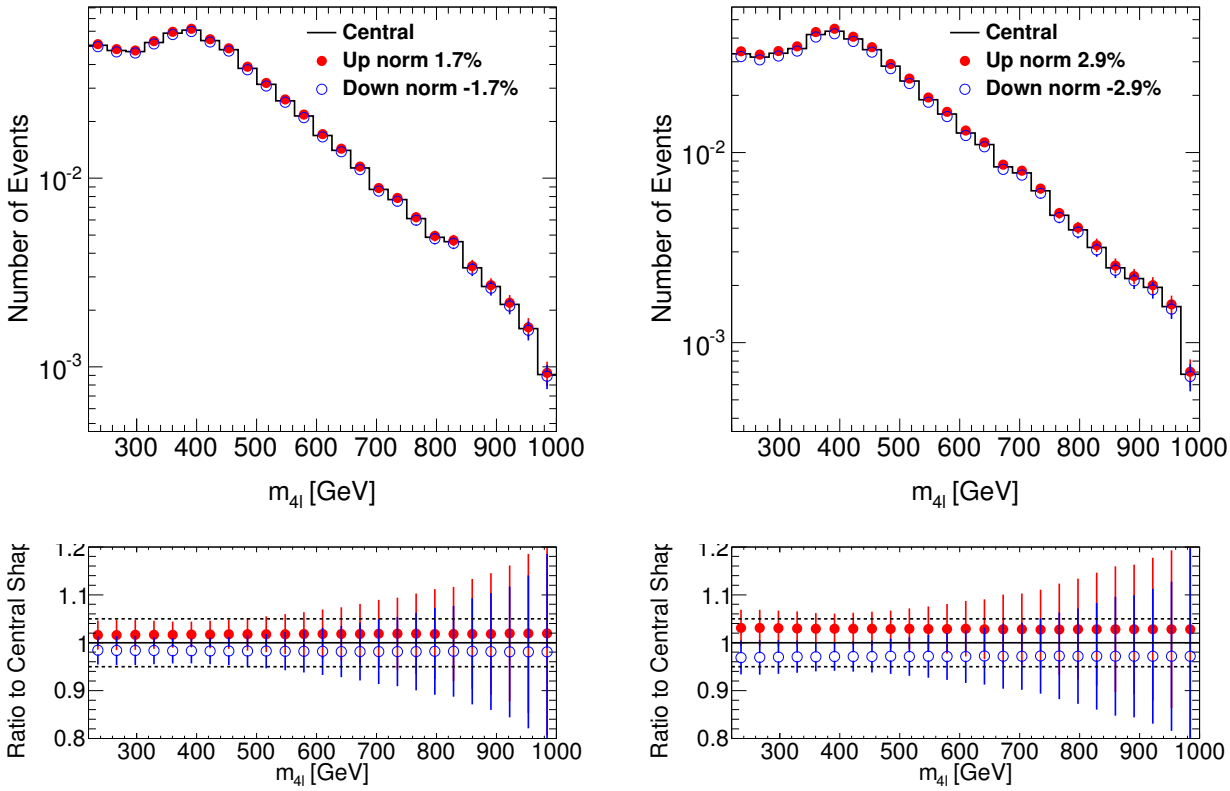

Figure 6.33: Experimental systematics on the muon efficiency in the 4μ channel (a) and on the electron efficiency in the 4e final state (a) affecting the m_{4l} spectrum. The ratio plots of the scale variations to the central shape are also present.

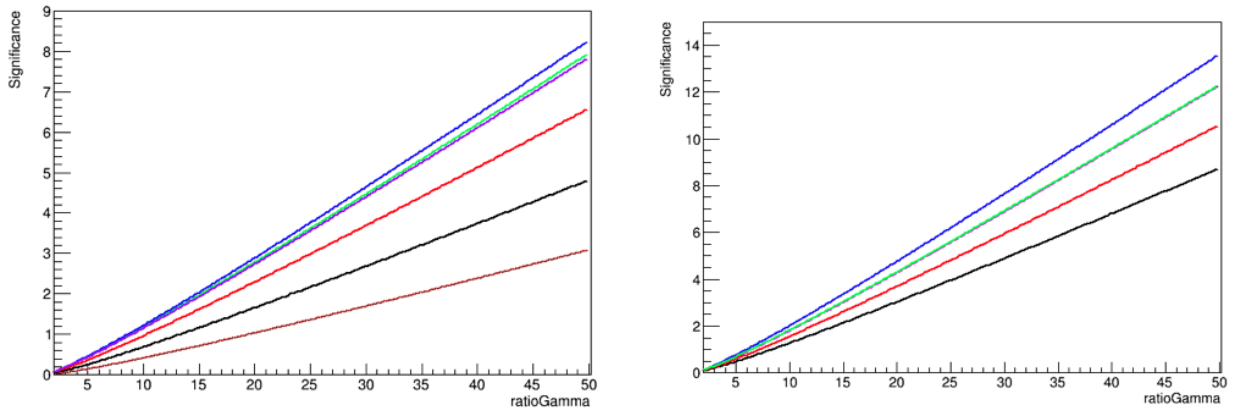

(a) **(b)**

Figure 6.34: Figure of merit $\mathcal{S}$ defined in equation (6.15) as a function of $r = \mu_{\text{off-shell}}$ for various m_{4l} (a) and BDT cuts (b), fixing $m_{4l} > 220$ GeV as in the standard analysis. The colours in (a) label different mass cuts applied to the template samples: brown $m_{4l} > 200$ GeV, black $m_{4l} > 250$ GeV, red $m_{4l} > 300$ GeV, green $m_{4l} > 350$ GeV, blue $m_{4l} > 400$ GeV, purple $m_{4l} > 450$ GeV. In the BDT-optimised figure of merit plot (b), the colour legend is the following: black BDT>0, red BDT>0.2, green BDT>0.4, blue BDT>0.6, purple BDT>0.8.

- The cut on m_{4l} is optimised by varying it between 200 and 450 GeV in steps of 50 GeV. Its best value, e.g. the one that minimises the 95 % C.L. on r, is found at 400 GeV. Results are reported in Figure 6.34 (a) where various significance curves as a function on r are plotted according to their mass cut.

- A cut-and-count approach using the BDT discriminant is also exploited. The BDT training and the samples used in the algorithm are the same as the ones described in Section 6.7. The figure of merit $\mathcal{S}$ is calculated for each BDT cut spanning from 0 to 1 with steps of 0.2 without any modification on the mass cut, i.e. $m_{4l} > 220$ GeV. The limit is reached when BDT>0.6 and its value is ~ 15 as in Figure 6.34 (b). This last result has been validated using a shape-based analysis built on 1-bin templates.
  Since m_{4l} is a constituent of the BDT, an extra mass optimisation on top of the BDT cut does not lead to any improvement in sensitivity on r compared to the optimisation of the BDT alone.

In Table 6.3 the number of expected events combining all lepton final states are charted. The event yields in the signal region are compared to the Higgs on-peak region and to a $q\bar{q} \to ZZ$ background enriched region.

Given the modest results extracted by the cut-based approach, it is decided to replace it with a shape-based algorithm that profits from the shape discrimination power of the various template configurations.
Sections 6.10.3 and 6.10.4 will be devoted to the documentation of this approach for the ME and the BDT algorithms respectively while Section 6.10.2 will define the main aspects of the fit parametrisation, the technical implementation as well as the validations performed.

sample	H on-peak	Background region	Signal region (optimised cut on m_{4l})
	m_{4l}: 110-140 GeV	m_{4l}: 160-220 GeV	m_{4l}: 400-1000 GeV
$gg \to H^* \to ZZ$	14.2	0.22	1.1
$gg \to ZZ$ (B)	1.2	26.1	2.8
$gg \to ZZ$ (S+B+I)	16.1	25.3	2.4
$q\bar{q} \to ZZ$	17.5	112.2	21.31

Table 6.3: Expected number of events for 8 TeV (4e, 2e2μ, 2μ2e, 4μ channels) in the various m_{4l} regions.

6.10.2 Shape-based analysis - The fit parametrisation

The analysis relies on a simultaneous binned maximum likelihood fit to extract the constraints on the off-shell Higgs couplings and the total Higgs width. The likelihood fit is constituted by histogram templates of signal and background processes ($gg \to$ ZZ and $q\bar{q} \to$ ZZ) as well as the SBI and the VBF contributions for the ME and the BDT distributions. The 4 lepton mass, m_{4l} has also been fitted: it was found that its sensitivity is 30% worse than the one characterising the ME or the BDT analyses, hence this approach has been abandoned.

The probability density function (PDF) components are parametrised and scaled as a function of $\mu_{\text{off-shell}}$ as explained in Section 6.8. The validation of the method is done using Monte Carlo samples generated at $\mu_{\text{off-shell}}$=10 for the SBI process. As indicated in Figure 6.35 for the 2e2μ channel, there is no significant deviation between the histogram scaling defined in Section 6.8 starting from the templates for $\mu_{\text{off-shell}}$=1 and the direct Monte Carlo production at $\mu_{\text{off-shell}}$=10. The same investigation has been accomplished for the BDT as well leading to similar results. This closure test guarantees the correctness of the scaling method, furthermore the fitting procedure is internally cross-checked by using two distinct frameworks, one of that based on the HistFactory [165] tool both for the ME-based approach (Section 6.10.3) and the BDT (Section 6.10.4). No smoothing is applied on the output histograms used in the likelihood fit. Assuming the same on-shell and off-shell couplings, $\frac{\Gamma_H}{\Gamma_{SM}}$ can be calculated with a simultaneous fit on the low mass and high mass as presented in Section 6.12. A comprehensive look at the statistical tests and tools employed in the following Sections is given in Appendix C.

The typical off-shell mass scales tested by the analyses are in the range ($400 < m_{VV} <$1000) GeV, with a small fraction of the expected $H^* \to$ WW signal extending to substantially higher mass scales. This is illustrated in Figure 6.36, which shows the generated m_{VV} mass for the gg$\to H^{(*)} \to$ VV and the VBF signal processes weighted by the expected S/B ratio in each bin of the final discriminant for the ZZ$\to$ 4l and ZZ$\to 2l2\nu$ and for all signal events in the signal region for the WW$\to l\nu l\nu$ analysis.

6.10.3 Shape-based analysis on the ME

The histograms in Figure 6.20 are produced for the 4 final states as input to the fit. The first step of the fitting validation, before performing the scanning in $\mu_{\text{off-shell}}$, consists in executing a fit in the presence of large $\mu_{\text{off-shell}}$ (10 or 25). Hence, Asimov datasets are created from Monte Carlo samples generated at $\mu_{\text{off-shell}}$=10 and $\mu_{\text{off-shell}}$=25 and PDF scaled with the formula in Section 6.8 from $\mu_{\text{off-shell}}$=1 and subsequently fitted without systematics. The results are provided below and the corresponding likelihood scans are in Figure 6.37 (a):

- Asimov dataset generated from PDF $\Rightarrow$ μ=$10^{+4.3}_{-3.8}$ (μ_{inj}=10), μ=$25^{+5.2}_{-4.8}$ (μ_{inj}=25).

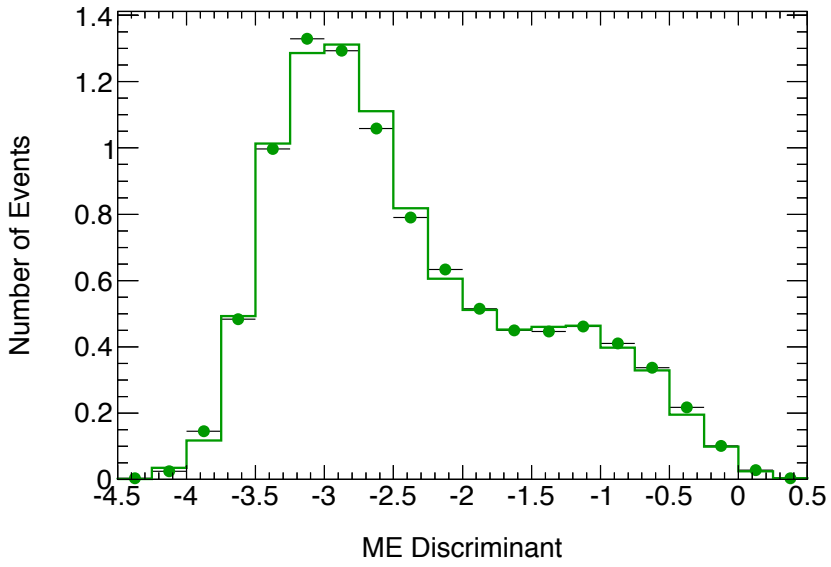

Figure 6.35: Distributions of the ME discriminants in the 2e2μ final state after the baseline off-peak selection for the SBI template. Lines are from the PDF parametrisation s using the scaling formula reported in Section 6.8 from the SM scenario to $\mu_{\text{off-shell}}$=10, while the dots are from the Monte Carlo generated at $\mu_{\text{off-shell}}$=10.

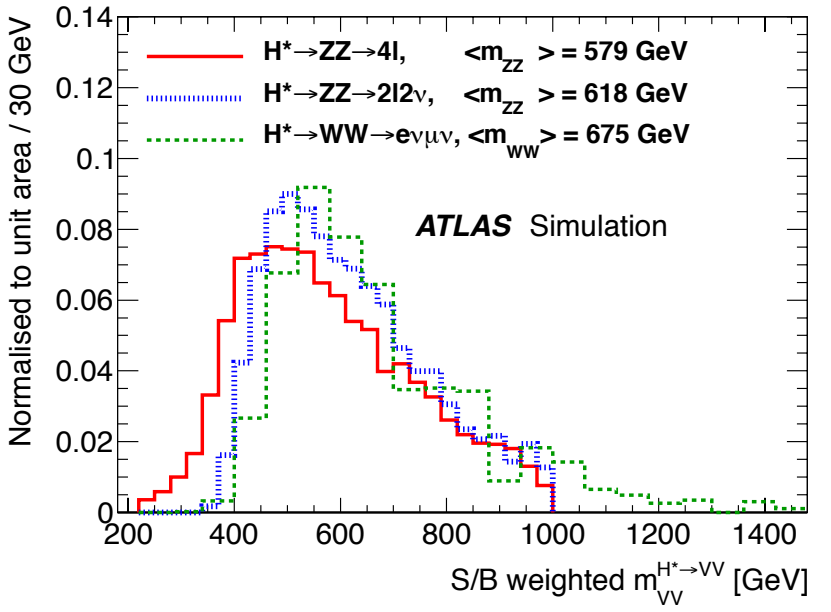

Figure 6.36: Normalised distribution of the generated mass m_{VV} for the $gg \to (H^*) \to$ ZZ and the VBF signal processes weighted by the expected S/B ratio in each bin of the final discriminant for the ZZ$\to$ 4l and ZZ$\to$ 2l2ν and for all signal events in the signal region for the WW$\to$ $l\nu l\nu$ analysis.

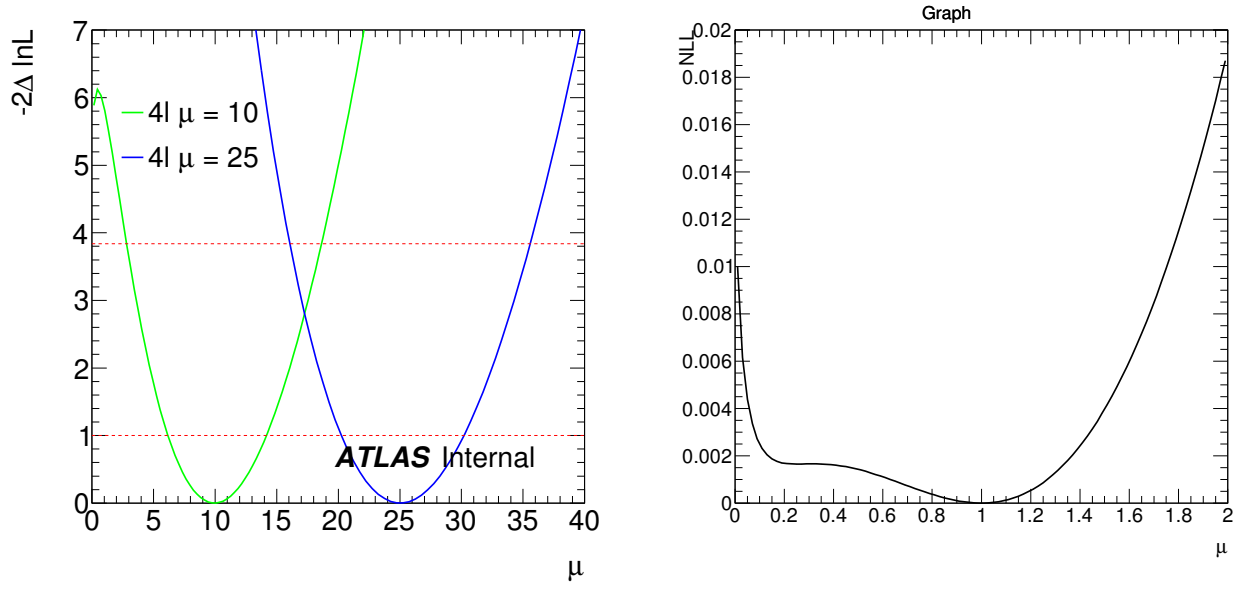

Figure 6.37: (a) Likelihood scan of $\mu_{\text{off-shell}}$ in the fit to Asimov data generated from Monte Carlo sample generated at $\mu_{\text{off-shell}}$=10 and $\mu_{\text{off-shell}}$=25 using the ME discriminant based shape analysis. (b) Likelihood scan of $\mu_{\text{off-shell}}$ in the fit to Asimov generated from Monte Carlo sample with $\mu_{\text{off-shell}}$=1 and zoomed in the region close to the minimum of the parabola.

- Asimov dataset built from Monte Carlo templates $\Rightarrow \mu = 10^{+4.3}_{-3.8}$ (μ_{inj}=10), $\mu = 25^{+5.2}_{-4.8}$ (μ_{inj}=25).

Given that the value of the off-shell coupling injected is returned by the fit, the procedure has no bias.

The expected sensitivity of the 95% C.L. upper limit on $\mu_{\text{off-shell}}$ is then evaluated assuming SM Higgs coupling. Figure 6.40 shows the likelihood scan on BDT and ME with and without the systematic uncertainty contribution whereas Table 6.4 shows the values of the limits on $\mu_{\text{off-shell}}$ as well as the breakdown of the systematics.
If we zoom close to the minimum of the likelihood parabola, a double-minimum structure between 0 and 1 is displayed as in Figure 6.37 (b). This is due to the presence of the double solution of the second order polynomial dependence of $gg \to$ ZZ to $\mu_{\text{off-shell}}$.

6.10.4 Shape-based analysis on the BDT and comparison with the ME-based approach

Analogously to the matrix element-based approach, the expected sensitivity of the BDT discriminant is extracted and the two methods are compared. The systematic uncertainties, both theoretical and experimental, determined in Section 6.9 are kept in common between the ME and the BDT. As for Section 6.10.3, the dominant systematic uncertainty is given by the higher order QCD on the background $gg \to$ ZZ contribution (Figure 6.38). Furthermore, as addressed in Section 6.9.2, additional systematics on the QCD scales raise from the usage of the ZZ system information inside the BDT training. The envelope of the largest deviations is consequently propagated to the final BDT templates entering the fit to produce the up and down variations. Figure 6.39 displays the impact of the up/down variations when varying the relevant scales of the process with the SHERPA generator. These are shape-only systematics, the overall normalisation of the templates is therefore not affected.

The expected 95% C.L. limit on $\mu_{\text{off-shell}}$ is extracted for the BDT and the ME configurations (Figure 6.40). To assess the impact of the systematic uncertainty on the two methods, its full breakdown is presented in Table 6.4. The final results on the fitted mean as well as on the 95% C.L. upper limit on $\mu_{\text{off-shell}}$ in parenthesis assuming the SM Higgs couplings and including gluon-gluon fusion and vector boson fusion production mechanisms are listed below:

- ME: Without systematics: 1.00 (8.85), with systematics: 1.00 (10.28);
- BDT: Without systematics: 1.00 (8.52), with systematics: 1.00 (10.08).

The gain of the BDT discriminant is approximately 4% with respect to the ME-based approach and $\sim$ 2% including all systematics. As reported in Table 6.4, the influence of the various sources of uncertainties is similar within the two methods and the extra p_T-related uncertainties account for less than 1%. Provided that the gain of the BDT-based analysis is small compared to the ME, the ME-based discriminant approach is chosen to be the baseline for the measurement.

Source of systematic uncertainties	BDT	ME
Luminosity	8.6 (1.2%)	8.9 (1.1%)
electron efficiency	8.5 (<1%)	8.9 (1.1%)
μ efficiency	8.5 (<1%)	8.9 (1.1%)
QCD scale for $q\bar{q} \to ZZ$	8.6 (1.2%)	9.0 (2.2%)
QCD scale for $gg \to ZZ$	9.5 (10.5%)	9.7 (9.3%)
QCD scale for the $gg \to (H^* \to)ZZ$ interference	9.0 (5.6%)	9.3 (5.4%)
PDF for $pp \to ZZ$	8.6 (1.2%)	8.9 (1.1%)
EW for $q\bar{q} \to ZZ$	8.5 (1.2%)	8.9 (1.1%)
ZZ p_T systematics	8.5 (<1%)	not needed
All systematic	10.0 (18.2%)	10.3 (16%)
No systematic	8.5	8.8

Table 6.4: Expected 95% C.L. upper limit on $\mu_{\text{off-shell}}$ in BDT and ME discriminant based shape analyses in the 4 lepton channel, including each systematic uncertainty individually compared to including no systematic uncertainty and all systematic uncertainties. Numbers in parenthesis represent the percentage change compared to the expected values without any systematic uncertainty.

6.11 Observed results in the 4l final state

6.11.1 Background-enriched regions

As a preliminary cross-check of the background estimation for the $q\bar{q} \to$ ZZ process prior to unblinding the signal region of the analysis, two background-enriched control-regions are defined:

- control region A: (160< m_{4l} <220) GeV;
- control region B: (220< m_{4l} <1000) GeV and ME<-1.5;

The background enhancement is guaranteed by the explicit usage of the signal-free m_{4l} region (control region A) or by a specific cut on the ME in order to select the background-like region. Tables 6.5 and 6.6 report the expected number of events in the control region A and B respectively as well as the observed events in data. The observed data is in good agreement with the total expected prediction within 1-2 σ. The corresponding inclusive distributions of m_{4l} and ME are exhibited in Figure 6.41 for control region A and in Figure 6.42 for control region B. In consideration of the

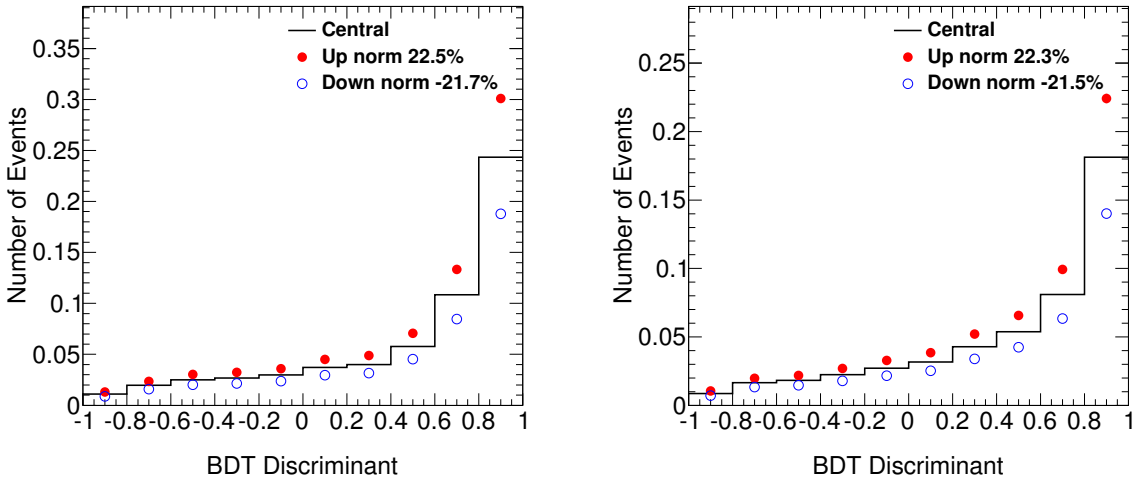

(a) $2e2\mu$

(b) $2\mu2e$

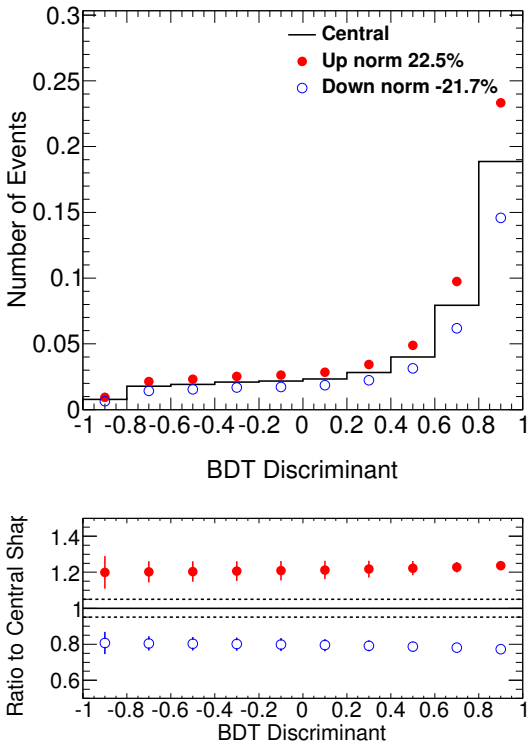

(c) $4e$

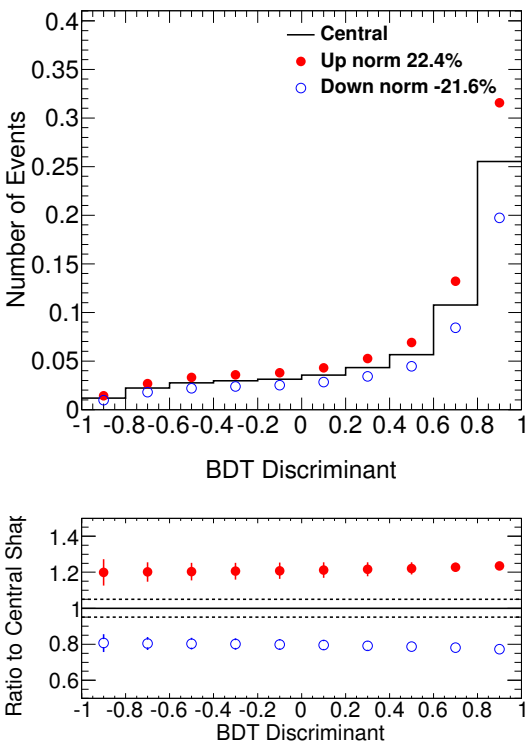

(d) 4μ

Figure 6.38: QCD scale uncertainties for the BDT discriminant shapes in the four different lepton final states for the $gg \to H \to ZZ$ process.

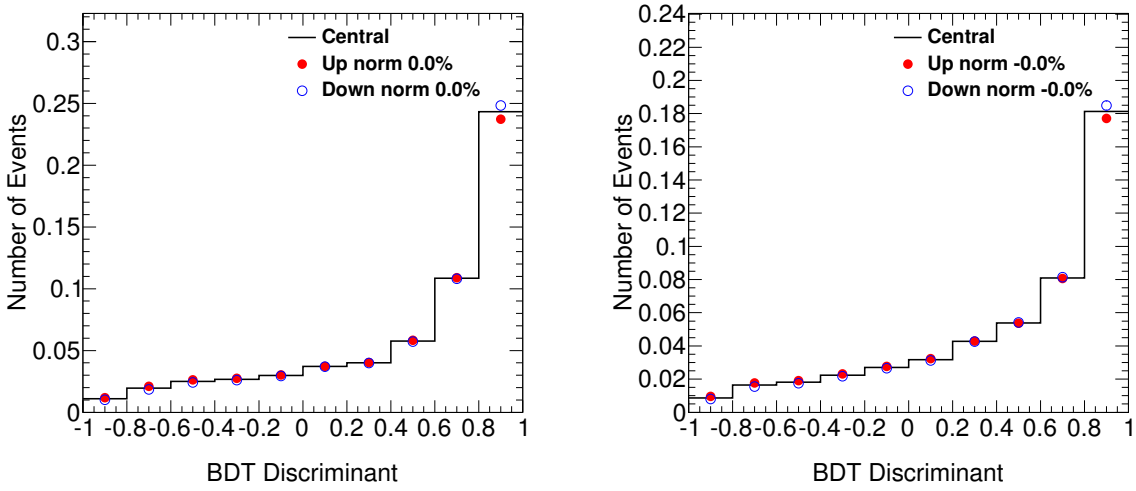

(a) $2e2\mu$

(b) $2\mu2e$

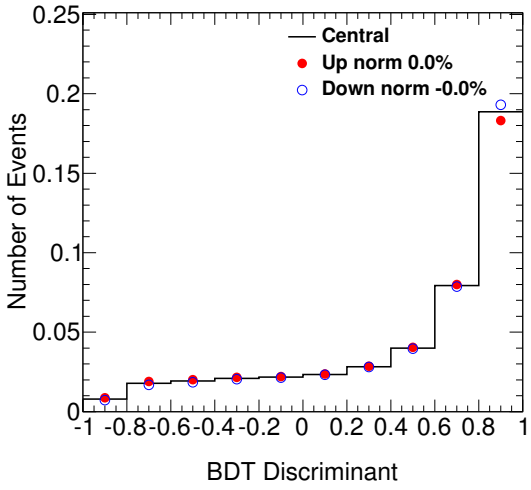

(c) $4e$

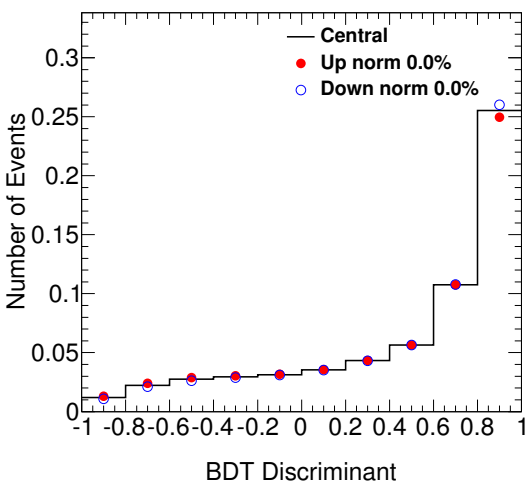

(d) 4μ

Figure 6.39: $p_T(ZZ)$ related systematics for the BDT discriminant shapes in the four different lepton final states for the $gg \to H \to \mathrm{ZZ}$ process.

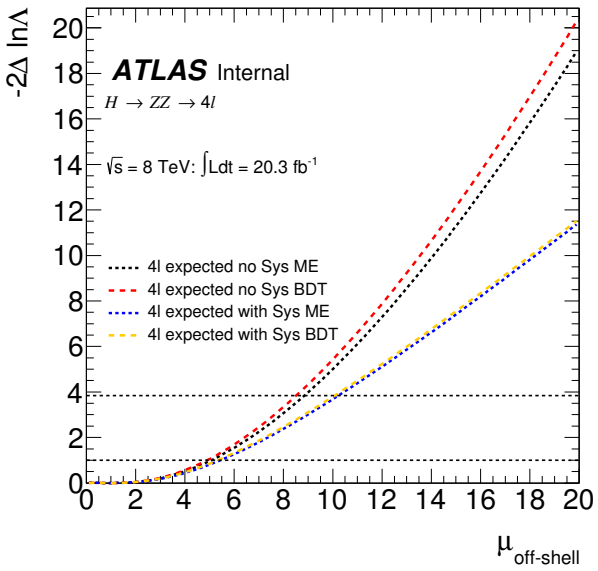

Figure 6.40: Scan of the negative log-likelihood, $-2\ln\Lambda$, as a function of $\mu_{\text{off-shell}}$ in the 4 lepton channel, comparing the BDT and ME-based discriminant analyses. The red long dashed (black dashed) line reproduces the expected value for the BDT (ME)-based analysis with no systematic uncertainty included, while the orange long dashed (blue dashed) line is for the expected value including all systematics.

data-to-Monte Carlo match in the background-enriched regions A and B, this study is extended in the signal region to extract the final values on the $\mu_{\text{off-shell}}$ upper limit at 95% C.L.

As noted in Section 6.10.1, the cut-based approach does not result in sufficiently competitive upper limit on the off-shell signal strength, hence it will not be pursued in this Section.

sample	$2\mu2e$	$2e2\mu$	4μ	4e	TOTAL
$gg \to H^* \to$ ZZ (S)	0.06 ± 0.00	0.05 ± 0.00	0.07 ± 0.00	0.04 ± 0.00	0.2 ± 0.0
$gg \to$ ZZ (B)	6.75 ± 0.03	6.01 ± 0.03	8.15 ± 0.03	5.17 ± 0.02	26.1 ± 0.1
$gg \to (H^*) \to$ ZZ (SBI)	6.58 ± 0.04	5.79 ± 0.03	7.87 ± 0.03	4.99 ± 0.02	25.2 ± 0.1
$gg \to (H^*) \to$ ZZ (SBI $\mu_{\text{off-shell}} = 10$)	6.24 ± 0.03	5.53 ± 0.03	7.48 ± 0.03	4.76 ± 0.02	24.0 ± 0.1
VBF $H^* \to$ ZZ (S)	0.01 ± 0.00	0.01 ± 0.00	0.01 ± 0.00	0.00 ± 0.00	0.0 ± 0.0
VBF ZZ (B)	0.13 ± 0.00	0.11 ± 0.00	0.16 ± 0.00	0.10 ± 0.00	0.5 ± 0.0
VBF $(H^*) \to$ ZZ (SBI)	0.12 ± 0.00	0.11 ± 0.00	0.15 ± 0.00	0.10 ± 0.00	0.5 ± 0.0
VBF $(H^*) \to$ ZZ (SBI, $\mu_{\text{off-shell}}$ =10)	0.16 ± 0.00	0.15 ± 0.00	0.19 ± 0.01	0.12 ± 0.00	0.6 ± 0.0
$q\bar{q} \to$ ZZ	28.9 ± 0.3	25.3 ± 0.2	36.1 ± 0.2	21.8 ± 0.2	112.2 ± 0.5
Reducible backgrounds	0.59 ± 0.08	0.59 ± 0.07	0.76 ± 0.06	0.58 ± 0.08	2.5 ± 0.1
Total Expected (SM)	36.2 ± 0.3	31.8 ± 0.2	44.9 ± 0.2	27.4 ± 0.2	140 ± 0
Observed	37	43	36	27	143

Table 6.5: Expected and observed number of events for the ZZ→ 4l channel for all processes in the $q\bar{q} \to$ ZZ-enriched region where (160< m_{4l} <220) GeV (control region A). The uncertainties are statistical only.

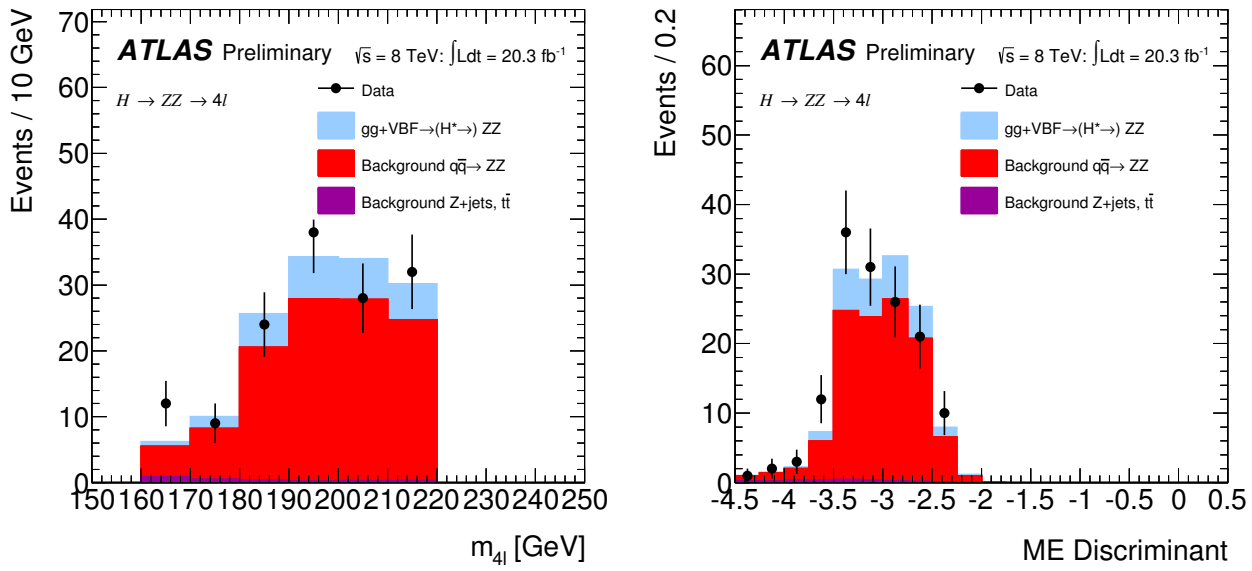

Figure 6.41: Distributions for the various Monte Carlo components and for data, corresponding to an integrated luminosity of 20.3 fb^{-1} generated at $\sqrt{s}$= 8 TeV, of m_{4l} (a) and ME (b) in the inclusive four different lepton final states using the $q\bar{q} \rightarrow$ ZZ-enriched region where (160< m_{4l} <220) GeV (control region A).

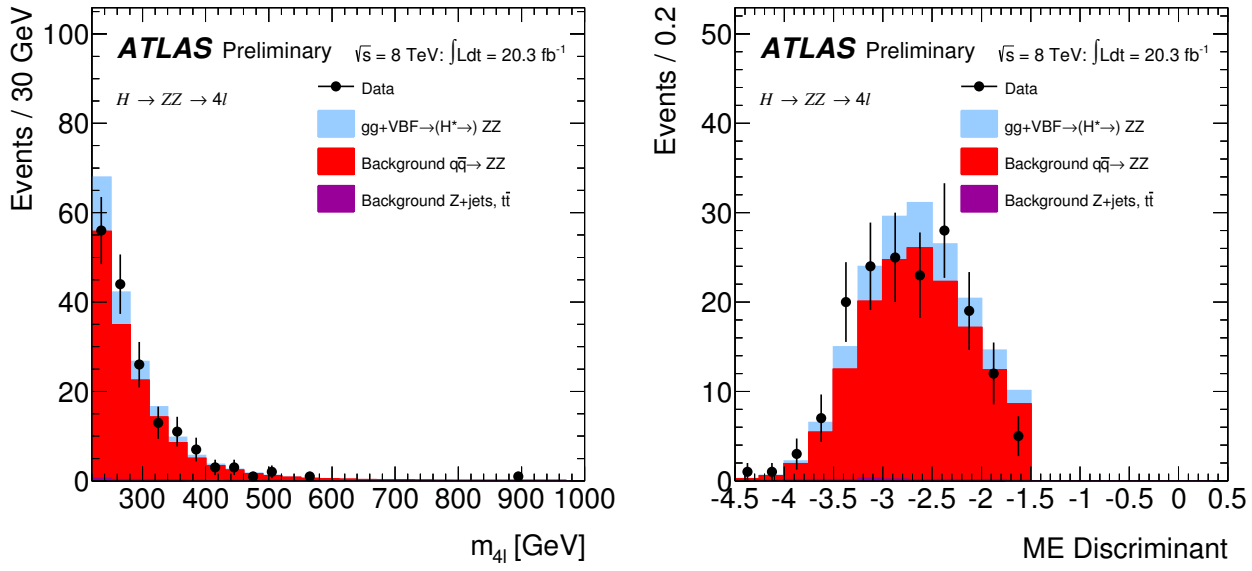

Figure 6.42: Distributions for the various Monte Carlo components and for data corresponding to an integrated luminosity of 20.3 fb^{-1} generated at $\sqrt{s}$= 8 TeV of m_{4l} (a) and ME (b) in the inclusive four different lepton final states using the $q\bar{q} \rightarrow$ ZZ-enriched region where (220< m_{4l} <1000) GeV and ME<-1.5 (control region B).

sample	2μ2e	2e2μ	4μ	4e	TOTAL
$gg \to H^* \to$ ZZ (S)	0.23 ± 0.00	0.24 ± 0.00	0.18 ± 0.00	0.11 ± 0.00	0.8 ± 0.0
$gg \to$ ZZ (B)	7.47 ± 0.03	7.24 ± 0.03	8.64 ± 0.03	5.28 ± 0.02	28.6 ± 0.1
$gg \to (H^*) \to$ ZZ (SBI)	7.20 ± 0.04	6.94 ± 0.04	8.31 ± 0.03	5.12 ± 0.02	27.6 ± 0.1
$gg \to (H^*) \to$ ZZ (SBI $\mu_{\text{off-shell}} = 10$)	7.88 ± 0.04	7.75 ± 0.04	8.58 ± 0.03	5.24 ± 0.02	29.4 ± 0.1
VBF $H^* \to$ ZZ (S)	0.02 ± 0.00	0.01 ± 0.00	0.02 ± 0.00	0.01 ± 0.00	0.1 ± 0.0
VBF ZZ (B)	0.41 ± 0.01	0.43 ± 0.01	0.44 ± 0.01	0.28 ± 0.00	1.6 ± 0.0
VBF $(H^*) \to$ ZZ (SBI)	0.40 ± 0.01	0.43 ± 0.01	0.42 ± 0.01	0.27 ± 0.01	1.5 ± 0.0
VBF $(H^* \to)$ ZZ (SBI, $\mu_{\text{off-shell}}$ =10)	0.49 ± 0.01	0.51 ± 0.01	0.51 ± 0.01	0.32 ± 0.01	1.8 ± 0.0
$q\bar{q} \to$ ZZ	39.5 ± 0.3	37.8 ± 0.3	46.6 ± 0.3	26.6 ± 0.2	150.6 ± 0.5
Reducible backgrounds	0.38 ± 0.06	0.29 ± 0.06	0.32 ± 0.06	0.38 ± 0.06	1.4 ± 0.1
Total Expected (SM)	47.5 ± 0.3	45.5 ± 0.3	55.6 ± 0.3	32.4 ± 0.2	181 ± 1
Observed	35	56	52	25	168

Table 6.6: Expected number of events for the ZZ→ 4l channel for all processes in the $qq \to ZZ$-enriched region where (220< m_{4l} <1000) GeV and ME<-1.5 (control region B). The uncertainties are statistical only.

6.11.2 ME discriminant response in the signal region

The signal-region of the analysis in the m_{4l}-ME phase space is:

- (220< m_{4l} <1000) GeV and -4.5< ME <0.5.

The observed and expected number of events for the various physics processes involved in the ME shape analysis are listed in Table 6.7 for the signal region. The reducible background component, comprising Z+jets and $t\bar{t}$, accounts for less than 1% on the total background contribution and is not added in the final computation of the limit. The expected events for the $gg \to$ ZZ and VBF processes, including the Higgs signal, background and interference (SBI templates) are calculated for both the SM case and for $\mu_{\text{off-shell}}$ =10. Figure 6.43 illustrates the observed and the expected m_{4l} and ME-discriminant distributions combining all lepton final states in the signal region.

Conclusively, the scan of the negative log likelihood, -2ln Λ, extracted by fitting the ME discriminant as a function of the $\mu_{\text{off-shell}}$ parameter, for data and for Monte Carlo with and without systematic uncertainties, is reported in Figure 6.44 (a). Besides, the observed and expected 95% C.L. upper limit on $\mu_{\text{off-shell}}$ as a function of the unknown ratio of background and signal k-factors involving gg-initiated processes, R^B_{H*}, is also present in Figure 6.44 (b) in the region 0.5< R^B_{H*}<2. The numerical values of the expected and observed 95% C.L. limits on $\mu_{\text{off-shell}}$ expressed for discrete steps of R^B_{H*} (0.5-1, 1.5,2) are charted in Table 6.8. The upper 95% C.L. limits are calculated from the CL_s method [166], the null hypothesis being $\mu_{\text{off-shell}}$=1 (SM scenario) and the alternative hypothesis the $\mu_{\text{off-shell}}$ value extracted from the fit. The expected 95% C.L. limits on $\mu_{\text{off-shell}}$ with and without systematic uncertainties are 8.8 and 10.3 respectively; the observed limit is $\mu^{obs}_{\text{off-shell}}$ =6.7 when assuming that the signal-to-background k-factor ratio, R^B_{H*}, is set to 1.

6.12 2l2ν and WW→ lνlν analyses

6.12.1 The analysis in the 2l2ν final state

The analysis of the $ZZ \to$ 2l2ν channel follows strategies similar to those used in the invisible Higgs boson search in the ZH channel [167]. The definitions of the reconstructed objects (electrons,

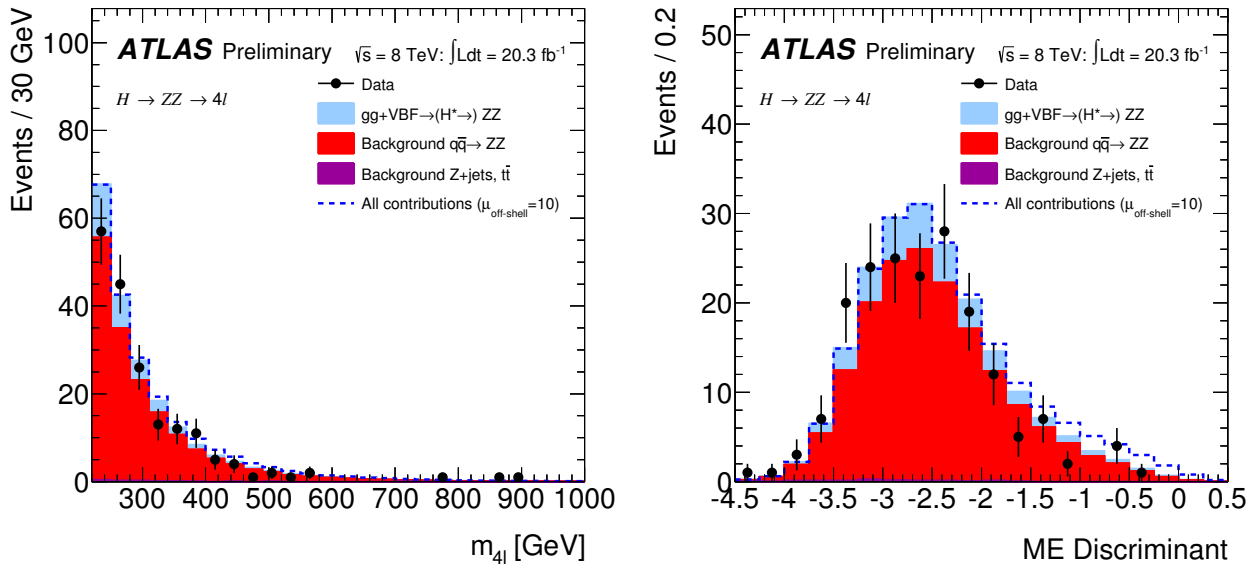

Figure 6.43: Distributions for the various Monte Carlo components and for data corresponding to an integrated luminosity of 20.3 fb^{-1} generated at $\sqrt{s}$= 8 TeV of m_{4l} (a) and ME (b) in the inclusive four different lepton final states using the signal region (220< m_{4l} <1000) GeV and -4.5< ME <0.5.

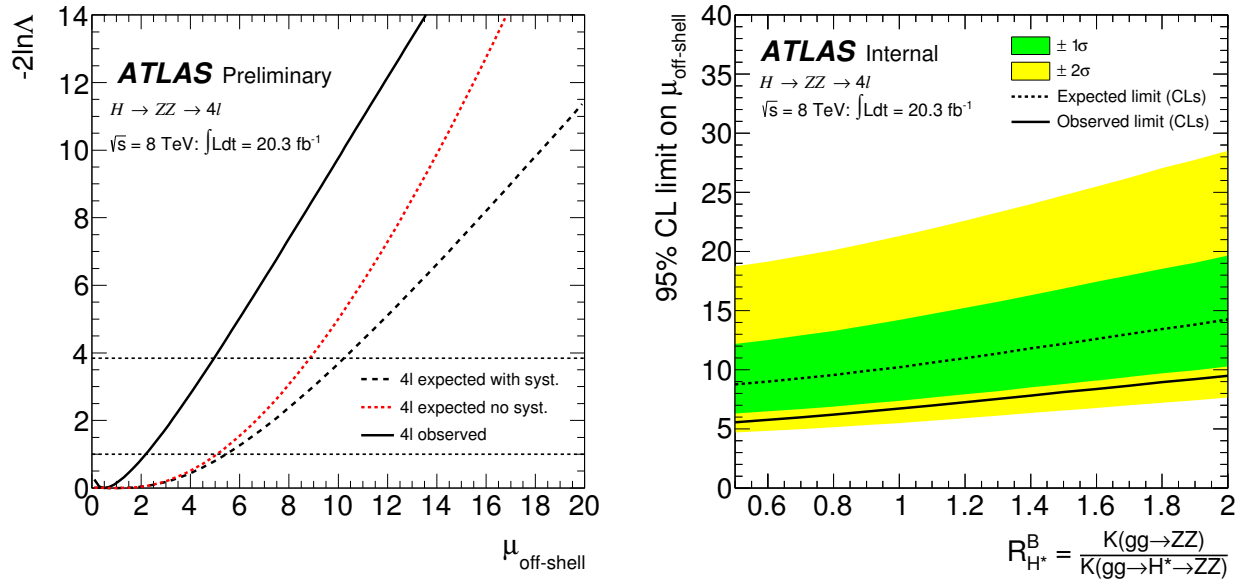

Figure 6.44: (a) Scan of the negative log-likelihood, -2ln Λ, as a function of $\mu_{\text{off-shell}}$ in the 4 lepton final state in the ME-based discriminant analysis. The black solid (dashed) line represents the observed (expected) value including all systematic uncertainty, while the red dotted line is for the expected value without systematic uncertainties. (b) Observed and expected 95% C.L. upper limit on $\mu_{\text{off-shell}}$ in the ME discriminant based analysis as a function of R^B_{H*}. The upper limits are calculated from the CL$_s$ method, the null hypothesis being $\mu_{\text{off-shell}}$=1.

	2μ2e	2e2μ	4μ	4e	Total
$gg \to H^* \to$ ZZ (S)	0.48 ± 0.11	0.60 ± 0.14	0.62 ± 0.14	0.45 ± 0.10	2.1 ± 0.5
$gg \to$ ZZ (B)	7.94 ± 1.81	7.87 ± 1.80	9.88 ± 2.25	6.18 ± 1.41	31.9 ± 7.3
$gg \to (H^*) \to$ ZZ (SBI)	7.61 ± 1.74	7.45 ± 1.70	9.41 ± 2.15	5.91 ± 1.35	30.4 ± 6.9
$gg \to (H^*) \to$ ZZ (SBI, $\mu_{\text{off-shell}}$ =10)	9.92 ± 2.27	10.5 ± 2.4	12.4 ± 2.8	8.10 ± 1.85	41.0 ± 9.4
VBF $H^* \to$ ZZ (S)	0.04 ± 0.00	0.05 ± 0.01	0.06 ± 0.01	0.04 ± 0.00	0.2 ± 0.0
VBF ZZ (B)	0.51 ± 0.03	0.56 ± 0.03	0.66 ± 0.03	0.44 ± 0.02	2.2 ± 0.1
VBF $(H^*) \to$ ZZ (SBI)	0.48 ± 0.03	0.53 ± 0.03	0.60 ± 0.03	0.40 ± 0.02	2.0 ± 0.1
VBF $(H^*) \to$ ZZ (S+B+I, $\mu_{\text{off-shell}} = 10$)	0.69 ± 0.04	0.79 ± 0.04	0.91 ± 0.05	0.60 ± 0.03	3.0 ± 0.2
$q\bar{q} \to$ ZZ	41.9 ± 3.3	40.7 ± 3.2	53.8 ± 4.2	31.3 ± 2.5	167.7 ± 13.1
Reducible backgrounds	0.36 ± 0.06	0.30 ± 0.06	0.29 ± 0.06	0.35 ± 0.06	1.3 ± 0.1
Total Expected (SM)	50.4 ± 3.7	49.0 ± 3.6	64.1 ± 4.7	37.9 ± 2.8	201 ± 15
Observed	35	59	59	29	182

Table 6.7: Expected and observed number of events in the ZZ→ 4l channel in the ME shape based analysis signal region, (220 GeV $< m_{4l} <$ 1000) GeV and -4.5 < ME < 0.5. Both statistical and systematic uncertainties are included.

R^B_{H*}	Observed	Median	1 σ band	2 σ band
0.5	5.5	8.8	[6.3, 12.2]	[4.7, 18.7]
1.0	6.7	10.2	[7.4, 14.2]	[5.5, 21.3]
1.5	8.1	12.2	[8.8, 16.9]	[6.5, 24.7]
2.0	9.5	14.3	[10.3, 19.7]	[7.7, 28.5]

Table 6.8: Observed and expected 95% C.L. upper limit on $\mu_{\text{off-shell}}$ in the ME discriminant shape based analysis as a function of R^B_{H*}. The upper limits are calculated from the CL_s method, with the null hypothesis $\mu_{\text{off-shell}}$=1.

muons, jets, and missing transverse momentum) are identical, but some of the kinematic cuts are optimised for the current analysis. As the neutrinos in the final state do not allow for a kinematic reconstruction of m_{ZZ}, the transverse mass (m_T^{ZZ}) reconstructed from the transverse momentum of the dilepton system (p_T^{ll}) and the magnitude of the missing transverse momentum (E_T^{miss}) is calculated as follows:

$$m_{\text{T}}^{ZZ} \equiv \sqrt{\left(\sqrt{m_Z^2 + \left|p_{\text{T}}^{\ell\ell}\right|^2} + \sqrt{m_Z^2 + \left|E_{\text{T}}^{\text{miss}}\right|^2}\right)^2 - \left|p_{\text{T}}^{\ell\ell} + E_{\text{T}}^{\text{miss}}\right|^2} . \tag{6.16}$$

This variable is chosen as the discriminant parameter to enhance the sensitivity to the gg-initiated signal.

The kinematic selection has been conceived to maximise the signal significance over the background.

- Events with two oppositely charged electron or muons in the mass window (76< m_{ll} < 106) GeV are selected.
- A series of kinematic requirements are employed to suppress the Drell-Yan background, i.e. $E_T^{\text{miss}} > 180$ GeV and (380< m_T^{ZZ} <1000) GeV. Furthermore, a cut on the azimuthal angle between the transverse momentum of the dilepton system and the missing transverse momentum is exploited, i.e. $\Delta\phi(p_T^{ll}, E_T^{\text{miss}})$ <2.5.

- Events with a b-jet whose p_T is greater than 20 GeV are rejected to suppress the top-quark background.
- Finally, another requirement on the azimuthal angle between the two leptons, $\Delta\phi_{ll}$ <1.4, is applied.

The dominant background of the analysis is the $q\bar{q}$ $\rightarrow$ZZ production as well as $q\bar{q}$ $\rightarrow$WZ. Background contributions from events having an isolated lepton pair originate from WW, $t\bar{t}$, Wt and $Z \rightarrow \tau\tau$ final states. Subdominant background processes are represented by Z $\rightarrow$ee or $Z \rightarrow \mu\mu$ where the E_T^{miss} term is poorly reconstructed.

- The $q\bar{q}$ $\rightarrow$ZZ background is estimated, in a similar way as for the 4 lepton final state, with the POWHEG generator; additional electroweak corrections are applied.
- The WZ background is also estimated with the simulation and validated in data using a signal-free control region with three leptons in the final state.
- The WW, $t\bar{t}$, Wt and $Z \rightarrow \tau\tau$ components are estimated in data in a eμ control region using a relaxed selection.
- The Z boson background ($Z \rightarrow \mu\mu$ and Z $\rightarrow$ee) is estimated in data using a two-dimensional sideband created by reversing the $\Delta\phi(p_T^{ll}, E_T^{\text{miss}})$ and the $\Delta\phi_{ll}$ cuts.

The observed event yields agree with the total predicted ones from the SM within the uncertainties. Figure 6.45 (a) illustrates the distribution of the transverse mass of the ZZ system for the ee and $\mu\mu$ final states in the signal region compared to the predicted contributions from the SM and to a Higgs boson generated with $\mu_{\text{off-shell}}$=10.

6.12.2 The analysis in the WW $\rightarrow$ e$\nu\mu\nu$ final state

As in the previous paragraph, the neutrinos in the final states do not allow for a kinematic reconstruction of m_{VV}. Hence, a transverse mass (m_{WW}^T) is calculated from the dilepton system transverse energy and the vectorial sum of neutrino transverse momenta:

$$m_{\text{T}}^{WW} = \sqrt{\left(E_{\text{T}}^{\ell\ell} + p_{\text{T}}^{\nu\nu}\right)^2 - \left|\boldsymbol{p}_{\text{T}}^{\ell\ell} + \boldsymbol{p}_{\text{T}}^{\nu\nu}\right|^2}. \tag{6.17}$$

In order to isolate the off-shell Higgs boson production, a new variable, R_8, is used:

$$R_8 = \sqrt{m_{ll}^2 + (a \cdot m_T^{WW})^2}. \tag{6.18}$$

The coefficient a is set to 0.8 and the analysis is run for $R_8 > 450$ GeV. These values are optimised for the off-shell signal sensitivity.

The distribution of the R_8 variable is shown in Figure 6.45 (b) in the signal region of the analysis (380-1000 GeV) for the SM expectation and for a Higgs boson generated at $\mu_{\text{off-shell}}$=10.

The two backgrounds with the largest expected event yields are the top and $q\bar{q} \rightarrow$ WW productions.

- Control regions are determined to compute the contributions of the top and the $q\bar{q} \rightarrow$ WW backgrounds in the signal region; transfer factors are calculated and applied in the signal regions.
- The remaining background components are negligible and are estimated from Monte Carlo simulations.

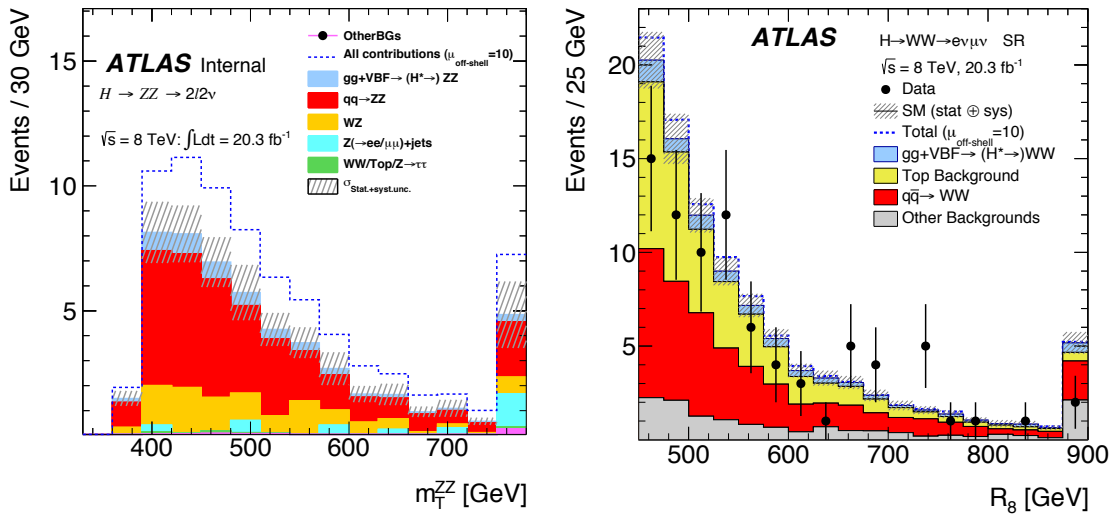

(a) **(b)**

Figure 6.45: (a) Observed distribution of m_{ZZ}^T in the range of the analysis (380< m_{ZZ}^T <1000) GeV combining the 2e2ν and the 2μ2ν channels. The hatched area shows the combined statistical and systematic uncertainties whilst the dashed line corresponds to the total expected event yield including all backgrounds and the Higgs boson signal generated with $\mu_{\text{off-shell}}$=10. (b) Observed distributions of R_8 for the signal region above 450 GeV, compared to the expected contributions from the SM including the Higgs boson. The dashed line corresponds to the total expected event yield, including all backgrounds and the Higgs boson with $\mu_{\text{off-shell}}$=10.

6.13 Statistical combination of the ZZ→4l, ZZ→2l2ν and WW→ νlν final states

The present Section will give an overview of the statistical combination of the ZZ and WW analyses for what concerns the off-shell-only contribution and the off+on-shell combination with the low mass coupling analysis. These results have been obtained by fixing the Higgs mass to its ATLAS measured value m_H=125.36 GeV [20].

In Section 6.13.1 the off-shell studies in the ZZ→ 4l, ZZ→ 2l2ν and WW→ $l\nu l\nu$ ($l = e, \mu$) are combined. As stated in the theoretical introduction in Section 6.1, the essential assumption is that the couplings of the Higgs boson to other particles are the same as for the Standard Model. Regarding the off-shell-only combination, two different approaches are presented in Section 6.13.1. In the second part of this paragraph (Section 6.13.2), the off-shell analyses in the ZZ→ 4l, ZZ→ 2l2ν and WW→ $l\nu l\nu$ are combined with the on-shell results of the same channels. The combination is performed only for the 2012 dataset ($\sqrt{s}$=8 TeV). The various assumptions supporting the different combination procedures are expressed in Section 6.13.2. The on-shell signal strength for the VH production is assumed to scale as the VBF one whereas the on-shell signal strength for $t\bar{t}H$ is scaled as the ggF one. Besides, the $t\bar{t}H$ production is expected to provide negligible contribution to the off-shell measurement.

The tests statistics, profile likelihood ratio and CL_s, employed in this Section to probe the upper limits on the off-shell signal strength and extract the Higgs total width are described in Appendix C. The final 95% C.L. limits with the CL_s method are generated as a function of the unknown ratio

of the background-to-signal k-factor (Sections 6.1 and 6.2.1), $R^B_{H*} = \frac{KH^*_{gg}(m_{ZZ})}{KH^*(m_{ZZ})}$, while comparisons between observed and Monte Carlo expected limits are calculated in the soft collinear approximation, i.e. R^B_{H*}=1.

The results presented in this Section rely on the asymptotic assumption. This hypothesis has been corroborated with Monte Carlo tests in the range of parameters where the limits are derived (Appendix C). In order to reduce the typical CPU-time for each fit instance, the systematic uncertainties (nuisance parameters) entering the fit are removed (*pruned*) if their impact on the final limit is negligible. The bias on the extraction of the upper limit introduced by the pruning was extracted and found to be extremely small. In order to ensure the validity of the results, the outcomes of the off and off+on-shell fits are internally cross-checked with two independent procedures and results are found to be fully consistent between the two methods.

6.13.1 Off-shell combination

The first step of the off-shell combination between the ZZ and WW final states is the treatment of the systematic uncertainties in the two channels. The main systematics for both ZZ and WW are related to the theory uncertainties on the gg and qq-initiated processes. These systematics are kept as fully correlated in the various channels. As indicated in Section 6.9.3, the experimental systematic uncertainties are very small and their impact on the final combined limit is imperceptible. The parameter of interest ($\mu_{\text{off-shell}}$) is correlated between the WW and ZZ final states while $R^B_{H*} = \frac{KH^*_{gg}(m_{ZZ})}{KH^*(m_{ZZ})}$ is kept fixed in order to derive the scanning of $\mu_{\text{off-shell}}$ as a function of this parameter.

The different fitting options are expressed below:

- fit on $\mu_{\text{off-shell}}$ - fixing the ratio of the signal strength ggF and VBF to the SM expectation, namely:
$$\frac{\mu^{ggF}_{\text{off-shell}}}{\mu^{ggF}_{\text{off-shell}}} = 1; \tag{6.19}$$
- fit on $\mu^{ggF}_{\text{off-shell}}$ - fixing the VBF off-shell signal strength to the SM expectation, i.e. $\mu^{VBF}_{\text{off-shell}}$=1.

Observed and expected values for $\mu_{\text{off-shell}}$ and $\mu^{ggF}_{\text{off-shell}}$ for the combined ZZ and WW analyses in the soft collinear approximation (R^B_{H*}=1) are listed in what follows:

$$\mu_{\text{off-shell}} = 0.6^{+1.8}_{-0.6},\ 1.0^{+3.7}_{-1.0}, \tag{6.20}$$

$$\mu^{ggF}_{\text{off-shell}} = 0.4^{+1.8}_{-0.4},\ 1.0^{+4.0}_{-1.0}. \tag{6.21}$$

In the two cases the negative uncertainty is given by the lower bound of $\mu_{\text{off-shell}} > 0$. These limits are obtained under the asymptotic assumption (Appendix C) by looking at the value of the parameter of interest at which the likelihood function increases by 3.84 (2-sided convention).

Figure 6.46 (a) shows the scan of the negative log-likelihood, -2ln Λ, as a function of the off-shell signal strength when fixing the same scale factor for the ggF and VBF off-shell couplings for the WW+ZZ channels. Figure 6.46 (b) displays the scan of the negative log-likelihood when setting the VBF off-shell signal strength to the SM. The limit on $\mu_{\text{off-shell}}$ and $\mu^{ggF}_{\text{off-shell}}$ computed with the CL_s method taking as null hypothesis the SM off-shell rates as a function of the unknown background-to-signal ratio k-factor R^B_{H*} are reported in Figures 6.47 (a) assuming one single scale factor for

both ggF and VBF processes and Figure 6.47 (b) fixing the VBF production to the SM expectation. The values of the observed and expected limits on $\mu_{\text{off-shell}}$ and $\mu^{ggF}_{\text{off-shell}}$ extracted at 95% C.L. for the full off-shell combination are illustrated in Table 6.9. Observed and expected 95% C.L. upper limits on $\mu_{\text{off-shell}}$ and $\mu^{ggF}_{\text{off-shell}}$ for the ZZ+WW final states within the range $0.5 < R^{B}_{H*} < 2$ are also shown in the same Table.

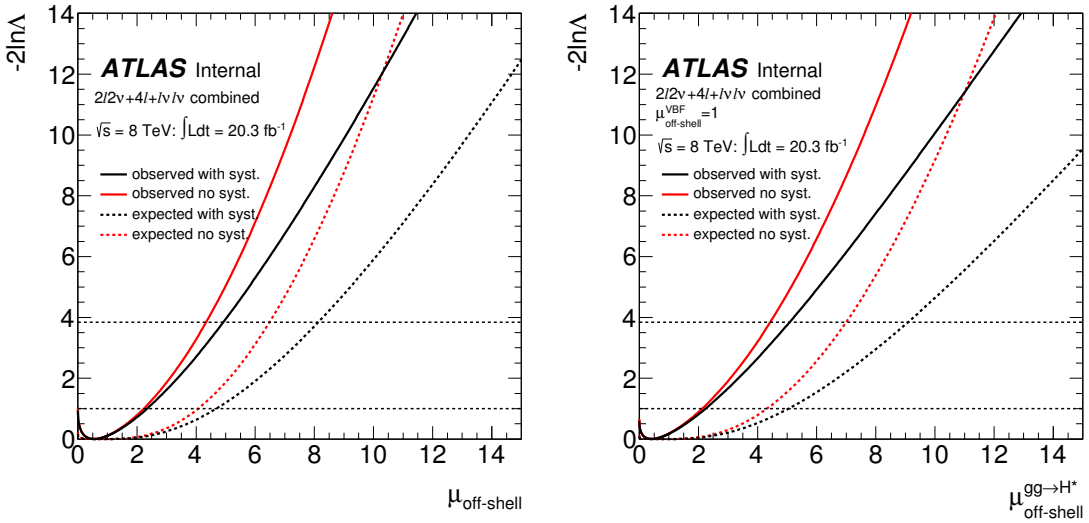

Figure 6.46: Scan of the negative log-likelihood as a function of $\mu_{\text{off-shell}}$ (a) and $\mu^{ggF}_{\text{off-shell}}$ (b) for the combined ZZ and WW channels. The black (red) dashed line represents the expected value with (and without) systematic uncertainties, solid black (red) line indicates the observed value with (without) systematic uncertainties.

$\mu_{\text{off-shell}}$ 95% CL		Observed	Expected
-2ln Λ	with sys	4.92	8.13
-2ln Λ	no sys	4.34	6.48
CL_s	with sys	6.23	8.12
CL_s	no sys	5.27	6.48
R^{B}_{H*}	0.5	**1**	2
Observed	5.1	**6.2**	8.6
Expected	6.7	**8.1**	11.0

$\mu^{ggF}_{\text{off-shell}}$ 95% CL		Observed	Expected
-2ln Λ	with sys	5.08	9.08
-2ln Λ	no sys	4.43	6.99
CL_s	with sys	6.71	9.07
CL_s	no sys	5.58	6.99
R^{B}_{H*}	0.5	**1**	2
Observed	5.3	**6.7**	9.8
Expected	7.3	**9.1**	13.0

Table 6.9: Observed and expected limits on $\mu_{\text{off-shell}}$ (left) and $\mu^{ggF}_{\text{off-shell}}$ (right) extracted at 95% C.L. for the off-shell ZZ+WW final states. Observed and expected 95% C.L. upper limits on $\mu_{\text{off-shell}}$ (bottom left table) and $\mu^{ggF}_{\text{off-shell}}$ (bottom right table) for the ZZ+WW final states within the range $0.5 < R^{B}_{H*} < 2$.

The *pull* distributions are generated for three different configurations when the parameter of interest μ is set to the following values:

- observed value in data $\hat{\mu} = 0.55$;
- observed value at 95% C.L. ($\mu = 4.92$);
- value near the expected limit on ($\mu = 8$).

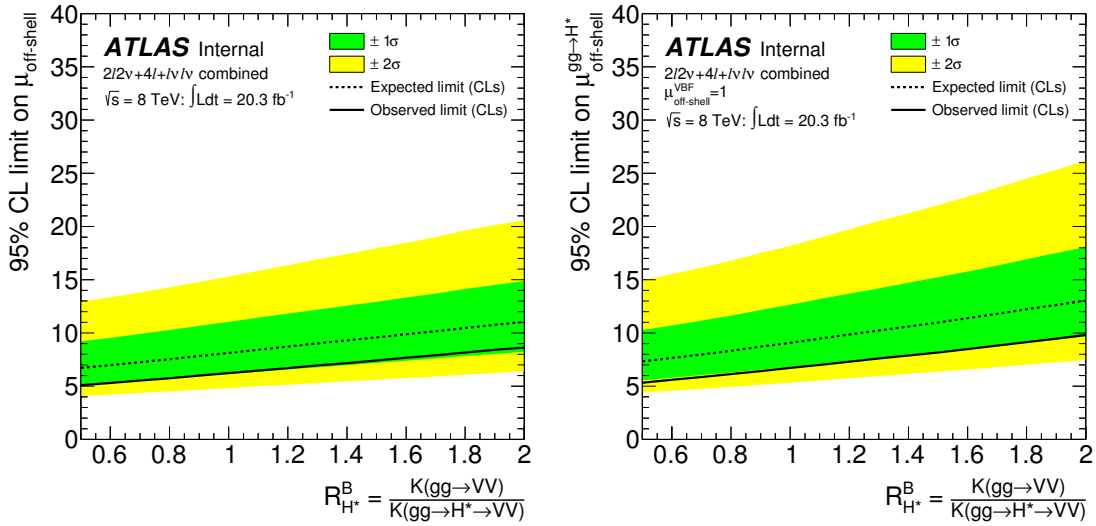

(a) **(b)**

Figure 6.47: Observed and expected combined 95% C.L. upper limit on $\mu_{\text{off-shell}}$ (a) and on $\mu^{ggF}_{\text{off-shell}}$ (b) as a function of R^B_{H*} for the ZZ+WW off-shell final states. The upper limits are calculated from the CL_s method, being the SM the null hypothesis.

Figure 6.48 shows the pull distributions for the nuisance parameters used in the analysis, employing the first fitting configuration namely $\mu^{\text{VBF}}_{\text{off-shell}} = \mu^{\text{ggF}}_{\text{off-shell}}$. The red points with error bars are the fitted values of the nuisance parameters (post-fit results) and the error bars are the uncertainties. The yellow bands show the Hesse correlation with the fitted parameter of interest ($\mu_{\text{off-shell}}$). The most pulled nuisance parameters (second fitting configuration, e.g. pulls generated when the parameter of interest μ is set to its observed value, μ=4.92 at 95% C.L.) are mainly associated to the most sensitive systematics entering the model, namely the QCD scales uncertainties for the gg-initiated signal and its background as well as the one related to the interference term.

6.13.2 Off-shell and on-shell combination

In this Section, the off-shell results are combined with the on-shell $H \to$ ZZ and $H \to$ WW analyses. The most relevant theoretical nuisance parameters as well as all the experimental systematics that are identified as coming from the same source of uncertainty are correlated between the off-shell and the on-shell analyses. The fit options employed in this analysis are listed below. In parenthesis the relevant Figures and Tables are indicated.

- Fit on $\frac{\Gamma_H}{\Gamma_{SM}}$ - when using the equation (6.19) to profile a common μ (Figure 6.49, Table 6.10 left).
- Fit on $\frac{\Gamma_H}{\Gamma_{SM}}$ - when profiling μ_{ggF} and fixing μ_{VBF} to its SM expectation (Figure 6.50, Table 6.10 right).
- Fit on $\frac{\Gamma_H}{\Gamma_{SM}}$ - when profiling both μ_{ggF} and μ_{VBF} (Figure 6.51, Table 6.11 left).
- Fit on R_{gg} defined as:

$$R_{gg} = \frac{\mu^{ggF}_{\text{off-shell}}}{\mu^{ggF}_{\text{on-shell}}}. \tag{6.22}$$

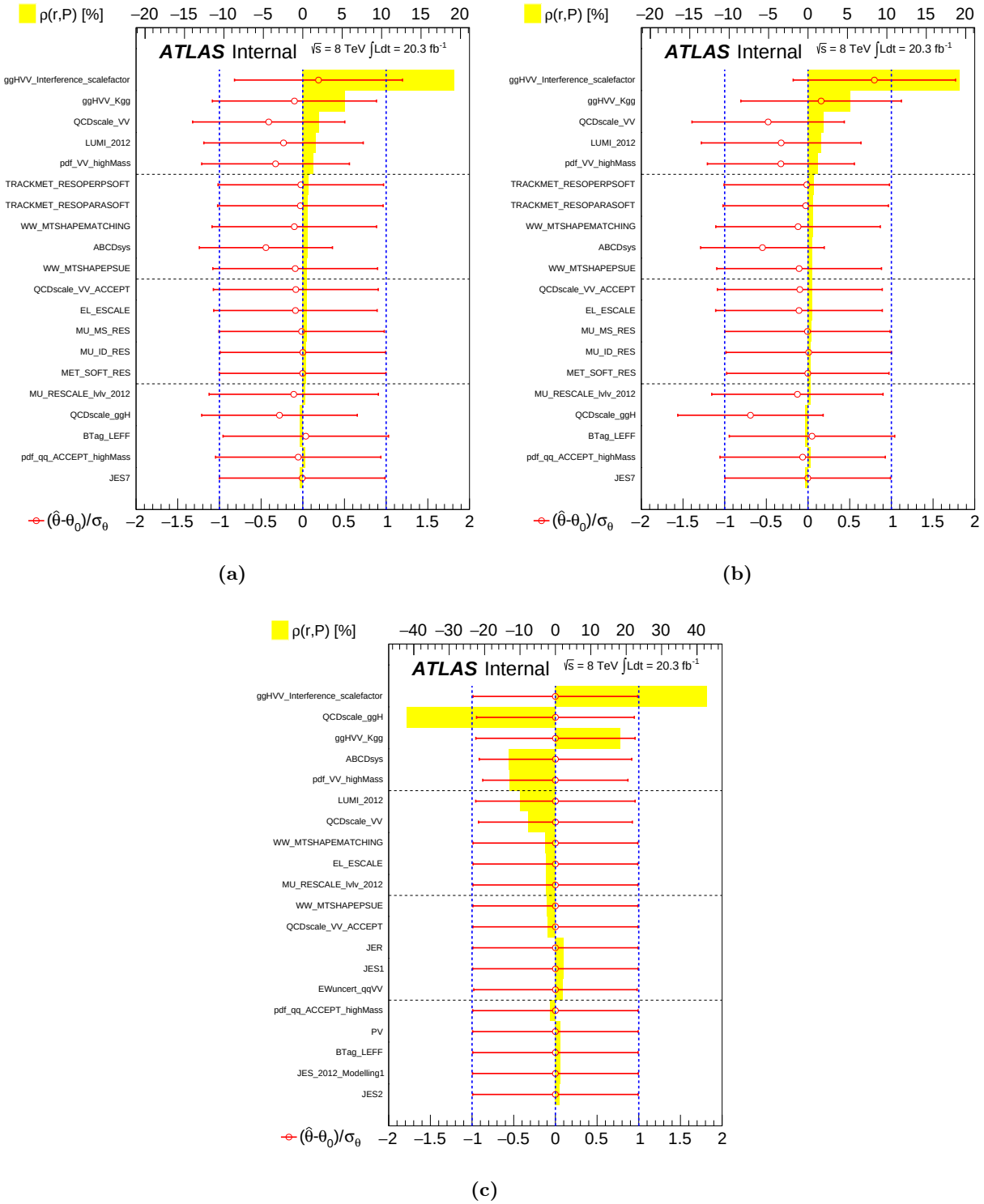

Figure 6.48: Pulls for various nuisance parameters using the full off-shell $\mu^{\mathrm{VBF}} = \mu^{\mathrm{ggF}}$ combination from (a) the observed unconditional fit ($\hat{\mu} = 0.55$), (b) the observed conditional fit with μ fixed at its 95% C.L. ($\mu = 4.92$), and (c) an unconditional fit to Asimov generated near the expected limit on μ ($\mu = 8$). In each case, the red points show the fitted value of the nuisance parameters and the error bars are the uncertainties from the Hessian.

while profiling μ_{VBF} under the assumption that $\mu_{VBF} = \mu^{VBF}_{\text{off-shell}} = \mu^{VBF}_{\text{on-shell}}$ and fixing the ratio $\frac{\Gamma_H}{\Gamma_{SM}} = 1$ (Figure 6.52, Table 6.11 right). The parameter R_{gg} is introduced because it is sensitive to possible modifications of the gluon couplings in the high mass range with respect to the off-shell value.

As for the previous Sections, the limits are computed with the CL_s method taking as null hypothesis the SM rates. The best fit values (observed and expected) from the negative log likelihood scan for the last two fitting configurations are:

$$\frac{\Gamma_H}{\Gamma_{SM}} = 0.4^{+1.4}_{-0.4},\ 1.0^{+3.5}_{-1.0}; \tag{6.23}$$

$$R_{gg} = 0.3^{+1.4}_{-0.4},\ 1.0^{+3.9}_{-1.0}. \tag{6.24}$$

$\frac{\Gamma_H}{\Gamma_{SM}}$ 95% C.L.		Observed	Expected
-2ln Λ	with sys	3.78	8.02
-2ln Λ	no sys	3.38	6.49
CL_s	with sys	5.44	7.99
CL_s	no sys	4.80	6.49
R^B_{H*}	0.5	**1**	2
Observed	4.4	**5.4**	7.5
Expected	6.5	**8.0**	11.2

$\frac{\Gamma_H}{\Gamma_{SM}}$ 95% CL		Observed	Expected
-2ln Λ	with sys	3.84	8.03
-2ln Λ	no sys	3.42	6.52
CL_s	with sys	5.49	8.00
CL_s	no sys	4.85	6.52
R^B_{H*}	0.5	**1**	2
Observed	4.5	**5.5**	7.6
Expected	6.5	**8.0**	11.1

Table 6.10: Left: Observed and expected limits on $\frac{\Gamma_H}{\Gamma_{SM}}$ when profiling a common μ for ggF and VBF contributions. R^B_{H*} spans within the range 0.5< R^B_{H*} <2. **Right**: Observed and expected limits on $\frac{\Gamma_H}{\Gamma_{SM}}$ when profiling μ_{ggF} and fixing μ_{VBF} to its SM expectation.

$\frac{\Gamma_H}{\Gamma_{SM}}$ 95% CL		Observed	Expected
-2ln Λ	with sys	3.77	8.04
-2ln Λ	no sys	3.41	6.52
CL_s	with sys	5.46	8.01
CL_s	no sys	4.83	6.52
R^B_{H*}	0.5	**1**	2
Observed	4.5	**5.5**	7.5
Expected	6.5	**8.0**	11.2

R_{gg} 95% CL		Observed	Expected
-2ln Λ	with sys	3.97	9.05
-2ln Λ	no sys	3.52	7.12
CL_s	with sys	5.95	9.01
CL_s	no sys	5.20	7.11
R^B_{H*}	0.5	**1**	2
Observed	4.7	**6.0**	8.6
Expected	7.1	**9.0**	13.4

Table 6.11: Left: Observed and expected limits on $\frac{\Gamma_H}{\Gamma_{SM}}$ when profiling both μ_{ggF} and μ_{VBF}. R^B_{H*} spans within the range 0.5< R^B_{H*} <2. **Right**: Observed and expected limits on R_{gg} when profiling μ_{VBF}.

The pull distributions are reported in Figure 6.53.

6.14 Conclusions

The measurement in the high mass region of the ZZ and WW final states provides a unique handle to infer the off-shell signal strength and indirectly constrain the total Higgs width. In this Chapter, the analysis on the determination of the off-shell signal strength in the ZZ→ 4l channel is performed with data collected at $\sqrt{s}$=8 TeV using a total integrated luminosity of 20.3 fb^{-1}. The observed 95% confidence level upper limit using the CL_s method on the off-shell signal strength is in the

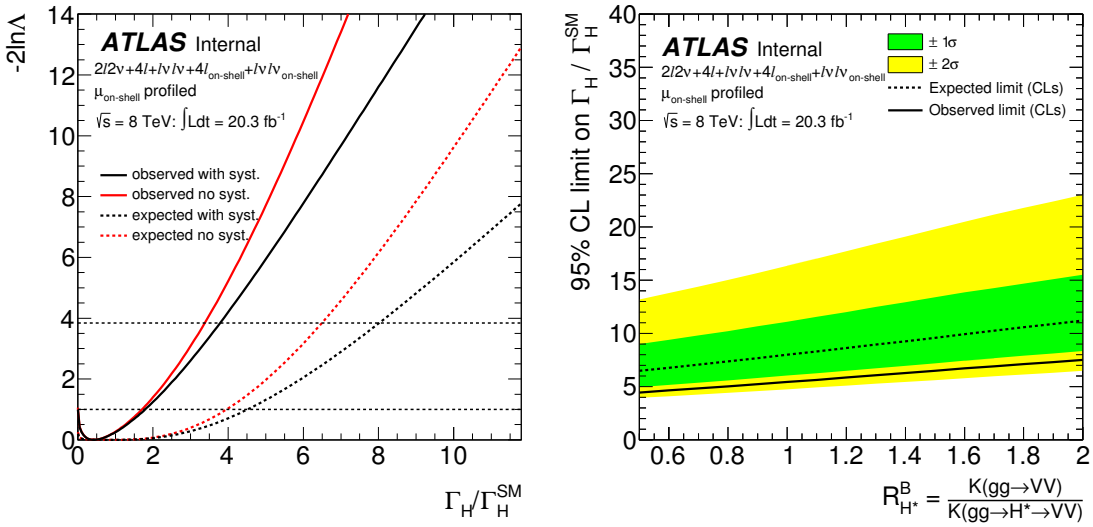

Figure 6.49: (a) Scan of the negative log likelihood as a function of $\frac{\Gamma_H}{\Gamma_{SM}}$ when profiling a common μ by fixing the ratio of the ggF and VBF signal strengths to the SM expectation. The black (red) dashed line represents the expected value with (and without) systematic uncertainties, while the solid black line indicates the observed value. (b) Observed and expected combined 95% CL upper limit on R^B_{H*} with the same assumption of (a).

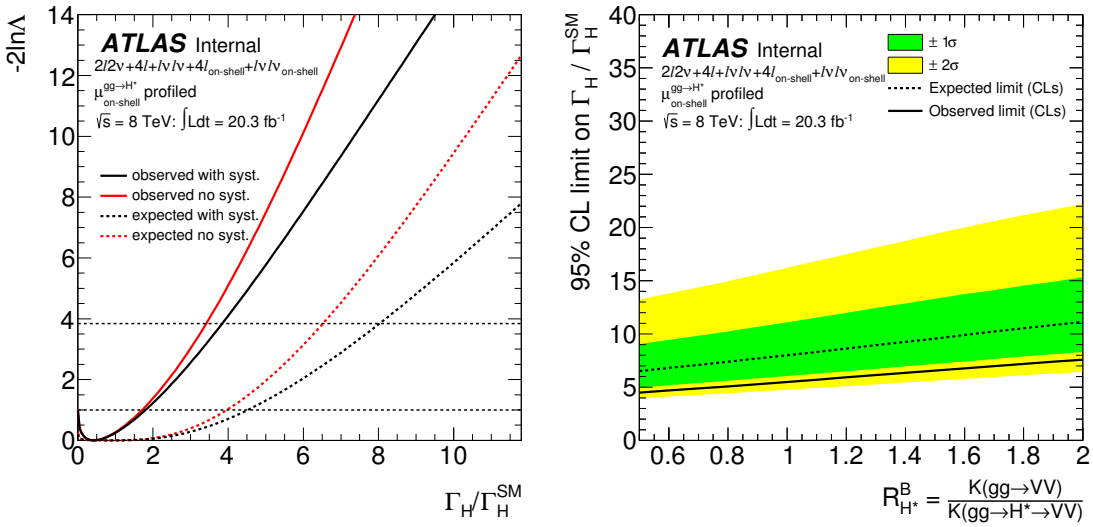

Figure 6.50: (a) Scan of the negative log likelihood as a function of $\frac{\Gamma_H}{\Gamma_{SM}}$ when profiling μ^{ggF} and fixing μ^{VBF} to its SM expectation. The black (red) dashed line represents the expected value with (and without) systematic uncertainties, while the solid black line indicates the observed value. (b) Observed and expected combined 95% CL upper limit on R^B_{H*} with the same assumption of (a).

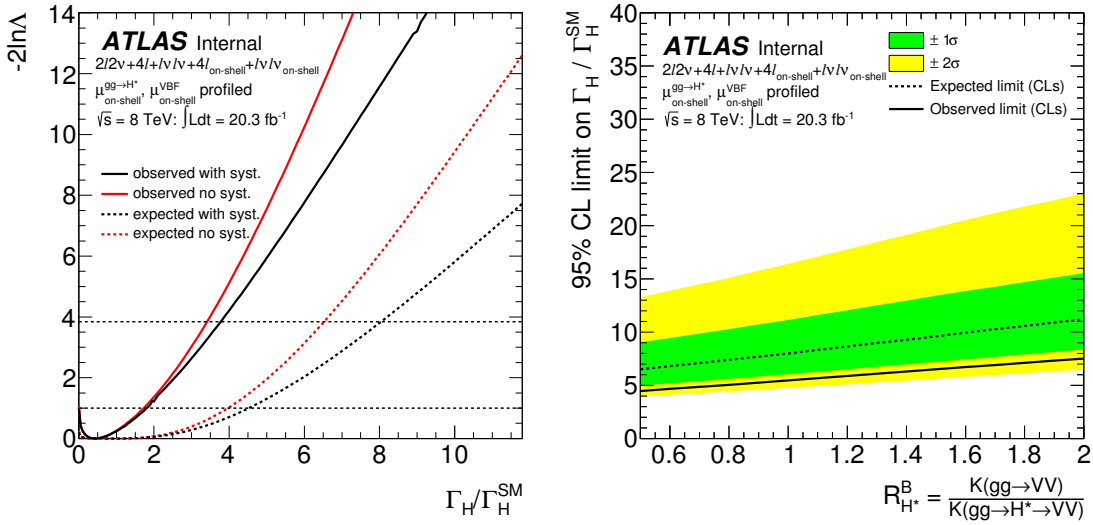

(a) **(b)**

Figure 6.51: (a) Scan of the negative log likelihood as a function of $\frac{\Gamma_H}{\Gamma_{SM}}$ when profiling both μ^{ggF} and μ^{VBF}. The black (red) dashed line represents the expected value with (and without) systematic uncertainties, while the solid black line indicates the observed value. (b) Observed and expected combined 95% CL upper limit on R^B_{H*} with the same assumption of (a).

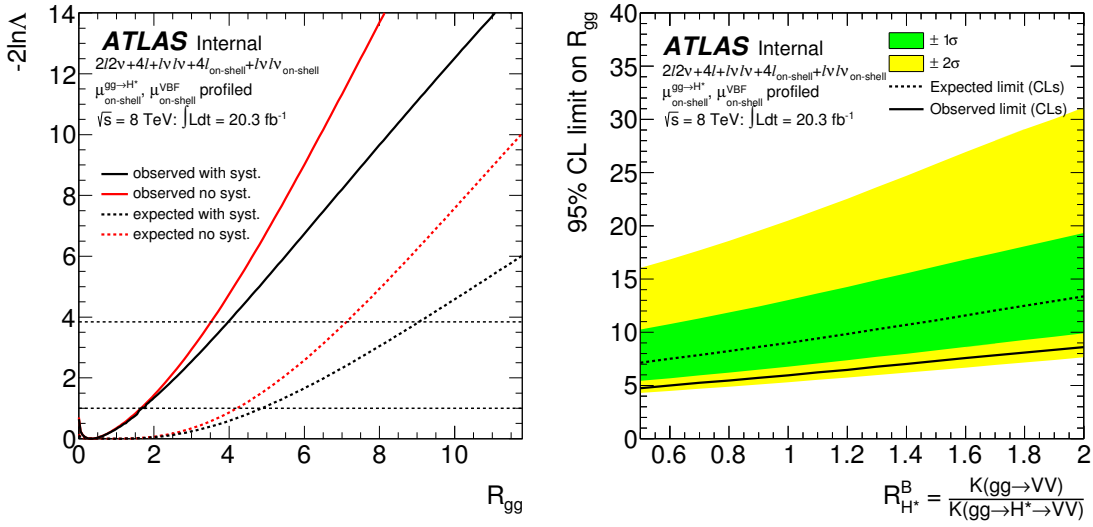

(a) **(b)**

Figure 6.52: (a) Fit of R_{gg} when profiling μ^{VBF}. The ratio $\frac{\Gamma_H}{\Gamma_{SM}}$ is set to 1. (b) Observed and expected combined 95% CL upper limit on R^B_{H*} with the same assumption of (a).

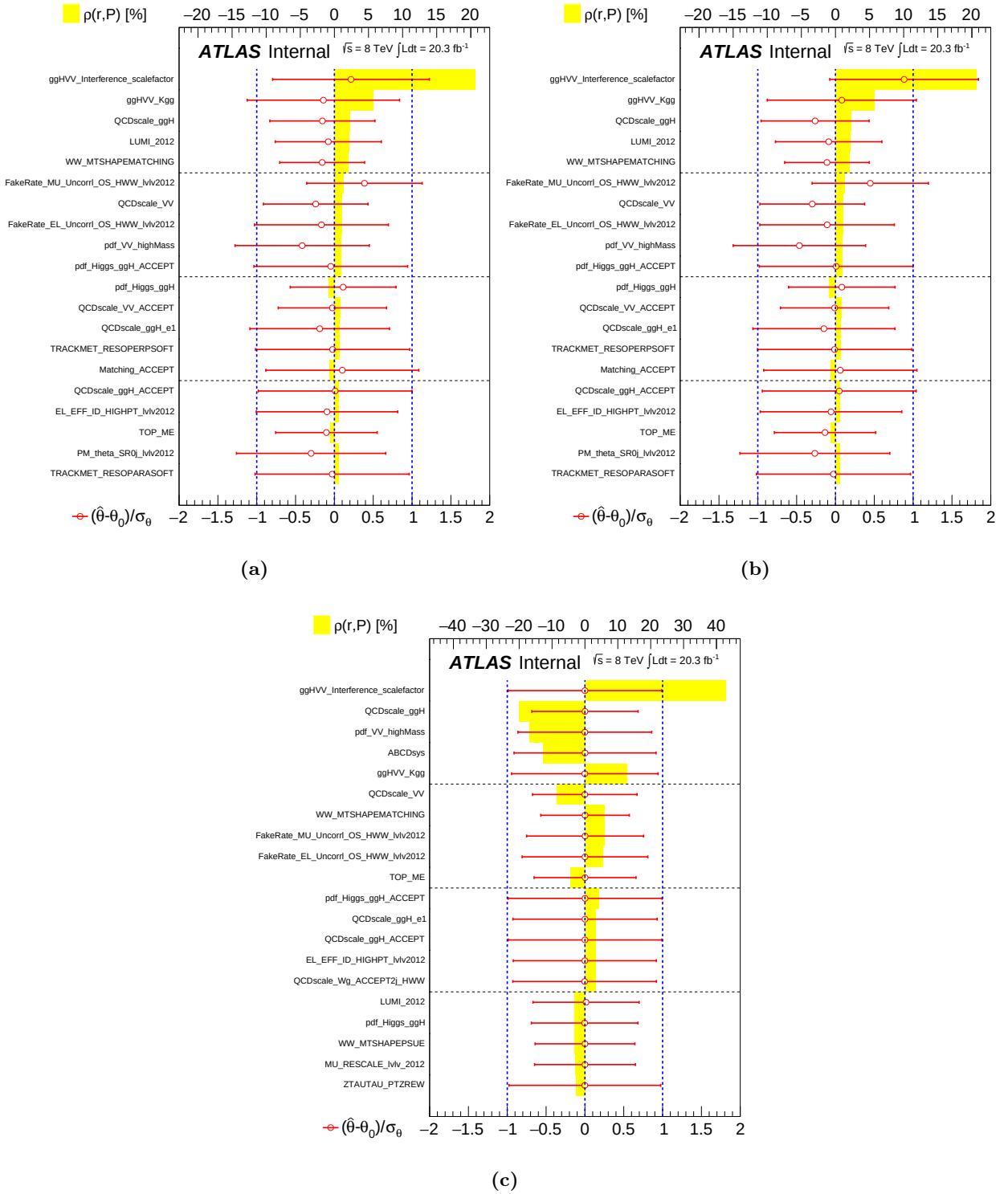

Figure 6.53: Pulls for various nuisance parameters from the on+off-shell combination with μ^{ggF} and μ^{VBF} floating from (a) the observed unconditional fit ($\hat{\mu} = 0.44$), (b) the observed conditional fit with μ fixed at its 95%CL ($\mu = 3.77$), and (c) an unconditional fit to Asimov generated near the expected limit on μ ($\mu = 8$). In each case, the red points show the fitted value of the nuisance parameters and the error bars are the uncertainties from the Hessian.

range 5.5-9.5 when the unknown background-to-signal k-factor ratio R^B_{H*} is varied between 0.5 and 2 being the median expected range 8.8-14.3. As for the off-shell signal strength, the observed 95% C.L. upper limit on $\mu_{\text{off-shell}}$ lies in the range 5.1-8.6 (expected 6.7-11) when varying the unknown k-factor between half and twice the known signal k-factor. A similar computation has been performed to determine the gluon-initiated contribution of the off-shell signal strength, namely $\mu^{ggF}_{\text{off-shell}}$. Its value encompasses the range 5.3-9.8 (observed) and 7.3-13 (expected). A combination of the off-shell results with the on-shell measurements of ZZ and WW is exploited. Various assumptions are tested (Section 6.13.2): the most general result quoted in [141] is based on the fit of $\frac{\Gamma_H}{\Gamma_{SM}}$ when profiling μ_{ggF} and μ_{VBF}. The observed (expected) 95% C.L. upper limits on the total Higgs width ratio to the SM value span from 4.5 (6.5) to 7.5 (11.2). Adopting the soft collinear approximation, R^B_{H*}=1, these values translate into an observed (expected) 95% C.L. upper limit on the Higgs boson total width of 22.7 (33.0) MeV.

Chapter 7

Off-shell Higgs couplings measurement using diboson events at HL-LHC

Contents

This Chapter will report on prospects studies on the Higgs off-shell couplings in the *High-Luminosity* LHC (HL-LHC) configuration using a simplified version of the main analysis employed in Chapter 5 (toy model). Section 7.1 will cover the production and validation of MCFM samples at $\sqrt{s}$=13 TeV and $\sqrt{s}$=14 TeV. Section 7.2 will describe the method to extract the extrapolation for the HL-LHC scenario starting from the generated samples at $\sqrt{s}$=13 TeV and $\sqrt{s}$=14 TeV while Section 7.3 will report the results of the off-shell coupling measurement. Similarly to the analysis previously carried out, this study includes the $H \to ZZ \to$ 4l final state only.

7.1 Monte Carlo event generation at $\sqrt{s}$=13 TeV and $\sqrt{s}$=14 TeV

Monte Carlo generation with MCFM is performed for $\sqrt{s}$=13 TeV and $\sqrt{s}$=14 TeV on $gg \to H^* \to ZZ \to$ 4l signal, $gg \to$ ZZ continuum background and $gg \to (H^*) \to ZZ \to$ 4l (comprising signal, background and interference between signal and background, SBI). As for the previous Monte Carlo production, the input Higgs mass is set to m_H=125.5 GeV whereas the QCD factorisation and renormalisation scales are taken as $\frac{m_{ZZ}}{2}$. In order to ensure consistency with the baseline generation at $\sqrt{s}$=8 TeV, the generation cuts applied at the grid level are the same as the ones detailed in Section 6.2. In addition, the $q\bar{q} \to$ ZZ POWHEG sample has been generated at $\sqrt{s}$=13 and 14 TeV.

Figure 7.1 illustrates the m_{4l} distribution plotted for the various gg-related processes in the 2e2μ channel at $\sqrt{s}$=13 TeV as well as the contribution of the signal-to-background negative interference.

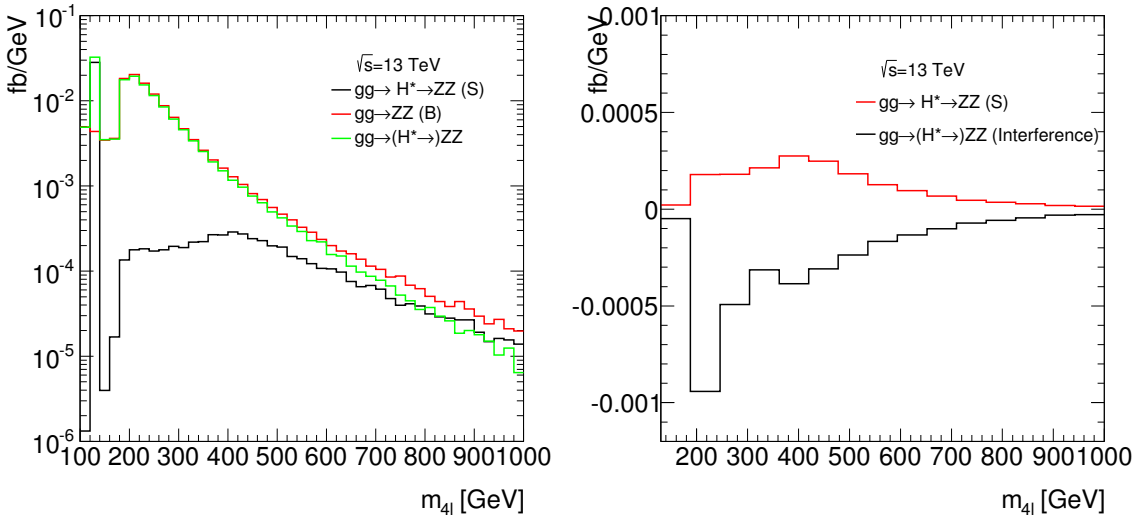

(a) **(b)**

Figure 7.1: (a) Differential cross sections generated with MCFM at $\sqrt{s}$=13 TeV for the gg-initiated processes in the 2e2μ channel at the matrix element level. (b) Comparison of the Higgs signal with the interference contribution.

7.2 Outline of the method

In order to extract the upper limit on the off-shell signal strength for the HL-LHC scenario, the matrix element-based kinematic discriminant presented in Sections 6.6 and 6.10.3 is adopted. The various checks on the validity of the PDF extraction are repeated with this new configuration.

The workflow of the analysis is articulated as follows:

- the m_{4l} distributions for the gg-initiated processes, namely signal, background and SBI, and for the $q\bar{q} \rightarrow$ ZZ process are generated with MCFM and POWHEG respectively at $\sqrt{s}$= 8 TeV as well as at $\sqrt{s}$= 14 TeV. The m_{4l} scaling factors are then computed as a function of the invariant mass for these four contributions (Figure 7.2) and the ME-based discriminant is reweighted according to the mass of the event.

- The $pp \rightarrow$ VV +2j (Section 6.3) contribution has been scaled as the gg-related initial state cross section with respect to the generation performed at $\sqrt{s}$=14 TeV because no Monte Carlo production at $\sqrt{s}$= 13 and $\sqrt{s}$= 14 TeV is currently available. Anyhow, this term provides a negligible impact on the final upper limit on the off-shell Higgs couplings.

The generation at $\sqrt{s}$=13 TeV was performed as a validation check of the method; as for the production at $\sqrt{s}$=14 TeV, two different configurations are explored in the analysis:

i $L_1 = \int \mathcal{L} dt$= 300 fb^{-1};

ii $L_2 = \int \mathcal{L} dt$= 3000 fb^{-1}.

The results on the off-shell coupling extraction will be documented in Sections 7.3. The main assumption underneath this simplified parametrisation [168] is that the signal and background efficiencies for $\sqrt{s}$=8 TeV are preserved in the high-luminosity-high-energy scenario. Furthermore, the 4 leptons invariant mass kinematic phase-space of the analysis is identical to that of the main analysis, e.g. (220< m_{4l} <1000) GeV.

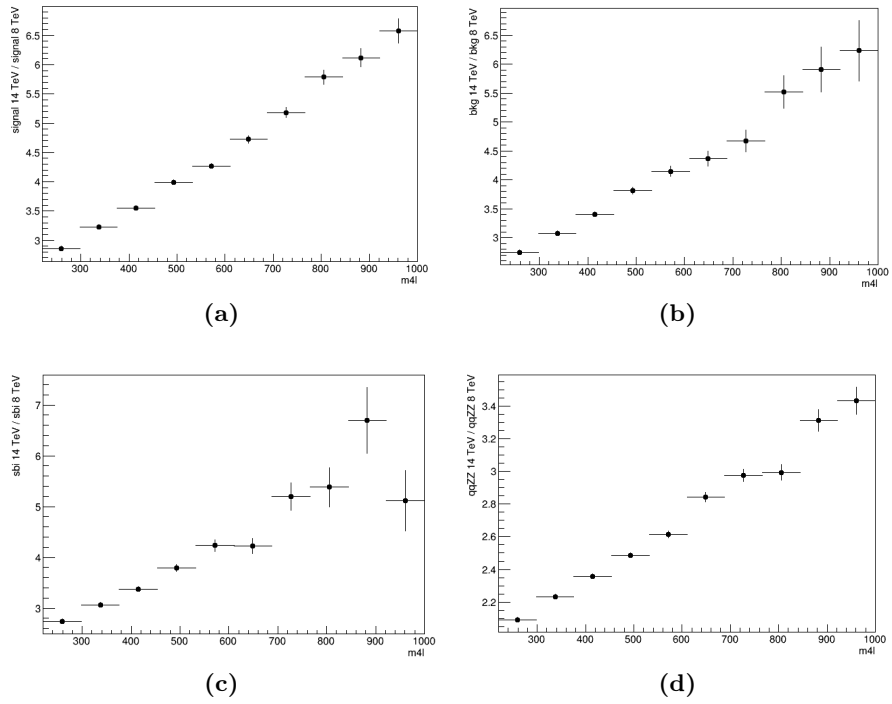

(a) **(b)** **(c)** **(d)**

Figure 7.2: m_{4l}-dependent reweighting functions from $\sqrt{s}$=8 TeV to $\sqrt{s}$=14 TeV for the $gg \to H^* \to$ 4l signal sample (a), the background gg→ZZ contribution (b), the SBI, comprising signal, background and interference (c) and the $q\bar{q}$ →ZZ term (d).

7.2.1 Treatment of the systematic uncertainties

Since the experimental systematics do not play a major role in the off-shell limit determination (their impact is of the order of 0.3% on the final upper limit on $\mu_{\text{off-shell}}$) as observed in Section 6.9.3, these uncertainties are not included in the final computation of the limit.

Recalling equation (6.12), the parametrisation for the gg-scaling of the templates in the fit is:

$$\begin{aligned} \mathrm{MC}_{gg\to(H^*)\to ZZ}(\mu_{\text{off-shell}}) &= \left(K^{H^*}(m_{ZZ})\cdot\mu_{\text{off-shell}} - K^{H^*}_{gg}(m_{ZZ})\cdot\sqrt{R^B_{H^*}\cdot\mu_{\text{off-shell}}}\right)\cdot \mathrm{MC}^{\mathrm{SM}}_{gg\to H^*\to ZZ} \\ &+ K^{H^*}_{gg}(m_{ZZ})\cdot\sqrt{R^B_{H^*}\cdot\mu_{\text{off-shell}}}\cdot \mathrm{MC}^{\mathrm{SM}}_{gg\to(H^*)\to ZZ} \\ &+ K^{H^*}_{gg}(m_{ZZ})\cdot\left(R^B_{H^*} - \sqrt{R^B_{H^*}\cdot\mu_{\text{off-shell}}}\right)\cdot \mathrm{MC}^{\mathrm{cont}}_{gg\to ZZ}. \end{aligned} \quad (7.1)$$

The treatment of the systematic uncertainties exploited in this model is expressed below:

- $\underline{K^{H^*}(m_{ZZ})}$ is the signal LO-to-NNLO k-factor → As in the main analysis (QCD scale uncertainty), 30% fully correlated, among S, SBI and B, systematic uncertainties are assessed.
- $\underline{R^B_{H^*}(m_{ZZ})}$ is the background-to-signal k-factor defined in Section 6.2.2 → 10% systematic uncertainty is given on this term following the prescriptions in [152].
- An additional 10% normalisation systematics is quoted for the $q\bar{q} \to$ ZZ sample due to QCD and PDF scale uncertainties as reported in Section 6.9.

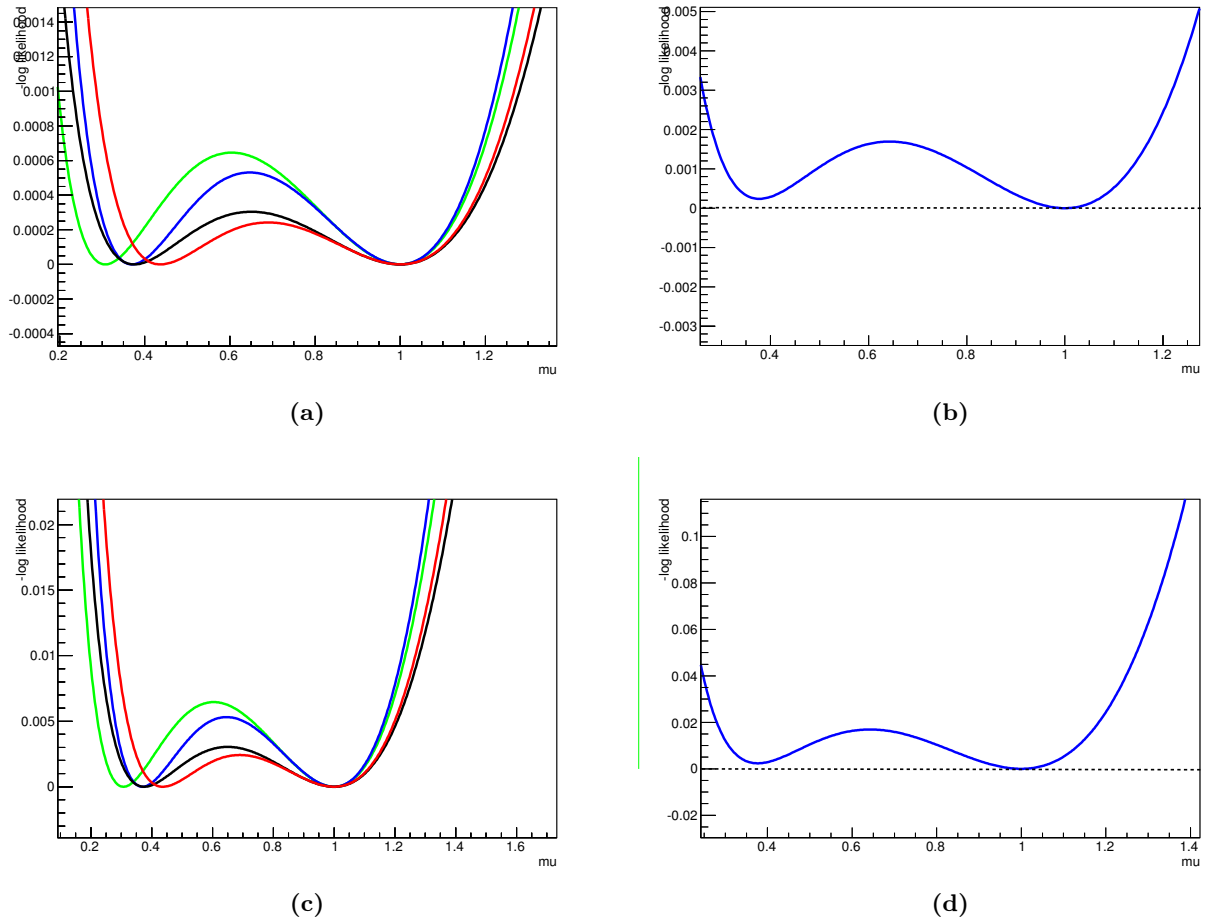

Figure 7.3: Likelihood scans on $\mu_{\text{off-shell}}$ without systematic uncertainties for the configuration L_1 (a), (b) and L_2 (c), (d) when using templates with one bin. The left plots indicate the zoom of the likelihood functions close to the minimum and the colours define the different final states: 4e in green, 4μ in red, $2\mu 2$e in black and $2\text{e}2\mu$ in blue. The right plots show the combined likelihood curves for all the channels together.

The only missing term with respect to the previous approach in Chapter 5 is the systematics on the interference contribution in the formula (7.1), accounting for a conservative 30% variation on the templates. The explanation of this addition was demonstrated by the definition of $R^B_{H^*}(m_{ZZ})$ that leads to large cancellations between the interference and the background. This item is now replaced by an *ad hoc* systematic uncertainty on $R^B_{H^*}(m_{ZZ})$ (second point of the list) for a less conservative approach. This simple model of uncertainties does not contain shape uncertainties but only normalisation systematics.

7.3 Results in the 4l channel

The primary step of the process is an internal validation of the results generated at $\sqrt{s}$=8 TeV against the ones of the main analysis. For this reason, a maximum likelihood fit is performed using PDFs generated at 8 TeV for 20.3 fb^{-1} and the statistics-only upper limits on $\mu_{\text{off-shell}}$ in the 4 lepton channel are found to be fully consistent with the ones reported in Chapter 5.

The 1 bin configuration (no systematic uncertainties are included in the model) has been exploited

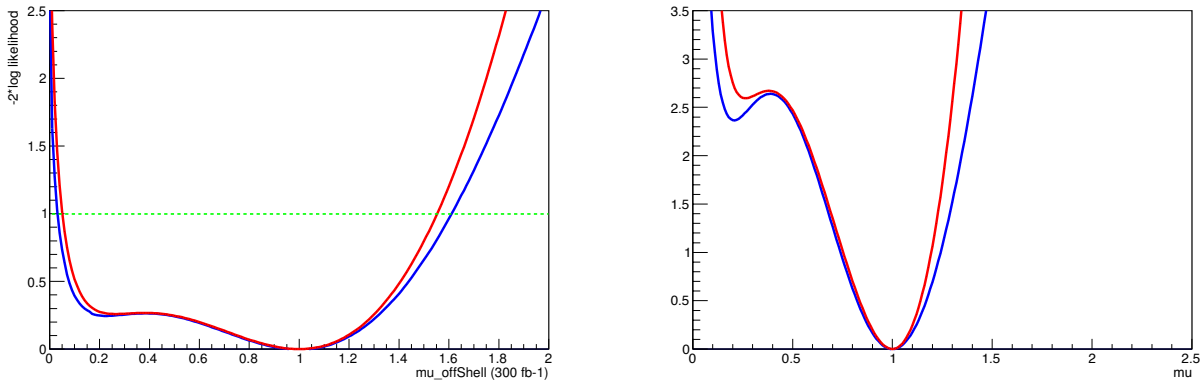

(a) **(b)**

Figure 7.4: Likelihood scans on $\mu_{\text{off-shell}}$ with (blue) and without (red) systematic uncertainties for the configuration L_1 and L_2. The error on μ is computed at the 1σ level.

first: likelihood plots for the configurations L_1 and L_2 are derived for the four different decay channels, 4e, 4μ, 2e2μ, 2μ2e and using the four states combination in Figure 7.3. A common minimum at $\mu_{\text{off-shell}}$=1 is observed for each channel, consistent with the injected value of the signal strength in the fit. Additionally, the likelihood functions are characterised by a second minimum for $\mu_{\text{off-shell}}$ <1. This is due to the presence of the double solution on $\mu_{\text{off-shell}}$ in equation (7.1). The position of the second minimum is not coincident for the various channel configurations: given that the expected total yields in the four channels are different, i.e. the second solution of the equation (7.1), the second minimum is displaced according to the channel.

Figure 7.4 shows the likelihood curves with and without systematic uncertainties on the configurations L_1 and L_2 respectively for the shape-based analysis. The flex observed for $\mu_{\text{off-shell}}$ <1, already present in Figure 6.37 for the main analysis at 20.3 fb^{-1}, gets more and more resolved as the statistics grows so that the likelihood function becomes parabolic in around $\pm$ 1σ around its minimum, for 3000 fb^{-1}. The value of the fitted $\mu_{\text{off-shell}}$ at the 1σ level in the two configurations, labelled with a superscript 1 and 2, are:

$$\mu^{(1)}_{\text{off-shell}} = 1.00^{+0.55}_{-0.94} \text{ (no sys)}, \; \mu^{(1)}_{\text{off-shell}} = 1.00^{+0.63}_{-0.97} \text{ (with sys)}. \tag{7.2}$$

$$\mu^{(2)}_{\text{off-shell}} = 1.00^{+0.23}_{-0.30} \text{ (no sys)}, \; \mu^{(2)}_{\text{off-shell}} = 1.00^{+0.26}_{-0.31} \text{ (with sys)}. \tag{7.3}$$

The values of the likelihood curves at the 2σ level for $\mu_{\text{off-shell}}$ are: $\mu^{(1)}_{\text{off-shell}} = 1.00^{+0.98}_{-0.97}$ (no sys), $\mu^{(1)}_{\text{off-shell}} = 1.00^{+1.22}_{-1.00}$ (with sys) for the configuration at 300 fb^{-1} and $\mu^{(2)}_{\text{off-shell}} = 1.00^{+0.36}_{-0.85}$ (no sys), $\mu^{(2)}_{\text{off-shell}} = 1.00^{+0.50}_{-0.90}$ (with sys) for the model generated at 3000 fb^{-1}.

In order to understand the behaviour of the likelihood curves that are characterised by a second minimum at $\mu_{\text{off-shell}} \sim 0.2$ and abruptly rise to $\mu_{\text{off-shell}}$=0, the m_{4l} distributions are plotted for different values of the off-shell couplings, e.g. close to the second minimum, $\mu_{\text{off-shell}} \sim 0.2$, the real minimum, $\mu_{\text{off-shell}}$=1, for the configuration where no signal is present ($\mu_{\text{off-shell}}$=0) and for the signal-only component (Figure 7.5 (a)). This study has been performed at 3000 fb^{-1} generated for $\sqrt{s}$=14 TeV. The distributions for $\mu_{\text{off-shell}}$=0.2 and $\mu_{\text{off-shell}}$=1 are very similar. This results in a relatively small $-2\Delta \log \mathcal{L}$ between the real minimum of the likelihood curve at 1 and the second minimum at 0.2 as observed in Figure 7.5 (b). On the contrary, the mass spectrum for $\mu_{\text{off-shell}}$=0

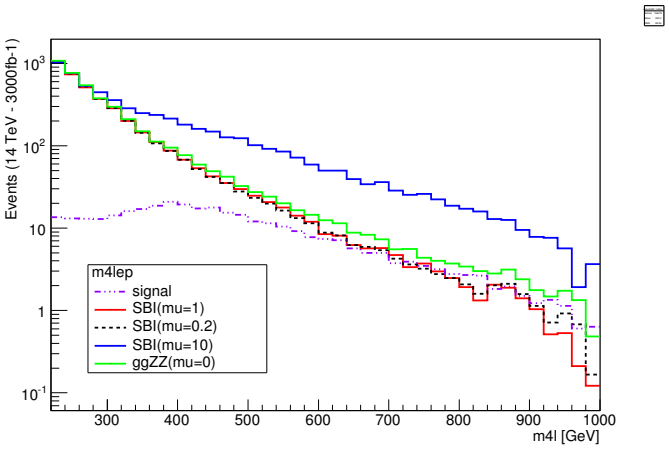

(a)

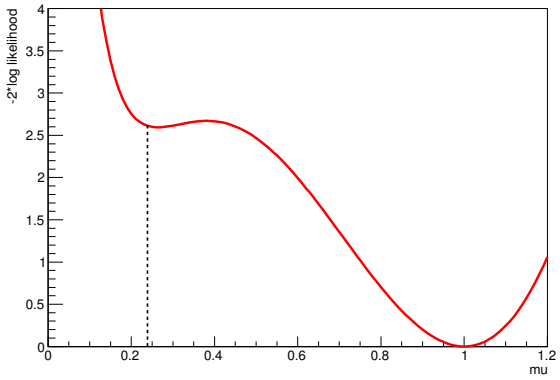

(b)

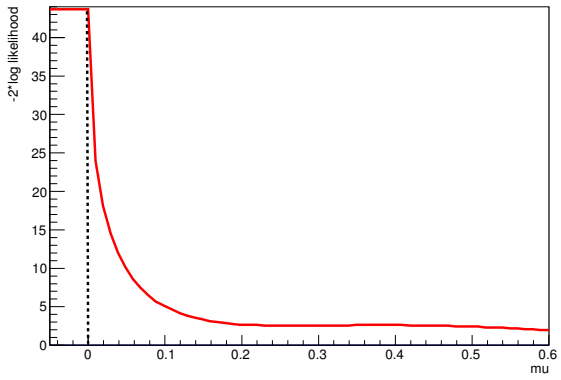

(c)

Figure 7.5: Invariant mass distribution generated at $\sqrt{s}$=14 TeV using an integrated luminosity of 3000 fb^{-1} in the phase space of the analysis (220< m_{4l} <1000) GeV for the signal components and different SBI contributions ($\mu_{\text{off-shell}}$=0, 0.2, 1 and 10). (b) and (c) Different zooms of the likelihood curves without systematic uncertainties, close to the value $\mu_{\text{off-shell}}$=0 and $\mu_{\text{off-shell}}$=1, illustrated in Figure 7.4 (b) for 3000 fb^{-1}.

(background-only hypothesis) is different with respect to the other two described before. This leads to a high value of the $-2\Delta \log \mathcal{L}$ estimator between $\mu_{\text{off-shell}}$=0 and $\mu_{\text{off-shell}}$=0.2, as in Figure 7.5 (c) causing the enhancement in sensitivity for $\mu_{\text{off-shell}} \to 0$.

The coupling parametrisation model

Another aspect of this analysis is the opportunity to re-parametrise the fitting model (7.1) by employing the following transformation on the parameter of interest μ:

$$\mu \to \kappa^2 \tag{7.4}$$

where κ is the product of the couplings of the Higgs boson to the initial and final states, $\kappa = \kappa_g \cdot \kappa_V$. This parametrisation is particularly suitable for the description of beyond SM scenarios because it is sensitive to possible non-SM positive interference resulting in values of κ below 0. The likelihood curves for the projections at 300 fb^{-1} and 3000 fb^{-1} are illustrated in Figure 7.6. The treatment of the systematic uncertainties on this measurement follows the prescriptions reported in Section

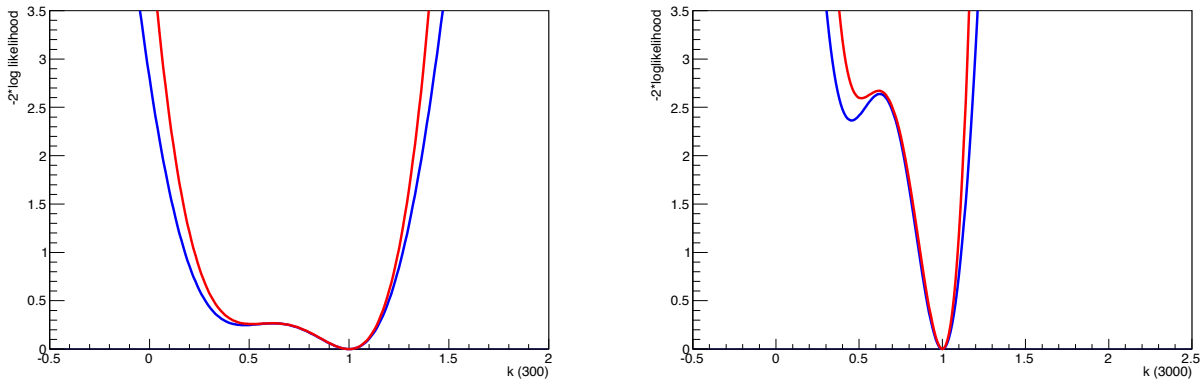

(a) **(b)**

Figure 7.6: Likelihood scans on κ with (blue) and without (red) systematic uncertainties for the configuration L_1 and L_2. The error on the limit on μ is computed at the 1σ level.

7.2.1. As for the previous case, the error on the fitted value is represented by the 1σ band in the plot:

$$\kappa^{(1)} = 1.00^{+0.24}_{-0.81} \text{ (no sys)}, \; \kappa^{(2)} = 1.00^{+0.25}_{-0.85} \text{ (with sys)}. \tag{7.5}$$

$$\kappa^{(2)} = 1.00^{+0.12}_{-0.14} \text{ (no sys)}, \; \kappa^{(2)} = 1.00^{+0.13}_{-0.14} \text{ (with sys)}. \tag{7.6}$$

The limits from the likelihood curves on the parameter of interest κ at the 2σ level are: $\kappa^{(1)} = 1.00^{+0.42}_{-0.97}$ (no sys), $\kappa^{(1)} = 1.00^{+0.48}_{-1.03}$ (with sys) for the model associated to 300 fb^{-1} and $\kappa^{(2)} = 1.00^{+0.17}_{-0.64}$ (no sys), $\kappa^{(2)} = 1.00^{+0.22}_{-0.72}$ (with sys) for the configuration generated at 3000 fb^{-1}.

7.4 Conclusions

The measurement of the off-shell signal strength of the Higgs boson using ZZ events in the 4l channel has been explored in the HL-LHC scenarios, i.e. $\sqrt{s}$=14 TeV for integrated luminosities of 300 fb^{-1} and 3000 fb^{-1}.

Monte Carlo samples of gg and $q\bar{q}$-initiated processes are generated with different center-of-mass energies with MCFM and POWHEG respectively. The measurement of $\mu_{\text{off-shell}}$ is carried out in the same way as in the standard analysis (Chapter 5), explicitly by employing a likelihood fit using matrix-element based templates that have been scaled in order to account for different luminosity and energy conditions. A simple treatment of the theoretical uncertainties is also introduced in the model. The best fitted value returned by the likelihood fit on $\mu_{\text{off-shell}}$ at 3000 fb^{-1} allows to determine the parameter of interest in the fit with an accuracy of approximately 25% at the 1σ level.

Conclusions

The theme of the analyses presented in this Thesis is the measurement of the Higgs boson properties in the $H \to ZZ \to 4l$ decay channel with the ATLAS experiment at the LHC. The main contributions of my studies throughout the period 2012-2015 are reported in Chapters 4, 5, 6 and 7 and comprised in the ATLAS Run 1 legacy papers.
After the description of the Standard Model framework, the ATLAS detector and the object reconstructions, Chapter 4 covers a detailed overview on the electron calibration process. In this regard, the track-cluster combination algorithm is found to improve the energy resolution of low E_T electrons by exploiting both track and cluster information into a template-based maximum likelihood fit. The method has been optimised on a Monte Carlo sample of single electrons and validated on data and Monte Carlo productions of J/Ψ and the Z dielectron resonances. Conclusively, the performance is evaluated with Monte Carlo-simulated $H \to ZZ \to 4l$ gauging the improvement on the 4-lepton invariant mass resolution. The improvement in resolution is approximately 18-20% for J/Ψ dielectron decays, and of the order of 3% for $Z \to ee$ events. The impact of this algorithm has been finally tested in the Higgs decay into 4e, 2e2μ and 2μ2e. An approximate gain of $\sim 4\%$ on the gaussian kernel resolution is found. In light of this result, the algorithm was adopted in the $H \to ZZ \to 4l$ analysis. The systematic uncertainties of the method associated to detector geometry and material were also determined and found to be small.

The main core of this manuscript is however represented by Chapter 5, 6 and 7 where the Higgs mass and its off-shell signal strength are evaluated.
The Higgs mass is measured in the 4l decay channel with particular interest on the beneficial effects brought by the improved electron calibration and the track-cluster combination. The mass on the full 2011 and 2012 sample generated at center-of-mass energies of $\sqrt{s}$=7 TeV and $\sqrt{s}$=8 TeV respectively is worked out with a 2 dimensional fit on the invariant mass of the 4 lepton final state, m_{4l}, and on a BDT-based output, explicitly conceived against the main ZZ irreducible background. The best-fitted value is m_H =124.51$\pm$0.52 GeV.

The results provided in Chapter 6 are based on a relatively recent approach aimed at indirectly constraining the Higgs boson width exploiting the m_{4l} high-mass region where the Higgs boson acts as a propagator. Limits on the Higgs width can be therefore set when merging the off-shell results with the on-shell ones. Final values are presented as a function of the unknown signal-to-background $gg \to (H^*) \to$ZZ k-factor. The observed 95% confidence level upper limit employing the CL_s method on the off-shell signal strength is in the range 5.5-9.5 when the unknown background-to-signal k-factor ratio is varied between 0.5 and 2 for a median expected range of 8.8-14.3. Combining with the on-shell measurement and using all the decay channels in the analysis, i.e. $H \to ZZ \to 4l$, $H \to ZZ \to 2l2\nu$ and $H \to WW \to l\nu l\nu$, the results lead to an observed (expected) 95% C.L. upper limit on the Higgs boson total width of 22.7 (33.0) MeV, when the signal-to-background k-factor ratio is set to 1 (soft collinear approximation).

Appendix A

$E - p$ combination software

Two versions of the software to perform the $E - p$ combination currently exist at different stages of the ATLAS offline reconstruction. An offline reconstruction implementation of the combination code (via Athena) is available in the `EMFourMomBuilder` class in the `egammaTools` package on the ATLAS offline reconstruction SVN. A D3PD-level implementation of the routine has also been developed, and is available in the `egammaFourMomentumError` class in the `egammaUtils` repository, which is compiled and run using the `RootCore` software package.
Two C++ classes were developed to implement the likelihood-based combination method. The first class, `CombinedPT_calculator`, performs the maximum-likelihood fit of cluster and track distributions. The second class is `CombinedPT_manager`, which instantiates each calculator subclass, and chooses the necessary calculator for a given set of track and cluster measurements. The various parameters for cluster and track PDFs (mean, σ, α, and n of the fitted Crystal Ball distributions) are stored in this class, according to the electron transverse momentum, pseudorapidity, and brem categories. The main function of the class, `getCombinedPt`, produces the likelihood-based combined transverse momentum (the `CombinedPT_calculator` class is therefore called once per electron) and calculates the fit error on this value, given as,

```
getCombinedPt(ptTrk, ptCl, etaCl, etaTrk, ECl, dPPin, ptComb, ptErr);
```

`ptTrack`, `etaCluster`, `etaTrack`, `Ecluster` and `fbrem` are user-defined inputs, whereas `ptComb` and `ptErr` are the outputs of the fit.

Both classes are built into a modular subclass of `egammaFourMomentumError` called `FourMomCombiner`, which contains implementations of the likelihood combination method, as well as decision-making methods based around the respective combination criteria. The motivation for using this modular subclass is to be able to efficiently modify the methods of one implementation, ensuring consistency between the two packages. At RootCore level, the combined four momentum is obtained by way of a `TLorentzVector` using the following user-facing function,

```
TLorentzVector buildfourmom(TLorentzVector track,
                            TLorentzVector cluster,
                            double qp_LM, double cov_qp,
                            int charge, double &comb_error);
```

The values of the PDF's for track and cluster distributions are extracted both for 2011 and 2012 Monte Carlo single electron samples.

Appendix B

Boosted decision tree discriminant

A decision tree is a binary tree structured as a classifier similar to the one sketched in Figure B.1 [118]. The phase space is split in such a way that the repeated binary decisions are exploited on single variables of interest in order to classify an event as *signal* or *background*. The boosting of a decision tree allows to accomplish this binary choice in a *forest*-like environment. The trees are derived in the same training ensemble by reweighting events and then are combined in an output classifier given by the weighted average of the decision trees.
The algorithm works in two different steps: the training is the process that defines the splitting criteria aiming at demarcating the phase space of each node. It starts with a single node where an initial working criteria for the splitting is worked out. Consequently, this procedure is iterated until the whole structure is constructed. The split is determined by finding the variables among the discriminant inputs that correspond to the best signal-to-background separation. Hence, the leaf nodes are classified as being signal or background according to the class the majority of events belongs to.

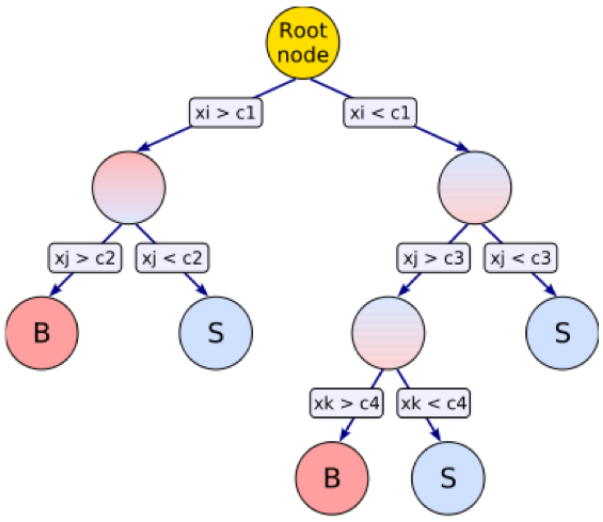

Figure B.1: Schematic sketch of a decision tree. Starting from the root node, a sequence of binary splits using the discriminating variables x_i is applied to the input data. Each split uses the variable that, at a given node, gives the best separation between signal and background when being cut on. The leaf nodes at the bottom end of the tree are labelled S for signal and B for background depending on the majority of events that end up in the respective nodes.

Appendix C

Statistical treatment of the limit extraction

The main results on the off-shell coupling measurement reported in Chapter 6 are based on the the *profile likelihood ratio* and on the CL_s method. These statistical concepts will be analysed in this Appendix.

C.1 Profile likelihood ratio

The likelihood $\mathcal{L} = \mathcal{L}(\mu, \vec{\theta})$ is a function of a parameter of interest μ and nuisance parameters $\vec{\theta}$. The hypothesis testing performed in the analysis in Chapter 6 are based on the profile likelihood ratio [131]. The hypothesised values for a parameter of interest μ are tested with the function:

$$q_\mu = -2\ln\Lambda(\mu,\vec{\theta}) = -2\ln\frac{\mathcal{L}(\mu,\hat{\hat{\vec{\theta}}})}{\mathcal{L}(\hat{\mu},\hat{\vec{\theta}})} \tag{C.1}$$

being $\hat{\mu}$ and $\hat{\vec{\theta}}$ the best values of the parameters obtained by maximising the likelihood function and $\hat{\hat{\vec{\theta}}}$ the values of the nuisance parameters obtained by maximising the likelihood function at a fixed (injected) value of the parameter of interest μ. Asymptotically, a test statistic $-2\ln\Lambda(\mu)$ of one parameter of interest μ is distributed as a χ^2 distribution with one degree of freedom, for which the 2-sided 1σ (68% confidence level) uncertainties are given by $-2\ln\Lambda(\mu) = 1$ and the 2-sided 95% confidence level uncertainties are given by $-2\ln\Lambda(\mu) = 3.84$.

C.2 Hypothesis testing and the CL_s method

The CL_s method [166], also called *modified frequentist approach*, is employed in the analysis and is defined with the following equation:

$$CL_s(\mu) = \frac{CL_{s+b}(\mu)}{CL_b(\mu)} = \frac{p_0(\mu_{\text{alt hyp}})}{1 - p_0(\mu_{\text{null hyp}})}, \tag{C.2}$$

where:

$$p_0^{\text{null hyp}}(\mu) = \int_m^\infty q(\mu)dq \tag{C.3}$$

and

$$p_0^{\text{alt hyp}}(\mu) = \int_{-\infty}^m q(\mu)dq \tag{C.4}$$

are the *p-values* for the null and alternative hypotheses. The null hypothesis coincides with the PDF for $\mu_{\text{off-shell}}$=1 and the alternative hypothesis represents the fitted $\mu_{\text{off-shell}}$. q is the employed test statistic - in our dissertation the profile likelihood ratio defined in (C.1) - that is accomplished to separate the two hypotheses and m is the median value of the null hypothesis distribution. The 95% C.L. limit is extracted with respect to the unknown variable $\mu_{\text{off-shell}}$ for CL_s=5%. Values of the parameter of interest $\mu_{\text{off-shell}}$ fulfilling the condition $\mu_{\text{off-shell}} > \mu^{95\%}_{\text{off-shell}}$ are excluded at 95% confidence level (C.L.).

C.3 Check on the validity of the asymptotic behaviour

The assumption on the validity of the asymptotic hypothesis that holds throughout the whole analysis in Section 6.12, has been carefully tested. In case of asymptotic behaviour, the test statistic, q, defined as the profile likelihood ratio formula in (C.1) is distributed as a χ^2 with one degree of freedom. For this test statistics a scan is applied on the Asimov set generated at $\mu_{\text{off-shell}} = 1$ and the value of q as a function of of the parameter of interest $\mu_{\text{off-shell}}$ is obtained, $q_1(\mu_{\text{off-shell}})$. The systematic uncertainties are set to their nominal value to get the distributions of the test statistics in the statistic-only scenario. The asymptotic behaviour is investigated by throwing 4000 toy Monte Carlos for different values of injected $\mu_{\text{off-shell}}$ ($\mu_{\text{off-shell}}$=3, 6).
Figures C.1 (a) to (d) show the distributions of the fitted off-shell signal strength as well as the distributions of the test statistic q for the different injected $\mu_{\text{off-shell}}$. The blue lines represent the $q_1(\mu_{\text{off-shell}})$ as a function of $\mu_{\text{off-shell}}$ obtained from the Asimov set generated at $\mu_{\text{off-shell}}$= 1. A χ^2 distribution with one degree of freedom (red line in the plots) is also superimposed to the histogram of q. The asymptotic behaviour is checked by comparing the p-values obtained with integral of the χ^2 distribution above $q_1(\mu)$ (the blue line in the plots) with the p-value obtained as the fraction of toys with the test statistics above $q_1(\mu_{\text{off-shell}})$. For a value of $\mu_{\text{off-shell}}$ =6 (close to the value at which the corresponding 95% asymptotic limit is derived as in Section 6.12), the asymptotic behaviour is reached and the p-values derived with the pseudo-experiments and the asymptotic assumption agree within the statistical accuracy of the samples. As soon as the injected $\mu_{\text{off-shell}}$ gets smaller, the integral of the pseudo-experiments for the test statistic above the $q_1(\mu_{\text{off-shell}})$ value does not match any longer with the asymptotic one.

C.4 Check on the validity of the limit extracted with the CL_s

Another check is performed on the CL_s method in light of the hypothesis testing for the ZZ only combination without systematic uncertainties. Toys are generated for the null hypothesis $\mu_{\text{off-shell}}$=1 and for the other alternative hypotheses, $\mu_{\text{off-shell}}$=5 and $\mu_{\text{off-shell}}$=6. The test statistic q (profile likelihood ratio) is calculated as a function of the null hypothesis and for the various alternative hypotheses as in equation (C.1). Figures C.1 (e) and (f) display the distributions of the test statistic q when using the null hypothesis $\mu_{\text{off-shell}}$=1 and the various alternative hypotheses. The CL_s value close 0.05 determining the exclusion of the injected $\mu_{\text{off-shell}}$ is found at $\mu_{\text{off-shell}}$=6, fully compatible with the result extracted by the fitting procedure in Section 6.12 for the ZZ only configuration.

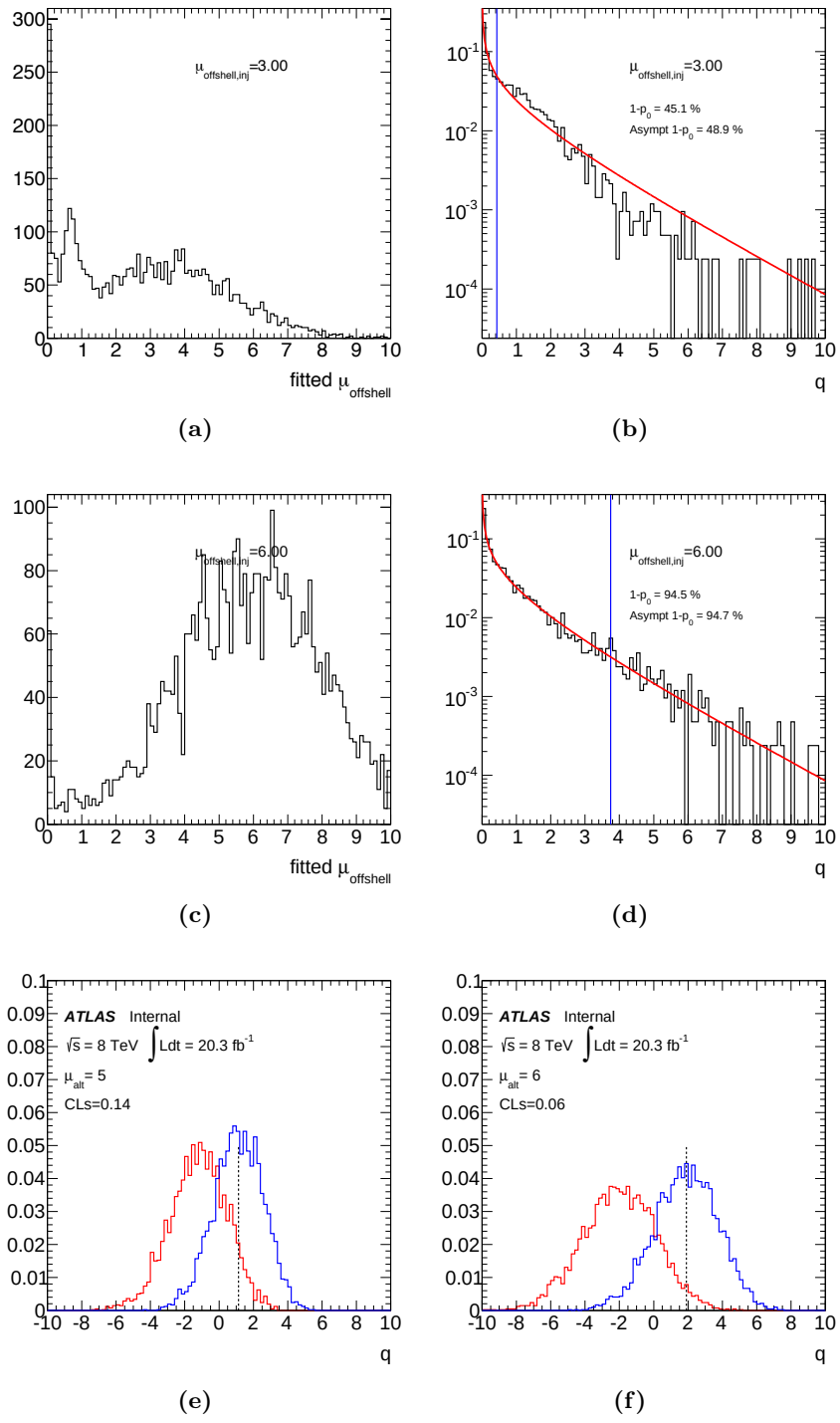

Figure C.1: Histograms of the fitted $\mu_{\text{off-shell}}$ when throwing toys injecting $\mu_{\text{off-shell}}$= 3 (a) and 6 (c). Distributions of the test statistic q (profile likelihood ratio) extracted for different values of the injected $\mu_{\text{off-shell}}$= 3 (b) and 6 (d). The blue lines represent the $q_1(\mu_{\text{off-shell}})$ as a function of $\mu_{\text{off-shell}}$ obtained in the null hypothesis configuration, $\mu_{\text{off-shell}}$= 1. A χ^2 distribution with one degree of freedom (red line in the plots) is also superimposed to the histogram of q. Distributions of the test statistic q when injecting $\mu_{\text{off-shell}}$=1 as null hypothesis (blue histograms) and of the other alternative hypotheses on $\mu_{\text{off-shell}}$ (red lines) generated at $\mu_{\text{off-shell}}$=5 (e) and $\mu_{\text{off-shell}}$=6 (f).

Appendix D

Extraction of the asymptotic formula to assess the expected significance for the BDT cut-based approach

The asymptotic formula to estimate the expected significance of the cut-based approach on the BDT output detailed in Section 5.3 is given below:

$$f(S,B) = \sqrt{2 \cdot \left[(S+B) \cdot \left(1 + \frac{S}{B} \right) - S \right]}. \tag{D.1}$$

The likelihood function $\mathcal{L}$ for the S+B hypothesis is written as follow:

$$\mathcal{L}(S+B) = \frac{e^{-(S+B)}(S+B)^N}{N!} \tag{D.2}$$

where S is the number of signal events, B is the number of background events and N is the number of entries. Likewise, for the background-only hypothesis, equation (D.2) becomes:

$$\mathcal{L}(B) = \frac{e^{-B}B^N}{N!} \tag{D.3}$$

Let us define $\mathcal{R}$ the likelihood ratio:

$$\mathcal{R} = \frac{\mathcal{L}(S+B)}{\mathcal{L}(B)} = \frac{e^{-S}(S+B)^N}{B^N} = e^{-S}(1+\frac{S}{B})^N \tag{D.4}$$

Starting from (D.4), the following statement holds:

$$-2\log\mathcal{R} = 2S - 2N \cdot \log(1+\frac{S}{B}). \tag{D.5}$$

This equation shows the value of the ratio $\frac{\mathcal{L}(S+B)}{\mathcal{L}(B)}$, defined in (D.4) when N varies. When the quantity on the left part of (D.5) is small, the value of the likelihood ratio $\mathcal{R}$ is large and vice-versa. Be $N = S + B$ the number of observed events in data. Should we replace the observed value of N in (D.5), we could obtain:

$$2\log\mathcal{R} = 2\,(S+B) \cdot \log\left(1 + \frac{S}{B}\right) - 2S. \tag{D.6}$$

It is therefore trivial to demonstrate that the equation above coincides with the asymptotic formula in (5.4) when extracting the square root:

$$\sqrt{2\log\mathcal{R}(N=S+B)} = \sqrt{2\cdot\left[(S+B)\cdot\left(1+\frac{S}{B}\right)-S\right]}. \tag{D.7}$$

Appendix E

Expected and observed distributions in the $H \to ZZ \to 4l$ analysis

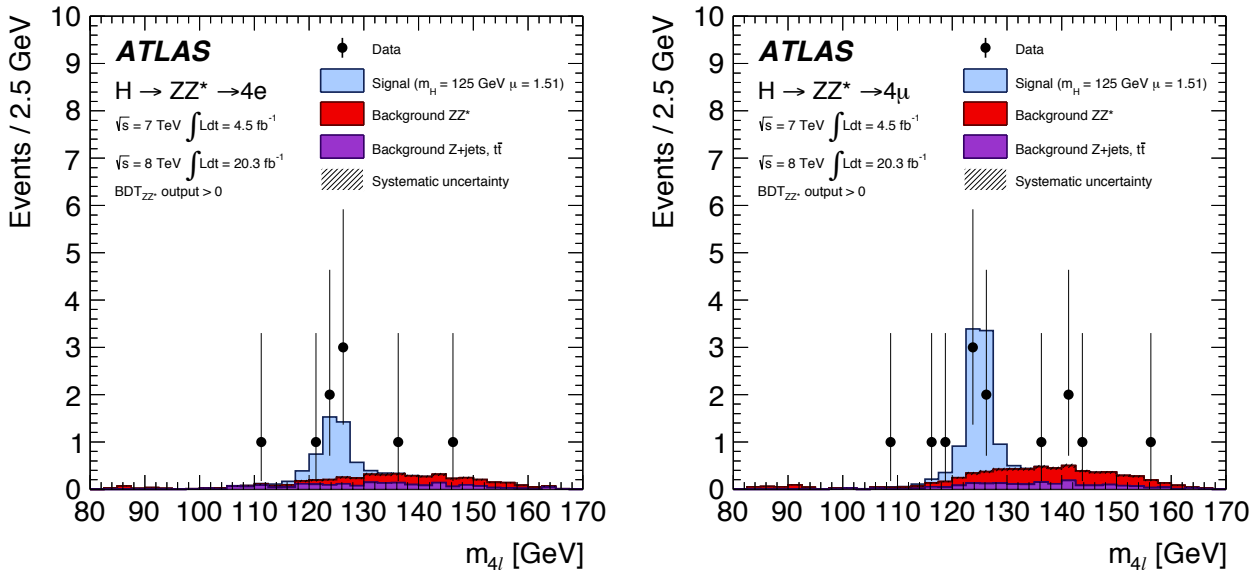

(a) 4e **(b)** 4μ

Figure E.1: m_{4l} distribution of the selected candidates for $\sqrt{s}$= 7 TeV and $\sqrt{s}$= 8 TeV for 4e and 4μ sub-channels of the analysis compared to the background expectations when BDT>0 to select the *signal-like* region of the BDT phase-space. The contribution of the reducible background is also shown separately as well as the systematic uncertainties drawn as a hatched grey area.

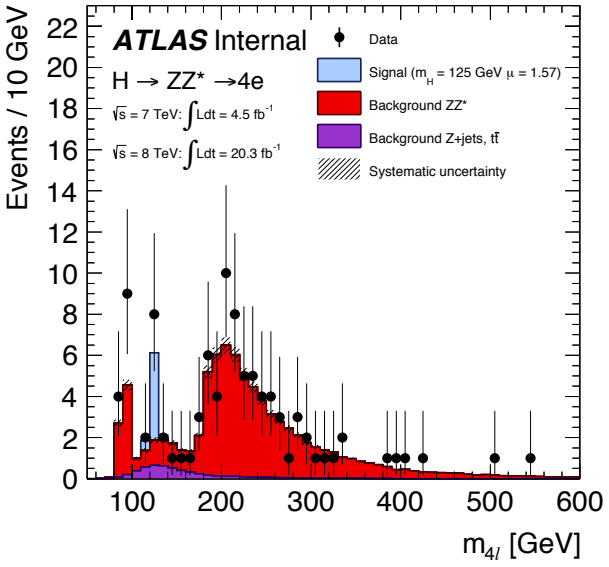

(a) 4e

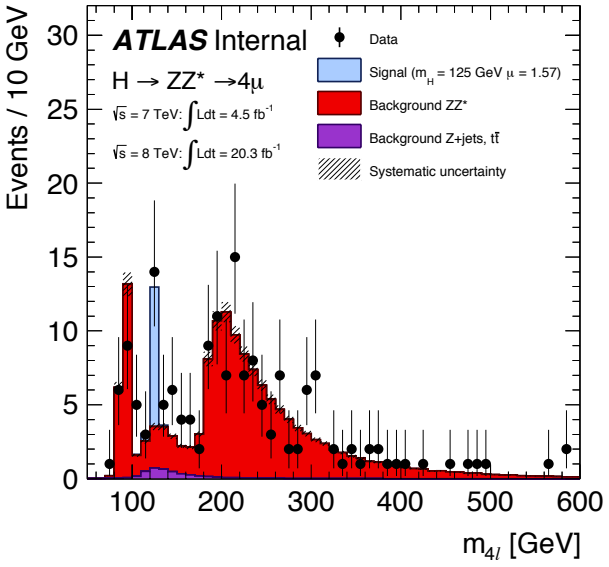

(b) 4μ

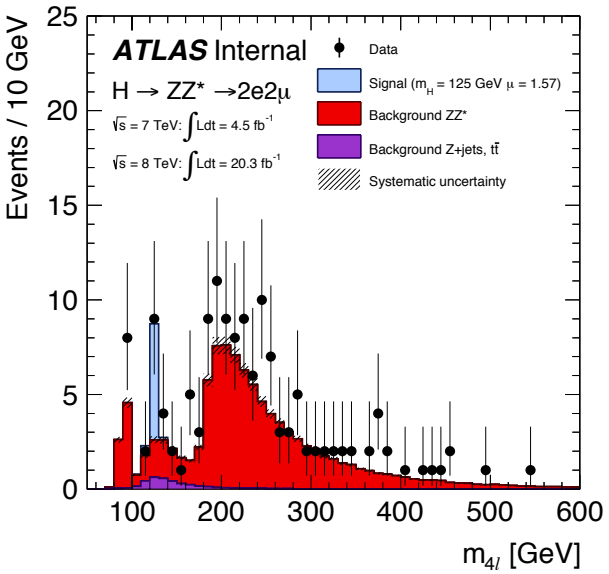

(c) 2e2μ

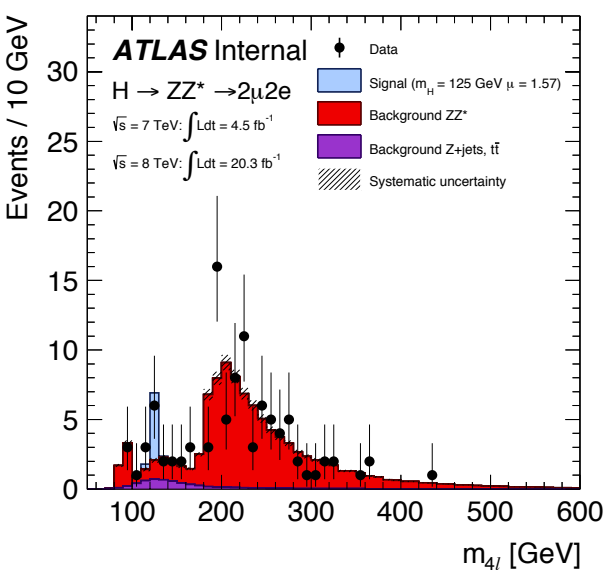

(d) 2μ2e

Figure E.2: m_{4l} distribution of the selected candidates for $\sqrt{s}$= 7 TeV and $\sqrt{s}$= 8 TeV for the different *sub*-channels of the analysis compared to the background expectations. The contribution of the reducible background is also shown separately as well as the systematic uncertainties drawn as a hatched grey area.

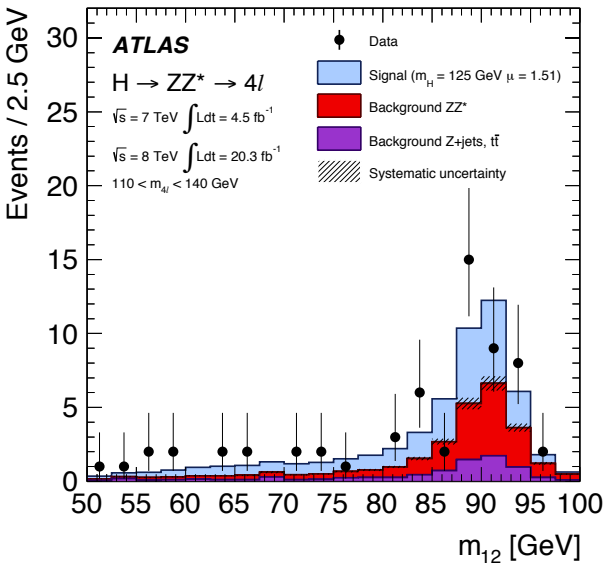

(a)

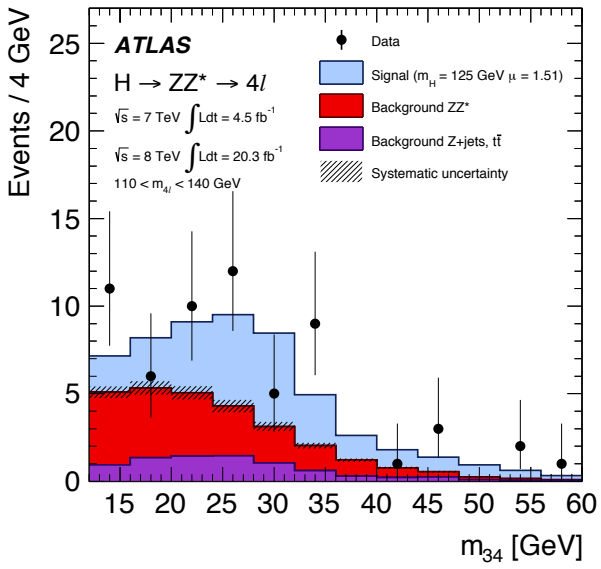

(b)

Figure E.3: m_{12} (a) and m_{34} (b) distribution of the selected candidates for $\sqrt{s}$= 7 TeV and $\sqrt{s}$= 8 TeV compared to the background expectations in the region 110-140 GeV. The contribution of the reducible background is also shown separately as well as the systematic uncertainties drawn as a hatched grey area.

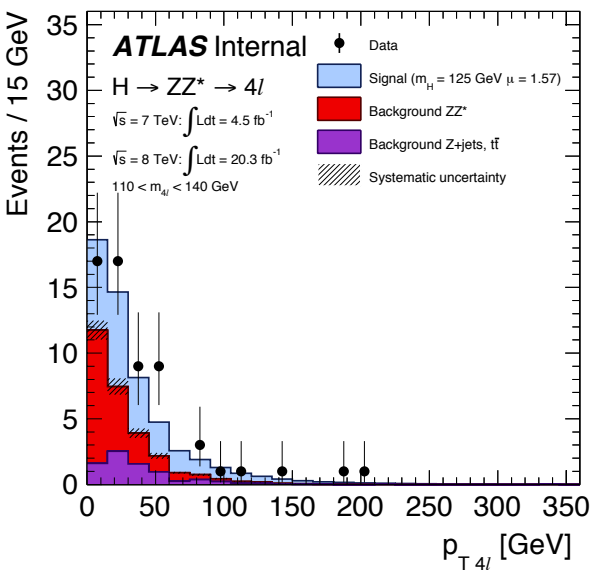

(a)

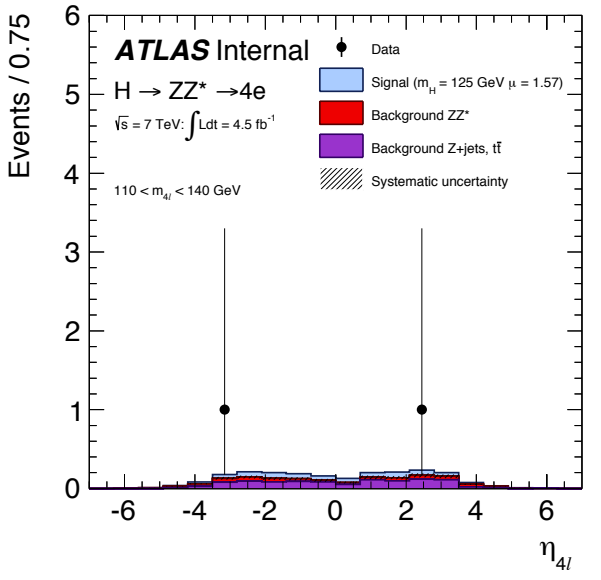

(b)

Figure E.4: Higgs p_T (a) and η (b) distribution of the selected candidates for $\sqrt{s}$= 7 TeV and $\sqrt{s}$= 8 TeV compared to the background expectations in the region 110-140 GeV. The contribution of the reducible background is also shown separately as well as the systematic uncertainties drawn as a hatched grey area.

Bibliography

[1] A. Halzen, F. Martin, *Quarks and Leptons.* John Wiley and Sons, 1984.

[2] E. Landau, L. Lifschitz, *Quantum Field Theory.* Bollati Boringhieri, 1981.

[3] L. Maiani, O. Benhar, *Relativistic Quantum Mechanics - An Introduction to Quantum Field Theory.* Editori Riuniti, 2013.

[4] M. Gell-Mann, *A schematic Model of Baryons and Mesons*, Physics Letter (1964).

[5] I. Dissertori, G. Knowles and M. Schmelling, *Quantum Chromodynamics - High Energy Experiments and Theory.* Oxford Science Publications, 2003.

[6] The JADE collaboration, *Observation of planar three-jet events in e^+ e^- annhilation and evidence for gluon bremsstrahlung*, Physics Letters B (1980).

[7] E. Fermi, *Tentativo di una Teoria dei raggi β*, Il Nuovo Cimento (1934).

[8] C.S. Wu, E. Ambler, R.W. Hayward, D.D Hoppes and R.P. Hudson, *Experimental Test of Parity Conservation in Beta Decay*, Phys. Rev. (1957).

[9] M. Goldhaber, L. Grodzins and A.W. Sunyar, *Helicity of neutrinos*, Phys. Rev. (1958).

[10] S.L. Glashow, *Partial-symmetries of weak interactions*, Nuclear Physics (1961).

[11] P.W. Higgs, *Spontaneous Symmetry Breakdown without Massless Bosons*, Phys. Rev. (1964).

[12] F. Englert and F. Brout, *Broken symmetry and the mass of Gauge Vector Mesons*, Phys. Rev. (1966).

[13] S. Weinberg, *Electromagnetic and Weak Interactions*, Il Nuovo Cimento (1959).

[14] A. Salam, J. Ward, *Electromagnetic and Weak Interactions*, Il Nuovo Cimento (1959).

[15] N. Cabibbo, L. Maiani and R. Petronzio, *Bounds on the fermions and Higgs boson masses in Grand Unified Theories*, Nuclear Physics B (1979).

[16] J. Ellis, J.R. Espinosa, G.F. Giudice, A. Hoecker, A. Riotto, *The Probable Fate of the Standard Model*, `arXiv:0906.0954v2 [hep-ph]`.

[17] The LEP collaborations (ALEPH, DELPHI, L3 and OPAL), *Search for the Standard Model Higgs Boson at LEP*, Phys. Lett.B (2003).

[18] The Tevatron collaborations (CDF and D0), *Updated combination of CDF and D0 Searches for Standard Model Higgs Boson Production with up to 10 fb-1 of Dtata*, `arXiv:1207.0449 [hep-ph]`.

[19] M. Baak, M. Goebel, J. Haller, A. Hoecker et al., *Updated Status of the Global Electroweak Fit and Constraints on New Physics*, arXiv:1107.0975 [hep-ph].

[20] The ATLAS collaboration, *Measurement of the Higgs Boson mass from the H→ γγ and H→ ZZ → 4l channels with the ATLAS detector using 25fb^{-1} of pp collisions data*, arXiv:1406.3827 [hep-ph].

[21] Y.L. Dokshitzer, V.A. Khoze, A.H. Muller, S. I. Troyan , *Basics of perturbative QCD*, http://www.lpthe.jussieu.fr/ yuri/BPQCD/BPQCD.pdf.

[22] J. C. Collins, *Sudakov form factors*, arXiv:0312336 [hep-ph].

[23] G. Altarelli, G. Parisi, *Asymptotic Freedom in Parton Language*, Nucl.Phys (1977).

[24] Y.L. Dokshitzer, *Calculation of the Structure Functions for Deep Inelastic Scattering and e^+e- Annihilation by Perturbation Theory in Quantum Chromodynamics.*, Sov. Phys. JETP (1977).

[25] V.N. Gribov, L.N. Lipatov, *e^+e- pair annihilation and deep inelastic e p scattering in perturbation theory.*, Sov. J. Nucl.Phys. (1972).

[26] P. Nadolsky, J. Gao, M. Guzzi, J. Huston, H.-L. Lai, Z. Li, J. Pumplin, D. Stump, C.-P. Yuan, *Progress in CTEQ-TEA PDF analysis*, arXiv:1206.3321 [hep-ph].

[27] A. D. Martin, W. J. Stirling, R. S. Thorne, G. Watt, *Parton distributions for the LHC*, arXiv:0901.0002 [hep-ph].

[28] R. D. Ball et al., *Impact of heavy quark masses on parton distributios and LHC phenomenology*, arXiv:1101.1300 [hep-ph].

[29] LHC Higgs Cross Section Working Group: S. Dittmaier, C. Mariotti, G. Passarino, R. Tanaka (eds) et al., *Handbook of LHC Higgs CrossSections: Inclusive Observables*, arXiv:1101.0593 [hep-ph].

[30] LHC Higgs Cross Section Working Group: S. Dittmaier, C. Mariotti, G. Passarino, R. Tanaka (eds) et al., *Handbook of LHC Higgs CrossSections: Differential distributions*, arXiv:1201.3084 [hep-ph].

[31] T. Sjostrand, S. Mrenna and P. Z. Skands, *PYTHIA 6.4 physics and manual*, arXiv:0603175 [hep-ph].

[32] T. Sjostrand and M. van Zijl, *A multiple interaction model for the event structure in hadron collisions*, Phys. Rev. D36 (1987).

[33] S. Aioli, P. Nason, C. Oleari and E. Re, *A general framework for implementing NLO calculations in shower Monte Carlo programs: The POWHEG BOX*, arXiv:1002.2581 [hep-ph].

[34] P. Golonka, Z. Was, *PHOTOS Monte Carlo: a precision tool for QED corrections in Z and W decays*, arXiv:0506026 [hep-ph].

[35] M. Ciccolini, A. Denner, S. Dittmaier, *Strong and electroweak corrections to the production of Higgs+2jets via weak interactions at the LHC*, arXiv:0707.0381 [hep-ph].

[36] P. Bolzoni, F. Maltoni, S. Moch, M. Zaro, *Higgs production via vector-boson fusion at NNLO in QCD*, arXiv:1003.4451 [hep-ph].

[37] T. Han and S. Willenbrock Phys. Lett. B (1991).

[38] O. Brein, A. Djouadi, R. Harlander, *NNLO QCD corrections to the Higgs-strahlung processes at hadron colliders*, arXiv:0307206 [hep-ph].

[39] M. Ciccolini, S. Dittmaier, M. Kramer, *Electroweak Radiative Corrections to Associated WH and ZH Production at Hadron Colliders*, arXiv:0306234 [hep-ph].

[40] W. Beenakker, S. Dittmaier, M. Kramer, B. Plumper, M. Spira, P.M. Zerwas , *Higgs Radiation of Top Quarks at the Tevatron and the LHC*, arXiv:0107081 [hep-ph].

[41] W. Beenakker et al. , *NLO QCD corrections to $t\bar{t}H$ production in hadron colliders*, arXiv:0211352 [hep-ph].

[42] L. Reina and S. Dawson , *Next-to-leading order results for $t\bar{t}H$ production at the Tevatron*, arXiv:0107101 [hep-ph].

[43] S. Dawson, L.H. Orr, L. Reina and D. Wackeroth, *Associated top quark Higgs boson production at the LHC*, arXiv:0211438 [hep-ph].

[44] S. Dittmaier, M. Kramer , M. Spira , *Higgs Radiation of Bottom Quarks at the Tevatron and the LHC*, Phys. Rev. D 70 074010 (2004)., arXiv:0309204 [hep-ph].

[45] S. Dawson, C. B. Jackson, L. Reina, D. Wackeroth, *Higgs Boson Production with Bottom Quarks at Hadron Colliders*, arXiv:0409345 [hep-ph].

[46] R. V. Harlander and W. B. Kilgore, *Higgs boson production in bottom quark fusion at next-to-next-to leading order*, arXiv:0304035 [hep-ph].

[47] A. Djouadi, J. Kalinovski, M. Spira , *HDECAY: a Program for Higgs Boson Decays in the Standard Model and its Supersymmetric Extension*, arXiv:970448 [hep-ph].

[48] A. Bredenstein, A. Denner, S. Dittmaier, M.M. Weber, *Precise predictions for the Higgs-boson decay $H \to W\ W/Z\ Z \to 4$ leptons*, arXiv:0604011 [hep-ph].

[49] C. Anastasiou, R. Boughezal, F. Petriello, *Mixed QCD-electroweak corrections to Higgs boson production in gluon fusion*, arXiv:0811.3458 [hep-ph].

[50] D. de Florian and M. Grazzini, *Higgs production through gluon fusion: Updated cross-sections at the Tevatron and the LHC*, Phys. Lett. B674, arXiv:0901.2427 [hep-ph].

[51] G. Passarino et al., *The Higgs Boson lineshape* , arXiv:1112.5517 [hep-ph].

[52] S. Actis, G. Passarino, C. Sturm and S. Uccirati, *NLO electroweak correctons to the Higgs boson production at hadron colliders*, Phys. Lett. B670, arXiv:0809.1301 [hep-ph].

[53] R. V. Harander and W. B. Kilgore, *Next-to-next-to-leading order Higgs production at hadron colliders*, Phys. Lett., arXiv:0201206 [hep-ph].

[54] D. de Florian, G. Ferrera, M. Grazzini and D. Tommasini, *Higgs boson production at the LHC: transverse momentum resummation effects in the $H \to \gamma\gamma$, $H \to WW$ and $H \to ZZ$ decay modes*, arXiv:1203.6321 [hep-ph].

[55] T. Melia, P. Nason, R. Rontsch, G. Zanderighi, *$W^+\ W^-$, WZ and ZZ production in the POWHEG-BOX*, arXiv:1107.5051 [hep-ph].

[56] T. Binoth, N. Kauer, P. Mertsch, *Gluon-induced QCD corrections to* $pp \to ZZ \to l\bar{l}l'\bar{l}'$, arXiv:0807.0024 [hep-ph].

[57] M. Botje et al., *The PDF4LHC working group interim reccomendations*, arXiv:1101.0538 [hep-ph].

[58] H.-L. Lai et al., *New parton distributions for collider physics*, arXiv:1007.2241 [hep-ph].

[59] M.L. Mangano, M. Moretti, F. Piccinini, R. Pittau, A.D. Polosa, *ALPGEN: a generator for hard multiparton processes in hadron collisions*, arXiv:0206293 [hep-ph].

[60] M.L. Mangano, M. Moretti, F. Piccinini, M. Treccani, *Matching matrix elements and shower for top-quark production in hadronic collisions*, arXiv:0611129 [hep-ph].

[61] S. Jadach, Z. Was, R. Decker, J.H. Kuhn, *The tau library decay TAUOLA: Version 2.4*, Comput. Phys. Commun. 76 3161 (1993).

[62] L. Evans, P. Bryant, *LHC Machine*, Journal of Instrumentation - IOP Science (2008).

[63] The ATLAS collaboration, *ATLAS Technical Proposal for a general-purpose pp experiment at the Large Hadron Collider at CERN*, CERN-LHCC-94-43 (1994).

[64] The CMS collaboration, *CMS Technical Proposal*, CERN-LHCC-94-38 ; LHCC-P-1 (1994).

[65] The ALICE collaboration, *ALICE Technical Proposal for a Large Ion Collider Experiment at the CERN LHC*, CERN-LHCC-95-71 (1995).

[66] The LHCb collaboration, *LHCb Technical Proposal*, CERN-LHCC-98-004 (1998).

[67] The TOTEM collaboration, *TOTEM Technical Proposal - Total Cross Section, Elastic Scattering and Diffractrion Dissociation at the LHC* , CERN-LHCC-99-7 (1999).

[68] The LHCf collaboration, *LHCf Technical Proposal*, CERN-LHCC-2005-032 (2005).

[69] CERN, *Design Study of the Large Hadron Collider (LHC): A multi particle collider in the LEP tunnel* , CERN-91-03 (1991).

[70] M. Aiba et al., *First beta-beating measurement and optics analysis for the CERN Large Hadron Collider*, Phys. Rev. ST Accel. Beams 12, 081002 (2009).

[71] Particle Data Group, *Review of Particle Physics*, Phys. Rev. D **86** (2012) 010001.

[72] V. Balagura, *Notes on Van der Meer Scan for Absolute Luminosity Measurement* , arXiv:1103.1129 [hep-ph].

[73] The ATLAS collaboration, *Improved luminosity determination in pp collision at* $\sqrt{s}$*= 7 TeV using the ATLAS detector at the LHC*, arXiv:1302.4393 [hep-ph].

[74] The ATLAS collaboration, *ATLAS Magnet System - Technical Design Report*, CERN-LHCC-97-018 (1997).

[75] The ATLAS collaboration, *ATLAS Central Solenoid - Technical Design Report*, CERN-LHCC-97-021 (1997).

[76] The ATLAS collaboration, *ATLAS Barrel Toroid - Technical Design Report*, CERN-LHCC-97-019 (1997).

[77] The ATLAS collaboration, *ATLAS Endcap Toroids - Technical Design Report*, CERN-LHCC-97-020 (1997).

[78] The ATLAS collaboration, *Inner Detector - Technical Design Report*, CERN-LHCC-97-16 (1997).

[79] M. Capeans, G. Darbo, K. Einsweiller, M. Elsing, T. Flick, M. Garcia-Sciveres, C. Gemme, H. Pernegger, O. Rohne, R. Vuillermet, *ATLAS Insertable B-Layer - Technical Design Report*, CERN-LHCC-2010-013 (2010).

[80] The ATLAS collaboration, *ATLAS pixel detector: Technical Design Report*, CERN-LHCC-98-013 (1998).

[81] Y. Unno, *ATLAS Silicon Microstrip detector system (SCT)*, Nuclear Instruments and Methods in Physics Research A 511 (2003).

[82] E. Abat et al., *The ATLAS Transition Radiation Tracker (TRT) proportional drift tube: Design and performance*, JINST, vol. 3 (2008).

[83] The ATLAS collaboration, *ATLAS Liquid Argon - Technical Design Report*, CERN-LHCC-96-41 (1996).

[84] The ATLAS collaboration, *ATLAS Tile Calorimeter: Technical Design Report*, CERN-LHCC-96-42 (1996).

[85] A. Artamonov et al., *The ATLAS Forward Calorimeters*, JINST, vol. 3 (2008).

[86] The ATLAS collaboration, *ATLAS Forward Detectors for Luminosity Measurement and Monitoring*, CERN-LHCC-2004-010 (2004).

[87] The ATLAS collaboration, *Zero Degree Calorimeter for ATLAS*, CERN-LHCC-2007-001 (2007).

[88] S. Diglio on behalf of the ATLAS collaboration, *The ATLAS Forward Physics program*, ATL-GEN-PROC-2013-005 (2007).

[89] The ATLAS collaboration, *ATLAS Computing - Technical Design Report*, CERN-LHCC-2005-022 (2005).

[90] A. Farbin for the ATLAS collaboration, *ATLAS Analysis Model*, Journal of Physics - Conference Series 119 042012 (2008).

[91] The ATLAS collaboration, *Performance of the ATLAS Inner Detector Track and Vertex Reconstruction in the High Pile-Up LHC Environment*, ATLAS-CONF-2012-042 (2012).

[92] The ATLAS collaboration, *Alignment of the ATLAS Inner Detector and its performance in 2012*, ATLAS-CONF-2014-047 (2012).

[93] S. Zambito, *Measurement of the Higgs Boson Production and Couplings in the Four-Lepton Decay Channel with the ATLAS detector.* PhD thesis, Brandeis University, 2014.

[94] The ATLAS collaboration, *Performance of the ATLAS Electron and Photon Trigger in p-p Collisions at* $\sqrt{s} = 7$ *TeV in 2011*, ATLAS-CONF-2012-048 (2012).

[95] The ATLAS collaboration, *Electron efficiency measurements with the ATLAS detector using the 2012 LHC proton-proton collision data*, ATLAS-CONF-2014-032 (2014).

[96] G. Artoni, *Search for a Standard Model Higgs boson in the H→ ZZ → 4l decay channel with the ATLAS experiment at CERN.* PhD thesis, Scuola di Dottorato in Fisica, Universitá degli Studi di Roma - La Sapienza, 2012.

[97] T. Cornelissen, M. Elsing, S. Fleischmann, W. Liebif, E. Moyse and A. Salzburger, *Concepts, design and implementation of the ATLAS new tracking (NEWT)*, ATLAS-SOFT-PUB-2007-006 (2007).

[98] T. G. Cornelissen, M. Elsing, I. Gavrilenko, J. Laporte, W. Liebig, M. Limper, K. Nikolopoulos, A. Poppleton, and A. Salzburger, *The global χ^2 track fitter in ATLAS*,.

[99] The ATLAS collaboration, *Improved electron reconstruction in ATLAS using the Gaussian Sum Filter-based model for bremsstrahlung*, ATLAS-CONF-2012-047 (2012).

[100] The ATLAS collaboration, *Muon reconstruction efi¬ciencyandmomentumresolutionoftheATLASexperimentinprotonprotoncollisionsat$\sqrt{s}$ = 7 TeV in 2010*, ATLAS-PERF-2011-01 (2011).

[101] The ATLAS collaboration, *Measurement of the muon reconstruction performance of the ATLAS detector using 2011 and 2012 LHC proton-proton collision data*, `arXiv:1407.3935 [hep-ph]`.

[102] The ATLAS collaboration, *Performance of the ATLAS muon trigger in 2011*, ATLAS-CONF-2012-099 (2012).

[103] The ATLAS collaboration, *Performance of the ATLAS muon trigger in pp collisions at $\sqrt{s}$= 8 TeV*, ATLAS-CONF-2014-154 (2014).

[104] R. Nicolaidou, L. Chevalier, S. Hassani, J.F. Laporte, E. Le Menedeu and A. Ouraou, *Muon identification procedure for the ATLAS detector at the LHC using Muonboy reconstruction package and tests of its performance using cosmic rays and single beam data*, Journal of Physics - Conference Series vol. 219 n.3 (2010).

[105] T. Laguori, D. Adams, K.A. Assamagan, M. Biglietti, G. Carlino, G. Cataldi, F. Conventi, A. Farilla, Y. Fisyak, S. Goldfarb, E. Gorini, K. Mair, L. Merola, A. Nairz, A. Poppleton, M. Primavera, S. Rosati, S. Shank, S. Spagnolo, S. Spogli, G.D. Stavropoulos, M. Verducci and T. Wenaus, *A Muon Identification and Combined Reconstruction Procedure for the ATLAS Detector at the LHC at CERN*, ATLAS-CONF-2003-011 (2003).

[106] V. Ippolito, *Measurement of the properties of the new particle observed within the search of the Standard Model Higgs Boson in the H→ ZZ → 4l decay channel at ATLAS.* PhD thesis, Scuola di Dottorato in Fisica, Universitá degli Studi di Roma - La Sapienza, 2013.

[107] The ATLAS collaboration, *Jet energy measurement with the ATLAS detector in proton-proton collisions at $\sqrt{s}$= 7 TeV*, `arXiv:1112.6426 [hep-ph]`.

[108] The ATLAS collaboration, *Jet energy measurement and its systematic uncertainty in proton proton collisions at $\sqrt{s}$= 7 TeV*, `arXiv:1406.0076 [hep-ph]`.

[109] M. Cacciari, G. P. Salam, and G. Soyez, *The anti-k_T jet clustering algorithm*, `arXiv:0802.1189 [hep-ph]`.

[110] The ATLAS collaboration, *Performace of Missing Transverse Momentum Reconstruction in ATLAS studied in Proton-Proton Collsions recorded in 2012 at $\sqrt{s}$=8 TeV*, ATLAS-CONF-2013-082 (2013).

[111] The ATLAS collaboration, *Electron and photon energy calibration with the ATLAS detector using LHC Run1 data*, arXiv:1407.5063 [hep-ph].

[112] The ATLAS collaboration, *Determination of the τ energy scale and the associated systematics uncertainty in proton-proton collisions at $\sqrt{s}$=7 TeV with the ATLAS detector at the LHC in 2011*, ATLAS-CONF-2012-054 (2012).

[113] The ATLAS collaboration, *Jet energy measurement with the ATLAS detector in proton-proton collisions at 7 TeV*, arXiv:1108.5602 [hep-ph].

[114] The ATLAS collaboration, *Luminosity Determination in pp Collisions at $\sqrt{s}$=7 TeV using the ATLAS detector at the LHC* , arXiv:1101.2185 [hep-ph].

[115] The ATLAS collaboration, *Measurement of the inelastic Proton-Proton cross section at $\sqrt{s}$=7 TeV with the ATLAS detector*, ATLAS-CONF-2011-002 (2011).

[116] ATLAS Collaboration, *Expected Performance of the ATLAS Experiment - Detector, Trigger and Physics*, arXiv:0901.0512 [hep-ex].

[117] R. Turra, *Energy Calibration and the Observation of the Higgs boson in the diphoton decay with the ATLAS experiment.* PhD thesis, Corso di Dottorato in Fisica, Astrofisica e Fisica Applicata, Universitá degli studi di Milano - Dipartimento di Fisica, Milano, Italy, 2013.

[118] A. Hoecker, P. Speckmayer, J. Stelzer, J. Therhaag, E. von Toerne, H. Voss et al., *TMVA: Toolkit for Multivariate Data Analysis*, arXiv:0703039 [hep-ph].

[119] The ATLAS collaboration, *Expected performance of the ATLAS experiment - Detector, trigger and physics*, arXiv:0901.0512 [hep-ph].

[120] B. P. Roe, H. J. Yang, J. Zhu, Y. Liu, I. Stancu, and G. McGregor, *Boosted decision trees as an alternative to artificial neural networks for particle identification*, arXiv:0408124 [hep-ex].

[121] The ATLAS collaboration, *Measurement of the Higgs boson production in the diphoton decay channel in pp collision at center of mass energies of 7 and 8 TeV with the ATLAS detector*, arXiv:1408.7084 [hep-ph].

[122] The ATLAS collaboration, *Measurements of the properties of the Higgs-like boson in the four lepton decay channel with the ATLAS detector using 25fb^{-1} of proton-proton collision data*, ATLAS-CONF-2013-013 (2013).

[123] W. Verkerke, D. Kirkby, *The RooFit toolkit for data modelling*, arXiv:0306116 [hep-ph].

[124] S. Alioli, P. Nason, C. Oleari, and E. Re, *A general framework for implementing NLO calculations in shower Monte Carlo programs: the POWHEG BOX*, arXiv:1002.2581 [hep-ph].

[125] S. Frixione, P. Nason, and C. Oleari, *Matching NLO QCD computations with Parton Shower simulations: the POWHEG method*, arXiv:0709.2092 [hep-ph].

[126] ATLAS Collaboration, *Summary of ATLAS Pythia 8 tunes*, ATL-PHYS-PUB-2012-003, CERN, Geneva, Aug, 2012.

[127] J. Allison, K. Amako, J. Apostolakis, H. Araujo, P.A. Dubois et al., *GEANT4 developments and applications*, IEEE Trans. Nucl. Sci. **53** (2006) 270.

[128] GEANT4 Collaboration, S. Agostinelli et al., *GEANT4: A Simulation toolkit*, Nucl. Instrum. Meth. **A506** (2003).

[129] The ATLAS collaboration, *Reconstruction of collinear final-state-radiation photons in Z decays to muons in $\sqrt{s}$=7 TeV of proton-proton collisions*, ATLAS-CONF-2012-143 (2012).

[130] J. Alwall, M. Herquet, F. Maltoni, O. Mattelaer and T. Stelzer, *MadGraph 5: Going beyond*, arXiv:1106.0522 [hep-ph].

[131] G. Cowan, K. Cranmer, E. Gross and O. Vitells, *Asymptotic formulae for likelihood-based tests of new physics*, arXiv:1007.1727 [hep-ph].

[132] The ATLAS collaboration, *Measurements of the Higgs boson production and couplings in the four lepton decay channel with the ATLAS detector using 25 fb^{-1} of proton-proton collision data*, arXiv:1408.5191 [hep-ph].

[133] G. Cowan, *Statistical Data Analysis*. Oxford University Press, 1998.

[134] K.S. Cramer, *Kernel Estimation in High Energy Physics*, arXiv:0011057 [hep-ph].

[135] L.A. Piegl and W.Tiller, *The NURBS book: Monographs in visual communication,*.

[136] N. Kauer, G. Passarino, *Inadequacy of zero-width approximation for a light Higgs boson signal*, arXiv:1206.4803 [hep-ph].

[137] F. Caola, K. Melnikov, *Constraining the Higgs boson width with ZZ production at the LHC*, arXiv:1307.4935 [hep-ph].

[138] J.M. Campbell, R.K. Ellis, C. Williams, *Bounding the Higgs width at the LHC using full analytic result for $gg \to 2e2\mu$*, arXiv:1311.3589 [hep-ph].

[139] The CMS Collaboration, *Constraints on the Higgs boson width from off-shell production and decay to Z-boson pairs*, arXiv:1405.3455 [hep-ph].

[140] The ATLAS collaboration, *Determination of the off-shell Higgs boson signal strength in the high-mass ZZ final state with the ATLAS detector*, ATLAS-CONF-2014-042 (2014).

[141] The ATLAS collaboration, *Determination of the off-shell Higgs boson signal strength in the high-mass ZZ and WW final state with the ATLAS detector*, arXiv:1503.01060 [hep-ph].

[142] G. Cacciapaglia, A. Deandrea, G.D. La Rochelle and J.-B. Flament, *Higgs couplings: disentangling New Physics with off-shell measurements*, arXiv:1406.1757 [hep-ph].

[143] C. Englert and M. Spannowsky, *Limitations and Opportunities of Off-shell Coupling Measurements*, arXiv:1405.0285 [hep-ph].

[144] F. Krauss, *Introduction to Event Generators*, Academic lectures on phenomenology at collider experiments, Monte Carlo event generatons: Series of four lectures, at the MCnet School (2009).

[145] F. Krauss, *QCD and Monte Carlo tools*, Academic lectures on phenomenology at collider experiments, Monte Carlo event generatons: Series of lectures, at the Fermilab-CERN Hadron Collider school (2007).

[146] gg2VV Monte Carlo generator (http://gg2VV.hepforge.org/).

[147] J. Campbell, K. Ellis, C. Williams, *MCFM - Monte Carlo for FeMtobarn processes*, http://mcfm.fnal.gov/.

[148] G. P. Lepage, *VEGAS: An Adaptie Multi-dimensional Integration Program*, Cornell preprint CLNS 80-447 (1980).

[149] J. Alwall et al., *A standard format for Les Houches Event Files*, arXiv:0609017 [hep-ph].

[150] M. Guzzi, P. Nadolsky, E. Berger, H.L. Lai, F. Olness et al., *CT10 parton distributions and other developments in the global QCD analysis*, arXiv:1101.0561 [hep-ph].

[151] G. Passarino, *Higgs CAT*, arXiv:1312.2397 [hep-ph].

[152] M. Bonvini, F. Caola, S. Forte, K. Melnikov and G. Ridolfi, *Signal-background interference effects for $gg \to H \to WW$ beyond leading order*, arXiv:1304.3053 [hep-ph].

[153] S. Hoeche, F. Krauss, N. Lavesson, L. Lonblad, M. Mangano, A. Schalicke, S. Schumann, *Matching parton showers and matrix element*, 0602031 [hep-ph].

[154] G. Corcella et al., *HERWIG : An event generator for hadron emission reactions with interfering gluons (including supersymmetric processes)*, arXiv:0011363 [hep-ph].

[155] The ATLAS collaboration, *First tuning of HERWIG/JIMMY to ATLAS data*, ATL-PHYS-PUB-2010-014 (2010).

[156] F. Cascioli, S. Hoeche, F. Krauss, P. Maierhoefer, S. Pozzorini, et al., *Precise Higgs-background predictions: merging NLO QCD and squared quark-loop corrections to four-lepton + 0,1 jet production*, arXiv:1309.0500 [hep-ph].

[157] A. Ballestrero, A. Belhouari, G. Bevilacqua, V. Kashkan, E. Maina, *PHANTOM: a Monte Carlo event generator for six parton final state at high energy colliders*, arXiv:0801.3359 [hep-ph].

[158] F. Cascioli, T. Gehrmann, M. Grazzini, S. Kallweit, P. Maierhfer et al., *ZZ production at hadron colliders in NNLO QCD*, arXiv:1405.2219 [hep-ph].

[159] A. Bierweiler, T. Kasprzik and J.H. Kuhn, *Vector-boson pair production at the LHC to $\mathcal{O}(\alpha^3)$ accuracy*, arXiv:1305.5402 [hep-ph].

[160] J. Baglio, L.D. Ninh and M.M. Weber, *Massive gauge boson pair production at the LHC: a next-to-leading order story*, arXiv:1307.4331 [hep-ph].

[161] S. Gieseke, T. Kasprzik and J.H. Kuhn, *Vector-boson pair production and electroweak corrections in HERWIG++*, arXiv:1401.3964 [hep-ph].

[162] Kolmogorov-Smirnov Test (http://www.physics.csbsju.edu/stats/KS-test.html).

[163] The Atlas collaboration, *Fiducial and differential cross section of Higgs boson production measured in the four-lepton decay channel in pp collisions at $\sqrt{s}$=8 TeV with the ATLAS detector*, arXiv:1408.3226 [hep-ph].

[164] T. Gleisberg, S. Hoeche, F. Krauss, M. Schonherr, S. Schumann, et al., *Event generation with SHERPA 1.1*, arXiv:0811.4622 [hep-ph].

[165] K. Cranmer, G. Lewis, L. Moneta, A. Shibata, W. Verkerke, *HistFactory: A tool for creating statistical model for use with RooFit and RooStats*, CERN-OPEN-2012-016 (2012).

[166] A. L. Read, *Presentation of search resuts: The CLs technique*, J. Phys. G28 (2002) 2693 (2002).

[167] The ATLAS collaboration, *Search for Invisible Decays of a Higgs Boson Produced in Association with a Z Boson in ATLAS*, arXiv:1402.3244 [hep-ph].

[168] The ATLAS collaboration, *Performance assumptions for an upgraded ATLAS detector at High-Luminosity LHC*, ATLAS-PHYS-PUB-2013-004 (2013).

[169] G. Mandl, F. Shaw, *Quantum Field Theory.* John Wiley and Sons, 1984.

[170] J. Sakurai, *Advanced Quantum Mechanics.* Zanichelli, 1967.

[171] H.D. Politzer, *Asymptotic Freedom - An approach to strong interactions*, Physics Report 14 (1974).

[172] S. Actis, G. Passarino, C. Sturm, S. Uccirati, *NLO Electroweak Corrections to Higgs Boson Production at Hadron Colliders*, arXiv:0809.1301 [hep-ph].

[173] W. Lampl, S. Laplace, D. Lelas, P. Loch, H. Ma, S. Menke, S. Rajagopalan, D. Rousseau, S. Snyder, and G. Unal, *Calorimeter Clustering Algorithms: Description and Performance*, ATL-LARG-PUB-2008-002. ATL-COM-LARG-2008-003, CERN, Geneva, Apr, 2008.

[174] ATLAS Collaboration, *Expected photon performance in the ATLAS experiment*, ATL-PHYS-PUB-2011-007, CERN, Geneva, Apr, 2011.

[175] G. Bozzi, S. Catani, D. de Florian, M. Grazzini, *The p_T spectrum of the Higgs boson at the LHC in QCD perturbation theory*, arXiv:0302104 [hep-ph].

[176] G. Bozzi, S. Catani, D. de Florian, M. Grazzini, *Transverse-momentum resummation and the spectrum of the Higgs boson at the LHC*, arXiv:0508068 [hep-ph].

[177] D. de Florian, G. Ferrera, M. Grazzini and D. Tommasini, *Transverse-momentum resummation: Higgs boson production at the Tevatron and the LHC*, arXiv:1109.2109 [hep-ph].

[178] F. Krauss, S. Schumann, *A parton shower algorithm based on Catani-Seymour dipole factorization*, 0709.1027 [hep-ph].

[179] S. Hoeche, F. Krauss, M. Schonherr, F. Siegert, *Automating the POWHEG method in Sherpa*, 1005.5399 [hep-ph].

[180] The ATLAS collaboration, *ATLAS Forward Detectors for Measurement of Elastic Scattering and Luminosity*, CERN-LHCC-2008-004 (2008).

[181] The ATLAS collaboration, *Performance of the ATLAS Trigger System in 2010*, arXiv:1110.1530 [hep-ph].

[182] The ATLAS collaboration, *ATLAS Muon Spectrometer - Technical Design Report*, CERN-LHCC-97-22 (1997).

[183] C. Anastasiou, S. Buehler, F. Herzog and A. Lazapoulos, *Inclusive Higgs boson cross-section for the LHC at 8 TeV*, arXiv:1202.3638 [hep-ph].

Acknowledgements

The completion of a doctoral thesis is by no means a singular effort: there is an infinite amount of people to whom I am grateful for their invaluable help.

First and foremost, I am deeply indebted to Bruno Mansoulié, my thesis director and mentor, for having offered me such an interesting analysis topic, for his scrupulous supervision and for the attention dedicated to my formation and growth as a physicist. Above all, being part of the off-shell determination effort has really been an incredible experience for which I am truly thankful for and it was by far the most exciting time all along my Ph.D period. Thanks for the fruitful and enriching discussions, for your precious suggestions, for supporting my ideas and for all the revision work of my thesis. I am grateful and glad for having grasped a bit of your huge knowledge of particle physics and your rigorous approach to physics analyses.

I would also like to thank my thesis referees, Chiara Mariotti and Yves Sirois, who read and thoroughly examined my manuscript as well as Anne-Isabelle Etienvre, Frank Krauss, Achille Stocchi, Christos Anastopoulos for accepting to be part of my jury. A special thanks goes to Christos for his numberless comments and inspiring discussions (sometimes on the tram 18 on our way back to Servette from CERN in the evening!) on the implementation of the E-p combination for electrons.

I thank Anne-Isabelle Etienvre and Claude Guyot as directors of SPP and ATLAS team leader of the Saclay group for having welcomed me in the lab and my fellow students at CEA-Saclay, Remie Hanna, Sofia Protopapadaki, Camilla Maiani, Fabrice Balli, Joao Firmino da Costa. Thanks to Maria Hoffmann with whom we shared Monte Carlo productions and nice chats on physics, life and future at CERN always from a "nordic" perspective.

As for the analysis in the EGamma working group, I thank Maarten Boonekamp for his invaluable suggestions on the possible advancements of the E-p combination algorithm during his convenership of the EGamma Calibration group. That was really educational for me! I acknowledge Paolo Mastrandrea with whom I worked in close contact for the J/Ψ validation and David Divalentino who I collaborated with for the track-cluster combination software.

Thank you to Stefano Rosati, Christos Anastopoulos and Fabien Tarrade who led the HSG2 group and always supported my presentations and welcomed my idea proposed to the group. Thanks equally to Rosy Nikolaidou, Roberto Di Nardo, Robert Harrington who took over as conveners of the working group. Specifically, I am thankful to Rosy Nikolaidou whose support was fundamental in the course of these years.

Regarding the 4 lepton analysis, my participation to the *task-force* for the off-shell measurement was unquestionably enriching. In this regard, I would like to acknowledge Michael Duehrssen and Yanyan Gao who effectively led the effort towards the analysis publication for the ICHEP confer-

ence in Valencia in July 2014 and beyond. They taught me how to perform a physics analysis from the beginning to the very last plots performed the night before the Higgs approval. In addition, I would also want to acknowledge Jochen Meyer whose inestimable cooperation allowed me to join the Monte Carlo simulation effort: thanks for your clear explanations and the quick answers to all my questions and doubts!

A number of people deserve special mention due to their direct contribution to the off-shell determination and for my close work with them. My collaboration with Fabio Cerutti, Monica Verducci, Roberto Di Nardo, Stefano Rosati was particularly fulfilling for me: we worked on the development of the BDT-based algorithm, on its validation, on the computation of the systematic uncertainties and so forth. Thanks Monica for the huge amount of time spent trying to build and debug workspaces. Thank you all for the essential discussions on the preparation of the analysis, on the physics results as well as on the possible improvements. Thanks Fabio, Roberto for the numerous and useful inputs and ideas developed for the off-shell measurement at High-Luminosity LHC and for your familiarity and expertise in all the statistics-related issues of particle physics.

This time would not have been nearly as enjoyable if it were not for friends around. Thanks to all my friends, old and new alike, in Rome, in Geneva, in Gaeta and the other ones scattered throughout Europe for being part of my life all along. Thank you to my "Italian-French" part of family in Paris, Siuan and Laurine.

Thank you to my flatmates in Geneva and in Paris, Mehdi, Xiaoyi, Hideyuki, Arabella, Jui-Fa, Bastien (Rue Hoffmann), to Corrado (Avenue Philippe Auguste), to Khoi (Rue de Lausanne) and to Terhi (Rue Saint-Jean) for sharing days, dinners, anecdotes, different existence experiences and geographical flavours with me. Thanks to StefanoZ, Alessio, and our amazing coast to coast trip in US in 2013, Matteo, Marco, Thanu, StefanoC, Alberto for daily lunches, dinners, and for having made living in Geneva agreeable and amusing.

Thanks to my high-school fellows, Ludovico, MarcoS, MarcoDL, Sissi, Francesca, Daniel, Alberto, Flaminia, and university friends, Ferdinando, Alessandro, Riccardo, Corrado, Elena, Edoardo, Gabriele who have always been there.

To my family, to my father and my mother, to their stubborn support in my grumpiest moments.

To Terhi, who is the sun in my life.